GDAŃSK UNIVERSITY OF TECHNOLOGY

The author of the doctoral dissertation: Marta Kowalkińska
Scientific discipline: Chemical Sciences

DOCTORAL DISSERTATION

Title of doctoral dissertation: Photocatalysts based on titanium(IV) oxide and scheelite-type compounds for the degradation of contaminants of emerging concern

Title of doctoral dissertation (in Polish): Fotokatalizatory na bazie tlenku tytanu(IV) i związków o strukturze szelitu do degradacji mikrozanieczyszczeń

Supervisor *signature*
prof. dr hab. Inż. Anna Zielińska-Jurek

Gdańsk, year 2025

GDAŃSK UNIVERSITY OF TECHNOLOGY

STATEMENT

The author of the doctoral dissertation: Marta Kowalkińska

I, the undersigned, declare that I am aware that in accordance with the provisions of Art. 27 (1) and (2) of the Act of 4th February 1994 on Copyright and Related Rights (Journal of Laws of 2021, item 1062), the university may use my doctoral dissertation entitled:
Photocatalysts based on titanium(IV) oxide and scheelite-type compounds for the degradation of contaminants of emerging concern
for scientific or didactic purposes.[1]

Gdańsk,..... .....
signature of the PhD student

Aware of criminal liability for violations of the Act of 4th February 1994 on Copyright and Related Rights and disciplinary actions set out in the Law on Higher Education and Science(Journal of Laws 2021, item 478), as well as civil liability, I declare, that the submitted doctoral dissertation is my own work.

I declare, that the submitted doctoral dissertation is my own work performed under and in cooperation with the supervision of prof. dr hab. inż. Anna Zielińska-Jurek.

This submitted doctoral dissertation has never before been the basis of an official procedure associated with the awarding of a PhD degree.

All the information contained in the above thesis which is derived from written and electronic sources is documented in a list of relevant literature in accordance with Art. 34 of the Copyright and Related Rights Act.

I confirm that this doctoral dissertation is identical to the attached electronic version.

Gdańsk,..... .....
signature of the PhD student

I, the undersigned, agree to include an electronic version of the above doctoral dissertation in the open, institutional, digital repository of Gdańsk University of Technology.

Gdańsk,..... .....
signature of the PhD student

[1] Art 27. 1. Educational institutions and entities referred to in art. 7 sec. 1 points 1, 2 and 4–8 of the Act of 20 July 2018 – Law on Higher Education and Science, may use the disseminated works in the original and in translation for the purposes of illustrating the content provided for didactic purposes or in order to conduct research activities, and to reproduce for this purpose disseminated minor works or fragments of larger works.

2. If the works are made available to the public in such a way that everyone can have access to them at the place and time selected by them, as referred to in para. 1, is allowed only for a limited group of people learning, teaching or conducting research, identified by the entities listed in paragraph 1.

GDAŃSK UNIVERSITY OF TECHNOLOGY

DESCRIPTION OF DOCTORAL DISSERTATION

The Author of the doctoral dissertation: Marta Kowalkińska

Title of doctoral dissertation: Photocatalysts based on titanium(IV) oxide and scheelite-type compounds for the degradation of contaminants of emerging concern

Title of doctoral dissertation in Polish: Fotokatalizatory na bazie tlenku tytanu(IV) i związków o strukturze szelitu do degradacji mikrozanieczyszczeń

Language of doctoral dissertation: English

Supervisor: prof. dr hab. inż. Anna Zielińska-Jurek

Date of doctoral defense:

Keywords of doctoral dissertation in Polish: fotokataliza heterogeniczna, oczyszczanie wody, nadtlenomonosiarczan, mikrozanieczyszczenia

Keywords of doctoral dissertation in English: heterogeneous photocatalysis, water treatment, peroxymonosulfate, contaminants of emerging concern

Summary of doctoral dissertation in Polish:

Poprawa jakości wody pitnej to jedno z kluczowych wyzwań współczesnego świata. Woda jest zanieczyszczana m.in. farmaceutykami, pestycydami i związkami fenolowymi, które są trudno usuwalne przez konwencjonalne metody oczyszczania. Celem niniejszej rozprawy doktorskiej było zastosowanie zaawansowanych technik utleniania, fotokatalizy heterogenicznej oraz fotokatalizy wspomaganej solami nadtlenomonosiarczanowymi (PMS), do eliminacji tych mikrozanieczyszczeń. Zakres prac badawczych obejmował syntezę fotokatalizatorów, charakterystykę ich struktury i właściwości fizykochemicznych oraz ocenę ich aktywności fotokatalitycznej. W rozprawie doktorskiej opisano następujące fotokatalizatory: wolframiany i molibdeniany metali ziem alkalicznych (ABO_4, gdzie *A* = Ca, Sr, Ba i *B* = W, Mo), fluorowany tlenek tytanu(IV) (F-TiO_2) oraz ortowanadan bizmutu ($BiVO_4$). Zbadano wpływ morfologii wspomnianych materiałów, a także wskazano rolę ekspozycji płaszczyzn krystalicznych. Przedstawiono również dwa zastosowania tlenofluorku tytanu ($TiOF_2$) - jako prekursor w syntezie F-TiO_2 oraz komponent w kompozycie {0 0 1} TiO_2/$TiOF_2$. W ramach modyfikacji warunków syntezy i zwiększenia aktywności fotokatalitycznej, zaproponowano nowe syntezy $TiOF_2$ i metawanadanu amonu (NH_4VO_3) o zróżnicowanej morfologii. Finalnie, zbadano wpływ modyfikacji powierzchniowej sub-nanoklastrami miedzi CuO_x na efektywność reakcji fotokatalitycznej i aktywację PMS.

Summary of doctoral dissertation in English:

Enhancing the quality of drinking water is one of the key challenges of the modern world. Contaminants of emerging concern (CECs), such as pharmaceuticals, pesticides, and phenolic compounds, are frequently detected in aquatic ecosystems and are often persistent in conventional wastewater treatment processes. In this regard, this doctoral dissertation aimed to investigate the application of advanced oxidation processes (AOPs), specifically heterogeneous photocatalysis and peroxymonosulfate (PMS)-assisted photocatalysis, for the effective CECs degradation. The scope of described research studies includes the synthesis of the photocatalysts, their structural characterization, determination of physicochemical properties, and evaluation of the photocatalytic activity. Alkaline-earth metal tungstates and molybdates (ABO_4, in which *A* = Ca, Sr, Ba and *B* = W, Mo), fluorinated titanium(IV) oxide (F-TiO_2), and bismuth orthovanadate ($BiVO_4$) were selected for investigation. The role of morphology and crystal facets exposition were examined for selected photocatalysts. Moreover, dual application of titanium oxyfluoride ($TiOF_2$) was indicated – as a precursor in F-TiO_2 preparation and a component in binary photocatalyst {0 0 1} TiO_2/$TiOF_2$. Novel methods

of precursor fabrication, $TiOF_2$ and ammonium metavanadate (NH_4VO_3), were also proposed. Finally, the effect of copper CuO_x sub-nanoclusters deposition on photocatalytic activity and PMS activation was investigated.

The research presented in the PhD dissertation was part of the projects:

Design, synthesis, and physicochemical characterization of 2D nanosheet-based hybrid photocatalysts for degradation of pharmaceuticals, Polish National Science Centre, UMO-2018/30/E/ST5/00845,

Development of multifunctional materials for thermo-photocatalytic reduction of carbon dioxide and photodegradation of persistent organic pollutants, Polish National Science Centre, UMO-2021/43/B/ST5/02983.

The main motivation for undertaking the research presented in the PhD dissertation was to take action within the framework of The United Nations Sustainable Development Goals, specifically Goal 6: *Clean Water and Sanitation*.

ACKNOWLEDGEMENT

"My soul is painted like the wings of butterflies.
Fairytales of yesterday will grow but never die.
I can fly my friends!"

~ Queen "The show must go on"

During the PhD journey, I had an opportunity to meet a lot of beautiful people. Without their assistance and encouragement, the completion of doctoral thesis would not have been possible. I would like to express my sincere gratitude to them.

First and foremost, I extend my heartfelt appreciation to my Supervisor, **Professor Anna Zielińska-Jurek**, for giving me the opportunity to pursue my PhD, for her trust in my abilities, and for her invaluable scientific guidance throughout this process.

My dearest husband **Szymon**, who has been my constant source of strength, never letting me down and always lifting me up when the challenges felt overwhelming.

I would like to sincerely thank the **members of The Department of Process Engineering and Chemical Technology**, especially *basement children*: Jakub Smoliński, Agnieszka Fiszka Borzyszowska, Izabela Frąckiewicz, Elvana Çako, Dahar Janwari, Samuel Latebo Majamo.

I am deeply grateful to **my parents, my grandparents, my family-in-law** and closest friends for their unwavering support and for always being there when I needed them most. Their belief in me, even in moments of doubt, have meant more than I can express.

I would like to extend my heartfelt thanks to: **Dr. Nicolas Keller** (University of Strasbourg/CNRS, France), **Dr. Eng. Adam Ostrowski** (Institute of Molecular Physics Polish Academy of Sciences), and **Dr. Eng. Aleksandra Szkudlarek** (AGH University of Krakow), for their time and expertise generously shared with me, which significantly enhanced my research and deepened my understanding of the subject.

Lastly, my purrrrfect white beast Iki, who has spent countless hours sitting on my knees (or on the keyboard) purring as I have been working at home. Thanks, meow.

I would like to dedicate this doctoral dissertation to my Grandfather, who always supported my education from buying the first computer and learning Moon phases to trying to understand what I am doing during PhD studies. I miss you, Dziadzia

TABLE OF CONTENTS

SUMMARY OF SCIENTIFIC ACHIEVEMENTS

List of publications and book chapters included in the PhD dissertation

[P1] M. Kowalkińska*, P. Głuchowski, T. Swebocki, T. Ossowski, A. Ostrowski, W. Bednarski, J. Karczewski, A. Zielińska-Jurek*, *Scheelite-Type Wide-Bandgap ABO_4 Compounds (A = Ca, Sr, and Ba; B = Mo and W) as Potential Photocatalysts for Water Treatment,* The Journal of Physical Chemistry C, 125(46), 2021, 25497-25513.
Impact Factor = 4.126, **Q2** quartile, **MNISW** = 140

[P2] S. Dudziak, M. Kowalkińska, A. Zielińska-Jurek*, book Chapter 3: Crystal Facet Engineering of TiO_2 from Theory to Application*, *From the book 'Updates on Titanium Dioxide'*, 2023, publisher: IntechOpen.
MNISW = 20

[P3] M. Kowalkińska*, K. Sikora, M. Łapiński, J. Karczewski, A. Zielińska-Jurek*, *Non-toxic fluorine-doped TiO_2 nanocrystals from $TiOF_2$ for facet-dependent naproxen degradation*, Catalysis Today, 413, 2023, 113959.
Impact Factor = 5.3, **Q1** quartile, **MNISW** = 140

[P4] M. Kowalkińska*, J. Karczewski, A. Zielińska-Jurek*, *The Effect of Titanium Oxyfluoride Morphology on Photocatalytic Activity of Fluorine-Doped Titanium(IV) Oxide*, Crystals, 13(2), 2023, 356.
Impact Factor = 2.7, **Q2** quartile, **MNISW** = 70

[P5] M. Kowalkińska*, N. Keller, F. Fresno, C. Colbeau-Justin, A. Zielińska-Jurek*, *Insight into charge carrier dynamics and interface design of {0 0 1} TiO_2 coupled with $TiOF_2$ for photocatalytic degradation of contaminants of emerging concern*, Applied Surface Science, 695, 2025, 162893.
Impact Factor = 6.3, **Q1** quartile, **MNISW** = 140

[P6] M. Kowalkińska*, A. Maximenko, A. Szkudlarek, K. Sikora, A. Zielińska-Jurek*, *Addressing challenges of $BiVO_4$ light-harvesting ability through vanadium precursor engineering and sub-nanoclusters deposition for peroxymonosulfate-assisted photocatalytic pharmaceuticals removal*, Separation and Purification Technology, 351, 2024, 127643.
Impact Factor = 8.6, **Q1** quartile, **MNISW** = 140

***** corresponding author

Total IF for publications: 27.026
Total number of Ministry points: 650

List of other publications

1. M. Kowalkińska, *Probing the surface of photoactive semiconductors using X-ray photoelectron spectroscopy*, Nature Reviews Clean Technology (Tools of the Trade; published 19th August 2025)
   Invited by The Editor Dr Rita Leones; MNISW = 5
2. S. Dudziak, M. Kowalkińska, J. Karczewski, M. Pisarek, J. D. Gouveia, J. R. B. Gomes, A. Zielińska-Jurek, *Surface and Trapping Energies as Predictors for the Photocatalytic Degradation of Aromatic Organic Pollutants*, The Journal of Physical Chemistry C, 126(35), 2022, 14859-14877.
   Impact Factor = 4.177, **Q2** quartile, **MNISW** = 140
3. M. Kowalkińska, A. Fiszka Borzyszkowska, A. Grzegórska, J. Karczewski, P. Głuchowski, M. Łapiński, M. Sawczak, A. Zielińska-Jurek, *Pilot-Scale Studies of WO_3/S-Doped g-C_3N_4 Heterojunction toward Photocatalytic NO_x Removal*, Materials, 15, 2022, 15, 633.
   Impact Factor = 3.748, **Q2** quartile, **MNISW** = 140
4. S. Dudziak, M. Kowalkińska, J. Karczewski, M. Pisarek, K. Siuzdak, A. Kubiak, K. Siwińska-Ciesielczyk, A. Zielińska-Jurek, *Solvothermal growth of {0 0 1} exposed anatase nanosheets and their ability to mineralize organic pollutants. The effect of alcohol type and content on the nucleation and growth of TiO_2 nanostructures*, Applied Surface Science, 563, 2021, 150360.
   Impact Factor = 6.707, **Q1** quartile, **MNISW** = 140
5. M. Kowalkińska, S. Dudziak, J. Karczewski, J. Ryl, G. Trykowski, A. Zielińska-Jurek, *Facet effect of TiO_2 nanostructures from $TiOF_2$ and their photocatalytic activity*, Chemical Engineering Journal, 404, 2021, 126493.
   Impact Factor = 10.652, **Q1** quartile, **MNISW** = 200
6. M. Kowalkińska, A. Zielińska-Jurek, *Różne oblicza nanostruktur tlenku tytanu(IV)*, Laborant 14/2020, 1-14.
   MNISW = 5

The provided journal metrics (Impact Factor, quartile, Ministerial points) were valid at the time of publication.

Total IF: 52.31
Total number of Ministry points: 1280
***h*-index:** 6

Involvement in projects

04.2025 – present Ministry of Science and Higher Education
Łatfizna. Łatwa nauka fizyki (English: Easy learn physics)
POWR.03.04.00-00-P023/21

09-2022 – 08.2025 Polish National Science Centre, OPUS 22
Development of multifunctional materials for thermo-photocatalytic reduction of carbon dioxide and photodegradation of persistent organic pollutants
Contract No. UMO-2021/43/B/ST5/02983

03-2024 – 09.2024 European Regional Development, Interreg Baltic Sea Region Programme
AdvIQwater - Improving quality of BSR waters by advanced treatment processes

03-2021 – 05.2022 The National Centre for Research and Development, European Regional Development Fund
Ecobituminen
Contract No. POIR. 01. 01. 01-00-0071/20-00

09-2019 – 06.2022 Polish National Science Centre, Sonata-Bis 8
Designing, synthesis and characterization of 2D hybrid photocatalyst for degradation of pharmaceuticals in aqueous phase
Contract No. UMO-2018/30/E/ST5/00845

Internships during PhD studies

1. 15th September – 14th December 2024

   Internship at R&D Photoactivated Processes Unit, IMDEA Energy Institute, Madrid, Spain

   Mentors: Dr Marta Liras, Dr Freddy E. Oropeza

   This internship was financed by the Polish National Agency for Academic Exchange (NAWA), under the Programme *"STER - Internationalisation of Doctoral Schools"* (BPI/STE/2023/1/00018/DEC/01).

2. 14th March – 13th May 2022

   Internship at The Institute of Chemistry and Processes for Energy, Environment and Health (ICPEES), University of Strasbourg, Strasbourg, France

   Mentor: Professor Nicolas Keller

   This internship was financed by the Erasmus+ programme.

Active participation in conferences as a presenting author

1. Poster presentation and flash talk during 12th European Conference on Solar Chemistry and Photocatalysis: Energy and Environmental Applications (SPEA12), 17-21.06.2024, Belfast, United Kingdom
   M. Kowalkińska, A. Maximenko, A. Szkudlarek, A. Zielińska-Jurek, *New strategies of $BiVO_4$ synthesis and modification for PMS-assisted photocatalytic degradation of pharmaceuticals*
   This poster received Best Poster Award from Royal Society of Chemistry.
2. Poster presentation during 12th European Conference on Solar Chemistry and Photocatalysis: Energy and Environmental Applications (SPEA12), 17-21.06.2024, Belfast, United Kingdom
   A. Zasada, M. Kowalkińska, A. Zielińska-Jurek, *Silver, copper and ruthenium surface modification of octahedral $BiVO_4$ with exposed {1 2 0} and {0 2 1} facets for peroxydisulfate activation and efficient photodegradation of naproxen*
3. Poster presentation and flash talk during 8th International Conference on Semiconductor Photochemistry (SP8), 11-15.09.2023, Strasbourg, France
   M. Kowalkińska, A. Zielińska-Jurek, *Visible Light-Driven Peroxymonosulfate-Assisted Degradation of Pharmaceuticals using Facet-Engineered $BiVO_4$-based Photocatalysts*
4. Poster presentation during SYLINDA International Symposium, 7-8.03.2024, Cracow, Poland
   M. Kowalkińska, A. Maximenko, A. Szkudlarek, A. Zielińska-Jurek, *CuO_x clusters anchored on $BiVO_4$ for visible-light-induced degradation of pharmaceuticals*
5. Poster presentation during 7th Fluorine Days, 18-22.06.2023, Poznań, Poland
   M. Kowalkińska, K. Sikora, M. Łapiński, J. Karczewski, A. Zielińska-Jurek, *The Role of Exposed Crystal Facets in F-doped TiO_2 Photocatalysts Synthesized from $TiOF_2$ for Naproxen Removal and Toxicity Rate*
6. Poster presentation during 24th Polish Conference of Chemical and Process Engineering, 13-16.06.2023, Szczecin, Poland
   M. Kowalkińska, A. Zielińska-Jurek, *Enhanced photocatalytic naproxen degradation under visible light by Cu_2O anchored on multifaceted monoclinic $BiVO_4$ photocatalysts*
7. Poster presentation during Non-linear Phenomena in Electrochemistry and Photovoltaics Conference & Workshop, 16-18.11.2022, Cracow, Poland

M. Kowalkińska, S. Dudziak, A. Zielińska-Jurek, *Crystal facets engineering of semiconductors for photocatalytic water treatment*

8. Oral presentation during VII Interdisciplinary Academic Conference on Environmental Protection (IAKOŚ), 21-23.09.2022, Gdańsk, Poland
   M. Kowalkińska, S. Dudziak, A. Zielińska-Jurek, *Tailoring photocatalytic water treatment using TiO_2 nanostructures with exposed {1 0 1}, {0 0 1} and {1 0 0}*
9. Poster presentation during 15th Pannonian International Symposium on Catalysis, 04-08.09.2022, Jastrzębia Góra, Poland
   M. Kowalkińska, S. Dudziak, A. Zielińska-Jurek, *Titanium oxyfluoride as a valuable precursor for the synthesis of anatase nanostructures with exposed crystal facets*
10. Poster presentation and flash talk during The 11th European Conference on Solar Chemistry and Photocatalysis: Environmental Applications (SPEA11), 6-10.06.2022. Turin, Italy
    M. Kowalkińska, A. Zielińska-Jurek, *Crystal Facets Engineering of F-Doped TiO_2 Prepared from $TiOF_2$ for Photocatalytic Degradation of Pharmaceuticals*
11. Oral presentation during The 6th International Conference on New Photocatalytic Materials for Environment, Energy and Sustainability (NPM-6) & The 7th International Conference on Photocatalytic and Advanced Oxidation Technologies for the Treatment of Water, Air, Soil and Surfaces (PAOT-7), 4-6.04.2022, Ljubljana, Slovenia
    M. Kowalkińska, P. Głuchowski, J. Karczewski, A. Zielińska-Jurek, *Insulators in photocatalysis: Investigation of alkaline-earth metal scheelite-type compounds as potential photocatalysts for solar-driven degradation of xenobiotics in the water system*
12. Conference paper during The 2nd International Electronic Conference on Catalysis Sciences – A Celebration of Catalysts 10th Anniversary, 15-30.10.2021, online
    M. Kowalkińska, S. Dudziak, J. Karczewski, A. Zielińska-Jurek, *Fluorine ions in photocatalysts' synthesis: an obstacle or an ally? The investigation of photocatalysts in Ti-O-F system*

Other conference activities

1. Invited lecture during The 27th International Conference on Semiconductor Photocatalysis and Solar Energy Conversion (SPASEC-27), 11-14.06.2024, Limassol, Cyprus
   A. Zielińska-Jurek (presenter), A. Grzegórska, M. Kowalkińska, A. Zasada, *The growing problem of water pollution with pharmaceuticals. Challenges, prospects and solutions*
2. Oral presentation during 5th International Conference on Applied Surface Science, 25-28.04.2022, Palma de Mallorca, Spain
   S. Dudziak, A. Grzegórska, M. Kowalkińska, A. Zielińska-Jurek (presenter), *Pharmaceuticals degradation over TiO_2-based photocatalyst exposed with different crystal facets*
3. Invited lecture during VI Forum EMR – PL, 19-22.09.2022, Szczecin, Poland
   A. Ostrowski (presenter), W. Bednarski, I. Malinowska, M. Kowalkińska, A. Zielińska-Jurek, *ESR photochemical measurements of new photocatalysts for water treatment by spin-trapping method*

Awards and scholarships

1. Distinction in the X edition of the Polish Academy of Sciences in Gdańsk Award for young scientists, for the publication **[P6]**
2. Outgoing mobility grant from the Polish National Agency for Academic Exchange (NAWA), STER programme
3. Best Poster Award during 12th European Conference on Solar Chemistry and Photocatalysis: Energy and Environmental Applications (SPEA12)
4. Distinction in national competition *ECOInnovators 2022* for scientific achievements, organized by the Institute of Sustainable Energy
5. Distinction in XX edition of Romuald Szczęsny Competition
6. Best Paper Award, during The 2nd International Electronic Conference on Catalysis Sciences – A Celebration of Catalysts 10th Anniversary, organized by MDPI publisher
7. Diploma of The Year 2020 for the best Master thesis, received from Faculty of Physics and Applied Mathematics, Gdańsk University of Technology
8. FRANCIUM scholarship for the best PhD students received in 2021/2022, 2022/2023 and 2023/2024, Gdańsk University of Technology

Didactic and organizational activities

1. Lecturer and organizer of laboratory classes during Summer School on Advanced Water Treatment Technologies within ENHANCE Alliance Programme, 24.06-11.07.2025, Gdańsk, Poland
2. Participation in Zero Waste Fashion Show, organized during 4th Fahrenheit Science Picnic, 24.05.2025, Gdańsk, Poland
3. Participation in national action #Odważnewnauce (EN: #Braveinscience) organized by Natalia Schmidt-Polończyk, PhD Eng., within International Day of Women and Girls in Science, 11.02.2025, Instagram
4. Organizing Committee Member of Thematic School for PhDs & Young Researchers, organized together with 8th International Conference on Semiconductor Photochemistry (SP8), 11–15.09.2023, Strasbourg, France
5. Co-organizer of laboratory workshops *Podróż do świata nanomateriałów* (EN: *A journey to the world of nanomaterials*) during Baltic Science Festival, 25-27.05.2023, Gdańsk, Poland
   These workshops received a distinction from The Association of Chemical Industry Engineers and Technicians (SITPChem)
6. Lecturer during Tri-City Scientific Café twice, Gdańsk, Poland

Other activities

1. Invited foreign lecturer at Handan University, China (01.11.2025–28.11.2025), within the Polish-Chinese Educational Development Foundation
2. Reviewer in journals from JCR list (total 40 performed reviews): Journal of Environmental Chemical Engineering (21), Chemical Engineering Journal (6), Separation and Purification Technology (5), Advanced Composites and Hybrid Materials (2), Catalysis Today (2), International Journal of Hydrogen Energy (2), Applied Surface Science (1), Materials Chemistry and Physics (1)

SYMBOLS AND ABBREVIATIONS

AOP	Advanced Oxidation Processes
BET	Brunauer, Emmet and Teller isotherm
CECs	Contaminants of Emerging Concern
COD	Crystallography Open Database
DFT	Density Functional Theory
DR	Diffuse Reflectance
e^-	Electron
ECOSAR	Ecological Structure Activity Relationship Class Program
EDX	Energy-Dispersive X-ray Spectroscopy
ESR	Electron Spin Resonance Spectroscopy
FTIR	Fourier Transform Infrared Spectroscopy
h^+	Hole
HPLC	High-Performance Liquid Chromatography
IC	Ion Chromatography
ICP-OES	Inductively Coupled Plasma Optical Emission Spectroscopy
IEP	Isoelectric Point
LC-MS	Liquid Chromatography–Mass Spectrometry
LIBs	Lithium-ion Batteries
LVRPA	Local Volume Rate of Photon Absorption
NSAIDs	Non-steroidal anti-inflammatory drugs
PBN	α-phenyl-N-tert-butylnitrone
PDS	Peroxydisulfate
PhACs	Pharmaceutically Active Compounds
PL	Photoluminescence
PMS	Peroxymonosulfate
ROS	Reactive Oxygen Species
SAED	Selected Area Electron Diffraction
SEM	Scanning Electron Microscopy
TEM	Transmission Electron Microscopy
TGA	Thermal Gravimetry Analyses
TL	Thermoluminescence
TOC	Total Organic Carbon
TRMC	Time-resolved Microwave Conductivity
TRPL	Time-resolved Photoluminescence Spectroscopy
UV	Ultraviolet light (around 100-400 nm according to IUPAC)

Vis	Visible light (around 400-760 nm according to IUPAC)
WWTP	Wastewater Treatment Plant
XANES	X-ray Absorption Near Edge Structure
XAS	X-ray Absorption Spectroscopy
XPS	X-ray Photoelectron Spectroscopy
XRD	X-ray Diffraction
7-OHC	7-hydroxycoumarin
Γ	Gamma value (arb. units)
Φ	Work function (eV)
λ	Wavelength (nm)
v	Frequency (Hz)
CB	Conduction band (eV)
E^0	Redox potential (mostly shown as V vs. NHE at pH = 7)
E_{ph}	Photon energy (eV)
E_g	Band gap energy (eV)
F_{KM}	Kubelka-Munk function (arb. units)
VB	Valence band (eV)
h	Planck constant ($6.626 \cdot 10^{-34}$ J · s)
k	Apparent kinetic rate constant (min^{-1})

1. INTRODUCTION

Access to safe drinking water is the most basic human need for health and well-being. According to the United Nations, the global urban population facing water scarcity will double from 930 million in 2016 to even 2.4 billion people in 2050 [1]. Rapid population growth continues to push water demand upward, while ongoing urbanization and industrialization are progressively reducing available water resources due to excessive emissions of harmful substances into water reservoirs. The main pollutants include dyes, heavy metal ions, surfactants, pesticides, pharmaceuticals, oils and microplastics. They pose significant risks to environmental health, aquatic ecosystems, and human well-being. Their persistence in the environment and potential to bioaccumulate make them a pressing issue. However, these contaminants, often introduced through industrial discharges, agricultural runoff, and domestic wastewater, might not be fully degraded in conventional wastewater treatment plants (WWTPs) [2]. Therefore, a proper management system for polluted water streams, as well as the development of effective, environmentally friendly and economically justified wastewater treatment processes, are a priority for sustainability and ecological preservation.

1.1. Contaminants of emerging concern (CECs)

Recently, there has been significant attention focused on a broad category of chemicals named as *contaminants of emerging concern* (CECs) or its synonym *emerging contaminants* (ECs). According to the U.S. Environmental Protection Agency (EPA), they can be defined as chemicals and other substances that have no regulatory standards, have been recently detected in natural water and potentially cause detrimental effects on aquatic life at environmentally relevant concentrations. These terms refer to pollutants that persist in the environment for a long time, although their presence and impact are only now being recognized and assessed [3].

There are several chemicals which can be classified as contaminants of emerging concern, including: polycyclic aromatic hydrocarbons, pesticides, pharmaceuticals and personal care products, phenolic compounds, UV filters, flame retardants, and microplastics [3,4]. However, the list of chemicals is continuously changing as new contaminants or effects are identified. Generally, the most dangerous effects of CECs' presence in the environment are:

- bioaccumulation – gradual accumulation of chemical compounds in the tissues of organisms over time,
- biomagnification – accumulation of chemical substances in successive links of the trophic chain,

- chronic toxicity – the effects of repeated or long-term exposure to a substance, which can often become visible after a long time period,
- carcinogenic and mutagenic properties.

In the PhD dissertation, three groups of contaminants were selected for investigation: phenolic compounds, pharmaceutically active compounds and pesticides. The reasons for their selection as well as their impact on the environment are presented below.

1.1.1. Pharmaceutically active compounds (PhACs)

Pharmaceutically active compounds (PhACs) became an important innovation in modern society, significantly improving public health, extending life expectancy, and enhancing the quality of life. PhACs have revolutionized the treatment and prevention of countless diseases, from infections and chronic conditions to mental health disorders and rare genetic illnesses. The COVID-19 pandemic highlighted how crucial the rapid development and widespread distribution of medications and vaccines are for protection the global health [5].

The pharmaceutical industry generates profits comparable to those of the arms industry. The global pharmaceutical market was valued at 1,205 billion USD in 2018, which is an increase of 208.8% compared to 2001. It is estimated that in 2025, this value would reach even 1,606 billion USD [6]. Moreover, the progress in medicine and pharmacy has contributed to the global increase in drug consumption and the introduction of new pharmaceutically active compounds to the market. For example, the European Patent Office received 7441 patent applications related to the pharmacy industry in 2018 [6].

The report about PhACs distribution in Poland revealed that the average Polish resident buys 34 packages of medicines within a year. These statistics created Poland as one of the leading countries in the world with high PhACs consumption [7]. The main reason for this state is the facile availability of PhACs, especially the over-the-counter medicines that can be purchased without a prescription. The overconsumption of PhACs, together with the production processes of the pharmaceutical industry, became the key reasons for their undesired occurrence in the natural environment. These compounds have been detected in a wide variety of environmental samples, including sewage, surface waters, groundwater, and potable water, at levels from a few parts per billion to parts per million [8]. Due to a detrimental effect on the environment, the EPA classified PhACs as contaminants of emerging concern [3]. Selected examples of the influence of PhACs on the flora and fauna are presented in Table 1.1.

Pharmaceutical and cosmetic residues are currently the primary sources of micropollutants found in urban wastewater, regardless of geography. In this regard, the revised Urban Wastewater Treatment Directive, which entered into force on 1st January 2025, addresses remaining pollution as new challenges in urban wastewater management. Although primary, secondary, and tertiary treatments can eliminate some micropollutants, an additional quaternary treatment stage is required to effectively remove the remaining micropollutants from urban wastewater [9].

Table 1.1. Examples of the impact of selected PhACs on non-target organisms.

Compound	Application	Its impact on non-target organisms	Ref.
Naproxen	NSAIDs	Naproxen induced lower heart rate and morphological abnormalities in zebrafish during embryonic development. Zebrafish larvae exhibited apparent histopathological liver damage.	[10,11]
Carbamazepine	Antiepileptic drug	Carbamazepine induced a decline in *Daphnia pulex* population, inhibiting the decomposition of organic matter.	[12]
Ofloxacin	Antibiotic	Bioaccumulation was noticed in *Bellamya aeruginosa* snail tissues when they were exposed to water contaminated with ofloxacin.	[13]
Sulfamethoxazole	Antibiotic	Toxic effect on green microalga, *Scenedesmus obliquus*, when sulfamethoxazole exists with different popular antibiotic sulfamethazine.	[14]

1.1.2. Pesticides

The significant increase in the global human population has resulted in higher demand for food crops and a corresponding expansion of agricultural activities. However, crops are attacked by various harmful organisms, such as insects, fungi, bacteria, weeds, and some animals. These pests can cause significant economic loss for the agronomist. To avoid crops damage, pesticides have come to aid in the agricultural practices to prevent, control and protect plants or plant products against pests. Pesticides include a broad range of substances, both synthetic and naturally occurring, and they can be categorized as insecticides, herbicides, bactericides, fungicides, termiticides, insecticides, and rodenticides, based on the target organisms they are intended to remove [15,16]. Due to their efficiency against a wide variety of harmful organisms, pesticides offer several advantages, particularly in agriculture and public health. They increase agricultural productivity by controlling pests, weeds, and diseases that would otherwise reduce crop yields, allowing farmers to produce better-quality food on the same land. Moreover, they can prevent the spread of some diseases, e.g. Lyme

disease, malaria, dengue, by controlling the population of vectors like mosquitoes, ticks, rodents [17].

Pesticides can be composed of organochlorines, organophosphorus, phenoxy derivatives, pyrethrins and pyrethroids, triazines, carbamates, dipyridyl derivatives, glycine derivatives, and benzimidazoles. These substances can infiltrate groundwater and be transported into rivers, lakes, or ponds, volatilize into the atmosphere, or sorb to soil constituents, ultimately affecting non-target organisms. Therefore, pesticides are also classified as contaminants of emerging concern as their uncontrolled release into the environment, even at trace amounts, may contribute to their accumulation in tissues of organisms, with potentially adverse effects to both aquatic ecosystems and human health, especially when the water is used for drinking or food production. They are of growing concern due to their unknown long-term effects and persistence to conventional treatment processes [18,19]. The potential impact of selected compounds used as pesticides on non-target organisms is presented in Table 1.2.

The detrimental effect of pesticides on aquatic life caused that their approval on the market in the European Union is governed by Regulation 1107/2009, considered as one of the strictest pesticide laws worldwide [20]. Moreover, numerous pesticides are included in the Watch List under the Water Framework Directive [21].

Table 1.2. Examples of the impact of selected pesticides on non-target organisms.

Compound	Chemical composition	Application	Its impact on non-target organisms	Ref.
Myclobutanil	Triazole	Fungicide	Toxic effects associated with oxidative stress, e.g. hepatocellular hypertrophy, nuclear pyknosis, vacuolation, and non-zonal macrovesicular lipid accumulation, were observed for *Eremias argus* lizards treated with myclobutanil enantiomers.	[22]
Glyphosate	Organophosphorus	Herbicide	Downregulation of the expression of host-produced antimicrobial peptides in the honey bee *Apis mellifera*, and melanization in the bee hemolymph; these two components are crucial for the innate immune system of honey bees.	[23]
Chlorpyrifos	Organophosphorus	Insecticide	Significant correlations between prenatal exposures to chlorpyrifos and postnatal neurological complications in adult rats, particularly cognitive deficits (associated with disruption of the structural integrity of the brain).	[24]

Methomyl	Carbamate	Insecticide	In male rats, methomyl led to a notable reduction in the fertility index, the function of accessory sexual glands, serum testosterone levels, and both sperm motility and count, while it caused an increase in sperm cell abnormalities.	[25]

1.1.3. Phenolic compounds

Phenolic compounds, also known as phenols, are characterized by an aromatic ring bonded with one or more hydroxyl substituents. All ranges from simple phenolic molecules to highly polymerized compounds with numerous aromatic rings can be found within this group. Many of the phenolic substances are naturally occurring in the environment and are beneficial for living organisms. For example, polyphenols are abundant in plants and plant-based food, such as fruits, vegetables, herbs, spices, tea, and wine. These compounds, including flavonoids, phenolic acids and curcuminoids, can act as antioxidants and have anti-inflammatory properties [26,27]. Additionally, environmental phenols can be of anthropogenic origin, which is linked to the manufacturing and application of pesticides, surfactants, plastics, and pharmaceutically active compounds. Due to their application in the chemical, petroleum, dye, or pharmaceutical sectors, many phenolic compounds have been detected in surface waters [28,29].

However, the occurrence of many phenol-based substances possess a detrimental effect on ecosystems. Some of the examples are listed in Table 1.3. Generally, their toxicity is related to the hydrophobicity of the individual compound and the possible formation of free radicals [30]. Due to limited solubility in water, phenols can interact with specified cell and tissue structures of living organisms. For example, the hydrophobicity of chlorophenols relies on the number of chlorine atoms, which enhances the toxicity of individual compounds [31,32]. Therefore, many phenolic compounds can be classified as contaminants of emerging concern, and their concentration in wastewater has to be strictly monitored, e.g. pentachlorophenol, octylphenols and nonylphenols were included in the List of Priority Substances in the Field of Water Policy, valid in the European Union [33].

Table 1.3. Examples of the impact of selected phenolic compounds in the environment.

Compound	Application	Its impact on the environment	Ref.
Phenol	Production of phenol formaldehyde resins and aspirin; can be used as antiseptics	Chronic exposure to sublethal phenol concentrations resulted in reduced feeding rates, decreased growth, reduced reproductive parameters of fish tilapia and lower zooplanktion populations compared to control	[34]
Chlorophenols	Synthesis of pesticides and wood preservatives	They can directly bind to DNA through their metabolites, resulting in DNA damage and potential cancerogenic effects.	[31,35]
Aminophenols	Synthesis of paracetamol, precursor for indole synthesis, production of dyes and lubricants	Both 2- and 4-aminophenol are nephrotoxic, 2-amoniphenol causes acute liver injury, linked to oxidative stress and glutathione depletion.	[36,37]
Bisphenol A	Synthesis of polycarbonate plastics, epoxy resin and other polymer materials	Bisphenol A shows endocrine disrupting effects on humans by interacting with estrogen receptor, androgen receptor, and thyroid hormone receptor.	[38,39]

1.2. Application of advanced oxidation processes for CECs removal

Among methods of wastewater treatment, Advanced Oxidation Processes (AOPs) have become a promising technology to remove contaminants of emerging concern from the aqueous phase. The basis of AOPs lies in their ability to produce reactive oxygen species (ROS), which are known for their strong oxidative potential and high reactivity. They can effectively break down a wide range of organic pollutants, including pharmaceutically active compounds, pesticides, and phenols, into less harmful or biodegradable compounds [40]. AOPs can be classified into homogeneous and heterogeneous processes, each involving different combinations of chemical reagents, light introduction, catalysts, or oxidants. The general classification of AOPs processes is presented in Figure 1.1.

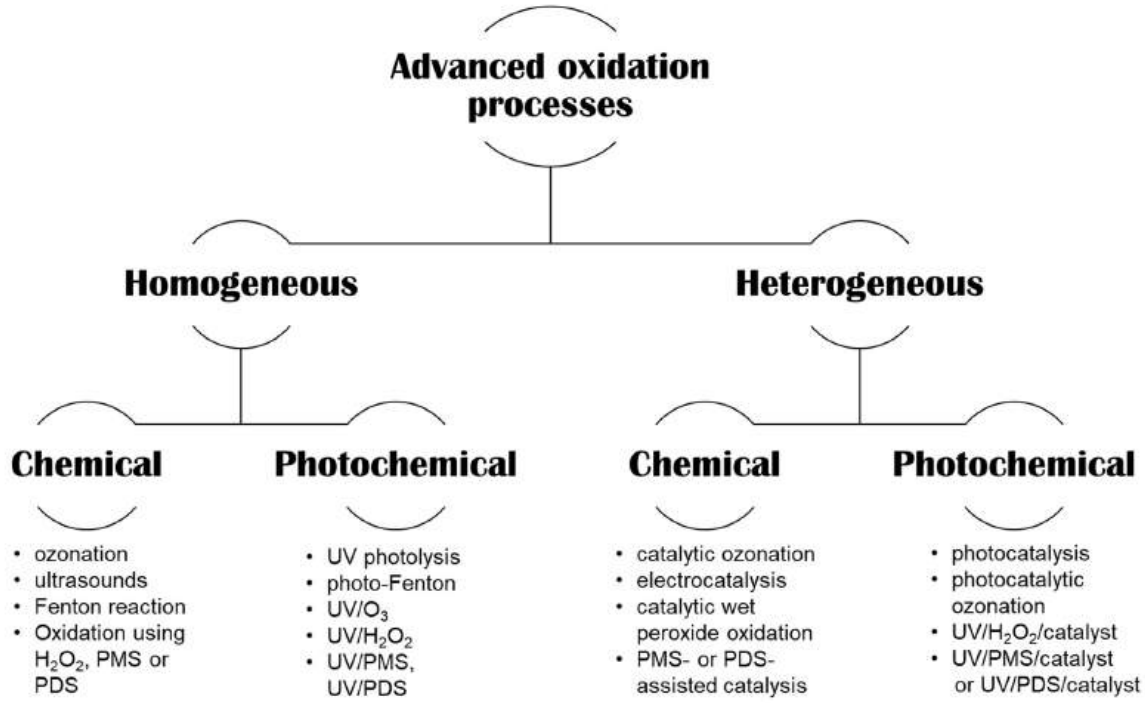

Figure 1.1. General classification of advanced oxidation processes.

Among AOPs, heterogeneous processes were selected for further investigation. Heterogeneous systems are more stable under a range of environmental conditions, making them suitable for long-term operation. Moreover, homogeneous processes often require low pH and high oxidant dosages. Finally, it is possible to design solid-state catalysts for targeted activation under specific light wavelengths or other conditions, improving the process control [41,42].

1.2.2. Heterogeneous catalytic activation of persulfates

The most typical approach of wastewater purification and disinfection is the introduction of oxidizing agents, including oxygen (O_2), ozone (O_3), hydrogen peroxide (H_2O_2) or chlorine dioxide (ClO_2). These oxidants can be applied standalone or in combination with UV light, ultrasounds or the presence of a catalyst [40,43].

Over recent years, persulfate-based oxidants like peroxydisulfates (PDS) and peroxymonosulfates (PMS) have been extensively investigated for the degradation of organic pollutants with minimal interference from water parameters. These compounds are white solid powders with high solubility in water, forming acidic water solutions. The commercial compounds used as oxidants are sodium or potassium peroxydisulfate ($Na_2S_2O_8$, $K_2S_2O_8$) and Oxone® ($KHSO_5 \cdot 0.5\ KHSO_4 \cdot 0.5\ K_2SO_4$) [44,45]. Their stability depends on the pH of the water solution – both PMS and PDS are relatively stable in acidic (pH 3-7) and neutral (pH = 7) conditions [46]. The chemical data of both PDS and

PMS anions are listed in Table 1.4. In the PhD dissertation, only processes with PMS were investigated. The main reason for this selection is its unique asymmetric structure, resulting in easier activation of PMS by metal oxide catalysts than that of PDS, thus requiring lower energy input [47,48].

Table 1.4. Chemical data of PMS and PDS, based on [44–46]. Oxygen, sulfur and hydrogen atoms are labelled as red, yellow and white, respectively.

Chemical data	Peroxymonosulfate (PMS)	Peroxydisulfate (PDS)
Chemical structure of anions	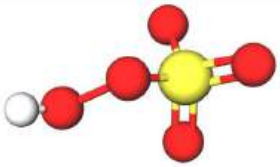	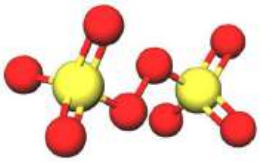
Chemical formula of anions	HSO_5^-	$S_2O_8^{2-}$
Molecular symmetry	Asymmetric oxidant, HO−O−SO_3	Symmetric oxidant, SO_3−O−O−SO_3
Comparison to H_2O_2	Replacement of one H atom in H_2O_2 with a SO_3 group	Replacement of two H atoms in H_2O_2 with two groups of SO_3
E^0 (V vs. NHE at pH = 7)	1.82	2.01

Generally, PMS and PDS are strong oxidizers, but they react directly with the organic pollutants at a low reaction rate. In this regard, appropriate activation of PMS and PDS is crucial for generating radicals with strong oxidation potential. The activation of persulfates involves breaking the O−O bond by homolytic or heterolytic cleavage. This can occur upon applying energy such as radiation, heat and ultrasounds, in alkaline conditions or in the presence of transition metals (e.g. Co, Fe, Mn, Cu) and carbonaceous materials [46,49]. Considering the advantages of heterogeneous catalytic systems, several materials based on the aforementioned elements were investigated for PMS/PDS activation. For example, the combination of $Co(OH)_2$ and g-C_3N_4 remarkably improved PMS activation, resulting in almost 96% of enrofloxacin degradation within 30 minutes [50].

As a result of PMS/PDS activation, highly reactive species can be obtained. The most characteristic feature of this method is the ability to produce sulfate radicals ($SO_4^{\bullet-}$), a powerful oxidant with a standard redox potential of +2.60-3.10 V vs. NHE. The possible mechanisms of $SO_4^{\cdot-}$ generation from PMS/PDS activation by metal ions and metal oxide are presented as reactions 1-2 [46,51]. Due to the possibility to generate this specific radical, oxidation processes using PMS and PDS are often described in the literature as *sulfate radical-based advanced oxidation processes* (SR-AOPs).

$$HSO_5^- + M^{n+} \rightarrow M^{(n+1)+} + SO_4^{\bullet-} + OH^- \quad (1)$$

$$S_2O_8^{2-} + M^{n+} \rightarrow M^{(n+1)+} + SO_4^{\bullet-} + SO_4^{2-} \quad (2)$$

However, labelling these oxidation processes as *sulfate radical-based AOPs* can be confusing, because both PMS and PDS can be a source of other reactive species. Persulfates can also decompose into hydroxyl radicals (•OH) as well, characterized by a high redox potential of 1.9–2.7 V vs. NHE. The possible formed •OH radicals can be a result of direct reaction with oxidant (the case of PMS is shown as reaction 3) or reaction with water over $M^{(n+1)+}$ and sulfate radicals (reactions 4-5) [49,52].

$$HSO_5^- + M^{n+} \rightarrow M^{(n+1)+} + \bullet OH + SO_4^{2-} \quad (3)$$

$$M^{(n+1)+} + H_2O \rightarrow M^{n+} + \bullet OH + H^+ \quad (4)$$

$$SO_4^{\bullet-} + H_2O \rightarrow SO_4^{2-} + \bullet OH + H^+ \quad (5)$$

Furthermore, non-radical pathways for PMS or PDS activation have been reported, which included singlet oxygen ($^1O_2$) or direct electron transfer between pollutant and oxidant mediated by the catalyst. The generation of $^1O_2$ is often associated with dissolved oxygen in water, as shown in the schematic route in Equation 6. The reaction between PMS/PDS and H_2O could also contribute to the formation of H_2O_2 [52,53].

$$O_2 \rightarrow H_2O_2 \rightarrow O_2^{\bullet-} \rightarrow {}^1O_2 \quad (6)$$

Compared with the most common oxidant, hydrogen peroxide, the application of PMS and PDS in wastewater treatment has many advantages:

- persulfates exist in solid form and are more stable during storage and transportation than H_2O_2,
- more ROS types can be generated in the process,
- PMS and PDS can be activated in several ways, in opposite to H_2O_2, which primarily relies on Fenton or photo-Fenton reactions (requiring Fe^{2+} and acidic conditions).

1.2.3. Heterogeneous photocatalysis

Heterogeneous photocatalysis has evolved into one of the most extensively researched technological processes, with a growing number of publications each year. According to Scopus database, 63,964 publications were published in 2024 with the keyword “photocatalysis”.

International Union of Pure and Applied Chemistry (IUPAC) defines photocatalysis as a process in which a change in the rate of a reaction or its initiation occurs under the

influence of UV, visible or infrared radiation in the presence of a photocatalyst. Essentially, a photocatalyst is a semiconductor which can absorb irradiation from solar spectrum and participate in the chemical transformation of the reaction substrates [54].

The process of heterogeneous photocatalysis using a semiconductor is initiated when the incident photon has energy equal to or greater than the energy required to transfer an electron from the valence band (VB) to the conduction band (CB), i.e. energy equal to the band gap (E_g). Then, an absorbed photon induces electron (e^-) excitation to the higher energy state. Simultaneously, the low-energy state, which remains unoccupied due to the e^- excitation, acts as an electron acceptor and can be attributed to the electron deficiency, namely a positively hole (h^+). Then, photogenerated electron-hole pairs migrate to the photocatalyst surface and react with the adsorbed molecules, e.g. H_2O, organic molecules, CO_2 [55,56]. A graphical representation of the photocatalytic reactions (photooxidation and photoreduction), is presented in Figure 1.2.

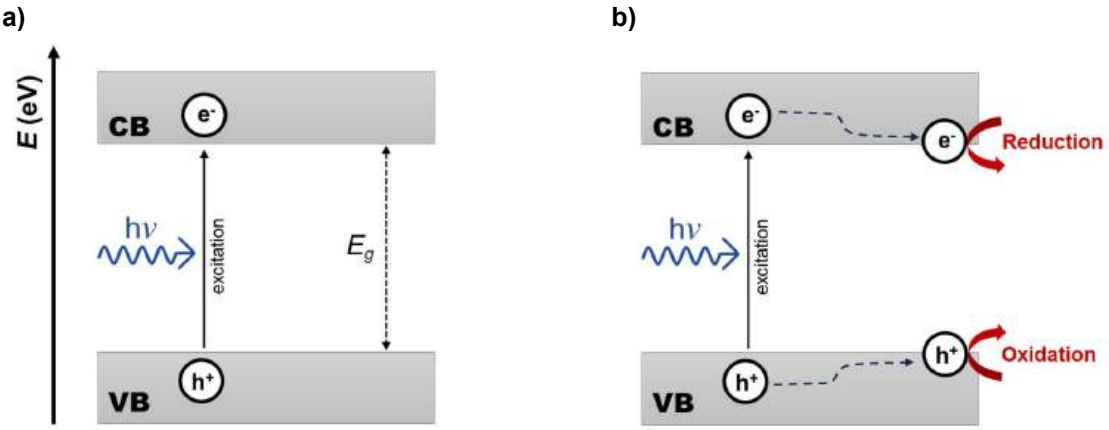

Figure 1.2. Illustration of **a)** photocatalyst excitation and **b)** possible redox reactions.

Photocatalytic processes have been extensively studied for solar energy conversion into chemical energy, degradation of organic pollutants, hydrogen evolution reaction (HER), oxygen evolution reaction (OER), carbon(IV) oxide reduction reaction (CO_2RR) into potential liquid and gaseous fuels. Additionally, these processes are investigated for heavy metal ions removal and in facilitating organic synthesis. The fundamental requirement which allows to initiate the photocatalytic reaction is that the band position of the used photocatalysts must be consistent with the redox potentials of the reaction of interest, as presented in Table 1.5. Especially oxidation reaction is correlated with the ability to generate reactive oxygen species upon irradiation, usually identified as hydroxyl radicals (·OH), superoxide radicals ($O_2^{\cdot-}$), hydrogen peroxide (H_2O_2) or rarely singlet oxygen ($^1O_2$) [57].

Table 1.5. Redox potential of selected reactions, based on [58,59].

Reaction (the main products were **bolded)**	**E^0 (V) vs. NHE at pH = 7**
$2\ H^+ + 2\ e^- \rightarrow \mathbf{H_2}$	-0.41
$2\ H_2O + 4\ h^+ \rightarrow \mathbf{O_2} + 4\ H^+$	+0.82
$H_2O + h^+ \rightarrow \mathbf{\cdot OH} + H^+$	+2.29
$O_2 + e^- \rightarrow \mathbf{\cdot O_2^-}$	-0.33
$O_2 + 2\ H^+ + 2\ e^- \rightarrow \mathbf{H_2O_2}$	+0.28
$CO_2 + 2\ H^+ + 2\ e^- \rightarrow \mathbf{CO} + H_2O$	-0.53
$CO_2 + 8\ H^+ + 8\ e^- \rightarrow \mathbf{CH_4} + 2\ H_2O$	-0.20

Based on the redox potentials, photocatalysts can be classified into reduction photocatalysts and oxidation photocatalysts [58]. As shown in Figure 1.3, reduction photocatalysts with high CB positions can produce photogenerated electrons with strong reducing power, for example: Cu_2O, g-C_3N_4, ZnS, CdS. However, too high VB position does not provide the strong oxidizing power of photogenerated holes, necessary for e.g. water oxidation to hydroxyl radicals and molecular oxygen. Meanwhile, oxidation photocatalysts, e.g. WO_3, $BiVO_4$, Fe_2O_3, BiOCl, are capable of producing photogenerated holes with strong oxidizing potential due to their low VB positions, but the photogenerated electrons have weak reducing abilities due to the low CB positions. Considering practical applications, reduction photocatalysts are mainly used for the production of solar fuels *via* CO_2 reduction or hydrogen evolution reaction, while oxidation photocatalysts are used for pollutant degradation and selective oxidation of organic compounds [58,59].

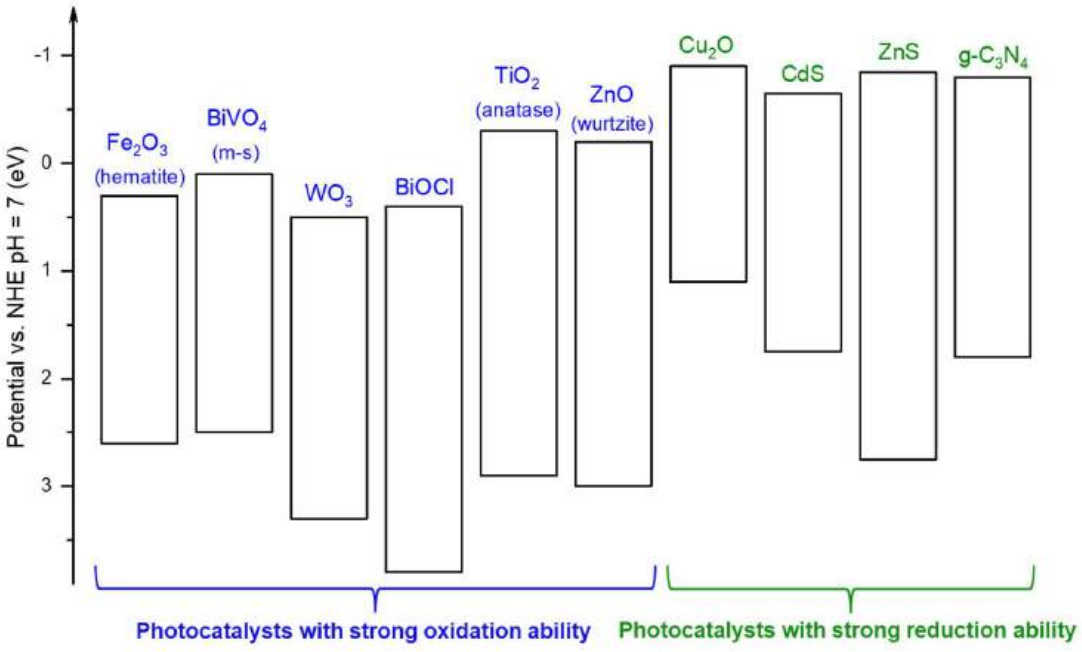

Figure 1.3. Approximate band positions of selected photocatalysts, based on [58,59].

Among the different semiconductors investigated, titanium(IV) oxide (TiO_2) has been the most extensively studied photocatalyst. Due to its strong oxidizing ability, high photo- and chemical stability and resistance to corrosion, TiO_2 became a promising semiconductor for photocatalytic applications, including wastewater treatment processes. For example, I. Rapti *et al.* described photocatalytic degradation of PhACs from hospital effluent in a pilot-scale 300 dm^3 reactor under natural sunlight using commercial TiO_2 P25 (Evonik). Measurements of toxicity rate confirmed that effluents were non-toxic after photocatalytic treatment [60]. There are at least 11 reported polymorphs of TiO_2, but three phases of TiO_2 are commonly recognized to occur naturally: anatase, rutile (both exhibit a tetragonal unit cell) and brookite with orthorhombic crystal structure [61]. Their visualized unit cells are presented in Figure 1.4. Among the polymorphs, anatase exhibits the highest photocatalytic activity due to two features of the electronic structure. First, anatase is an indirect band gap semiconductor, in opposite to both rutile and brookite, which belong to the direct band gap semiconductors. Secondly, compared to other polymorphs, anatase has the lightest average effective mass of photogenerated electrons and holes, which facilitates the migration of photogenerated charge carriers to the photocatalyst's surface [62]. The band structure of anatase is suitable for the generation of several ROS, such as hydroxyl and superoxide radicals, important for initiating redox reactions and CECs degradation.

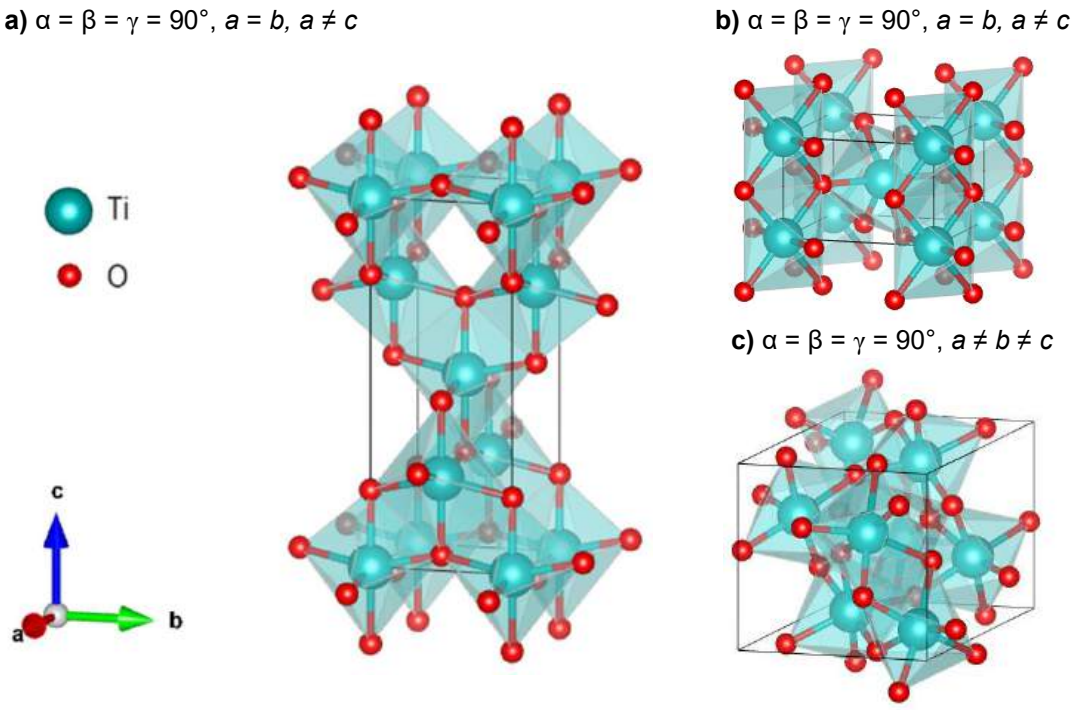

Figure 1.4. Unit cells of TiO_2 polymorphs: **a)** anatase, **b)** rutile and **c)** brookite, visualized in VESTA software [63]. CIF files 2310710, 1534781 and 8104269 from the Crystallography Open Database were used for visualization.

However, unmodified anatase is not able to fully utilize solar light due to the wide band gap energy of 3.20 eV, which corresponds to the absorption thresholds at ~388 nm. In this regard, research attention is focused on visible-light-active semiconductors such as bismuth orthovanadate ($BiVO_4$). In nature, three main polymorphs of $BiVO_4$ can be found: pucherite with orthorhombic crystal structure, dreyerite with tetragonal zircon (t–z) structure, and clinobisvanite with monoclinic scheelite (m–s) structure [64]. However, the fourth polymorph with tetragonal scheelite (t–s) structure can be obtained from the reversible transition of $BiVO_4$ (m–s) [65]. All these unit cells were visualized and shown in Figure 1.5. The highest photocatalytic activity under visible light was observed for $BiVO_4$ (m–s), besides noticeable similarities between polymorphs presented in Figures 1.5.c and 1.5.d. Herein, the minor structural changes have a detrimental effect on the electronic structure of $BiVO_4$. In tetragonal (t–s) $BiVO_4$, only a transition from O_{2p} to V_{3d} occurs, resulting in a UV absorption band (E_g = 2.9 eV). In the case of monoclinic (m–s) $BiVO_4$, an additional transition from Bi_{6s} is possible, which requires lower energy input. Therefore, (m–s) $BiVO_4$ is a visible-light-responsive photocatalyst with a band gap energy of about 2.4-2.5 eV [66].

$BiVO_4$ has been frequently investigated in solar-assisted photocatalytic processes due to its suitable band gap energy for absorbing visible light. The most described application of pristine $BiVO_4$ includes photocatalytic O_2 evolution (OER) [67,68]. Although $BiVO_4$ exhibits strong oxidation ability, the formation of particular ROS is different from that for TiO_2. Especially, the formation of superoxide radicals is not possible *via* single electron reduction due to the low position of the conduction band (presented in Figure 1.3). Moreover, Nakabayashi *et al.* suggested that water oxidation to ·OH is not favourable for $BiVO_4$ [69]. Therefore, considering the application of $BiVO_4$ in photocatalytic CECs degradation, a detailed investigation into radical formation and strategies for enhancing the photocatalytic activity are needed.

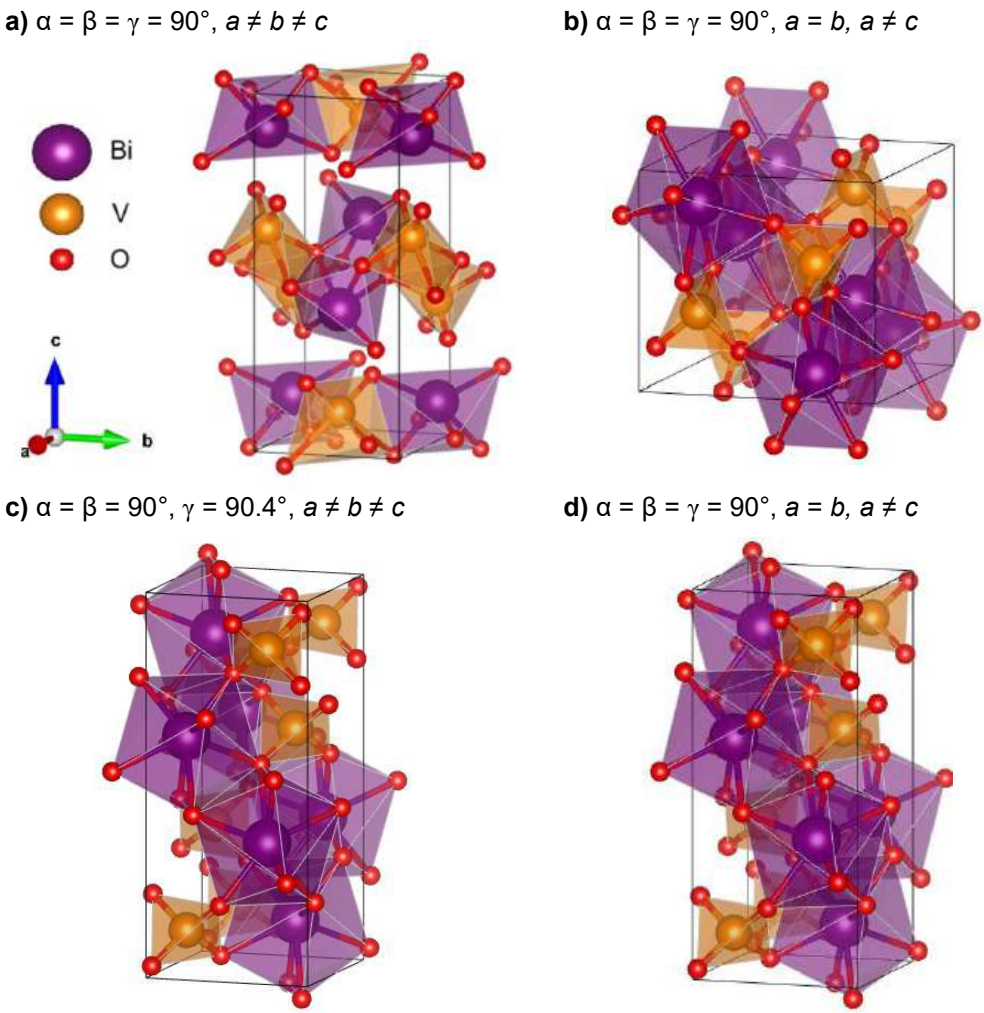

Figure 1.5. Unit cells of $BiVO_4$ polymorphs: **a)** orthorhombic, **b)** tetragonal zircon (t–z), **c)** monoclinic scheelite (m–s) and **d)** tetragonal scheelite (t–s), visualized in VESTA software [63]. CIF files 9000054, 9011741, 9013437 and 9012062 from the Crystallography Open Database were used for visualization.

1.2.4. Persulfate-assisted photocatalysis

While heterogeneous photocatalysis with semiconductors takes advantage of its ability to achieve total mineralization of a large variety of persistent organic pollutants in a broad pH range, the kinetic reaction rate is usually lower than that of homogeneous processes using oxidants [70]. This method is also limited by the absorption of visible light and not satisfactory quantum yield of reactive species generation [59,71]. On the other side, pollutants degradation using oxidants is strongly pH-dependent and still suffers from incomplete mineralization yield [70,72].

Therefore, coupling heterogeneous photocatalysis with persulfate activation can be a sustainable solution to overcome the aforementioned challenges and to achieve a more efficient system of CECs removal with a satisfactory reaction rate. In this system,

the semiconductor has a dual role, as a photocatalyst and PMS/PDS activator. Moreover, persulfates can capture photogenerated electrons, leading to the suppression of electron-hole pair recombination and promoting the photocatalytic process [42,73]. Therefore, persulfate-assisted photocatalysis may become a promising technology able to remove contaminants of emerging concern under solar light and at mild conditions.

1.3. Strategies for enhancing photocatalytic activity and PMS activation

Several approaches for enhancing the photocatalytic activity and PMS activation have been developed to achieve a high degradation rate of CECs and expand the potential applications of these technologies. These strategies focus on optimizing key parameters, including light absorption, charge separation, surface reactivity, and mass transfer. By manipulating the morphology, surface properties, and electronic structure of the (photo)catalysts, significant improvements in their performance and functionality can be achieved.

1.3.1. Morphology control and crystal facets engineering

Generally, the properties of bulk solid materials result from the combined effects of interactions of a large number of particles, determined by the type of these particles (atoms, ions, molecules) and their interdependencies. At the macroscale, the number of particles on the surface is small compared to the number of particles in the volume and the surface-area-to-volume ratio (S/V) is close to zero. Although the surface properties can be different than those for the bulk, the final physicochemical features of the material, such as colour, refractive index, thermal and electrical conductivity, are the result of the structure and interactions primarily within the volume of the material. In the case of nanomaterials with dimensions less than 100 nm, a large number of atoms are localized either at the surface or in its vicinity, leading to a high S/V parameter [74,75].

Reducing particle size and tailoring catalyst morphology are key factors that influence the properties of the final materials. First, specific surface area and pore volume are increased, which facilitate the adsorption and diffusion of reactants. Moreover, the electron and hole diffusion path can be shortened, allowing for a faster migration of charge carriers from the bulk to the photocatalyst's surface and reducing recombination rate [76,77]. Moreover, the thermodynamics and phase equilibria can be changed at the nanoscale. For example, among TiO_2 polymorphs, rutile is the most stable at large particle size and anatase for the smallest particles [78]. The hydrated forms are also favourable for nanomaterials, because phases with structural water or hydroxylated have smaller surface energies than their anhydrous counterparts [79]. Finally, nanostructured

semiconductors may exhibit different light absorption and light harvesting ability due to antenna and quantum size effects [80].

Considering the tunable optoelectronic properties and enhanced surface area, nanotechnological approaches have been extensively investigated for advanced oxidation processes and water purification technologies. The role of catalyst morphology was observed by Y. Wang *et al.*, who investigated hierarchically structured MnO_2 for PMS-assisted catalytic oxidation of phenol. In these studies, all the presented nanostructures (2D nanosheets, 3D sea urchin-like and 1D tetragonal nanorods) demonstrated remarkably enhanced catalytic activity compared to commercial bulk MnO_2, which provided only 15% phenol degradation after 60 min. Among synthesized nanostructures, the highest reaction kinetics was obtained when 2D nanosheets were used as PMS catalytic activator, achieving 100% phenol removal within 30 min. Therein, the nanostructuration led to the phase composition and porosity of MnO_2 [81]. Hence, the particle size and morphology adjustment have a significant impact on the (photo)catalytic performance.

Finally, precursor morphology-controlled synthesis can be an effective strategy for tailoring the properties of photocatalysts. By carefully designing the morphology of the substrate, it is possible to adjust the crystal growth, specific surface area, and active site distribution of the final material. For example, J. Zheng *et al.* described the effect of NH_4VO_3 morphology (butterfly-like, rhombohedral, and flower-like) on the electrochemical properties of V_2O_5, which can be used as electrodes for supercapacitors. The precursor morphology affected the initial specific capacitance and cycling stability of the final electrode material [82]. However, far less attention has been given to how precursor morphology may affect the crystal growth, surface properties and photocatalytic activity of the semiconductors. Meanwhile, this strategy could provide new opportunities to achieve enhanced light utilization and the generation of reactive oxygen species. Therefore, a systematic study on precursor morphology was performed in the doctoral dissertation for the development of metal oxide-based photocatalyst design. The morphology of titanium oxyfluoride ($TiOF_2$) and ammonium metavanadate (NH_4VO_3) was selected for investigation, as these compounds had not been applied for precursor morphology-controlled synthesis of the photocatalysts yet.

Within the term *'morphology control'*, crystal facets engineering can also be included. Crystallography reveals that each crystal lattice consists of atoms periodically arranged in a highly ordered microscopic structure. However, if the crystal lattice were cut in specific directions, a different atom arrangement at the surface would be obtained. Each crystal facet represents a specific plane along which the atoms or molecules are arranged in a regular, repeating pattern [83,84].

Atom arrangement and coordination of the surface intrinsically determine surface energy, geometry, and adsorption energy (with potential dissociation), which affect the electronic properties of the surface. The photocatalytic activity is affected by the surface structure, which can be controlled by specific crystal facets exposure to the environment. Therefore, the exposition of a particular crystal facet has emerged as a promising approach of photocatalysts design with the possibility to tailor the physicochemical properties for specific applications. The arrangement of exposed facets determines a specific shape of the particle. By the analysis of material morphology, it is possible to ascribe crystal facets in the material [84,85].

Among crystal facet engineering of inorganic semiconductors, TiO_2, especially the anatase polymorph, became one of the most extensively studied materials. According to the Wulff construction and calculated surface energy for a particular crystal facet, the shape of anatase under equilibrium conditions is a truncated tetragonal bipyramid enclosed with the eight isosceles trapezoidal surfaces composed of {1 0 1} facets (94% of their exposition) and two top squares at base composed of {0 0 1} facets [86,87]. Figure 1.6 presents the equilibrium shape and atom arrangement in the most investigated anatase crystal facets, namely {1 0 1}, {1 0 0} and {0 0 1}. Their corresponding surface energies are 0.44 J/m^2, 0.53 J/m^2 and 0.90 J/m^2 [83,86]. What is worth attention, {1 0 0} facets are not present in the equilibrium shape, although they are more thermodynamically stable than {0 0 1}. In the case of highly-energetic {0 0 1} facets, fluorine ions can stabilize their structure, promoting their exposition instead of the thermodynamically favoured {1 0 1} [88]. Depending on the synthesis conditions and F^- content, anatase can form several euhedral shapes, including: octahedra with exposed {1 0 1} crystal facets, plates with dominant {0 0 1} facets, decahedra with mixed {1 0 1}/{0 0 1} and elongated rods with topped off with truncated pyramids, containing also {1 0 0} facets [83,89,90]. These possible shapes are presented in Figure 1.7.f.

The idea of crystal facets engineering can be extended to other photocatalytic materials, such as bismuth orthovanadate. The most investigated shape of (m–s) $BiVO_4$ is decahedral with exposed {0 1 0} and {1 1 0} crystal facets, with corresponding surface energies equal to 0.27 J/m^2 and 0.28 J/m^2 [91]. Moreover, high-index crystal facets like {1 2 0} in octahedra and {1 1 1} in octadecahedra (combined with {0 1 0} and {1 1 0}) were also reported [92,93]. All these described crystal planes and possible shapes are presented in Figure 1.7. However, the formation of other multifaceted microcrystals also occurs. For example, X. Zhai *et al.* synthesized and characterized $BiVO_4$ microcrystals enclosed with up to 42 low- and high-index facets [94].

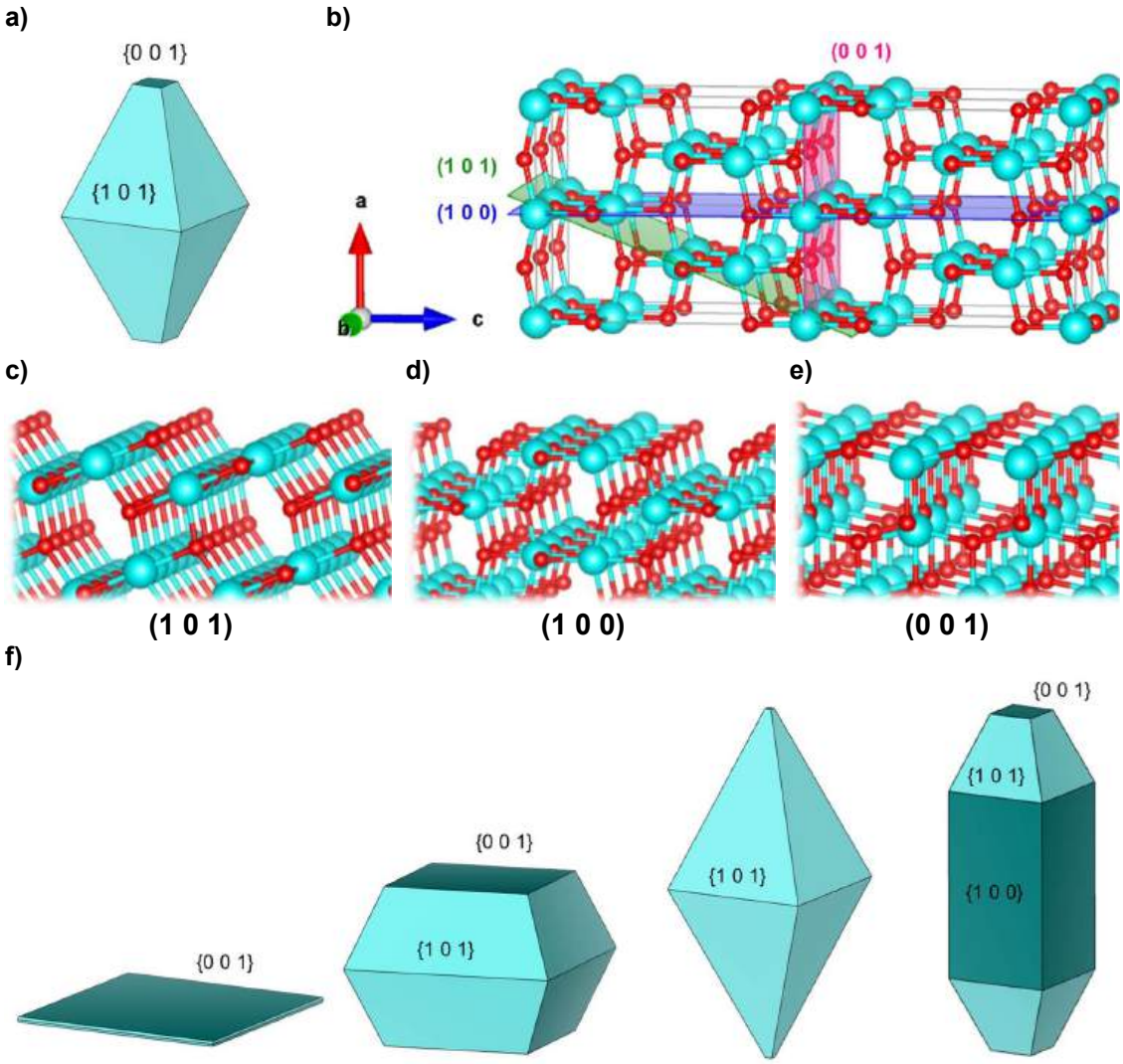

Figure 1.6. a) Anatase shape under equilibrium conditions, visualization of the **b)** 4 anatase unit cells with highlighted lattice planes, **c)** (1 0 1), **d)** (1 0 0) and **e)** (0 0 1) surfaces in anatase, **f)** possible shapes of anatase crystals. Crystal structures were visualized using VESTA software [63]. CIF file 2310710 from COD was used for visualization.

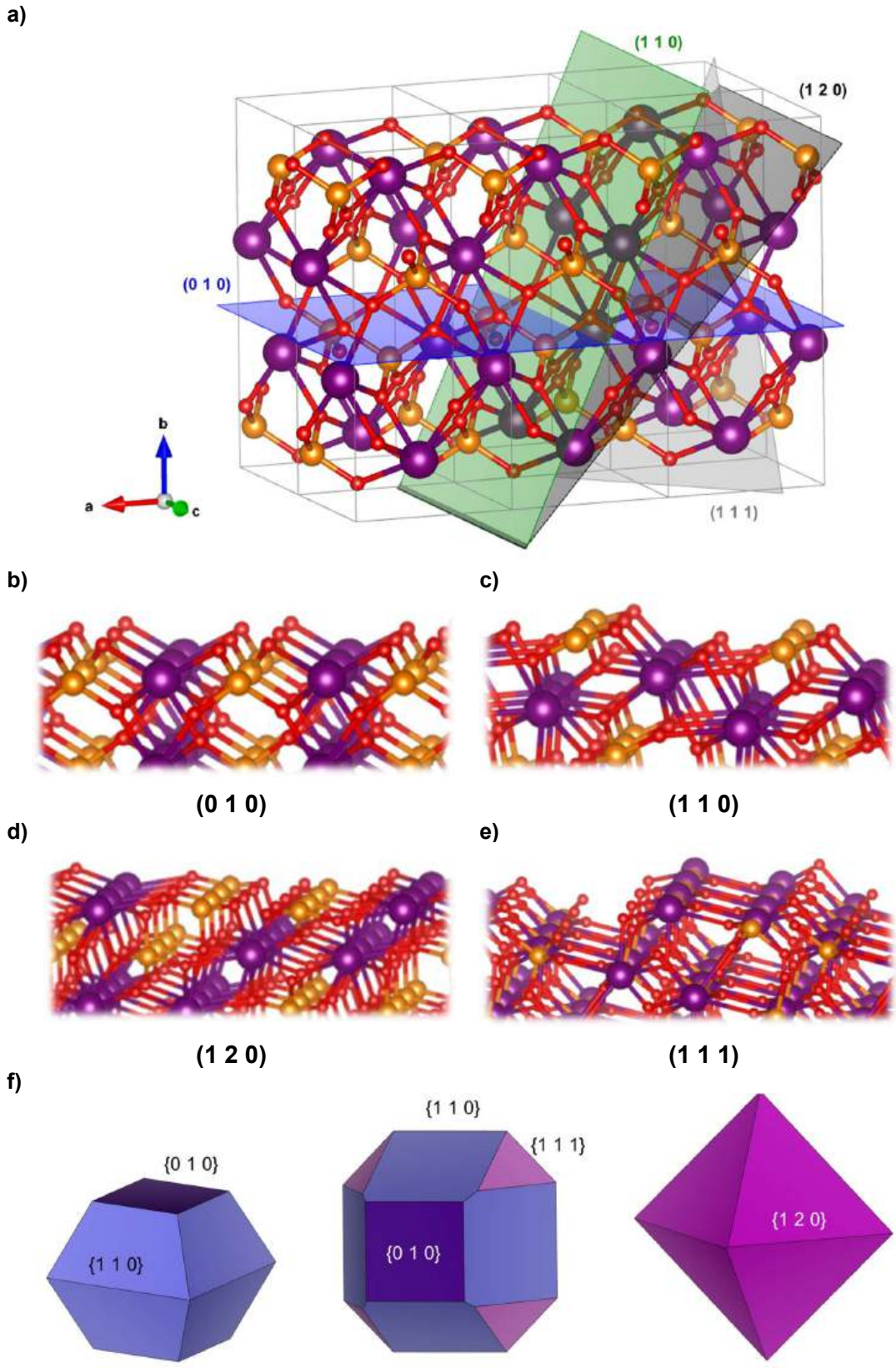

Figure 1.7. a) 6 unit cells of (m–s) $BiVO_4$ with highlighted lattice planes, visualization of the **b)** (0 1 0) and **c)** (1 1 0) surfaces, **d)** (1 2 0) and **e)** (1 1 1) surfaces, **f)** possible shapes of (m–s) $BiVO_4$ crystals. Crystal structures were visualized using VESTA software [63]. CIF file 9013437 from COD was used for visualization.

The shape-controlled synthesis is the possibility to create a homojunction with facet-selective reduction and oxidation facets within the single-component material, leading to the separation of photogenerated charge carriers. This effect is especially investigated for decahedral shapes like anatase with combined {0 0 1}/{1 0 1} facets and (m–s) $BiVO_4$ with {0 1 0}/{1 1 0} ones. Spatial separation of photogenerated charge carriers among decahedral (m–s) $BiVO_4$ was confirmed by R. Li *et al.,* who performed selective deposition of the reduction (Au, Pt, Ag) and oxidation (MnO_x, PbO_2) co-catalysts [95]. Moreover, facet-dependent effects can be obtained in both photocatalysis and PMS activation due to changes in adsorption/desorption energies and different charge distributions. Y. Zhao *et al.* investigated Fe(III) impregnated on anatase TiO_2 with different exposition of {0 0 1} and {1 0 1} crystal facets for PMS-assisted photocatalytic degradation of bisphenol A. The enhanced degradation rate of the pollutant was observed for Fe-TiO_2 with high contribution of {1 0 1} facets, due to stronger charge transfer between iron and TiO_2 and, in consequence, faster redox cycle Fe(III)/Fe(II) [96].

Therefore, atomic-scale design of the photocatalyst's surface should be of particular attention, considering the expected maximization of the reaction rate and selectivity. In this regard, crystal facets-engineered photocatalysts based on TiO_2 and $BiVO_4$ were investigated in a doctoral dissertation for facet-dependent photocatalytic CECs degradation. Moreover, a literature study of crystal facets exposure in TiO_2 polymorphs (anatase, rutile and brookite) was demonstrated in a published book chapter **[P2]**.

1.3.2. Surface modification

Despite promising possibilities of heterogeneous photocatalysis, the low efficiency of the single-component photocatalysts limits their practical applications. The key challenge is to inhibit the recombination of the photogenerated electrons and holes, which undergo recombination due to the strong Coulomb attraction. Moreover, for a pristine photocatalyst, it is difficult to find a compromise between strong redox ability and a broad light absorption range [97,98]. On the one hand, a large band gap would include redox potential for both oxidation and reduction processes. However, to improve the efficiency of solar light utilization, a smaller band gap, which increases the capability of light harvesting, is required [99]. Therefore, facile strategies to overcome these challenges are crucial for enhancing the photocatalytic performance.

In this regard, surface modification can be a strategy to enhance both the photocatalytic performance and PMS activation. Common approaches include the deposition of nanoscale species on the (photo)catalyst surface, including nanoparticles, clusters and single atoms. The difference between particular species is presented in

Figure 1.8. Due to their size in the range of nanometers, they exhibit unique properties like quantum size effects, abundant surface-active sites, and flexible compositional tunability, which can be designed with atomic-level precision [56,100]. Therefore, surface modification by sub-nanometer species can be a promising way to enhance the light absorption, charge carriers separation, and to adjust interfacial reaction pathways.

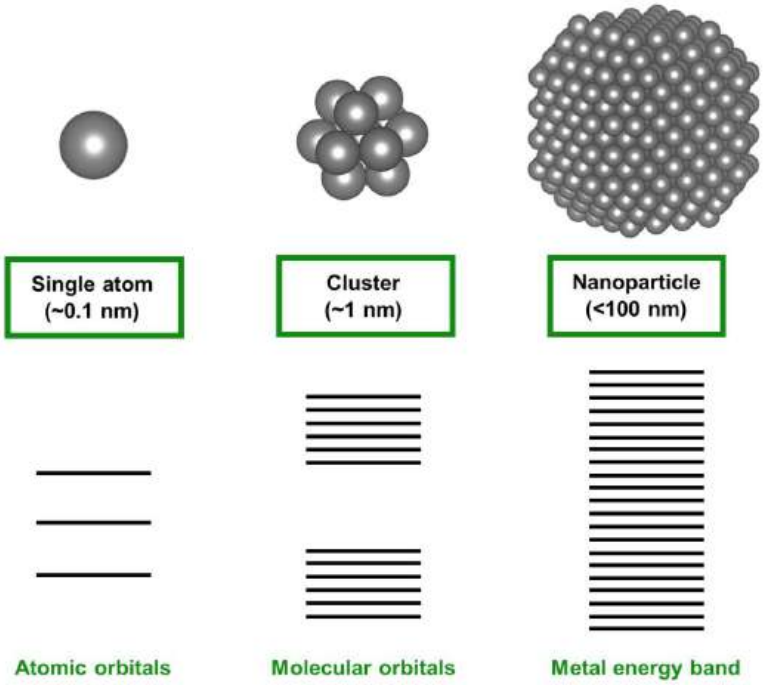

Figure 1.8. Geometric and electronic structures of the single atom, cluster and nanoparticle.

Several effects are accompanied with surface modification by metallic compounds. Firstly, as a result of the interface interaction between a noble metal nanocrystal (e.g. Pt, Pd, Ag, Ru) and a semiconductor structure, a junction is formed. Since the work function of metals is larger than that of n-type semiconductor, but smaller than that of p-type semiconductor, a charge transfer is possible when combined. When n-type semiconductors are in contact with metal nanoparticles, electrons are transferred from the CB of the semiconductor to the Fermi level of a metallic compound, thus building up an equilibrium state of Fermi levels between these two components. As a result, the surface of the metallic component accumulates negative charges, while the holes in the VB of the semiconductor lead to a positively charged surface [101]. Moreover, localized surface plasmon resonance (LSPR) may occur for metal nanoparticles, in which, when a nanoparticle absorbs light, oscillating electrons become excited and subsequently relax by colliding with the lattice of plasmonic materials. Thus, the surrounding environment heats up, accelerating the redox reaction and mass transfer rate, leading to the enhancement of the photocatalytic activity [102,103].

The most frequently studied type of surface modification is the deposition of metallic nanoparticles. However, single-atom catalysts (SACs) have been of great interest since 2011, when Qiao *et al.* showed that anchoring highly dispersed Pt_1 atoms on FeO_x crystals caused unusual catalytic activity [104]. In this regard, the number of publications about surface manipulation using clusters and isolated atoms has grown over the last years. Due to their ultrasmall size (below 2 nm), they exhibit nonmetallic behaviors with energy quantization without demonstrating the LSPR effect. Instead, they provide a high surface area-to-volume ratio, which can bring precise control of the active site dispersion and tailored surface reaction kinetics at low metal loading [105,107].

Concerning unique metal-support interaction, surface-modified materials have been thoroughly explored for (photo)catalytic applications. For example, S. Saedy *et al.* investigated the promotional effect of Cu_xO clusters grown on TiO_2 on photocatalytic H_2 production. Deposition of clusters enhanced photocatalytic activity due to induced substantial reduction of Ti^{4+} to Ti^{3+} on the surface, leading to increased charge carrier separation and improved light absorption [108]. Such atomic-precise control can be beneficial for PMS activation as well. J. Miao *et al.* presented single-atom transition metals (Co, Fe, Mn and Ni) in M−N moieties anchored on carbon nanotubes for PMS-assisted catalytic sulfamethoxazole degradation [109]. Experimental studies and theoretical calculations confirmed that a large effective magnetic moment with a high spin state (like in Co−N) favoured the overlap of d orbitals with oxygen-containing adsorbates on metal active sites. This effect promoted electron transfer and facilitated PMS adsorption, strongly determining their catalytic activity. Therefore, careful engineering of the (photo)catalyst surface using sub-nanometer species can be a solution for achieving high reaction rates in CECs degradation.

1.3.3. Formation of heterojunction

Next to surface modification, the design of heterojunction-based photocatalysts is a promising approach due to the ability to enhance the charge carriers separation while integrating the benefits of each component. A heterojunction can be defined as the interface between two different semiconductors with unequal band structure, leading to the band alignments [110]. Typically, three types of conventional heterojunction can be distinguished: with a straddling alignment (type-I), those with a staggered alignment (type-II), and with a broken gap (type-III) [71,97]. The schematic illustration of these heterojunctions is presented in Figure 1.9. Generally, type-I heterojunction with straddling alignment (Figure 1.9.a) does not allow to separate charge carriers, due to the accumulation of photogenerated electrons and holes in the same semiconductor [111].

However, N. Imanuella *et al.* proposed an inverted F-scheme heterojunction based on straddling alignment, in which electrons as CB of the semiconductor A have two possible electron migration channels – recombination with holes in VB in semiconductor B or transfer to another CB. This mechanism should promote charges carriers' separation and preserve the high oxidation ability of holes in semiconductor A [112]. In the case of the type-III heterojunction (Figure 1.9.b), the band gaps do not overlap, so the migration of electrons and holes cannot occur, making it unsuitable for enhancing the separation of charge carriers. Therefore, among the heterojunction types, only staggered (type-II) alignments allow to both migrate electrons and holes and their spatial separation. However, there are two main mechanisms of charge carriers separation for this alignment. As shown in Figure 1.9.c, a substantial separation of electrons and holes is achieved, but at the expense of the redox abilities of transferred charge carriers. Moreover, electrostatic repulsive forces between holes or electrons are huge to restrain their migration in a type-II heterojunction. These problems do not occur in a typical direct Z-scheme heterojunction (Figure 1.9.d), in which strong oxidation/reduction abilities of photogenerated charge carriers are preserved, besides the recombination of electrons and holes with inferior redox power. As a result, a Z-scheme heterojunction-based photocatalyst has simultaneously the strong redox ability for initiating photocatalytic reactions and the spatially separated reductive and oxidative active sites [97,98].

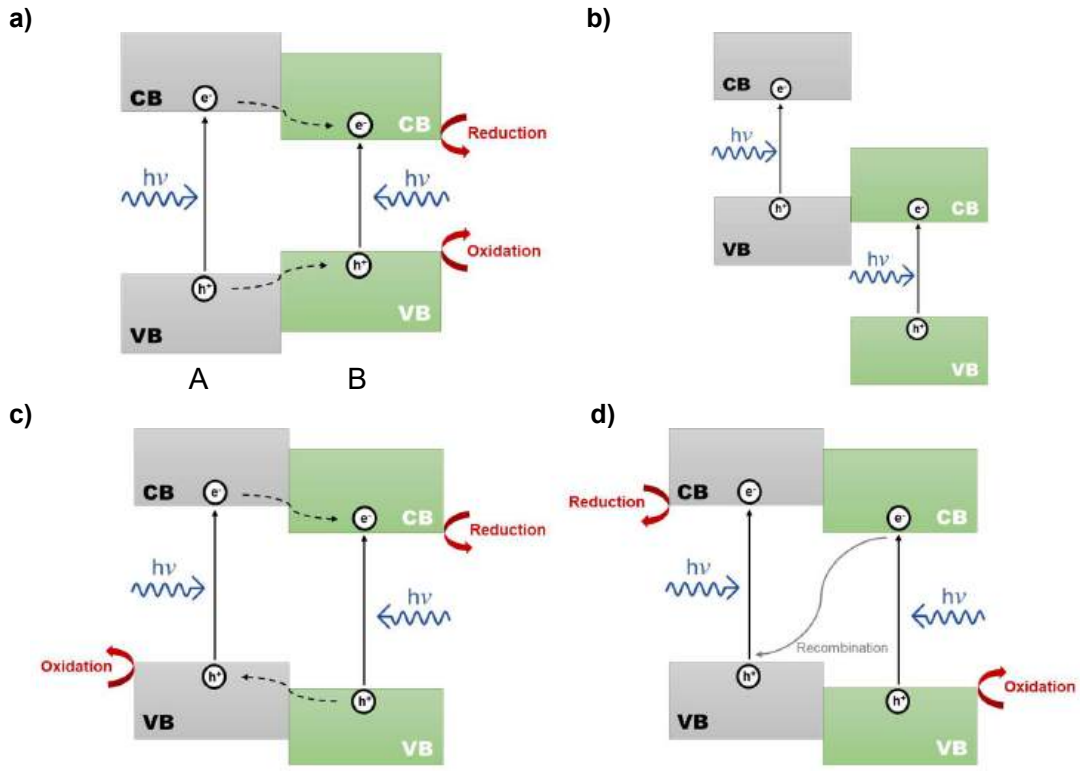

Figure 1.9. The most common types of heterojunctions formed by two semiconductors: **a)** straddling (type-I), **b)** broken gap (type-III) and **c), d)** staggered (type-II) alignments; figure d) refers to the direct Z-scheme heterojunction.

Formation of the heterojunction in the semiconductor can be *a game-changer* for the photocatalytic activity. For example, T.-Y. Liang *et al.* reported the superior photocatalytic activity of Ag_2S deposited onto Cu_2O cubes toward methyl orange removal, although both single-component materials were photocatalytically inactive. An unexpected high photocatalytic activity could be attributed to the charge carriers' separation due to the creation of a Z-scheme heterojunction [113]. Therefore, this approach is expected to be a promising solution considering solar light utilization and enhancing photocatalytic activity.

2. RESEARCH OBJECTIVES AND HYPOTHESES

The literature overview highlighted the importance of eliminating contaminants of emerging concern, including pesticides, pharmaceutically active compounds and phenols from water. Advanced oxidation processes became a promising approach for degrading several organic contaminants, especially those persistent to conventional treatment methods. Especially heterogeneous-based AOPs have been of particular attention due to higher stability under a wide range of environmental conditions and the possibility to tailor the properties of solid-state materials for specific reactions.

In the PhD dissertation, two AOP techniques were selected for investigation: heterogeneous photocatalysis and PMS-assisted photocatalysis. Both processes are based on solid-state photocatalysts, therefore, the presented investigation focused on the synthesis and characterization of the materials, designed for contaminants of emerging concern oxidation under specific conditions. To achieve the highest efficiency of CECs removal, several strategies for enhancing photocatalytic activity and PMS activation were considered, primarily the impact of morphology and crystal facets exposition, formation of heterojunction and interface modification.

In this regard, two groups of photocatalysts were studied, whose selection was based on their band positions and possible strong oxidation ability:

- **TiO_2-based photocatalysts:** F-TiO_2 and TiO_2/$TiOF_2$,
- **Scheelite-type compounds:** (m–s) $BiVO_4$, $CaWO_4$, $SrWO_4$, $BaWO_4$, $CaMoO_4$, $SrMoO_4$ and $BaMoO_4$.

Although photocatalytic materials and catalytic PMS activators have been extensively studied over the last decade, there are still several research gaps within the existing literature. Therefore, to achieve the intended goal, several studies have been undertaken to explain:

I. How does the morphology of the precursor affect the photocatalytic activity of the photocatalyst?
II. Can $TiOF_2$ be used as a precursor for TiO_2 synthesis?
III. Can degradation of contaminants of emerging concern and their toxicity assessment be facet-dependent?
IV. What is the role of $TiOF_2$ in the TiO_2/$TiOF_2$ binary photocatalyst, although pristine $TiOF_2$ is not photocatalytically active?
V. Which crystal facet of (m–s) $BiVO_4$ is the most favourable for photocatalytic oxidation processes and PMS activation?
VI. Is the surface of (m–s) $BiVO_4$ always stoichiometric?

VII. Can alkaline-earth-metal tungstates and molybdates be used in photocatalytic oxidation processes, despite the wide band gap energy?
VIII. What is the mechanism of ROS generation in PMS-assisted photocatalysis with $BiVO_4$?

The aforementioned aspects are still in the minority of research interests. Therefore, the goal of the presented study was not only fundamental studies of the possible photocatalysts, but also to find the relationships between the material structure (chemical and phase composition, crystal facets exposition, morphology) and actual activity toward oxidation and mineralization of contaminants of emerging concern, toxicity rate and/or ROS generation.

Following identified research gaps and raised questions, hypotheses derived directly from analyses of existing studies and as a result of ongoing work are formulated as follows:

H1. Alkaline-earth metal tungstates and molybdates can be used as photocatalysts.
H2. The morphology of the precursor for semiconductor synthesis influences the photocatalytic activity of the final photocatalyst.
H3. Degradation of contaminants of emerging concern, toxicity rate of treated water and PMS activation can be facet-dependent.
H4. $TiOF_2$ has a dual role – as a precursor for F-TiO_2 synthesis and as a photocatalyst if coupled with other semiconductors.
H5. Deposition of Cu sub-nanometer species enhances the photocatalytic activity and PMS activation.
H6. Surface non-stoichiometry of $BiVO_4$ is a critical factor for photocatalytic activity and PMS activation.
H7. Increased generation of hydroxyl radicals is the main reason of enhanced degradation rate when PMS is introduced to the photocatalytic process.

In this regard, the canon of PhD thesis [P1-P6] includes the studies conducted to gain a better understanding of the effects of precursor type and photocatalyst morphology on physicochemical properties and photocatalytic activity. As presented schematically in Figure 2.1, the main criterion was the material selected for investigation. Depending on its properties, such as phase composition, morphology, band gap value, specific research aspects were considered.

The main objective of publication [P1] was to explore the potential of alkaline-earth metal tungstates and molybdates in photocatalytic degradation of phenol, including also

differences between tungstates and molybdates. The research study described in [P3] and [P4] was devoted to the application of titanium oxyfluoride ($TiOF_2$) in F-TiO_2 synthesis. The role of crystal facets exposition of obtained F-TiO_2 toward photocatalytic naproxen degradation [P3] and the effect of the precursor morphology [P4] were investigated. $TiOF_2$ was also used as a component in {0 0 1} TiO_2/$TiOF_2$ binary photocatalyst, as described in [P5]. Since all the studied photocatalysts primarily exhibited UV activity, the research focus was also on the ability to activate the semiconductor under visible light. In this regard, the same aspects investigated within F-TiO_2 were also considered for $BiVO_4$, including the morphology of the precursor (herein: ammonium metavanadate) in [P6] and crystal facets exposure. Moreover, research studies concerning $BiVO_4$ also involved PMS-assisted photocatalysis.

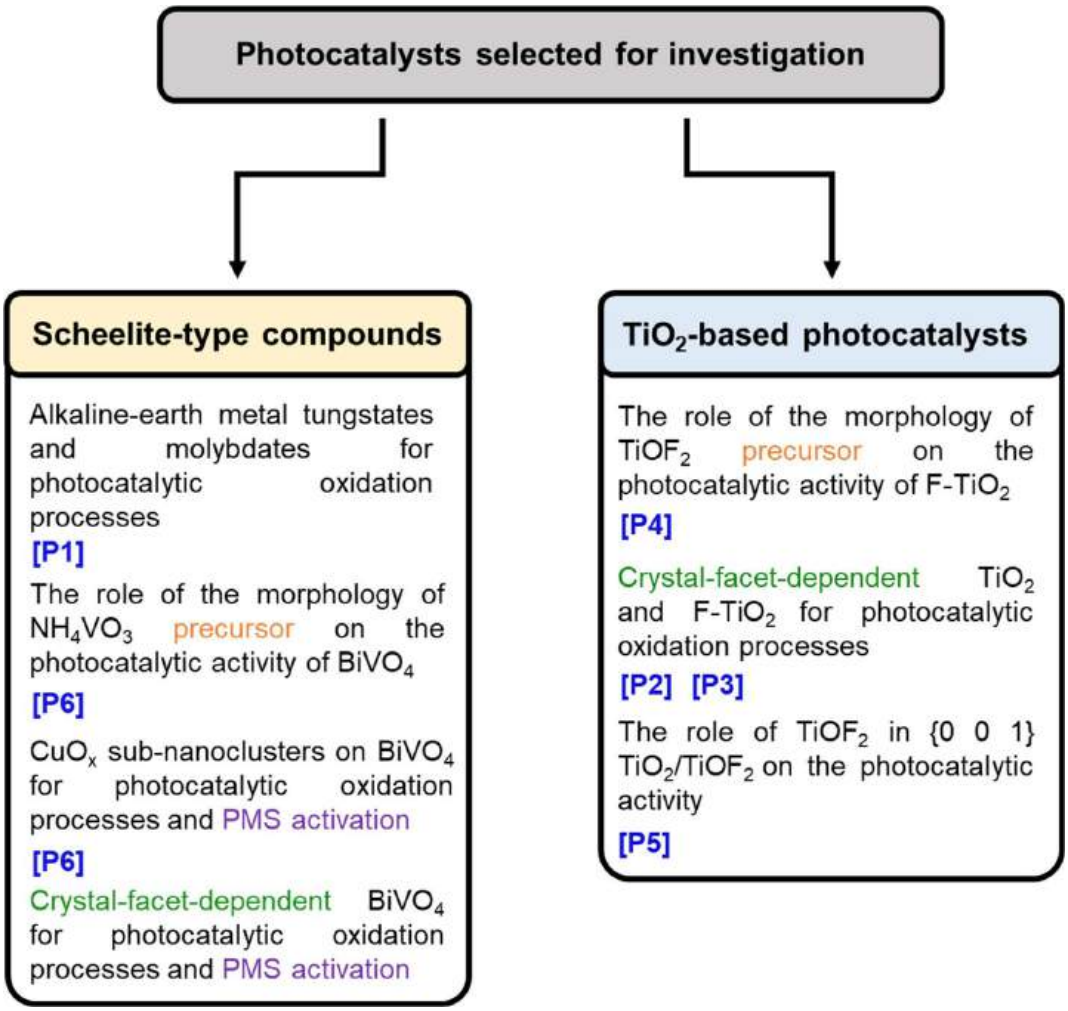

Figure 2.1. Thematic correlation between the manuscripts that constitute the scientific achievement in the PhD dissertation.

3. RESEARCH METHODOLOGY

3.1. Synthesis procedures

Most of the photocatalysts and precursors described in the doctoral dissertation were prepared using the solvothermal method. However, there were a few exceptions when chemical reduction was selected for material preparation. The synthesis time, temperature, duration, reactants, and environment were adjusted based on the work and the material being designed. Exact descriptions of the synthesis procedure are presented in publications, but general information about important aspects of particular syntheses are presented in the subsections below.

3.1.1. Alkaline-earth metal tungstates and molybdates

Alkaline-earth metal scheelite-type compounds ($CaWO_4$, $SrWO_4$, $BaWO_4$, $CaMoO_4$, $SrMoO_4$, $BaMoO_4$) were synthesized *via* a hydrothermal route. Two aqueous solutions were prepared separately, first with alkali metal salts and the second containing $Na_2WO_4 \cdot 2\ H_2O$ (for tungstates) or $Na_2MoO_4 \cdot 2\ H_2O$ (for molybdates), and then mixed with each other. After obtaining uniform stable suspensions, the mixture was transferred into a 200 cm^3 Teflon-lined stainless-steel autoclave and was heated at 160 °C for 6 h. After cooling down naturally to room temperature, the obtained white solids were washed by deionized water several times, separated through centrifugation and dried to a dry mass.

3.1.2. $TiOF_2$ precursor and TiO_2-based photocatalysts

Generally, synthesis of $TiOF_2$ precursors requires solvothermal conditions and a source of fluorine. The most common procedure of $TiOF_2$ preparation in doctoral dissertation, used in **[P3]** and **[P4]**, included HF-free method, in which TiF_4 substrate was mixed in 120 cm^3 of 1-butanol. This suspension was then transferred into a Teflon-lined stainless-steel autoclave and heated at 210 °C for 24 h. More $TiOF_2$ syntheses were proposed in **[P4]**, considering morphological differences. The procedure was then modified and an appropriate amount of 48% hydrofluoric acid (HF) was added to the reaction mixture. Moreover, to achieve cubic $TiOF_2$, different substrates were used for synthesis; titanium(IV) isopropoxide (TTIP) was dissolved in acetic acid in the presence of HF and underwent solvothermal treatment at 200 °C in 12 h.

$TiOF_2$ powders were then used as the precursors for F-TiO_2 preparation. In this regard, 0.2 g $TiOF_2$ was dispersed in deionized water and mixed in aqueous NH_4F solution in different NH_4F:$TiOF_2$ molar ratio. Optionally, $NH_{3(aq)}$ solution in different amounts was added as a capping agent. The obtained mixtures were then transferred

into a 200 cm^3 Teflon-lined stainless-steel autoclave and heated at 200 °C for 20 h. After cooling naturally, beige solids were centrifuged and washed several times with water and anhydrous ethanol to remove residual NH_4^+ and F^- ions, then dried to dry mass. The effect of synthesis parameters was a part of **[P3]** publication. **[P4]** manuscript included only one synthesis condition – the aqueous mixture of $TiOF_2$ precursor and NH_4F in molar ratio 4:1 was prepared, and 10 cm^3 of $NH_{3(aq)}$ was added.

$TiOF_2$ was also used as a component of binary {0 0 1} TiO_2/$TiOF_2$ photocatalysts with controllable $TiOF_2$ content, described in **[P5]**. To achieve this goal, 17 cm^3 of titanium(IV) butoxide (TBT) was dissolved in 30 cm^3 of 1-hexanol. After obtaining a uniform mixture, 3.4 cm^3 of 48% HF was slowly added to the reaction environment. Then, the resulting milky suspension was transferred into a 200 cm^3 Teflon-lined stainless-steel reactor and was kept at 210 °C. The content of $TiOF_2$ in the binary photocatalyst depended on the time of solvothermal synthesis, so durations of 3 h, 6 h, 8 h, 10 h, 12 h, 16 h and 24 h were investigated. After cooling down naturally, the precipitate was centrifuged and washed with water, anhydrous ethanol and 0.1 M NaOH solution to remove residual organic reagents and excess fluoride ions, then finally dried to dry mass.

3.1.3. NH_4VO_3 precursor and $BiVO_4$-based photocatalysts

In case of $BiVO_4$ synthesis, the morphology and crystal facets exposure is mainly dependent on two factors: pH of the solution and the presence of surfactants. Especially vanadium plays the key role in the formed morphology and crystal growth, as water and V^{5+} can act as Lewis base and acid, respectively. Therefore, electrons can be transferred to the vacant 3d orbital of vanadium, which has a strong polarizing power. This transfer induces the formation of a complex $[V(OH)_h(OH_2)^{6-h}]^{(5-h)}$, in which *h* is a ratio of water hydrolyzed by solvation of V^{5+}. The parameter *h* depends on the pH value of the environment and leads to the different stoichiometry of the vanadium complex. Finally, the reaction of these vanadium forms can result in the formation of H_2O–V–OH or HO–V–OH bonds and a different morphology of the final vanadium-based material [114,115].

In most $BiVO_4$ synthesis, the most frequently used vanadium source is ammonium metavanadate (NH_4VO_3), a compound with a polymeric structure consisting of chains of $[VO_3]^-$ connected by hydrogen bonds [116]. Changes of pH directly influence the formation of hydrogen bonds by affecting the degree of ionization of molecules, which can lead to changes in material properties. Moreover, the morphology of the NH_4VO_3 can also be a key parameter, because of different contributions of V=O and V-O-V bonds and the amount of hydrolyzed water.

In this regard, two samples of NH_4VO_3 precursors were compared and described in **[P6]** – the commercial one from Merck and the as-synthesized one. The self-made precursor procedure was as follows: 0.25 g of vanadium(V) oxide (V_2O_5) was dispersed in 300 cm^3 of 1.25 M aqueous solution of ammonium acetate using an ultrasonic bath. Then, the yellow uniform solution was left for 24 h to achieve the precipitated white solids. Finally, this precipitate was washed several times with anhydrous ethanol and centrifuged. The final NH_4VO_3 was dried at 40 °C in a vacuum oven to dry mass.

(m–s) $BiVO_4$ was synthesized *via* a hydrothermal route. For investigating the role of precursor morphology, three solutions in 2 M aqueous nitric acid were prepared separately: with NH_4VO_3 (vanadium source), $Bi(NO_3)_3 \cdot 5\ H_2O$ (Bi source) and sodium dodecyl sulfate (SDS). After ensuring that all the reagents were dissolved, these three solutions were mixed. Subsequently, the mixture was diluted by deionized water and transferred into a 100 cm^3 Teflon-lined stainless-steel reactor. The conditions of hydrothermal treatment were 150 °C and 24 h. After cooling down naturally, the yellow precipitates were centrifuged and washed with deionized water and anhydrous ethanol to purify the sample from excess ions and surfactant residues.

The described above synthesis procedure was also repeated for obtaining polyhedra with Bi-rich surfaces. The parameter conditions were exactly the same for multifaceted $BiVO_4$, but the commercial NH_4VO_3 from Merck was used. In case of octahedral $BiVO_4$, the only difference was a surfactant – SDS was replaced by sodium dodecylbenzene sulfonate (SDBS). Regarding decahedral $BiVO_4$, no surfactant was used. Instead, the substrates (NH_4VO_3 and $Bi(NO_3)_3 \cdot 5\ H_2O$) were dissolved in 1.5 M HNO_3 solution. This mixture was extremely acidic with pH = 0.45, so 2 M $NH_{3(aq)}$ solution was required to adjust the pH to 0.89. The final mixture was transferred to a 100 cm^3 Teflon-lined stainless-steel autoclave and heated at 200 °C for 24 h.

Within **[P6]**, the interface modification by CuO_x sub-nanoclusters was also performed. To achieve this, $BiVO_4$ sample was added to an aqueous solution with SDS, and then, 1.5 cm^3 of 0.1 M $CuCl_2$ water solution was dropped into the mixture. Cu^{2+} cations were further reduced by 2.5 cm^3 of 0.2 M $NH_2OH \cdot HCl$ aqueous solution. Finally, $CuO_x/BiVO_4$ was washed several times with deionized water and anhydrous ethanol, centrifuged and dried to dry mass in vacuum conditions.

3.2. Characterization techniques

All the described materials were characterized considering their: crystal structure and phase composition. Their crystal structure and phase composition were analyzed using powder X-ray diffraction (XRD) with Cu Kα radiation. Phase identification was performed based on the available reference cards of the standard compounds, provided by The International Centre for Diffraction Data (ICDD) database. If possible, the Rietveld refinement was performed using X'Pert HighScore Plus 2006 software (Malvern Panalytical), including lattice parameters, specimen displacement, polynomial coefficients for the background function, profile parameters and Gaussian/Lorentzian profile coefficients. For Rietveld refinement [117], crystallographic information files (.cif) were obtained from Crystallography Open Database (COD). The amorphous phase content was analyzed using NiO as an internal standard (provided by Sigma-Alrich). The average crystallite size, defined as the size of the coherent diffracting domains, was estimated from the Scherrer equation with the usual assumption of spherical crystallites.

For selected solid materials, the bond identification was determined by Fourier-transform infrared spectroscopy (FTIR) in the transmittance mode. In each measurement, pellets containing KBr and a powder sample were performed.

The morphology of solid materials, especially considering the exposition of specific crystal facets, was investigated using electron microscopy techniques: mostly scanning electron microscopy (SEM) and transmission electron microscopy (TEM) for fine particles. Depending on the specific features like chemical composition or crystal phase identification, the morphological observations were supported by energy-dispersive X-ray spectroscopy (EDX) and selected area electron diffraction (SAED), respectively. The parameters of surface area and pore volume were investigated using low-temperature nitrogen sorption based on Brunauer–Emmett–Teller (BET) method. Before each measurement, the analyzed photocatalysts were degassed.

The effect of pH on the photocatalyst's surface charge was measured as zeta potential. For each measurement, the diluted suspension of a sample in KCl water solution was prepared.

The surface chemical composition and chemical state of the photocatalysts were analyzed by X-ray photoemission spectroscopy (XPS), carried out at room temperature under ultrahigh vacuum conditions. The carbon C1s peak position was calibrated to 285.0 eV and used as an internal standard to determine other photoelectron peaks' binding energy. This method was also used to determine the position of the valence band (VB) in relation to the Fermi level.

The thermal stability and phase transition of $TiOF_2$, were demonstrated using thermal gravimetric analyzes (TGA) in a range of 25–800 °C at a heating rate of 10 °C·min^{-1} under a nitrogen atmosphere.

X-ray absorption spectroscopy (XAS) at the Cu K edge was performed in [P6] to investigate the presence and nature of copper sub-nanoclusters. This analysis was carried out at the ASTRA beamline of the SOLARIS National Synchrotron Radiation Centre in Kraków, Poland. The investigated sample was ground in an agate mortar and spread on the Kapton tape. Cu foil was used to calibrate and align collected spectra, whereas commercial copper oxides (Cu_2O and CuO) were the Cu(I) and Cu(II) reference materials, respectively. Reference compounds were measured in transmission mode, whereas the as-synthesized sample was measured in fluorescence mode. Data processing and analysis were examined by ATHENA software from Demeter software package [118].

The diffuse reflectance UV-Vis spectroscopy (DR/UV-vis) measurements were performed to determine the light absorption range and calculate band gap energy based on Tauc's method [119]. All these spectra were recorded in relation to barium sulfate ($BaSO_4$). Photoluminescence spectroscopy (PL) was performed to check the intensity of radiative emission upon excitation. For selected series, time-resolved photoluminescence (TRPL) spectroscopy was demonstrated to determine the average lifetime of photogenerated charge carriers. The excitation wavelength was adjusted to the bandgap of materials. The presence of trapping centers in the alkaline-earth metal scheelite-type compounds was confirmed by thermoluminescence (TL) spectroscopy. Finally, the time-resolved microwave conductivity (TRMC) spectroscopy was employed to study the charge-carrier dynamics in TiO_2/$TiOF_2$ series under UV light excitation.

Electrochemical measurements were also performed for selected photocatalysts. For electrochemical studies, the photocatalyst powders were dispersed in aqueous or water/alcohol solutions, sonicated to obtain stable suspensions, and deposited onto conductive substrates such as fluorine-doped tin oxide (FTO) or carbon screen-printed electrodes by drop-casting, followed by drying. To improve the stability of layers, the electrode surfaces were blocked with a thin Nafion layer applied either by drop-casting or spin-coating. Then, prepared electrodes were placed in a three-electrode configuration, in which Ag/AgCl was a reference electrode and aqueous Na_2SO_4 solution was a supporting electrolyte. Optionally, $[Fe(CN)_6]^{3-/4-}$ was used as a redox probe. Measurements were conducted using potentiostat-galvanostat systems, enabling techniques such as cyclic voltammetry (CV), electrochemical impedance spectroscopy (EIS), and Mott-Schottky diagrams. Additionally, photocurrent experiments were

performed under controlled LED illumination to evaluate photocurrent density upon irradiation.

3.3. Evaluation of the photocatalytic activity and toxicity assessment, ROS generation

Most of the photocatalytic and PMS-assisted processes were performed as a suspension in 25 or 50 cm^3 quartz photoreactor (1) with a cooling jacket connected to a thermostat to maintain a constant temperature of 20 °C. The photocatalytic set-up, placed in a black box, included also: a magnetic stirrer (2), hoses for the sample collection and connection to airflow and a quartz window as the light's entry. The light source was 300 W xenon lamp with IR filter (4), optionally equipped with cut-off filter $\lambda >$ 420 nm (3), if visible-light responsive photocatalysts were investigated. The schematic illustration of this experimental set-up is presented in Figure 3.1. (also shown in [P6]).

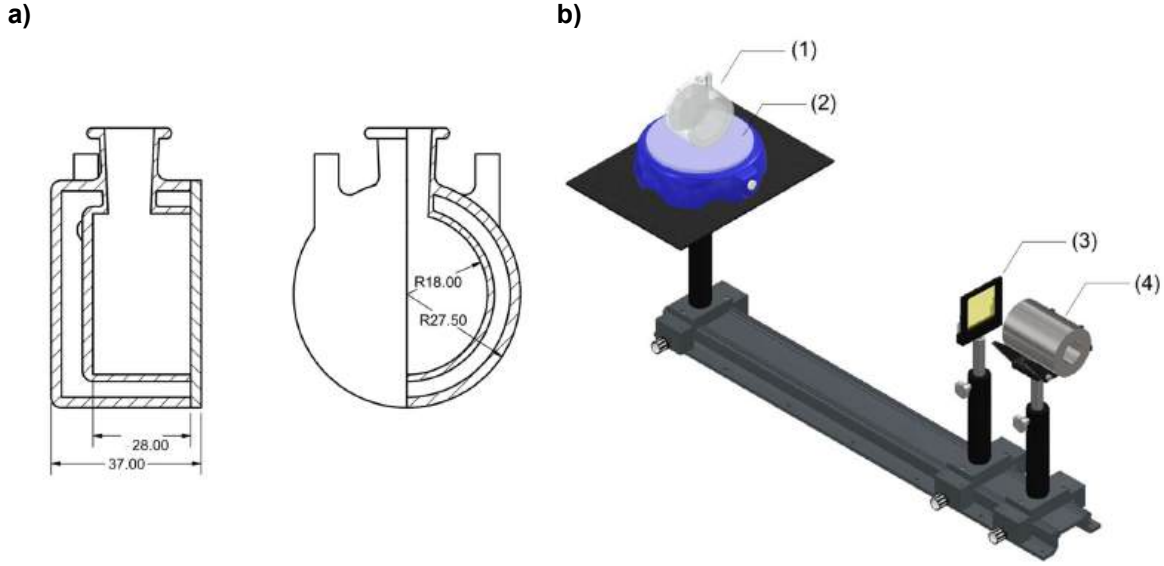

Figure 3.1. Schematic illustration of **a)** 25 cm^3 quartz reactor and **b)** experimental set-up. For better clarity of illustrations, Xenon lamp and thermostat were not presented. Adapted from [P6].

Moreover, the publication [P5] includes another experimental set-up. In that case, the experiments were carried out in a batch beaker-type glass reactor with a volume of 100 cm^3. The slurry photocatalyst suspension was exposed to 24 W UV-A light centered at 365 nm with a light intensity equal to 6 mW/cm^2.

In a typical experimental procedure, an appropriate concentration of the photocatalyst was dispersed under stirring in an aqueous solution of CECs. Before light introduction, the photocatalyst suspension was stirred for min. 30 minutes in the darkness to achieve the adsorption–desorption equilibrium. In case of PMS-assisted

processes, an Oxone® solution with appropriate concentration was added to the slurry system. The total PMS concentration in the reactor.

In the PhD dissertation, several organic contaminants classified as CECs were investigated, mostly PhACs and phenols, and listed in Table 3.1.

Table 3.1. CECs selected for investigation during PhD studies.

Name	CECs type	Molecular structure	λ_{max} (nm)
Phenol	Phenolic compound	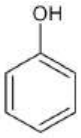	271
4-chlorophenol	Phenolic compound		224
Myclobutanil	Pesticide	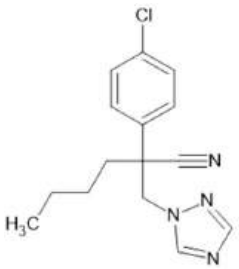	220
Naproxen	PhACs	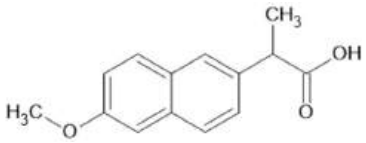	230
Ofloxacin	PhACs	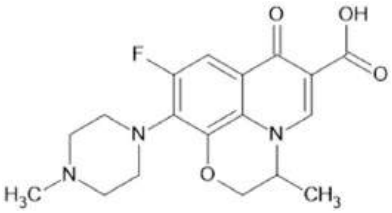	294
Carbamazepine	PhACs	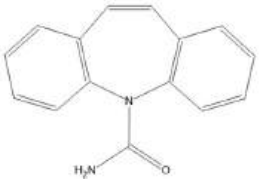	285

The concentration of degraded CECs was mostly monitored using a high-performance liquid chromatography (HPLC) combined with a photodiode array detector (PDA). Quantitative analysis of CECs was performed using the external calibration method with solutions of standard compounds. Optionally, the efficiency of the photocatalytic reaction was monitored as a change in the concentration of total organic carbon (TOC) before and after reaction, which is often attributed to the mineralization of

CECs to CO_2. In this regard, TOC analyzer was used. The concentrations of selected inorganic ions, mainly SO_4^{2-}, Cl^- and F^-, were monitored by Dionex ICS-1100 Ion Chromatography. Dionex™ Combined Seven Anion Standard II was used as an external standard to prepare the calibration curve. Metal leaching was monitored by inductively coupled plasma optical emission spectroscopy (ICP-OES). Intermediate products of CECs degradation were also examined in selected studies. In this regard, the high-performance liquid chromatography–mass spectrometry (LC-MS) system was employed. The mass spectrometer was operated in two modes: full scan and fragmentation ions monitoring.

The toxicity assessment of solutions after photocatalytic and PMS-assisted photocatalytic treatment was evaluated by Microtox® bioassay, based on the inhibition of luminescence from *Vibrio fischeri* bacteria. The measurements of light output were carried out after 5 min and 15 min. The toxic environment induces a decline in the light output, so the percent decrease in light output was recorded.

ROS generation by selected photocatalysts was also monitored by electron spin resonance (ESR) spectroscopy in the presence of spin traps. For spin trapping experiments, chemicals 5,5-Dimethyl-1-pyrroline N-oxide (DMPO), α-phenyl-N-tert-butylnitrone (PBN) and 2,2,6,6-tetramethyl-4-piperidinol (HTMP) were used. The measurements were performed at room temperature under aerobic and hypoxic conditions. Moreover, the photocatalytic generation of hydroxyl radicals (•OH) was examined by studying the selective oxidation of coumarin to 7-hydroxycoumarin (7-OHC) [120]. The concentration of 7-OHC was monitored by photoluminescence spectroscopy using an external calibration curve for quantification.

3.4. Computational techniques

Computational simulations of the electronic structure and energetics of the selected materials were performed based on density functional theory (DFT). Quantum Espresso software package was used for the calculations [121,122]. The preparation of all models was based on the existing crystallographic information files of the bulk crystal structures (.cif files), which were optimized concerning positions of all atoms and unit cell dimensions, following the Broyden–Fletcher–Goldfarb–Shanno algorithm (BFGS). Next, surface models were built from the optimized bulk structure, and geometry was further relaxed under the fixed cell dimensions, including all atoms in each case. Depending on the research study, further point defects, interfaces and adsorbing molecules were introduced, followed by analogous optimizations. Optimized models were used for further analysis of charge density (Bader [123]), its differences, density of states (DOS)

distributions and adsorption energies for the analyzed system(s). All procedures were calculated to the default threshold values of Quantum Espresso with Perdew-Burke-Ernzerhof (PBE) functionals [124]. Further details, like specific pseudopotentials, k-point grids, introduction of Hubbard on-site corrections (U), wave functions energy cut-off, *etc.* differed between the studies; however, they were always selected following the existing studies of similar systems (TiO_2, $TiOF_2$, $BiVO_4$).

In case of the publication [P5], the preparation of (0 0 1) TiO_2/$TiOF_2$ interface utilized fact of the almost identical unit cell lengths along the respective (0 0 1) and (1 0 0) planes of both structures (a_{TiO2} = 3.7845 Å and a_{TiOF2} = 3.798 Å, a 0.36% difference) and the known mechanism of the (1 0 0) $TiOF_2$ plane being an intermediate product for the growth of the anatase (0 0 1). Therefore, no detailed optimization of the interface model was needed, and the corresponding surfaces were directly connected *via* the planes created by OX and OY axes.

To estimate the ecological toxicity of selected by-products, the Ecological Structure Activity Relationships (ECOSAR) software was used to assess acute and chronic toxicity potential.

4. RESULTS

The canon of doctoral dissertation [P1-P6] includes the theoretical and experimental approach to better understand the role of morphology and phase composition of the photocatalyst on physicochemical properties, photocatalytic activity and PMS activation. During PhD studies, numerous aspects were considered for investigation. Based on the research performed, five research articles and one book chapter were published. All the studies and related manuscripts listed in the dissertation have three features in common:

- material characterization was performed and described in each research article,
- each photocatalyst was applied in the degradation of contaminants of emerging concern in the aqueous phase,
- only heterogeneous advanced oxidation processes based on photocatalysis were considered for investigation.

The most important aspects discussed in chapters are presented in Table 4.1.

Table 4.1. The summary of the research considered in chapters and articles, marked in green.

Key aspects under consideration	**Chapters**					
	I	**II**	**III**	**IV**	**V**	**VI**
TiO_2-based photocatalysts						
Photocatalysts with scheelite-type structure						
Precursor design ($TiOF_2$ or NH_4VO_3)						
Crystal facets engineering						
Surface modification/Formation of heterojunction						
UV-light active photocatalysts						
Visible-light active photocatalysts						
PMS-assisted photocatalytic oxidation						
Degradation of phenolic compounds						
Degradation of pharmaceutically active compounds						
Degradation of pesticides						
Analysis of TOC conversion						
Generation of radicals						
Toxicity assessment						
DFT calculations						

4.1. Chapter I: Photocatalytic activity of alkaline-earth metal scheelite-type tungstates and molybdates

Based on **[P1]** M. Kowalkińska, P. Głuchowski, T. Swebocki, T. Ossowski, A. Ostrowski, W. Bednarski, J. Karczewski, A. Zielińska-Jurek, *Scheelite-Type Wide-Bandgap ABO_4 Compounds (A = Ca, Sr, and Ba; B = Mo and W) as Potential Photocatalysts for Water Treatment,* The Journal of Physical Chemistry C, 125(46), 2021, 25497-25513.

In the present study, alkaline-earth metal compounds with scheelite-type structure and general formula ABO_4 (*A* = Ca, Sr, Ba and *B* = Mo, W) were investigated for photocatalytic phenol degradation. The main motivation was to develop earth-abundant materials for photocatalytic applications. Many of these compounds occur naturally as minerals, such as $CaWO_4$ (scheelite) and $CaMoO_4$ (powellite) [125]. Therefore, the main goal of these studies was analyses of alkaline-earth metal tungstates and molybdates as potential photocatalytic active materials.

Structural characterization confirmed that all synthesized materials crystallized in the tetragonal scheelite structure with high crystallinity, while morphological analyses using SEM microscopy revealed microspheres for Ca- and Sr-based compounds and formation of microcrystals for Ba-based ones. The specific surface areas were extremely low (less than 10 m^2/g for almost all samples), particularly for $BaWO_4$ and $BaMoO_4$, which would suggest poor photocatalytic performance due to low dispersion in aqueous solution. All the obtained materials absorb light in the UV range (as shown in Figure 4.1.a), which is typical for wide-bandgap compounds and could be a limiting factor that affects the photocatalytic performance in the UV-vis range.

However, the experimental results revealed that as-synthesized tungstates and molybdates were capable of degrading phenol despite their low specific surface area and wide band gap energy, depicted in Figure 4.1.b. HPLC analyses confirmed the formation of catechol and hydroquinone as the main intermediate products of phenol oxidation. The highest rates of phenol degradation were achieved for $BaWO_4$ and $SrWO_4$, which exhibited the longest average charge carrier lifetimes, as proved by time-resolved photoluminescence spectroscopy. Thermoluminescence (TL) glow curves revealed that trap depths strongly influenced the photocatalytic activity. Tungstates exhibited shallower traps which promoted the electron transfer, in opposite to molybdates' deeper. These results, collected and presented in Table 4.2, were consistent with electrochemical measurements, which shown that AWO_4 tungstates had less insulating character than $AMoO_4$, and more efficient charge transfer can be achieved.

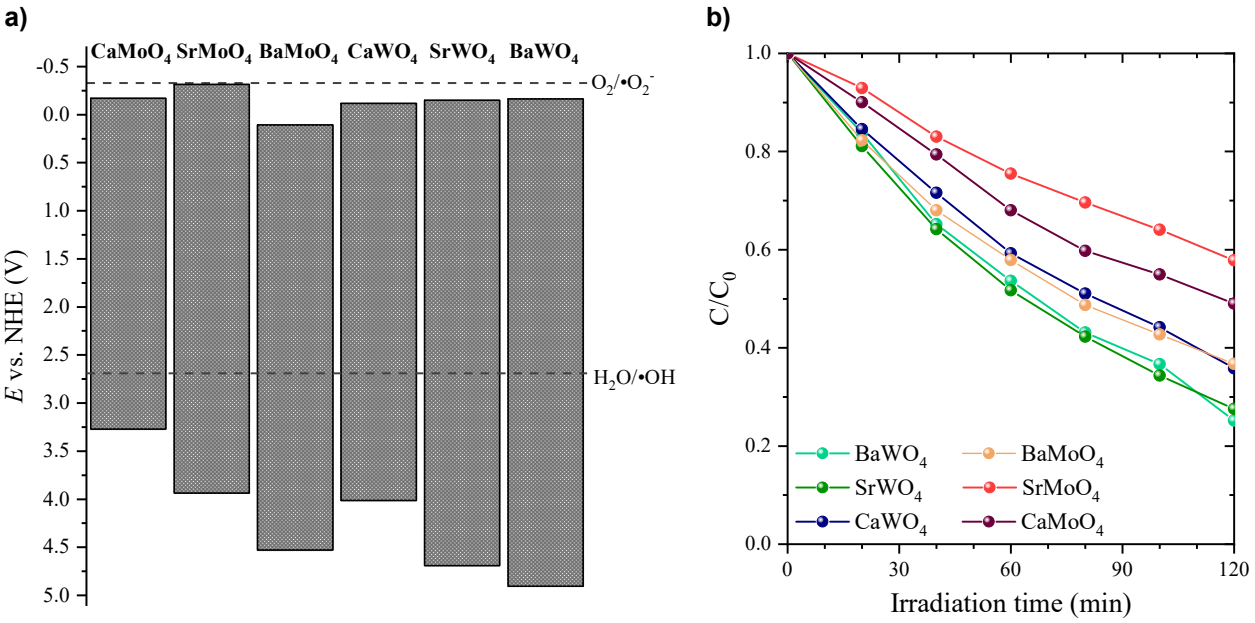

Figure 4.1. a) Band edge positions determined from the Mott−Schottky analysis and UV−vis absorption and **b)** photocatalytic phenol degradation over ABO_4 compounds under UV-vis light.

Table 4.2. The photoluminescence carrier lifetimes and energy traps for scheelite-type compounds, derived from TRPL and TL spectroscopy.

Compound	τ_1 (μs)	τ_2 (μs)	<τ> (μs)	Trap energy (eV)
$CaMoO_4$	20.11 ± 2.03	10.89 ± 1.26	17.08 ± 3.71	0.71 ± 0.02 0.89 ± 0.04
$SrMoO_4$	35.53 ± 0.13	4.17 ± 0.03	8.61 ± 0.10	0.70 ± 0.01
$BaMoO_4$	61.62 ± 2.53	29.98 ± 1.85	50.76 ± 5.22	0.74 ± 0.02
$CaWO_4$	129.61 ± 7.39	10.16 ± 0.03	12.38 ± 0.75	0.65 ± 0.01 0.87 ± 0.03
$SrWO_4$	110.12 ± 0.35	-	110.12 ± 0.35	0.63 ± 0.01
$BaWO_4$	110.25 ± 0.29	-	110.25 ± 0.29	0.70 ± 0.02

Finally, the mechanism of ROS generation was investigated for $SrWO_4$ and $BaWO_4$ using electron spin resonance (ESR) spectroscopy with PBN as a spin trap. The ESR spectra of the UV-irradiated suspensions, shown in Figure 4.2, contained signals typical for hydroxyl radicals. However, the comparison of ESR spectra under aerobic and hypoxic conditions suggested that superoxide radicals can also be formed, although they were not directly detected.

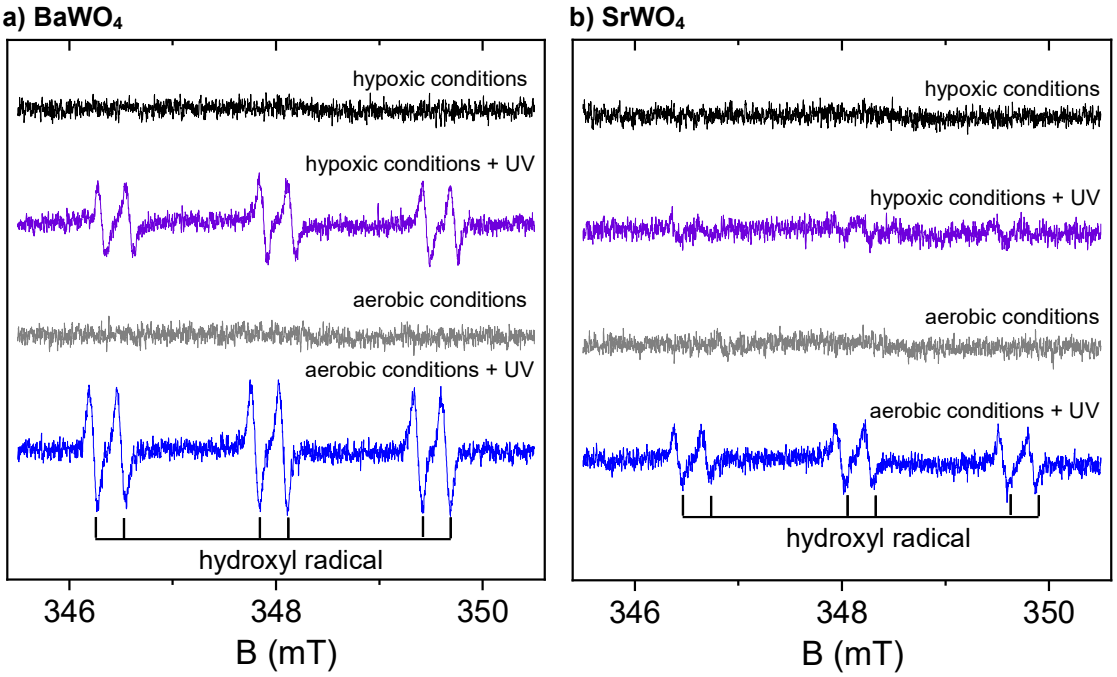

Figure 4.2. ESR spectra of **a)** $BaWO_4$ and **b)** $SrWO_4$ aqueous suspension, contained PBN as a spin trap performed under hypoxic and aerobic conditions before and after UV irradiation.

The presented results confirmed that alkali-earth metal scheelite-type compounds can be used as photocatalysts upon UV irradiation. However, their photocatalytic activity remains low compared to other wide-band gap semiconductors like TiO_2. In this regard, the investigation of scheelite-type compounds in the photocatalytic degradation of organic contaminants was further shifted to bismuth orthovanadate.

THE JOURNAL OF PHYSICAL CHEMISTRY C
A JOURNAL OF THE AMERICAN CHEMICAL SOCIETY

pubs.acs.org/JPCC

Article

Scheelite-Type Wide-Bandgap ABO_4 Compounds (A = Ca, Sr, and Ba; B = Mo and W) as Potential Photocatalysts for Water Treatment

Marta Kowalkińska,* Paweł Głuchowski, Tomasz Swebocki, Tadeusz Ossowski, Adam Ostrowski, Waldemar Bednarski, Jakub Karczewski, and Anna Zielińska-Jurek*

Cite This: *J. Phys. Chem. C* 2021, 125, 25497−25513

Read Online

ACCESS | Metrics & More | Article Recommendations | Supporting Information

ABSTRACT: In the present study, alkaline earth metal scheelite-type ABO_4 compounds (A = Ca, Sr, and Ba; B = Mo and W) synthesized by a hydrothermal method were systematically studied. The as-obtained photocatalysts were characterized by X-ray diffraction (XRD), scanning electron microscopy (SEM), Brunauer−Emmett−Teller (BET) surface area analysis, UV−vis diffuse reflectance (DR/UV−vis) spectroscopy, photoluminescence, and thermoluminescence (TL) spectroscopy together with charge carrier lifetime measurements, electron paramagnetic resonance (EPR) spectroscopy, and electrochemical impedance spectroscopy (EIS). The photocatalytic activity was studied in the reaction of phenol degradation under simulated solar light. The obtained tungstates and molybdates revealed excellent photocatalytic activity despite the low surface area and wide bandgap typical for insulators. The mechanism of phenol degradation proceeded through hydroquinone and catechol formation in the presence of hydroxyl and superoxide radicals. The presence of electron traps allowed absorption of light with lower energy than resulting from the absorption edge. $BaWO_4$ and $SrWO_4$, with the most extended average carrier lifetime, were the most efficient photocatalysts from the obtained series. In general, molybdates exhibited lower photocatalytic activity toward phenol degradation due to deeper trap states and lower average charge carrier lifetimes than tungstates. Additionally, electrochemical studies demonstrated that molybdates exhibit more insulating behavior than tungstates. The overall results showed that wide-bandgap semiconductors, mainly tungstates, can be applied as earth-abundant photocatalytic materials for the degradation of persistent organic pollutants.

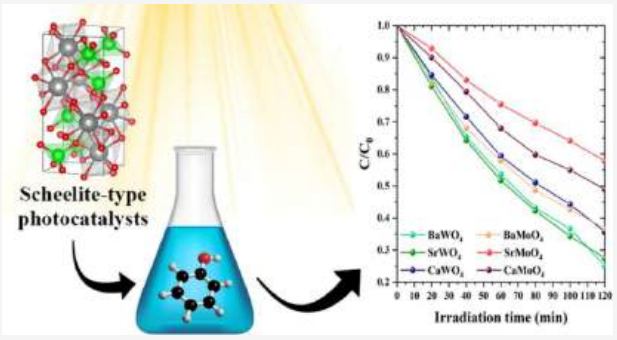

1. INTRODUCTION

The environmental pollution due to increased agricultural, industrial, and domestic activities has led to the global need to develop advanced and more effective water treatment technologies. Heterogeneous photocatalysis belonging to the group of advanced oxidation processes (AOPs) has been demonstrated as a green technology for removing toxic contaminants and energy production. The main advantage is the possibility of light-induced degradation of the broad spectrum of recalcitrant organic pollutants.[1−5] The most frequently studied photocatalysts include oxides, sulfides, selenides, and iodides as single and hybrid compounds.[6] However, the ability to apply heterogeneous photocatalysis in wastewater treatment at a full technological scale requires the application of earth-abundant photocatalytic materials, whose preparation method will not be expensive or sophisticated.

Many inorganic solids from the class of materials with ABO_4 composition occur naturally, including $CaWO_4$ (scheelite) or $CaMoO_4$ (powellite).[7] Scheelite-type compounds with the composition ABO_4, in which A and B cations are different elements with various oxidation states, have been investigated in recent years due to their attractive properties and potential applications as Raman lasers,[8,9] cryogenic scintillation detectors,[10,11] white light-emitting diodes,[12] and a highly suitable host for luminescent materials due to thermal and chemical stability.[12−14] The synthesis of these materials can be cost-effective and simple; the most popular method is a facile co-precipitation.[15] Scheelite-type compounds possess a tetragonal structure characterized by a $I41/a$ space group (no. 88). Each of the B atoms (B = Mo and W) is 4-fold-coordinated, forming the $[BO_4]^{2-}$ tetrahedral configuration, while each divalent metal A^{II} shares corners with eight adjacent oxygen atoms from the $[BO_4]^{2-}$ tetrahedra, composing the AO_8 polyhedra (bisdisphenoid).[16] The scheelite structure, which

Received: July 20, 2021
Revised: October 28, 2021
Published: November 12, 2021

was visualized using the VESTA program,[17] is presented in Figure 1.

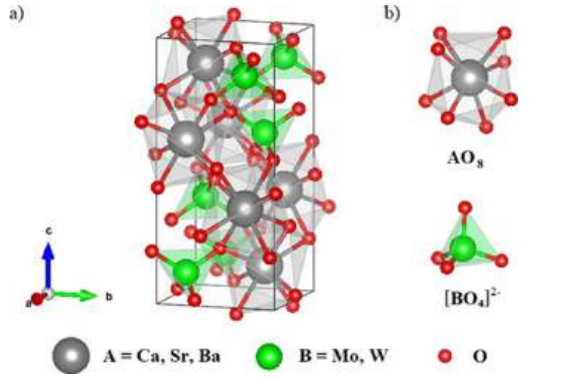

Figure 1. Visualization of the (a) scheelite structure, (b) AO_8, and $[BO_4]^{2-}$ polyhedra.

Since scheelite-type compounds are mainly semiconductors, they are supposed to have photocatalytic properties. Previous sparse studies have focused on the possibility of application ABO_4 compounds in photocatalytic degradation of organic dyes,[18−20] salicylic acid,[21] tetracycline, or hydrogen generation.[22] However, in these reports, for scheelite-type compounds due to their wide bandgaps of about 4−5 eV, only high energy-consuming ultraviolet radiation was applied to study the efficiency of photocatalytic processes. However, the high value of E_g does not have to be an obstacle for the application of scheelite-type materials as photocatalysts because it may increase the valence band maximum to higher energy levels relative to the redox potentials of adsorbed molecules. This rise might contribute to the higher reactivity of electrons in semiconductors.[23] For example, Dong *et al.* demonstrated the O-vacancy defects present in the typical insulator $BaCO_3$, which played dominant roles in the photocatalytic removal of NO.[24] Similar observations were also noticed by Cui *et al.* in $BaSO_4$ with intrinsic Ba vacancy.[25] All of these examples suggest that scheelite-type compounds containing Ba, Sr, or Ca cations might exhibit good photocatalytic performance, despite large values of E_g. The wide-bandgap photocatalysts can be used as a co-catalyst to facilitate the migration of charge carriers from the semiconductor photocatalyst or a locked layer to prevent the recombination of charge carriers.[26]

In this regard, in the present study, the alkaline earth tungstates and molybdates with interesting luminescence and structural properties were studied for the first time as potential alkali earth metal-abundant photocatalytic materials. Alkaline earth metal scheelite-type ABO_4 compounds (A = Ca, Sr, and Ba; B = Mo and W) as examples of wide-bandgap semiconductors were applied for phenol photodegradation. Phenol was selected as a model pollutant since it is photostable and non-volatile, and the mechanism of phenol degradation is well established. Moreover, phenol is produced by chemical, food-processing, or biotechnological industries. Phenol and its derivatives are hardly biodegradable and have a phytotoxic effect on the microorganisms responsible for their biological degradation.[27,28] Also, the current phenol levels and removal of their derivatives from water, which can be achieved using conventional water treatment technologies, are often unsatisfactory. The photocatalytic degradation of phenol in water starts with the formation of a phenoxy radical due to the reaction between phenol molecules and photocatalytically generated hydroxyl radicals ($^{\bullet}OH$). These phenoxy radicals are in resonance with two radical structures in the ortho- and para-positions; thus, di-hydroxylated side products, such as catechol and hydroquinone, are formed. After that, further oxidation of phenol derivatives occurs, and finally, the photocatalytic process leads to the opening of the benzene ring and the formation of shorter aliphatic compounds, which can be easily mineralized to carbon(IV) dioxide.[29,30] However, phenol photocatalytic degradation is still challenging because it is dependent on the efficiency of the generation of reactive oxygen species (ROS), especially $^{\bullet}OH$ and $^{\bullet}O_2^-$ radicals. Aslam *et al.* have reported that superoxide radicals were the major contributors in phenol degradation because only the $^{\bullet}O_2^-$ radicals can open the phenyl ring and contribute to the loss of aromaticity. These observations were noticed for disc-shaped WO_3 photocatalysts.[31]

The main aim of the present work was the demonstration of alkaline earth metal tungstates and molybdates as potential photocatalysts in a broad sense, including also crucial differences between tungstates and molybdates. The ABO_4 compounds were studied for the first time as potential alkali earth metal-abundant materials for UV−vis light-induced phenol photocatalytic degradation. Furthermore, the effects of morphology, their electrochemical and optical properties, and their influence on the mechanism of phenol degradation were also studied in detail.

2. METHODS

2.1. Fabrication of Metal Tungstates and Molybdates. Alkaline earth metal tungstates and molybdates, namely, $CaWO_4$, $SrWO_4$, $BaWO_4$, $CaMoO_4$, $SrMoO_4$, and $BaMoO_4$, were synthesized by a hydrothermal method without using any surfactant or stabilizing agent. Calcium chloride ($CaCl_2$), strontium chloride hexahydrate ($SrCl_2{\cdot}6H_2O$), barium nitrate ($Ba(NO_3)_2$), sodium tungstate dihydrate ($Na_2WO_4{\cdot}2H_2O$), and sodium molybdate dihydrate ($Na_2MoO_4{\cdot}2H_2O$) were used as received from Sigma-Aldrich without any purification. In a typical synthesis of scheelite-type compounds, a stoichiometric amount of alkali metal salts and $Na_2WO_4{\cdot}2H_2O$ (metal tungstates) or $Na_2MoO_4{\cdot}2H_2O$ (metal molybdates) were dissolved in 50 cm^3 distilled water separately. The solution containing sodium molybdates or tungstates was placed inside a 200 cm^3 Teflon-lined reactor, and the second solution was added dropwise to the reactor. The obtained mixtures were stirred for 30 min to form stable suspensions using a Teflon-coated magnetic stirrer bar. After that, the reactor was transferred into a stainless steel autoclave immediately and was heated at 160 °C for 6 h in an oven and then cooled down to room temperature. The obtained products were separated through centrifugation and were washed thoroughly with deionized water to remove the residual contamination. After drying at 80 °C to dry mass, the white powders were obtained.

2.2. Material Characterization. The structure and phase composition of the obtained compounds were investigated by powder X-ray diffraction (XRD). XRD patterns were recorded on the Rigaku MiniFlex 600 X-ray diffractometer with Cu Kα radiation (λ = 1.5405 Å) in the 10−80° range (step 1°/min). Rietveld refinements of the diffraction data were performed using the X'Pert HighScorePlus software package (PANalytical, 2006) with data fitting based on the pseudo-Voigt profile

https://doi.org/10.1021/acs.jpcc.1c06481
J. Phys. Chem. C 2021, 125, 25497−25513

function. The specimen displacement, lattice parameters, polynomial coefficients for the background function, profile parameters, and Gaussian and Lorentzian profile coefficients were refined.

The alkaline earth tungstates and molybdate morphologies were characterized by scanning electron microscopy (SEM) with a field emission gun, model FEI Quanta FEG 250. In addition, the Micromeritics Gemini V instrument was used to determine the porous structure parameters of the scheelite-type compounds and adsorption isotherms, including Brunauer–Emmett–Teller (BET) surface area and pore volume, using low-temperature nitrogen sorption. Before measurement, the analyzed materials were degassed at 200 °C for 2 h. The surface area was determined by the multipoint BET method in the p/p_0 range from 0.05 to 0.30. The total pore volumes were estimated from the adsorbed amount of nitrogen at p/p_0 = 0.995. The average pore diameters were calculated from adsorption isotherms according to the procedure described in Soltanali and Darian.[32] By using the Barrett–Joyner–Halenda (BJH) method, pore size distributions were derived from the branches of the adsorption isotherms.

2.3. Optical Properties. The UV–visible diffuse reflectance spectra (DRS/UV–vis) were measured on a Thermo Fisher Scientific Evolution 220 spectrophotometer using $BaSO_4$ as a reflectance standard. Based on the obtained data, the bandgap energy calculations were performed using Tauc's method.[33] The excitation and luminescence spectra were recorded using an FLS980 fluorescence spectrophotometer from Edinburg Instruments equipped with a 450 W xenon lamp as an excitation source and a Hamamatsu 928 PMT detector. Measured spectra were corrected for the sensitivity and wavelength of the experimental setup. The slit width was 2 μm (excitation spectra) or 0.3 μm (emission spectra). The same equipment was used for decay measurements, and the lamp was changed to a 150 W pulse xenon lamp. All spectra were recorded at room temperature. Based on these measurements, the carrier lifetime of photocatalysts was calculated. The best luminescence decay curve fits of the data were noticed from a poly-phase exponential decay function with time constant parameters (eq 1)

$$I(t) = \sum_{i=1}^{n} \alpha_i \cdot \exp\left(-\frac{t}{\tau_i}\right) + y_0 \tag{1}$$

where $I(t)$ is the intensity, α_i is the pre-exponential scaling factor, $\langle\tau\rangle$ is the lifetime of the ith exponential component, and y_0 is a constant. The average lifetime $\langle\tau\rangle$ is given by eq 2

$$\langle\tau\rangle = \frac{\sum_{i=1}^{n} \alpha_i \tau_i^2}{\sum_{i=2}^{n} \alpha_i \tau_i} \tag{2}$$

The errors associated with the carrier lifetime evaluations consider only the uncertainty in decay curve fitting.[34,35]

The thermoluminescence (TL) glow curves were collected from room temperature up to 300 °C with a heating rate of 5 K/s after 5 min of X-ray irradiation. A Varian VF-50J/S RTG tube with a tungsten core and copper case as an X-ray radiation source was used as an irradiation source. The voltage and amperage for the X-ray source were 35 kV and 0.7 mA, respectively. The signal was collected with an R13456 PMT (Hamamatsu Photonics) monitoring the global emission from the whole spectral response (from 185 to 980 nm) with an integration (channel) time of 0.1 s without a filter. The energy of the traps was calculated according to the general-order expression describing intensity I as a function of temperature T (eq 3)[36,37]

$$I(T) = sn_0 \cdot \exp\left(\frac{E}{k_B T}\right) \cdot \left[\frac{(l-1)s}{\beta} \cdot \int_{T_0}^{T} \exp\left(-\frac{E}{k_B T}\right) dT + 1\right]^{-l(l-1)} \tag{3}$$

where n_0 is the trap concentration at t = 0, k_B is Boltzmann's constant, and β is the heating rate. The kinetics order l was determined from the peak asymmetry defined as the thermal activation energy E. The parameter E is associated with the trap depth, assuming no re-trapping. The frequency factor s was obtained by taking the derivative of eq 3 with respect to T and setting it to zero at the peak temperature.

2.4. Electrode Surface Preparation, Electrochemical Measurements, and EPR Studies. Preparation of the electrode substrates modified with ABO_4 photocatalysts, suitable for electrochemical measurements, was performed in three stages: pretreatment, deposition of the sample, and surface blockage. Each sample was deposited onto FTO electrodes (7 Ω/sq) (Sigma Aldrich), 35 × 15 mm by size, by drop-casting a suspension of samples (V_{drop} = 0.005 cm^3). The suspension was prepared by mixing water/isopropanol solution (v/v: 3/1) with *ca.* 0.06 mol of the given sample. The suspension were then sonicated for a couple of seconds and drop-cast onto the electrode, followed by drying to evaporate the solvent completely. The surface blockage was carried out by spin-coating 0.1 cm^3 of Nafion (Sigma-Aldrich) onto the FTO surface (200 rpm). After this step, the electrodes were placed in the electrochemical cell for further experiments.

Electrochemical measurements were performed in a glass cell with a built-in cylindrical glassy carbon (GC) auxiliary electrode. A silver chloride (3 M KCl) electrode was used as a reference. A 0.25 M Na_2SO_4 was used as a supporting electrolyte, and a 2.5 mM solution of potassium hexacyanoferrate(II/III) $[Fe(CN)_6]^{3-/4-}$ was chosen as a redox probe. An Autolab Multi M204 potentiostat/galvanostat with the FRA32 module (Metrohm) was used for electrochemical measurements, and a built-in software, Nova 2.1.4., was used for EIS spectra fitting.

In the photochemical EPR experiments, the samples were prepared as an aqueous suspension of $BaWO_4$ or $SrWO_4$ (concentration 0.4 g cm^{-3}) in the presence of α-phenyl-*N*-*tert*-butylnitrone (PBN) spin trap (concentration 60 mmol dm^{-3}) at room temperature. Approximately 0.017 cm^3 mixture of PBN and $BaWO_4$ or $SrWO_4$ aqueous suspension was placed into a thin-walled quartz tube with 0.8 mm ID and put in an EPR cavity. LG UV LED (3 W, λ_{max} = 365 nm) was used as an irradiation source. During photochemical EPR experiments, the samples were irradiated directly in the EPR resonator with a light power of about 70 mW/cm^2. EPR measurements were performed both for samples obtained under aerobic and hypoxic conditions. For studies under aerobic or hypoxic conditions, air or N_2 was passed over the sample at a rate of a few dm^3 h^{-1}.

2.5. Determination of Photocatalytic Activity. The photocatalytic activity of the obtained samples was tested in a phenol degradation reaction performed in the black box. All mentioned chemicals were used as delivered by the provider

https://doi.org/10.1021/acs.jpcc.1c06481
J. Phys. Chem. C 2021, 125, 25497−25513

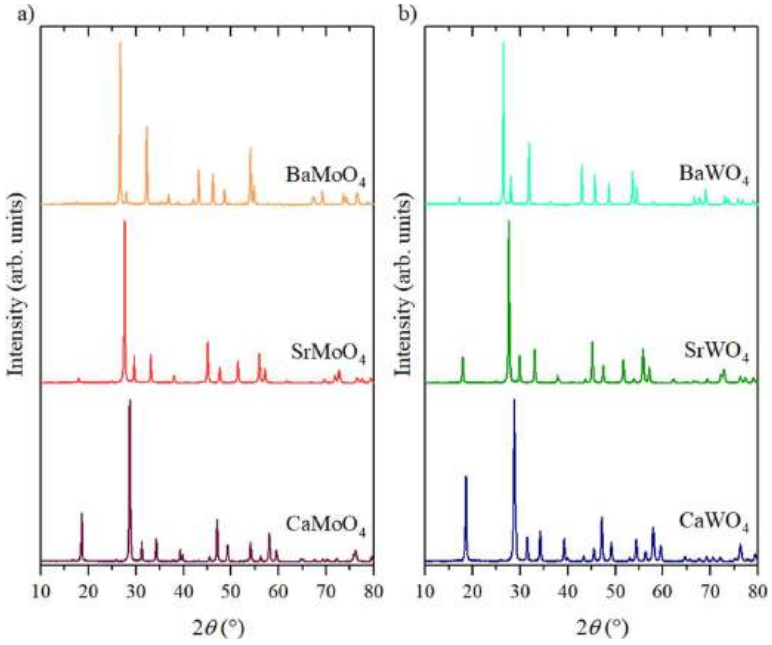

Figure 2. XRD patterns of obtained (a) molybdates and (b) tungstates.

Table 1. Structural Parameters of the Obtained Samples Using Rietveld Analysis

		lattice parameters			cation−oxygen distance		Rietveld refinement[a]		
compound	crystallite size estimation (nm)	a, b (Å)	c (Å)	V (Å^3)	A−O (Å)	B−O (Å)	R_{exp}(%)	R_{wp} (%)	χ^2
$CaMoO_4$	50	5.225	11.432	312.18	2.448	1.749	10.76	13.51	1.58
					2.477				
$SrMoO_4$	43	5.395	12.023	350.01	2.619	1.735	9.39	11.99	1.63
					2.626				
$BaMoO_4$	47	5.582	12.823	399.50	2.800	1.697	9.43	12.80	1.35
					2.808				
$CaWO_4$	31	5.240	11.368	312.10	2.358	1.890	10.20	12.70	1.55
					2.514				
$SrWO_4$	41	5.415	11.945	350.21	2.529	1.862	9.16	11.82	1.67
					2.533				
$BaWO_4$	75	5.612	12.721	401.70	2.704	1.825	9.73	12.52	1.30
					2.753				

[a]The uncertainty of structural parameters, including lattice constants and bond lengths, is strictly correlated with a Rietveld refinement quality. The insight into how well the model fits the experimental data is determined by expected profile residual (R_{exp}), weighted profile residual (R_{wp}), and goodness of fit (χ^2).

and were used without any purification. In a typical experiment of phenol photocatalytic degradation, 25 cm^3 of 0.21 mmol dm^{-3} phenol solution and 50 mg of the photocatalyst were put into a quartz reactor under magnetic stirring. A xenon lamp (model 6271H, Oriel, USA) was used as a simulated solar light source with a narrow range of UV light.[38] The UV spectrum flux intensity at the reactor border was set as 45 mW cm^{-2}. A constant air flow of 5 dm^3 h^{-1} was introduced during the reaction through suspension, which was thermostated to 20 °C. Before irradiation, the whole system was kept in the dark for 30 min to achieve the adsorption−desorption equilibrium. After that, the process was initiated by turning on the Xe lamp. The samples were collected at −30, 0, 20, 40, 60, 80, 100, and 120 min of the process, where 0 is the point of light introduction. The degradation efficiency was monitored using a high-performance liquid chromatography system (HPLC, model Shimadzu LC-6A), combined with a photodiode array detector (SPD-M20A) and a C18 column (Phenomenex Gemini 5 μm; 150 × 4.6 mm) working at 45 °C. During HPLC measurements, the mobile phase composed of (v/v) 70% acetonitrile, 29.5% water, and 0.5% orthophosphoric acid (85% w/w solution) was used at a flow rate of 0.3 cm^3 min^{-1}. Quantitative analysis of all the observed species was performed using standard compounds from Sigma-Aldrich using the external calibration method. An HPLC-grade acetonitrile and orthophosphoric acid solution was provided by Merck. Charge carrier scavengers, such as ammonium oxalate, silver nitrate, isopropyl alcohol, and benzoquinone, were provided by Sigma-Aldrich. Simultaneously, the total organic carbon (TOC) concentration after each process was monitored using the Shimadzu TOC-L analyzer.

https://doi.org/10.1021/acs.jpcc.1c06481
J. Phys. Chem. C 2021, 125, 25497−25513

3. RESULTS AND DISCUSSION

3.1. Structural and Morphological Analysis. To confirm the presence of single-phase metal tungstates and molybdates, XRD was performed, and the obtained patterns are presented in Figure 2. According to Rietveld analysis and CIF files, single-phase compounds with high crystallinity were successfully obtained. The refinement results revealed that all compounds crystallized in the tetragonal scheelite structure with the space group $I41/a$ and a good agreement between the recorded and calculated patterns were observed. The refined structural parameters of scheelite compounds are presented in Table 1. The lattice parameters (a and c) and the unit cell volume rise with the increasing ionic radii of alkaline earth ions (Ca^{2+} = 0.112 nm, Sr^{2+} = 0.125 nm, and Ba^{2+} = 0.142 nm) due to the change in the charge density of AO_8 together with the rise of metal's ionic radii.[16]

Additionally, the relative intensity of some peaks was changed in the same relation. For example, the signal at 20° 2θ originating from the (101) $CaMoO_4$ plane was lowered when the Ca atom was replaced by a heavier one and almost completely vanished in $BaMoO_4$. The average crystallite size was estimated from the (112) peaks at 30° 2θ using Scherrer's equation. The greatest crystallite size was noticed for $BaWO_4$, in which both the heaviest cation and transition metal were present.

The morphologies of alkali earth metal molybdates and tungstates were further studied by scanning electron microscopy analysis. Size distributions of particles or microcrystals are presented in Figure S1 in the Supporting Information. Figure 3a shows the uniform $CaWO_4$ microspheres with an average size of *ca.* 7 μm. These spheres consist of agglomerated nanoparticles with an average size of 79 ± 14 nm (Figure 3b). A similar morphology was observed for the $CaMoO_4$ (Figure 3c,d), $SrWO_4$ (Figure 4a,b), and $SrMoO_4$ (Figure 4c,d) samples, but in comparison with $CaWO_4$, their aggregates were more deformed. Additionally, nanoparticles present in $SrMoO_4$ microspheres were polyhedral, and the exposed crystal facets of nanocrystals can be easily observed. In the case of $BaWO_4$ (Figure 5a) and $BaMoO_4$ (Figure 5b) samples, polyhedra-shaped microcrystals presenting a polydisperse nature were observed. Similar morphologies were noticed by Cavalcante *et al.*[39] and Oliveira *et al.*,[40] suggesting enhanced crystal growth when heavy cations such as barium are introduced to the system. Although the nucleation rate of barium-based materials is slower than for strontium and calcium ones, the crystal growth is the fastest with Ba^{2+}. This effect explains the formation of microcrystals only for $BaMoO_4$ and $BaWO_4$.

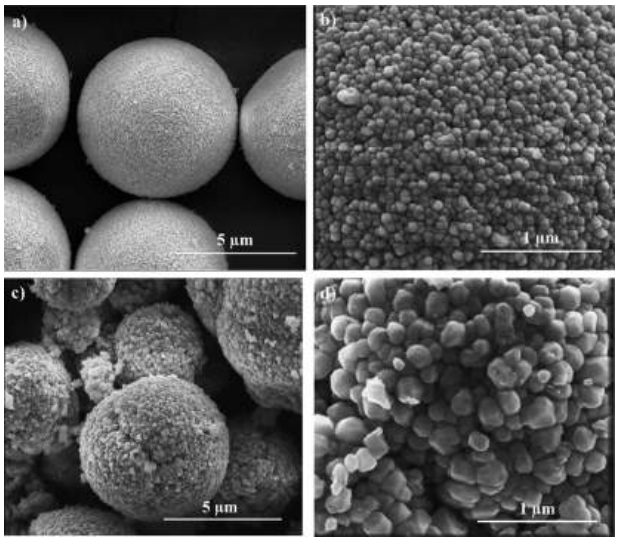

Figure 3. SEM images of $CaWO_4$ (a,b) and $CaMoO_4$ (c,d) microspheres and nanoparticles, respectively.

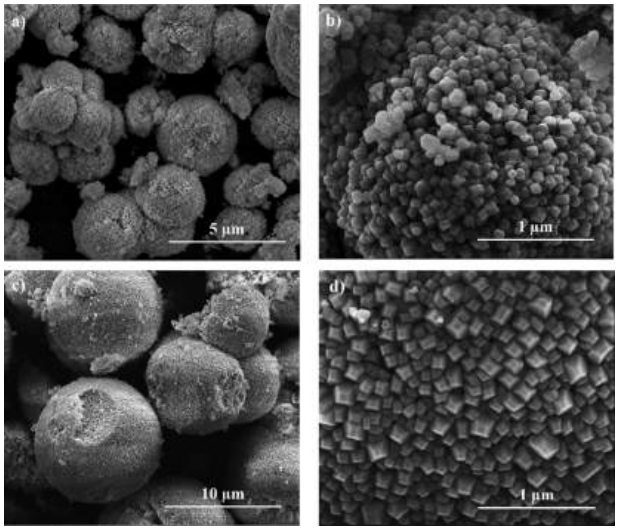

Figure 4. SEM images of $SrWO_4$ (a,b) and $SrMoO_4$ (c,d) microspheres and nanoparticles, respectively.

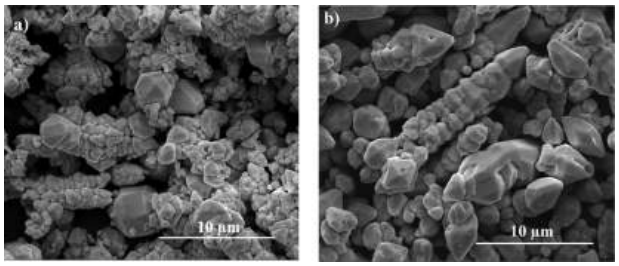

Figure 5. SEM images of $BaWO_4$ (a) and $BaMoO_4$ (b) microcrystals.

The data from electron microscopy were completed by surface area and pore analysis using the BET and BJH methods, as presented in Table 2. More detailed information, including adsorption isotherms and pore size distribution, are presented in Figure S2 in the Supporting Information. All samples were characterized by low surface area. Calcium and strontium compounds, which created the microspheres consisting of agglomerated nanoparticles, had surface areas ranging from 4 to 10 $m^2\ g^{-1}$, while $BaWO_4$ and $BaMoO_4$ possessed a reduced surface area of about 0.4−1 $m^2\ g^{-1}$. These results can be explained as the beginning of the aggregation process and the formation of microcrystals with smooth facets, as observed under SEM images. In the previous reports, the morphology of barium compounds was studied for $BaWO_4$ crystals with {1 1 2}, {0 0 1}, and {1 0 0} as predominantly exposed facets, in which the {1 1 2} facet is commonly the most exposed. However, edge-truncated octahedra can be noticed due to the destabilization of the {1 1 2} surface.[41] The preferential growth was also observed for $BaMoO_4$ crystals,

https://doi.org/10.1021/acs.jpcc.1c06481
J. Phys. Chem. C 2021, 125, 25497−25513

Table 2. Specific Surface Area and Morphology Summation of the Obtained Samples

Sample	surface area (m^2g^{-1})[a]	pore volume (cm^3g^{-1})[a]	mean agglomerate diameter (μm)	mean nanoparticle size (nm)
$CaMoO_4$	3.88 ± 0.17	0.0264 ± 0.0012	5.22 ± 1.18	195 ± 37
$SrMoO_4$	4.21 ± 0.04	0.0386 ± 0.0004	8.62 ± 1.81	141 ± 30
$BaMoO_4$	0.42 ± 0.20	0.0003 ± 0.0001	1.55 ± 0.56	-
$CaWO_4$	10.15 ± 0.29	0.0781 ± 0.0023	6.96 ± 0.94	79 ± 14
$SrWO_4$	6.98 ± 0.13	0.0537 ± 0.0011	2.39 ± 0.67	107 ± 22
$BaWO_4$	1.03 ± 0.14	0.0043 ± 0.0006	1.08 ± 0.70	-

[a]An average of three measurements ± the standard error.

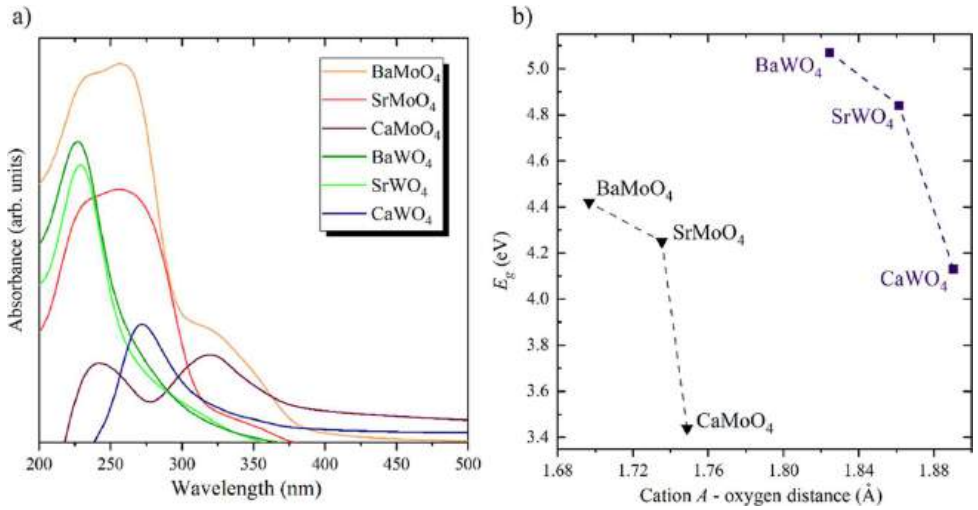

Figure 6. (a) DR/UV−vis spectra of the obtained tungstates and molybdates and (b) relation between the bandgap and the cation−oxygen distance of the obtained samples.

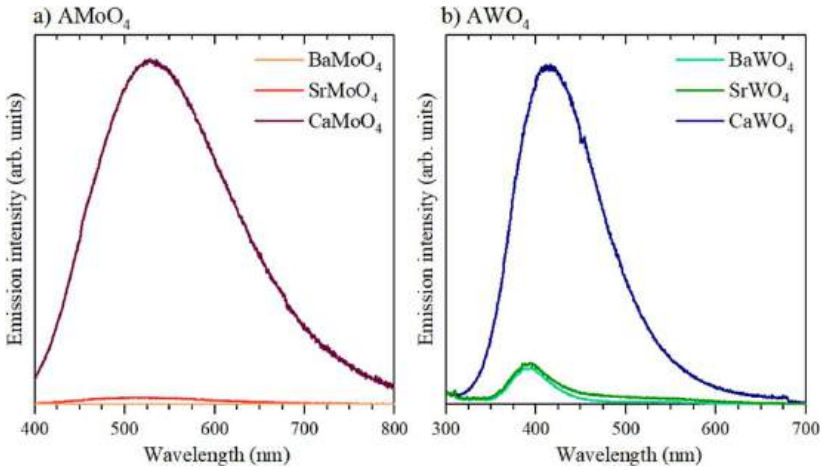

Figure 7. Emission spectra of alkali earth metals: (a) molybdates (λ_{exc} = 260 nm for $BaMoO_4$, λ_{exc} = 265 nm for $SrMoO_4$, and λ_{exc} = 261 nm for $CaMoO_4$) and (b) tungstates (λ_{exc} = 250 nm).

which occur along with the [0 0 1] direction of the micro-octahedrons.[39−41]

3.2. Absorption and Emission Spectroscopy Analysis.

The DR/UV−vis spectra of the obtained ABO_4 photocatalysts are presented in Figure 6a. All the obtained materials absorb light in the UV range, which is typical for wide-bandgap compounds. Therefore, the absorption of solar light irradiation can be limited because only 3−5% of the solar spectrum is ultraviolet light.[42,43] According to the recorded spectra, strontium and barium compounds possess the highest absorbance in the series; however, the absorption behavior is different for tungstates and molybdates. The spectra bands for AWO_4 materials are narrow, and probably single excitation states are observed. In contrast, the bands of $AMoO_4$ compounds are broader, with more overlapping excitation states.

After converting spectra to the Kubelka−Munk functions, the bandgaps of scheelite-type compounds were calculated. The transformations of these functions are presented in the Supporting Information (Figure S3). All photocatalysts are

https://doi.org/10.1021/acs.jpcc.1c06481
J. Phys. Chem. C 2021, 125, 25497−25513

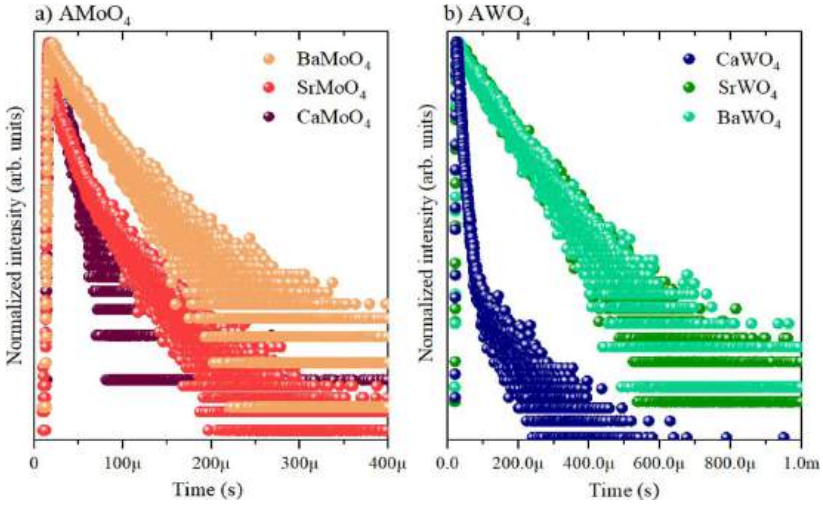

Figure 8. Luminescence decay curve of (a) molybdates (λ_{exc} = 260 nm for $BaMoO_4$, λ_{exc} = 265 nm for $SrMoO_4$, and λ_{exc} = 261 nm for $CaMoO_4$) and (b) tungstates (λ_{exc} = 250 nm).

Table 3. Carrier Lifetimes and Energy Traps for Scheelite-Type Photocatalysts

sample	τ_1 (μs)	τ_2 (μs)	$\langle\tau\rangle$ (μs)	trap energy (eV)
$CaMoO_4$	20.11 ± 2.03	10.89 ± 1.26	17.08 ± 3.71	0.71 ± 0.02
				0.89 ± 0.04
$SrMoO_4$	35.53 ± 0.13	4.17 ± 0.03	8.61 ± 0.10	0.70 ± 0.01
$BaMoO_4$	61.62 ± 2.53	29.98 ± 1.85	50.76 ± 5.22	0.74 ± 0.02
$CaWO_4$	129.61 ± 7.39	10.16 ± 0.03	12.38 ± 0.75	0.65 ± 0.01
				0.87 ± 0.03
$SrWO_4$	110.12 ± 0.35	-	110.12 ± 0.35	0.63 ± 0.01
$BaWO_4$	110.25 ± 0.29	-	110.25 ± 0.29	0.70 ± 0.02

wide-bandgap semiconductors close to the range typical for insulators.[24,44,45] Remarkably for *A* cations, the cation−oxygen distance decreases with the increase of the *A* ionic radius (see in Table 1 and Figure 6b). The reduction of the size of $[BO_4]^{2-}$ tetrahedra with simultaneous changes in AO_8 polyhedra (bisdisphenoid) led to the structural disorder and, in consequence, changed the crystal fields of each cation. The reduced strength of the coordinative bond from O atoms at larger distances led to lower crystal-field splitting. Therefore, it can be observed that the energy gap rises with a decrease of the cation *A*−oxygen distance (an increase of the *A* ionic radius). The same situation occurs if we take into account the cation *B* radii. The larger ion deforms the $[BO_4]^{2-}$ tetrahedra and may lead to a decrease of cation−oxygen distance and, in consequence, increasing the energy gap. This contributes to changes in the absorption properties of the scheelite-type compounds.

The emission spectra of the obtained scheelite-type photocatalysts are presented in Figure 7, while the excitation results are presented in Figure S4 in the Supporting Information. Among the series, the most intense photoluminescence was observed for calcium compounds. These bands, located at about 527 nm ($CaMoO_4$) or 413 nm ($CaWO_4$), were attributed to the intrinsic luminescence of the host lattice.[46,47] It is worth mentioning that the blue emission from $CaWO_4$ and green from $CaMoO_4$ were visible with the naked eye under UV light excitation. While comparing the emission spectra of molybdates (Figure 7a) with those of tungstates (Figure 7b), a blue shift can be seen, especially for $SrWO_4$ and $BaWO_4$. According to Puma and Yue,[48] the degradation rates can be significantly enhanced by shifting the irradiation toward a lower wavelength (higher energy). Therefore, although the emission intensity for $BaWO_4$ and $SrWO_4$ is lower (compared with $CaWO_4$ and $CaMoO_4$), their photoactivity can be higher due to the higher emission energy.

Generally, the photoluminescence emission is strongly connected with radiative recombination processes because they result from optically excited semiconductors. The excitonic photoluminescence signal can origin from surface oxygen vacancies or defects of semiconductors. The lattice distortions may positively impact the photocatalytic performance because they can easily bind electrons to form excitons in the sub-band.[49,50] As the result of the defect binding of the photoinduced electrons, the photoluminescence signal can easily occur. In that case, the stronger the emission signal, the higher the photocatalytic activity, so oxygen vacancies and lattice distortions might favor photocatalytic reactions.[50] On the contrary, lattice distortions can also act as recombination centers that influence the lower photocatalytic performance compared to defect-free samples, as was shown by Liqiang *et al.*[51] Thus, the relation between structural defects and photocatalytic activity is challenging to determine based only on the photoluminescence signals.

In this regard, the optical properties of scheelite-type photocatalysts were completed by decay measurements. The luminescence decay curves and carrier lifetimes calculated from curve fits are presented in Figure 8 and Table 3, respectively. All materials in this series possess an average carrier lifetime in the range *ca.* 9−110 μs. In the $AMoO_4$ series, barium molybdate has the most extended carrier lifetime, whereas, in

https://doi.org/10.1021/acs.jpcc.1c06481
J. Phys. Chem. C 2021, 125, 25497−25513

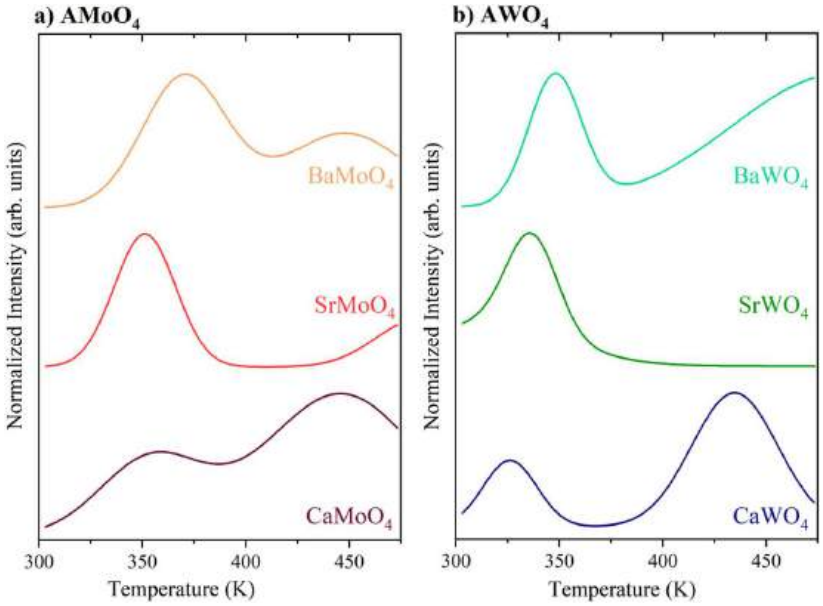

Figure 9. Thermoluminescence glow curves of alkali earth metals: (a) molybdates and (b) tungstates. The measurement was performed after 5 min of X-ray irradiation.

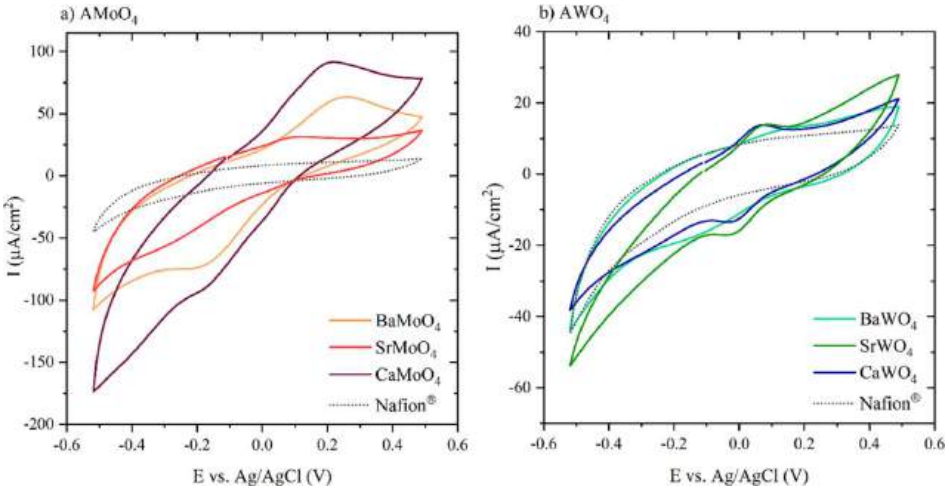

Figure 10. Cyclic voltammograms of (a) $AMoO_4$ and (b) AWO_4 (A = Ba, Ca, and Sr) recorded in the degassed 0.25 M Na_2SO_4 and 2.5 mM $[Fe(CN)_6]^{3-/4-}$ system.

the AWO_4 ones, both strontium and barium tungstates were characterized by the highest $\langle\tau\rangle$ value (110 μs). In general, the carrier lifetime of tungstates was more prolonged than that of molybdates, although the average lifetime for $CaWO_4$ was lower than for $CaMoO_4$. However, the τ_1 parameter for $CaWO_4$ was much higher than for other AWO_4 compounds, suggesting the presence of charge carrier traps. Several attempts at fitting the luminescence decay curves by a single exponential function have been made; however, these calculations were finished successfully only for $SrWO_4$ and $BaWO_4$. The remaining samples required poly-phase exponential decay models, which further suggest that these materials have structural defects in the lattice or the presence of recombination and trapping centers.[51,52] Optical measurements were further followed by electrochemical studies to complete photocatalyst characterization. However, it can be assumed that although the light absorption is limited, the photon amount is sufficient to create photogenerated charge carriers, which are necessary for initiating the photocatalytic reaction.

To confirm the presence of trapping centers in the obtained scheelite-type compounds, thermoluminescence (TL) spectroscopy was performed. Thermoluminescence is a phenomenon that refers to the light emission as a result of heating from an insulator or a wide-bandgap semiconductor that has already been irradiated by a radiation source. High temperatures cause emptying the filled trapping centers obtained from electrons, which then move toward the delocalized bands and finally undergo radiative recombination. The TL parameters of the thermal activation energy are associated with a trap depth.[53] The TL glow curves are presented in Figure 9. A distinct glow in Figure 9a was observed at ~371 and ~352 K for $BaMoO_4$ and $SrMoO_4$, respectively. A similar observation was noticed from Figure 9b for $BaWO_4$ (~348 K) and $SrWO_4$ (~336 K). It

https://doi.org/10.1021/acs.jpcc.1c06481
J. Phys. Chem. C 2021, 125, 25497−25513

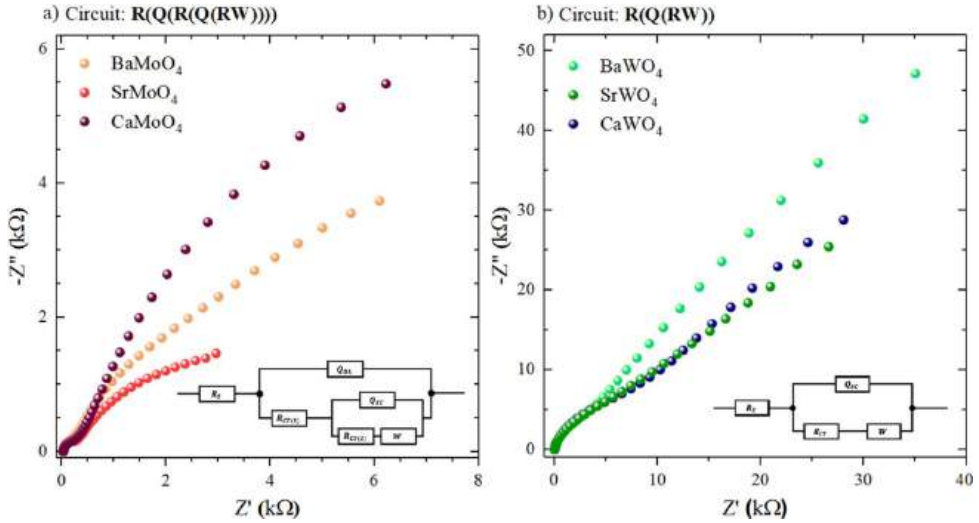

Figure 11. EIS spectra of (a) $AMoO_4$s and (b) AWO_4s (A = Ba, Ca, and Sr) recorded in the degassed 0.25 M Na_2SO_4 and 2.5 mM $[Fe(CN)_6]^{3-/4-}$ system.

is worth highlighting that the calcium compounds can be characterized by two glow peaks (~355 and ~446 K for $CaMoO_4$ and ~327 and ~435 K for $CaWO_4$), which suggest the presence of more than one trapping center.

Considering that the traps are located below the conduction band, it can be supposed that these compounds also absorb light with lower energy than determined by the absorption edge. Therefore, these materials are supposed to be applied as solar-driven photocatalysts. Moreover, the distribution and energy of traps affect photocatalytic efficiency. According to Kong *et al.*, the photocatalytic efficiencies increased with the increasing ratio of the amount of surface to total defects.[54] It was also shown that shallow traps (up to 0.7 eV) have higher electron-transfer efficiency from the defects to the species adsorbed on the surface.[55] The TL studies indicated a significant role of the type of cations *A* and *B* in the creation of electron traps in the scheelite structure, which, consequently, greatly impacts the photocatalytic process. The simple calculation of the energy of the traps (see Table 3) showed that molybdates have deeper traps and therefore should have lower photocatalytic efficiency compared to tungstates. It can also be seen that the scheelite with the smaller *A* cation are characterized by shallower traps, so more electrons can react with molecules such as phenol or water.

3.3. Electrochemical Studies. The profile of the as-synthesized photocatalysts was complemented by electrochemical measurements. First, cyclic voltammograms (CV) were recorded, as presented in Figure 10. By using a negatively charged inorganic probe ($[Fe(CN)_6]^{3-/4-}$), the behavior of the scheelite-type structures incorporated into the Nafion electrode surface was studied. As $[Fe(CN)_6]^{3-/4-}$ is a quasi-reversible probe, both the oxidation and reduction of Fe(II) and Fe(III) form of the probe on a bare, non-modified electrode should be observed. These processes are usually represented on voltammograms by current peaks. By studying the changes in peak height and position, different phenomena regarding the electron transfer can be discussed. The introduction of the Nafion film to the surface of the FTO electrode resulted in complete blockage of the electrode surface as we did not observe the reduction or oxidation process of $[Fe(CN)_6]^{3-/4-}$. This phenomenon can be explained by the nature of Nafion, which is rich in negatively charged SO_3- groups. These groups prevent charge transfer from $[Fe(CN)_6]^{3-/4-}$ due to the electrostatic repulsion of the redox probe.[56]

Meanwhile, implementing scheelite-type compounds into the conductive layer structure resulted in an appearance of slight $[Fe(CN)_6]^{3-/4-}$ peaks and an increase of capacitive currents of the electrode. Molybdates exhibited a much more significant rise in peak currents, with the anodic peak better shaped than the cathodic peak. It is worth mentioning that the difference of redox potential (ΔE) after modification of the surface is equal to *ca.* 370−390 mV. The unequal current response for the redox process together with high values of ΔE indicates the complex mechanism of charge transfer through the layer. We can observe the dependence on the divalent cation for the shape of CV voltammograms and measured currents.

On the other hand, tungstates demonstrated different electrochemical behaviors than molybdates. The recorded voltammograms seem to be less dependent on the cation present in the AWO_4 photocatalyst. Again, the $[Fe(CN)_6]^{3-/4-}$ peaks became visible but with much lower values of the faradaic currents of the probe. The electrochemical process seems to be reversible due to the difference in the reduction and oxidation voltage values of around ΔE *ca.* 82−90 mV. The comparison of the values of the oxidation and reduction current $|I_{pa}/I_{pk}| \approx 1$ confirms the reversibility of the $[Fe(CN)_6]^{3-/4-}$ process. Comparing the results for both groups, the barium and calcium compounds exhibited significantly better electrochemical features than strontium, which impeded the redox process on the electrode.

However, due to the chemical nature of the system and equivocal current changes, electron impedance spectroscopy (EIS) measurements were performed in order to explain the observed phenomenon. The Nyquist plot of EIS spectra of alkali earth metal tungstates and molybdates is presented in Figure 11. Few circuits were tested for data fitting, including R(Q(RW)), R(QR)(QR), and R(Q(R(Q(RW)))), with the last one fitting the best for all the $AMoO_4$ spectra and R(Q(RW)) for AWO_4. The recorded spectra differed in shape—two semi-circles were visible for molybdates, while for

https://doi.org/10.1021/acs.jpcc.1c06481
J. Phys. Chem. C 2021, 125, 25497−25513

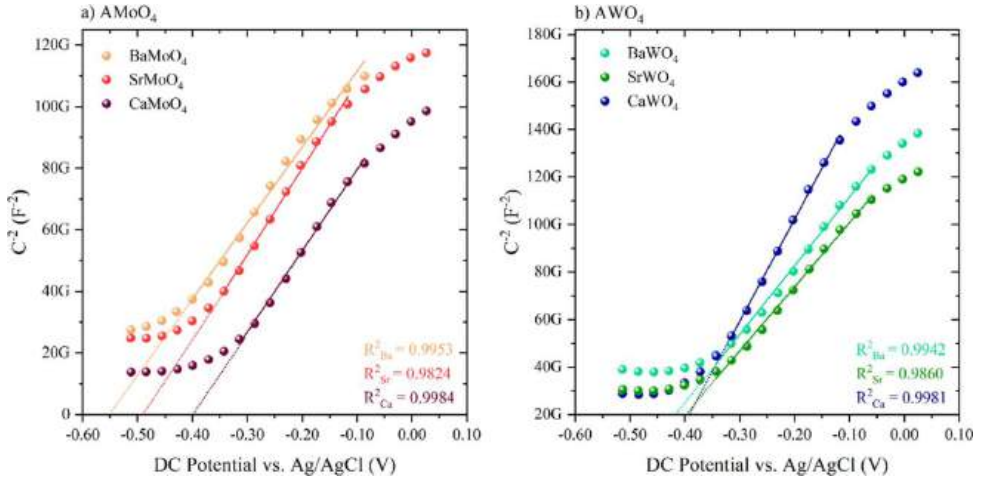

Figure 12. Mott–Schottky diagrams of (a) $AMoO_4$s and (b) AWO_4s (A = Ba, Ca, and Sr).

tungstates, no curvature of mid- to low-frequency impedance plot was observed. The shape of the $AMoO_4$ spectra indicated the possible presence of at least two charge-transfer resistances—one for the obtained material and the other one for FTO itself (*ca.* 200–300 Ω), whereas AWO_4 spectra showed only one charge-transfer resistance, which was a total resistance of FTO and the photocatalyst. The separated FTO resistance was not observed due to the high resistance of scheelite-type compounds, which impedes charge transfer resulting in the collapse of two resistances. By analyzing both coherent data, a distinct behavior of each group of samples can be observed. The obtained results suggest that the presence of tungstates changes the double layer so that it exhibits a more resistive nature than molybdates. Additionally, cyclic voltammograms indicated that AWO_4 compounds are better conductors than the $AMoO_4$ ones. Another possible explanation of improved reversibility for alkali earth metal tungstates suggests a formation of charge carrier channels in the layer of the conductive polymer. Both hypotheses are planned to be studied at a further stage of research.

In order to determine the flat band potential of the obtained samples, a Mott–Schottky analysis was performed (Figure 12). The flat bands (E_{FB}) and capacities (C_{SC}) of these photocatalysts are presented in Figure S5 and Table S1 in the Supporting Information. The positive slope in the linear region of the $f(E) = C_{SC}^{-2}$ (where C_{SC} is the capacitance of the semiconductor) plot was observed. The flat band potential (E_{FB}) was determined from the intersection of the slope with the *X*-axis (*x* position at $y = 0$). The obtained potential was later considered as a conductive band (E_{CB}) of investigated scheelite-type compounds. All the investigated samples are considered n-type semiconductors, which is in agreement with the previous reports.[22,57] Connecting these data with the EIS measurements, a significant difference between alkali earth metal tungstates and molybdates becomes even more visible. $AMoO_4$ compounds exhibited higher values of flat band potential compared to AWO_4. Moreover, the values of C_{SC} and E_{FB} for tungstates were more stable and did not differ very much between samples. On the other hand, the values of molybdates differed depending on the cation present in the compound.

According to Mott–Schottky diagrams and bandgap calculations from DR/UV–vis spectroscopy, the band positions of photocatalysts were calculated (Figure 13). This parameter determines the position of band edges at the

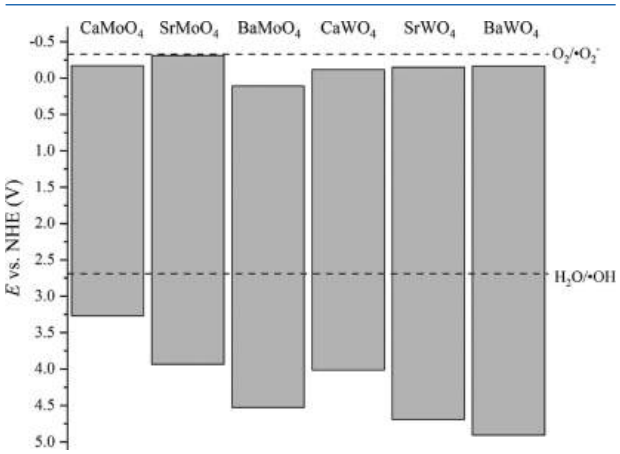

Figure 13. Band edge positions of the obtained photocatalysts determined from the Mott–Schottky analysis and UV–vis absorption. The length of the gray stripes corresponds to the bandgap energy values.

interface between the electrode material and the electrolyte.[58] Therefore, the potential of conduction band electrons and considering the obtained bandgap value, the valence band edge position can be estimated. Based on band positions, it is possible to predict the photocatalytic performance by monitoring the behavior of reactive oxygen species (ROS). The degradation of organic pollutants depends on ROS generation, especially $^{\bullet}OH$ and $^{\bullet}O_2^-$ through water oxidation and reduction of the adsorbed oxygen on the photocatalyst surface.[59] As can be observed in both diagrams, all the semiconductors exhibited a suitable conduction and valence band position to perform the reduction of water. Therefore, there is a possibility of oxidizing phenol using alkali earth metal tungstates and molybdates due to suitable band position to hydroxyl radical generation. It is worth noticing that in the first step of the reaction, the oxidation of phenol by hydroxyl radicals led mainly to the ortho- and para-oriented hydroxy derivatives.[60]

https://doi.org/10.1021/acs.jpcc.1c06481
J. Phys. Chem. C 2021, 125, 25497–25513

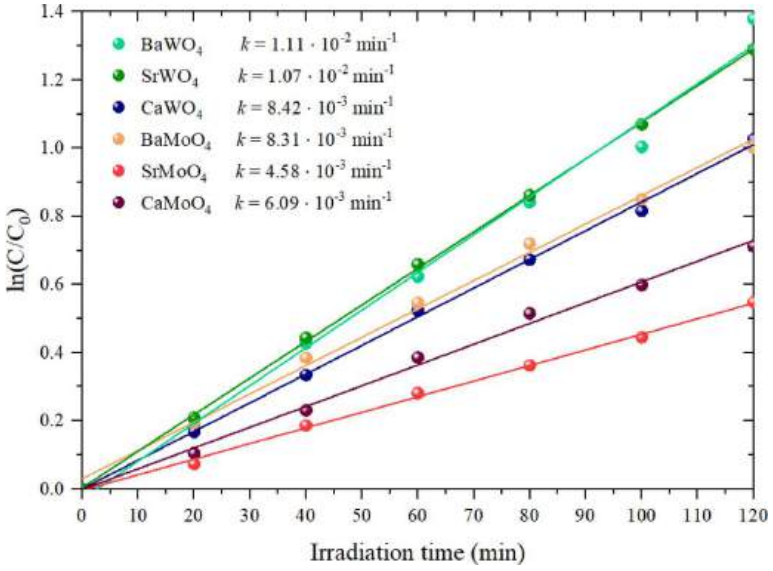

Figure 14. Photocatalytic phenol degradation for different alkali earth scheelite-type compounds.

Table 4. Comparison of ABO_4 with the Reported Unmodified Catalysts for Phenol Degradation

catalyst	initial phenol concentration (mg/L) and catalyst mass (g)	light source	surface area (m^2/g)	rate constant (10^{-3} min^{-1})	surface-area-normalized rate constants[a]	ref.
TiO_2 (Degussa P25)	20 mg/L 0.05 g	300 W Xe lamp, 45 mW/cm^2	55	90	0.033	68
TiO_2 (TBT hydrolysis)	20 mg/L 0.05 g	300 W Xe lamp, 30 mW/cm^2	169	9.8	0.015	69
ZnO	25 mg/L 0.02 g	300 W, light flux not mentioned	no information	5	-	70
WO_3 (Shanghai Chemicals)	40 mg/L 0.12 g[a]	300 W Hg lamp, light flux not mentioned	2.3	0.15	0.0005	71
CeO_2	40 mg/L 0.10 g	Hg lamp 4.4 mW	89	0.80	~0.0001	72
SnO_2	10 mg/L 0.065 g	8 W Hg lamp, 8 mW/cm^2	28	6.20[a]	0.003	73
$CaMoO_4$	20 mg/L 0.05 g	300 W Xe lamp, 45 mW/cm^2	3.88 ± 0.17	6.09 ± 0.20	0.031 ± 0.003	present work
$SrMoO_4$	20 mg/L 0.05 g	300 W Xe lamp, 45 mW/cm^2	4.21 ± 0.04	4.58 ± 0.10	0.022 ± 0.001	present work
$BaMoO_4$	20 mg/L 0.05 g	300 W Xe lamp, 45 mW/cm^2	0.42 ± 0.20	8.31 ± 0.24	0.396 ± 0.201	present work
$CaWO_4$	20 mg/L 0.05 g	300 W Xe lamp, 45 mW/cm^2	10.15 ± 0.29	8.42 ± 0.15	0.017 ± 0.001	present work
$SrWO_4$	20 mg/L 0.05 g	300 W Xe lamp, 45 mW/cm^2	6.98 ± 0.13	10.7 ± 0.09	0.031 ± 0.001	present work
$BaWO_4$	20 mg/L 0.05 g	300 W Xe lamp, 45 mW/cm^2	1.03 ± 0.14	11.1 ± 0.50	0.216 ± 0.040	present work

[a]For better comparison, some parameters were calculated based on the experimental results described in cited reports.

Except for $BaMoO_4$, each photocatalyst has a negative conduction band position. However, the occurrence of a one-electron process of O_2 reduction potential to $^{\bullet}O_2^-$ is doubtful (−0.33 eV for the standard gas state of 1 atm[61]) due to an

https://doi.org/10.1021/acs.jpcc.1c06481
J. Phys. Chem. C 2021, 125, 25497−25513

unsuitable band position. This indicates that the participation of superoxide radicals in the degradation reaction might be limited during the photocatalytic process.[62] However, the redox potential is not constant and is changed with process parameters such as a type of gas or a gas flow. Wardman[63] has calculated the redox potential of $O_2/^{\bullet}O_2^-$ process for 0.2 atm in air and in the case of oxygen concentration equals to 1 M in water. These values were estimated to be −0.29 and −0.16 V, respectively. Therefore, scheelite-type compounds may be capable of generating $^{\bullet}O_2^-$ radicals because the introduction of air and dissolved oxygen in the water system leads to lowering the absolute value of the redox potential. Another possible explanation of these results is that the reduction potential of O_2 might be changed due to the adsorption on the photocatalyst surface. Finally, $^{\bullet}O_2^-$ radicals can also derive from the two-electron process from hydrogen peroxide and further reaction with holes according to eqs 4 and 5

$$O_2 + 2H^+ + 2e \rightarrow H_2O_2 \quad (4)$$

$$H_2O_2 + h^+ \rightarrow^{\bullet} O_2^- + 2H^+ \quad (5)$$

The redox potential of hydrogen peroxide generation is +0.30 eV,[61] so this process can occur in the photocatalytic process with scheelite-type compounds.

3.4. Photocatalytic Activity Analysis. The photocatalytic activity of the as-prepared scheelite-type compounds was evaluated in the reaction of phenol photodegradation. No phenol was degraded in the absence of illumination, indicating no dark reaction at the surface of the obtained samples. Photolysis tests of phenol under UV−vis irradiation without the presence of photocatalyst were also performed. Under the experimental conditions, phenol photolysis was not observed.

The results of phenol degradation in the presence of the obtained materials are presented in Figure 14. The highest photocatalytic activity was observed for $SrWO_4$ and $BaWO_4$ materials. Although their light absorption is limited, scheelite-type compounds exhibited good photocatalytic performance. The comparison of *k*-constant rates with other photocatalysts described in the literature is presented in Table 4. In addition, the surface-area-normalized rate constants were calculated due to better comparison photocatalysts with different specific surface areas.[64] Regarding ABO_4 compounds with a low specific surface area, especially $BaMoO_4$ and $BaWO_4$, the ratio for these materials is similar or higher, even 1 order of magnitude than TiO_2. Therefore, it can be concluded that developing the surface area of tungstates and molybdates may cause more efficient phenol degradation. Remarkably, no information about the photocatalytic performance of alkali earth metal scheelite-type compounds was reported in the literature.

Another observation is the trend to decrease the efficiency while the bandgap value was decreasing. Generally, both photocatalytic and photochemical processes require sufficient energy to generate the electron−holes pairs responsible for the reduction and oxidation processes.[5,65] Therefore, almost all of the reported photocatalysts are semiconductor-based materials with a suitable band structure. It is commonly believed that insulators cannot be used for photocatalytic water treatment due to large bandgaps to be excited by the usual UV and visible light sources.[66,67] However, barium ($BaWO_4$ and $BaMoO_4$) and strontium ($SrWO_4$) compounds possess the highest photocatalytic activity despite the E_g value in the range 4−5 eV.

The light absorption properties and bandgap values are not the main factors influencing the phenol degradation efficiency. In this regard, photoluminescence properties were also studied in detail. While comparing the values of carrier lifetimes with *k*-constants, it can be noted that $SrWO_4$ and $BaWO_4$ revealed the highest $\langle\tau\rangle$ values. By analogy, the short carrier lifetimes contributed to low phenol degradation. It can be assumed that the average lifetime calculated from time-resolved PL decay curves is the main factor that affected the photocatalytic performance. This observation is not entirely consistent with $CaWO_4$, which has a lower $\langle\tau\rangle$ value than $BaMoO_4$, although their phenol photocatalytic degradation is similar. The luminescence decay curve fits the data from a poly-phase exponential decay function with constant parameters τ_1 and τ_2. Meanwhile, the τ_1 value is higher for $CaWO_4$ (129.61 μs) than for $BaMoO_4$ (61.62 μs). The explanation of this discrepancy can be found in thermoluminescence spectra.

$SrWO_4$ and $BaWO_4$ are the most efficient photocatalysts within this scheelite-type series, so this can be explained by no or very low recombination states, which reduce the carrier lifetimes. This observation was described by Wang *et al.*, whose research includes nitrogen-doped anatase titania nanobelts.[74] Although the N 2p levels near the valence band contribute to the visible light absorbance, the band originated from the risen oxygen vacancies. The associated Ti^{3+} species were relatively deep and acted as the recombination centers for the photoinduced electrons and holes, reducing the photocatalytic activity. By analogy, tungstates revealed higher photocatalytic activity than molybdates due to more shallow traps and higher average charge carrier lifetimes. The only exception is probably $CaWO_4$. The photocatalytic activity of $CaWO_4$ can be explained as the presence of trapping centers, which allows for elongating the lifetime carriers. Kato *et al.* have reported that Na-doping in $SrTiO_3$ enhances the activity because new mid-gap states are introduced. The photoexcited electrons were trapped into these states after excitation, so trapped electrons had a longer lifetime than those in undoped $SrTiO_3$.[75] This hypothesis can be confirmed while comparing the τ_1 in this series. This value is the highest from presented scheelite-type compounds, so $CaWO_4$ had a similar photocatalytic performance to $BaMoO_4$. This observation is also in agreement with the TL spectra—two distinct glow peaks were detected for $CaWO_4$, in which the first electron trap causes the prolongation of charge carrier lifetime, whereas the second one is responsible for radiative recombination. However, the second trap was probably a reason for low photocatalytic activity in the AWO_4 series.

3.5. Degradation Mechanism Discussion. During a photocatalytic process, phenol derivatives are formed, indicating the degradation pathway of the organic pollutant. In the case of photoreaction with alkali earth scheelite-type compounds, by HPLC analysis, catechol (CT) and hydroquinone (HQ) were detected as the main intermediate products during the phenol photodegradation reaction. The production of CT and HQ during the reaction is typical for many photocatalysts.[30,68,76] Some works also suggest the formation of benzoquinone (BQ) being in possible equilibrium with hydroquinone.[77,78] However, in this study, BQ presence and the slowdown of the photocatalytic process were not observed. The evolution of phenol removal with the monitored formation of catechol and hydroquinone concentration as a function of photoreaction time using different photocatalysts is presented in Figure S6 in the Supporting Information.

https://doi.org/10.1021/acs.jpcc.1c06481
J. Phys. Chem. C 2021, 125, 25497−25513

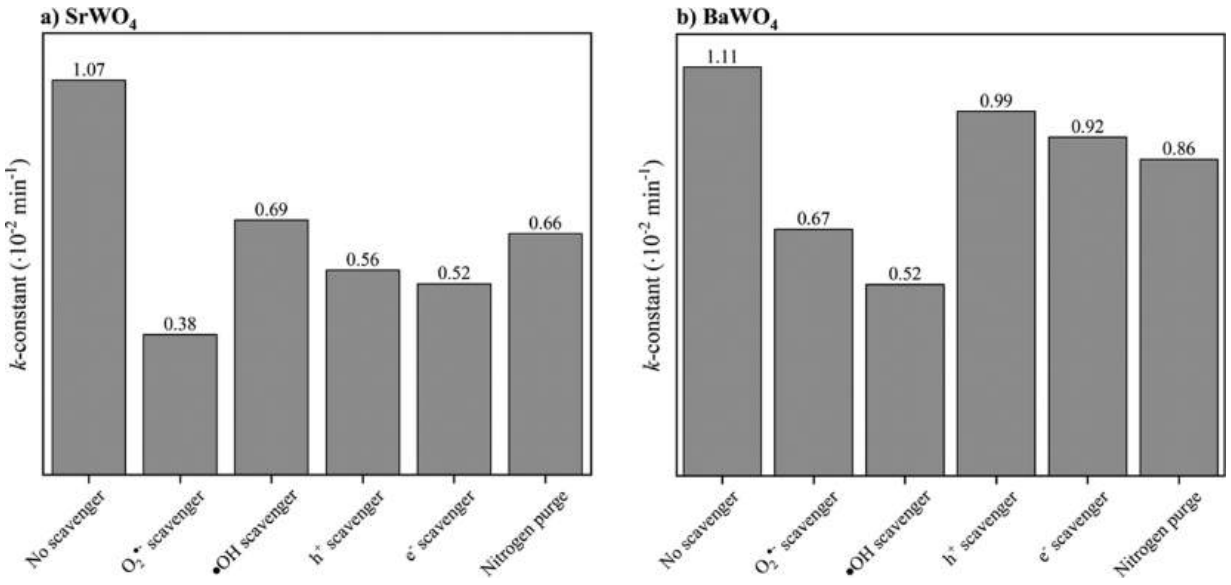

Figure 15. Photocatalytic degradation of phenol in the presence of (a) $SrWO_4$ and (b) $BaWO_4$ and charge carrier scavengers.

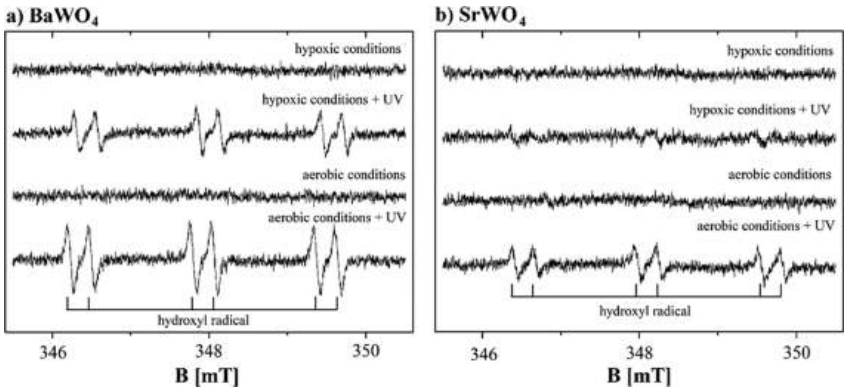

Figure 16. EPR spectra of PBN in (a) $BaWO_4$ and (b) $SrWO_4$ aqueous suspension recorded under hypoxic and aerobic conditions before and after UV irradiation (70 s).

According to the graph, the phenol concentration decreased with the reaction time, whereas the concentration of hydroquinone and catechol increased.

Overall, the photocatalysis mechanism is depicted as the generation of photoexcited electrons and holes in the conduction band and valence band. These charge carriers migrate to the photocatalyst surface and undergo reactions with a water molecule to form reactive oxygen species (ROS). Therefore, the phenol degradation analyses were carried out in the presence of $^{\bullet}O_2^-$, $^{\bullet}OH$, e^-, and h^+ scavengers and under anaerobic conditions (N_2 purging) to understand the phenol degradation pathway. The results of the photocatalytic activity of $BaWO_4$ and $SrWO_4$ in the presence of e^-, h^+, $^{\bullet}O_2^-$, and $^{\bullet}OH$ scavengers, that is, silver nitrate, ammonium oxalate, benzoquinone, and isopropyl alcohol, respectively, and during N_2 purging are presented in Figure 15. $BaWO_4$ and $SrWO_4$ were selected as the most effective photocatalysts in solar-driven phenol degradation.

A significant contribution of both $^{\bullet}OH$ and $^{\bullet}O_2^-$ on the photocatalytic process was observed in both samples. These observations are in agreement with other reports, which confirm that hydroxyl and superoxide radicals are the main factors that contribute to phenol oxidation.[60,76] It suggests that water oxidation, as well as oxygen reduction, can be efficiently performed in the presence of $BaWO_4$ or $SrWO_4$ photocatalysts. Furthermore, in the case of $SrWO_4$, oxygen reduction was predominant in comparison with $BaWO_4$ due to the higher observed effect of $^{\bullet}O2^-$ scavenger as well as an e^- scavenger and N_2 purge to eliminate O_2 from the suspension. On the other hand, $BaWO_4$ seems more suitable for the $^{\bullet}OH$ generation, which agrees with the observed lowering of the valence band potential for this compound. Our overall results suggest that changing the cation in the AWO_4 structure affects the generation ability of ROS generated during irradiation. This effect might be possible due to (i) morphology change of the sample or facet effect in the case of $BaWO_4$ or (ii) modified electronic structure of the conduction band.

$BaWO_4$ and $SrWO_4$ were selected for photochemical EPR measurements. Figure 16 shows the EPR spectra of PBN in $BaWO_4$ (Figure 16a) and $SrWO_4$ (Figure 16b) aqueous suspension. The presented spectra of the suspensions that were not irradiated showed no signals from short-lived $^{\bullet}O_2-$ and $^{\bullet}OH$ radicals trapped on PBN for both hypoxic conditions or aerobic. The spectra of the UV-irradiated suspensions consist

https://doi.org/10.1021/acs.jpcc.1c06481
J. Phys. Chem. C 2021, 125, 25497−25513

of sextets described by spin Hamiltonian parameters (A^N = 1.56 mT, A^H = 0.27 mT, and g = 2.0057),[79−81] which clearly indicate that the PBN traps hydroxyl radicals. It should be noted that the intensity of the EPR spectra recorded under hypoxic conditions was less intense than the spectra obtained under aerobic conditions. The formation of hydroxyl radicals can take place under hypoxic conditions, in opposite to superoxide radicals. On the other hand, the superoxide radical anion can transform directly into a non-paramagnetic form or participate in the formation of the hydroxyl radical. The above statement explains the EPR results in which, due to aerobic conditions, a higher concentration of trapped hydroxyl radicals was observed. Despite the lack of lines in EPR spectra that could be attributed to the $^{\bullet}O_2-$ radical, the decrease in the number of trapped $^{\bullet}OH$ radicals under hypoxic conditions is also an indirect evidence of the superoxide radical creation.

The possible mechanism of the phenol degradation can be described as follows: the $^{\bullet}OH$ radicals initiate the oxidation of phenol molecules, explaining the decline of k-constant for both tungstates. The performed analysis is consistent with HPLC analysis, which indicates the formation of catechol and hydroquinone. These derivatives are the results of phenol oxidation by hydroxyl radicals. After further oxidation of phenol derivatives, superoxide radicals ($^{\bullet}O_2^-$) are needed to break the benzyl ring and mineralize it to CO_2. An increased ability of $SrWO_4$ to reduce oxygen would especially explain the higher TOC removal observed for this sample due to the possible aromatic ring breaking with $^{\bullet}O_2^-$. In the case of $BaWO_4$, the concentration of superoxide radicals is probably too low to open the benzyl ring; therefore, no mineralization was observed[82] (see Figure S7 in the Supporting Information).

3.6. Stability Test. $SrWO_4$ and $SrMoO_4$ compounds with the highest mineralization efficiency measured as a TOC removal were selected to study the stability and reusability of ABO_4 photocatalysts. After each 120 min cycle, photocatalysts were separated and used in another run without any treatment. The obtained results of phenol degradation are presented in Figure S8 in the Supporting Information. No significant loss in photocatalytic activity was noticed after three subsequent cycles of degradation. Moreover, XRD analyses (Figure S9 in the Supporting Information) performed after a single photocatalytic degradation reaction and three subsequent degradation cycles confirmed that scheelite-type compounds are stable after the photocatalytic process and can be reused without specific treatment. Finally, the SEM images of photocatalysts after degradation processes (Figures S10 and S11 in the Supporting Information) indicate that only partial deagglomeration is observed, which is typical for photocatalytic reactions in water systems.

4. CONCLUSIONS

To summarize, a simple synthesis of alkaline earth metal scheelite-type compounds was developed. The photocatalytic activity under simulated solar light irradiation for phenol degradation using AWO_4- and $AMoO_4$-based photocatalysts (A = Ca, Sr, and Ba) was reported for the first time. The morphologies of the potential photocatalyst, together with BET measurements, were described. Despite the microcrystals or microsphere formation and low surface area, all samples exhibit photocatalytic activity toward phenol degradation. Although ABO_4 compounds absorb mainly UV light, the photon amount was sufficient to create photogenerated electron−hole pairs. The thermoluminescence glow curves showed the presence of energy traps, which allow absorbing light at higher wavelengths that it could be suggested by bandgap calculations. Remarkably, the charge carrier lifetime was the crucial factor influencing the photocatalytic performance of the as-synthesized materials. $BaWO_4$ and $SrWO_4$, with the longest $\langle\tau\rangle$ value, demonstrated the highest photodegradation rate constants. Ultimately, AWO_4s are more efficient photocatalysts than $AMoO_4$s because of the possible conduction through charge carrier channels as well as more resistive characteristic, which was observed during electrochemical studies. In addition, molybdates had deeper electron traps than tungstates, which was a reason for their lower photocatalytic activity. Finally, the photocatalytic processes with charge carrier scavengers indicate the significant role of $^{\bullet}OH$ and $^{\bullet}O_2^-$ radicals, which oxidize phenol to hydroquinone and catechol. An increased ability of $SrWO_4$ to reduce oxygen explained the observed phenol mineralization due to the predominant role of $^{\bullet}O_2^-$, e^- and dissolved oxygen in phenol photocatalytic degradation.

The obtained results provide information about the unique physicochemical properties of alkali earth metal scheelite-type compounds and shed new light on the photocatalytic performance of AWO_4 and $AMoO_4$. The precise characteristics facilitate further investigation of these compounds and find novel solutions for enhancing photocatalytic performance in wide-bandgap semiconductors.

■ ASSOCIATED CONTENT

Supporting Information

The Supporting Information is available free of charge at https://pubs.acs.org/doi/10.1021/acs.jpcc.1c06481.

Size distribution of nanoparticles or microcrystals of scheelite-type compounds; adsorption isotherms and pore distributions of scheelite-type compounds; bandgap calculations based on Tauc's method for scheelite-type compounds; excitation spectra of scheelite-type compounds; determination of flat bands and capacity of ABO_4 compounds; phenol, hydroquinone, and catechol concentration *versus* irradiation time during photocatalytic process for all samples; TOC measurements for scheelite-type compounds after 120 min of photocatalytic process; stability tests of scheelite-type compounds (XRD patterns and SEM images), stability tests of $SrWO_4$ and $SrMoO_4$ after three degradation cycles (XRD patterns and SEM images); and efficiency of phenol degradation after 120 min of the photocatalytic process after three degradation cycles (PDF)

■ AUTHOR INFORMATION

Corresponding Authors

Marta Kowalkińska − *Department of Process Engineering and Chemical Technology, Faculty of Chemistry, Gdańsk University of Technology, Gdańsk 80-233, Poland;* orcid.org/0000-0003-0518-7508; Email: marta.kowalkinska@pg.edu.pl

Anna Zielińska-Jurek − *Department of Process Engineering and Chemical Technology, Faculty of Chemistry, Gdańsk University of Technology, Gdańsk 80-233, Poland;* orcid.org/0000-0002-9830-1797; Email: annjurek@pg.edu.pl

https://doi.org/10.1021/acs.jpcc.1c06481
J. Phys. Chem. C 2021, 125, 25497−25513

Authors

Paweł Głuchowski — *Institute of Low Temperature and Structural Research, Polish Academy of Sciences, Wrocław 50-422, Poland;* orcid.org/0000-0003-2566-1422

Tomasz Swebocki — *Department of Analytical Chemistry, Faculty of Chemistry, University of Gdansk, Gdańsk 80-308, Poland; Institute of Interdisciplinary Research (USR 3078), French National Centre for Scientific Research, Villeneuve-d'Ascq F-59652, France*

Tadeusz Ossowski — *Department of Analytical Chemistry, Faculty of Chemistry, University of Gdansk, Gdańsk 80-308, Poland*

Adam Ostrowski — *Institute of Molecular Physics, Polish Academy of Sciences, Poznań 60-179, Poland*

Waldemar Bednarski — *Institute of Molecular Physics, Polish Academy of Sciences, Poznań 60-179, Poland*

Jakub Karczewski — *Institute of Nanotechnology and Materials Engineering, Faculty of Applied Physics and Mathematics, Gdańsk University of Technology, Gdańsk 80-233, Poland*

Complete contact information is available at: https://pubs.acs.org/10.1021/acs.jpcc.1c06481

Notes

The authors declare no competing financial interest.

■ ACKNOWLEDGMENTS

This research was financially supported by the Polish National Science Centre (grant no. NCN 2018/30/E/ST5/00845). We also acknowledge Bogusław Macalik from the Polish Academy of Sciences for reflectance spectra measurements.

■ REFERENCES

(1) Oturan, M. A.; Aaron, J.-J. Advanced Oxidation Processes in Water/Wastewater Treatment: Principles and Applications. A Review. *Crit. Rev. Environ. Sci. Technol.* **2014**, *44*, 2577−2641.

(2) Howe, R. F. Recent Developments in Photocatalysis. *Dev. Chem. Eng. Miner. Process.* **1998**, *6*, 55−84.

(3) Ahmed, S. N.; Haider, W. Heterogeneous Photocatalysis and Its Potential Applications in Water and Wastewater Treatment: A Review. *Nanotechnology* **2018**, *29*, 342001.

(4) Schneider, J.; Matsuoka, M.; Takeuchi, M.; Zhang, J.; Horiuchi, Y.; Anpo, M.; Bahnemann, D. W. Understanding TiO_2 Photocatalysis: Mechanisms and Materials. *Chem. Rev.* **2014**, *114*, 9919−9986.

(5) Fujishima, A.; Zhang, X.; Tryk, D. TiO_2 Photocatalysis and Related Surface Phenomena. *Surf. Sci. Rep.* **2008**, *63*, 515−582.

(6) Li, W.; Ismat Shah, S. Semiconductor Nanoparticles for Photocatalysis. *Encycl. Nanosci. Nanotechnol.* **2004**, *9*, 669−695.

(7) Hsu, L. C.; Galli, P. E. Origin of the Scheelite-Powellite Series of Minerals. *Econ. Geol.* **1973**, *68*, 681−696.

(8) Fan, L.; Fan, Y. X.; Duan, Y. H.; Wang, Q.; Wang, H. T.; Jia, G. H.; Tu, C. Y. Continuous-Wave Intracavity Raman Laser at 1179.5 Nm with $SrWO_4$ Raman Crystal in Diode-End-Pumped Nd:YVO_4 Laser. *Appl. Phys. B: Lasers Opt.* **2009**, *94*, 553−557.

(9) Šulc, J.; Jelínková, H.; Basiev, T. T.; Doroschenko, M. E.; Ivleva, L. I.; Osiko, V. V.; Zverev, P. G. Nd:$SrWO_4$ and Nd:$BaWO_4$ Raman Lasers. *Opt. Mater.* **2007**, *30*, 195−197.

(10) Michail, C.; Valais, I.; Fountos, G.; Bakas, A.; Fountzoula, C.; Kalyvas, N.; Karabotsos, A.; Sianoudis, I.; Kandarakis, I. Luminescence Efficiency of Calcium Tungstate ($CaWO_4$) under X-Ray Radiation: Comparison with Gd_2O_2S:Tb. *Meas.: J. Int. Meas. Confed.* **2018**, *120*, 213−220.

(11) Zhang, X.; Lin, J.; Mikhailik, V. B.; Kraus, H. Studies of Scintillation Properties of $CaMoO_4$ at Millikelvin Temperatures. *Appl. Phys. Lett.* **2015**, *106*, 241904.

(12) Dutta, S.; Som, S.; Sharma, S. K. Luminescence and Photometric Characterization of K+ Compensated $CaMoO_4$:Dy3+ Nanophosphors. *Dalton Trans.* **2013**, *42*, 9654−9661.

(13) Zhang, J.; Wang, Y.; Zhai, Z.; Chen, G. Investigations on Morphology, Photoluminescence and Cathodoluminescence of $SrWO_4$ and $SrWO_4$:Tb^{3+}. *Opt. Mater.* **2014**, *38*, 126−130.

(14) Abreu, M. F. C.; Motta, F. V.; Lima, R. C.; Li, M. S.; Longo, E.; Marques, A. P. D. A. Effect of Process Parameters on Photophysical Properties and Barium Molybdate Phosphors Characteristics. *Ceram. Int.* **2014**, *40*, 6719−6729.

(15) Gou, Y.; Liu, Q.; Shi, X.; Asiri, A. M.; Hu, J.; Sun, X. $CaMoO_4$ Nanosheet Arrays for Efficient and Durable Water Oxidation Electrocatalysis under Alkaline Conditions. *Chem. Commun.* **2018**, *54*, 5066−5069.

(16) Gonçalves, R. F.; Cavalcante, L. S.; Nogueira, I. C.; Longo, E.; Godinho, M. J.; Sczancoski, J. C.; Mastelaro, V. R.; Pinatti, I. M.; Rosa, I. L. V.; Marques, A. P. A. Rietveld Refinement, Cluster Modelling, Growth Mechanism and Photoluminescence Properties of $CaWO_4$:Eu^{3+} Microcrystals. *CrystEngComm* **2015**, *17*, 1654−1666.

(17) Momma, K.; Izumi, F. VESTA 3 for Three-Dimensional Visualization of Crystal, Volumetric and Morphology Data. *J. Appl. Crystallogr.* **2011**, *44*, 1272−1276.

(18) Shivakumara, C.; Saraf, R.; Behera, S.; Dhananjaya, N.; Nagabhushana, H. Scheelite-Type MWO_4 (M = Ca, Sr and Ba) Nanophosphors: Facile Synthesis, Structural Characterization, Photoluminescence and Photocatalytic Properties. *Mater. Res. Bull.* **2015**, *61*, 422−432.

(19) Zhu, Y.; Zheng, G.; Dai, Z.; Zhang, L.; Ma, Y. Photocatalytic and Luminescent Properties of $SrMoO_4$ Phosphors Prepared via Hydrothermal Method with Different Stirring Speeds. *J. Mater. Sci. Technol.* **2017**, *33*, 23−29.

(20) Ghoreishi, S. M. Facile Synthesis and Characterization of $CaWO_4$ Nanoparticles Using a New Schiff Base as Capping Agent: Enhanced Photocatalytic Degradation of Methyl Orange. *J. Mater. Sci. Mater. Electron.* **2017**, *28*, 14833−14838.

(21) Bi, J.; Wu, L.; Zhang, Y.; Li, Z.; Li, J.; Fu, X. Solvothermal Preparation, Electronic Structure and Photocatalytic Properties of PbMoO4 and $SrMoO_4$. *Appl. Catal., B* **2009**, *91*, 135−143.

(22) Huerta-Flores, A. M.; Juárez-Ramírez, I.; Torres-Martínez, L. M.; Carrera-Crespo, J. E.; Gómez-Bustamante, T.; Sarabia-Ramos, O. Synthesis of $AMoO_4$ (A = Ca, Sr, Ba) Photocatalysts and Their Potential Application for Hydrogen Evolution and the Degradation of Tetracycline in Water. *J. Photochem. Photobiol., A* **2018**, *356*, 29−37.

(23) Luttrell, T.; Halpegamage, S.; Tao, J.; Kramer, A.; Sutter, E.; Batzill, M. Why Is Anatase a Better Photocatalyst than Rutile? - Model Studies on Epitaxial TiO_2 Films. *Sci. Rep.* **2015**, *4*, 4043.

(24) Dong, F.; Xiong, T.; Sun, Y.; Lu, L.; Zhang, Y.; Zhang, H.; Huang, H.; Zhou, Y.; Wu, Z. Exploring the Photocatalysis Mechanism on Insulators. *Appl. Catal., B* **2017**, *219*, 450−458.

(25) Cui, W.; Chen, L.; Li, J.; Zhou, Y.; Sun, Y.; Jiang, G.; Lee, S. C.; Dong, F. Ba-Vacancy Induces Semiconductor-like Photocatalysis on Insulator $BaSO_4$. *Appl. Catal., B* **2019**, *253*, 293−299.

(26) Li, K.; Zhang, S.; Tan, Q.; Wu, X.; Li, Y.; Li, Q.; Fan, J.; Lv, K. Insulator in Photocatalysis: Essential Roles and Activation Strategies. *Chem. Eng. J.* **2021**, *426*, 130772.

(27) Adán, C.; Bahamonde, A.; Fernández-García, M.; Martínez-Arias, A. Structure and Activity of Nanosized Iron-Doped Anatase TiO_2 Catalysts for Phenol Photocatalytic Degradation. *Appl. Catal., B* **2007**, *72*, 11−17.

(28) Dang, T. T. T.; Le, S. T. T.; Channei, D.; Khanitchaidecha, W.; Nakaruk, A. Photodegradation Mechanisms of Phenol in the Photocatalytic Process. *Res. Chem. Intermed.* **2016**, *42*, 5961−5974.

(29) Krivec, M.; Pohar, A.; Likozar, B.; Dražić, G. Hydrodynamics, Mass Transfer, and Photocatalytic Phenol Selective Oxidation Reaction Kinetics in a Fixed TiO_2 Microreactor. *AIChE J.* **2015**, *61*, 572−581.

(30) Sobczyński, A.; Duczmal, Ł.; Zmudziński, W. Phenol Destruction by Photocatalysis on TiO_2: An Attempt to Solve the Reaction Mechanism. *J. Mol. Catal. A: Chem.* **2004**, *213*, 225−230.

(31) Aslam, M.; Ismail, I. M. I.; Chandrasekaran, S.; Hameed, A. Morphology Controlled Bulk Synthesis of Disc-Shaped WO_3 Powder and Evaluation of Its Photocatalytic Activity for the Degradation of Phenols. *J. Hazard. Mater.* **2014**, *276*, 120−128.
(32) Soltanali, S.; Darian, J. T. Synthesis of Mesoporous SAPO-34 Catalysts in the Presence of MWCNT, CNF, and GO as Hard Templates in MTO Process. *Powder Technol.* **2019**, *355*, 127−134.
(33) Tauc, J. Optical Properties and Electronic Structure of Amorphous Ge and Si. *Mater. Res. Bull.* **1968**, *3*, 37−46.
(34) Bailiff, I. K. Characteristics of Time-Resolved Luminescence in Quartz. *Radiat. Meas.* **2000**, *32*, 401−405.
(35) Jones, M.; Nedeljkovic, J.; Ellingson, R. J.; Nozik, A. J.; Rumbles, G. Photoenhancement of Luminescence in Colloidal CdSe Quantum Dot Solutions. *J. Phys. Chem. B* **2003**, *107*, 11346−11352.
(36) Wang, Y.; Xu, K.; Li, D.; Zhao, H.; Hu, Z. Persistent Luminescence and Photocatalytic Properties of Ga_2O_3:Cr^{3+},Zn^{2+} Phosphors. *Opt. Mater.* **2014**, *36*, 1798−1801.
(37) Cooke, D. W.; Bennett, B. L.; Farnum, E. H.; Hults, W. L.; Muenchausen, R. E.; Smith, J. L. Thermally Stimulated Luminescence from X-Irradiated Porous Silicon. *Appl. Phys. Lett.* **1997**, *70*, 3594−3596.
(38) Winer, A. M.; Breuer, G. M.; Carter, W. P. L.; Darnall, K. R.; Pitts, J. N. Effects of Ultraviolet Spectral Distribution on the Photochemistry of Simulated Polluted Atmospheres. *Atmos. Environ.* **1979**, *13*, 989−998.
(39) Cavalcante, L. S.; Sczancoski, J. C.; Tranquilin, R. L.; Varela, J. A.; Longo, E.; Orlandi, M. O. Growth Mechanism of Octahedron-like $BaMoO_4$ Microcrystals Processed in Microwave-Hydrothermal: Experimental Observations and Computational Modeling. *Particuology* **2009**, *7*, 353−362.
(40) Oliveira, M. C.; Gracia, L.; Nogueira, I. C.; do Carmo Gurgel, M. F.; Mercury, J. M. R.; Longo, E.; Andrés, J. Synthesis and Morphological Transformation of $BaWO_4$ Crystals: Experimental and Theoretical Insights. *Ceram. Int.* **2016**, *42*, 10913−10921.
(41) Alencar, L. D. S.; Mesquita, A.; Feitosa, C. A. C.; Balzer, R.; Probst, L. F. D.; Batalha, D. C.; Rosmaninho, M. G.; Fajardo, H. V.; Bernardi, M. I. B. Preparation, Characterization and Catalytic Application of Barium Molybdate ($BaMoO_4$) and Barium Tungstate (BaWO4) in the Gas-Phase Oxidation of Toluene. *Ceram. Int.* **2017**, *43*, 4462−4469.
(42) Iervolino, G.; Zammit, I.; Vaiano, V.; Rizzo, L. Limitations and Prospects for Wastewater Treatment by UV and Visible-Light-Active Heterogeneous Photocatalysis: A Critical Review. *Top. Curr. Chem.* **2020**, *378*, 7.
(43) Loeb, S. K.; Alvarez, P. J. J.; Brame, J. A.; Cates, E. L.; Choi, W.; Crittenden, J.; Dionysiou, D. D.; Li, Q.; Li-Puma, G.; Quan, X.; et al. The Technology Horizon for Photocatalytic Water Treatment: Sunrise or Sunset? *Environ. Sci. Technol.* **2019**, *53*, 2937−2947.
(44) Jędrzejczyk, M.; Zbudniewek, K.; Rynkowski, J.; Keller, V.; Grams, J.; Ruppert, A. M.; Keller, N. Wide Band Gap Ga_2O_3 as Efficient UV-C Photocatalyst for Gas-Phase Degradation Applications. *Environ. Sci. Pollut. Res.* **2017**, *24*, 26792−26805.
(45) Zhang, Y.; Holzwarth, N. A. W.; Williams, R. T. Electronic band structures of the scheelite materialsCaMoO4, $CaWO_4$, $PbMoO_4$ and $PbWO_4$. *Phys. Rev. B: Condens. Matter Mater. Phys.* **1998**, *57*, 12738−12750.
(46) Singh, A.; Dutta, D. P.; Ramkumar, J.; Bhattacharya, K.; Tyagi, A. K.; Fulekar, M. H. Serendipitous Discovery of Super Adsorbent Properties of Sonochemically Synthesized Nano BaWO4. *RSC Adv.* **2013**, *3*, 22580−22590.
(47) Thongtem, T.; Kungwankunakorn, S.; Kuntalue, B.; Phuruangrat, A.; Thongtem, S. Luminescence and Absorbance of Highly Crystalline $CaMoO_4$, $SrMoO_4$, $CaWO_4$ and $SrWO_4$ Nanoparticles Synthesized by Co-Precipitation Method at Room Temperature. *J. Alloys Compd.* **2010**, *506*, 475−481.
(48) Li Puma, G.; Yue, P. L. Effect of the Radiation Wavelength on the Rate of Photocatalytic Oxidation of Organic Pollutants. *Ind. Eng. Chem. Res.* **2002**, *41*, 5594−5600.
(49) Jing, L.; Xin, B.; Yuan, F.; Xue, L.; Wang, B.; Fu, H. Effects of Surface Oxygen Vacancies on Photophysical and Photochemical Processes of Zn-Doped TiO_2 Nanoparticles and Their Relationships. *J. Phys. Chem. B* **2006**, *110*, 17860−17865.
(50) Liqiang, J.; Yichun, Q.; Baiqi, W.; Shudan, L.; Baojiang, J.; Libin, Y.; Wei, F.; Honggang, F.; Jiazhong, S. Review of Photoluminescence Performance of Nano-Sized Semiconductor Materials and Its Relationships with Photocatalytic Activity. *Sol. Energy Mater. Sol. Cells* **2006**, *90*, 1773−1787.
(51) Liqiang, J.; Xiaojun, S.; Baifu, X.; Baiqi, W.; Weimin, C.; Honggang, F. The Preparation and Characterization of La Doped TiO_2 Nanoparticles and Their Photocatalytic Activity. *J. Solid State Chem.* **2004**, *177*, 3375−3382.
(52) Fujihara, K.; Izumi, S.; Ohno, T.; Matsumura, M. Time-Resolved Photoluminescence of Particulate TiO_2 Photocatalysts Suspended in Aqueous Solutions. *J. Photochem. Photobiol., A* **2000**, *132*, 99−104.
(53) Rajashekharaiah, A. S.; Vidya, Y. S.; Anantharaju, K. S.; Darshan, G. P.; Lalitha, P.; Sharma, S. C.; Nagabhushana, H. Photoluminescence, Thermoluminescence and Photocatalytic Studies of Sonochemical Synthesis of $Bi_2Zr_2O_7$:Sm^{3+} Nanomaterials. *J. Mater. Sci. Mater. Electron.* **2020**, *31*, 15627−15643.
(54) Kong, M.; Li, Y.; Chen, X.; Tian, T.; Fang, P.; Zheng, F.; Zhao, X. Tuning the Relative Concentration Ratio of Bulk Defects to Surface Defects in TiO_2 Nanocrystals Leads to High Photocatalytic Efficiency. *J. Am. Chem. Soc.* **2011**, *133*, 16414−16417.
(55) Kohtani, S.; Kamoi, Y.; Yoshioka, E.; Miyabe, H. Kinetic Study on Photocatalytic Hydrogenation of Acetophenone Derivatives on Titanium Dioxide. *Catal. Sci. Technol.* **2014**, *4*, 1084−1091.
(56) Cirocka, A.; Zarzeczańska, D.; Wcisło, A.; Ryl, J.; Bogdanowicz, R.; Finke, B.; Ossowski, T. Tuning of the Electrochemical Properties of Transparent Fluorine-Doped Tin Oxide Electrodes by Microwave Pulsed-Plasma Polymerized Allylamine. *Electrochim. Acta* **2019**, *313*, 432−440.
(57) Luo, J.; Bai, X.; Li, Q.; Yu, X.; Li, C.; Wang, Z.; Wu, W.; Liang, Y.; Zhao, Z.; Liu, H. Band Structure Engineering of Bioinspired Fe Doped $SrMoO_4$ for Enhanced Photocatalytic Nitrogen Reduction Performance. *Nano Energy* **2019**, *66*, 104187.
(58) Luévano-Hipólito, E.; Torres-Martínez, L. M. Ink-Jet Printing Films of Molybdates of Alkaline Earth Metals with Scheelite Structure Applied in the Photocatalytic CO_2 Reduction. *J. Photochem. Photobiol., A* **2019**, *368*, 15−22.
(59) Augugliaro, V.; Bellardita, M.; Loddo, V.; Palmisano, G.; Palmisano, L.; Yurdakal, S. Overview on Oxidation Mechanisms of Organic Compounds by TiO_2 in Heterogeneous Photocatalysis. *J. Photochem. Photobiol., C* **2012**, *13*, 224−245.
(60) Lv, K.; Guo, X.; Wu, X.; Li, Q.; Ho, W.; Li, M.; Ye, H.; Du, D. Photocatalytic Selective Oxidation of Phenol to Produce Dihydroxybenzenes in a TiO_2/UV System: Hydroxyl Radical versus Hole. *Appl. Catal., B* **2016**, *199*, 405−411.
(61) Nosaka, Y.; Nosaka, A. Y. Generation and Detection of Reactive Oxygen Species in Photocatalysis. *Chem. Rev.* **2017**, *117*, 11302−11336.
(62) Augugliaro, V.; Palmisano, L.; Sclafani, A.; Minero, C.; Pelizzetti, E. Photocatalytic Degradation of Phenol in Aqueous Titanium Dioxide Dispersions. *Toxicol. Environ. Chem.* **1988**, *16*, 89−109.
(63) Wardman, P. Reduction Potentials of One Electron Couples Involving Free Radicals in Aqueous Solution. *J. Phys. Chem. Ref. Data* **1989**, *18*, 1637−1755.
(64) Zhong, J.; Zhao, Y.; Ding, L.; Ji, H.; Ma, W.; Chen, C.; Zhao, J. Opposite Photocatalytic Oxidation Behaviors of BiOCl and TiO_2: Direct Hole Transfer vs. Indirect OH Oxidation. *Appl. Catal., B* **2019**, *241*, 514−520.
(65) Chen, X.; Shen, S.; Guo, L.; Mao, S. S. Semiconductor-Based Photocatalytic Hydrogen Generation. *Chem. Rev.* **2010**, *110*, 6503−6570.

https://doi.org/10.1021/acs.jpcc.1c06481
J. Phys. Chem. C 2021, 125, 25497−25513

(66) Li, R.; Wang, X.; Jin, S.; Zhou, X.; Feng, Z.; Li, Z.; Shi, J.; Zhang, Q.; Li, C. Photo-Induced H_2 Production from a CH_3OH-H_2O Solution at Insulator Surface. *Sci. Rep.* **2015**, *5*, 13475.
(67) Yu, Z.; Chen, X.-Q.; Kang, X.; Xie, Y.; Zhu, H.; Wang, S.; Ullah, S.; Ma, H.; Wang, L.; Liu, G.; et al. Noninvasively Modifying Band Structures of Wide-Bandgap Metal Oxides to Boost Photocatalytic Activity. *Adv. Mater.* **2018**, *30*, No. e1706259.
(68) Dudziak, S.; Kowalkińska, M.; Karczewski, J.; Pisarek, M.; Siuzdak, K.; Kubiak, A.; Siwińska-Ciesielczyk, K.; Zielińska-Jurek, A. Solvothermal Growth of {0 0 1} Exposed Anatase Nanosheets and Their Ability to Mineralize Organic Pollutants. The Effect of Alcohol Type and Content on the Nucleation and Growth of TiO_2 Nanostructures. *Appl. Surf. Sci.* **2021**, *563*, 150360.
(69) Bielan, Z.; Dudziak, S.; Sulowska, A.; Pelczarski, D.; Ryl, J.; Zielińska-Jurek, A. Preparation and Characterization of Defective TiO_2. The Effect of the Reaction Environment on Titanium Vacancies Formation. *Materials* **2020**, *13*, 2763.
(70) Jiang, J.; Wang, H.; Chen, X.; Li, S.; Xie, T.; Wang, D.; Lin, Y. Enhanced Photocatalytic Degradation of Phenol and Photogenerated Charges Transfer Property over BiOI-Loaded ZnO Composites. *J. Colloid Interface Sci.* **2017**, *494*, 130−138.
(71) Wan, L.; Sheng, J.; Chen, H.; Xu, Y. Different Recycle Behavior of Cu^{2+} and Fe^{3+} Ions for Phenol Photodegradation over TiO_2 and WO_3. *J. Hazard. Mater.* **2013**, *262*, 114−120.
(72) Castañeda, C.; Gutiérrez, K.; Alvarado, I.; Martínez, J. J.; Rojas, H.; Tzompantzi, F.; Gómez, R. Effective Phosphated CeO_2 Materials in the Photocatalytic Degradation of Phenol under UV Irradiation. *J. Chem. Technol. Biotechnol.* **2020**, *95*, 3213−3220.
(73) Al-Hamdi, A. M.; Sillanpää, M.; Bora, T.; Dutta, J. Efficient Photocatalytic Degradation of Phenol in Aqueous Solution by SnO_2 :Sb Nanoparticles. *Appl. Surf. Sci.* **2016**, *370*, 229−236.
(74) Wang, J.; Tafen, D. N.; Lewis, J. P.; Hong, Z.; Manivannan, A.; Zhi, M.; Li, M.; Wu, N. Origin of Photocatalytic Activity of Nitrogen-Doped TiO_2 Nanobelts. *J. Am. Chem. Soc.* **2009**, *131*, 12290−12297.
(75) Kato, K.; Jiang, J.; Sakata, Y.; Yamakata, A. Effect of Na-Doping on Electron Decay Kinetics in $SrTiO_3$ Photocatalyst. *ChemCatChem* **2019**, *11*, 6349−6354.
(76) Wysocka, I.; Kowalska, E.; Trzciński, K.; Łapiński, M.; Nowaczyk, G.; Zielińska-Jurek, A. UV-Vis-Induced Degradation of Phenol over Magnetic Photocatalysts Modified with Pt, Pd, Cu and Au Nanoparticles. *Nanomaterials* **2018**, *8*, 28.
(77) Devi, L. G.; Rajashekhar, K. E. A kinetic model based on non-linear regression analysis is proposed for the degradation of phenol under UV/solar light using nitrogen doped TiO_2. *J. Mol. Catal. A: Chem.* **2011**, *334*, 65−76.
(78) Murcia, J. J.; Hidalgo, M. C.; Navío, J. A.; Araña, J.; Doña-Rodríguez, J. M. Study of the Phenol Photocatalytic Degradation over TiO2 Modified by Sulfation, Fluorination, and Platinum Nanoparticles Photodeposition. *Appl. Catal., B* **2015**, *179*, 305−312.
(79) Tero-Kubota, S.; Ikegami, Y.; Kurokawa, T.; Sasaki, R.; Sugioka, K.; Nakano, M. Generation of Free Radicals and Initiation of Radical Reactions in Nitrones−Fe^{2+}−Phosphate Buffer Systems. *Biochem. Biophys. Res. Commun* **1982**, *108*, 1025−1031.
(80) Dodd, N. J. F.; Jha, A. N. Photoexcitation of Aqueous Suspensions of Titanium Dioxide Nanoparticles: An Electron Spin Resonance Spin Trapping Study of Potentially Oxidative Reactions. *Photochem. Photobiol.* **2011**, *87*, 632−640.
(81) Janzen, E.; Kotake, Y.; Randalld, H. Stabilities of Hydroxyl Radical Spin Adducts of PBN-Type Spin Traps. *Free Radic. Biol. Med.* **1992**, *12*, 169−173.
(82) Kowalkińska, M.; Dudziak, S.; Karczewski, J.; Ryl, J.; Trykowski, G.; Zielińska-Jurek, A. Facet Effect of TiO_2 Nanostructures from $TiOF_2$ and Their Photocatalytic Activity. *Chem. Eng. J.* **2021**, *404*, 126493.

https://doi.org/10.1021/acs.jpcc.1c06481
J. Phys. Chem. C 2021, 125, 25497−25513

Supporting Information

Scheelite-Type Wide-Bandgap ABO_4 Compounds (*A* = Ca, Sr and Ba, *B* = Mo, W) as Potential Photocatalysts for Water Treatment

Marta Kowalkińska[1], Paweł Głuchowski[2], Tomasz Swebocki[3,4], Tadeusz Ossowski[3], Adam Ostrowski[5], Waldemar Bednarski[5], Jakub Karczewski[6], Anna Zielińska-Jurek[1*]*

[1] Department of Process Engineering and Chemical Technology, Faculty of Chemistry, Gdańsk University of Technology, Gabriela Narutowicza 11/12, 80-233 Gdańsk, Poland,

[2] Institute of Low Temperature and Structural Research, Polish Academy of Sciences, Okólna 2, 50-422 Wrocław, Poland,

[3] Department of Analytical Chemistry, Faculty of Chemistry, University of Gdansk, Wita Stwosza 63, 80-308 Gdańsk, Poland,

[4] Institute of Interdisciplinary Research (USR 3078), French National Centre for Scientific Research, F-59652 Villeneuve-d'Ascq, France

[5] Institute of Molecular Physics, Polish Academy of Sciences, Mariana Smoluchowskiego 17, 60-179 Poznań, Poland,

[6] Institute of Nanotechnology and Materials Engineering, Faculty of Applied Physics and Mathematics, Gdańsk University of Technology, Gabriela Narutowicza 11/12, 80-233 Gdańsk, Poland.

---

* Corresponding authors: marta.kowalkinska@pg.edu.pl (MK), annjurek@pg.edu.pl (AZJ)

1. Size distribution of nanoparticles or microcrystals

Normal distribution of nanoparticles (for calcium and strontium compounds) or microcrystals (for barium compounds) size was performed for each sample. All the size distributions are presented in Figure S1. To determine the size distribution of nanoparticles and agglomerates, SEM images of all samples were measured. Then the ImageJ software was applied to analyze the nanoparticles' and agglomerates' sizes. All measurements were carried out manually. For each considered sample, the morphological parameters were measured at least min. 100 times (for nanoparticles' size) or 50 times (for agglomerates' size). Finally, the obtained data were a basis of size distribution and were used to calculate the mean agglomerate diameter and mean nanoparticle size as well as to plot histograms.

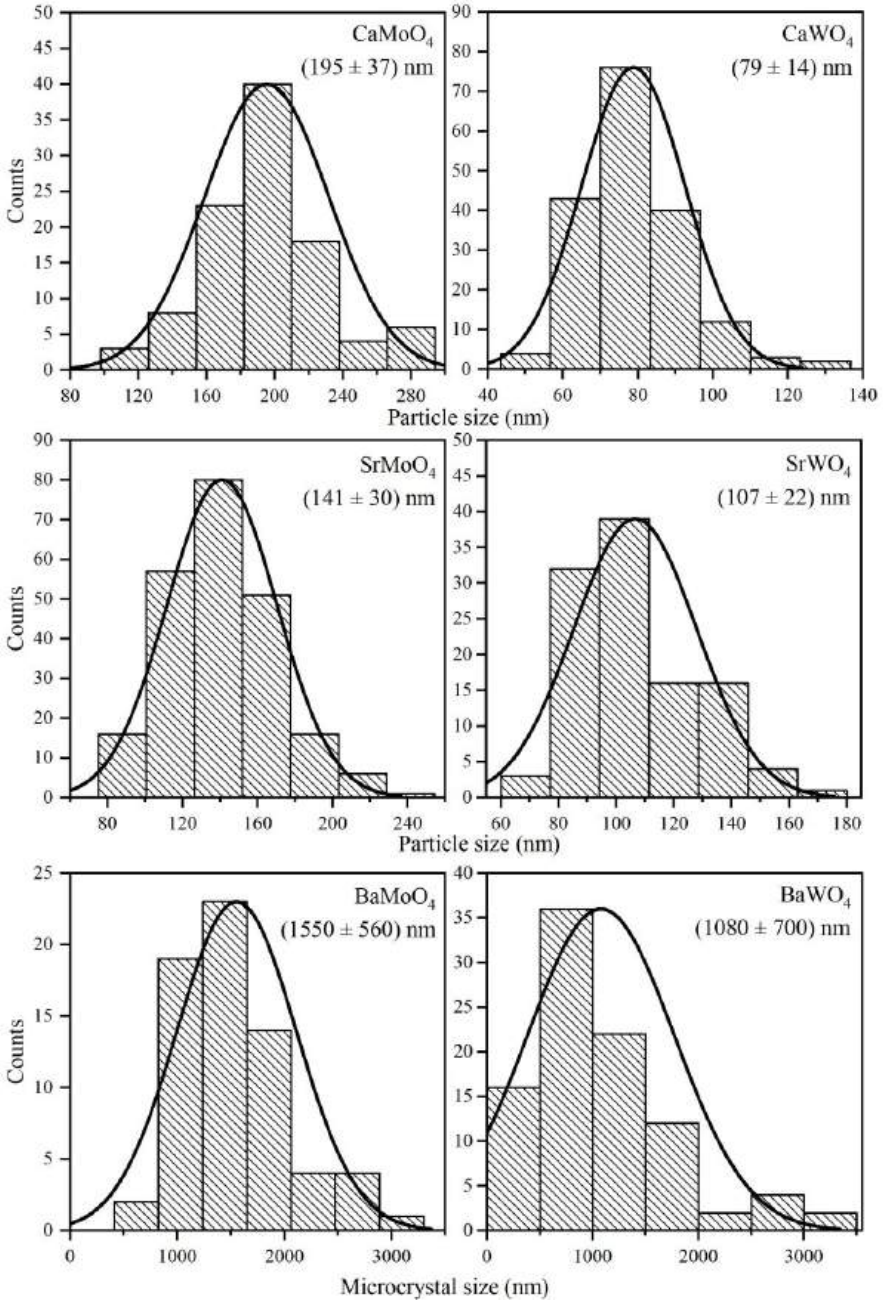

Figure S1. Size distribution graphs of nanoparticles ($CaMoO_4$, $CaWO_4$, $SrMoO_4$, $SrWO_4$) and microcrystals ($BaMoO_4$, $BaWO_4$)

2. Adsorption isotherms

The SEM analyzes were completed by adsorption isotherm measurements (Figure S2).

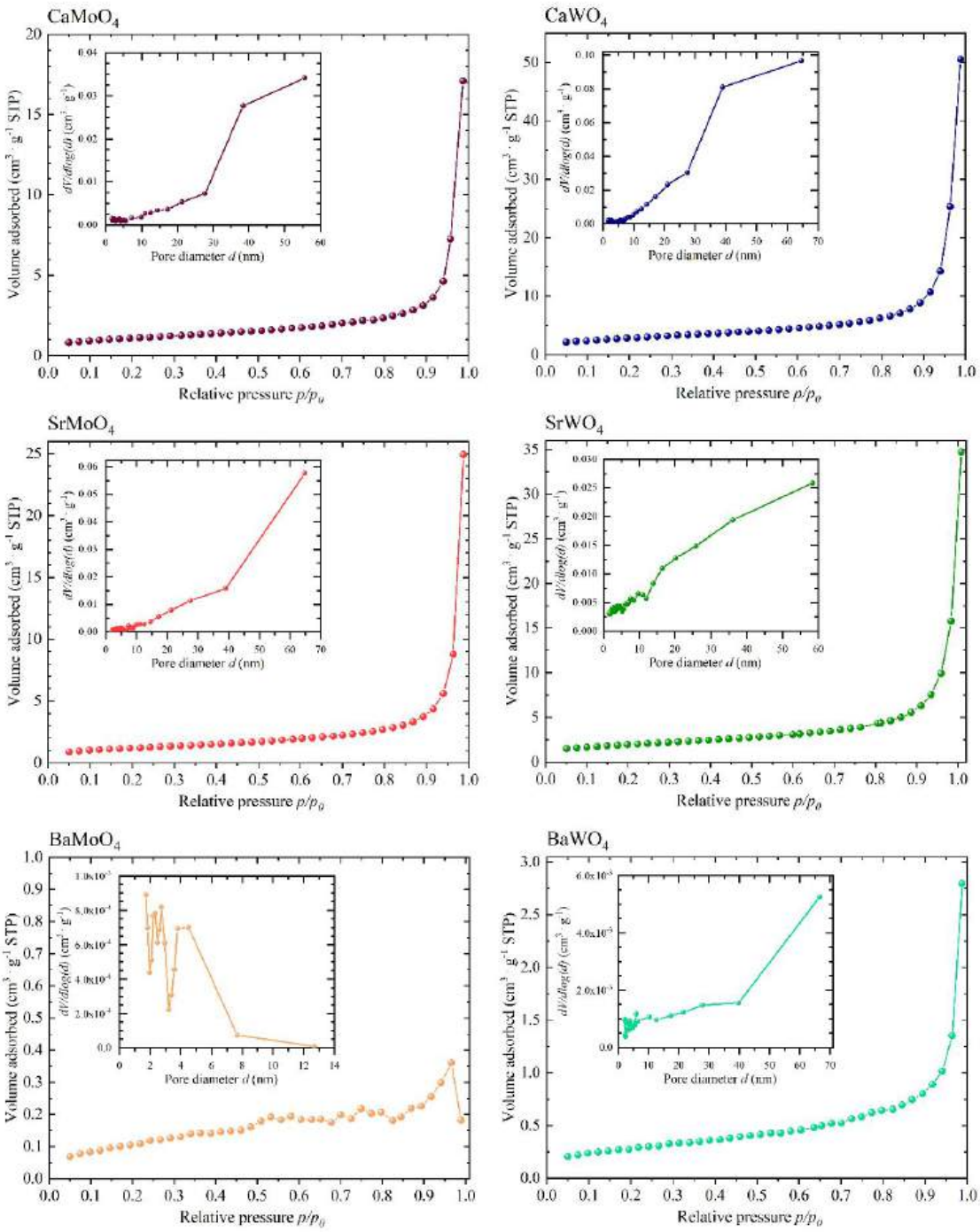

Figure S2. Low-temperature N_2 adsorption isotherms measured for the obtained samples. The inset shows the pore size distributions

3. Band gap calculations

The band gap of obtained scheelite-type photocatalysts was calculated using the Tauc method. This method includes the fact that the optical band gap is associated with the absorbance and the photon energy by the equation: $(F_{KM} \cdot h\nu)^n = A\ (h\nu - E_g)$, where F_{KM} is a Kubelka-Munk function, $h\nu$ is the photon energy, A is the absorption coefficient, E_g is the optical bandgap of the material and n is the constant associated with the different types of electronic transitions. In the case of the molybdates and tungstates with scheelite-type tetragonal structure, directed electronic transition is allowed (n=2), so the band gap value was determined by extrapolating the straight portion of the curve to y=0.

The transformations of Kubelka-Munk function versus photon energy were presented in Figure S3. The uncertainties of measurements came from the least-squares approximation of linear jump of $(F_{KM} \cdot E_{ph})^{½}$ data and included in the graphs. Due to the discrepancy in the literature, it is hard to compare results of E_g values in this work with other reports. In general, band gap values are in ranges 3.4-4.4 eV (molybdates) or 4.2-6.2 eV (tungstates). The differences in band gaps can be explained by different structural defects, e.g., oxygen vacancies, which can promote the formation of intermediate energy states within the bandgap.

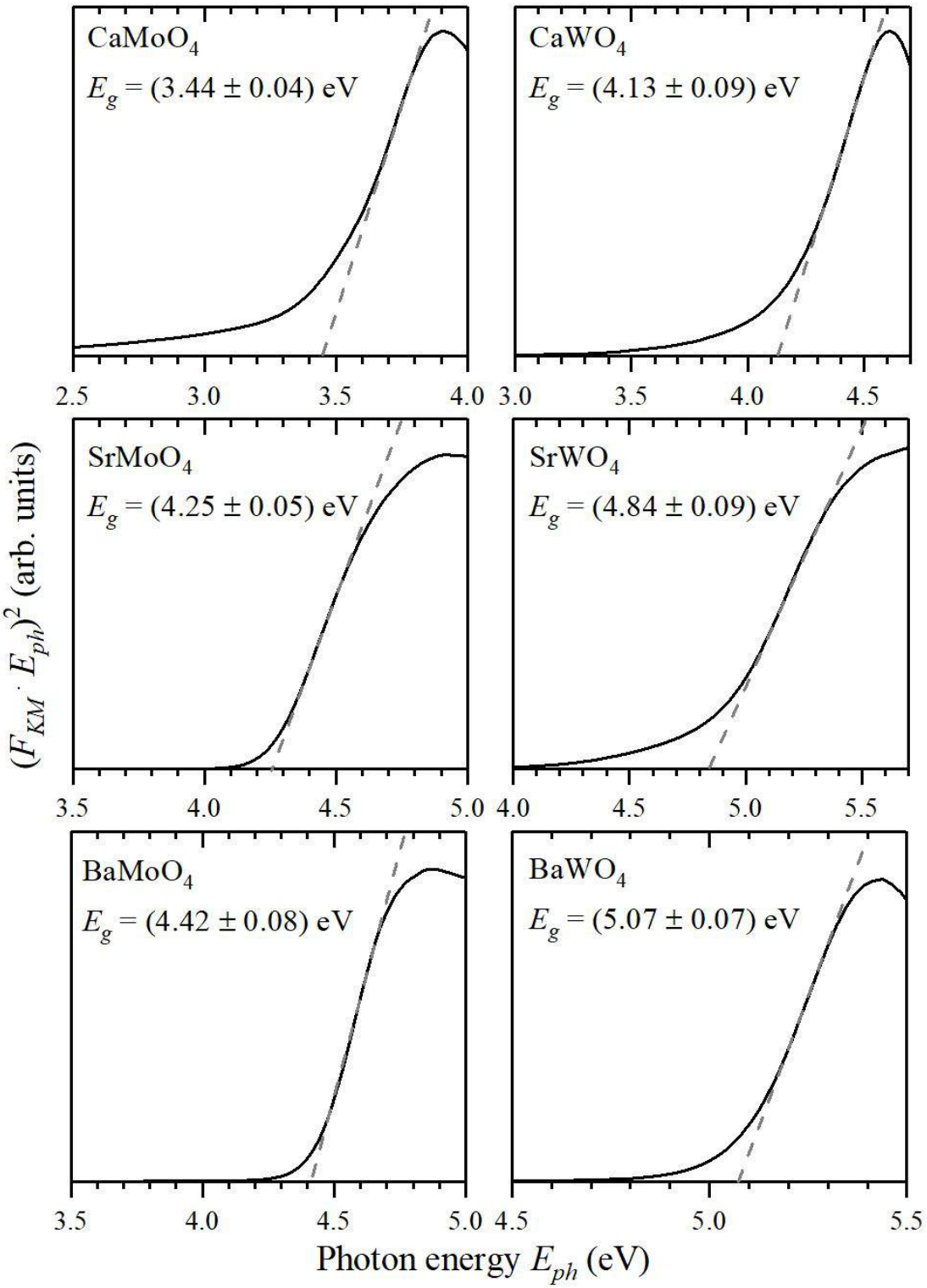

Figure S3. The transformation of Kubelka-Munk functions vs. photon energy for alkali-earth metal tungstates and molybdates.

4. Additional information about optical properties of ABO_4 compounds

The excitation spectra of obtained samples are presented in Figure S4. The highest intensity of excitation is noticed only for calcium compounds. These observations are in agreement with emission spectra (see Fig. 7 in the main text) of photocatalysts and confirm the photoluminescence properties of $CaWO_4$ and $CaMoO_4$.

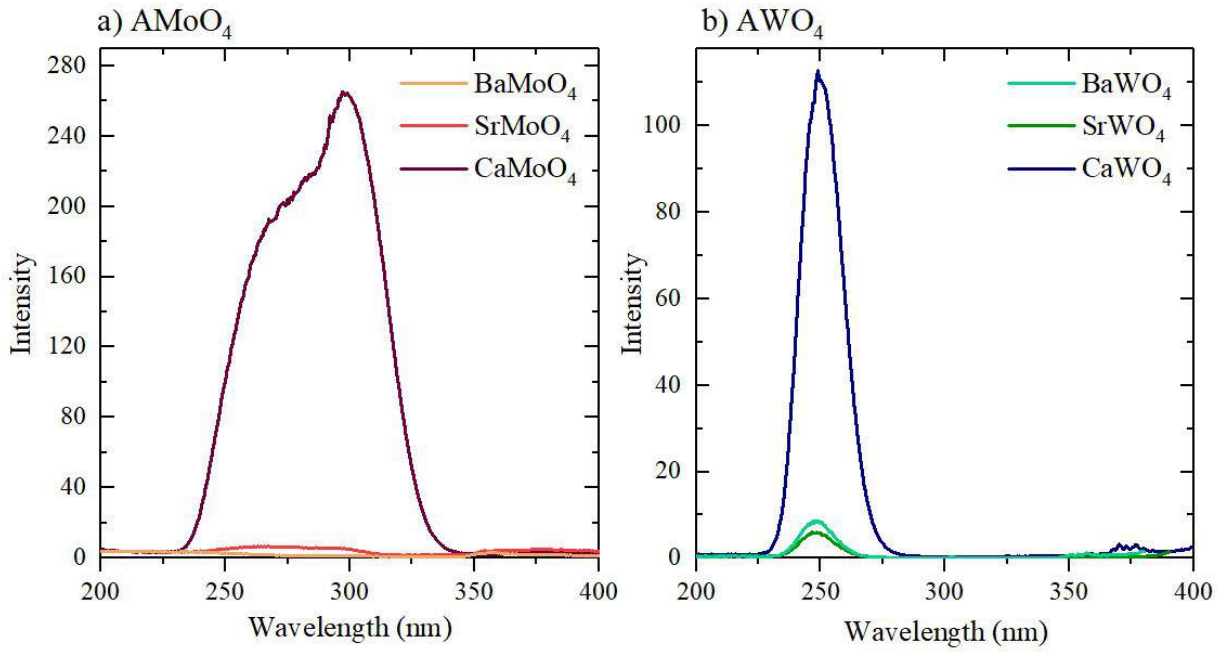

Figure S4. Excitation spectra of alkali-earth metal a) molybdates (λ_{em} = 510 nm for $BaMoO_4$, λ_{em} = 513 nm for $SrMoO_4$ and λ_{em} = 528 nm for $CaMoO_4$), b) tungstates (λ_{em} = 392 nm for $BaWO_4$, λ_{em} = 399 nm for $SrWO_4$ and λ_{em} = 413 nm for $CaWO_4$).

5. Flat bands and capacity of ABO_4 compounds determination

Based on EIS spectra, flat bands and the capacity of the obtained scheelite-type compounds were determined. These parameters were presented in Figure S5 and Table S1, together with the uncertainty of these values.

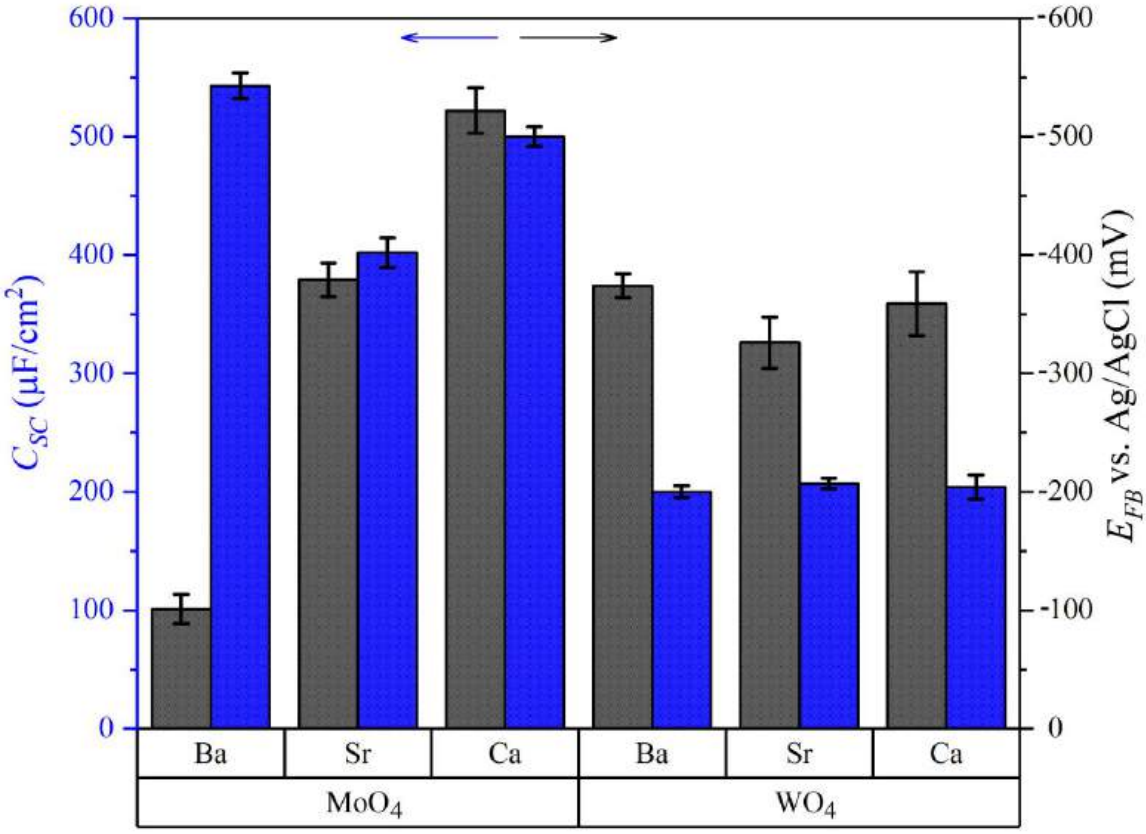

Figure S5. The E_{FB} (blue) and C_{SC} (grey) parameters of alkali-earth metal tungstates and molybdates obtained using EIS.

Table S1. The E_{FB} and C_{SC} parameters of presented photocatalysts obtained by means of EIS.

Sample	**E_{FB} vs. Ag/AgCl (mV)**	**C_{SC} (μF/cm^2)**
$CaMoO_4$	-379.28 ± 14.24	402 ± 12.45
$SrMoO_4$	-522.81 ± 19.22	500 ± 8.22
$BaMoO_4$	-101.50 ± 12.44	543 ± 10.82
$CaWO_4$	-326.15 ± 21.51	207 ± 4.54
$SrWO_4$	-359.91 ± 26.95	204 ± 10.33
$BaWO_4$	-374.45 ± 10.01	200 ± 4.91

6. Detailed study of phenol photocatalytic degradation

Additional results of phenol degradation for each sample are presented below in Figure S6. 1,2-dihydroxybenzene (catechol) and benzene-1,4-diol(hydroquinone) are the two main derivatives that appear during the photocatalytic process. The reaction kinetics are shown in the main manuscript.

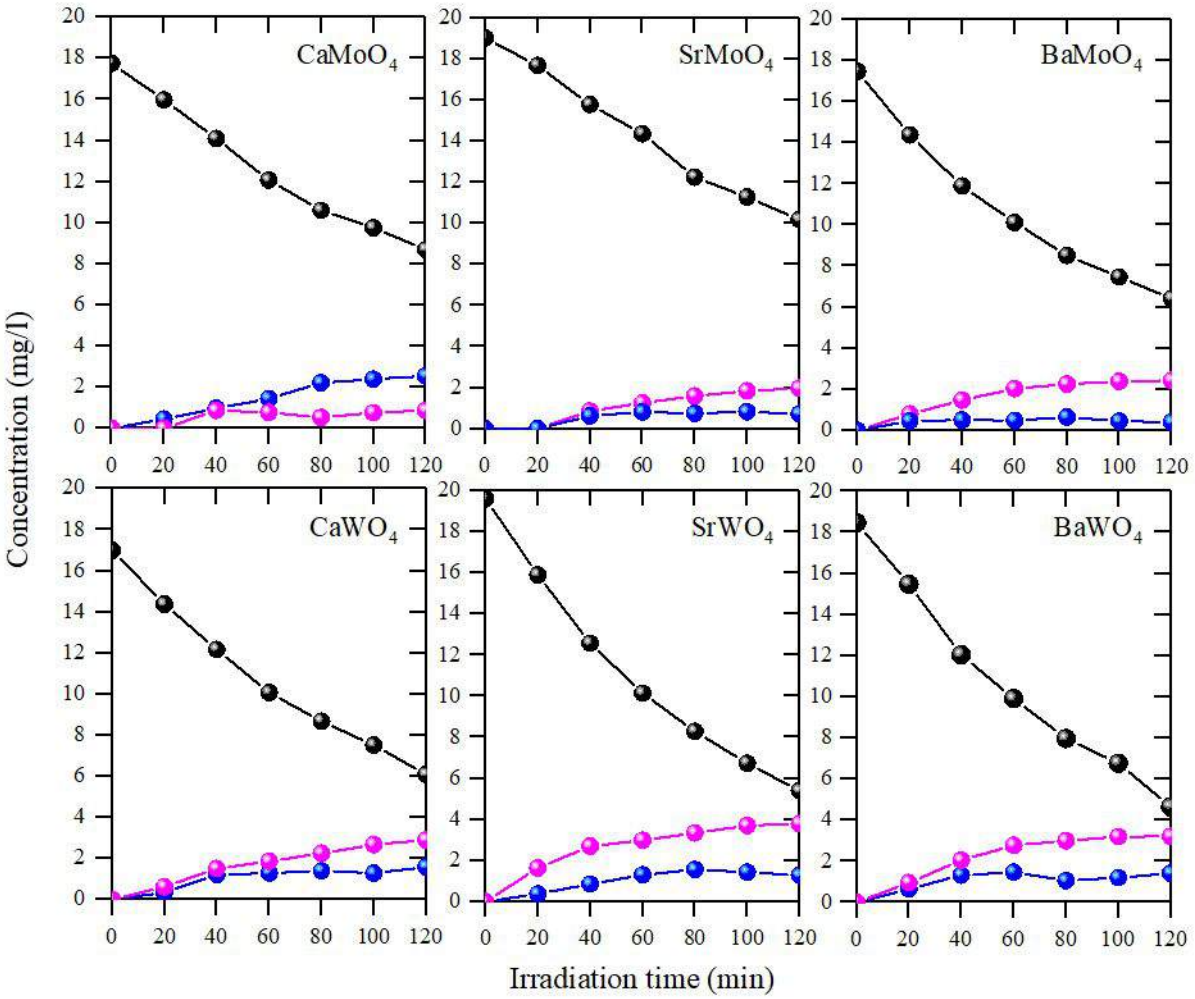

Figure S6. Phenol (black lines), hydroquinone (blue lines), and catechol (pink one) concentration vs. irradiation time for different scheelite-type photocatalysts.

Small differences in phenol removal can result from minor photocatalyst loss during filtration, which is necessary for preparing samples for HPLC analysis.

To study the mineralization efficiency, the total organic carbon (TOC) measurements were performed (Figure S7). No significant decline of TOC in comparison with phenol (20 ppm) was observed. Minor deviations resulted from measurement uncertainty (2%).

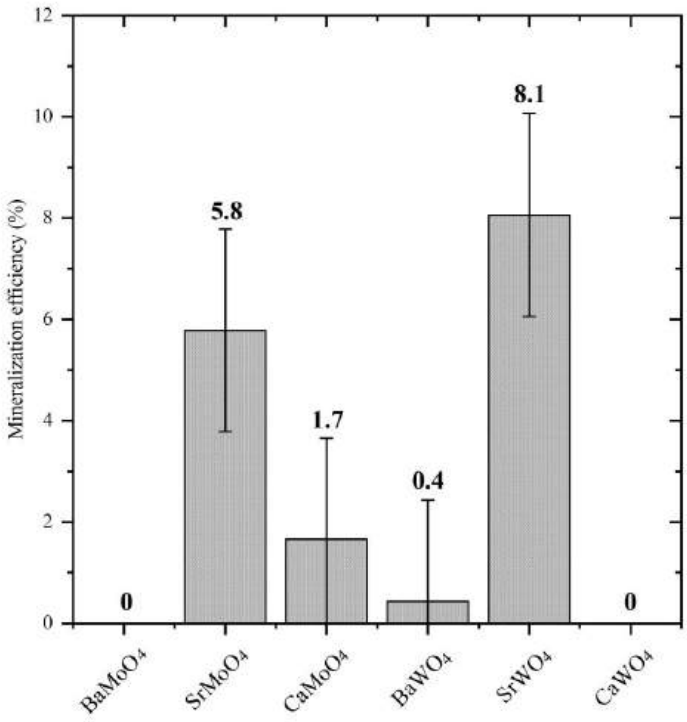

Figure S7. TOC measurements for scheelite-type compounds after the photocatalytic process.

7. Stability of scheelite-type compounds

To confirm the stability of the presented materials, three cycles of the photocatalytic process were performed. The phenol degradation efficiency after cycles is presented in Figure S8.

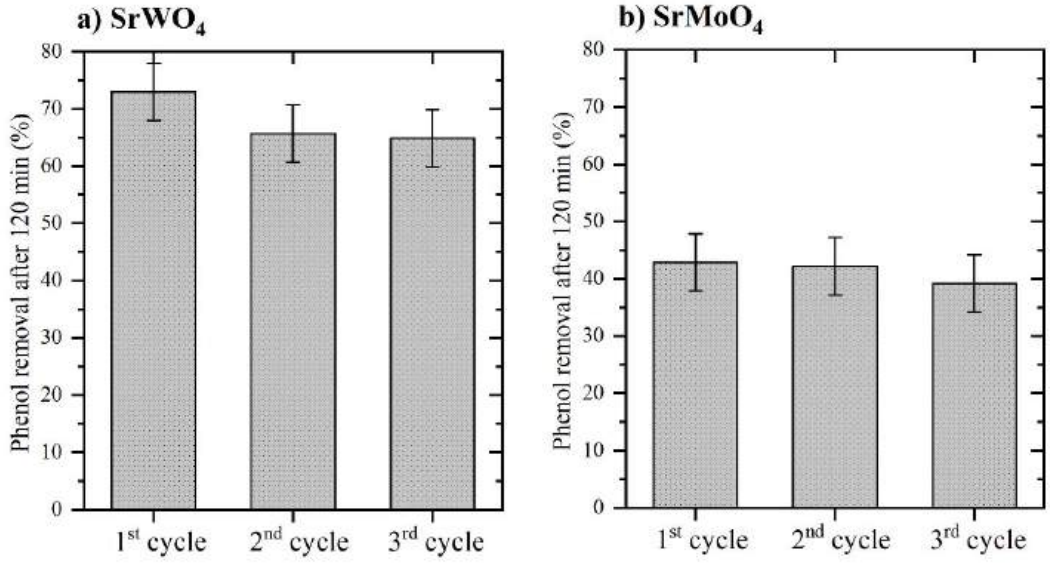

Figure S8. The efficiency of phenol degradation after 120 minutes of the photocatalytic process using a) $SrWO_4$ and b) $SrMoO_4$ after three degradation cycles.

In addition, X-Ray diffraction patterns are demonstrated for each photocatalyst (Figure S9). No additional peaks from other phases were detected, confirming that all scheelite-type compounds are stable after the photocatalytic process and can be reused without specific treatment. The same conclusions can be found after comparing the XRD patterns of $SrWO_4$ and $SrMoO_4$ after three cycles of the photocatalytic process. The investigations about the stability of ABO_4 materials were completed by SEM analysis, presented in Figures S10 and S11. It was shown that after the photocatalytic process, the agglomerates present in Figures 3 and 4 (main manuscript) had fallen apart, and in consequence, these microspheres are fragmented. These pieces of spheres can also join each other and create bigger agglomerates. However, the new formations are more irregular than before the photocatalytic process. After three degradation cycles, there were no significant changes in the morphology of $SrMoO_4$ and $SrWO_4$. In the case of barium compounds, the obtained microcrystals were also visible, but for $BaMoO_4$, the polyhedra created the single elongated agglomerates, whereas, for $BaWO_4$, the agglomerates consisted of many particles.

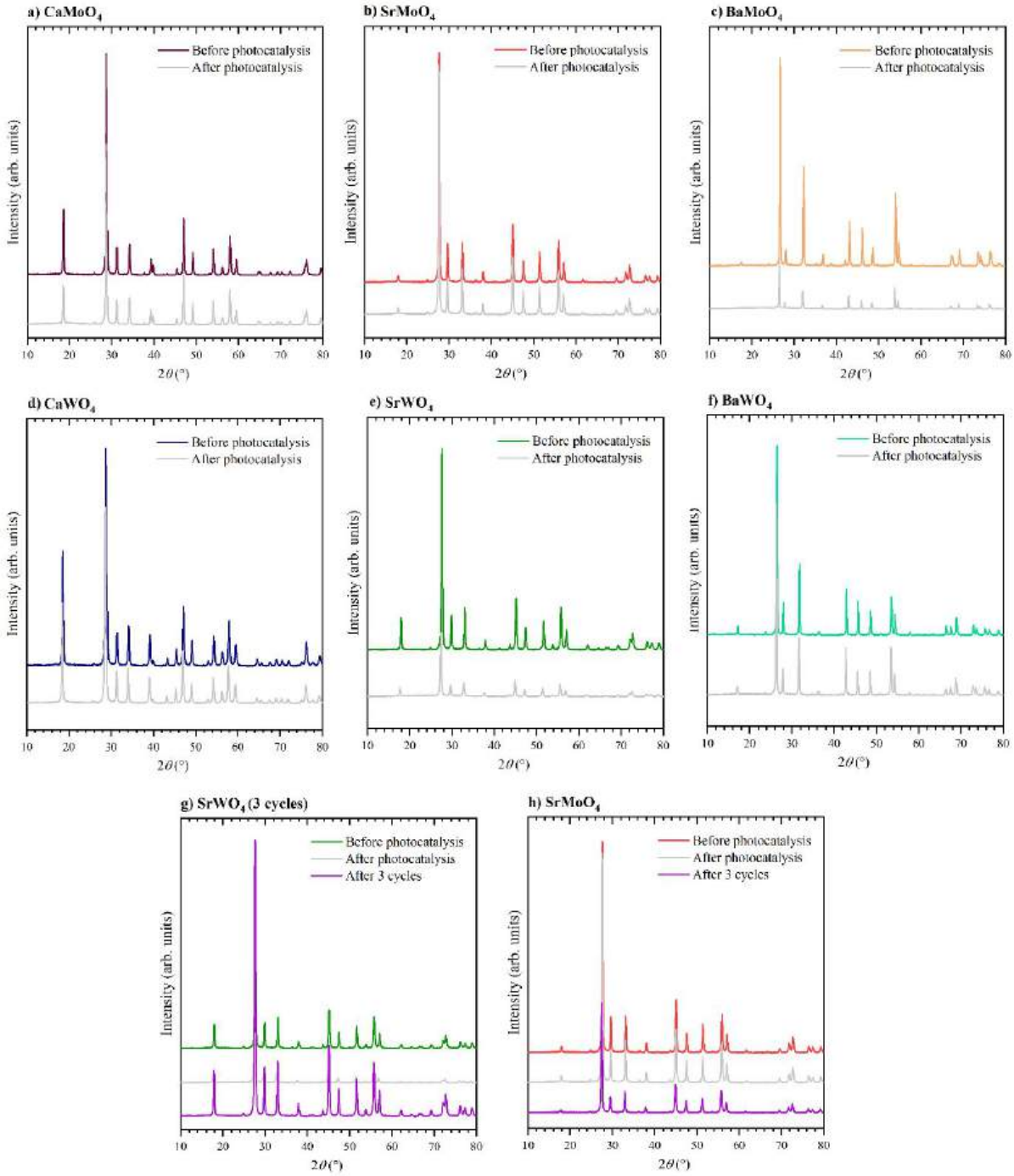

Figure S9. XRD patterns of ABO_4 compounds before and after the photocatalytic process.

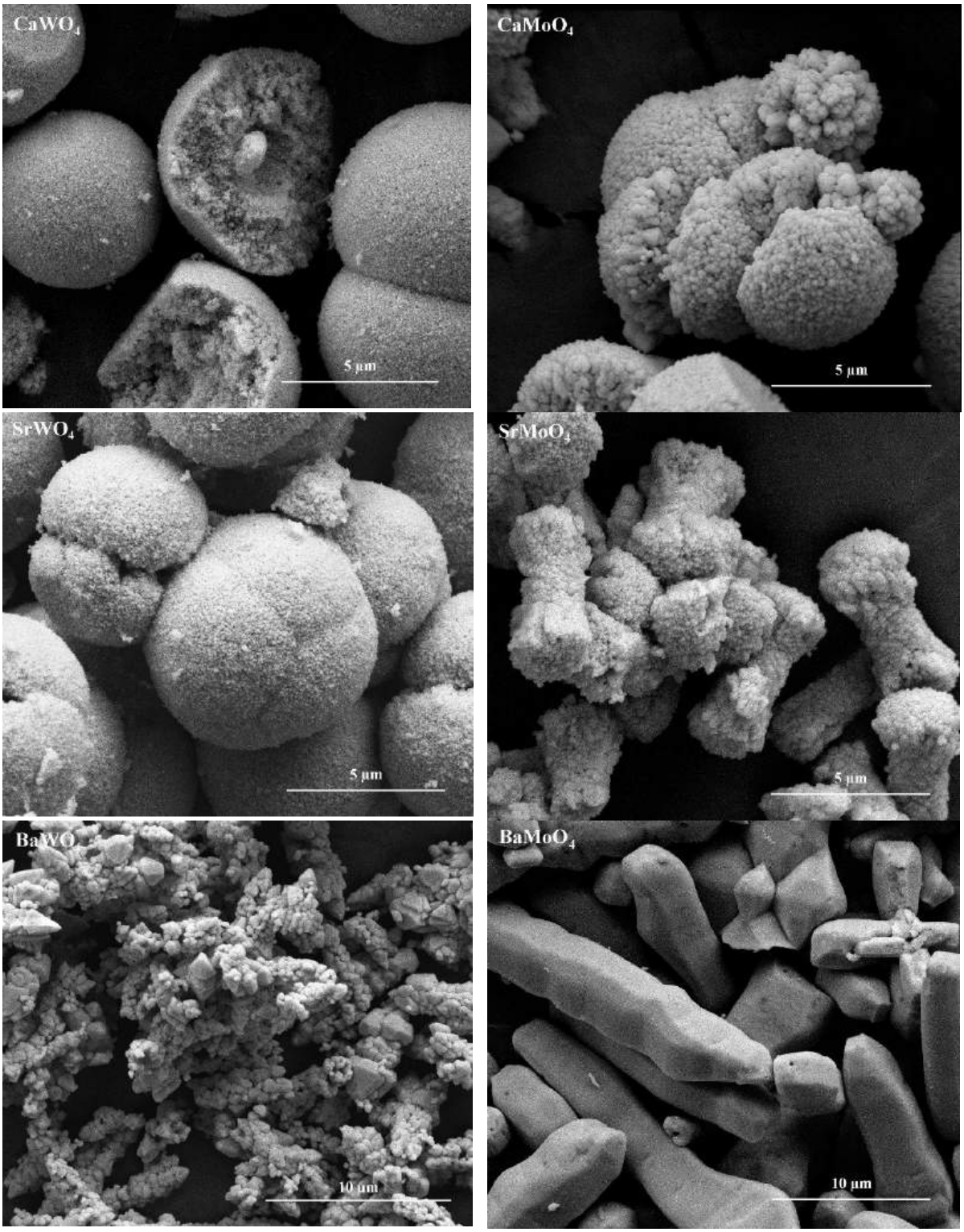

Figure S10. SEM images of ABO_4 compounds after the photocatalytic process.

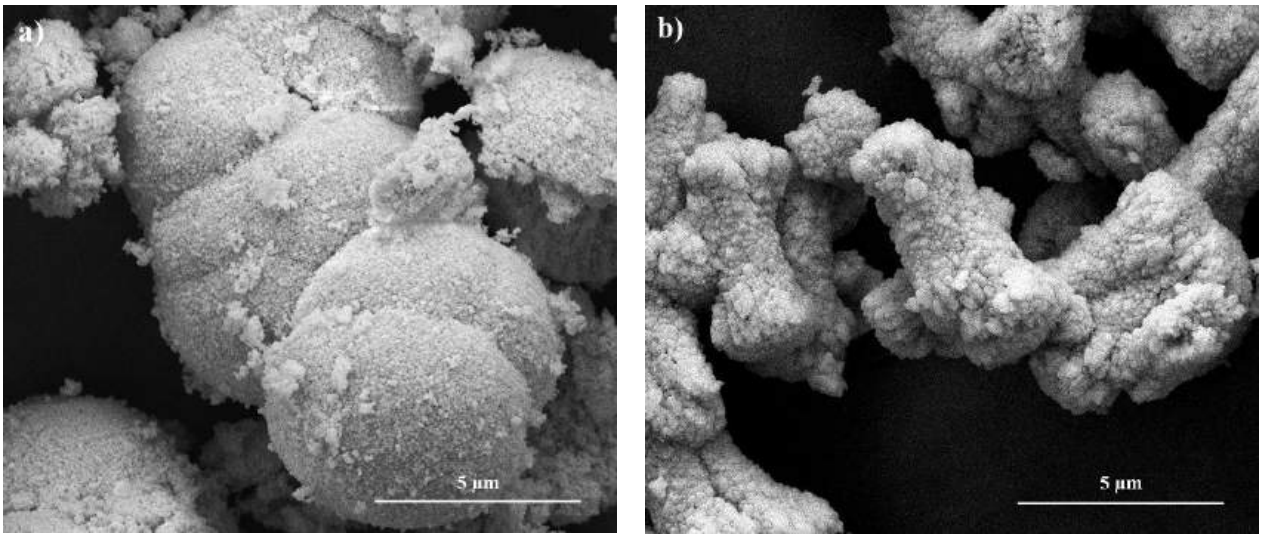

Figure S11. SEM images of a) $SrWO_4$ and b) $SrMoO_4$ after three degradation cycles.

4.2. Chapter II: Facet-dependent naproxen degradation over F-TiO_2 synthesized from $TiOF_2$

Based on **[P3]** M. Kowalkińska, K. Sikora, M. Łapiński, J. Karczewski, A. Zielińska-Jurek, *Non-toxic fluorine-doped TiO_2 nanocrystals from $TiOF_2$ for facet-dependent naproxen degradation*, Catalysis Today, 413, 2023, 113959.

Herein, titanium oxyfluoride ($TiOF_2$) was used for the first time as a precursor for crystal facet-engineered F-TiO_2, as it naturally introduced fluoride ions into the reaction environment. These photocatalysts were obtained through hydrothermal synthesis in the aqueous $NH_4F/TiOF_2$ mixture (series A:1), optionally with additional capping agents $NH_{3(aq)}$ or NaF.

SEM images, shown in Figure 4.3, revealed the agglomerates of F-TiO_2 composed of smaller nanocrystals. The presence of particular capping agents influenced the crystal facets exposition. After hydrothermal treatment of aqueous $NH_4F/TiOF_2$ mixture, the formation of decahedral F-TiO_2 with exposed {0 0 1} and {1 0 1} facets. Similar results were noticed for the sample, for which NaF was used during synthesis. When $NH_{3(aq)}$ was introduced to the reaction environment, the exposition of {1 0 1} and {1 0 0} crystal facets was favoured. EDX spectroscopy confirmed the presence of fluorine in all samples, although no surface fluorine was detected by XPS spectroscopy for samples synthesized with $NH_{3(aq)}$ as the capping agent. These results suggest that doping occurs instead of surface modification by fluoride ions.

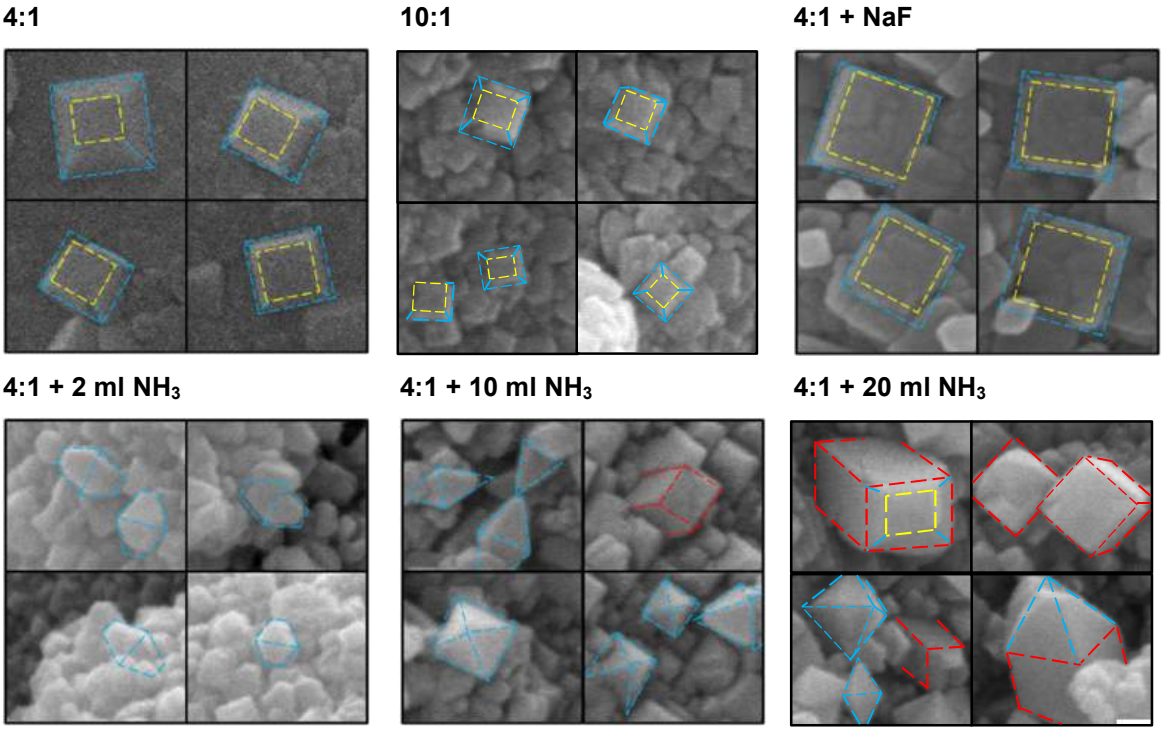

Figure 4.3. Zoomed SEM images of selected F-TiO_2 nanostructures with marked crystal shapes.

Then, F-TiO_2 photocatalysts were investigated toward photocatalytic degradation of naproxen (NPX) under UV-vis and visible light (λ > 420 nm), as presented in Figure 4.4. NPX undergoes rapid photolysis under UV-vis light, which makes difficulties in kinetics of photocatalytic processes. However, the effect of photolytic TOC conversion of NPX solution was relatively low, reaching 10% of TOC reduction, so this parameter was a direct confirmation that photocatalytic processes occur. Among the series, the most promising was sample 4:1 + 10 ml NH_3 due to the highest TOC conversion yield (65% of TOC reduction after 60 min) and the highest photocatalytic activity under visible light.

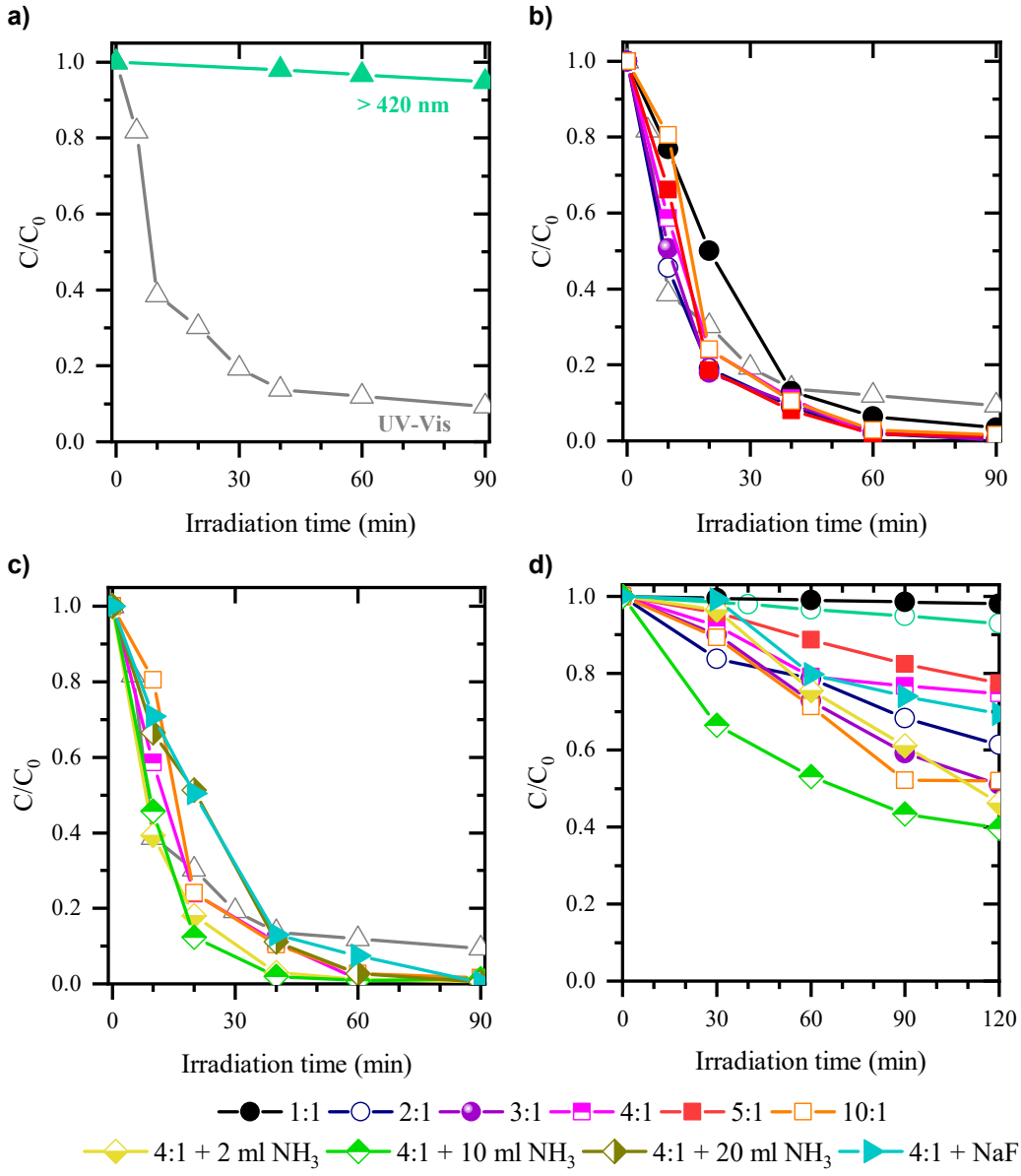

Figure 4.4. NPX degradation **a)** without photocatalysts (only photolysis), **b)** using F-TiO_2 photocatalysts from A:1 series, **c)** using photocatalysts with the addition of NH_3 or NaF to synthesis under UV-Vis and **d)** under visible (> 420 nm) light.

Then, the NPX photocatalytic degradation pathway was monitored using liquid chromatography-mass spectrometry (LC-MS). Remarkably, a dimer intermediate was detected when the NPX solution was treated by F-TiO_2 samples with exposed {0 0 1} facets. This by-product was not observed during photocatalysis with samples with mostly {1 0 1} crystal facets exposure. Moreover, the toxicity rate of post-process solutions was examined using Microtox® bioassay with *Vibrio fisheri* bioluminescence bacteria. Remarkably, no inhibition of bacteria's bioluminescence was noticed for solutions after photocatalytic treatment with F-TiO_2 synthesized in the presence of $NH_{3(aq)}$. Based on these results, we proposed that {0 0 1} facets induced dimer formation, leading to lower TOC removal and the highest toxicity rate of the post-process solution.

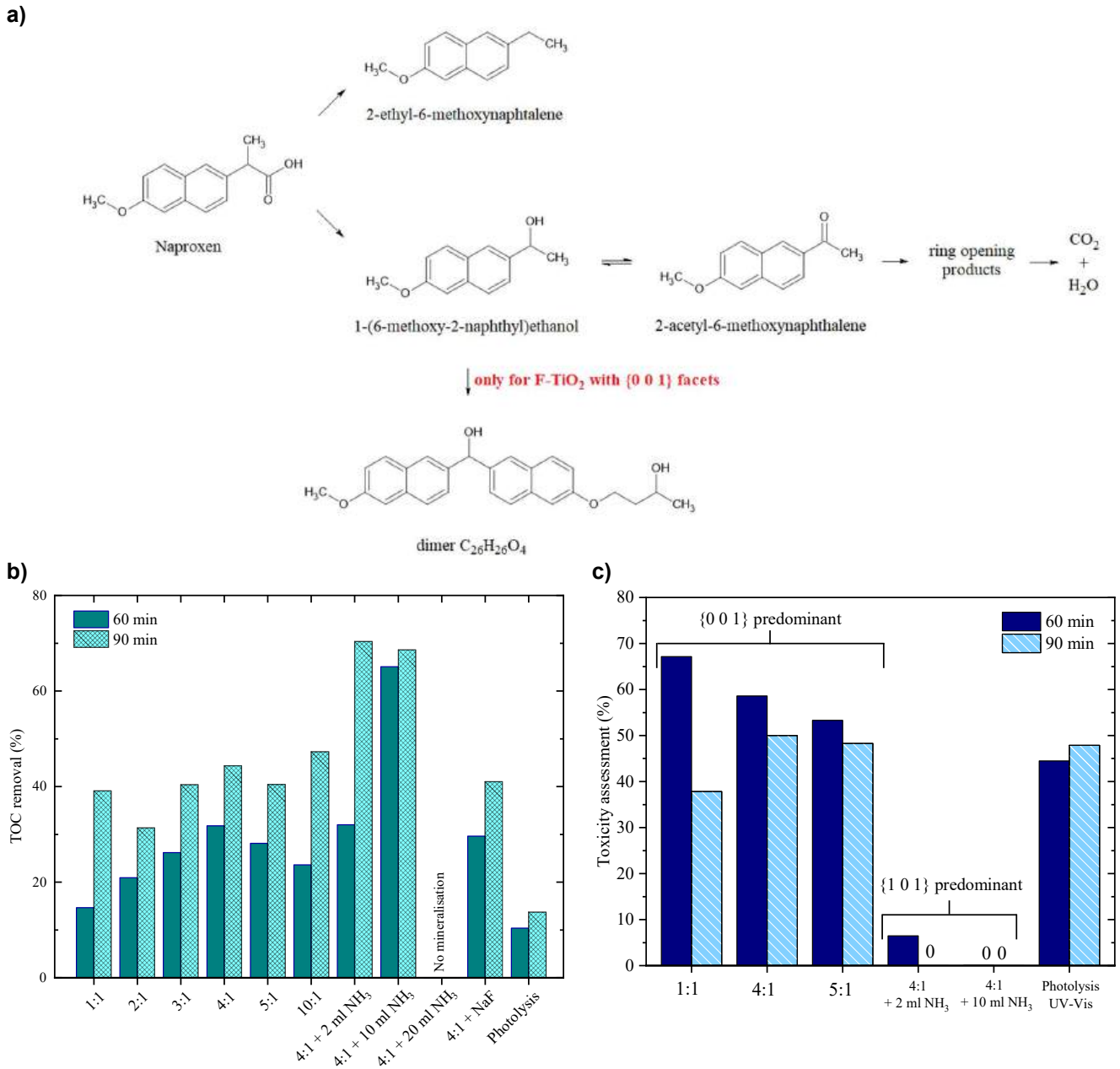

Figure 4.5. a) Products of NPX photocatalytic degradation under UV-vis irradiation, **b)** TOC conversion of NPX solution, **c)** Toxicity rate measurements using Microtox® bioassay.

Catalysis Today 413-415 (2023) 113959

Contents lists available at ScienceDirect

Catalysis Today

journal homepage: www.elsevier.com/locate/cattod

Non-toxic fluorine-doped TiO_2 nanocrystals from $TiOF_2$ for facet-dependent naproxen degradation

Marta Kowalkińska [a,*], Karol Sikora [b], Marcin Łapiński [c], Jakub Karczewski [c], Anna Zielińska-Jurek [a,*]

[a] Department of Process Engineering and Chemical Technology, Faculty of Chemistry, Gdansk University of Technology, Poland
[b] Department of Inorganic Chemistry, Faculty of Pharmacy, Medical University of Gdansk, Poland
[c] Institute of Nanotechnology and Materials Engineering, Faculty of Applied Physics and Mathematics, Gdansk University of Technology, Poland

ARTICLE INFO

Keywords:
Fluorine-doped TiO_2
Crystal facets engineering
Naproxen degradation
Titanium oxyfluoride
Microtox bioassay

ABSTRACT

In the present study, the photocatalytic degradation of naproxen (NPX), which is a nonsteroidal anti-inflammatory drug (NSAID), frequently detected in drinking water, was investigated. The F-doped TiO_2 with defined morphology was successfully obtained from $TiOF_2$ and applied for photocatalytic degradation under UV–vis and visible light. All samples were characterised by X-ray diffraction, scanning electron microscopy, X-ray photoelectron spectroscopy, zeta potential, diffuse reflectance spectroscopy, and Brunauer–Emmett–Teller surface area analyses. The effect of morphology on the photocatalytic activity of the F-TiO_2 nanostructures with exposed {1 0 1}, {0 0 1} and {1 0 0} facets was studied. Octahedral F-TiO_2 particles with exposed {1 0 1} facets revealed the highest photocatalytic activity, and degraded 100% of the initial NPX concentration after 40 min of the photodegradation process under simulated solar light (UV–vis). Moreover, this sample exhibited the highest TOC removal and NPX degradation under visible light (>420 nm). Based on HPLC-MS analysis, it was assumed that {0 0 1} facets present in fluorinated decahedral nanostructures promote the formation of a dimer, which further hinders the mineralisation rate. Therefore, decahedral nanostructures exposing {1 0 1} and {0 0 1} facets revealed lower photocatalytic activity than octahedral F-TiO_2 particles with exposed {1 0 1} facets, which is also consistent with DFT studies. Finally, toxicity assessment of post-process suspensions using Microtox bioassay confirmed that fluorine-doped octahedral anatase particles are non-toxic, although fluorine ions were the reactants of the synthesis from $TiOF_2$. Overall results showed the possibility of application of highly efficient and environmentally safe fluorine-doped anatase photocatalysts in improved degradation of naproxen.

1. Introduction

An excessive introduction of organic contaminants to water is a serious environmental hazard. The effluents may contain large amounts of toxic organic compounds, which are not susceptible to treatment using conventional methods [1,2]. Therefore, the efficient treatment of wastewaters is an ambitious challenge. Among the group of emerging contaminants, pharmaceuticals and personal care products (PPCP) are extensively and increasingly being detected in the water. PPCPs can be further classified as antibiotics, contrast agents, hormones, and nonsteroidal anti-inflammatory drugs (NSAIDs). Their presence in natural sediments, groundwater, surface water, and even drinking water can hinder the proper functioning of the human body and other organisms in the natural environment. The toxicity and persistence of some pollutants and limited drinking water resources have made it necessary to search for new advanced treatment technologies for environmental protection, applying innovative nanotechnology solutions to purify water from emerging contaminants [3].

Recently, the commonly used worldwide pharmaceuticals from the group of nonsteroidal anti-inflammatory drugs have gained attention due to the concern of possible effects on living aquatic organisms and humans. An example of a pain killer from the NSAIDs group, which occurs in the environment causing an emerging problem, is naproxen (NPX). It is a commonly used drug for treating osteoarthritis in patients, unlike diclofenac and other NSAIDs, because at high doses, it poses a lower vascular risk [4]. Moreover, the prolonged duration of action resulting from a long biological half-life and no need for a prescription are reasons for its popularity in the pharmaceutical market and, as a

* Corresponding authors.
E-mail addresses: marta.kowalkinska@pg.edu.pl (M. Kowalkińska), annjurek@pg.edu.pl (A. Zielińska-Jurek).

https://doi.org/10.1016/j.cattod.2022.11.020
Received 5 August 2022; Received in revised form 28 October 2022; Accepted 14 November 2022
Available online 15 November 2022

consequence, its presence in surface waters. Caban et al. have detected naproxen in ground and surface water in Gdańsk (Poland). In this study, naproxen, next to paracetamol, was one of the most frequently detected active pharmaceutical ingredients in drinking water [5]. Although the established concentration of NPX was at the $ng \cdot dm^{-3}$ level, it is not completely removed during wastewater treatment processes and can bioaccumulate and biomagnify in living organisms, which can cause antibiotic resistance, skin irritation, endocrine disruption or neurotoxic, and even immunotoxic reactions [6,7]. Therefore, the elimination and degradation methods of NPX in WWTP are highly desirable. Among water treatment technologies, heterogeneous photocatalysis is worthy of attention because it allows for the degradation of trace amounts (at the level of a few $mg \cdot dm^{-3}$ to several hundreds of $\mu g \cdot dm^{-3}$) of organic pollutants from water or air. If photocatalysts are active under visible light, they open up the possibility of utilising solar irradiation instead of highly energy-consuming UV lamps. However, so far, the low quantum efficiency under visible light and fast charge carriers recombination are still limiting factors in photocatalysis [8].

Titanium (IV) oxide is one of the most promising photocatalysts due to its strong oxidising potential, low cost, and long-term stability against photocorrosion and chemical corrosion [9,10]. However, the large bandgap energy of about 3.2 eV for anatase, and in consequence, the capability of being excited only by ultraviolet light is a limitation for the application of photocatalysis in the presence of solar light. In this regard, attention has been paid to extending the optical response of TiO_2-based photocatalyst. It is of great importance to develop photocatalysts that can be used in both UV and visible light regions. The first attitude is doping by using transition metal cations into TiO_2 lattice. However, this approach often leads to localising d-states deep in the bandgap of titanium (IV) oxide, which acts as the recombination centres for photoexcited electrons and holes and lowers the photocatalytic activity. Moreover, doping may contribute to unfavourably shifting the conduction band below the redox potential of adsorbates, which inactivates the photocatalyst [11]. Therefore, doping with anions, usually non-metal atoms, seems to be a promising alternative for structure modification because they result in the p-states near the valence band, much like other deep donor levels in TiO_2 [12].

Among modified photocatalysts, fluorinated titanium(IV) oxide has been reported as a promising photocatalytic material, including introducing defects to crystal lattice and surface fluorination. The great potential of F-TiO_2 results from strong complexation between F^- and Ti as well as the high electronegativity of fluorine leading to more efficient hole-induced direct water oxidation. Next to changes in surface structure, doping of TiO_2 with fluorine improves its photoreactivity through tailoring the band structure [12]. However, fluorine is toxic to the central nervous system, and excessive exposure to this element can cause harmful effects such as permanent damage to all brain structures, memory dysfunction, and behavioural problems [13]. Moreover, most described fluorinated TiO_2 were synthesised using hydrofluoric acid as a capping agent. The HF-assisted synthesis allows for stabilising high-energetic crystal facets, but their efficiency is low due to the etching of the anatase structure and dissolution–recrystallisation processes [14]. Therefore, titanium oxyfluoride ($TiOF_2$) is a desired precursor because it naturally introduces fluorine ions inside the reaction system. Our previous study showed that the application of $TiOF_2$ enables to control of the growth of selected crystal facets using simple stabilising agents [15].

In this regard, in the present study, faceted F-TiO_2 photocatalysts from the combination of NH_4F and $TiOF_2$ were for the first time successfully synthesised. Furthermore, the photocatalytic activity towards NPX degradation over F-doped titanium(IV) oxide together with the Microtox bioassay test were studied in detail. To our best knowledge, there are no studies of the toxicity assessment of fluorinated TiO_2 with defined morphology. The efficiency of proposed photocatalysts was studied on three parameters: (i) removal of NPX under simulated solar and visible light, (ii) total organic carbon removal, and (iii) toxicity assessment. Finally, the role of surface structure compared with DFT calculations and facets exposition toward NPX degradation pathway were discussed.

2. Experimental

2.1. Synthesis of F-TiO_2

The synthesis of titanium oxyfluoride ($TiOF_2$) by a facile and HF-free solvothermal method was described in our previous study [15]. Titanium (IV) tetrafluoride (TiF_4), 1-butanol, ammonium fluoride (NH_4F), sodium fluoride, and ammonia water (25%) were used as received from Sigma-Aldrich. The synthesis of F-TiO_2 was performed from $TiOF_2$ precursor (0.2 g) dispersed in 50 cm^3 of deionised water. Then, $TiOF_2$ suspension was added to 50 cm^3 of NH_4F solution in NH_4F: $TiOF_2$ molar ratios of 1:1, 2:1, 3:1, 4:1, 5:1 and 10:1. The obtained solution was transferred into a 200 cm^3 Teflon-lined stainless-steel autoclave and kept at 200 °C for 20 h, then cooled down naturally. After each reaction, beige precipitates were centrifuged and washed several times with water and ethanol to remove residual inorganic ions, then dried at 80 °C. The obtained photocatalysts were denoted as A:1, where *A* is the NH_4F: $TiOF_2$ molar ratio used in the synthesis. In addition, the effect of fluorine concentration was studied. In the first series, the appropriate amount of ammonia water was added, preserving the same volume of solution (100 cm^3) as earlier. The second part included the addition of NaF as a source of fluoride ions. In this case, the concentration of F^- was the same as in sample 10:1. Moreover, several attempts were performed with hydrofluoric acid but without success due to etching the anatase structure.

3. Materials characterisation

The characterisation methods applied in this work can be found in the subsection *2.1. Material characterisation* in the Supplementary Information (SI).

4. Results and discussion

The powder X-ray diffraction (XRD) analyses confirmed the phase-pure anatase crystallographic structure of the obtained photocatalysts (see Fig. S1 in Supplementary Information). No signal for any impurities was noticed. However, a close look into the (101) peak might suggest that the lattice is deformed. This peak is slightly shifted, indicating the lattice distortions due to the presence of a dopant. The more NH_4F was used in synthesis, the more remarkable shift was observed. A similar situation occurred when NH_3 or NaF was added during the synthesis. The lattice parameters and unit cell volumes calculated using Rietveld refinement are presented in Table S1.

The obtained photocatalysts' morphologies were examined using scanning electron microscopy. Fig. 1 shows the SEM images of F-TiO_2 prepared from $TiOF_2$. Moreover, SEM observations, including the truncation level and facet identification, are presented in Table S2 in SI. For all samples, the agglomerates composed of smaller nanostructures were observed. However, significant changes in individual photocatalysts can be noted. Firstly, the samples from the series without additives started the agglomeration process in hollow boxes on a bulk microparticle, which originates from the precursor, as well as creating crystal facets. The more NH_4F was used in the synthesis, the more faces from $TiOF_2$ cubes were unfolded, and more nanoparticles were distinguished on microscopy analyses. Therefore, samples n:1 and 4:1 + NaF are decahedral in shape with exposed {0 0 1} and {1 0 1} facets. However, this increased tendency has a limitation. Based on Yang et al., it was assumed that hydrothermal conditions, where water is the solvent, do not allow to stabilise only {0 0 1} facets [16]. Therefore, there is a limitation of synthesis nanostructures with {0 0 1} facets. There is a maximum value of truncation level (also the {0 0 1} to {1 0 1} ratio) and even higher

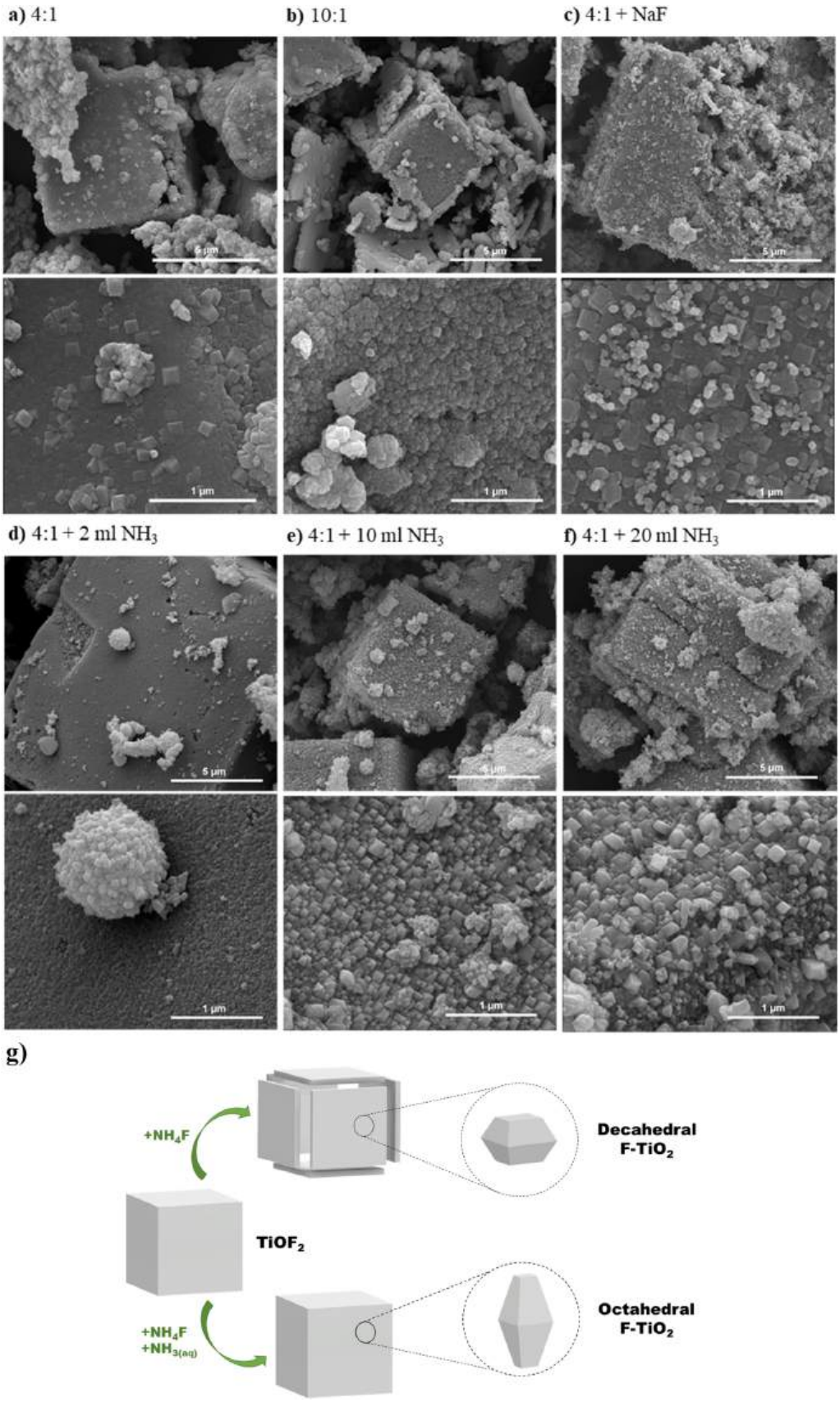

Fig. 1. (a-f) SEM images of F-TiO_2 nanostructures, g) Morphology evolution and transformation of F-TiO_2 from $TiOF_2$.

amount of fluorine in the reaction do not influence on the morphology of the photocatalyst. For further growth of {0 0 1} facets, changing the solvent from water to alcohol is needed [14].

Based on Lee and co-workers' study [17] and the above observations, the mechanism of anatase nanocrystals synthesis from titanium oxyfluoride and ammonium fluoride is proposed and can be described according to the following equations:

$$TiOF_2 + NH_4F \rightarrow NH_4TiOF_3 \quad (1)$$

$$NH_4TiOF_3 + 5H_2O \rightarrow [Ti(OH)_6]^{2-} + 2H^+ + 2HF + NH_4F \quad (2)$$

$$[Ti(OH)_6]^{2-} + 2H^+ \rightarrow TiO_2 + 4H_2O \quad (3)$$

According to Eqs. (1)–(3), three important roles of ammonium fluorine can be highlighted: i) a source of the intermediate product of NH_4TiOF_3, which can further hydrolyse to TiO_2, ii) capping agent, and iii) fluorine ions as the self-etching agent instantaneously produced in the system. However, the addition of $NH_{3(aq)}$ to the reaction system preserved the bulk cube originating from titanium oxyfluoride and prevented hollowing microparticles out. Ammonia molecules act as F^- scavengers, preventing adsorption on the photocatalyst's surface. Fluorine ions stabilise the {0 0 1} facet [18], which explains that on the cubes' faces, small nanoparticles with octahedral shapes with {1 0 1} facets are noted, as presented in Fig. 1d-e. For octahedral nanostructures, adding more ammonia to the synthesis caused lowering the truncation level and more distinct {1 0 1} facet exposition. So far, the synthesis of octahedral TiO_2 requires specific capping agents like a combination of hydrazine and sulphate ions [19] or using $Na_2Ti_3O_7$ phase [20]. The advantage of using $TiOF_2$ as a precursor is the simplification of the procedure of octahedral titanium (IV) oxide synthesis with good reproducibility. However, as presented in Fig. 1f, adding a high amount of $NH_{3(aq)}$ to the reaction system caused the formation of {1 0 0} facets, which was consistent with our previous study [15].

To confirm the presence of fluorine in the photocatalyst's structure, Energy Dispersive X-Ray Analysis (EDX) was performed for selected samples (Table S2 in Supplementary Information). The presence of fluorine was confirmed in most of the analysed samples. In the case of series + NH_3, the fluorine content is lower due to decreased amount of surface fluorine, replaced by -OH groups.

Based on SEM and EDX analysis, the schematic synthesis procedure of the fluorinated TiO_2 with defined morphology is presented in Fig. 1g. Overall, adding ammonium fluorine without additives enables to grow

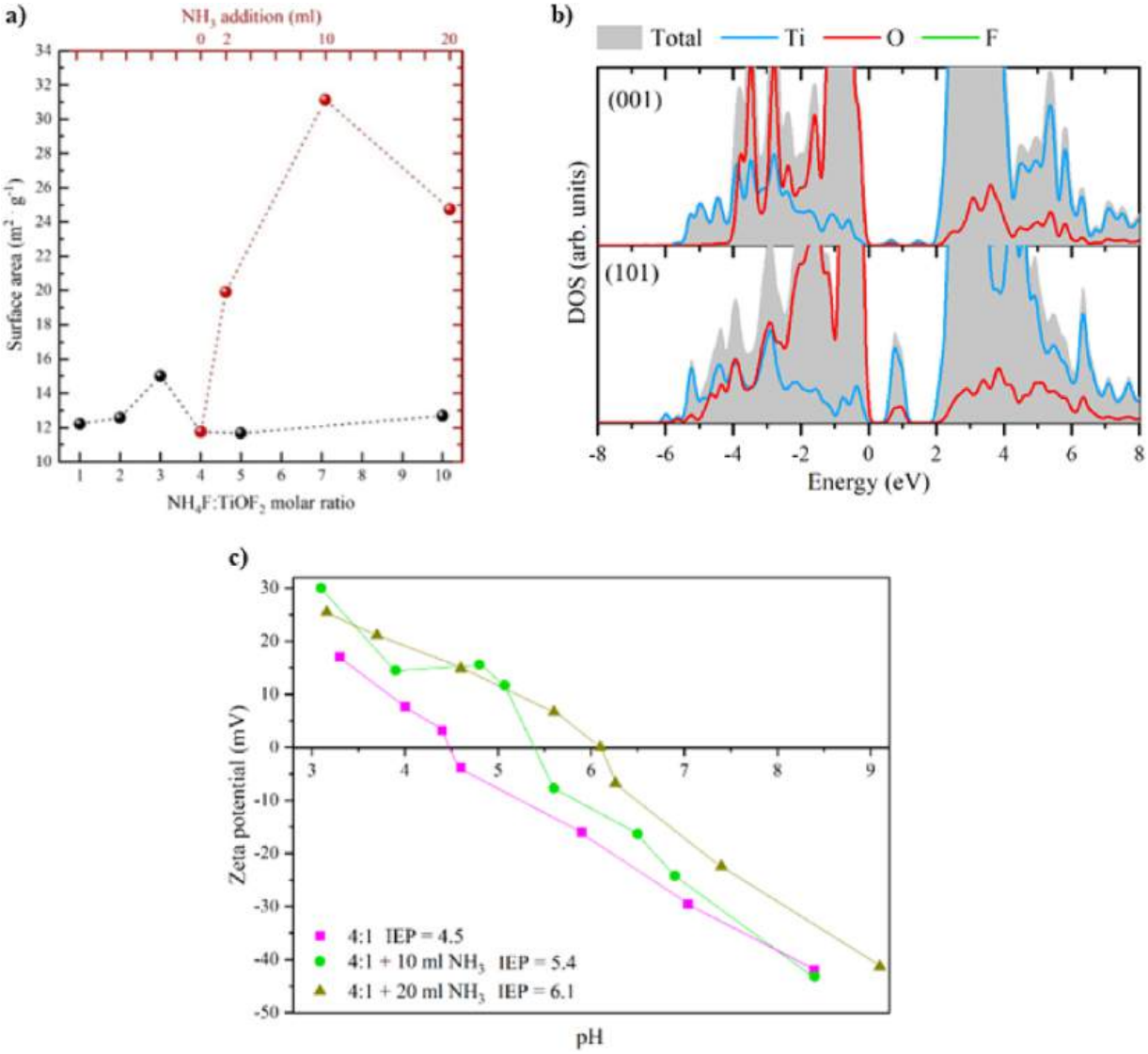

Fig. 2. a) A relationship between the surface area of photocatalysts and NH_4F: $TiOF_2$ ratio (black axis) or NH_3 volume used during synthesis (the dark red one), b) The total and partial density of states for F-doped (101), and (001) slab model, obtained with the GGAU methodology, c) Zeta potential determined from the electrophoretic mobility in dependence of the pH, $I = 1 \cdot 10^{-2}$ M KCl.

decahedral nanoparticles with exposed {1 0 1} and {0 0 1} facets. If a certain amount of ammonia water is introduced to the reaction system, only {1 0 1} facets are present in octahedral nanostructures. Furthermore, the XPS analysis showed that the surface of the series with $NH_{3(aq)}$ addition did not contain fluoride (see Fig. S2 in Supplementary Information). The most photocatalytic active sample of octahedral F-TiO_2 had negligible F^- ions on the surface. However, the fluorine atoms are present in the lattice, which was confirmed by EDX analysis. For sample with NaF presence, the content of F^- was about 7%, and it was slightly lower than for F-TiO_2 without additives.

Among the F-TiO_2 samples, the relatively highest surface area in the series is noticed for NH_4F: $TiOF_2$ with a 3:1 molar ratio, see in Fig. 2a. However, the addition of NH_3 to the reaction system contributed to the growth of {1 0 1} facets and increased the surface area of photocatalysts. However, an increase in S_{BET} value is limited, and the decrease of the surface area for the 4:1 + 20 cm^3 NH_3 sample is noted, which may be a result of nanocrystals formation with {1 0 0} facets.

To better understand the optical properties of F-TiO_2 nanostructures, DR/UV–vis spectra were analysed (Fig. S3 in SI) and compared with theoretical calculations using the Density Functional Theory (DFT) method. The DOS simulation is depicted in Fig. S4 in SI. The total and partial density of states for F-doped (101) and (0 0 1) slab model is presented in Fig. 2b. The bandgap of (0 0 1) and (1 0 1) F-doped surface were 1.84 eV and 1.64 eV, respectively. Therefore, the {1 0 1} facets in fluorine-doped anatase nanostructures are supposed to reveal better visible light response than {0 0 1} facets. Similar to bulk F-doped anatase, all models are characterised by the presence of midgap states. However, the significant difference between these two slabs is in the type of midgap states. A distinct DOS band in the (1 0 1) surface slab can be noted, opposite the small two bands in (0 0 1). This change in electronic structure is a reason for enhanced light absorption in the visible region. Therefore, the decahedral F-TiO_2 photocatalysts as a combination of {1 0 1} and {0 0 1} facets may exhibit lower photocatalytic activity under visible light compared to octahedral F-TiO_2 with exposed only {1 0 1} facets.

Furthermore, to study the surface properties of the F-TiO_2 photocatalysts, the electrophoretic mobility of these particles at different pH values (zeta potential) was investigated. The isoelectric point (IEP), which represents the pH where the electrophoretic mobility changes from positive to negative was determined for sample 4:1 of F-TiO_2 exposing {1 0 1} and {0 0 1} facets, sample 4:1 + 10 ml NH_3 of F-TiO_2 exposing {1 0 1} facets, and sample 4:1 + 20 ml NH_3 with exposed {1 0 1} and {1 0 0} facets (see Fig. 2c). In the case of 4:1 + 20 ml NH_3 with exposed {1 0 0} facets, the IEP = 6.1 is close to the values reported in the literature for anatase [21]. However, the shift towards acidic conditions was observed and the IEP for octahedral and decahedral F-TiO_2 were 5.4 and 4.5, respectively. So, the following order of IEP based on the facet exposition can be noticed: {0 0 1} < {1 0 1} < {1 0 0}. These results can be explained by differences in the surface atom rearrangement and electronic distribution on the surface. In consequence, there will be a different rate of surface hydroxylation and protonation for particular facets. The {0 0 1} facets, due to F^- stabilisation, are the most negatively charged in comparison with {1 0 1} and {1 0 0} facets, which is consistent with the existing literature [22]. The higher stability of suspension was noticed at a pH of about 4 and above 7. In addition, these results were compared with the initial pH of the photocatalyst suspension in NPX solution. The pH of the photocatalyst suspension was 4.8 for octahedral F-TiO_2 (sample 4:1 + 10 ml NH_3) and 4.3 for decahedral F-TiO_2 (sample 4:1), whereas pure NPX solution had the initial pH of 4.9. The pKa of NPX is about 4.2, so during photocatalysis with F-TiO_2, naproxen occurs in a deprotonated form with a negative charge. During NPX removal, the photocatalyst surface was positively charged (pH < pH_{IEP}), which facilitated the attraction of the deprotonated form of the naproxen molecule at the photocatalyst surface.

The photocatalytic activity of the as-prepared F-doped TiO_2 was investigated in the reaction of NPX degradation under UV–vis and visible (λ > 420 nm) light. The results are presented in Fig. 3. Firstly, the photolysis of NPX was analysed to notice the differences between processes with or without photocatalyst. The concentration of NPX decreased rapidly during photolysis under UV–vis light (Fig. 3a and c), and after 90 min of irradiation, the observed reduction of naproxen concentration was 91%. The high level of photolytic processes can be explained by deprotonation of carboxylic acid group in NPX molecule, which occurred, when pH > pKa. This deprotonated NPX molecule, having a $\pi \rightarrow \pi^*$ conjugation system, is supposed to easily undergo photolysis. Marotta et al. reported the photolysis of naproxen under monochromatic irradiation with a wavelength of 254 nm (UVC light), indicating a significant role of dissolved oxygen in a solution due to its predominant role in the generation of singlet oxygen at aerated conditions. The major by-product was 1-(6-methoxy-2-naphthyl)ethanol, which molecule differs from NPX compound replacement of -COOH group by -OH [23]. The photolysis of NPX in visible light was significantly lower than NPX removal under UV–vis light. The photocatalytic degradation process was more effective than the photolysis. All F-TiO_2 photocatalysts were highly photoactive in NPX decomposition. What is worth noticing, the removal rate was dependent on the morphology of the F-doped TiO_2 photocatalyst. In the case of samples 5:1 and 10:1, about 100% of NPX was degraded after 60 min of irradiation. Among the nanostructures with exposed {1 0 1} and {0 0 1} facets, samples with a higher molar ratio of NH_4F to $TiOF_2$ were the most active in the series without additives (NaF or NH_3). Furthermore, the presence of sodium fluoride in the synthesis (sample 4:1 + NaF) of decahedral fluorinated anatase particles negatively affected NPX degradation (see Fig. 3c). However, for octahedral F-TiO_2 with exposed {1 0 1} facets (sample 4:1 + 10 cm^3 NH_3), the degradation rate markedly increased, and after 40 min, naproxen was completely degraded.

Based on NPX degradation analyses performed in the presence of scavengers, it can be noticed that •OH are the predominant reactive oxygen species in NPX degradation using octahedral F-TiO_2, whereas $O_2^{\bullet -}$ are more important in the photodegradation in the presence of decahedral F-TiO_2 (see Fig. S5 in SI). Finally, the relative photonic efficiency was calculated and the value reached 2.94 for NPX solution. Detailed information about these calculations are in Supporting Information.

Regarding the photocatalytic activity under vis light, the higher NH_4F: $TiOF_2$ ratio resulted in increased and more efficient NPX photodegradation in the presence of the obtained F-doped decahedral anatase particles (see Fig. 3b and d). Furthermore, the series with F-doped octahedral anatase particles (samples 4:1 + NH_3) revealed much more efficient naproxen photodegradation than decahedral F-TiO_2 under vis light. The highest visible-light driven photocatalytic activity was observed for sample 4:1 + 10 ml NH_3. After 120 min, 63% of naproxen was degraded. The significant difference is noticed while comparing samples 10:1 and 4:1 +NaF, which have the same fluorine amount in the reaction system. For sample 10:1, 48% of NPX removal was observed after 120 min of visible light irradiation, whereas the sample 4:1 + NaF reached only 31% in the same process parameters. The results for this sample can be explained by the presence of Ti^{3+} on the 4:1 + NaF surface, which may act as recombination centres and, in consequence, decrease the photocatalytic activity. The calculated constant rates based on a pseudo-first order model are presented in Table S3 in Supplementary Information. The visible light-driven photocatalysts towards NPX degradation were reported previously, such as AgBr-α-$NiMoO_4$ [24], reduced graphene oxide/$ZnIn_2S_4$ [25], Ag/AgI/ZnO [26] or TiO_2 immobilised on polyacrylonitrile/multiwall carbon nanotubes composite (PAN-CNT/TiO_2-NH_2) [27]. These materials rapidly degraded NPX under visible light irradiation, although the light intensity used during the photocatalytic experiment was high (~100 mW/cm^2). Herein, we have focused on single-component photocatalyst with simple synthesis conditions and unsophisticated modifications. Our results showed that using photocatalysts for efficient naproxen removal without high-energy rays is possible.

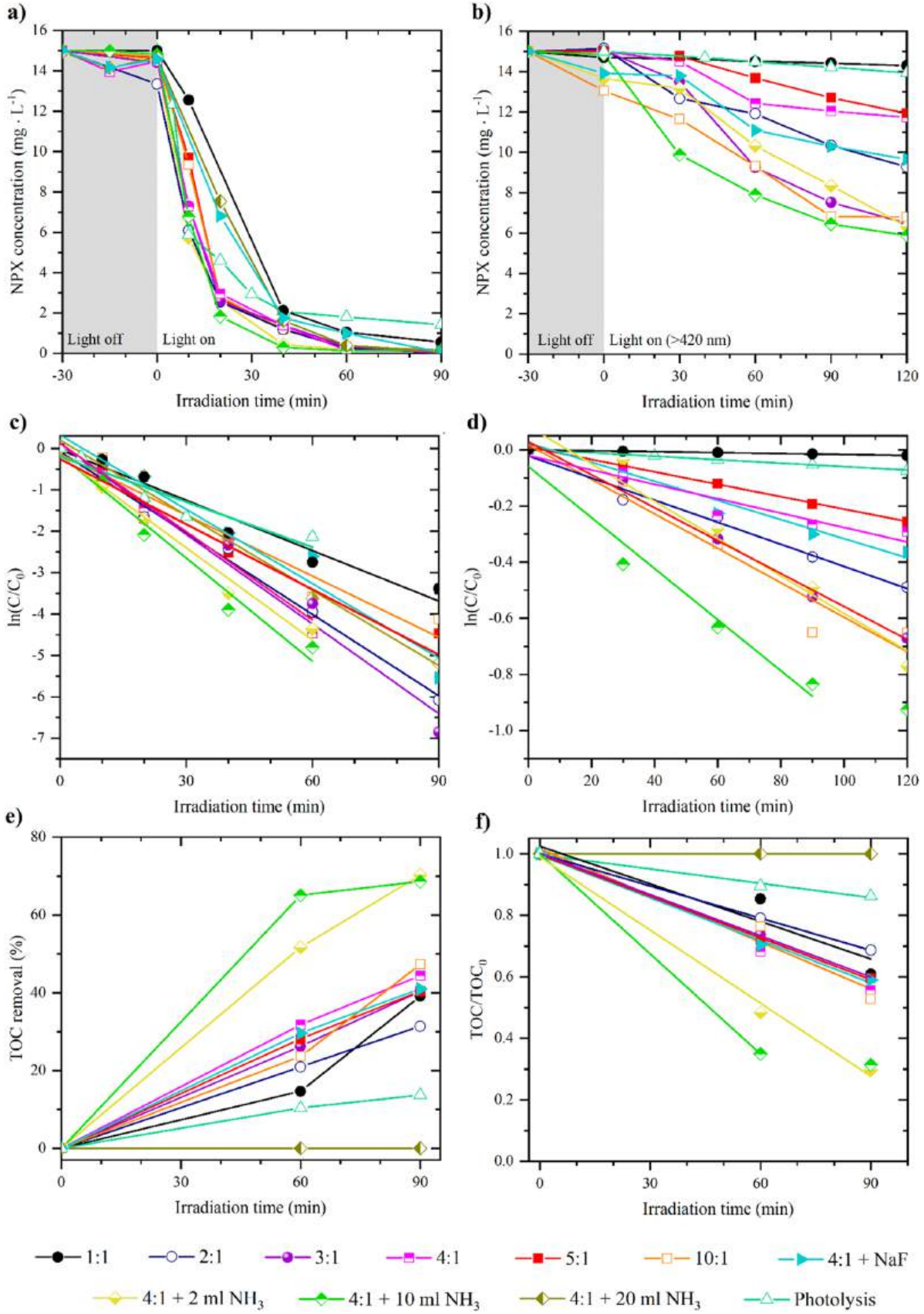

Fig. 3. Photocatalytic degradation of naproxen as a function of concentration (a, b) and ln(C/C$_0$) (c, d); photocatalytic performance was determined under UV–vis irradiation (a, c) and visible (> 420 nm) light (b, d); TOC removal in the presence of F-TiO$_2$ photocatalysts after photocatalytic process (e, f).

The TOC removal in the presence of F-TiO_2 photocatalysts after 60 and 90 min of UV–vis irradiation is presented in Fig. 3e. During photolysis, NPX molecules undergo partial mineralisation, but this reaction's mineralisation rate is slow. For the photocatalytic process, the efficiency of TOC reduction increased for all F-TiO_2 materials except the sample 4:1 + 20 cm^3 NH_3, probably due to the presence of {1 0 0} facets. These observations are consistent with Xu et al., who have suggested that {1 0 0} facets are strongly reductive, and electrons transferred to the surface can reduce H^+ into H_2 effectively [28]. For NH_4F+$TiOF_2$ series with decahedral nanostructures, all photocatalysts exhibit a similar TOC removal in the range of 30–50% after 90 min of the photocatalytic process. Similar results were obtained for the sample 4:1 + NaF, so the type of fluorine source does not influence the NPX conversion to CO_2. Meanwhile, a significant enhancement in TOC removal of about 70% was observed for series with ammonia water addition. The most efficient photocatalyst was the sample 4:1 + 10 cm^3 NH_3, for which 65% of TOC reduction was noticed after 60 min of the photocatalytic process. This sample also revealed the highest photocatalytic activity under UV–vis and vis light irradiation. Such high TOC removal rates have so far been observed for commercial P25 [29,30] or ternary photocatalysts like single atom-dispersed silver and carbon quantum dots co-loaded with carbon nitride [31]. However, the addition of a higher amount of $NH_{3(aq)}$ contributed to growing {1 0 0} facets, which in consequence, probably inhibited the degradation process and mineralisation. These results are in agreement with our previous study regarding facet-dependent photocatalytic activity towards phenol degradation using TiO_2 with defined morphology. The octahedral nanostructures with exposed {1 0 1} facets are more suitable for phenol mineralisation than decahedral ones due to the increased formation of $O_2^{\bullet-}$ on the {1 0 1} surface and favoured electron localisation on the surface [15]. In this study, octahedral F-TiO_2 is more efficient in NPX mineralisation than decahedral nanostructures, suggesting that the NPX degradation pathway can be facet-dependent.

For a better understanding of the NPX degradation pathway, post-process water after 10 and 20 min of photocatalysis and 90 min of photolysis were analysed using liquid chromatography-mass spectrometry (HPLC/MS). Table S4 shows the detected intermediate products, and Fig. 4a depicts the detected products of NPX photocatalytic degradation. In the case of photolysis, the presence of two principal pseudo-molecular ions representing - 2-acetyl-6-methoxynaphthalene (NPX 1) and dimer $C_{26}H_{26}O_4$ can be observed. It can be assumed that the dimerisation process leads to the creation of more complex compounds which are supposed to be less susceptible to photo-induced degradation processes. Therefore, the TOC removal will be lower when the dimer is formed. However, partial mineralisation during the photolytic process is observed, which is probably a result of partial naproxen decarboxylation [32,33]. Next to NPX 1, 1-(6-methoxy-2-naphthyl)ethanol (NPX 2) and 2-ethyl-6-methoxynaphtalene were noticed. Surprisingly, in the case of

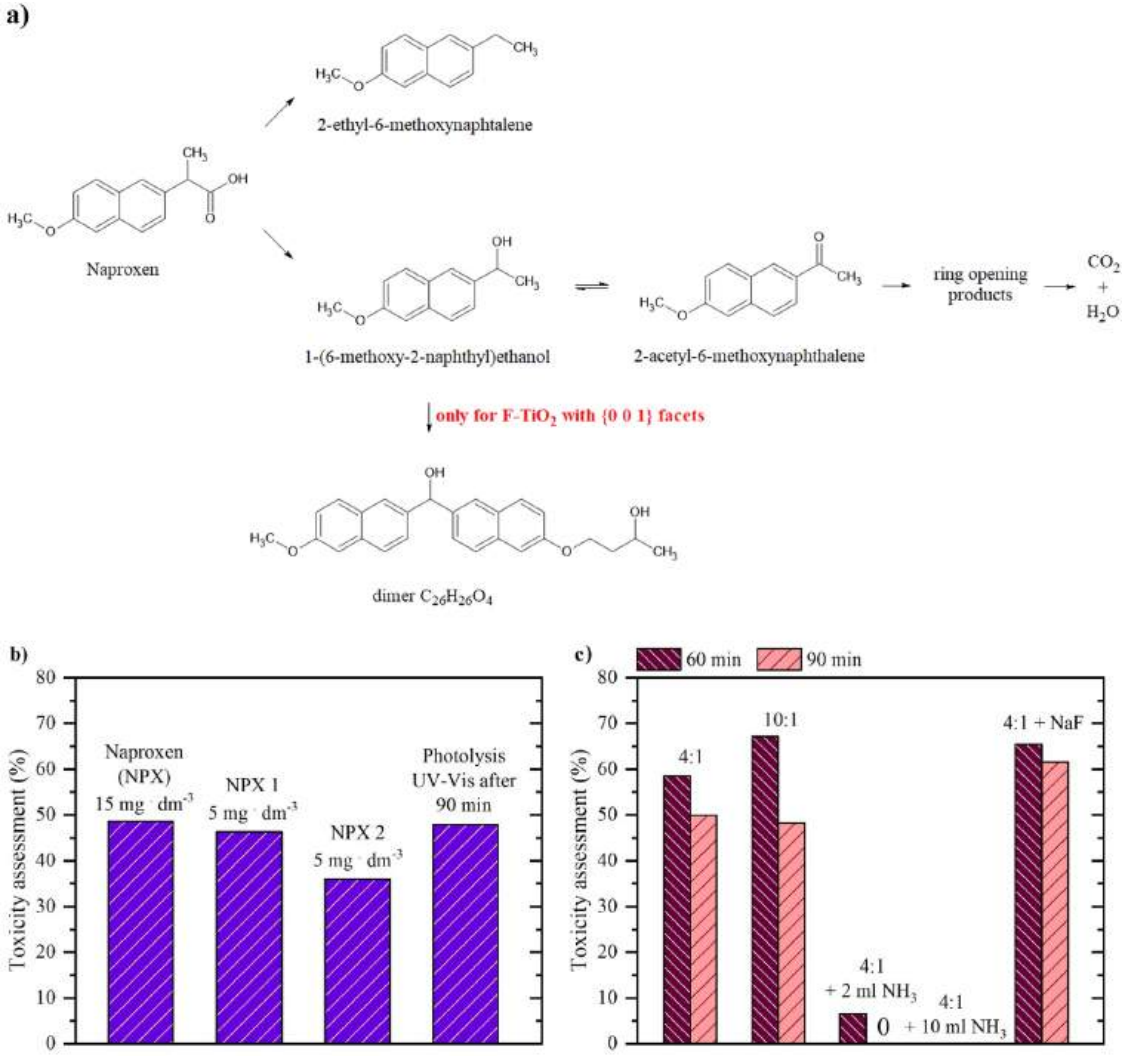

Fig. 4. a) Products of NPX photocatalytic degradation under UV–vis irradiation, Microtox test of b) NPX and derivatives solutions and c) post-treatment wastewater using selected photocatalysts.

octahedral F-TiO_2 with {1 0 1} facets, no products of dimerisation were detected, in opposite to decahedral particles. These results indicate different NPX degradation pathways depending on facet exposition. When {0 0 1} facets are exposed in the photocatalyst, the formation of dimer $C_{26}H_{26}O_4$ is induced, in opposite to {1 0 1} facets. By analogy to photolysis, the dimerisation process is unfavourable for NPX removal because it inhibits the mineralisation to CO_2 and H_2O. Therefore, the highest TOC removal was noticed for the photocatalyst 4:1 + 10 cm^3 NH_3, which is octahedral in shape, and dimer compounds were not produced during the degradation process. More detailed studies about by-products formation are presented in Fig. S7 in Supporting Information.

To study the toxicity of NPX mixture in the presence of F-TiO_2 photocatalysts, Microtox bioassays were performed. The results are presented in Fig. 4. Firstly, the NPX initial solution and two by-products were analysed. It can be observed that the toxicity of NPX is moderate (49%). The presented results of the NPX solution are comparable with the literature [29]. However, there is a lack of information about the toxicity of main by-products. In this regard, additional measurements were performed in the maximum concentration detected by HPLC analysis. Remarkably, 2-acetyl-6-methoxynaphthalene (NPX 1) is similarly toxic to naproxen, although the concentration of this intermediate is just 5 mg · dm^{-3}. This effect may be a result of changes in the aliphatic chain (-CH(CH_3)-COOH for NPX and -C(O)-CH_3 for NPX 1). The toxicity assessment for 1-(6-methoxy-2-naphthyl)ethanol (NPX 2) showed lower inhibition of *Vibrio fisheri* bioluminescence than two previous compounds, which may be a result of replacing the ketone group with the hydroxyl group.

What is worth noticing the direct NPX removal during the photolysis process did not decrease the toxicity (see Fig. 4c). In the case of photocatalysis using F-doped TiO_2, the rise in toxicity after 60 min of the photocatalytic degradation process is observed for 4:1 and 10:1 samples. Two reasons for this effect can be indicated. Firstly, F-TiO_2 decahedral nanostructures had fluorine ions on the surface, necessary to create {0 0 1} facets, which are supposed to be toxic. Secondly, {0 0 1} facets promote the formation of a dimer, which may be more toxic than other compounds presented in Figure 5a. Remarkably, no inhibition of bacterias' bioluminescence is observed in the presence of octahedral F-TiO_2 in NPX solution, which also correlates well with the high TOC removal of this sample. This photocatalyst also had negligible F^- ions on the surface, confirmed by the XPS analysis. Therefore, the application of F-TiO_2 with exposed {1 0 1} facets is supposed to be environmentally friendly. On the other hand, the post-treatment wastewater after the photocatalytic process in the presence of sample 4:1 + NaF is the most toxic in the series. By analogy to HPLC analysis, these nanostructures promote different degradation pathways without NPX 1 formation; therefore, these by-products may be more toxic than from other series.

5. Conclusions

Fluorine-doped anatase nanostructures synthesised from titanium oxyfluoride with defined morphology were for the first time obtained and applied for efficient naproxen photocatalytic degradation under UV–vis and vis light. The effect of NH_3, NaF and NH_4F introduced during solvothermal synthesis on preparation of F-TiO_2 nanocrystals with exposed {0 0 1}, {1 0 1} and {1 0 0} facets was investigated. The octahedral F-TiO_2 with exposed {1 0 1} facets and fluorine-free surface exhibited the highest photocatalytic activity. Moreover, this sample (4:1 + 10 cm^3 NH_3) revealed the highest efficiency of NPX removal under visible light (> 420 nm) and the highest TOC removal under simulated solar light. The high photocatalytic activity can be explained by DFT calculations, which suggest the presence of additional surface states when fluorine atoms are introduced to the (1 0 1) surface as well as a lower surface bandgap than (0 0 1). The facet dependence was crucial in changes in the concentration of 2-acetyl-6-methoxynaphthalene. Remarkably, our study showed that {0 0 1} facets of F-doped decahedral anatase particles promote the dimerisation process, inhibiting efficient NPX removal. Finally, Microtox bioassay tests confirmed that the application of octahedral fluorine-doped anatase particles is safe for the environment. In view of the excellent photocatalytic performance and non-toxicity, the fluorinated TiO_2 nanomaterial has the potential for practical application, thus providing a new idea for wastewater treatment from active pharmaceutical ingredients.

CRediT authorship contribution statement

Marta Kowalkińska: Conceptualization, Investigation, Formal analysis, Writing – original draft, Writing – review & editing. **Karol Sikora:** Investigation, Formal analysis. **Marcin Łapiński:** Investigation, Formal analysis. **Jakub Karczewski:** Investigation. **Anna Zielińska-Jurek:** Conceptualization, Methodology, Validation, Supervision, Writing – review & editing, Project administration, Funding acquisition.

Declaration of Competing Interest

The authors declare the following financial interests/personal relationships which may be considered as potential competing interests: Anna Zielińska-Jurek reports financial support was provided by National Science Centre Poland.

Data availability

Data will be made available on request.

Acknowledgements

The research was financially supported by the Polish National Science Centre, Grant No. 2018/30/E/ST5/00845.

Appendix A. Supplementary material

Supplementary data associated with this article can be found in the online version at doi:10.1016/j.cattod.2022.11.020.

References

[1] M. Pirilä, M. Saouabe, S. Ojala, B. Rathnayake, F. Drault, A. Valtanen, M. Huuhtanen, R. Brahmi, R.L. Keiski, Top. Catal. 58 (2015) 1085–1099.
[2] S.N. Ahmed, W. Haider, Nanotechnology 29 (2018), 342001.
[3] O. Fawzi Suleiman Khasawneh, P. Palaniandy, Civ. Environ. Eng. Rep. 29 (2019) 1–33.
[4] D.J. Angiolillo, S.M. Weisman, Am. J. Cardiovasc. Drugs 17 (2017) 97–107.
[5] M. Caban, E. Lis, J. Kumirska, P. Stepnowski, Sci. Total Environ. 538 (2015) 402–411.
[6] D. Wojcieszyńska, U. Guzik, Appl. Microbiol. Biotechnol. 104 (2020) 1849–1857.
[7] L. Corominas, P. Gimeno, C. Constantino, P. Daldorph, J. Comas, J. Hazard. Mater. 407 (2021).
[8] S.K. Loeb, P.J.J. Alvarez, J.A. Brame, E.L. Cates, W. Choi, J. Crittenden, D. D. Dionysiou, Q. Li, G. Li-Puma, X. Quan, D.L. Sedlak, T. David Waite, P. Westerhoff, J.H. Kim, Environ. Sci. Technol. 53 (2019) 2937–2947.
[9] G. Nabi, W. Raza, M.B. Tahir, J. Inorg. Organomet. Polym. Mater. 30 (2019) 1425–1429.
[10] M. Saif, S.M.K. Aboul-Fotouh, S.A. El-Molla, M.M. Ibrahim, L.F.M. Ismail, J. Nanopart. Res. 14 (2012).
[11] W. Choi, A. Termin, M.R. Hoffmann, J. Phys. Chem. 98 (1994) 13669–13679.
[12] J. Wang, D.N. Tafen, J.P. Lewis, Z. Hong, A. Manivannan, M. Zhi, M. Li, N. Wu, J. Am, Chem. Soc. 131 (2009) 12290–12297.
[13] K. Dec, A. Łukomska, D. Maciejewska, K. Jakubczyk, I. Baranowska-Bosiacka, D. Chlubek, A. Wąsik, I. Gutowska, Biol. Trace Elem. Res. 177 (2017) 224–234.
[14] S. Dudziak, M. Kowalkińska, J. Karczewski, M. Pisarek, K. Siuzdak, A. Kubiak, K. Siwińska-Ciesielczyk, A. Zielińska-Jurek, Appl. Surf. Sci. 563 (2021), 150360.
[15] M. Kowalkińska, S. Dudziak, J. Karczewski, J. Ryl, G. Trykowski, A. Zielińska-Jurek, Chem. Eng. J. 404 (2021), 126493.
[16] H.G. Yang, G. Liu, S.Z. Qiao, C.H. Sun, Y.G. Jin, S.C. Smith, J. Zou, H.M. Cheng, G. Q. Lu, J. Am. Chem. Soc. 131 (2009) 4078–4083.
[17] H.K. Lee, S.W. Lee, Chem. Lett. 44 (2015) 604–606.
[18] T.R. Gordon, M. Cargnello, T. Paik, F. Mangolini, R.T. Weber, P. Fornasiero, C. B. Murray, J. Am. Chem. Soc. 134 (2012) 6751–6761.
[19] L. Gai, Q. Mei, X. Qin, W. Li, H. Jiang, X. Duan, Mater. Res. Bull. 48 (2013) 4469–4475.

[20] P. Mikrut, M. Kobielusz, W. Macyk, Electrochim. Acta 310 (2019) 256–265.
[21] K. Kobayashi, M. Takashima, M. Takase, B. Ohtani, Catalysts 8 (2018).
[22] H. Park, W. Choi, J. Phys. Chem. B 108 (2004) 4086–4093.
[23] R. Marotta, D. Spasiano, I. Di Somma, R. Andreozzi, Water Res. 47 (2013) 373–383.
[24] S.K. Ray, D. Dhakal, S.W. Lee, Chem. Eng. J. 347 (2018) 836–848.
[25] K. Fun, Y. Pan, C. Ding, J. Shi, H. Deng, Catalysts 10 (2020).
[26] C. Ding, K. Fu, M. Wu, S. Gong, J. Liu, J. Shi, H. Deng, J. Photochem. Photobiol. A Chem. 414 (2021), 113283.
[27] A. Uheida, A. Mohamed, M. Belaqziz, W.S. Nasser, Sep Purif. Technol. 212 (2019) 110–118.
[28] H. Xu, S. Ouyang, P. Li, T. Kako, J. Ye, ACS Appl. Mater. Interfaces 5 (2013) 8262.
[29] D. Kanakaraju, C.A. Motti, B.D. Glass, M. Oelgemöller, Chemosphere 139 (2015) 579–588.
[30] A. Romeiro, M.E. Azenha, M. Canle, V.H.N. Rodrigues, J.P. Da Silva, H.D. Burrows, ChemistrySelect 3 (2018) 10915–10924.
[31] F. Wang, Y. Wang, Y. Feng, Y. Zeng, Z. Xie, Q. Zhang, Y. Su, P. Chen, Y. Liu, K. Yao, W. Lv, G. Liu, Appl. Catal. B 221 (2018) 510–520.
[32] G. Fan, J. Zhan, J. Luo, J. Zhang, Z. Chen, Y. You, Catal. Sci. Technol. 9 (2019) 4614–4628.
[33] F. Méndez-Arriaga, J. Gimenez, S. Esplugas, J. Adv. Oxid. Technol. 11 (2008) 435–444.

Supporting Information

Non-toxic fluorine-doped TiO_2 nanocrystals from $TiOF_2$ for facet-dependent naproxen degradation

Marta Kowalkińska[1*], Karol Sikora[2], Marcin Łapiński[3], Jakub Karczewski[3], Anna Zielińska-Jurek[1*]

[1] Department of Process Engineering and Chemical Technology, Faculty of Chemistry, Gdansk University of Technology, G. Narutowicza 11/12 Street, 80-233 Gdansk, Poland

[2] Department of Inorganic Chemistry, Faculty of Pharmacy, Medical University of Gdansk, M. Sklodowskiej-Curie 3a Street, 80-210 Gdansk, Poland

[3] Institute of Nanotechnology and Materials Engineering, Faculty of Applied Physics and Mathematics, Gdansk University of Technology, G. Narutowicza 11/12 Street, 80-233 Gdansk, Poland

Keywords: fluorine-doped TiO_2, crystal facets engineering, naproxen degradation, titanium oxyfluoride, Microtox bioassay

---

* Corresponding authors: marta.kowalkinska@pg.edu.pl (MK), annjurek@pg.edu.pl (AZJ)

2. Experimental

2.1. Material characterisation

The synthesised photocatalysts' crystal structure and phase composition were characterised by X-ray powder diffraction (Cu Kα radiation, Rigaku MiniFlex 600 X-Ray diffractometer) in the 5-80° 2θ range. The analyses and Rietveld refinements were performed with the HighScorePlus software package (PANalytical, 2006) and the Crystallographic Open Database with data fitting based on the pseudo-Voigt profile function. The specimen displacement, lattice parameters, polynomial coefficients for the background function, profile parameters, and Gaussian and Lorentzian profile coefficients were refined. The amorphous phase content was estimated using an internal standard (NiO, Sigma Aldrich). The morphologies of F-doped anatase nanostructures were investigated by scanning electron microscope (SEM) with a field emission gun, model FEI Quanta FEG 250. A truncation level, which is defined as a ratio between their top and a middle side (A/B) of a particle, was selected as a parameter to describe decahedral and octahedral nanostructures. The ImageJ software was used for measurements of A and B values. Next, Micromeritics Gemini V instrument was used to determine the porous structure parameters of the photocatalytic materials, including Brunauer–Emmett–Teller (BET) surface area and pore volume, using low-temperature nitrogen adsorption. Before measurement, the analysed materials were degassed at 200°C for 2 h. The surface area was determined by the multipoint BET method. To complete the surface properties analysis, the detailed chemical composition of the photocatalysts' surface was analysed by the X-ray photoemission spectroscopy method (XPS). XPS measurements were carried out at room temperature under ultrahigh vacuum conditions with pressures below $1.1 \cdot 10^{-6}$ Pa using Omicron NanoScience equipment with Argus hemispherical analyser. Spectra deconvolution was performed with the CASA XPS software package using the Shirley background subtraction and Gauss-Lorentz

curve fitting algorithm by the least-squares method - GL (30). The XPS spectra were calibrated to obtain binding energy of 285.00 eV for the C 1s peak.

Moreover, zeta potential was determined from the electrophoretic mobility in dependence of the pH using Malvern Nano Zetasizer (Malvern Instruments Ltd., Malvern, UK). These measurements were performed in 10^{-2} M KCl solution with the photocatalyst loading of 0.5 $g \cdot dm^3$. Finally, the optical properties were studied using a UV–Vis spectrophotometer (Thermo Fisher Scientific Evolution 220) to measure diffuse reflectance (DRS), using barium sulfate as a standard. Based on the obtained spectra and conversion to the Kubelka-Munk function, the bandgap energy calculations were performed using Tauc's method.

2.2. Theoretical studies

The electronic structure of pure and F-doped anatase, in bulk form as well as (101) and (001) surfaces, were determined computationally using density functional theory calculations (DFT) within the generalised gradient approximation (GGA), as implemented in Quantum Espresso 6.5 software package [1,2]. All calculations were performed using ultrasoft pseudopotentials with projector augmented wave method (PAW). The electronic wave functions were expanded to the energy cut-off of 500 eV. During the calculations of bulk materials, the 2 × 2 × 1 anatase supercell was used, while for the (001) and (101) surface, a single layer was created. K-point grids of 3 × 3 × 3 and 3 × 3 × 1 were used for the bulk and slab models, respectively. Fluorine doping was modeled next to the pure structures by removing a single O atom. During the calculations, the Hubbard parameter U = 5.5 eV was applied for Ti atoms. All calculations were performed under the same conditions to be comparative.

2.3. Determination of photocatalytic activity

Naproxen, (S)-(+)-2-(6-Methoxy-2-naphthyl)propionic acid was provided by Sigma-Aldrich. Photocatalytic activities of the obtained samples were analysed by measuring the rate of NPX decomposition in an aqueous solution under UV-vis irradiation using a xenon lamp

(model 6271H, Oriel, USA) as a simulated solar light source with a narrow range of UV light. However, water filter, which cut-off the infrared light, was always used for each photoinduced process. For each experiment, 25 cm^3 of pollutant solution (15 $mg \cdot dm^{-3}$) and 12.5 mg (0.5 $g \cdot dm^3$) photocatalyst were put into a quartz reactor under magnetic stirring. The UV-spectrum flux intensity at the reactor border was 45 $mW \cdot cm^{-2}$. In addition, a cut-off glass filter (GG420; $\lambda > 420$ nm) was used to test the photocatalytic activity under visible light. The photocatalyst suspension of the photocatalyst was thermostated at 20°C and bubbled with 6 $dm^3 \cdot h^{-1}$ of airflow. Before the photodegradation process, the aqueous suspension of the photocatalyst was mixed in darkness for 30 min to analyse the adsorption of NPX on the photocatalyst surface. The point '-30' corresponds to the concentration of the initial NPX solution (15 $mg \cdot dm^{-3}$). After the dark process, the NPX concentration was 15 ± 2 $mg \cdot dm^{-3}$. Then, the process was initiated by turning on the Xe lamp. All the experiments were studied for 90 minutes (UV-vis) or 120 minutes (Vis) of irradiation. The aqueous suspension's aliquots of 1 cm^3 were collected at regular periods during irradiation and passed through syringe filters (Ø = 0.2 μm) to remove the photocatalyst particles.

The evolution of NPX concentration and the first derivative 2-acetyl-6-methoxynaphthalene (NPX 1) was monitored using a high-performance liquid chromatography system (HPLC, model Shimadzu LC-6A), combined with a photodiode array detector (SPD-M20A) and C18 column (Phenomenex Gemini 5 μm; 150x4.6 mm) working at 45°C. During measurements, the mobile phase was composed of (v/v) 70% acetonitrile and 30% water with 0.1% formic acid at a flow rate of 0.35 $cm^3 \cdot min^{-1}$. Quantitative analysis of NPX and NPX 1 was performed utilising the external calibration method. An HPLC-grade acetonitrile and formic acid solution were provided by Sigma Aldrich. Additionally, the total organic carbon (TOC) concentration after each photocatalytic process was monitored using the Shimadzu TOC-L analyser. The high-performance LC-MS system employed consisted of an HCT Ultra spectrometer (Bruker

Daltonics, Billerica, Massachusetts, US) with an ESI source coupled with an Agilent 1200 liquid chromatography (Agilent Technologies, Santa Clara, California, US). Chromatographic separation was conducted on Eclipse XDB-C8, 4,6 x 150 mm, 5 um (Agilent) column. Mobile phase A was water with 0.1% formic acid and phase B acetonitrile with 0.1% formic acid. The gradient program was as follows: 0 min – 10% B, 20 min – 90% B, 25 min – 90% B, 30 min – 10% B. The flow was set at 0.4 $cm^3 \cdot min^{-1}$, and the injection volume was 50 µl. The column oven temperature was set to 25°C, and UV chromatograms were recorded at 230, 254, and 270 nm. Spectra were acquired in positive and negative ESI mode, the capillary voltage was set at 113 V, the scanned mass range was 50–850 m/z, and the accumulation time was 200,000 ms. The parameters capillary voltage, drying gas flow, nebulising gas, and source temperature was respectively: 4.0 kV, 10 $dm^3 \cdot min^{-1}$, 30 psi, and 350 °C. Helium (99.999%) was used as the collision gas in the ion trap. The mass spectrometer was operated in full scan and MS/MS modes. Finally, the effect of reactive oxygen species was determined by performing photocatalytic tests in the presence of scavengers. Isopropyl alcohol, sodium azide, and benzoquinone provided by Sigma Aldrich were used as •OH, $^1O_2$, and $O_2^{\bullet -}$ scavengers.

Finally, according to IUPAC recommendation [3], the relative photonic efficiency was calculated for naproxen, which is a comparison between the initial rate of NPX with initial rate of phenol. For these measurements, 0.5 $g \cdot dm^3$ of 4:1+10 ml NH_3 sample was used. The light source was a combination of 25 LEDs, with the maximum located at λ=375 nm. The photon flux was (4 ± 0.5) $mW \cdot cm^{-2}$. Under these conditions, the effect of photolysis was negligible. The rate constants of photocatalytic degradation of phenol and NPX were 0.0023 min^{-1} and 0.013 min^{-1}, respectively. Based on performed experiments, the relative photonic efficiency was 2.94. So, the efficiency of NPX degradation will be ca. 3 times higher compared to photocatalytic degradation of phenol (as a standard). These simple experiments can be useful in further comparison of the procedures for the degradation of organic pollutants.

2.4. Toxicity assessment

Microtox bioassay evaluated the toxicity of solutions treated during the photodegradation process. The Microtox tests using the inhibition of luminescence from *Vibrio fischeri* bacteria as an acute reagent was performed on a Microtox model M500 (Microbics Corp., Carlsbad, California). The measurements of light output were carried out after 15 minutes. The addition of toxic compounds was indicated by a decrease in the light output. The toxicity was recorded as the percent decline of light output, which was calculated using the formula:

$$Inhibition = 100\% \frac{Is - Ie}{Is}$$

in which I_s is the light level of blank and I_e - the light level of exposure sample. The reagents for the Microtox test were supplied by Microbic Corporation [4].

3. Results and discussion

3.1. Structural and morphological analyses

The phase structure of the photocatalysts was analysed using powder X-ray diffraction (XRD), as presented in Figure S1. All XRD patterns are ascribed to anatase, confirming the complete transformation from $TiOF_2$. The crystallite size from Scherrer's equation and amorphous phase content were also estimated. The hydrothermal treatment of $TiOF_2$ allows to obtain highly crystalline materials with low amorphous phase content. The only exceptions were samples 1:1, 2:1, and 4:1 + 10 cm^3 NH_3, for which the content of amorphous content is much greater than 0. Moreover, in the case of samples with the addition of NaF, 10 cm^3 NH_3 and 20 cm^3 NH_3 are characterised by decreased crystallite size compared to other photocatalysts from the series. These estimated parameters are also presented in Table S1.

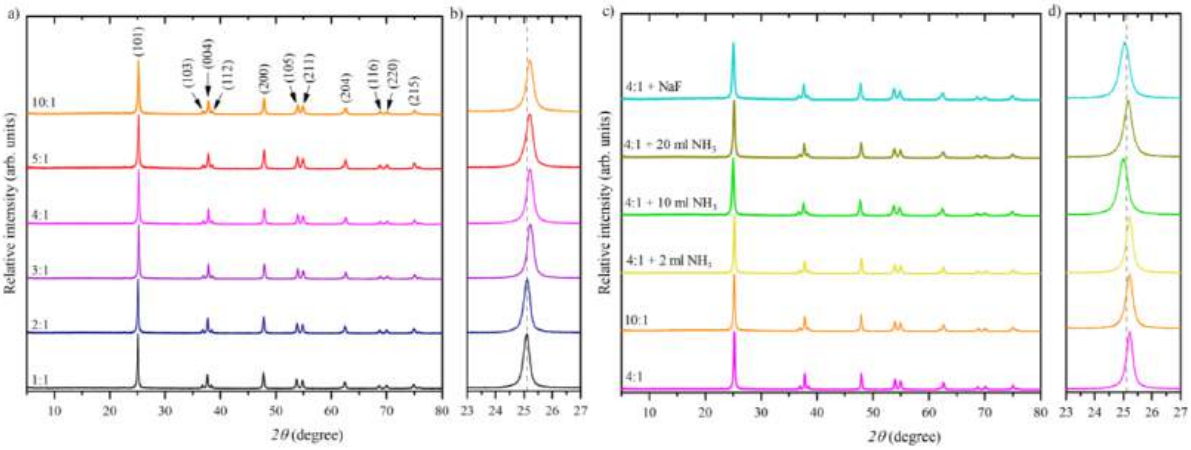

Figure S1. XRD patterns of samples from a) NH_4F+$TiOF_2$ series, c) effect of NH_3 and NaF addition. Main reflexes originating from anatase were indexed. The zoom into (101) peaks is presented in b) and d).

Table S1. Structural parameters of F-TiO_2 photocatalysts.

Sample name	Amorphous phase content (% w/w)	Crystallite size (nm)	Lattice parameters		
			***a, b* (Å)**	***c* (Å)**	***V* (Å^3)**
1:1	11	34	3.788	9.505	136.39
2:1	8	33	3.787	9.492	136.13
3:1	0	32	3.798	9.495	136.96
4:1	0	33	3.790	9.494	136.37
5:1	0	28	3.790	9.495	136.39
10:1	0	30	3.790	9.486	136.26
4:1 + 2 ml NH_3	0	32	3.788	9.498	136.29
4:1 + 10 ml NH_3	15	23	3.786	9.494	136.09
4:1 + 20 ml NH_3	0	24	3.788	9.503	136.36
4:1 + NaF	1	21	3.786	9.496	136.11

3.2. Surface properties

The photocatalytic performance strictly depends on photocatalysts' surface state because of the interactions with adsorbed water and pharmaceutical molecules. In this regard, the surface properties of fluorinated TiO_2 were intensively studied. Firstly, the surface area (S_{BET}) of F-TiO_2 photocatalysts using the Brunauer–Emmett–Teller (BET) method was analysed (see Table S2). The S_{BET} values for samples without additives were in the range of about 12 - 15 $m^2 \cdot g^{-1}$. The relatively highest surface area in this series is noticed for NH_4F: $TiOF_2$ of a 3:1 molar ratio. Further addition of NH_4F did not affect the increase of the surface area of F-TiO_2. The addition of NH_3 to the reaction system contributed to the growth of {1 0 1} facets and

increased the surface area of photocatalysts. However, an increase in S_{BET} value is limited, and the decrease of the surface area for the 4:1 + 20 cm^3 NH_3 sample is noted, which may be a result of nanocrystals formation with {1 0 0} facets. In the case of the sample with NaF addition, the highest surface area from the series was noted.

Table S2. The representation of the specific surface area, morphology, and elementary composition summation of F-TiO_2 samples.

Sample name	Surface area ($m^2 \cdot g^{-1}$)	Pore volume ($cm^3 \cdot g^{-1}$)	F content from EDX analysis (%)	Crystal shape	Identified facets	Truncation level *A/B*	Elementary content based on XPS studies (%)	
							Ti	F
1:1	12.2	0.0191	nd	-	-	nd	nd	nd
2:1	12.6	0.0197	nd	Decahedral	{0 0 1}, {1 0 1}	0.55 ± 0.09	nd	nd
3:1	15.0	0.0338	nd	Decahedral	{0 0 1}, {1 0 1}	nd	nd	nd
4:1	11.8	0.0250	3.88	Decahedral	{0 0 1}, {1 0 1}	0.61 ± 0.07	84	16
5:1	11.7	0.0058	nd	Decahedral	{0 0 1}, {1 0 1}	nd	nd	nd
10:1	12.7	0.0060	3.80	Decahedral	{0 0 1}, {1 0 1}	0.60 ± 0.08	89	11
4:1 + 2 ml NH_3	19.9	0.0098	2.74	Octahedral	{1 0 1}	0.19 ± 0.04	>99	<1
4:1 + 10 ml NH_3	31.1	0.0151	2.15	Octahedral	{1 0 1}	0.14 ± 0.04	~100	~0
4:1 + 20 ml NH_3	24.7	0.0122	nd	Rectangular with bipyramidal prisms	{1 0 1}, {1 0 0}	nd	nd	nd
4:1 + NaF	37.9	0.0183	5.54	Decahedral	{0 0 1}, {1 0 1}	nd	93	7

Simultaneously, samples 4:1, 10:1, and 4:1 with additives were analysed using X-ray photoelectron spectroscopy (XPS) to determine their surface chemical composition. We have focused mainly on titanium and fluorine content due to strong interactions between Ti and F. During the syntheses, F^- ions from ammonium fluorine and $TiOF_2$ were introduced to the reaction system. As reported previously, fluorine ions affect the surface structure of the growing anatase [5,6], according to the following equations:

$$TiOF_2 + H_2O \rightarrow TiO_2 + 2HF \quad (4)$$

$$TiO_2 + 4H^+ + 6F^- \rightarrow [TiF_6]^{2-} + 2H_2O \quad (5)$$

However, the presence of ammonium ions can also influence the course of reactions (4) and (5) and, in consequence, modify the surface properties of fluorinated TiO_2. In this regard, Ti2p and F1s spectra of selected samples were analysed (see Figure S2 and Table S2). For most of the

analysed samples, well-defined Ti^{4+} doublet ascribed to stoichiometric TiO_2 surface structure around ~458.7 eV ($2p_{1/2}$) and ~464.4 eV ($2p_{3/2}$) was noticed [7]. The majority of obtained F-TiO_2 samples showed a binding energy peak centered at ~684 eV in F1s spectra, typical of the Ti-F bond [8]. However, the sample 4:1+NaF exhibited an additional signal at the lower energies in Ti 2p spectra, which originated from the presence of Ti^{3+} states, despite the same amount of F^- in the reaction system as in the 10:1 sample. The 10% percentage of Ti^{3+} species can result from the surface presence of oxygen vacancies induced by the molecular HF formed during the hydrothermal process [9]. Significant changes are also noticed in surface fluorine content. The F^- amount for the photocatalysts 4:1 and 10:1was about 10-15%, but the addition of ammonium hydroxide to the synthesis markedly reduced the fluorine amount, and almost fluorine-free surfaces were obtained. Although the surface of the series with $NH_{3(aq)}$ addition did not contain fluoride, the fluorine atoms were present in the lattice, which was confirmed by EDX analysis. For samples with NaF presence, the content of F^- was 7%, and it was slightly lower than for F-TiO_2 without additives.

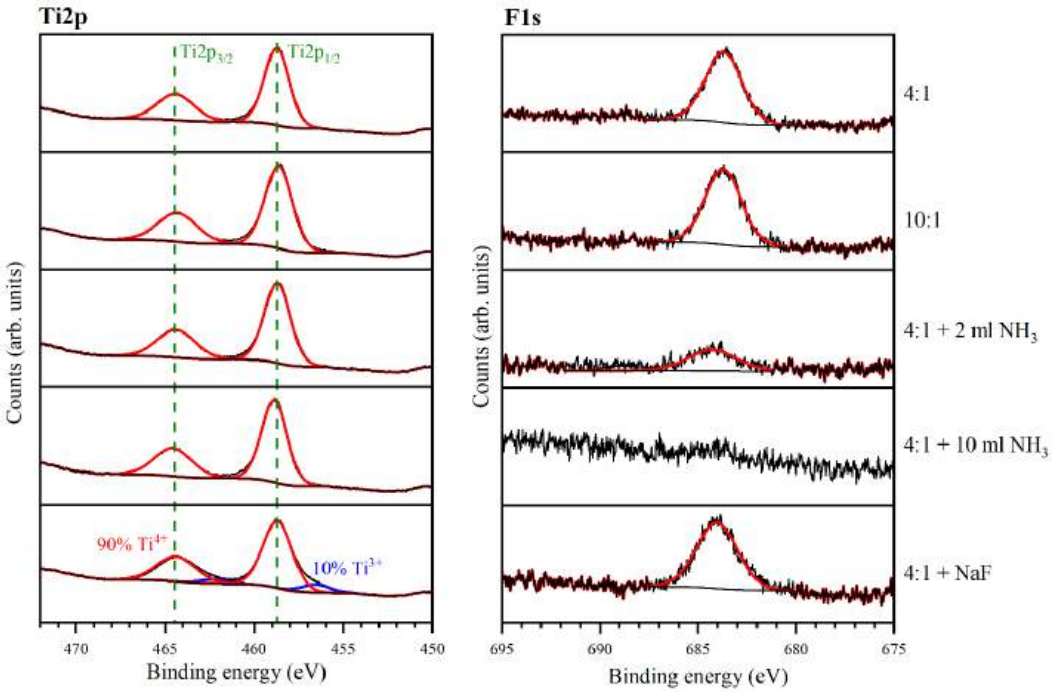

Figure S2. The XPS spectra of selected F-TiO_2 samples showing Ti2p and F1s signals with Lorentzian fits, respectively.

3.3. Optical properties and DOS calculations

The effect of fluorine doping on light absorption properties was analysed using DR/UV-vis spectroscopy (see in Figure S3). All samples were characterised by high absorbance in the UV range (< 350 nm). However, except for the 1:1 sample, most of the titanium (IV) oxide photocatalysts can absorb visible light, primarily samples 5:1 and the series with $NH_{3(aq)}$ addition. What is worth noticing, the sample 4:1 + NaF revealed a lower absorbance above 400 nm than sample 10:1, although the amount of fluorine in the reaction system was the same. The modification of the synthesis procedure influenced the fluorine content in bulk material as well as photocatalyst's surface, together with Ti^{3+} presence. Based on converted spectra to Kubelka-Munk function, the optical bandgap values were calculated using the Tauc method. Small changes of E_g compared with unmodified anatase (~ 3.2 eV) are noticed, indicating that F^- presence does not change band structure significantly. However, shallow traps originating from additional bands from F-doping are supposed to be present. In our previous study regarding scheelite-type compounds, based on thermoluminescence spectra, it was found that photocatalysts with deeper traps exhibited lower photocatalytic activity than those with shallower ones [10]. Kohtani *et al.* reported that for titanium (IV) oxide, shallow traps (up to 0.7 eV) revealed higher electron transfer efficiency from the defects to the species adsorbed on the surface, which led to better photocatalytic performance [11].

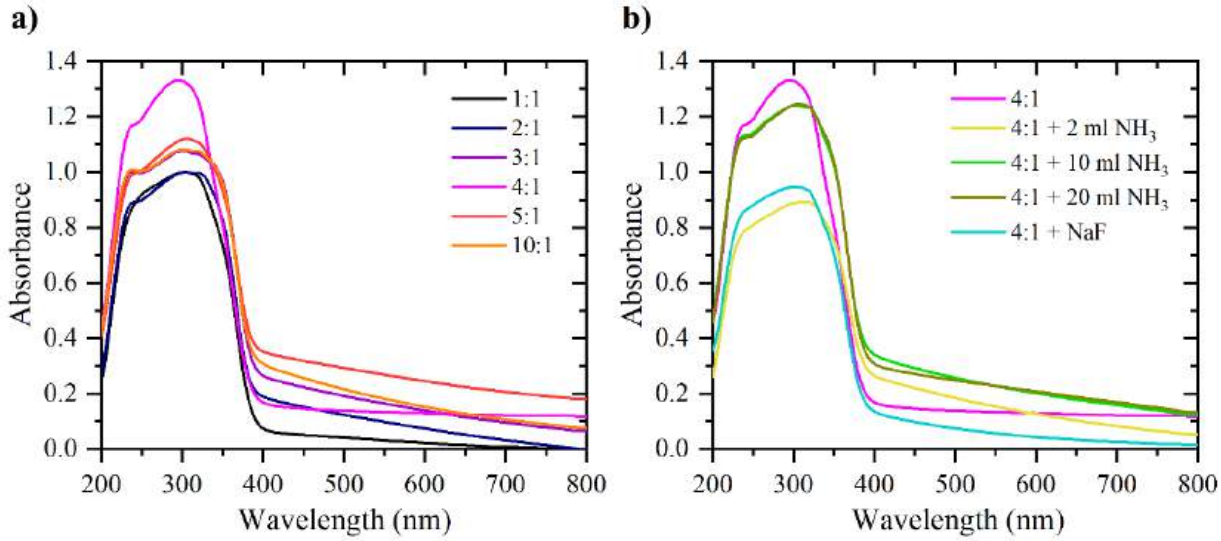

Figure S3. DR/UV-vis spectra of F-TiO_2 samples a) without and b) with NH_3 or NaF addition.

The calculated density of state (DOS) distributions is shown in Figure S4, including bulk, pure and fluorine doping samples. For this GGAU methodology in the bulk anatase bandgap energy (E_g) was 2.28 eV. This value does not change for F-doped bulk TiO_2, but introducing F atoms to crystal lattice allows the creation of the midgap states (~ 0.2 eV) near the conduction band, which is typical for non-metal doping [9,12]. However, additional states are not derived from F 2p orbital, so they do not originate directly from F presence in the structure. Remarkably, structural distortions caused by replacing oxygen atoms with fluorine influence the creation of new occupied states from Ti 3d orbitals, which confirms the charge transfer and the reduction of Ti^{4+} to Ti^{3+} or other degenerated Ti surface states. This observation is consistent with González-Torres *et al.* [13] study, which proved that the F atom distributes its unpaired electron towards neighbours Ti atoms. Therefore, in Figure 2c in the main manuscript, only partial DOS from Ti and O are depicted.

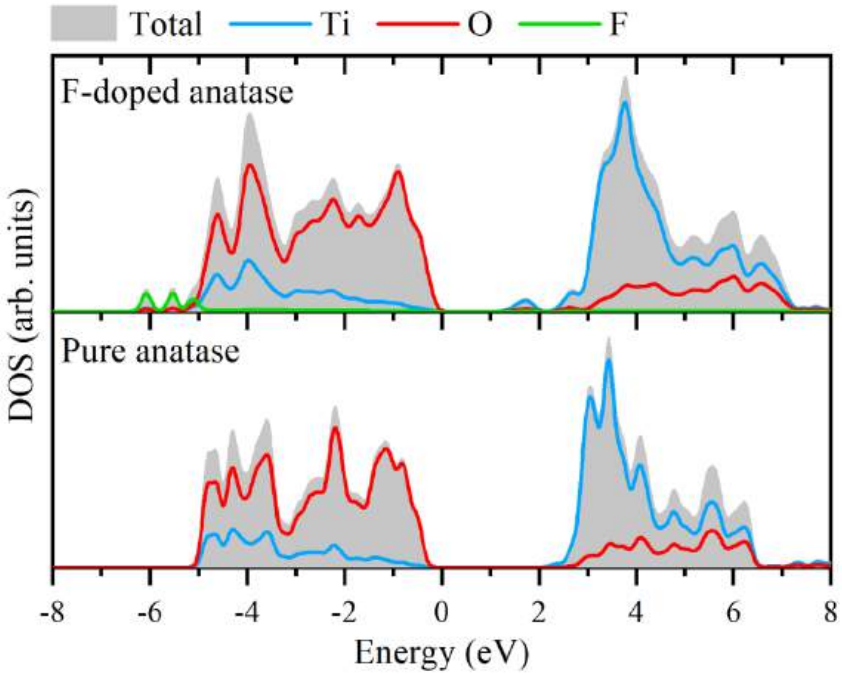

Figure S4. The total and partial density of states for bulk pure and modified anatase. Results were obtained with the GGAU methodology.

3.4. Photocatalytic naproxen degradation

The photocatalytic naproxen degradation was studied, and the results are presented in Figure 3 in the main manuscript. Furthermore, the corresponding rate constants for both naproxen degradation and TOC conversion were calculated using a pseudo-first and zero-order kinetic model, respectively. The reaction rate constants are presented in Table S3. However, it should be noted that in the case of reactions under UV-vis light, the kinetic model consists of photolysis and photocatalysis, due to the high rate constant of the photolytic reaction.

Table S3. Reaction rate constants of photocatalytic processes using F-TiO_2.

Sample name	Degradation under UV-vis light				Degradation under visible light (>420 nm)	
	k ($\cdot 10^{-2}$ min^{-1})	*RSSQ*	k_{TOC} ($\cdot 10^{-2}$ $mg \cdot L^{-1} \cdot min^{-1}$)	*RSSQ*	k ($\cdot 10^{-3}$ min^{-1})	*RSSQ*
Photolysis	3.65 ± 0.70	1.059	1.61 ± 0.17	0.011	0.62 ± 0.02	< 0.001
1:1	4.06 ± 0.41	0.376	4.21 ± 1.46	0.893	0.25 ± 0.01	< 0.001
2:1	6.55 ± 0.27	0.175	3.61 ± 0.01	< 0.001	3.94 ± 0.30	0.002
3:1	7.22 ± 0.59	0.791	4.69 ± 0.24	0.025	5.87 ± 0.35	0.003
4:1	5.64 ± 0.75	1.278	5.16 ± 0.28	0.033	2.56 ± 0.47	0.006
5:1	5.25 ± 0.65	0.960	4.68 ± 0.02	0.010	2.21 ± 0.11	< 0.001
10:1	4.92 ± 0.57	0.744	5.24 ± 1.01	0.427	6.14 ± 0.89	0.021
4:1 + 2 ml NH_3	7.42 ± 0.58	0.230	8.20 ± 0.61	0.156	6.66 ± 0.83	0.018
4:1 + 10 ml NH_3	8.31 ± 0.79	0.427	8.37 ± 2.48 *	2.577 *	9.09 ± 1.14	0.012
4:1 + 20 ml NH_3	6.05 ± 0.30	0.198	no mineralisation	-	-	-
4:1 + NaF	5.98 ± 0.60	0.816	4.78 ± 0.03	0.035	3.41 ± 0.56	0.008

* The kinetics of TOC conversion was changing after 60 minutes of the photocatalytic process and the non-linear tendency can be observed. Therefore, we calculated the second k_{TOC} excluding the point at t=90 min (only for two point). The value was $k_{TOC} = 11.23 \cdot 10^{-2}\ mg \cdot L^{-1} \cdot min^{-1}$.

In general, the photocatalytic process depends on a type of photocatalyst, including its surface properties. Herein, the fluorine-doped TiO_2 with different surface structures are investigated, which can affect the naproxen degradation pathway. The initial pH of the photocatalyst suspension was about 4.8 for octahedral anatase particles (sample 4:1 + 10 ml NH_3) and slightly lower (pH ~ 4.3) for decahedral anatase particles (sample 4:1). The pH of the irradiated solution changes during the photodegradation process with 4:1 + 10 ml NH_3 sample, reaching a pH value of about 6 after the complete mineralisation process.

Furthermore, the NPX degradation analyses were performed in the presence of scavengers of reactive oxygen species $O_2^{\bullet-}$, •OH, and $^1O_2$. The results of NPX removal are presented in Figure S5. It can be noticed that hydroxyl radicals are the predominant reactive oxygen species in NPX degradation using octahedral nanostructures, whereas superoxide anion radicals are more important in the photodegradation in the presence of decahedral anatase particles. Remarkably, for the 4:1 + NaF sample, which is characterised by surface Ti^{3+} presence, the degradation rate is similar to that observed in the presence of •OH scavenger. Therefore, the surface defects can lead to the formation of other reactive species like superoxide radicals and hinder the formation of hydroxyl radicals. Nowotny *et al.* [14], based on theoretical calculations,

have reported that Ti^{3+} sites are localised deeply below the conduction band edge of anatase. Therefore, the presence of surface defects may act as recombination centres instead of photogenerated electron traps, which hinders the radical formation crucial in the photocatalytic degradation process. This effect can be a reason for the lower NPX mineralisation rate of decahedral F-TiO_2 compared to octahedral nanostructures.

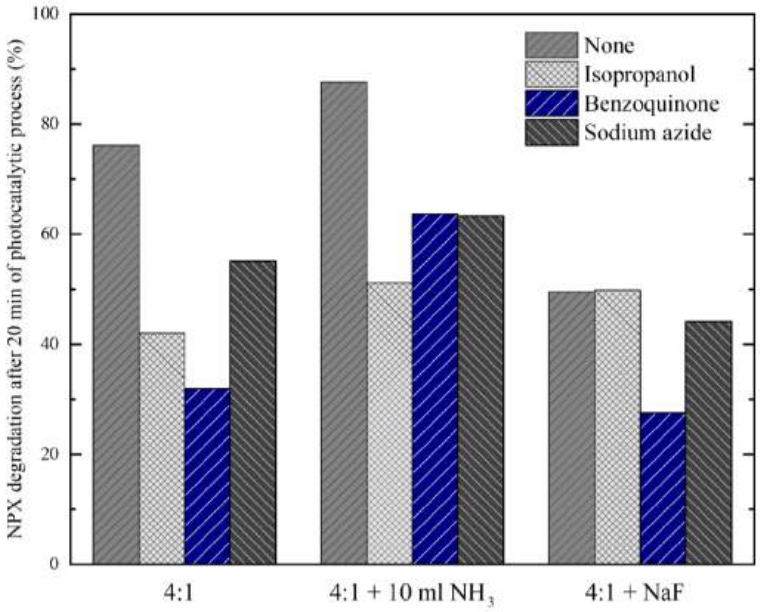

Figure S5. Photodegradation of naproxen using 4:1 series, 4:1 + 10 ml NH_3, and 4:1 + NaF under UV-vis irradiation in the presence of scavengers.

Moreover, NPX degradation products were detected using HPLC/DAD and HPLC/LC-MS analyses. During each photolytic and photocatalytic process, the most commonly found by-product was 6'-methoxy-2'-acetonaphtone (denoted as NPX 1, the chemical structure is presented in Table S4). Therefore, a quantitative analysis of this compound was performed (Figure S6). It can be noticed that the NPX 1 concentration increased to c.a. 6 mg $\cdot$ dm^{-3} in the first 10 minutes of photolysis (Fig. S6 a) and photocatalysis using octahedral F-TiO_2 (Fig. S6 c). Then, the concentration of this by-product decreased in time. In the case of the 4:1 + 10 cm^3 NH_3 sample, the process occurred fast, and after 40 minutes of the photocatalytic degradation process, the NPX 1 concentration was under the detection limit. At the same time, the naproxen concentration was almost zero. What is worth highlighting, the changes in concentration are

different for decahedral and octahedral nanostructures. In Figure S6 b, the formation of NPX 1 in the presence of the 4:1 sample occurred slower than for other ones. After reaching the value of about 1.5 mg · dm^{-3}, the NPX 1 concentration dropped slowly and reached ~0 after 60 minutes of the photocatalytic degradation process. The main difference between these samples is a facet exposition – {1 0 1} for octahedral TiO_2 and {0 0 1} coupled with {1 0 1} facets for decahedral TiO_2. Therefore, it can be concluded that the formation of NPX 1 is facet-dependent, and the morphology of anatase nanostructures influenced the degradation pathway at the initial step. What is worth noticing, completely different results were obtained using the 4:1 + NaF sample. Although decahedral shapes were confirmed, no NPX 1 was detected. The probable explanation for lacking this by-product is the presence of Ti^{3+} on the surface, which may change the NPX degradation pathway. This observation is in agreement with results in the photocatalytic process in the presence of scavengers. As a consequence, the limited formation of hydroxyl radicals may influence on NPX degradation pathway.

Table S4. Detected intermediate products in NPX photolysis and photocatalytic degradation reaction with F-TiO_2 nanostructures.

m/z	***t_R*** **(min)**	**Compound name**	**Chemical structure**
228.8 (-)	18.4	(S)-(+)-2-(6-Methoxy-2-naphthyl)propionic acid (Naproxen)	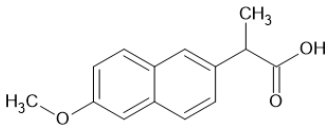
201.0 (+)	19.5	2-acetyl-6-methoxynaphthalene (NPX 1)	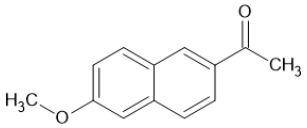
185.1 (+)	17.8	1-(6-methoxy-2-naphthyl)ethanol (NPX 2)	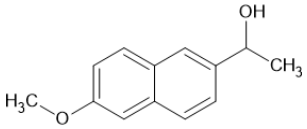
400.9 (-)	16.4	dimer $C_{26}H_{26}O_4$	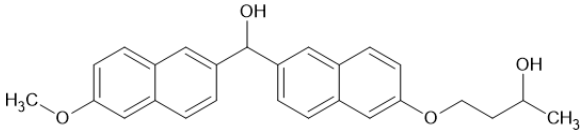
187.0 (+)	13.5	2-ethyl-6-methoxynaphtalene	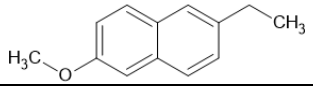

(+) - positive ionisation mode, (-) - negative ionisation mode

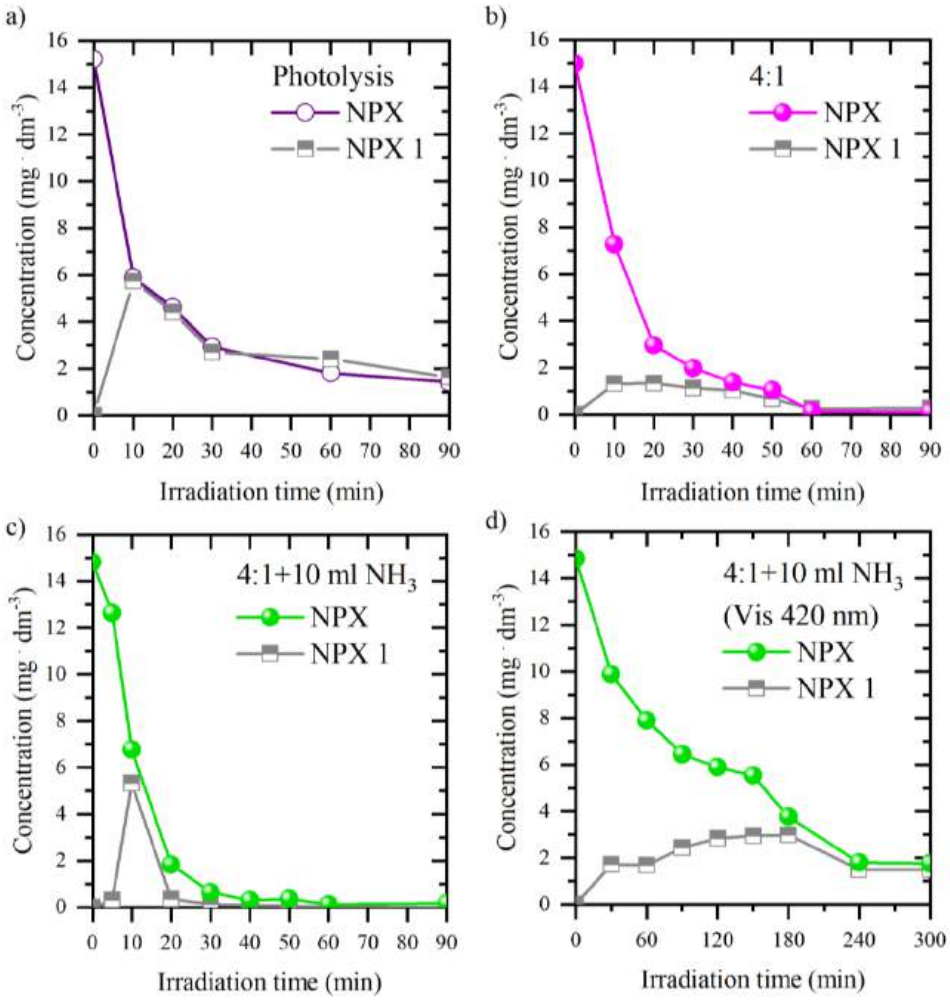

Figure S6. Changes in concentration of NPX and NPX 1 in the process a) without catalysts (only photolysis), b) using 4:1 sample (decahedral TiO_2), c) using 4:1 + 10 ml NH_3 (octahedral TiO_2) under UV-vis irradiation, d) using 4:1 + 10 ml NH_3 (octahedral TiO_2) under visible (> 420 nm) light.

Based on the LC-MS results and the related literature [15–17], the mechanism of naproxen degradation during photocatalytic process is proposed (Figure S7). Demethylation and decarboxylation are the principal initial processes in the degradation of naproxen molecule. At the beginning of the NPX degradation at aerobic conditions, reactive oxygen species, e.g. $O_2^{\bullet-}$ cause decarboxylation and the photodecarboxylated radicals are formed. These photodecarboxylated radicals are the precursors of three by-products: 2-ethyl-6-methoxynaphtalene, 1-(6-methoxy-2-naphthyl)ethanol (NPX 2) and organic superacid, which easily transform to 2-acetyl-6-methoxynaphtalene (NPX 1). The second intermediate product

can also oxidize to NPX 1. NPX 2 molecules undergo further demethylation during photocatalytic process to compound **B** and then aliphatic chain cleavage. However, holes can participate in further transformation to compound **C**. Simultaneously, several short-lived alcohol-based (like compound **A**) radicals originated from reaction of methyl and hydroxyl radicals can be formed, which then react with compounds B and C. These compounds (**A, B and C**) are supposed to participate in dimerization process. Remarkably, the dimer $C_{26}H_{26}O_4$ formation can be noticed only decahedral F-TiO_2. These transformation to dimer occurs only for samples with exposed {0 0 1} facets next to {1 0 1} ones. Actually, these NPX transformations are strongly attributed to the presence of oxygen in water phase and formation of ROS. However, {0 0 1} facets have the strongest affinity to trap holes [18,19], which may participate in further transformation of compound B. Finally, this statement can explain, why only for photocatalytic processes with decahedral F-TiO_2 the dimer is detected.

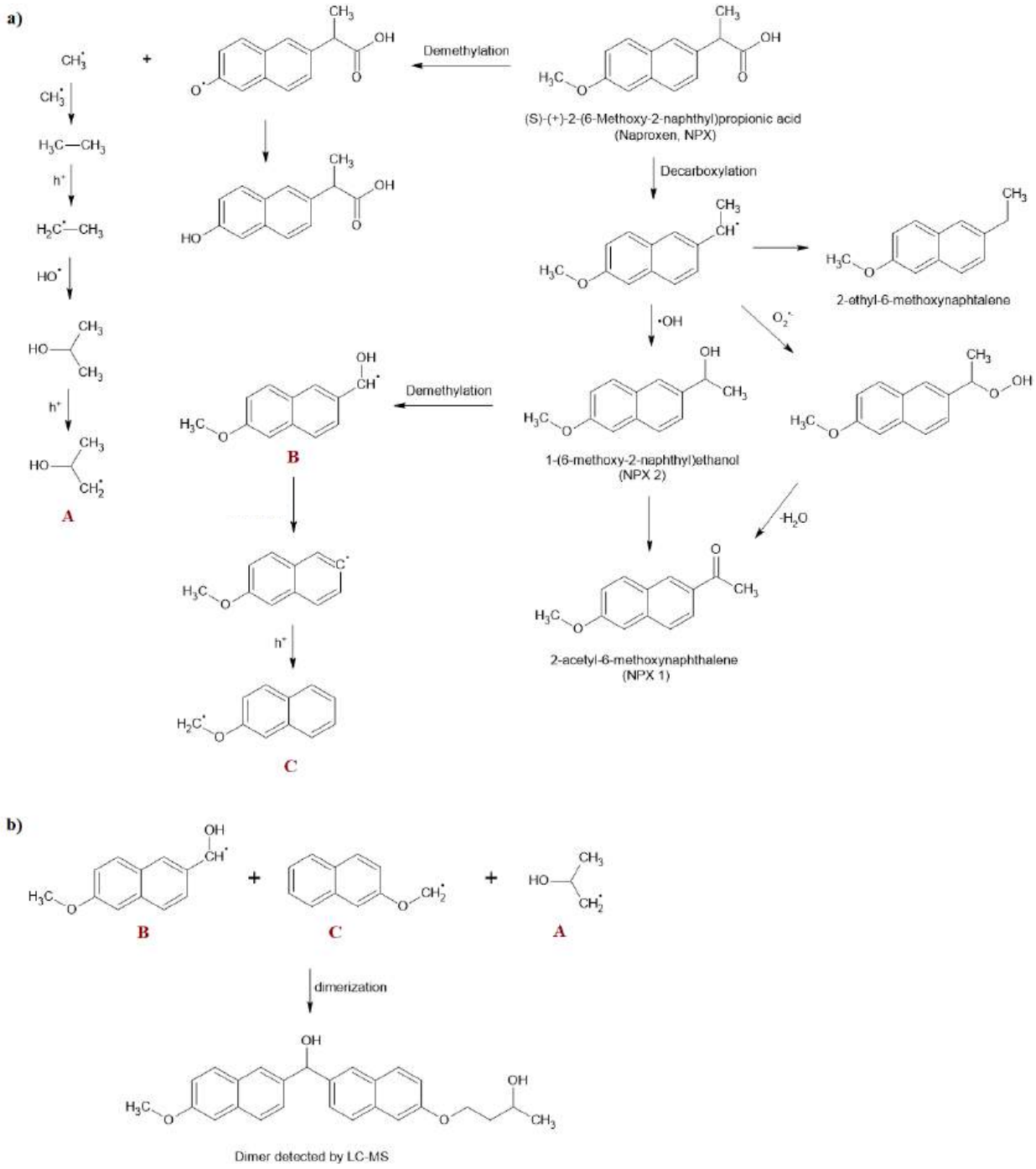

Figure S7. The proposed NPX degradation mechanism, including formation of NPX 1 and NPX 2 (a), dimer (b).

Acknowledgements

The research was financially supported by the Polish National Science Centre, grant no. 2018/30/E/ST5/00845.

References:

[1] P. Giannozzi, S. Baroni, N. Bonini, M. Calandra, R. Car, C. Cavazzoni, D. Ceresoli, G.L. Chiarotti, M. Cococcioni, I. Dabo, A. Dal Corso, S. De Gironcoli, S. Fabris, G. Fratesi, R. Gebauer, U. Gerstmann, C. Gougoussis, A. Kokalj, M. Lazzeri, L. Martin-Samos, N. Marzari, F. Mauri, R. Mazzarello, S. Paolini, A. Pasquarello, L. Paulatto, C. Sbraccia, S. Scandolo, G. Sclauzero, A.P. Seitsonen, A. Smogunov, P. Umari, R.M. Wentzcovitch, Journal of Physics Condensed Matter 21 (2009).

[2] P. Giannozzi et al., Journal of Physics: Condensed Matter PAPER 29 (2017).

[3] N. Serpone, A. Salinaro, Pure and Applied Chemistry 71 (1999) 303–320.

[4] Microbics Corporation Ed., Microtox Operating Manual, Carlsbad, California, 1991.

[5] M. Maisano, M.V. Dozzi, E. Selli, Journal of Photochemistry and Photobiology C: Photochemistry Reviews 28 (2016) 29–43.

[6] M. Sun, J.E. Paciga, R.I. Feldman, Z.Q. Yuan, D. Coppola, You Yong Lu, S.A. Shelley, S. V. Nicosia, J.Q. Cheng, Nature 530 (2016) 171–176.

[7] K. Lv, Q. Xiang, J. Yu, Appl Catal B 104 (2011) 275–281.

[8] T. Shi, Y. Duan, K. Lv, Z. Hu, Q. Li, M. Li, X. Li, Front Chem 6 (2018).

[9] S. Dudziak, M. Kowalkińska, J. Karczewski, M. Pisarek, K. Siuzdak, A. Kubiak, K. Siwińska-Ciesielczyk, A. Zielińska-Jurek, Appl Surf Sci 563 (2021) 150360.

[10] M. Kowalkińska, P. Głuchowski, T. Swebocki, T. Ossowski, A. Ostrowski, W. Bednarski, J. Karczewski, A. Zielińska-Jurek, The Journal of Physical Chemistry C 125 (2021) 25497–25513.

[11] S. Kohtani, Y. Kamoi, E. Yoshioka, H. Miyabe, Catal Sci Technol 4 (2014) 1084–1091.

[12] J. Wang, D.N. Tafen, J.P. Lewis, Z. Hong, A. Manivannan, M. Zhi, M. Li, N. Wu, J Am Chem Soc 131 (2009) 12290–12297.

[13] J.C. González-Torres, E. Poulain, V. Domínguez-Soria, R. García-Cruz, O. Olvera-Neria, International Journal of Photoenergy 2018 (2018) 30–32.

[14] J. Nowotny, T. Bak, M.K. Nowotny, L.R. Sheppard, Journal of Physical Chemistry B 110 (2006) 18492–18495.

[15] G. Fan, J. Zhan, J. Luo, J. Zhang, Z. Chen, Y. You, Catal Sci Technol 9 (2019) 4614–4628.

[16] F. Méndez-Arriaga, J. Gimenez, S. Esplugas, Journal of Advanced Oxidation Technologies 11 (2008) 435–444.

[17] N. Jallouli, K. Elghniji, O. Hentati, A.R. Ribeiro, A.M.T. Silva, M. Ksibi, J Hazard Mater 304 (2016) 329–336.

[18] J.J. Carey, K.P. McKenna, Journal of Physical Chemistry C 122 (2018) 27540–27553.

[19] M. Chen, J. Ma, B. Zhang, F. Wang, Y. Li, C. Zhang, H. He, Appl Catal B 223 (2018) 209–215.

4.3. Chapter III: The role of $TiOF_2$ morphology on the photocatalytic activity of F-TiO_2

Based on **[P4]** M. Kowalkińska, J. Karczewski, A. Zielińska-Jurek, *The Effect of Titanium Oxyfluoride Morphology on Photocatalytic Activity of Fluorine-Doped Titanium(IV) Oxide*, Crystals, 13(2), 2023, 356.

Following studies described in Chapter II [P3], the main goal was to verify if $TiOF_2$ morphology has an impact on the photocatalytic activity of F-TiO_2. A connection between the $TiOF_2$ morphology and the photocatalytic activity of the final photocatalyst structure was evaluated. In this regard, single-phase $TiOF_2$ were fabricated *via* the solvothermal method, including HF-assisted and acid-free reactions with TiF_4 or titanium tetraisopropoxide (TTIP) as a Ti source. SEM microscopy confirmed several morphological differences: cubic particles (TP), solid smooth structure with square-shaped openings (TF_0.17HF), a mixture of cubic and spherical particles (TF_0HF) and small ones with undefined shape (TF_0.085HF). BET surface area measurements indicated overall low S_{BET} values (<10 m²/g) for all $TiOF_2$ samples. The comparison of the precursors' morphology is presented in Figure 4.6.

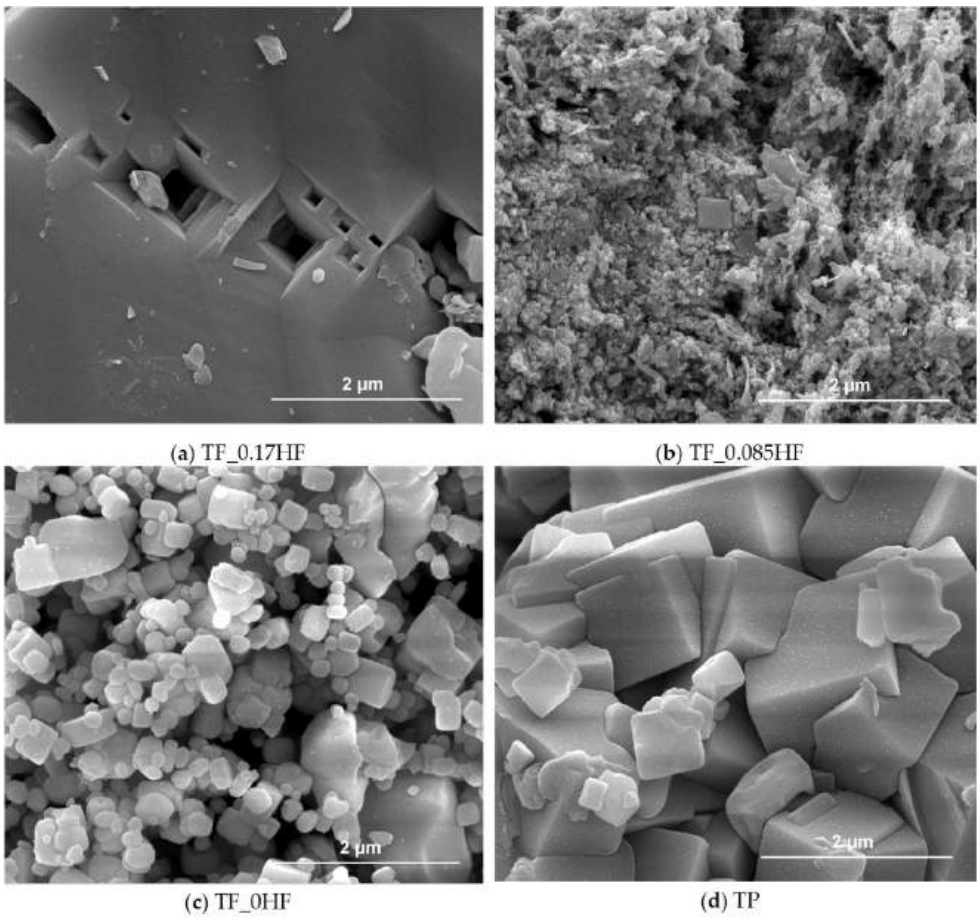

Figure 4.6. SEM images of $TiOF_2$ precursors.

Subsequently, $TiOF_2$ samples were used as precursors for F-TiO_2 synthesis under hydrothermal conditions. Finally, photocatalytic activity was assessed toward phenol degradation under UV-vis light, depicted in Figure 4.7. The highest kinetics of phenol oxidation was observed for photocatalysts derived from TiF_4, achieving nearly 100% degradation within 60 minutes. F-TiO_2 derived from TP, despite its high surface area, showed the lowest efficiency among the series.

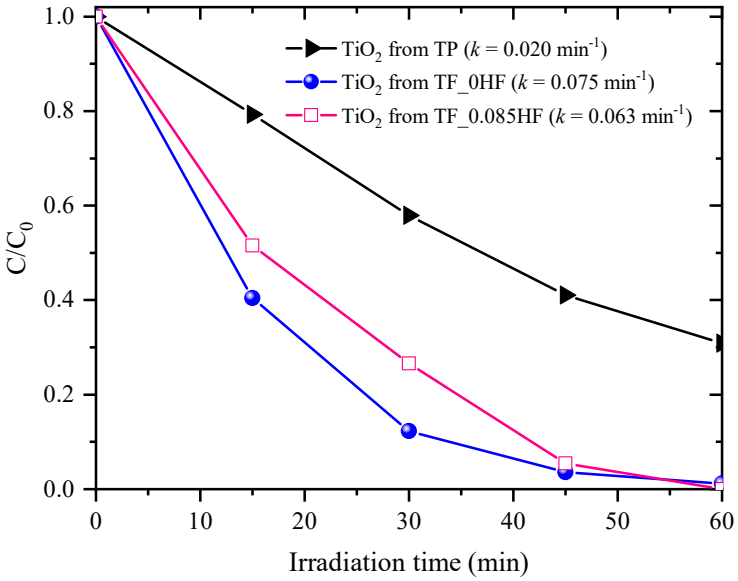

Figure 4.7. Photocatalytic degradation of phenol under UV-Vis light over F-TiO_2 synthesized from different $TiOF_2$ precursors.

To summarize, by systematically manipulating the morphology of the precursor, it is possible to tailor the photocatalytic activity of TiO_2 semiconductors.

crystals

MDPI

Article

The Effect of Titanium Oxyfluoride Morphology on Photocatalytic Activity of Fluorine-Doped Titanium(IV) Oxide

Marta Kowalkińska [1,*], Jakub Karczewski [2] and Anna Zielińska-Jurek [1,*]

[1] Department of Process Engineering and Chemical Technology, Gdansk University of Technology, Gabriela Narutowicza 11/12, 80-233 Gdansk, Poland
[2] Institute of Nanotechnology and Materials Engineering, Faculty of Applied Physics and Mathematics, Gdansk University of Technology, Gabriela Narutowicza 11/12, 80-233 Gdansk, Poland
* Correspondence: marta.kowalkinska@pg.edu.pl (M.K.); annjurek@pg.edu.pl (A.Z.-J.)

Abstract: Titanium oxyfluoride ($TiOF_2$) is a metastable product that can be obtained in a fluorine-rich environment. This material can also be a valuable precursor in the synthesis of titanium(IV) oxide (TiO_2). However, the effect of $TiOF_2$ morphology on the physicochemical properties of TiO_2 has not been studied so far. In this work, single-phase $TiOF_2$ was prepared by a solvothermal method. The as-synthesized samples exhibited a variety of morphologies, including different shapes and crystallite sizes. These materials were characterized by X-ray diffraction (XRD), scanning electron microscopy (SEM) combined with energy-dispersive X-ray spectroscopy (EDS), surface area measurements, thermal gravimetric analysis (TGA) and UV–vis diffuse reflectance spectroscopy (DR/UV–vis). Furthermore, $TiOF_2$ samples were used as precursors in the synthesis of fluorine-doped titanium(IV) oxide and applied in photocatalytic phenol degradation under UV-vis light. The experiments showed that the crystallite size of the precursor, as well as the number of fluoride ions used in the synthesis, were the predominant factors that affected the photocatalytic activity of the final photocatalyst.

Keywords: titanium oxyfluoride; morphology; titanium(IV) oxide; nanostructures; photocatalyst; phenol degradation

Citation: Kowalkińska, M.; Karczewski, J.; Zielińska-Jurek, A. The Effect of Titanium Oxyfluoride Morphology on Photocatalytic Activity of Fluorine-Doped Titanium(IV) Oxide. *Crystals* **2023**, *13*, 356. https://doi.org/10.3390/cryst13020356

Academic Editor: Dah-Shyang Tsai

Received: 2 February 2023
Revised: 14 February 2023
Accepted: 16 February 2023
Published: 19 February 2023

1. Introduction

Titanium oxyfluoride ($TiOF_2$) is a semiconducting material that exists in two polymorphs: a cubic structure and a hexagonal unit cell, which is thermodynamically less favoured [1]. $TiOF_2$ can be easily synthesized by a solvothermal route, usually with the addition of hydrofluoric acid [2–4]. Titanium oxyfluoride has been mainly investigated as an electrode material for lithium-ion batteries. The utilization of this compound could have numerous advantages, including air stability and low hygroscopicity [5]. According to Reddy et al., $TiOF_2$ with a cubic unit cell can intercalate four lithium atoms, while the accident-related energy capacity is higher than commercially available graphite nodes [6]. Nanostructured titanium oxyfluoride is also advantageous due to its more developed surface area, larger pore volume, and shorter diffusion path for ion transport than its macroscopic counterparts [5,7]. Therefore, further research on $TiOF_2$-based materials may be useful in terms of electrochemical applications.

Recently, $TiOF_2$ has also been proposed as a photocatalytic material in heterogeneous photocatalysis. However, this material does not actually demonstrate noticeable photocatalytic activity, as has been studied in H_2 evolution [8], hydroxyl radicals generation [9] and decomposition of organic pollutants so far [10,11]. Due to low photocatalytic activity and limited practical application, titanium oxyfluoride is still overlooked in the literature. However, in some studies, $TiOF_2$ is proposed as a precursor of titanium(IV) oxide (TiO_2), which is one of the most described and characterized photocatalysts in the literature [12–15]. Our recent studies showed that the hydrothermal treatment of $TiOF_2$ in the presence of capping agents allowed us to obtain anatase nanostructures or fluorine-doped TiO_2 nanocrystals,

with exposed {1 0 1}, {0 0 1} and {1 0 0} facets [4,16]. Therefore, considering the practical aspect of $TiOF_2$ utilization as a precursor, further investigation of this material is needed.

It is well known that the morphology of the material is a key factor that may influence either the photocatalytic performance or electrochemical properties [17–19]. However, the morphological design of the material may be applied to both the final product as well as the precursor. To our best knowledge, there are no studies concerning the $TiOF_2$ morphologies' effect on the final structure and properties of TiO_2-based materials. Therefore, the main aim of the present study was the design and synthesis of $TiOF_2$ with a desired structure, including HF-assisted and acid-free synthesis and physicochemical characterization of $TiOF_2$ samples. Furthermore, fluorine-doped TiO_2 from different $TiOF_2$ precursors was characterized and applied in photocatalytic phenol degradation under simulated solar light.

2. Materials and Methods

The synthesis of titanium oxyfluoride was proceeded via a solvothermal route. Titanium(IV) fluoride (TiF_4), titanium(IV) isopropoxide (TTIP), 1-butanol, hydrofluoric acid 48% (HF), acetic acid (CH_3COOH), ammonium fluoride (NH_4F) and ammonia water 25% ($NH_{3(aq)}$) were provided by Chemat, Poland.

2.1. Synthesis of Titanium Oxyfluoride and F-Modified Titanium(IV) Oxide

In a typical procedure of $TiOF_2$ synthesis, TiF_4 or TTIP are used as precursors. The samples obtained from TTIP are denoted as TP, whereas materials originating from TiF_4 are labeled as TF. In the case of TF series, the labels are completed by the volume of hydrofluoric acid used in the synthesis. The detailed parameters of synthesis conditions and the nomenclature are presented in Table 1 and the subsections below.

Table 1. Synthesis conditions and nomenclature of $TiOF_2$ samples.

Sample Name	Titanium Source	Titanium Source Amount	Solvent	Solvent Volume (cm^3)	HF Volume (cm^3)	Reaction Temperature and Time
TP	TTIP	10.2 cm^3	CH_3COOH	24.4	3.9	200 °C, 12 h
TF_0HF	TiF_4	10 g	1-butanol	120	-	210 °C, 24 h
TF_0.085HF		3.06 g			0.085	
TF_0.17HF					0.17	

2.1.1. Synthesis of $TiOF_2$–TP Series

The demonstrated synthesis of $TiOF_2$ was based on Chen et al., with modifications [20]. The appropriate amount of TTIP was mixed with acetic acid and kept under stirring using a Teflon-coated magnetic stirrer bar at room temperature. After 15 min, HF was slowly added and stirring was continued for 15 min. The obtained mixture was then transferred into a 200 cm^3 Teflon-lined stainless-steel autoclave and heated at 200 °C for 12 h. The obtained product was separated through centrifugation and washed several times thoroughly with ethanol and deionized water to remove the residual organic contamination. After drying at 80 °C overnight, the TP sample was harvested.

2.1.2. Synthesis of $TiOF_2$–TF Series

TF_0HF sample was synthesized using TiF_4 powder, which was added into a 200 cm^3 Teflon reactor with 120 cm^3 of 1-butanol. The obtained mixture was stirred for 30 min to form a uniform suspension. Furthermore, the reactor was transferred into a stainless-steel autoclave immediately and heated at 210 °C for 24 h. The obtained product was separated through centrifugation and washed several times with ethanol and deionized water. Finally, the grey powder was dried at 80 °C overnight.

A similar procedure was applied to obtain samples TF_0.085HF and TF_0.17HF, but a different mass of TiF_4 was used. In addition, after forming the stable suspension, the

desired amount of HF was slowly injected. After this step, the reactor was transferred into an autoclave immediately.

2.1.3. Synthesis of Fluorine-Modified TiO_2

Fluorine-modified photocatalysts were synthesized using $TiOF_2$ as precursors. In this regard, 0.2 g $TiOF_2$ sample was dispersed in 45 cm^3 of deionized water (DI). Simultaneously, 0.2904 g NH_4F was dissolved in 45 cm^3 DI. NH_4F solution was added to $TiOF_2$ mixture and stirred for 15 min using a magnetic stirrer. Next, 10 cm^3 of ammonia water was added to the mixture and the stirring was continued for 15 min. The obtained mixture was transferred into a 200 cm^3 Teflon-lined stainless-steel autoclave and kept at 200 °C for 20 h and then cooled down naturally. After each reaction, beige precipitates were centrifuged and washed several times with DI and ethanol to remove residual inorganic ions, then dried at 80 °C overnight.

2.2. Materials Characterization

The crystal structure of the samples and phase identification were investigated by X-ray powder diffraction (Rigaku MiniFlex 600 X-Ray diffractometer, Tokyo, Japan) with Cu Kα radiation. Data were collected in a 2θ range of 5°–80° with a scan speed 1° min^{-1} and scan steps 0.01°. The analysis and Rietveld refinements were performed with the HighScore Plus software package (Malvern Panalytical, Malvern, United Kingdom) and the Crystallography Open Database, with data fitting based on the pseudo-Voigt profile function. Several parameters were refined, i.e., the specimen displacement, lattice parameters, polynomial coefficients for the background function, profile parameters and Gaussian and Lorentzian profile coefficients. The estimation of the crystallite size was performed on the basis of Scherrer's equation. A field emission scanning electron microscope (SEM, FEI Quanta FEG 250, Hillsboro, OR, USA) was used to determine the morphologies of $TiOF_2$ samples. The presence of titanium and fluorine in all powders was confirmed by energy-dispersive X-ray spectroscopy (EDS). The Brunauer–Emmett–Teller (BET) surface area of $TiOF_2$ and F-TiO_2 samples was measured by nitrogen adsorption using a Micromeritics Gemini V instrument. All powders were degassed at 200 °C for 120 min prior to N_2 adsorption measurements. The BET surface area was determined by a multipoint BET method. To study the absorption properties, diffuse reflectance UV−visible spectra (DRS/UV−vis) were measured using a Thermo Fisher Scientific Evolution 220 spectrophotometer. Barium sulfate was used as a reflectance standard. Based on the obtained data, bandgap energy (E_g) calculations were performed using Tauc's method. To study the thermal stability and phase transition of $TiOF_2$, thermal gravimetric analyses (TGA) were performed using Thermal Analysis System 2 SF/1100 (Mettler Toledo, Greifensee, Switzerland). The measurements were performed in a range of 25–800 °C at a heating rate of 10 °C·min^{-1} under a nitrogen atmosphere.

2.3. Photocatalytic Phenol Degradation

The photocatalytic activity of F-TiO_2 photocatalysts was tested towards phenol degradation under UV-vis light, performed in a black box. In a typical experiment, 25 cm^3 of 20 mg·dm^{-3} phenol solution and 25 mg of the photocatalyst were put into a quartz reactor under magnetic stirring with a speed of 800 rpm. The suspension was aerated with a constant airflow of 5 dm^3·h^{-1}. For an experiment, a 300 W xenon lamp was used as simulated solar light. The UV spectrum flux intensity at the reactor border was set as 45 mW·cm^{-2}. Before irradiation, the whole system was kept in darkness for 30 min to provide the adsorption−desorption equilibrium. After that, the process was initiated by turning on the xenon lamp. The liquid samples (1.0 cm^3) were collected every 15 min and filtered through syringe filters (pore size = 0.2 μm) to remove the photocatalyst particles.

The phenol concentration was monitored using a high-performance liquid chromatography system (HPLC, model Shimadzu LC-6A, Kyoto, Japan), combined with a photodiode array detector (SPD-M20A) and a C18 column (Phenomenex Gemini 5 μm; 150 × 4.6 mm,

California, USA) working at a temperature of 45 °C. During measurements, the mobile phase, composed of (*v*/*v*) 70% acetonitrile, 29.5% water and 0.5% orthophosphoric acid, was used at a flow rate of 0.3 $cm^3 \cdot min^{-1}$. HPLC-grade acetonitrile, orthophosphoric acid solution and phenol were provided by Merck. Quantitative phenol analysis was performed using standard compounds using the external calibration method.

3. Results and Discussion

3.1. Structural and Morphological Analyses of $TiOF_2$

To confirm the presence of titanium oxyfluoride in the as-synthesized samples, powder X-Ray Diffraction (XRD) was performed. XRD patterns of investigated materials compared with the calculated model are presented in Figure 1. The experimental XRD patterns of the obtained samples were compared with the reference card 01-077-0132. The presence of the $TiOF_2$ phase with cubic structure and space group Pm-3 m is observed in all samples. The unit cell parameters from Rietveld refinement are presented in Table 2. No additional peaks, as well as low χ^2 as a parameter of the goodness of fit, indicated that the obtained samples are single phase. Moreover, the crystallite size estimated using Scherrer's equation is in a range of 40–49 nm in all cases.

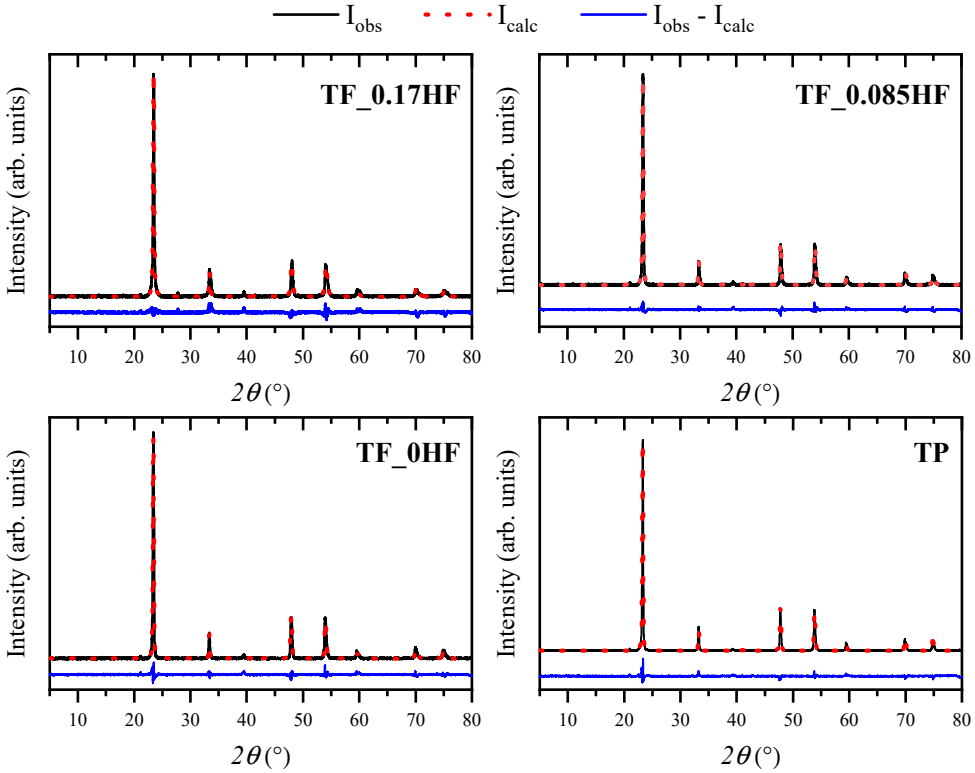

Figure 1. XRD patterns of synthesized $TiOF_2$ samples.

Table 2. Lattice and microstructural parameters of $TiOF_2$ obtained by XRD, BET and EDS analysis.

Sample Name	Crystallite Size (nm)	F/Ti Ratio Calculated from EDS Spectroscopy	Surface Area S_{BET} ($m^2 \cdot g^{-1}$)	Lattice Parameters $a = b = c$ (Å)	Goodness of Fit χ^2
TP	49	2.19	3.9	3.799	1.89
TF_0HF	43	2.13	5.2	3.794	1.48
TF_0.085HF	44	2.08	8.5	3.796	1.37
TF_0.17HF	40	-	-	3.788	2.62

The morphologies of $TiOF_2$ powders were further studied using scanning electron microscopy analysis. Figure 2 shows SEM images of the as-synthesized samples. Comparing

all the SEM images, the difference in morphology within obtained powders was distinct. The sample TF_0.17HF (Figure 2a) exhibited large agglomerates with a solid structure and smooth surface, in which smaller crystallites cannot be unambiguously distinguished. Within the solid structure, square-shaped openings can be observed. In contrast to this solid morphology, in the case of sample TF_0.085HF (Figure 2b), small particles with undefined shapes can be observed. This variation is in agreement with the literature because increased fluoride ion concentrations promote the growth of large particles [4,21]. However, solvothermal alcoholysis of TiF_4 without HF addition (Figure 2c) led to the formation of a mixture of cubic and spherical particles. The morphology is not uniform, which is probably due to the high amount of TiF_4 precursor with respect to 1-butanol. According to Wang et al., an oxidation process to $TiOF_2$ results from hydrolysis of the initially formed $(RO)_xTiF_{4-x}$ complex. At this stage, the particles are spherical and the further prolongation of solvothermal synthesis allows one to shape transformation to cubes [10]. A distinct cubic shape was noticed in the TP sample (Figure 2d). An addition of acetic acid was probably responsible for two effects: support in HF-assisted crystal growth and a factor determining the morphology [22].

In general, titanium oxyfluoride can undergo hydrolysis under air conditions and transform into anatase [23]. In this regard, theoretically, $TiOF_2$ should be stored under low humic conditions. However, only TF_0.17HF from the series, when stored in the presence of air, starts oxidizing to titanium(IV) oxide. In other cases, this reaction does not occur, and these samples are stable. The probable explanation of this phenomenon is the high Ti/F ratio used in the synthesis. The solvothermal route with TiF_4 and HF is also the method of synthesizing TiO_2 with exposed {0 0 1} facets [21,24]. Therefore, an increased F^- amount at the material's surface may promote the hydrolysis and formation of TiO_2.

Finally, EDS spectroscopy was used to estimate the presence of fluorine in $TiOF_2$ samples. Based on these results, the average atomic F/Ti ratio was calculated (see Table 2). These values are close to the theoretical F/Ti ratio from the general formula of titanium oxyfluoride, which equals 2.0.

Furthermore, the surface area analyses (S_{BET}) using the BET method for $TiOF_2$ samples were performed. The S_{BET} values are presented in Table 2. All powders possessed a surface area below 10 $m^2 \cdot g^{-1}$. The lowest S_{BET} value was observed for the TP sample, which can be explained by the high amount of hydrofluoric acid used in the synthesis and, in consequence, the largest crystallite size. Although in the preparation of TF series, titanium fluoride was used as a precursor, the absence or low amount of HF was probably responsible for the small crystallite size of $TiOF_2$ and increasing the surface area compared to the TP sample.

The optical properties, including light absorption, were determined using diffuse-reflectance (DR) UV-Vis spectroscopy. The DR/UV-vis spectra of as-prepared titanium oxyfluoride samples are presented in Figure 3. All samples possessed the highest absorbance in a range of 200–400 nm, which is similar to TiO_2 [25,26]. Moreover, all samples in the series were capable of absorbing light above 400 nm, which is in accordance with the fact that these powders are gray. Based on the transformation of the Kubelka–Munk function, the bandgap energies of titanium oxyfluoride samples were calculated. The E_g values equaled 3.2–3.3 eV, which is consistent with previous reports [2,4].

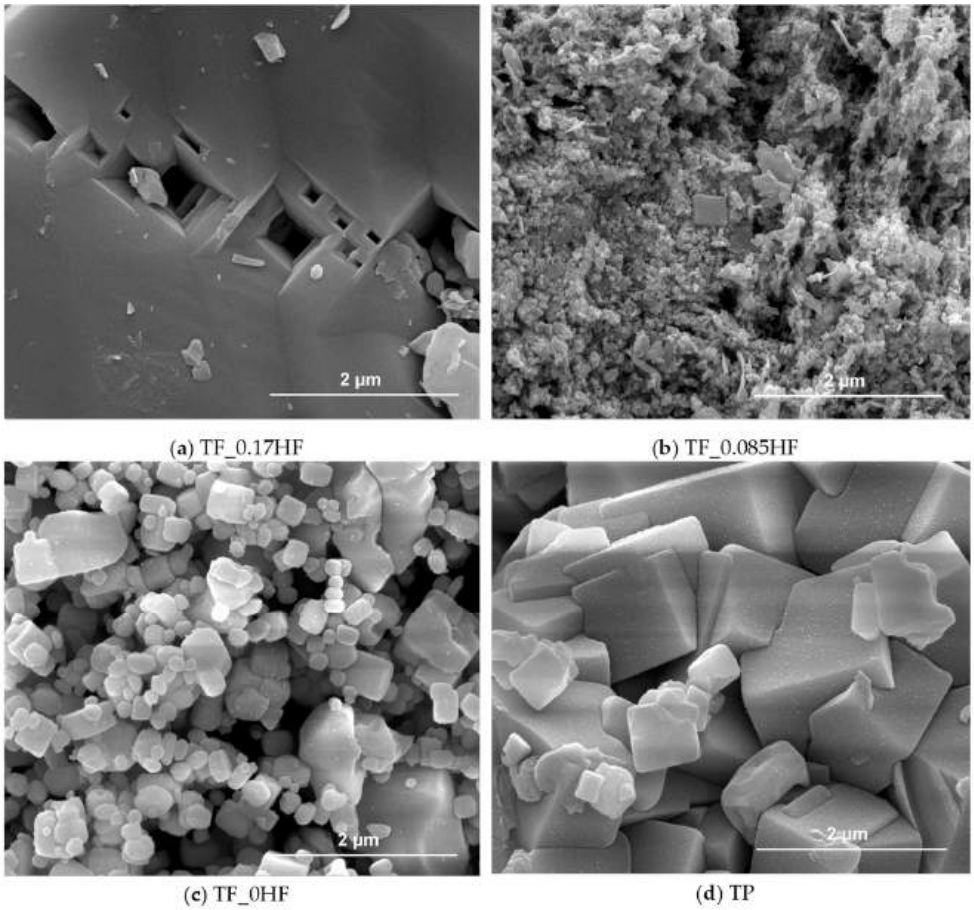

Figure 2. SEM images of as-prepared samples.

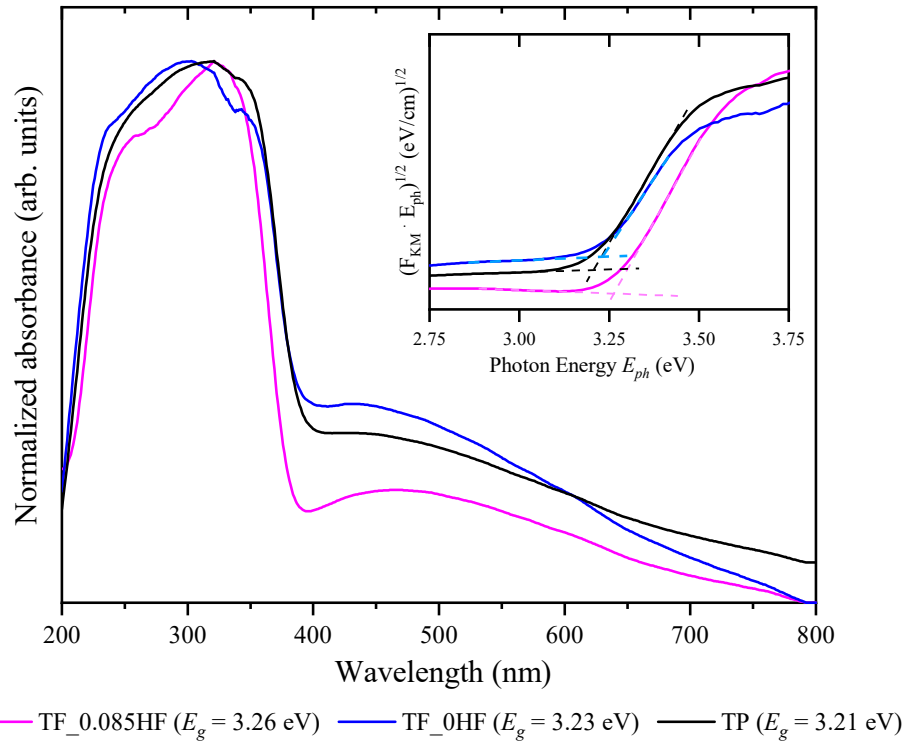

Figure 3. DR/UV-vis spectra of obtained $TiOF_2$. The inset shows the transformation of Kubelka–Munk function vs. photon energy.

For a better characterization of the thermal stability of titanium oxyfluoride samples, thermal gravimetry analyses (TGA) were performed. The TGA curves are presented in Figure 4. A distinct weight loss is observed at a temperature of around 550 °C in the case of all three samples. The mass variations at these temperatures are −45.17%, −46.75% and −48.16% for samples TP, TF_0HF and TF_0.085HF, respectively. These results showed that under a nitrogen atmosphere, $TiOF_2$ does not transform into TiO_2 directly; theoretically, in that case, the mass loss should achieve a value around c.a. −32%. According to Xie et al., the following transition may occur: 2 $TiOF_2 \rightarrow TiO_2 + TiF_4$ [27]. However, these measurements were performed under air conditions, whereas our samples were heated under a non-oxidizing atmosphere. Moreover, the powders after TGA analyses had a dark-blue-gray color, but X-ray diffraction confirmed the presence of anatase. Therefore, this phase transition may be more complex. The probable explanation is that weight loss results from $TiOF_2$ transformation to the Ti-O Magneli phase [28]. This product is apparently metastable and undergoes oxidation to anatase under air conditions. However, based on the powder color, the final material would be defective and oxygen deficient [25].

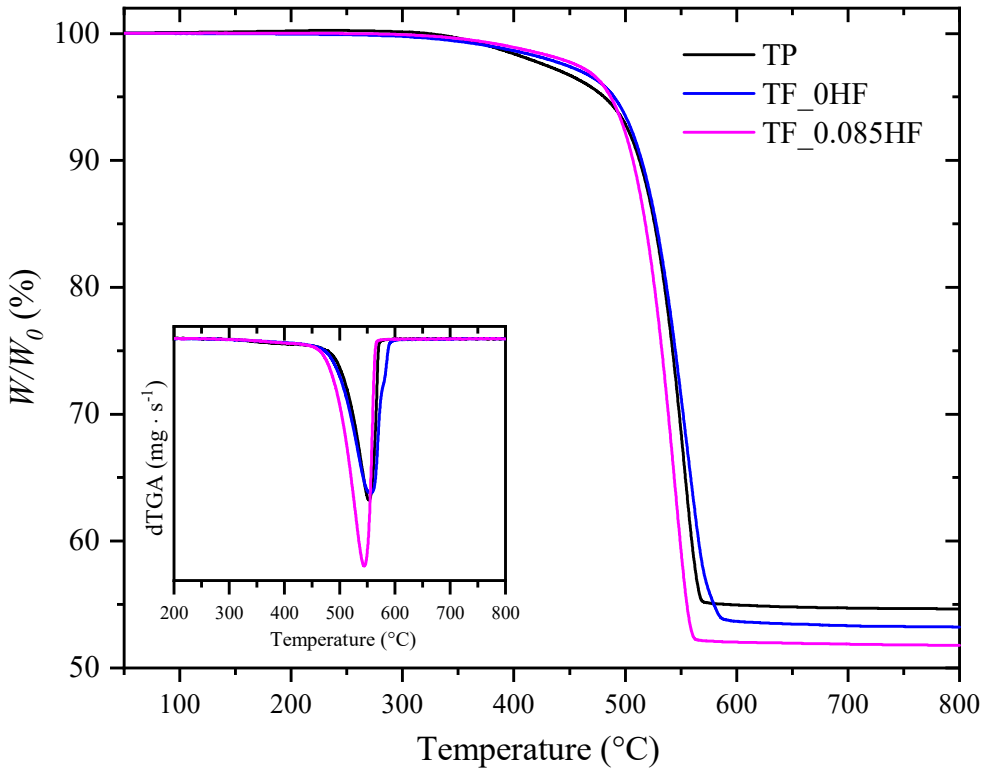

Figure 4. TGA curves of $TiOF_2$ samples. The inset shows the first derivative dTGA in relation to temperature.

3.2. Characterization and Photocatalytic Activity of TiO_2 Synthesized from $TiOF_2$

To study the effect of precursor morphology on the final photocatalyst properties, X-ray diffraction analyses were performed. The XRD patterns of F-TiO_2 are presented in Figure 5. The experimental XRD pattern of the obtained photocatalysts was compared with the reference card 03-065-5714. Each $TiOF_2$ precursor was successfully transformed to anatase under hydrothermal conditions. Moreover, comparing the crystallite size of anatase samples (Table 3) with the values from Table 2, it can be noticed that the transformation from titanium oxyfluoride to titanium(IV) oxide allows photocatalysts with small crystallite size to be achieved. Specifically, sample TP, which exhibited the largest crystallite size in the $TiOF_2$ series, was able to synthesize F-TiO_2 with the smallest crystallites. Finally, the presence of fluorine in the photocatalysts was confirmed by EDS spectroscopy. The results of the average F/Ti ratio for F-TiO_2 are presented in Table 3.

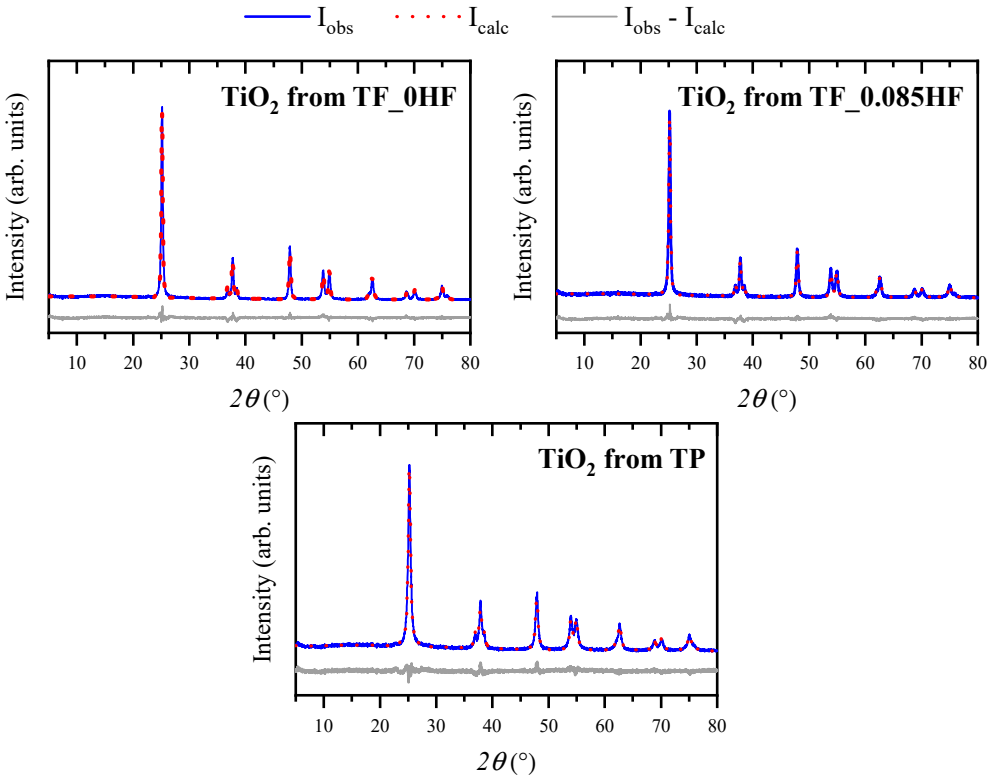

Figure 5. XRD patterns of F-modified TiO_2.

Table 3. Lattice and microstructural parameters of F-TiO_2 obtained by XRD, BET and EDS analysis.

Sample Name	Crystallite Size (nm)	F/Ti Ratio Calculated from EDS Spectroscopy	Surface Area S_{BET} ($m^2 \cdot g^{-1}$)	Lattice Parameter $a = b$ (Å)	Lattice Parameter c (Å)	Goodness of Fit χ^2
TiO_2 from TP	17	0.086	38.9	3.793	9.488	1.94
TiO_2 from TF_0HF	28	0.072	20.7	3.786	9.499	2.05
TiO_2 from TF_0.085HF	24	0.054	28.1	3.788	9.497	1.95

The differences in crystallite size between samples are correlated with the specific surface area, which is an important factor concerning the improvement in photocatalytic activity [29]. Therefore, to complete the characterization of F-TiO_2 samples, surface area measurements using the BET method were performed. The highest surface area of 38.9 $m^2 \cdot g^{-1}$ was observed in TiO_2 obtained from TP, although this precursor exhibited the lowest surface area in the $TiOF_2$ samples. However, these measurements are consistent with the estimated crystallite size by Scherrer's equation. In the case of the photocatalysts synthesized from precursors in the TF series, S_{BET} values of about 21–28 $m^2 \cdot g^{-1}$ were noticed.

Finally, the photocatalytic degradation of phenol under UV-vis light in the presence of F-TiO_2 was determined. The changes in phenol concentration during the photocatalytic process are presented in Figure 6a. Under these conditions, the effect of photolysis was negligible. All F-TiO_2 samples were capable of degrading phenol under simulated solar light. However, the reaction rate constants (Figure 6b) differed for particular photocatalysts. The lowest phenol degradation efficiency was observed for TiO_2 prepared from TP; this is the only sample that did not fully degrade phenol after 60 min of the photocatalytic process. For this photocatalytic process, the main phenol derivative detected by HPLC-DAD was 1,2-dihydroxybenzene (catechol). Remarkably, TiO_2 from TP was supposed to have the smallest crystallite size in the anatase series, but according to SEM images, the

formed cubes were bigger than crystallites in TF_0HF and TF_0.085HF. Moreover, these photocatalysts exhibited the highest surface area in the F-TiO_2 series. Meanwhile, the application of the TF series as precursors allowed us to achieve almost 100% degradation of initial phenol concentration after 1 h of irradiation. For both photocatalytic processes, two phenol derivatives were predominant: catechol and benzene-1,4-diol (hydroquinone). It is worth highlighting that the precursor TF_0HF was the only sample in which, during solvothermal synthesis, no hydrofluoric acid was used. For this photocatalyst, the highest reaction rate constant was noticed. No correlation between either specific surface area of fluorinated anatase or the atomic F/Ti was observed. The more important factor was the morphology of the precursors; $TiOF_2$ from the TF series exhibited smaller crystallite size and higher surface area than the TP sample. The crystallite size and surface area depended on the F^- content in the solvothermal reaction. Therefore, we can conclude that $TiOF_2$ precursor morphology primarily influences the photocatalytic activity of the anatase-based photocatalytic material. In particular, the crystallite size and the number of fluoride ions used in the synthesis significantly influenced the efficiency of phenol degradation.

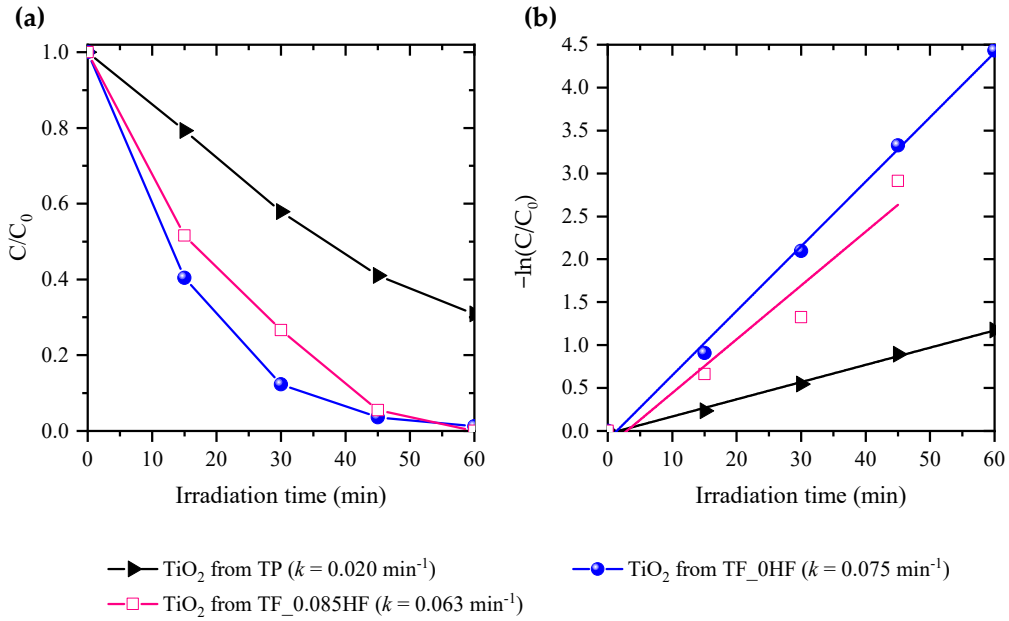

Figure 6. Photocatalytic degradation of phenol as a function of concentration to initial concentration (**a**) and $ln(C/C_0)$ (**b**).

Previously, it was reported that the morphology of the photocatalysts affects their photocatalytic activity. Our recent studies about anatase nanostructures with exposed crystal facets showed that facet exposition was responsible for photocatalytic activity as well as naproxen and phenol degradation pathways [4,16]. The role of morphology was also investigated by Sulowska et al., who studied organic–inorganic photocatalysts consisting of two-dimensional anatase nanosheets modified with PEDOT [30]. Various PEDOT morphologies were obtained, including; globular, stuck spindles and microvesicular structures. It was found that the highest photocatalytic hexavalent chromium removal was observed for 2D TiO_2 combined with microvesicular PEDOT.

Next to photocatalysts' morphology, a vital role of the substrate type used in photocatalyst synthesis was also described in certain studies. For example, in the synthesis of anatase nanocrystals with exposed {0 0 1} facets, the aliphatic chain length in alcohol solvent influenced the crystal growth rate and the final morphology of TiO_2 [25,31]. Next to the solvent type, it was found that the precursor used in the photocatalyst's preparation can affect the properties of the final product. This effect was comprehensively studied by Li et al., who investigated octahedral anatase nanostructures with exposed {1 0 1} facets [32]. A two-step synthesis was performed to obtain these nanocrystals with defined morphology,

where the titanium source was potassium titanate nanowires. It was found that an ion exchange between potassium and ammonium cations influenced the transformation mechanism to titanium(IV) oxide; instead of the in-site transformation and topochemical reaction, a dissolution–nucleation process was predominant. Therefore, the synthesis of TiO_2 with well-defined facets was more controllable. The effect of the precursor was also described by Xia et al., who investigated graphitic carbon nitride for photocatalytic H_2 evolution [33]. To obtain different g-C_3N_4 photocatalysts, thermal polycondensation syntheses using guanidine hydrochloride, melamine, urea, dicyandiamide and thiourea as the precursors were performed. Among the obtained photocatalysts, g-C_3N_4 synthesized from urea possessed the most desirable morphology, including the porous-layered structure and high specific surface area. The above examples showed that the morphology of the precursor is an important factor that should be considered when designing a new photocatalyst with desirable properties.

4. Conclusions

In this work, a facile approach to synthesize titanium oxyfluoride ($TiOF_2$) with different morphologies was developed. The solvothermal route was proposed to obtain this metastable material using TTIP or TiF4 as precursors and, optionally, HF as a reagent and capping agent. X-ray diffraction supported by Rietveld refinements confirmed the presence of single-phase materials. Based on electron microscopy analysis, various morphologies were confirmed, including different shapes and crystallite sizes. However, in most cases, the microstructure of titanium oxyfluoride had no influence on the thermal stability. The fluorine content in all samples and atomic F/Ti ratio determined by EDS spectroscopy were close to the theoretical F/Ti ratio from the general formula of titanium oxyfluoride. Thermal gravimetric analysis curves showed a distinct weight loss at a temperature of about 550 °C, which can be attributed to the formation of the oxygen-deficient oxide. Finally, these samples were applied in the synthesis of fluorine-doped titanium(IV) oxide. The hydrothermal conditions allowed us to complete $TiOF_2$ transformation to anatase with a small crystallite size and high surface area. These materials were applied for photocatalytic phenol degradation under simulated solar light. The analyses showed that F-TiO_2 prepared from the precursor TF_0HF exhibited the highest photocatalytic activity in the series. Surprisingly, the smallest crystallite size of the fluorinated anatase and high specific surface area did not influence phenol degradation efficiency under UV-vis light. Therefore, we supposed that the final photocatalytic activity depended on the crystallite size of titanium oxyfluoride and the number of fluoride ions used in the synthesis of the precursor. It can also be assumed that the morphology of the precursor is a crucial parameter affecting the final photocatalytic material physicochemical properties and should be worthy of attention in further investigations.

Author Contributions: Conceptualization, M.K. and A.Z.-J.; methodology, M.K. and A.Z.-J.; validation, M.K. and A.Z.-J.; formal analysis, M.K. and J.K.; investigation, M.K. and A.Z.-J.; writing—original draft preparation, M.K.; writing—review and editing, M.K. and A.Z.-J.; supervision, A.Z.-J.; project administration, A.Z.-J.; funding acquisition, A.Z.-J. All authors have read and agreed to the published version of the manuscript.

Funding: This research was funded by the Polish National Science Centre, contract No. UMO-2021/43/B/ST5/02983.

Institutional Review Board Statement: Not applicable.

Informed Consent Statement: Not applicable.

Data Availability Statement: The authors confirm that the data supporting the findings of this study are available within the article. Derived data supporting the findings of this study are available from the corresponding author [A.Z.-J.] on request.

Conflicts of Interest: The authors declare no conflict of interest.

References

1. Shian, S.; Sandhage, K.H. Hexagonal and Cubic $TiOF_2$. *J. Appl. Crystallogr.* **2010**, *43*, 757–761. [CrossRef]
2. Lu, Y.; Yan, H.; Huang, E.; Chen, B. Persistent Negative Compressibility Coupled to Optical Modulation in Empty-Perovskite $TiOF_2$. *J. Phys. Chem. C* **2021**, *125*, 8869–8875. [CrossRef]
3. Wang, Z.; Yu, K.; Feng, Y.; Qi, R.; Ren, J.; Zhu, Z. Stabilizing Ti3C2Tx-MXenes with $TiOF_2$ Nanospheres Intercalation to Improve Hydrogen Evolution Reaction and Humidity-Sensing Performance. *Appl. Surf. Sci.* **2019**, *496*. [CrossRef]
4. Kowalkińska, M.; Dudziak, S.; Karczewski, J.; Ryl, J.; Trykowski, G.; Zielińska-Jurek, A. Facet Effect of TiO_2 Nanostructures from $TiOF_2$ and Their Photocatalytic Activity. *Chemical. Eng. J.* **2021**, *404*, 126493. [CrossRef]
5. Louvain, N.; Karkar, Z.; El-Ghozzi, M.; Bonnet, P.; Guérin, K.; Willmann, P. Fluorination of Anatase TiO_2 towards Titanium Oxyfluoride $TiOF_2$: A Novel Synthesis Approach and Proof of the Li-Insertion Mechanism. *J. Mater. Chem. A Mater.* **2014**, *2*, 15308–15315. [CrossRef]
6. Reddy, M.V.; Madhavi, S.; Subba Rao, G.V.; Chowdari, B.V.R. Metal Oxyfluorides $TiOF_2$ and NbO_2F as Anodes for Li-Ion Batteries. *J. Power Sour.* **2006**, *162*, 1312–1321. [CrossRef]
7. Jung, M.J.; Kim, Y.; Lee, Y.S. Enhancement of the Electrochemical Capacitance of $TiOF_2$obtained via Control of the Crystal Structure. *J. Ind. Eng. Chem.* **2017**, *47*, 187–193. [CrossRef]
8. Wen, C.Z.; Hu, Q.H.; Guo, Y.N.; Gong, X.Q.; Qiao, S.Z.; Yang, H.G. From Titanium Oxydifluoride ($TiOF_2$) to Titania (TiO_2): Phase Transition and Non-Metal Doping with Enhanced Photocatalytic Hydrogen (H2) Evolution Properties. *Chem. Commun.* **2011**, *47*, 6138–6140. [CrossRef]
9. Wang, Z.; Lv, K.; Wang, G.; Deng, K.; Tang, D. Study on the Shape Control and Photocatalytic Activity of High-Energy Anatase Titania. *Appl. Catal. B* **2010**, *100*, 378–385. [CrossRef]
10. Wang, J.; Cao, F.; Bian, Z.; Leung, M.K.H.; Li, H. Ultrafine Single-Crystal $TiOF_2$ Nanocubes with Mesoporous Structure, High Activity and Durability in Visible Light Driven Photocatalysis. *Nanoscale* **2014**, *6*, 897–902. [CrossRef]
11. Lv, K.; Yu, J.; Cui, L.; Chen, S.; Li, M. Preparation of Thermally Stable Anatase TiO_2 Photocatalyst from $TiOF_2$ Precursor and Its Photocatalytic Activity. *J. Alloy. Compd.* **2011**, *509*, 4557–4562. [CrossRef]
12. Lv, K.; Guo, X.; Wu, X.; Li, Q.; Ho, W.; Li, M.; Ye, H.; Du, D. Photocatalytic Selective Oxidation of Phenol to Produce Dihydroxybenzenes in a TiO2/UV System: Hydroxyl Radical versus Hole. *Appl. Catal. B* **2016**, *199*, 405–411. [CrossRef]
13. Dalton, J.S.; Janes, P.; Jones, N.; Hallam, K.R.; Nicholson, J.A.; Allen, G.C. Photocatalytic Oxidation of NOx Gases Using TiO_2: A Spectroscopic Approach. *Environ. Pollut.* **2002**, *45120*, 415–422. [CrossRef] [PubMed]
14. Sobczyński, A.; Duczmal, L.; Zmudziński, W. Phenol Destruction by Photocatalysis on TiO_2: An Attempt to Solve the Reaction Mechanism. *J. Mol. Catal. A Chem.* **2004**, *213*, 225–230. [CrossRef]
15. Rej, S.; Hejazi, S.M.H.; Badura, Z.; Zoppellaro, G.; Kalytchuk, S.; Kment, Š.; Fornasiero, P.; Naldoni, A. Light-Induced Defect Formation and Pt Single Atoms Synergistically Boost Photocatalytic H2 Production in 2D TiO_2-Bronze Nanosheets. *ACS Sustain. Chem. Eng.* **2022**, *10*, 17286–17296. [CrossRef]
16. Kowalkińska, M.; Sikora, K.; Łapiński, M.; Karczewski, J.; Zielińska-Jurek, A. Non-Toxic Fluorine-Doped TiO2 Nanocrystals from $TiOF_2$ for Facet-Dependent Naproxen Degradation. *Catal. Today* **2022**. [CrossRef]
17. Nakata, K.; Fujishima, A. TiO_2 Photocatalysis: Design and Applications. *J. Photochem. Photobiol. C Photochem. Rev.* **2012**, *13*, 169–189. [CrossRef]
18. Zhang, Y.; Deng, B.; Zhang, T.; Gao, D.; Xu, A.W. Shape Effects of Cu_2O Polyhedral Microcrystals on Photocatalytic Activity. *J. Phys. Chem. C* **2010**, *114*, 5073–5079. [CrossRef]
19. Mazierski, P.; Sowik, J.; Miodyńska, M.; Trykowski, G.; Mikołajczyk, A.; Klimczuk, T.; Lisowski, W.; Nadolna, J.; Zaleska-Medynska, A. Shape-Controllable Synthesis of GdVO4 Photocatalysts and Their Tunable Properties in Photocatalytic Hydrogen Generation. *Dalton Trans.* **2019**, *48*, 1662–1671. [CrossRef]
20. Chen, L.; Shen, L.; Nie, P.; Zhang, X.; Li, H. Facile Hydrothermal Synthesis of Single Crystalline $TiOF_2$ Nanocubes and Their Phase Transitions to TiO_2 Hollow Nanocages as Anode Materials for Lithium-Ion Battery. *Electrochim Acta* **2012**, *62*, 408–415. [CrossRef]
21. Wen, C.Z.; Zhou, J.Z.; Jiang, H.B.; Hu, Q.H.; Qiao, S.Z.; Yang, H.G. Synthesis of Micro-Sized Titanium Dioxide Nanosheets Wholly Exposed with High-Energy {001} and {100} Facets. *Chem. Commun.* **2011**, *47*, 4400–4402. [CrossRef] [PubMed]
22. Ye, J.; Liu, W.; Cai, J.; Chen, S.; Zhao, X.; Zhou, H.; Qi, L. Nanoporous Anatase TiO_2 Mesocrystals: Additive-Free Synthesis, Remarkable Crystalline-Phase Stability, and Improved Lithium Insertion Behavior. *J. Am. Chem. Soc.* **2011**, *133*, 933–940. [CrossRef] [PubMed]
23. Wang, L.; Liu, J.; Min, Y.; Zhang, K. Nontopological Transformation of Hierarchical TiO_2 by Self-Regulated Etching and Capping Roles of F—For Photocatalytic H 2 Evolution. *Appl. Surf. Sci.* **2019**, *473*, 738–745. [CrossRef]
24. Gordon, T.R.; Cargnello, M.; Paik, T.; Mangolini, F.; Weber, R.T.; Fornasiero, P.; Murray, C.B. Nonaqueous Synthesis of TiO_2 Nanocrystals Using TiF4 to Engineer Morphology, Oxygen Vacancy Concentration, and Photocatalytic Activity. *J. Am. Chem. Soc.* **2012**, *134*, 6751–6761. [CrossRef] [PubMed]
25. Dudziak, S.; Kowalkińska, M.; Karczewski, J.; Pisarek, M.; Siuzdak, K.; Kubiak, A.; Siwińska-Ciesielczyk, K.; Zielińska-Jurek, A. Solvothermal Growth of {0 0 1} Exposed Anatase Nanosheets and Their Ability to Mineralize Organic Pollutants. The Effect of Alcohol Type and Content on the Nucleation and Growth of TiO_2 Nanostructures. *Appl. Surf. Sci.* **2021**, *563*, 150360. [CrossRef]

26. Kumar, M.M.; Badrinarayanan, S.; Sastry, M. Nanocrystalline TiO_2 Studied by Optical, FTIR and X-Ray Photoelectron Spectroscopy: Correlation to Presence of Surface States. *Thin Solid Film.* **2000**, *358*, 122–130. [CrossRef]
27. Xie, S.; Han, X.; Kuang, Q.; Fu, J.; Zhang, L.; Xie, Z.; Zheng, L. Solid State Precursor Strategy for Synthesizing Hollow TiO_2 Boxes with a High Percentage of Reactive {001} Facets Exposed. *Chem. Commun.* **2011**, *47*, 6722–6724. [CrossRef]
28. Okamoto, H. O-Ti (Oxygen-Titanium). *J. Phase Equilibria Diffus* **2011**, *32*, 473–474. [CrossRef]
29. Song, G.; Gao, R.; Zhao, Z.; Zhang, Y.; Tan, H.; Li, H.; Wang, D.; Sun, Z.; Feng, M. High-Spin State Fe(III) Doped TiO_2 for Electrocatalytic Nitrogen Fixation Induced by Surface F Modification. *Appl. Catal. B* **2022**, *301*. [CrossRef]
30. Sulowska, A.; Fiszka Borzyszkowska, A.; Cysewska, K.; Siwińska-Ciesielczyk, K.; Nikiforow, K.; Trykowski, G.; Zielińska-Jurek, A. The Effect of PEDOT Morphology on Hexavalent Chromium Reduction over 2D TiO_2/PEDOT Photocatalyst under UV–Vis Light. *Mater. Chem. Phys.* **2023**, 127430. [CrossRef]
31. Zheng, Y.; Wang, J.; Yang, P. Anatase TiO_2 Nanosheets Exposed {001} Facet: Solvent Effects on the Photocatalytic Performance. *J. Nanosci. Nanotechnol.* **2017**, *17*, 1204–1209. [CrossRef] [PubMed]
32. Li, J.; Yu, Y.; Chen, Q.; Li, J.; Xu, D. Controllable Synthesis of TiO_2 Single Crystals with Tunable Shapes Using Ammonium-Exchanged Titanate Nanowires as Precursors. *Cryst. Growth Des.* **2010**, *10*, 2111–2115. [CrossRef]
33. Xia, P.; Li, G.; Li, X.; Yuan, S.; Wang, K.; Huang, D.; Ji, Y.; Dong, Y.; Wu, X.; Zhu, L.; et al. Synthesis of G-C3N4 from Various Precursors for Photocatalytic H2 Evolution under the Visible Light. *Crystals* **2022**, *12*, 1719. [CrossRef]

4.4. Chapter IV: {0 0 1} TiO_2 coupled with $TiOF_2$ for photocatalytic degradation of contaminants of emerging concern – Insight into charge carrier dynamics and generation of ·OH radicals

Based on **[P5]** M. Kowalkińska, N. Keller, F. Fresno, C. Colbeau-Justin, A. Zielińska-Jurek, *Insight into charge carrier dynamics and interface design of {0 0 1} TiO_2 coupled with $TiOF_2$ for photocatalytic degradation of contaminants of emerging concern*, Applied Surface Science, 695, 2025, 162893.

Anatase TiO_2 nanocrystals with exposed {0 0 1} crystal facets have received significant research attention due to remarkably higher surface energy than other low-index facets, resulting in high reactivity. These facets can be synthesized mainly in a fluorine-rich environment [88,126]. This unique feature was beneficial for several photocatalytic reactions [127,128]. However, our previous studies revealed a low TOC conversion of aromatic compounds when {0 0 1} TiO_2 was used as a photocatalyst [129, 130]. Meanwhile, this parameter is important for CECs removal because it ensures that the initial substrate and any by-products formed during the process have been degraded.

The main motivation to conduct these studies was to find a one-step facile procedure to improve the TOC removal of {0 0 1} TiO_2, excluding co-catalyst deposition or interface modification with an external compound. In this regard, {0 0 1} TiO_2/$TiOF_2$ heterojunction photocatalysts with broad $TiOF_2$ content were proposed, because $TiOF_2$ phase can be easily achieved in a fluorine-rich environment as well. The synthesis of {0 0 1} TiO_2/$TiOF_2$ with adjustable $TiOF_2$ content has not been proposed in the literature yet. These binary photocatalysts were investigated toward photocatalytic degradation of 4-chlorophenol (4CP), myclobutanil (MCL) and carbamazepine (CBZ) under UV-A and simulated solar light. The study also aimed to clarify the role of $TiOF_2$ in the heterojunction.

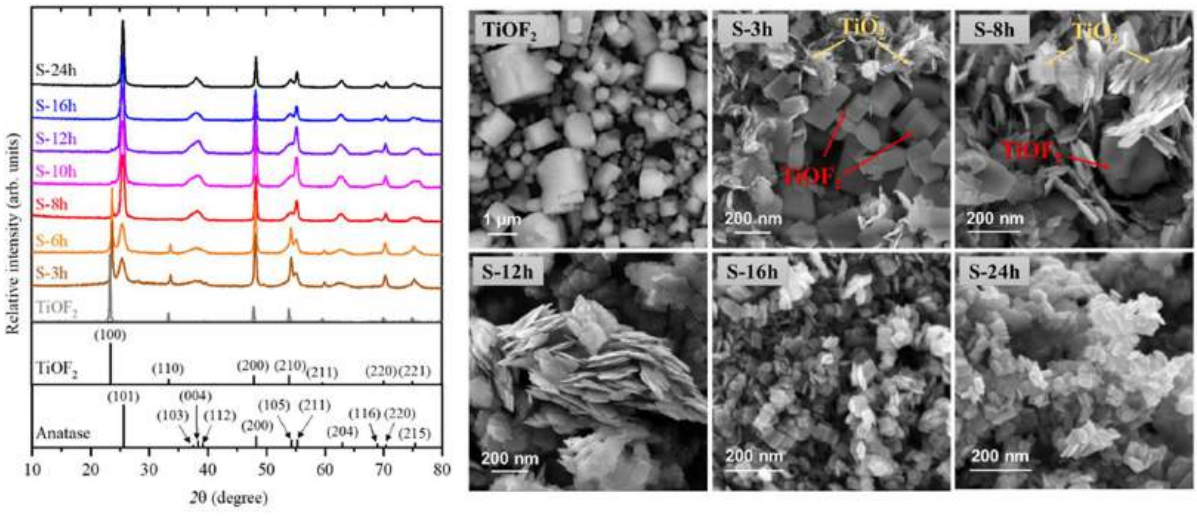

Figure 4.8. a) XRD pattern and **b)** SEM images of {0 0 1} TiO_2/$TiOF_2$ samples.

Experimental studies showed that introducing a small amount of $TiOF_2$ (1.5–6%) into {0 0 1} TiO_2 remarkably increased photocatalytic •OH radical generation and in consequence, degradation rates and TOC conversion for all investigated CECs compared to pristine {0 0 1} TiO_2.

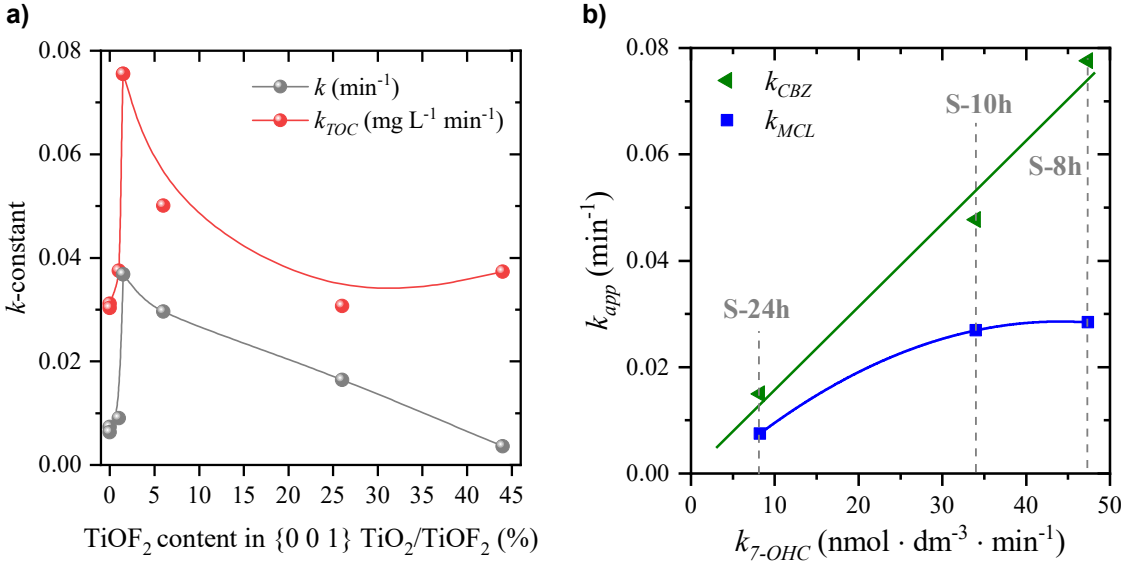

Figure 4.9. The relationships between the apparent kinetic rate constants of **a)** 4CP degradation and the $TiOF_2$ content, **b)** CBZ and MCL degradation and the 7-OHC production.

This enhancement was linked to the improved interfacial charge carriers separation and a high number of charge carriers available for initiating redox reactions, supported by TRMC and fluorescence lifetime spectroscopy (Figure 4.10). Moreover, DFT calculations revealed high potential barriers within $TiOF_2$ structure, explaining the optimum at a low level of $TiOF_2$ amount.

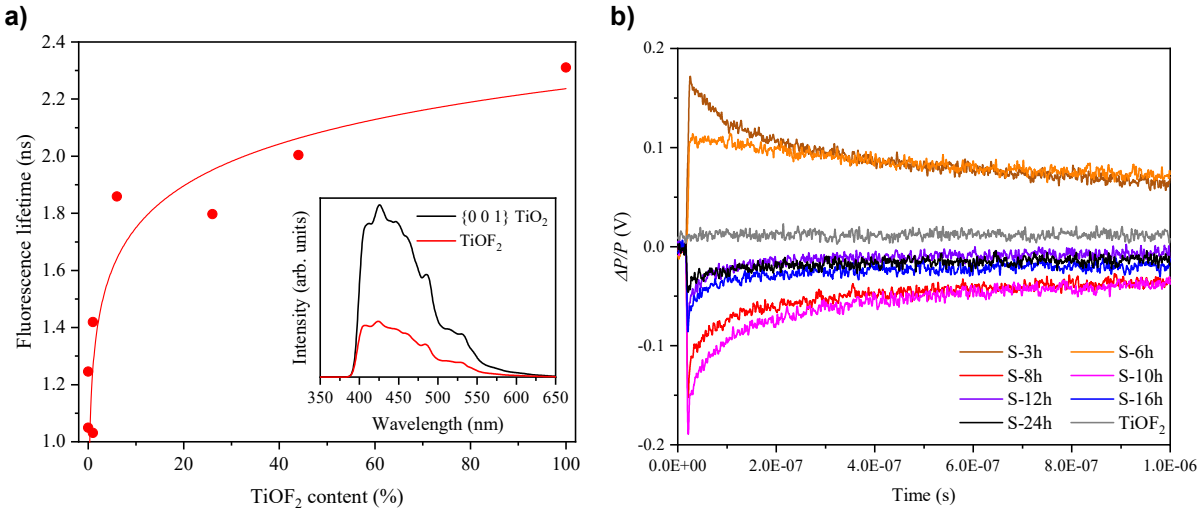

Figure 4.10. a) The relationship between fluorescence lifetime of different {0 0 1} TiO_2/$TiOF_2$ samples and $TiOF_2$ phase content; Inset shows the PL spectra of single-component materials, and **b)** TRMC signal after excitation for pure {0 0 1} anatase, $TiOF_2$ and {0 0 1} TiO_2/$TiOF_2$ photocatalysts.

Applied Surface Science 695 (2025) 162893

Contents lists available at ScienceDirect

Applied Surface Science

journal homepage: www.elsevier.com/locate/apsusc

Full Length Article

Insight into charge carrier dynamics and interface design of {0 0 1} TiO_2 coupled with $TiOF_2$ for photocatalytic degradation of contaminants of emerging concern

Marta Kowalkińska [a,*], Nicolas Keller [b], Fernando Fresno [c], Christophe Colbeau-Justin [d], Anna Zielińska-Jurek [a,*]

[a] Department of Process Engineering and Chemical Technology, Faculty of Chemistry, Gdansk University of Technology, 80-233 Gdansk, Poland
[b] Institut de Chimie et Procédés pour l'Energie, l'Environnement et la Santé (ICPEES) CNRS/University of Strasbourg, 25 rue Becquerel, 67087 Strasbourg, France
[c] Instituto de Catálisis y Petroleoquímica (ICP), CSIC, Marie Curie 2, 28049 Madrid, Spain
[d] ICP, Institut de Chimie Physique, CNRS UMR 8000, Université Paris-Saclay, Bâtiment 349, CEDEX, 91405 Orsay, France

ARTICLE INFO

Keywords:
TiO_2/$TiOF_2$
Titanium oxyfluoride
Hydroxyl radicals generation
Photocatalyst
TRMC

ABSTRACT

Herein, the role of titanium oxyfluoride ($TiOF_2$) on the charge carriers generation and electron transport in the {0 0 1} TiO_2/$TiOF_2$ heterojunction photocatalysts was examined. Time-resolved microwave conductivity (TRMC), fluorescence lifetime spectroscopy, and DFT calculations were applied to investigate the charge carriers dynamics. These binary photocatalysts in a broad $TiOF_2$ content were further studied in photocatalytic generation of hydroxyl radicals (•OH) and degradation of several organic contaminants of emerging concern (CECs), namely 4-chlorophenol (4CP), myclobutanil (MCL) and carbamazepine (CBZ). Regardless of the CEC tested, it was found that the combination of highly-energetic {0 0 1} TiO_2 with $TiOF_2$ phase improved the photocatalytic activity compared to the pristine anatase. The presence of the $TiOF_2$ phase in the heterojunction increased the interfacial charge carriers separation and enhanced the generation of •OH radicals. Maximised photocatalytic activity and TOC reduction were observed for composites with a $TiOF_2$ content of 1.5 %–6 %, which exhibited the highest number of photogenerated charge carriers and a longer lifetime compared to those with higher $TiOF_2$ content. DFT calculations revealed high potential barriers within the $TiOF_2$ structure, which explains the optimum at a low level of $TiOF_2$ amount. Finally, high photocatalytic activity was maintained in five consecutive degradation cycles.

1. Introduction

Nowadays, with progressive industrialisation, the amount of pollutants in ground and surface water is growing. According to the European Environmental Agency (EEA) report, between 2000 and 2017, the total number of synthetic chemicals in the market was estimated at 100,000 compounds, excluding transformation products from chemicals during their life cycles [1]. Some of the commonly used cosmetic ingredients, pigments, pesticides and medicines are persistent in the environment. This leads to ongoing exposure to chemical pollution and limitation of available drinking water, which negatively affects human health and the environment. Therefore, further advances in the deployment of eco-innovations are crucial for reaching effective wastewater treatment and consequently avoiding bioaccumulation and biomagnification of contaminants of emerging concern (CECs) in the environment.

One of the promising methods that are capable of removing persistent organic pollutants and that is classified as green technology is heterogeneous photocatalysis, in which charge carriers photogenerated upon the irradiation of a semiconductor material participate in the degradation of a wide span of CECs such as e.g. phenolic compounds, pesticides and pharmaceuticals [2–4]. One of the most studied semiconductors is TiO_2, which has been widely investigated for photocatalytic water treatment due to suitable conduction and valence band edges as well as superior photostability [5,6]. Among many efforts to improve the photocatalytic performance of TiO_2, the shape-controlled strategies have been the focus of much effort to obtain highly energetic surfaces as the photocatalytic activity critically depends on the

* Corresponding authors.
E-mail addresses: marta.kowalkinska@pg.edu.pl (M. Kowalkińska), annjurek@pg.edu.pl (A. Zielińska-Jurek).

https://doi.org/10.1016/j.apsusc.2025.162893
Received 29 November 2024; Received in revised form 15 February 2025; Accepted 4 March 2025
Available online 5 March 2025

crystal facets exposition [7–9]. Recently, anatase {0 0 1} crystal facets have been extensively studied since the research presented by Yang et al. proved that these facets, despite high surface energy, could be stabilized by F^- ions and formed instead of the thermodynamically stable {1 0 1} facets [10]. TiO_2 exposing a majority of {0 0 1} facets became prominent because it contains the high density of active unsaturated Ti atoms and active surface oxygen atoms, which renders numerous active sites and strong interactions with the adsorbates during the photocatalytic redox reactions [11,12]. However, our recent studies showed that anatase {0 0 1} nanosheets exhibited a low mineralisation rate of aromatic compounds, which is an important factor for CECs removal because high total organic carbon (TOC) reduction yield in the presence of the photocatalyst ensures that the substrate and any intermediate products formed during the process have been degraded [13,14].

In fluorine-rich environments during the solvothermal reaction of a Ti source, titanium oxyfluoride ($TiOF_2$), a wide bandgap semiconductor (~3.2 eV) with cubic structure, can also be formed next to anatase [15,16]. Due to the strong bonding energy of Ti—F, $TiOF_2$ is supposed to be stable at ambient conditions [17]. However, pristine $TiOF_2$ suffers from low photocatalytic activity [14,18,19], so practical applications for this material have been scarcely explored. The majority of the studies regarding titanium oxyfluoride includes phase conversion to anatase *via* calcination [16,18,20] or hydrothermal route [14,21]. The application of $TiOF_2$ in the heterojunction-based photocatalysts has not been studied yet and only a few recent studies have been reported, e.g. $TiOF_2$/g-C_3N_4 [22], Ag_3PO_4/$TiOF_2$ [23] and $TiOF_2$@$Ti_3C_2T_x$ [24]. Therefore, coupling $TiOF_2$ with facet-regulated {0 0 1} anatase may be a perfect solution for enhancing photocatalytic performance and inducing TOC reduction of aromatic pollutants, which is a serious limitation for these facets exposition. Two strong advantages support this combination: first, the comparable atomic density of states and electron binding energy between TiO_2 and $TiOF_2$ crystals lead to excellent interfacial alignment, facilitating efficient migration and separation of photogenerated electron-hole pairs [18,25]. Remarkably, the formation of {0 0 1} TiO_2/$TiOF_2$ can be performed *via* a one-step facile procedure, excluding co-catalyst deposition or interface modification with an external compound. Nevertheless, many aspects of $TiOF_2$-based photocatalysts remain unexplored, including the synthesis procedure for TiO_2/$TiOF_2$ with a controllable $TiOF_2$ content, the role of the $TiOF_2$ phase and the understanding of the photocatalytic activity enhancement [26].

Therefore, this study aims to demonstrate the promise of coupling highly energetic {0 0 1} anatase crystal facets with controlled amounts of $TiOF_2$ for the photocatalytic degradation of CECs in water under UV-A and simulated solar light. The synthesis of a span of {0 0 1} TiO_2/$TiOF_2$ binary photocatalysts in various $TiOF_2$ contents was performed under pronounced steric hindrance conditions, in order to study the mechanism of $TiOF_2$ formation. The activity of these binary photocatalysts was assessed in the degradation and mineralisation of several persistent organic pollutants aiming to expand the scope of the study, namely 4-chlorophenol (4CP), carbamazepine (CBZ) and myclobutanil (MCL). 4CP is a compound widely used in the textile industry, whereas the anticonvulsant drug CBZ has been proposed as an anthropogenic marker of water quality [27–29]. The degradation of the triazole pesticide MCL has been still rarely reported in the literature compared to that of other organic pollutants so this compound was also selected for investigation [30]. Moreover, the photocatalytic generation of hydroxyl radicals (•OH) was monitored and discussed. The behaviour of the photogenerated charge carriers and the electronic structure of {0 0 1} TiO_2/$TiOF_2$ were extensively studied by fluorescence lifetime measurements, time-resolved microwave conductivity (TRMC) analysis and density functional theory (DFT) calculations. Finally, reusability tests were performed for the most efficient photocatalyst.

2. Results and discussion

The synthesis protocol and characterisation methods applied in this work can be found in Supplementary Materials.

2.1. Material characterisation

Two distinct phases, namely anatase TiO_2 (reference ICDD no. 01-070-8505) and titanium oxyfluoride $TiOF_2$ (no. 01-077-0132), were noticed in the photocatalysts, as presented in Fig. 1a. No additional peaks corresponding to other compounds were detected. The detailed structural parameters of the photocatalyst series are presented in Table 1. Based on the XRD analysis, the predominant role of the synthesis time was confirmed. With the increasing time of solvothermal synthesis, the content of anatase rises and the (101) peak at $2\theta = 25.5°$ becomes more distinct. Simultaneously, the content of titanium oxyfluoride decreased with increasing the reaction time. This can be explained by the progressive transformation of $TiOF_2$ into TiO_2. For samples synthesised over times exceeding 16 h, *ie.* S-16 h and S-24 h, the main (100) peak at $2\theta = 23.7°$ related to $TiOF_2$ has completely vanished, and only pure anatase can be observed.

In addition to the phase composition, the synthesis time mainly influences three structural parameters, namely the mean anatase crystallite size, the amorphous phase content and the specific surface area. The relationship between these parameters and the time of solvothermal synthesis is presented in Fig. S1 in Supplementary Materials. Globally, the longer the synthesis time, the larger the mean anatase crystallite size, so pure anatase samples (S-16 h and S-24 h) exhibit larger mean crystallite sizes than the binary TiO_2/$TiOF_2$ samples. Also, the amorphous phase content increased during the first few hours of the solvothermal reaction, reaching a maximum content for 6 h of synthesis, before dropping down to reach a minimum value for S-24 h when decreasing the $TiOF_2$ content. This effect can be explained by the fact that freshly synthesised TiO_2 is not fully crystallised and contains a high fraction of the amorphous phase. During the solvothermal reaction, progressive crystallisation of the anatase structure occurs, resulting in the decrease of the amorphous phase contribution. Additionally, the specific surface area of the samples followed a volcano-like trend within the 80–100 m^2/g range with the increase in the synthesis time, the highest values being for S-8 h and S-10 h. Those features correlate well with the simultaneous occurrence of both $TiOF_2 \rightarrow TiO_2$ phase transformation and the progressive crystallisation process of the pure anatase phase. By contrast, a low specific surface area of 5 m^2/g was observed for pure $TiOF_2$.

Fig. 1b compares the FTIR spectra of $TiOF_2$, {0 0 1} TiO_2 and {0 0 1} TiO_2/$TiOF_2$ with different phase compositions. The stretching and bending vibrations due to adsorption of H_2O and the Ti—OH groups are found at 3100–3600 cm^{-1} and 1630 cm^{-1}, respectively [5]. Bands located at 539 cm^{-1} and 455 cm^{-1} can be attributed to Ti—O or Ti—O—Ti vibrations. Strong absorption peaks centered at 992 cm^{-1} are ascribed to Ti—F bonds [31]. Remarkably, the intensity of this band is dependent on the $TiOF_2$ content – for pristine titanium oxyfluoride it is the most distinct and decreases with increasing anatase content. Finally, for samples prepared with a solvothermal synthesis time exceeding 8 h, this band cannot be distinguished. This observation can be strictly correlated with the progressive tranformation from $TiOF_2$ to TiO_2.

SEM images in Fig. 2a revealed that the pristine $TiOF_2$ titanium oxyfluoride phase consists of irregular cubes. With increasing the synthesis time, the formation of two-dimensional anatase nanoparticles is observed, which resulted from the presence of F^- ions during the solvothermal synthesis. These ions stabilise the highly energetic {0 0 1} facets and promote growth in the *hk* direction [13,32]. However, differences between the anatase nanosheets can be noted, as binary

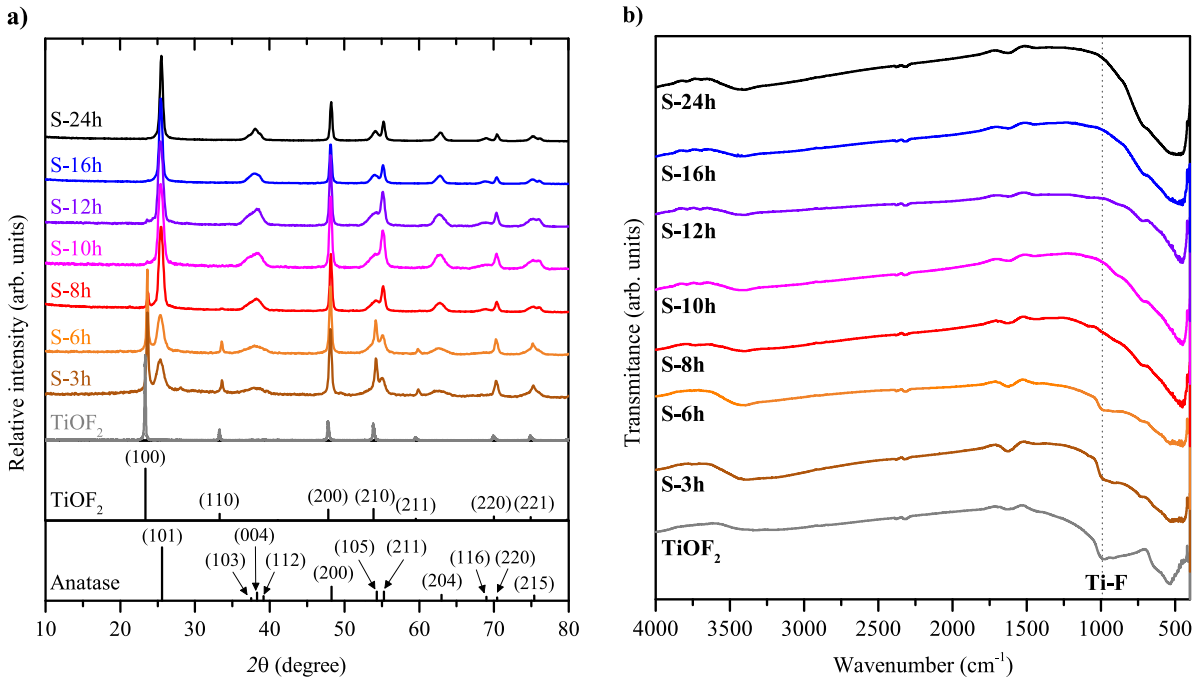

Fig. 1. a) XRD patterns and b) FTIR spectra of the {0 0 1} TiO_2/$TiOF_2$ series samples.

Table 1
Characterisation of the photocatalysts using XRD, BET and XPS analyses.

Sample name	Phase composition (%)		Mean anatase crystallite size (nm) *	Amorphous phase content (%)	Surface area (m^2/g)	Surface Ti/F ratio
	TiO_2	$TiOF_2$				
$TiOF_2$	-	100	43	-	5	0.5
S-3h	56	44	8	42	79	1.1
S-6h	74	26	9	60	78	1.2
S-8h	94	6	13	54	99	2.5
S-10h	98.5	1.5	11	54	102	3.7
S-12h	>99	<1	12	47	82	n.c.
S-16h	100	-	17	36	84	n.c.
S-24h	100	-	19	21	78	4.9

*For TiO_2-containing samples, the mean anatase crystallite size was calculated based on the (101) peak. For $TiOF_2$, the mean crystallite size was calculated based on the (100) peak. The mean crystallite size for anatase, defined as the average size of the coherent diffracting domains, remains an estimate as it was determined from the Scherrer equation with the usual assumption of spherical crystallites.
n.c.: non calculated.

samples S-3 h, S-8 h and S-12 h displayed thicker and wider TiO_2 nanostructures than in the single-phase counterpart (sample S-24 h). In the {0 0 1} TiO_2/$TiOF_2$ samples S-3 h, S-8 h and S-12 h, the irregular cubes assigned to the $TiOF_2$ titanium oxyfluoride phase displayed a larger size than the thick nanosheets. These bulk particles were not noticed in the S-12 h sample, as the $TiOF_2$ content remains by far much lower (<1 %) than for samples synthesised with shorter reaction times.

The synthesis time had an impact either on the TiO_2 content or on the morphology changes. Based on SEM and XRD results, the {0 0 1} TiO_2/$TiOF_2$ formation under solvothermal conditions with n-hexanol as a solvent and its transformation to pure anatase is proposed to rely on the following mechanism (Eqs. 1–3) [15,33,34]:

$$2\ \text{R-OH} \rightarrow \text{R-O-R} + H_2O, \quad (1)$$

$$(\text{R-O})_n TiF_{4-n} + n\ H_2O \rightarrow TiOF_2 + n\ \text{R-OH} + n\ \text{HF}, \quad (2)$$

$$TiOF_2 + H_2O \rightarrow TiO_2 + 2\ \text{HF}. \quad (3)$$

Generally, in the presence of alcohols and HF, the Ti precursor undergoes alcoholysis and forms $(\text{R-O})_n TiF_{4-n}$ complex. However, for further transformation to titanium oxyfluoride Eq. (2), H_2O molecules are needed, which amount is limited in solvothermal conditions. Therefore, alcohol condensation Eq. (1) is probably due to high temperature and increased pressure. The nucleation is slow due to the use of long-chain alcohol as a solvent and, in consequence, steric hindrance [13]. H_2O also participates in the hydrolysis of $TiOF_2$ to anatase Eq. (3). However, it is well-known that the subsequent {0 0 1} TiO_2 growth is a result of HF-mediated dissolution-recrystallisation processes, in which the Ti species are reversibly transferred between its solid oxide form and dissolved ion, preferably coordinated with 6 ligands in the form of bipyramid. In addition, an alcohol exchange with halide ligands is possible under solvothermal conditions [20,35]. The scheme of these transformations is presented in Fig. 2b. The more dissolution-recrystallisation processes occur, the more stable and defect-free TiO_2 structure is formed, which explains the relatively low amorphous phase content in the S-24 h sample. Finally, longer durations of solvothermal synthesis provide more H_2O to the reaction environment so that when the Ti precursor is fully transformed to anatase, this new structure is surrounded by F^- ions and water molecules. While the {0 0 1} facets can be stabilised mainly by fluoride ions, H_2O can promote the formation of low-energetic crystal facets like {1 0 0} [36]. This is a probable reason for the formation of wider nanosheets in the pure anatase S-24 h sample compared to the binary photocatalysts. The proposed mechanism of the

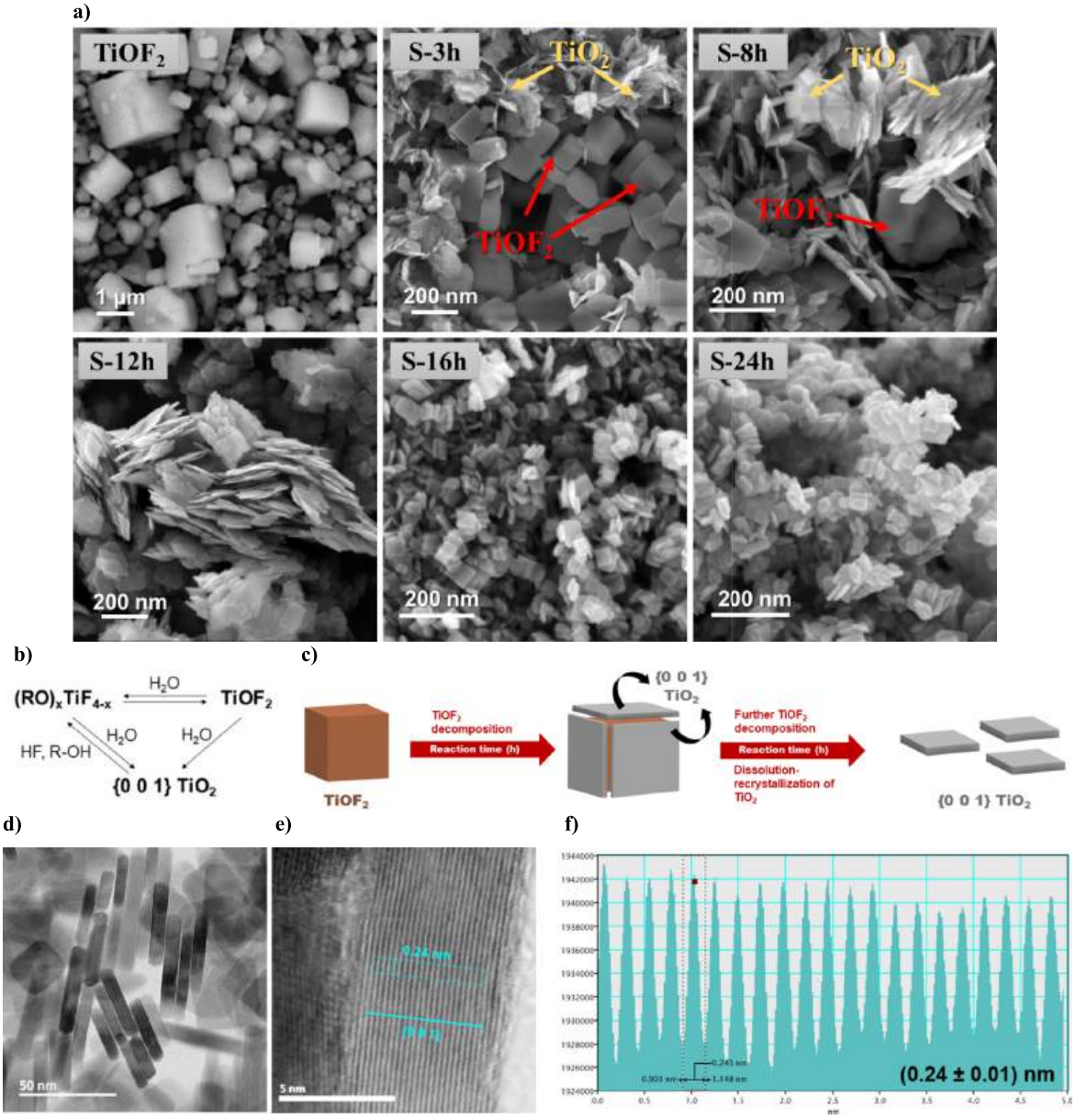

Fig. 2. a) SEM images of the $TiO_2/TiOF_2$ series samples, for samples S-3 h and S-8 h, $TiOF_2$ and anatase TiO_2 phases are marked with red and yellow arrows, respectively. b) Transformation of Ti species under solvothermal conditions and c) proposed mechanism of the morphology transformation from $TiOF_2$ cubes to {0 0 1} TiO_2. d) TEM and e) HRTEM image of the {0 0 1} TiO_2 (sample S-16 h) in bright-field mode, f) line profile image.

morphological changes is schematically presented in Fig. 2c.

The formation of {0 0 1} facets in anatase nanosheets was confirmed by transmission electron microscopy (TEM). The TEM images of S-16 h presented in Fig. 2d revealed a well-defined sheet-shaped structure. As shown in HRTEM images (Fig. 2e) and corresponding line profile image (Fig. 2f), the lattice spacing parallel to the front of the nanosheets was calculated to be ~0.24 nm, which is a direct confirmation that the exposed top and bottom facets belong to {0 0 1}, because these planes are arranged to [0 0 1] direction [37].

DRS analysis performed on the $TiO_2/TiOF_2$ series within the 200–800 nm range (Fig. 3a) exhibited the absorption band and edge characteristic for both anatase and titanium oxyfluoride phases [14,38]. Pure $TiOF_2$ is grey with a small band above 380 nm, which further vanishes during TiO_2 formation. The derived Tauc plot evidenced that the bandgap energy of the samples was not significantly influenced by the phase composition and the morphology changes (Fig. S2 in Supplementary Materials).

Furthermore, ζ potential as a function of pH was studied to investigate the interaction between the photocatalyst surface and the pollutant. Based on the zeta potential analysis presented in Fig. S3 in Supplementary Materials, the isoelectric point (IEP), which is defined as the pH where the electrophoretic mobility changes from positive to negative, was determined. For the samples S-24 h (pure anatase) and S-10 h ($TiO_2/TiOF_2$), the IEP values were 5.7 and 5.5, respectively. Compared to the literature value of the isoelectric point for TiO_2 (6.2) [39,40], a slight shift towards acidic conditions can be observed. This effect can be explained by differences in the surface atom arrangement due to the exposition of {0 0 1} facets stabilised by fluorine ions. The presence of F^- and the unique morphology obtained influence the rates of surface hydroxylation and protonation compared to bulk TiO_2 [41]. Moreover, $IEP_{S\text{-}10h}$ is slightly lower than $IEP_{S\text{-}24h}$, which is probably a result of the presence of the titanium oxyfluoride phase in the photocatalyst, which causes different electronic distribution on the surface compared to pure {0 0 1} anatase nanocrystals.

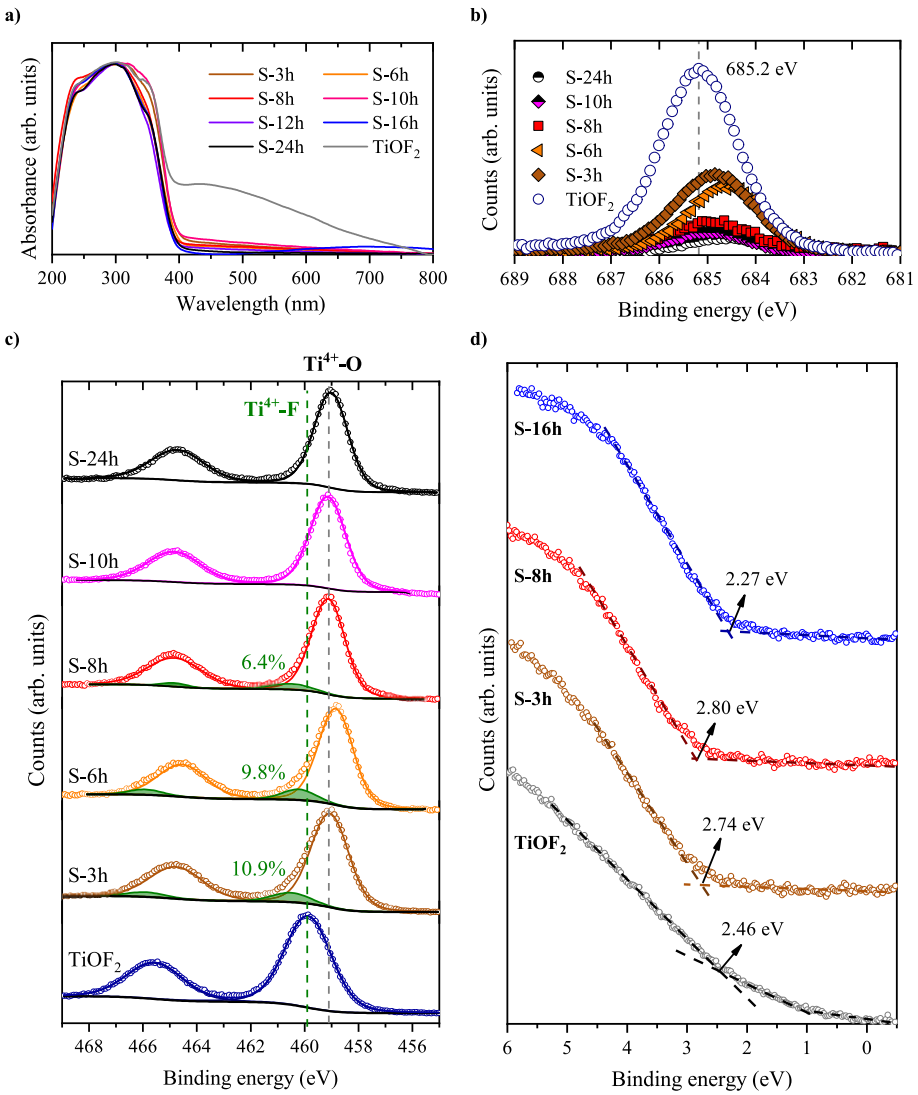

Fig. 3. a) DR/UV–vis absorption spectra of the photocatalysts, b) F1s and c) Ti2p orbital XPS spectra recorded on selected samples from the $TiO_2/TiOF_2$ series, d) VB-XPS spectra of selected photocatalysts.

The photocatalyst surface was also studied using X-ray photoelectron spectroscopy (XPS). The XPS spectra at F1s and Ti2p core orbital regions recorded on the binary $TiO_2/TiOF_2$ samples with different $TiOF_2$ contents and both pure $TiOF_2$ and anatase (S-24 h) samples are depicted in Fig. 3a-b. The survey scans of all the samples are shown in Fig. S4 in Supplementary Materials. The spectra recorded on the pure titanium oxyfluoride material showed a characteristic symmetrical contribution at 685.2 eV ascribed to F^- ions (F1s orbital), and a well-defined Ti^{4+} Ti $2p_{3/2}$-Ti $2p_{1/2}$ doublet at 459.9 eV and 465.6 eV with a spin–orbit coupling constant of 5.7 eV (Ti2p orbital) [13,15]. The bulk transformation of the $TiOF_2$ phase into TiO_2 with increasing the synthesis duration is accompanied by a surface change, and the Ti2p orbital spectra recorded on binary $TiO_2/TiOF_2$ samples were characterised by the presence of two well-defined Ti^{4+} doublets, with the contribution of Ti^{4+}—O bonds at ca. 459.1 eV and 464.8 eV, and an additional doublet at higher binding energy assigned to Ti—F bonds. Contrary to the bulk ratio, the Ti^{4+}—O contribution was dominant over its Ti—F counterpart already for the short synthesis duration of 3 h. Thereby the contribution of the Ti—F species was not evidenced for synthesis durations exceeding 6 h, while simultaneously the F1s orbital signal decreased significantly when increasing the TiO_2 content with increasing the synthesis duration. Consequently, the Ti/F surface atomic ratio increased strongly with the increase in the TiO_2 content (Table 1). With the electrostatic model of chemical shifts in XPS, the higher binding energy of the Ti-F bond contribution compared to that of Ti^{4+}—O results from the higher electronegativity of fluoride *vs.* oxygen. This was also observed by Jain et al. [42], who studied the surface chemical state of TiF_4. Similar F-induced chemical shifts were observed for a span of elements [43]. However, F atoms are randomly distributed in the titanium oxyfluoride structure [44], which makes it impossible to distinguish between Ti—F and Ti—O bonds in the Ti 2p XPS spectra of pure $TiOF_2$.

Valence-band XPS spectra (VB-XPS) presented in Fig. 3d revealed the position of the valence band relative to the Fermi level. The VB edges values for pristine $TiOF_2$, {0 0 1} TiO_2 (S-16 h), S-3 h and S-8 h were 2.46 eV, 2.27 eV, 2.74 eV and 2.80 eV, respectively. S-3 h and S-8 h samples, which correspond to {0 0 1} $TiO_2/TiOF_2$ photocatalysts, exhibit a shift toward higher binding energies compared to pure compounds, which can be attributed to the modulation of Fermi level in the heterojunction.

2.2. *Photocatalytic degradation of contaminants of emerging concern*

The photocatalytic activity of the samples was studied in the degradation of organic pollutants classified as contaminants of emerging concern and differing strongly in terms of chemical functions. Firstly, the degradation of 4-chlorophenol (4CP) under UV-A light was studied.

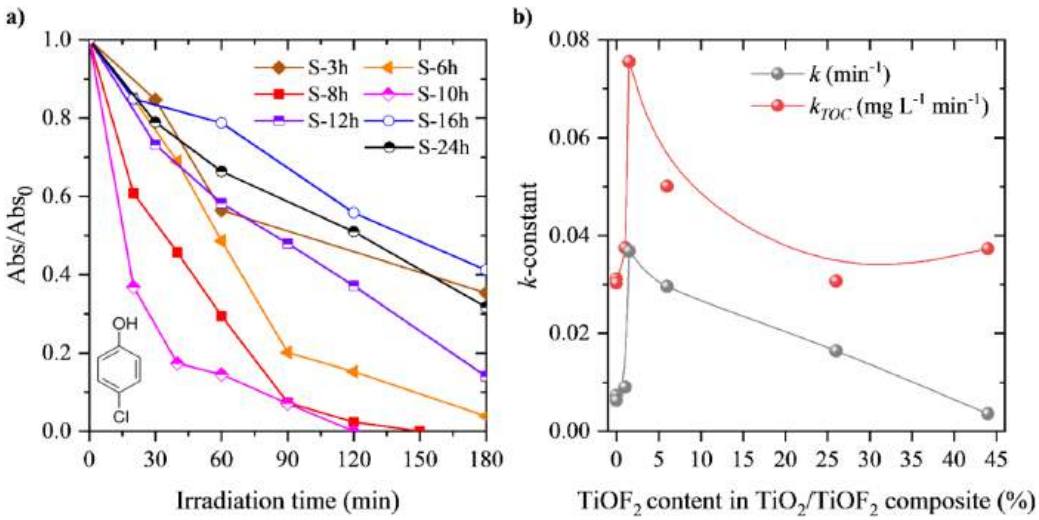

Fig. 4. a) Photocatalytic degradation of 4CP under UV-A light over $TiO_2/TiOF_2$ series, b) relationship between the *k*-constants and the $TiOF_2$ content. Process parameters: $[4CP]_0 = 20$ ppm, [cat] = 1 g/dm^3.

As presented in Fig. S5 in Supplementary Materials, pristine $TiOF_2$ revealed low photocatalytic activity, whereas Fig. 4a and Fig. S6 show that all the samples containing {0 0 1} anatase TiO_2 in the series could degrade and mineralise 4CP. The least efficient samples were S-16 h and S-24 h, which are composed of pure {0 0 1} anatase phase. Both degradation and mineralisation kinetics were accelerated when the $TiOF_2$ phase was present in the photocatalyst structure. The relationship between the $TiOF_2$ content in the heterojunction-based photocatalyst and both apparent kinetic rate constants for degradation and mineralisation evidenced a volcano-type behavior with increasing the $TiOF_2$ content (Fig. 4b). The highest apparent kinetic constants for both 4CP degradation and TOC reduction were achieved for the sample S-10 h, namely the heterojunction with a low and optimal $TiOF_2$ content of about 1.5 %. We observed that a too high titanium oxyfluoride content inhibited the photocatalytic degradation of the organic pollutant.

Based on the results of 4CP degradation, the photocatalytic activity of the samples was assessed in the degradation of CECs with more complex molecular structures, namely myclobutanil and carbamazepine. Fig. 5 depicts the evolution of the relative concentration of both pollutants for reactions conducted under pure UV-A light or simulated

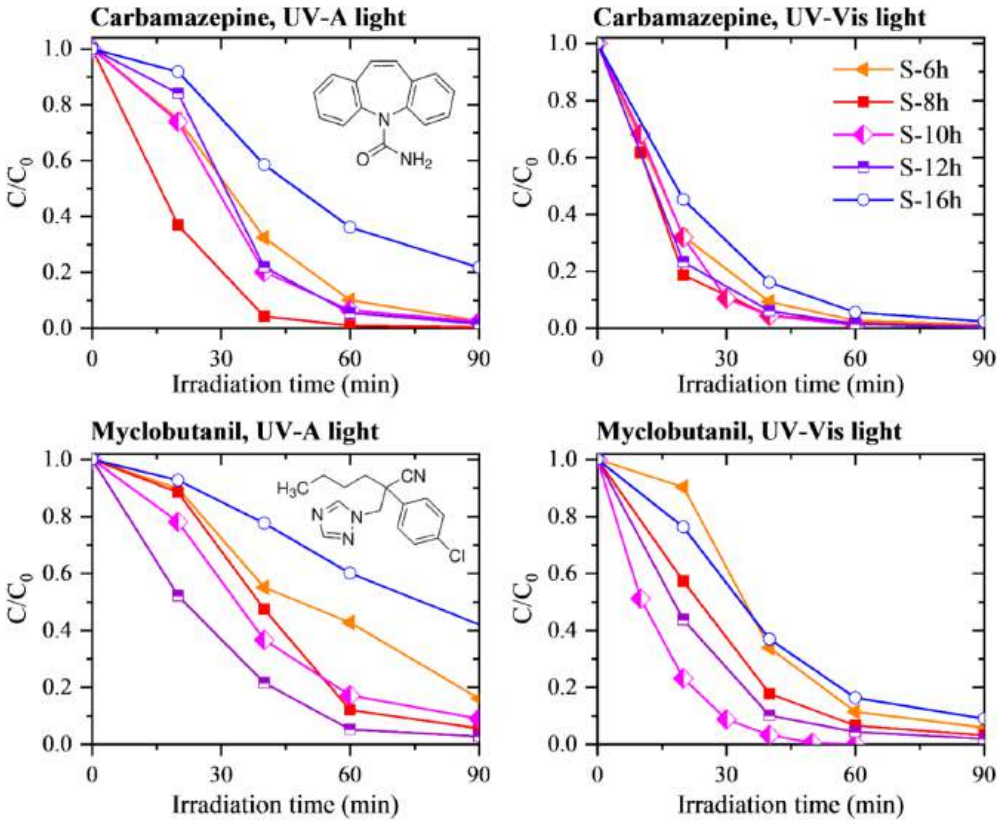

Fig. 5. Photodegradation of MCL and CBZ under UV–Vis and UV-A light using {0 0 1} TiO_2 and {0 0 1} $TiO_2/TiOF_2$. Conditions: $[CBZ]_0 = 14$ ppm, $[MCL]_0 = 20$ ppm, [cat] = 1.0 g/dm^3.

solar light, and the apparent kinetic rate constants for degradation are presented in Table S1 in Supplementary Materials. HPLC chromatograms of CBZ and MCL are shown in Fig. S7. Photolysis in the absence of photocatalysts and the linear plots of $\ln(C_0/C)$ *vs.* irradiation time are shown in Fig. S8. Pure {0 0 1} anatase samples (S-16 h and S-24 h) exhibited lower apparent kinetics than the heterojunction-based photocatalysts independently of the light source. The TOC reduction after 2 h of reaction is presented in Fig. 6. Similarly to the results with 4CP, the highest mineralisation efficiency was observed for samples with a very low $TiOF_2$ content. In the case of MCL and CBZ solutions, this corresponded to S-8 h and S-10 h samples that have a $TiOF_2$ content lower than 6 %. These samples exhibited excellent photocatalytic performance toward CECs oxidation, comparable or higher than the previous reports regarding CBZ and MCL removal (the comparison of apparent kinetic rate constants is presented in Table S2 in Supplementary Materials).

Although myclobutanil and carbamazepine are degraded, their interaction with the photocatalyst surface is different. The pH of the suspension before the photocatalytic MCL removal was 4.9. Herein, MCL occurs in the deprotonated form as pH > pKa (2.3) and therefore MCL is negatively charged in the degradation reaction conditions. The positively charged surface of the {0 0 1} $TiO_2/TiOF_2$ sample consequently favoured its interaction with the deprotonated form of the pesticide compound. After the photocatalytic process, the pH of the suspension slightly dropped down to 4.3, as a result of the release of acidic Cl^- ions during the MCL removal, which is consistent with IC chromatography analysis of the Cl^- ion concentration. By contrast, the CBZ molecule is neutral, as pH < pK_a (13.9), and therefore the electrostatic attraction with the photocatalyst surface is unlikely.

Based on Figs. 4-6, three samples – S-8 h, S-10 h and S-12 h – with a relatively low $TiOF_2$ content (below 6 %), can be distinguished as the most photocatalytically active binary systems with the highest kinetic rate constants, and for which the highest 4CP, MCL and CBZ removal, as well as the highest TOC reduction, were observed. Therefore, it can be assumed that the ability to create the $TiO_2/TiOF_2$ heterojunction is a predominant factor which affects the photocatalytic degradation of pollutants. The effect of surface fluorination also occurs, but based on our previous report [45], we can assume that the role of surface fluorination is relatively low compared to the formation of heterojunction.

However, these experiments showed that considering the degradation of MCL and CBZ, the apparent kinetic rate constant may not be correlated with the TOC reduction efficiency. For example, S-12 h exhibited *k*-constants comparable to those obtained with S-10 h and S-8 h, but the TOC conversion was significantly lower than with the aforementioned samples. This discrepancy was also observed in our previous studies about facet-engineered TiO_2 [14]. The probable reason is that the presence of titanium oxyfluoride influences the degradation pathway of the pollutant oxidation. Moreover, the interaction with the photocatalyst is different for particular CECs due to various pK_a values. Finally, the intermediate products formed during the degradation of the contaminant can have different adsorption features on the photocatalyst surface than the initial compound.

2.3. Hydroxyl radicals generation

The ability of the heterojunction photocatalysts to generate •OH radicals, which participate in the degradation and the mineralisation of the pollutant, was monitored using a coumarin fluorescence probe method. The more hydroxyl radicals are generated, the more 7-hydroxycoumarin (7-OHC) is formed by selective oxidation of the coumarin substrate. Fig. 7a shows the 7-OHC production under UV-A light obtained on selected photocatalysts, whereas the statistical analysis of coumarin fluorescence probe method is depicted in Fig. S9 in Supplementary Materials. A direct correlation is observed between the hydroxyl radicals formation (characterised by the formation of 7-OHC) and the degradation rate of CBZ and MCL, as shown in Fig. 7b. Indeed, the concentration of 7-OHC is significantly higher for the {0 0 1} $TiO_2/TiOF_2$ composites (S-8 h and S-10 h) than for pure anatase nanosheets (S-24 h). This indicates that the presence of the $TiOF_2$ phase helps in the separation of charge carriers and the enhancement of ROS generation. The high •OH generation yield obtained with the S-8 h sample is comparable to that shown by the Aeroxide© TiO_2 P25 (Degussa), as is presented in Fig. S10 in Supplementary Materials, which confirms the high photoactivity of the binary $TiO_2/TiOF_2$ photocatalysts.

Generation of •OH radicals is often the result of H_2O reaction with photogenerated holes [46,47]. Therefore, higher coumarin conversion to 7-OHC for {0 0 1} $TiO_2/TiOF_2$ can be explained by higher amount of charge carriers available to drive the reaction. This hypothesis was verified by the experiment of photocatalytic hexavalent chromium reduction, presented in Fig. S11 in Supplementary Materials. Similarly, the enhanced Cr(V) → Cr(III) conversion was observed for $TiO_2/TiOF_2$. Considering that electrons are responsible for reduction reactions, this suggests that the formation of heterojunction enhances the separation of electrons and holes.

2.4. The role of $TiOF_2$ – Charge carriers generation and separation, DFT calculations

Furthermore, to study the role of the $TiOF_2$ phase in the heterojunction at an atomic level, DFT calculations were performed. The optimised model of the (0 0 1) TiO_2/(1 0 0) $TiOF_2$ interface, along the

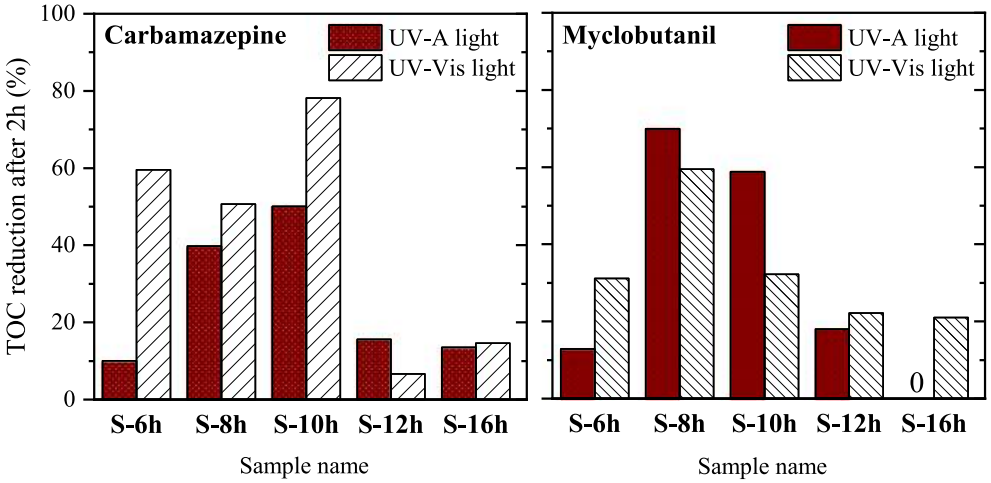

Fig. 6. TOC reduction achieved after 2 h of process under UV-A and UV–Vis light using {0 0 1} TiO_2 and {0 0 1} $TiO_2/TiOF_2$ photocatalysts.

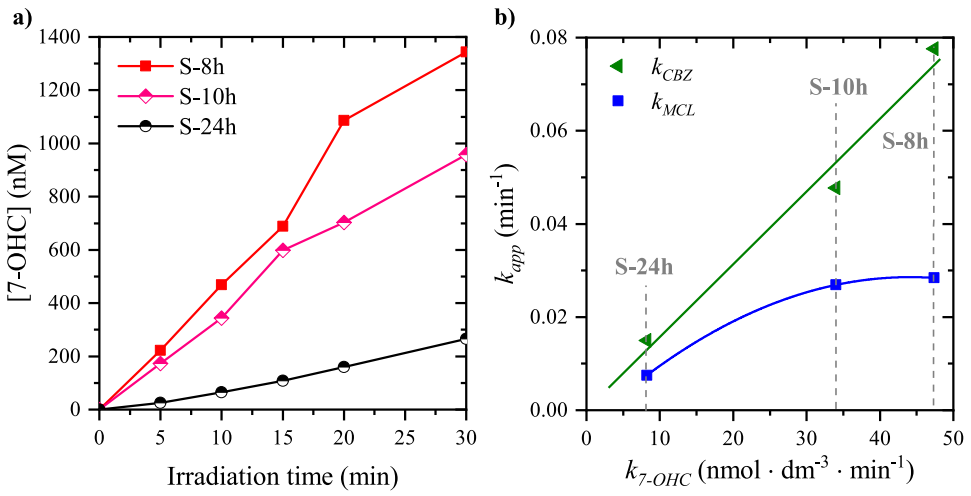

Fig. 7. a) 7-OHC generation under UV-A light, b) relationship between the apparent kinetic rate constants for CBZ and MCL degradation and the 7-OHC production derived from the slopes of Fig. 6a.

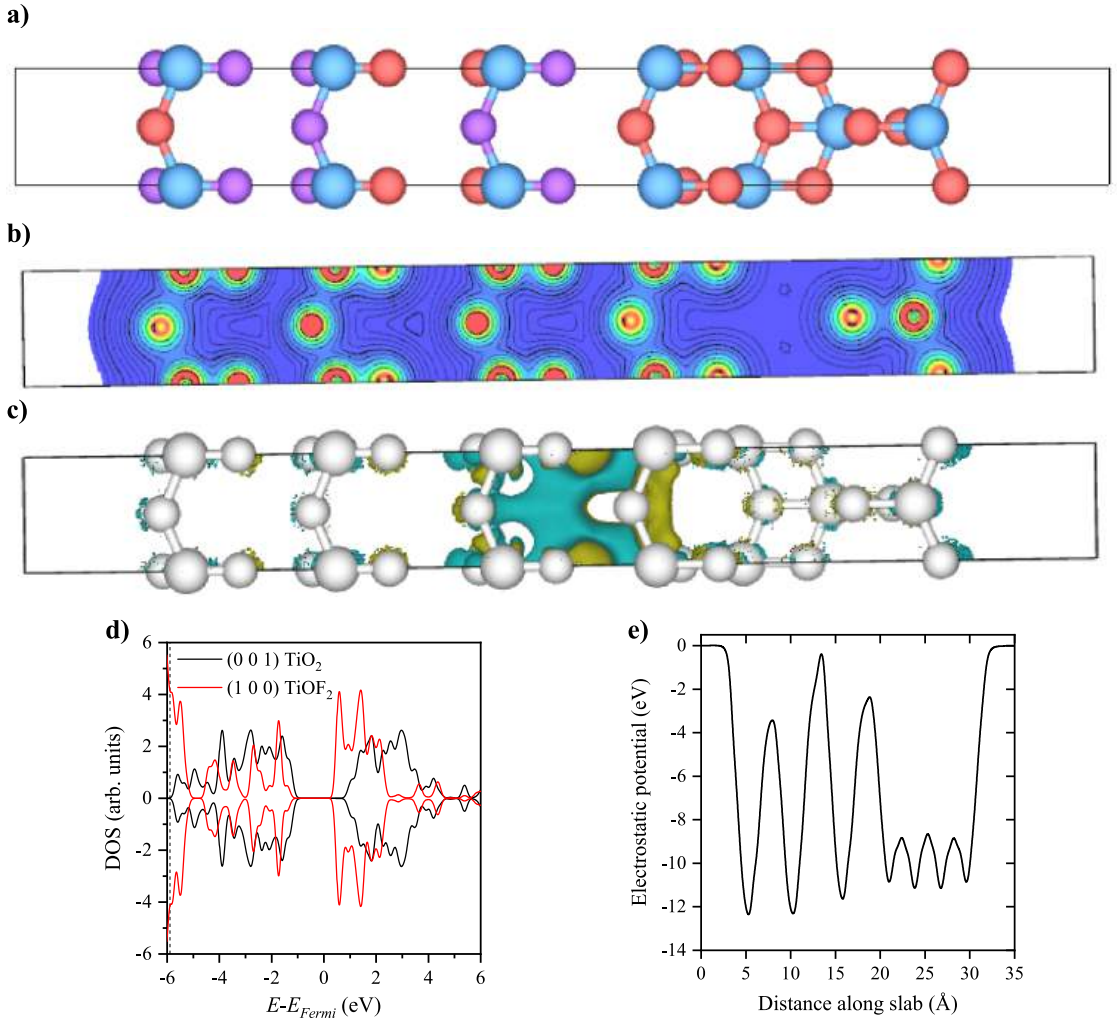

Fig. 8. a) Optimized model of the (001) TiO_2/(100) $TiOF_2$ interface, considering mutual [0 0 1] axis of both crystal structures, b) the corresponding calculated electron density distribution map, and c) charge density difference formed as the consequence of the interface formation, d) Total DOS of (0 0 1) TiO_2/(1 0 0) $TiOF_2$ interface and e) electrostatic potential plotted along the slab thickness. In panel a), Ti, O and F atoms are blue, red and purple, respectively; in panel c) element colours were omitted for better clarity.

analogical [0 0 1] axis, is presented in Fig. 8a. From the output file of SCF results (necessary for geometrical optimisation), work functions (Φ) of pristine compounds were obtained, equal to 5.87 eV and 6.76 eV for (0 0 1) TiO_2 and (1 0 0) $TiOF_2$, respectively. The $\Phi_{anatase}$ is consistent with the literature [48]. Noteworthy, the interface formation resulted in a noticeable distortion of the $TiOF_2$ geometry, with O/F atoms deviating from their cubic-phase positions and recreating lengths and angles analogical to the (0 0 1) plane of the anatase TiO_2. Following the geometry optimisation, the electronic properties of the interface were investigated based on the charge density map (Fig. 8b), and charge density difference (Fig. 8c, 3D model). As observed, overall charge density shows little difference within the model, with the most noticeable feature being preferred charge localization on the F atoms within the $TiOF_2$ structure, in agreement with the extremely high electronegativity of the fluorine. However, analysis of the charge density difference revealed further consequences of the interface formation. As presented in Fig. 8c, electron density became more affected at the interface, with a clear preference to localize charge at the interfacial F atoms and Ti-O-Ti bridge of the (0 0 1) anatase plane (dark-yellow regions in the figure). In this regard, it is expected that the formation of the $TiO_2/TiOF_2$ interface will form additional states that are especially beneficial for electron localization. To quantitatively investigate the charge change and transfer, Bader charge analysis was performed for pristine compounds and in heterojunction (Table S3 in Supplementary Materials). The positive Bader charge corresponds to electron donation, whereas negative values show the electrons gained by atoms. The highest interface effect is noticed for interfacial F atoms, which exhibited a positive value of Bader charge. These results are consistent with charge density difference plots.

The calculated density of states (DOS) of the interface between the anatase (0 0 1) surface and (1 0 0) $TiOF_2$ is presented in Fig. 8d. It can be seen that the band corresponding to $TiOF_2$ possesses lower energy than TiO_2, so the conduction band (CB) of TiO_2 will be located higher than that of $TiOF_2$. Consequently, the valence band (VB) positions also vary from each other and the VB of TiO_2 possesses higher energy than that of $TiOF_2$. Finally, plotting of the average electrostatic potential along the slab (Fig. 8e) revealed that high potential barriers exist within the $TiOF_2$ structure. Above all, this might be the reason behind the long lifetimes of the generated charge carriers observed for the $TiOF_2$, but might also contribute to its negligible photocatalytic activity, as the charge carriers might undergo trapping within the crystal structure, with the low possibility of migration and transfer after the excitation. However, as a consequence, efficient charge separation can be achieved only when $TiOF_2$ forms thin structures at the (0 0 1) TiO_2 surface. This is because further growth of the $TiOF_2$ may trap electrons at the interface and reduce their possible migration due to the high potential barriers

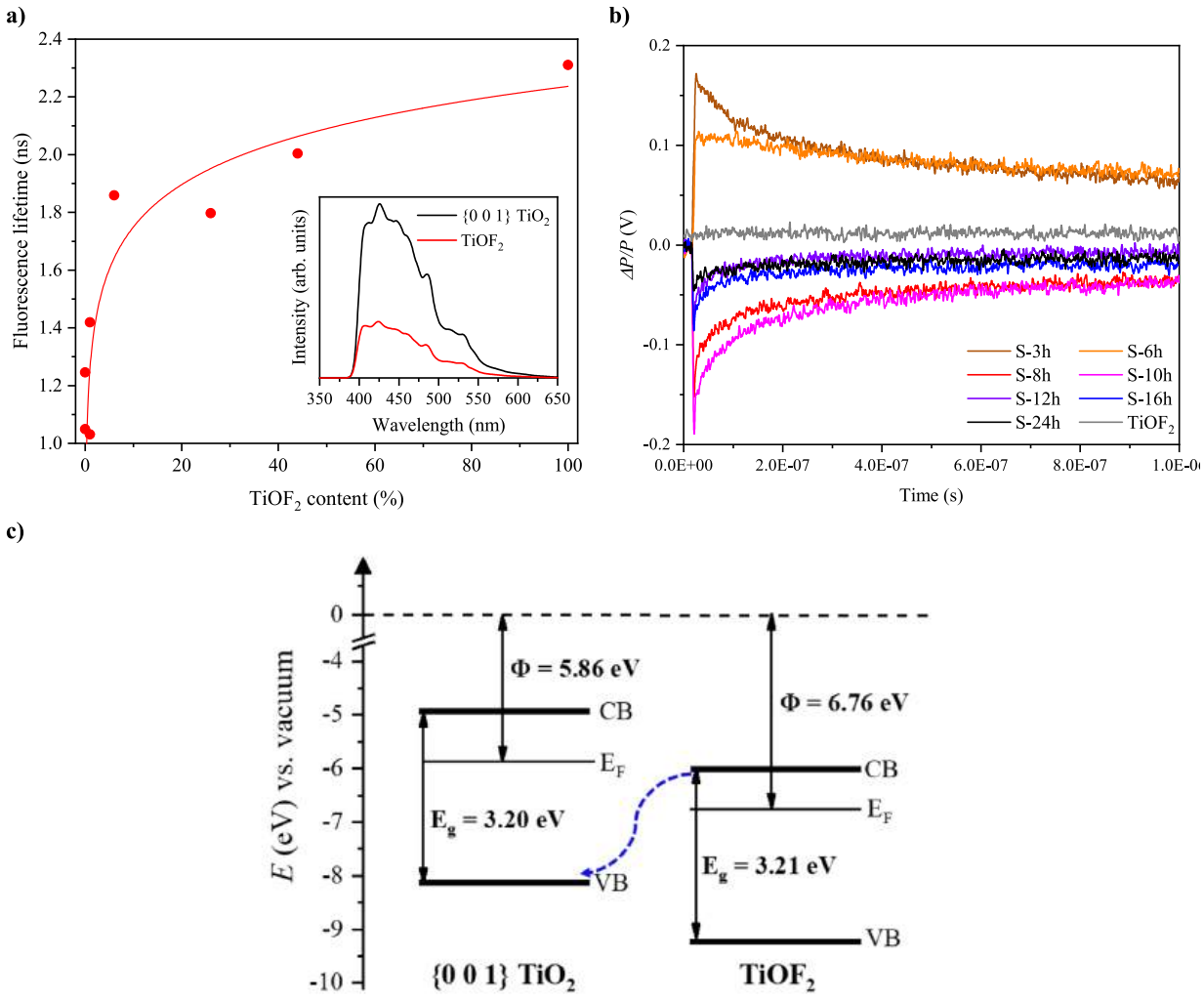

Fig. 9. a) Fluorescence lifetime for the different $TiO_2/TiOF_2$ samples *vs.* the $TiOF_2$ phase content. The solid line is a guide to the eye only; Inset shows the PL spectra of pure compounds at λ_{exc} = 320 nm, b) TRMC signal after excitation at λ = 360 nm for pure {0 0 1} anatase, $TiOF_2$ and $TiO_2/TiOF_2$ photocatalysts, c) Proposed mechanism of charge carriers separation in illuminated $TiO_2/TiOF_2$ based on lifetime measurements and DFT calculations; blue arrow shows the recombination process.

existing within its structure. In this regard, it seems reasonable that small amounts of $TiOF_2$ in the heterojunction can effectively withdraw both charge carriers from the composite structure, leading to boosted photocatalytic activity.

Considering the band structures of these two semiconductors, there are two possible charge carrier transfer pathways in the photocatalytic systems, that is, a traditional type-II heterojunction or a direct Z-scheme system. Therefore, DFT calculations were combined with fluorescence spectra to indicate the type of heterojunction between titanium oxyfluoride and {0 0 1} anatase. This time-resolved spectroscopy technique is supposed to be appropriate for heterojunction classification, as it provides insights into the evolution dynamics of photogenerated charge carriers within the heterojunction [49]. Fig. 9a shows the average fluorescence lifetimes obtained from exponential decay fittings of the fluorescence delay times measured for the different samples. An example of experimental and fitted exponential decay curves is presented in Fig. S12 in Supplementary Materials. Considering the single-phase compounds, $TiOF_2$ shows a remarkably longer fluorescence lifetime than TiO_2, which can be related to longer-lived electron-hole pairs. The composites show intermediate fluorescence lifetime values that reasonably follow an asymptotic trend with increasing $TiOF_2$ content. However, pure TiO_2 exhibited significantly higher fluorescence intensity than $TiOF_2$ (inset in Fig. 9a), so the determined fluorescence lifetimes in the composites originate from the anatase phase. Based on the presented trend, it can be noticed that $< \tau >$ increases for {0 0 1} TiO_2 when coupled to $TiOF_2$. In this system longer fluorescence lifetime, associated with higher number of photogenerated electrons, can be achieved when electrons from the CB of $TiOF_2$ recombine with holes from the VB of TiO_2. In the case of type-II heterojunction, electron flow should be into CB of $TiOF_2$, resulting in lower fluorescence intensity and lifetime. Therefore, according to the relative band positions obtained from DFT calculations, we suggest a Z-scheme heterojunction in {0 0 1} TiO_2/$TiOF_2$. This proposed heterojunction type aligns with the literature, where it has been studied using different techniques [50].

The TRMC measurements are presented in Fig. 9b. It can be observed that $TiOF_2$ itself does not show any signal, therefore this compound is supposed not to be photocatalytically active. All the compounds containing TiO_2 present a clear, typical high signal with well-defined decay. However, it can be noted that both S-3 h and S-6 h samples present a positive A sensitivity factor, whereas the others show signals with negative A factors. Therefore, it is not possible to compare I_{max} values of samples with opposite A factors. These differences in A factors for these series can be explained by significant variations in the microstructures. Composite structures consisting of two heterogeneous phases are always associated with important A factors variations. The structural analysis confirms this assumption – S-3 h and S-6 h are the only ones containing $TiOF_2$ in a significant amount with particular heterojunction structuration. The other photocatalysts with a low $TiOF_2$ content possess a similar behaviour to that of pure TiO_2 (S-16 h and S-24 h). However, in the range of synthesis time from 8 h to 24 h, it is possible to fully compare the TRMC signals. In this case, S-8 h and S-10 h exhibit the highest I_{max} values and slower decays, indicating a high number of charge carriers available for driving the surface redox reactions and the photocatalytic process.

Based on DFT calculations, VB-XPS spectroscopy and band gap measurements, we propose the band position of {0 0 1} TiO_2/$TiOF_2$ composite in relation to vacuum. Based on fluorescence lifetime measurements, the mechanism of electron and hole transport is suggested (Fig. 9c). This mechanism of charge carrier transfer is suitable for photocatalytic reactions because a Z-scheme photocatalyst has simultaneously a strong redox ability for driving photocatalytic reactions and spatially separated reductive and oxidative active sites. In the case of a type-II heterojunction, the advantage of charge carrier separation is at the expense of the redox abilities of charge carriers, which may weaken some specific surface redox reactions [51].

On the other hand, bulk $TiOF_2$ shows minimal photocatalytic activity in both oxidation and reduction processes. However, the low photoreactivity of a material does not preclude its efficient role in a heterojunction, as a material can produce electrons and holes under suitable irradiation while exhibiting minimal standalone photocatalytic activity. For example, Liang *et al.* reported the superior photocatalytic activity of Ag_2S/Cu_2O due to formation of Z-scheme heterojunction, although both pristine materials exhibited poor photocatalytic performance [52]. Although no signal was detected for pristine $TiOF_2$ in TRMC measurements, the calculated electron density distribution map revealed that its electronic structure significantly differs when used incorporated into the heterojunction compared to its standalone form. Due to this effect, comparing photocatalytic performance of $TiOF_2$ in the composite with its pristine form is challenging.

2.5. Stability and reusability tests of the optimum TiO_2/$TiOF_2$ photocatalyst

Reusability tests are of prime importance as leaching of fluorine ions from the {0 0 1} TiO_2/$TiOF_2$ photocatalysts can occur, whether it might come directly from the $TiOF_2$ phase or residual ions resulting from the HF-assisted solvothermal synthesis that forms the {0 0 1} TiO_2 facets. Using the most efficient S-8 h binary photocatalyst and the degradation of MCL under UV–vis irradiation, Fig. 10 shows the ability of the TiO_2/$TiOF_2$ system to be reused for five consecutive test cycles. The photocatalytic activity remained stable upon the first three cycles, with an average apparent kinetic rate constant k_{MCL} of 0.044 ± 0.002 min^{-1}. XRD patterns of the fresh and used photocatalysts showed that the {0 0 1} TiO_2/$TiOF_2$ photocatalysts undergo minor structural changes (Fig. S14 in Supplementary Materials) with similar crystallite size (14 nm), while XPS measurements evidenced an increase in the Ti/F surface ratio (Fig. S15 in Supplementary Materials) and a slight decrease in the Ti^{4+}–F contribution. The lower Ti^{4+}–F contribution than in the fresh sample and the slight increase in the Ti/F surface ratio were assigned to fluorine leaching, as confirmed by the ion chromatography (IC) analysis of the post-process water (Fig. S16 in Supplementary Materials). IC showed the presence of both F^- released by the photocatalyst, and Cl^- which originates from MCL mineralisation. The experimental Cl^- concentration was close to the theoretical value, which also confirmed the high efficiency of MCL dechlorination over three consecutive cycles. The slight decrease in the photocatalytic activity can be observed in fourth (0.0395 min^{-1}) and fifth cycle (0.0391 min^{-1}). Therefore, it is worth highlighting that although changes in the structure and surface, the photocatalytic activity is still high, so that the {0 0 1} TiO_2/$TiOF_2$ photocatalyst can be reused in water treatment.

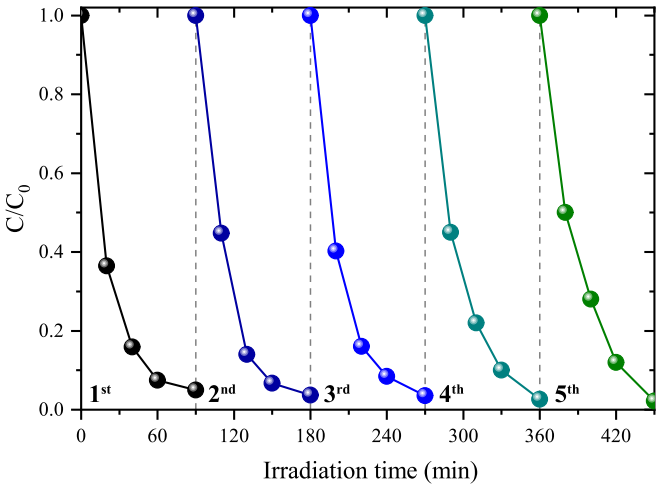

Fig. 10. Reusability tests of the MCL photocatalytic degradation on the S-8 h {0 0 1} TiO_2/$TiOF_2$ under UV–Vis light.

3. Conclusions

In the present work, the potential of {0 0 1} TiO_2/$TiOF_2$ heterojunction semiconductor photocatalysts was investigated for photocatalytic CECs oxidation and •OH generation. The combination of the $TiOF_2$ phase with highly energetic {0 0 1} crystal facets of anatase strongly enhanced both the degradation and the mineralisation of the organic pollutants. TRMC confirmed that the most photoactive samples (S-8 h and S-10 h) exhibited the highest number of charge carriers available for driving the surface redox reactions. Time-resolved fluorescence spectra revealed that charge carriers' lifetimes were prolonged when $TiOF_2$ was present in the final photocatalyst. DFT calculations and valence-band XPS spectra showed the favourable band position between both (0 0 1) TiO_2 and (1 0 0) $TiOF_2$ semiconductor phases, facilitating efficient migration and separation of photogenerated electron-hole pairs.

The $TiOF_2$ content in the binary photocatalyst, controlled by tuning the duration of the solvothermal synthesis, was a crucial factor which affected the photocatalytic performance. Regardless of the pollutant to degradation, the apparent kinetic rate constants for degradation as well as the TOC reduction efficiency feature a volcano-type behavior with increasing the $TiOF_2$ content. The highest performances were obtained on binary {0 0 1} TiO_2/$TiOF_2$ heterojunction photocatalysts with a low content of the $TiOF_2$ phase in the range 1.5–6 %, corresponding to synthesis durations of 8 h–12 h. These experimental results align well with DFT calculations which revealed a high potential barrier for $TiOF_2$ which is responsible for impeded electron migration. Therefore, efficient charge separation is achievable only when $TiOF_2$ forms thin structures at the (0 0 1) TiO_2 surface. Finally, reusability tests demonstrated high MCL degradation efficiency over five consecutive test cycles, despite minor structural changes.

The present study provides information about novel composition-controlled $TiOF_2$-based photocatalysts with improved charge carrier dynamics, as a key-factor for enhancing the degradation and mineralisation of a span of contaminants of emerging concern with varied chemical functions.

CRediT authorship contribution statement

Marta Kowalkińska: Writing – review & editing, Writing – original draft, Methodology, Investigation, Formal analysis, Conceptualization. **Nicolas Keller:** Writing – review & editing, Supervision, Methodology, Investigation, Formal analysis, Conceptualization. **Fernando Fresno:** Writing – review & editing, Investigation, Formal analysis. **Christophe Colbeau-Justin:** Investigation. **Anna Zielińska-Jurek:** Writing – review & editing, Validation, Supervision, Resources, Project administration, Methodology, Funding acquisition, Conceptualization.

Declaration of competing interest

The authors declare that they have no known competing financial interests or personal relationships that could have appeared to influence the work reported in this paper.

Acknowledgements

The research was financially supported by the Polish National Science Centre, grant no. UMO-2021/43/B/ST5/02983. The authors acknowledge the MEB-CRO platform in Strasbourg and T. Dintzer for SEM observations. V. Papaefthymiou (ICPEES, Strasbourg) is acknowledged for performing XPS characterisation. D. Ihiawakrim (IPCMS, Strasbourg) is thanked for performing TEM characterisation.

Appendix A. Supplementary data

Supplementary data to this article can be found online at https://doi.org/10.1016/j.apsusc.2025.162893.

Data availability

Data will be made available on request.

References

[1] European Environmental Agency, Chapter 10: chemical pollution, in: The European Environment-State and Outlook 2020. Knowledge for Transition to a Sustainable Europe, 2020, pp. 230–251, https://doi.org/10.2800/96749.
[2] V. Augugliaro, M. Bellardita, V. Loddo, G. Palmisano, L. Palmisano, S. Yurdakal, Overview on oxidation mechanisms of organic compounds by TiO_2 in heterogeneous photocatalysis, J. Photochem. Photobiol. C Photochem. Rev. 13 (2012) 224–245, https://doi.org/10.1016/j.jphotochemrev.2012.04.003.
[3] P. Garcia-Muñoz, F. Fresno, J. Ivanez, D. Robert, N. Keller, Activity enhancement pathways in $LaFeO_3$@TiO_2 heterojunction photocatalysts for visible and solar light driven degradation of myclobutanil pesticide in water, J. Hazard. Mater. 400 (2020) 123099, https://doi.org/10.1016/j.jhazmat.2020.123099.
[4] A. Habibi-Yangjeh, K. Pournemati, Z. Ahmadi, A. Khataee, Decoration of carbon dots on oxygen-vacancy-enriched s-scheme TiO_2 quantum Dots/TiO_2 oxygen vacancies photocatalysts: impressive quantum-dot-sized photocatalysts for remediation of antibiotics, bacteria, and dyes, Langmuir 40 (2024) 8503–8519, https://doi.org/10.1021/acs.langmuir.4c00060.
[5] K. Pournemati, A. Habibi-Yangjeh, S.R. Pouran, A. Khataee, Fabrication of TiO_2/CeO_2/$CeFeO_3$ tandem n-n heterojunction nanocomposites for visible-light-triggered photocatalytic degradation of tetracycline and colored effluents, Ceram. Int. 48 (2022) 22393–22402, https://doi.org/10.1016/j.ceramint.2022.04.241.
[6] A. Zielińska-Jurek, Z. Wei, M. Janczarek, I. Wysocka, Size - controlled synthesis of Pt particles on TiO_2 surface : physicochemical characteristic and photocatalytic activity, Catalysts 9 (2019) 1–18, https://doi.org/10.3390/catal9110940.
[7] F. Fang, Y. Liu, X. Sun, C. Fu, Y. Prakash Bhoi, W. Xiong, W. Huang, TiO_2 Facet-dependent reconstruction and photocatalysis of CuO_x/TiO_2 photocatalysts in CO_2 photoreduction, Appl. Surf. Sci. 564 (2021) 150407, https://doi.org/10.1016/j.apsusc.2021.150407.
[8] Y. Chen, L. Soler, C. Cazorla, N.G. Bastús, V.F. Puntes, J. Llorca, Facet-engineered TiO_2 drives photocatalytic activity and stability of supported noble metal clusters during H_2 evolution, Nat. Commun. 14 (2023) 6165, https://doi.org/10.1038/s41467-023-41976-2.
[9] S. Dudziak, M. Kowalkińska, A. Zielińska-Jurek, Chapter 3: crystal facet engineering of TiO_2 from theory to application, in: Updates on Titanium Dioxide, IntechOpen, 2023, https://doi.org/10.5772/intechopen.104130.
[10] H.G. Yang, C.H. Sun, S.Z. Qiao, J. Zou, G. Liu, S.C. Smith, H.M. Cheng, G.Q. Lu, Anatase TiO_2 single crystals with a large percentage of reactive facets, Nature 453 (2008) 638–641, https://doi.org/10.1038/nature06964.
[11] X. Han, Q. Kuang, M. Jin, Z. Xie, L. Zheng, Synthesis of titania nanosheets with a high percentage of exposed (001) facets and related photocatalytic properties, J. Am. Chem. Soc. 131 (2009) 3152–3153, https://doi.org/10.1021/ja8092373.
[12] J. Yu, J. Low, W. Xiao, P. Zhou, M. Jaroniec, Enhanced photocatalytic CO2-reduction activity of anatase TiO2 by co-exposed 001 and 101 facets, J. Am. Chem. Soc. 136 (2014) 8839–8842, https://doi.org/10.1021/ja5044787.
[13] S. Dudziak, M. Kowalkińska, J. Karczewski, M. Pisarek, K. Siuzdak, A. Kubiak, K. Siwińska-Ciesielczyk, A. Zielińska-Jurek, Solvothermal growth of 0 0 1 exposed anatase nanosheets and their ability to mineralize organic pollutants. The effect of alcohol type and content on the nucleation and growth of TiO2 nanostructures, Appl. Surf. Sci. 563 (2021) 150360, https://doi.org/10.1016/j.apsusc.2021.150360.
[14] M. Kowalkińska, S. Dudziak, J. Karczewski, J. Ryl, G. Trykowski, A. Zielińska-Jurek, Facet effect of TiO_2 nanostructures from $TiOF_2$ and their photocatalytic activity, Chem. Eng. J. 404 (2021) 126493, https://doi.org/10.1016/j.cej.2020.126493.
[15] J. Wang, F. Cao, Z. Bian, M.K.H. Leung, H. Li, Ultrafine single-crystal $TiOF_2$ nanocubes with mesoporous structure, high activity and durability in visible light driven photocatalysis, Nanoscale 6 (2014) 897–902, https://doi.org/10.1039/c3nr04489k.
[16] C.Z. Wen, Q.H. Hu, Y.N. Guo, X.Q. Gong, S.Z. Qiao, H.G. Yang, From titanium oxydifluoride ($TiOF_2$) to titania (TiO_2): phase transition and non-metal doping with enhanced photocatalytic hydrogen (H_2) evolution properties, Chem. Comm. 47 (2011) 6138–6140, https://doi.org/10.1039/c1cc10851d.
[17] L. Chen, L. Shen, P. Nie, X. Zhang, H. Li, Facile hydrothermal synthesis of single crystalline $TiOF_2$ nanocubes and their phase transitions to TiO_2 hollow nanocages as anode materials for lithium-ion battery, Electrochim. Acta 62 (2012) 408–415, https://doi.org/10.1016/j.electacta.2011.12.058.
[18] K. Lv, J. Yu, L. Cui, S. Chen, M. Li, Preparation of thermally stable anatase TiO_2 photocatalyst from $TiOF_2$ precursor and its photocatalytic activity, J. Alloys Compd. 509 (2011) 4557–4562, https://doi.org/10.1016/j.jallcom.2011.01.103.

[19] Z. Wang, K. Lv, G. Wang, K. Deng, D. Tang, Study on the shape control and photocatalytic activity of high-energy anatase titania, Appl. Catal. B 100 (2010) 378–385, https://doi.org/10.1016/j.apcatb.2010.08.014.

[20] L. Wang, J. Liu, Y. Min, K. Zhang, Nontopological transformation of hierarchical TiO_2 by self-regulated etching and capping roles of F^- for photocatalytic H_2 evolution, Appl. Surf. Sci. 473 (2019) 738–745, https://doi.org/10.1016/j.apsusc.2018.12.077.

[21] M. Kowalkińska, K. Sikora, M. Łapiński, J. Karczewski, A. Zielińska-Jurek, Non-toxic fluorine-doped TiO_2 nanocrystals from $TiOF_2$ for facet-dependent naproxen degradation, Catal. Today 415 (2022) 113959, https://doi.org/10.1016/j.cattod.2022.11.020.

[22] Y. Liu, Z. Ma, $TiOF_2$/g-C_3N_4 composite for visible-light driven photocatalysis, Colloids Surf. A. Physicochem. Eng. Asp. 618 (2021) 126471, https://doi.org/10.1016/j.colsurfa.2021.126471.

[23] P. Dong, E. Cui, G. Hou, R. Guan, Q. Zhang, Synthesis and photocatalytic activity of Ag_3PO_4/$TiOF_2$ composites with enhanced stability, Mater. Lett. 143 (2015) 20–23, https://doi.org/10.1016/j.matlet.2014.12.063.

[24] Z. Wang, K. Yu, Y. Feng, R. Qi, J. Ren, Z. Zhu, Stabilizing $Ti_3C_2T_x$-MXenes with $TiOF_2$ nanospheres intercalation to improve hydrogen evolution reaction and humidity-sensing performance, Appl. Surf. Sci. 496 (2019) 143729, https://doi.org/10.1016/j.apsusc.2019.143729.

[25] X. Ding, Z. Hong, Y. Wang, R. Lai, M. Wei, Synthesis of square-like anatase TiO_2 nanocrystals based on $TiOF_2$ quantum dots, J. Alloys Compd. 550 (2013) 475–478, https://doi.org/10.1016/j.jallcom.2012.10.049.

[26] Z. Liu, X. Liu, Q. Lu, Q. Wang, Z. Ma, $TiOF_2$/TiO_2 composite nanosheets: effect of hydrothermal synthesis temperature on physicochemical properties and photocatalytic activity, J. Taiwan Inst. Chem. Eng. 96 (2019) 214–222, https://doi.org/10.1016/j.jtice:2018.11.013.

[27] S. Dudziak, Z. Bielan, P. Kubica, A. Zielinska-Jurek, Optimization of carbamazepine photodegradation on defective TiO_2-based magnetic photocatalyst, J. Environ. Chem. Eng. 9 (2021) 105782, https://doi.org/10.1016/j.jece:2021.105782.

[28] E. Donner, T. Kosjek, S. Qualmann, K.O. Kusk, E. Heath, D.M. Revitt, A. Ledin, H. R. Andersen, Ecotoxicity of carbamazepine and its UV photolysis transformation products, Sci. Total Environ. 443 (2013) 870–876, https://doi.org/10.1016/j.scitotenv.2012.11.059.

[29] J.M. Monteagudo, A. Durán, R. González, A.J. Expósito, In situ chemical oxidation of carbamazepine solutions using persulfate simultaneously activated by heat energy, UV light, Fe^{2+} ions, and H_2O_2, Appl. Catal. B 176–177 (2015) 120–129, https://doi.org/10.1016/j.apcatb.2015.03.055.

[30] P. Garcia-Muñoz, W. Dachtler, B. Altmayer, R. Schulz, D. Robert, F. Seitz, R. Rosenfeldt, N. Keller, Reaction pathways, kinetics and toxicity assessment during the photocatalytic degradation of glyphosate and myclobutanil pesticides: influence of the aqueous matrix, Chem. Eng. J. 384 (2020) 123315, https://doi.org/10.1016/j.cej.2019.123315.

[31] C. Hou, H. Liu, F.B. Mohammad, Preparation of ordered mesoporous F–$H_2Ti_3O_7$ nanosheets using orthorhombic $HTiOF_3$ as a precursor and their highly efficient degradation of tetracycline hydrochloride under simulated sunlight, J. Solid State Chem. 300 (2021) 122288, https://doi.org/10.1016/j.jssc.2021.122288.

[32] X. Han, Q. Kuang, M. Jin, Z. Xie, L. Zheng, Synthesis of titania nanosheets with a high percentage of exposed (001) facets, J. Am. Chem. Soc. 131 (2009) 3152–3153, https://doi.org/10.1021/ja8092373.

[33] H.G. Yang, G. Liu, S.Z. Qiao, C.H. Sun, Y.G. Jin, S.C. Smith, J. Zou, H.M. Cheng, G. Q. Lu, Solvothermal synthesis and photoreactivity of anatase TiO2 nanosheets with dominant 001 facets, J. Am. Chem. Soc. 131 (2009) 4078–4083, https://doi.org/10.1021/ja808790p.

[34] Z. Huang, Z. Wang, K. Lv, Y. Zheng, K. Deng, Transformation of TiOF2 cube to a hollow nanobox assembly from anatase TiO2 nanosheets with exposed 001 facets via solvothermal strategy, ACS Appl. Mater. Interfaces 5 (2013) 8663–8669, https://doi.org/10.1021/am4023048.

[35] R. Ragsdale, B.B. Stewart, Fluorine-19 nuclear magnetic resonance study of some pentafluorotitanate complexes, Inorg. Chem. 2 (1963) 1002–1004, https://doi.org/10.1021/ic50027a031.

[36] Z. Lai, F. Peng, Y. Wang, H. Wang, H. Yu, P. Liu, H. Zhao, Low temperature solvothermal synthesis of anatase TiO2 single crystals with wholly 100 and 001 faceted surfaces, J. Mater. Chem. 22 (2012) 23906–23912, https://doi.org/10.1039/c2jm34880b.

[37] Q. Cheng, Y.J. Yuan, R. Tang, Q.Y. Liu, L. Bao, P. Wang, J. Zhong, Z. Zhao, Z.T. Yu, Z. Zou, Rapid hydroxyl radical generation on (001)-facet-exposed ultrathin anatase TiO_2 nanosheets for enhanced photocatalytic lignocellulose-to-H_2 conversion, ACS Catal. 12 (2022) 2118–2125, https://doi.org/10.1021/acscatal.1c05713.

[38] X. Zhao, G. Wei, J. Liu, Z. Wang, C. An, J. Zhang, Synthesis of heterostructured Pd@TiO_2/$TiOF_2$ nanohybrids with enhanced photocatalytic performance, Mater. Res. Bull. 80 (2016) 337–343, https://doi.org/10.1016/j.materresbull.2016.04.018.

[39] K. Kobayashi, M. Takashima, M. Takase, B. Ohtani, Mechanistic study on facet-dependent deposition of metal nanoparticles on decahedral-shaped anatase titania photocatalyst particles, Catalysts 8 (2018) 542, https://doi.org/10.3390/catal8110542.

[40] A. Zielińska-Jurek, Z. Bielan, S. Dudziak, I. Wolak, Z. Sobczak, T. Klimczuk, G. Nowaczyk, J. Hupka, Design and application of magnetic photocatalysts for water treatment The effect of particle charge on surface functionality, Catalysts 7 (2017) 360, https://doi.org/10.3390/catal7120360.

[41] H. Park, W. Choi, Effects of TiO_2 surface fluorination on photocatalytic reactions and photoelectrochemical behaviors, J. Phys. Chem. B 108 (2004) 4086–4093, https://doi.org/10.1021/jp036735i.

[42] A. Jain, S. Agarwal, S. Kumar, S. Yamaguchi, H. Miyaoka, Y. Kojima, T. Ichikawa, How does TiF_4 affect the decomposition of MgH_2 and its complex variants? - An XPS investigation, J. Mater. Chem. A 5 (2017) 15543–15551, https://doi.org/10.1039/c7ta03081a.

[43] G. Nansé, E. Papirer, P. Fioux, F. Moguet, A. Tressaud, Fluorination of carbon blacks: an X-ray photoelectron spectroscopy study: I. A literature review of XPS studies of fluorinated carbons. XPS investigation of some reference compounds, Carbon (1997) 175–194, https://doi.org/10.1016/S0008-6223(96)00095-4.

[44] S. Shian, K.H. Sandhage, Hexagonal and cubic $TiOF_2$, J. Appl. Crystallogr. 43 (2010) 757–761, https://doi.org/10.1107/S0021889810016730.

[45] S. Dudziak, M. Kowalkińska, J. Karczewski, M. Pisarek, J.D. Gouveia, J.R. B. Gomes, A. Zielińska-Jurek, Surface and trapping energies as predictors for the photocatalytic degradation of aromatic organic pollutants, J. Phys. Chem. C 126 (2022) 14859–14877, https://doi.org/10.1021/acs.jpcc.2c02775.

[46] Y. Nosaka, A.Y. Nosaka, Understanding hydroxyl radical (•OH) generation processes in photocatalysis, ACS Energy Lett. 1 (2016) 356–359, https://doi.org/10.1021/acsenergylett.6b00174.

[47] Y. Nosaka, A.Y. Nosaka, Generation and detection of reactive oxygen species in photocatalysis, Chem. Rev. 117 (2017) 11302–11336, https://doi.org/10.1021/acs.chemrev.7b00161.

[48] K. Cieślik, D. Wrana, M. Rogala, C. Rodenbücher, K. Szot, F. Krok, The effect of reduction and oxidation processes on the work function of metal oxide crystals: TiO_2(110) and $SrTiO_3$(001) case, Crystals 13 (2023) 1–17, https://doi.org/10.3390/cryst13071052.

[49] K. Spilarewicz, K. Mróz, M. Kobielusz, W. Macyk, When the fate of electrons matters — strategies for correct heterojunction classification in photocatalysis, Curr. Opin. Chem. Eng. 45 (2024) 101041, https://doi.org/10.1016/j.coche.2024.101041.

[50] Y. Chen, X. Wang, Z. Zeng, M. Lv, K. Wang, H. Wang, X. Tang, Towards molecular understanding of surface and interface catalytic engineering in TiO_2/$TiOF_2$ nanosheets photocatalytic antibacterial under visible light irradiation, J. Hazard. Mater. 465 (2024) 133429, https://doi.org/10.1016/j.jhazmat.2024.133429.

[51] Q. Xu, L. Zhang, J. Yu, S. Wageh, A.A. Al-Ghamdi, M. Jaroniec, Direct Z-scheme photocatalysts: principles, synthesis, and applications, Mater. Today 21 (2018) 1042–1063, https://doi.org/10.1016/j.mattod.2018.04.008.

[52] T.Y. Liang, S.J. Chan, A.S. Patra, P.L. Hsieh, Y.A. Chen, H.H. Ma, M.H. Huang, Inactive Cu_2O cubes become highly photocatalytically active with Ag_2S deposition, ACS Appl. Mater. Interfaces 13 (2021) 11515–11523, https://doi.org/10.1021/acsami.1c00342.

Supplementary Materials

Insight into charge carrier dynamics and interface design of {0 0 1} TiO_2 coupled with $TiOF_2$ for photocatalytic degradation of contaminants of emerging concern

Marta Kowalkińska[1*], Nicolas Keller[2], Fernando Fresno[3], Christophe Colbeau-Justin[4], Anna Zielińska-Jurek[1*]

[1] Department of Process Engineering and Chemical Technology, Faculty of Chemistry, Gdansk University of Technology, G. Narutowicza 11/12 Street, 80-233 Gdansk, Poland

[2] Institut de Chimie et Procédés pour l'Energie, l'Environnement et la Santé (ICPEES) CNRS/University of Strasbourg, 25 rue Becquerel, 67087 Strasbourg, France

[3] Instituto de Catálisis y Petroleoquímica (ICP), CSIC, Marie Curie 2, 28049 Madrid, Spain

[4] ICP, Institut de Chimie Physique, CNRS UMR 8000, Université Paris-Saclay, Bâtiment 349, CEDEX, 91405 Orsay, France

---

* Corresponding authors: marta.kowalkinska@pg.edu.pl (MK), annjurek@pg.edu.pl (AZJ)

TABLE OF CONTENT

Experimental details

EXPERIMENTAL DETAILS

Chemicals were purchased from Sigma Aldrich and used without purification: titanium(IV) fluoride (TiF_4, MQ200), titanium(IV) butoxide (TBT, ≥97%), 1-butanol (≥98%), 1-hexanol (≥98%), hydrofluoric acid 48% (HF), 4-chlorophenol (4CP, 99+%), myclobutanil PESTANAL® (MCL, analytical standard) and carbamazepine (CBZ, analytical standard). The aqueous solutions were prepared using deionised water from Milli-Q® integral water purification systems.

Synthesis of $TiOF_2$ and {0 0 1} TiO_2/$TiOF_2$ heterojunction photocatalysts

For the preparation of pristine $TiOF_2$, 10 g of TiF_4 was added into a 200 cm^3 Teflon reactor with 120 cm^3 of 1-butanol. After stirring the suspension for 15 min at 600 rpm, the reactor was transferred into a stainless-steel autoclave and heated at 210 °C for 24 h in an electric oven. The final product was separated through centrifugation and washed thoroughly with absolute ethanol and deionised water to remove residual contamination and fluorine species. After drying at 80 °C to dry mass, the $TiOF_2$ grey powder was harvested.

The synthesis of {0 0 1} TiO_2/$TiOF_2$ was performed by solvothermal reaction. In this regard, 17 cm^3 of TBT was dissolved in 30 cm^3 of 1-hexanol. The solution was stirred for 20 min before 3.4 cm^3 of 48% hydrofluoric acid was slowly added to the solution and mixed for 5 min. The obtained mixture was transferred into a 200 cm^3 Teflon-lined stainless-steel reactor and was kept at 210 °C in an electric oven for durations of 3 h, 6 h, 8 h, 10 h, 12 h, 16 h and 24 h, then cooled down naturally. After the reaction, the precipitate was centrifuged and washed four times with water, twice with anhydrous ethanol and twice with 0.1 M NaOH

solution to remove residual organic reagents, then finally dried at 80 °C to dry mass. The samples were denoted as S-xh, where x is the time of solvothermal reaction.

Material characterisation

The phase identification and the composition of the samples were investigated by X-ray powder diffraction (Bruker D8 Advance diffractometer) equipped with a monochromatic copper radiation source (Cu Kα = 1.54 Å), with a scan step of 0.02°. The analyses of the XRD patterns were performed with the HighScorePlus software package (PANalytical, 2006) and the Crystallographic Open Database. The amorphous phase content was analysed using an internal standard (NiO, Sigma Aldrich, Germany). The mean crystallite size defined as the average size of the coherent diffracting domains, was determined from the Scherrer equation with the usual assumption of spherical crystallites. The bond identification in samples was determined by Fourier-transform infrared spectroscopy (FTIR) in the transmittance mode using FTIR Nicolet iS10 (Thermo Fisher Scientific, Waltham, MA, USA) spectrometer. The pellets containing KBr and a photocatalyst were analysed in each measurement.

The morphology of the photocatalysts was studied by field emission scanning electron microscopy (model JEOL JSM-6700 F FEG) in secondary electrons (SE) mode, EHT = 3.00 kV, WD = 3.5 mm, aperture size = 20.00 μm. Transmission electron microscopy (TEM) images of the {0 0 1} TiO_2 (S-16h) were acquired in a JEOL 2100 F. A Gemini V instrument was used to measure the surface area of the photocatalysts based on the Brunauer-Emmett-Teller (BET) method. All samples were degassed at 200 °C for 2 h before N_2 adsorption measurements.

The surface composition and the surface chemical states of the photocatalysts were determined by X-ray photoelectron spectroscopy (XPS) using a Thermo VG Multilab ESCA3000 spectrometer (Al Kα anode at $h\nu$ = 1486.6 eV). The obtained XPS spectra were fitted using the CasaXPS software (version 2.3.25), using a Shirley-type background and an

Asymmetric Lorentzian function with 50% Gaussian character (LA(50)). The surface atomic ratio Ti/F was calculated using the appropriate experimental sensitivity factors, as determined by Scofield. The spectra were corrected from electrostatic charging using the adventitious sp^2 carbon C1s peak at 285.0 eV as an internal standard. The effect of the pH on the photocatalysts' surface charge was measured as zeta potential (mV) using Malvern Nano Zetasizer (Malvern Instruments Ltd., Malvern, UK). The dispersion of the catalyst at the concentration of 0.2 g/dm^3 in 10^{-2} M KCl solution was used for measurements.

The optical properties of the photocatalysts were studied by diffuse reflectance spectroscopy (DRS) using a UV–Vis spectrophotometer (Thermo Fisher Scientific Evolution 220) and barium sulfate as standard material. Absorption spectra were recorded with a slot width of 2 nm and an integration time of 1.1 s. The bandgap energy values (E_g) were graphically derived using the Tauc's method and the Kubelka-Munk transformation [1].

Photocurrent density were measured obtained using potentiostat–galvanostat Autolab PGSTAT204 (Metrohm Autolab) with a 0.5 M Na_2SO_4 solution as an electrolyte and a built-in software, Nova 2.1.4. was used for data analysis. Preparation of the electrode substrates modified with the as-synthesised photocatalysts, suitable for electrochemical measurements, was performed as follows: firstly, the sample suspension in isopropanol was sonicated for 20 min. Then, photocatalyst dispersion was dropped-cast onto carbon screen-printed electrodes with Ag/AgCl reference electrode (Metrohm DropSens 11L), followed by drying to evaporate the solvent completely. Finally, surface blockage was carried out by adding a small drop of Nafion (Sigma-Aldrich) onto the electrode. A switchable LED revolver (Instytut Fotonowy, Kraków, Poland) was used as a light source. The measurements were performed for λ_{max} = 372 nm, P = 30.5 mW.

Fluorescence lifetime was measured through time-correlated single photon counting (TCSPC) in a Mini-τ device from Edinburgh Instruments, using as an excitation source a 372

nm laser with a pulse width of 61.2 ps at a repetition rate of 1 MHz and with an emission bandpass filter at 450 ± 25 nm. Experimental data were fitted to exponential decay curves to obtain average lifetimes. Fluorescence spectra were recorded on a Perkin-Elmer LS50B spectrometer, with an excitation wavelength of 320 nm, slit widths of 10 nm for excitation and emission, and an emission cut-off filter at 400 nm.

The time-resolved microwave conductivity (TRMC) technique was employed to study the charge-carrier dynamics under UV excitation. The incident microwaves were generated by a Gunn diode (30 GHz). A laser (EKSPLA, NT342B) tunable between 200 and 2000 nm, equipped with an optical parametric oscillator (OPO), was used as a pulsed light source. The wavelength used was 360 nm, with an excitation energy of 1.1 mJ/cm^2. TRMC technique measures the relative change ($\frac{\Delta P(t)}{p}$) in microwave power reflected by a semiconductor material during its excitation by a laser pulse (Equation below). This change ($\Delta\sigma(t)$) correlates to the variation of sample conductivity for small perturbations.

$$\frac{\Delta P(t)}{p} = A\Delta\sigma(t) = Ae\mu_e\Delta n_e(t) \ ,$$

where n_e(t) is the number of excess free electrons at time t, μ_e is the mobility of free electrons, and e is the charge. The sensitivity factor A is independent of time but is dependent on both the microwave frequency and the sample conductivity, and can be positive or negative. The primary data provided by TRMC include the maximum signal value (I_{max}), which represents the number of excess charge carriers generated by the laser pulse, and the decay that results from the decrease of the excess electrons (free electrons) and relates to the lifetime of charge carriers. Details can be found in [2,3].

Theoretical calculations

The interface between anatase {0 0 1} and $TiOF_2$ was determined computationally using density functional theory calculations (DFT) within the generalised gradient approximation

with Hubbard parameter (GGA+U), as implemented in Quantum Espresso 6.5 software package [4,5]. All calculations were performed using Perdew–Burke-Ernzerhof (PBE) functionals and projector augmented wave (PAW) pseudopotentials. Since $TiOF_2$ transforms to TiO_2, they exhibited similar unit cell *a* and *b* parameters [32]. Therefore, during calculations, both crystal lattices have a common OX axis. The fluorine atom was the bridge between (0 0 1) TiO_2 and (1 0 0) $TiOF_2$ surface. These two slabs were separated by vacuum at a distance of 10 Å. The electronic wave functions were expanded to the energy cut-off of 450 eV. During the calculations of the density of states (DOS) of the TiO_2/$TiOF_2$ interface, K-point grids of 4 × 4 × 1 were used. The first two Ti-O and Ti-O-F layers were used for plotting the DOS of the interface itself. During the calculations, the Hubbard parameter U = 3.9 eV was applied for Ti atoms, based on the previous report [6]. All calculations were performed under the same conditions to be comparative.

Photocatalytic activity analysis

The evaluation of the photocatalytic activity was carried out in two set-ups depending on the light source used. The experiments under UV-A were carried out in a batch beaker-type glass reactor with a volume of 100 cm^3. The photocatalyst suspension was exposed to a 6 mW/cm^2 irradiance UV-A light centred at 365 nm, provided by Philips 24 W/10/4 P lamps[7,8]. In the case of experiments with simulated solar light, the reactions were performed in a quartz reactor with a volume of 50 cm^3, using as a light source a 300 W xenon lamp (model 6271H, Oriel, USA) with a UV irradiance fraction of 21 mW/cm^2 (measured in the center of the reactor) and equipped with a water IR filter. For measurements using an Xe lamp, the quartz reactor was connected to a thermostat to maintain the temperature at 20 °C.

In a typical reaction procedure, the powder photocatalyst was dispersed at the concentration of 1 g/dm^3 under stirring in an aqueous solution of the organic pollutant. The initial 4CP, MCL

and CBZ concentration was 20 ppm (TOC_{4CP} = 15.4 ppm, TOC_{MCL} = 14.3 ppm) and 14 ppm (TOC_{CBZ} = 11.4 ppm), respectively. Before irradiation, the photocatalyst suspension was stirred for 60 min at 600 rpm in the dark to ensure the establishment of the adsorption-desorption equilibrium.

The concentration of 4CP was determined by UV-vis spectrophotometry by following the disappearance of the main absorption peak at λ_{max} = 224 nm. The degradation efficiency for MCL and CBZ was monitored using a high-performance liquid chromatography system (HPLC, model Shimadzu LC-6A), combined with a photodiode array detector (SPD-M20A) and C18 column (Phenomenex Gemini 5 µm; 150x4.6 mm). The mobile phase includes (v/v): 60% H_2O, 0.5% H_3PO_4, 39.5% acetonitrile for CBZ detection and 60% acetonitrile, 40% H_2O + 0.1% formic acid for MCL analysis. The concentration of these compounds was measured at λ_{max} = 285 nm and 220 nm for CBZ and MCL, respectively. The retention time (t_R) of CBZ and MCL were 4.73 min and 6.99 min, respectively. Quantitative analysis of the pollutants was performed using standard compounds from Sigma-Aldrich using the external calibration method. An HPLC-grade acetonitrile, formic acid and orthophosphoric acid solution was provided by Merck. The apparent kinetic rate constants k for the degradation of the pollutants were calculated according to a pseudo-first-order kinetic model.

Moreover, Total Organic Carbon (TOC) measurements were performed using a TOC analyser (Shimadzu, model TOC-L) to determine the organic carbon content in the post-process wastewater. The TOC concentration evolution curve was fitted with a zero-order kinetic model to obtain the apparent kinetic rate constants for mineralisation k_{TOC}. The anion concentration was monitored by Dionex ICS-1100 Ion Chromatography (Thermo Fisher Scientific) and Dionex™ Combined Seven Anion Standard II was used to perform the quantitative analysis.

The generation of hydroxyl radicals (•OH) was investigated under UV-A light by studying the selective oxidation of coumarin to 7-hydroxycoumarin (7-OHC) [9,10]. The experiments

were carried out in the set-up with UV-A irradiation. The photocatalyst suspension at the concentration 0.5 g/dm^3 in 0.7 mM aqueous coumarin solution was exposed to a flux of 6 mW/cm^2 UV-A light centered at 365 nm. The 7-OHC evolution was monitored by photoluminescence (PL) spectroscopy using a Shimadzu spectrofluorophotometer RF-6000, using an external calibration curve for quantification. During the measurements, the excitation and emission wavelengths were 332 nm and 454 nm, respectively.

The photocatalytic hexavalent chromium reduction in CrO_4^{2-} aqueous solution was investigate to elucidate the electrons generation. These experiments were also carried out in the set-up with UV-A irradiation light centered at 365 nm. The photocatalyst suspension had the concentration 1 g/dm^3 and the concentration of Cr(VI) solution was 25 mg/dm^3. The suspension was adjusted to pH = 3. The progress of Cr(VI) reduction was monitored by the colorimetric method using diphenylcarbazide as a complexing agent. The absorbance was measured at λ = 540 nm.

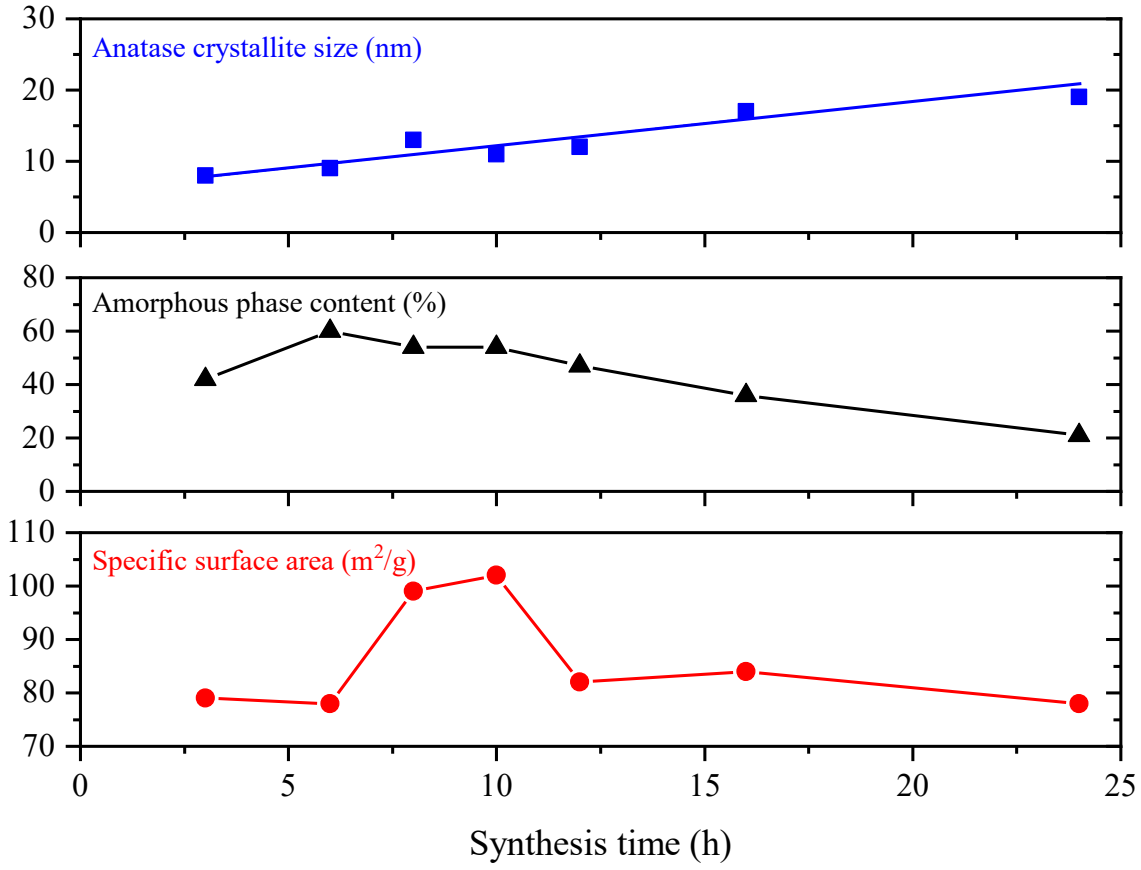

Figure S1. Evolution of the mean anatase crystallite size, the amorphous phase content and the specific surface area of the photocatalysts as a function of the synthesis time.

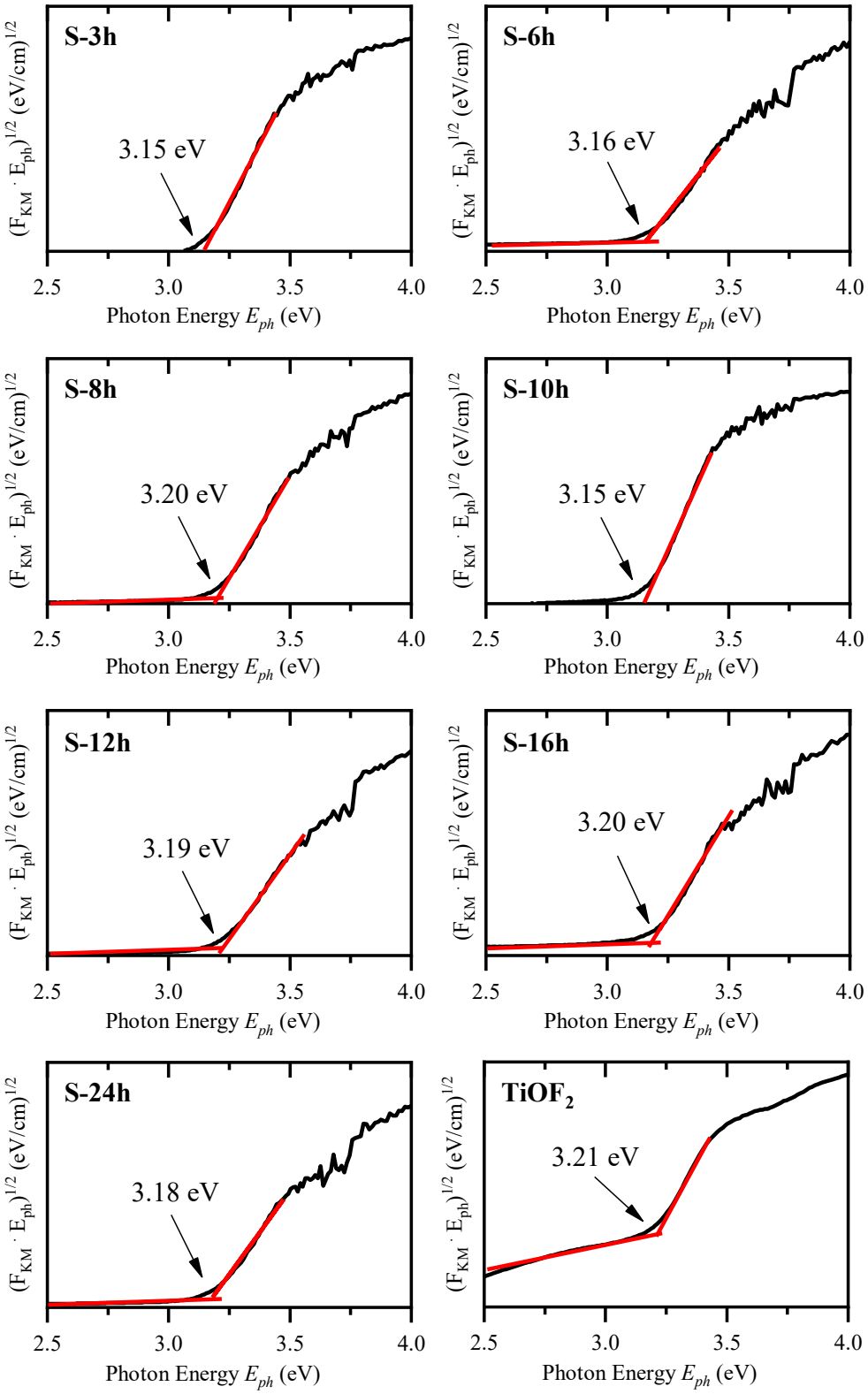

Figure S2. Tauc plots as the transformed Kubelka-Munk function *vs.* photon energy for the photocatalysts and $TiOF_2$.

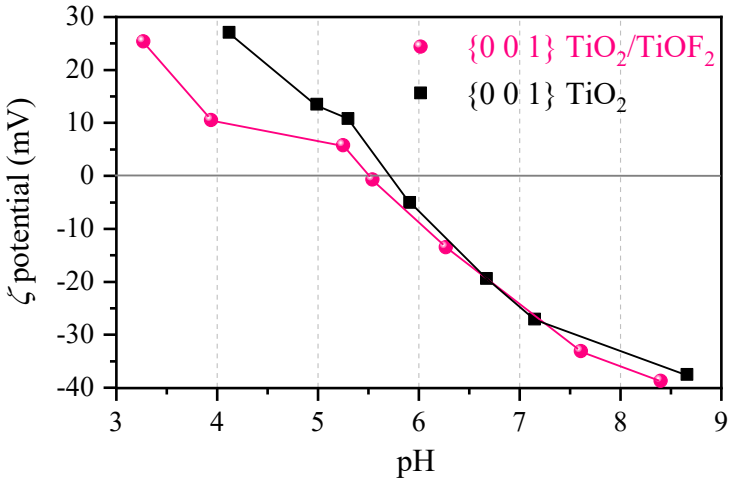

Figure S3. Zeta potential as a function of the pH for the pure {0 0 1} anatase and the composite with $TiOF_2$, I = 10^{-2} M KCl, [cat] = 0.2 g/L.

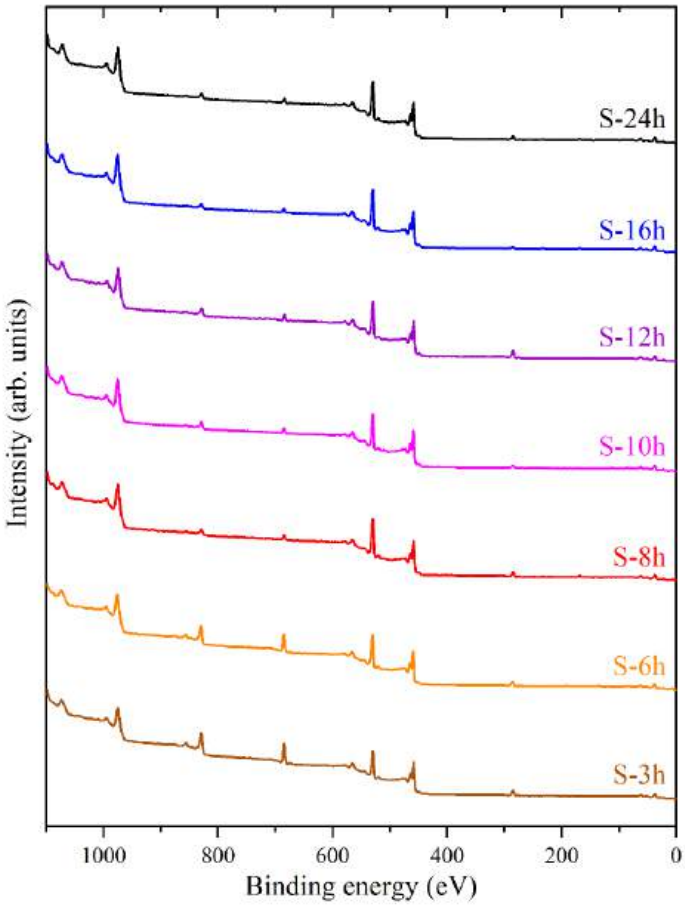

Figure S4. XPS survey spectrum for the photocatalysts.

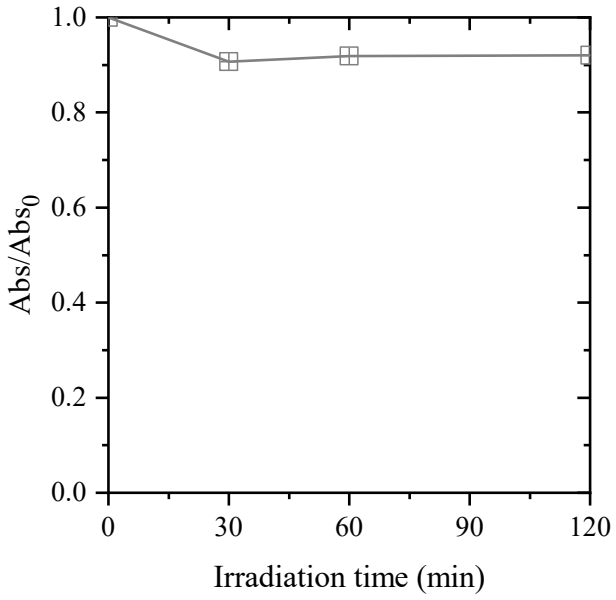

Figure S5. Time-evolution of the relative 4CP concentration during the photocatalytic degradation of 4CP under UV-A light using $TiOF_2$.

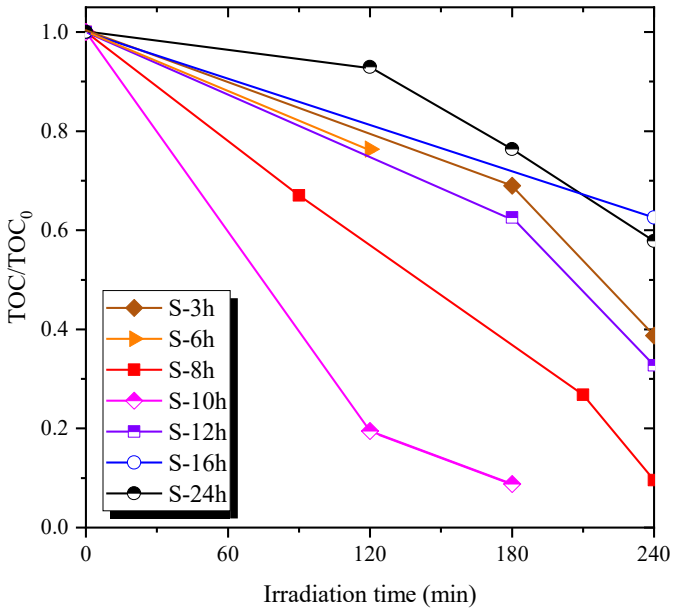

Figure S6. Time-evolution of the relative TOC concentration during the photocatalytic degradation of 4CP under UV-A light using the different photocatalysts.

a)

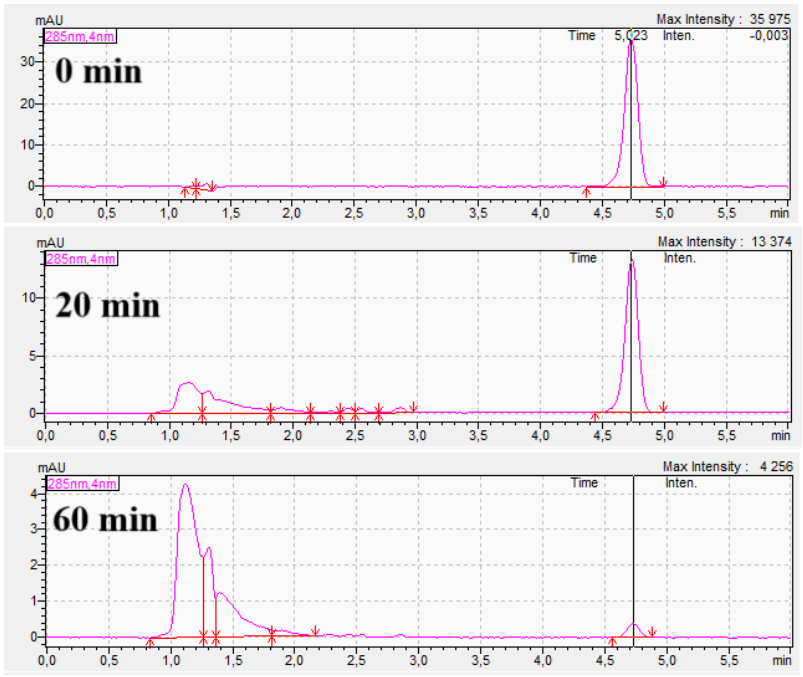

b)

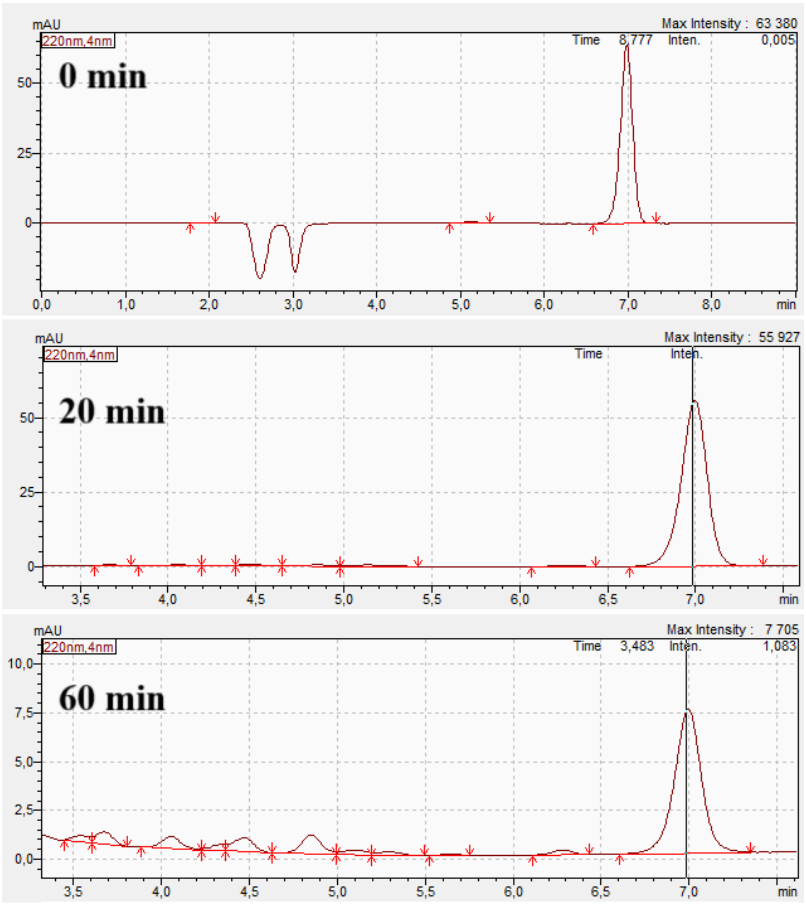

Figure S7. HPLC chromatograms during photocatalytic **a)** CBZ and **b)** MCL degradation under UV-A light over S-8h sample.

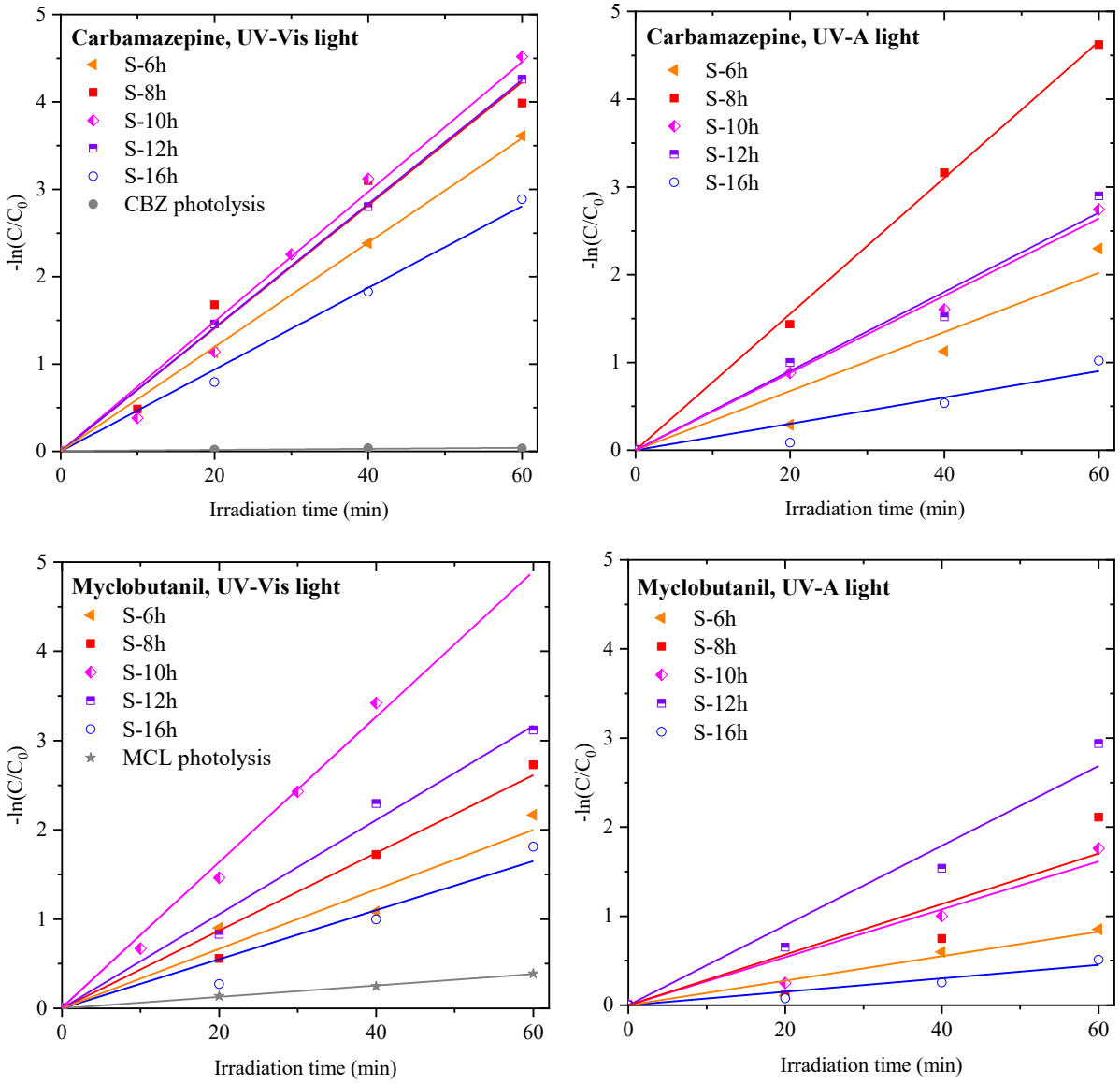

Figure S8. Linear relationship between *ln(C₀/C)* and the irradiation time in the case of the degradation of MCL and CBZ under UV-vis light and UV-A light using the different photocatalysts.

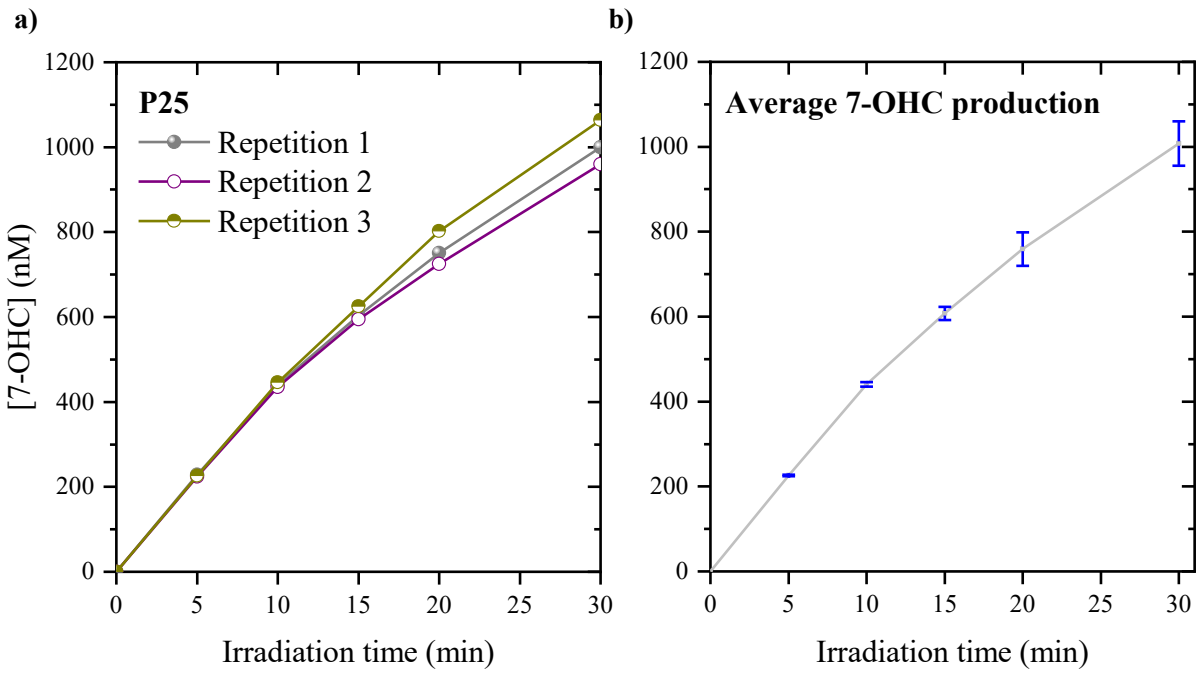

Figure S9. Statystical analysis of photocatalytic 7-OHC production observed under UV-A light using the Aeroxide P25 TiO_2 from Degussa: **a)** photocatalytic 7-OHC production in three independent measurements, **b)** average photocatalytic 7-OHC production and error bars.

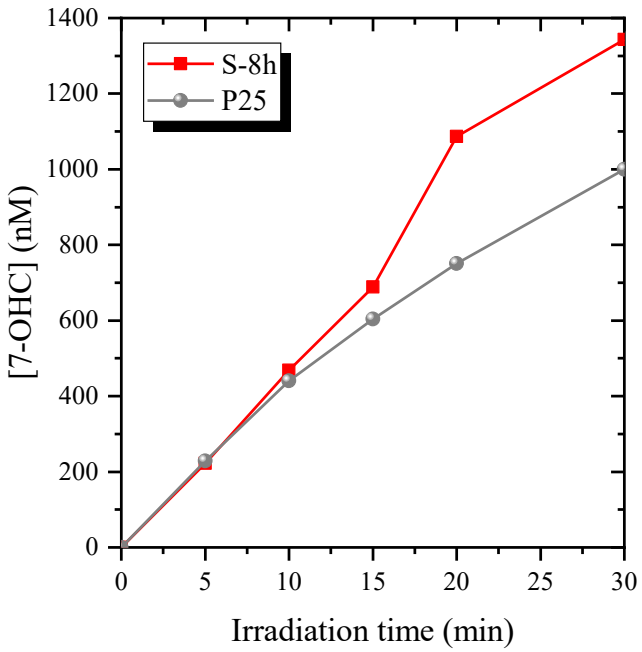

Figure S10. Photocatalytic 7-OHC production observed under UV-A light using the Aeroxide P25 TiO_2 from Degussa and the S-8h $TiO_2/TiOF_2$ photocatalyst.

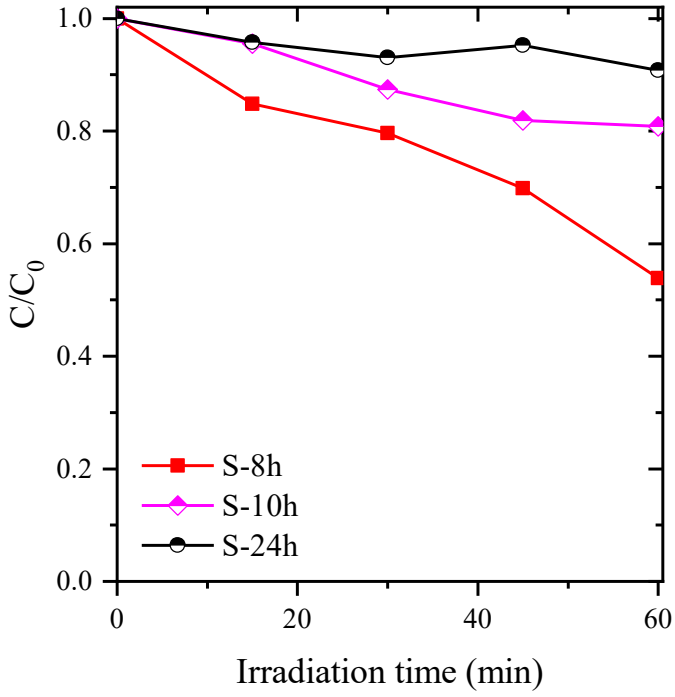

Figure S11. Photocatalytic Cr(VI) reduction observed under UV-A light over the {0 0 1} TiO_2 and {0 0 1} $TiO_2/TiOF_2$ photocatalysts.

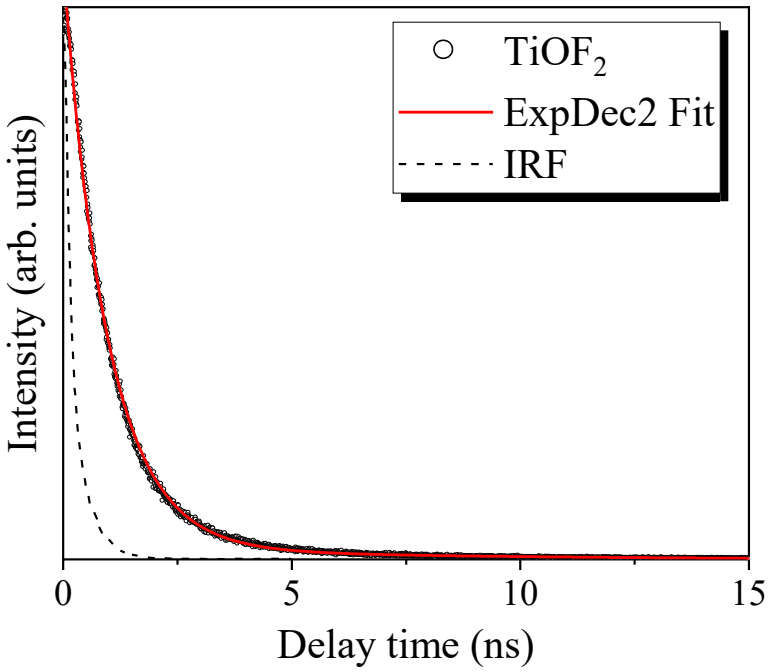

Figure S12. Example of experimental and fitted fluorescence decay curves. IRF: instrument response function.

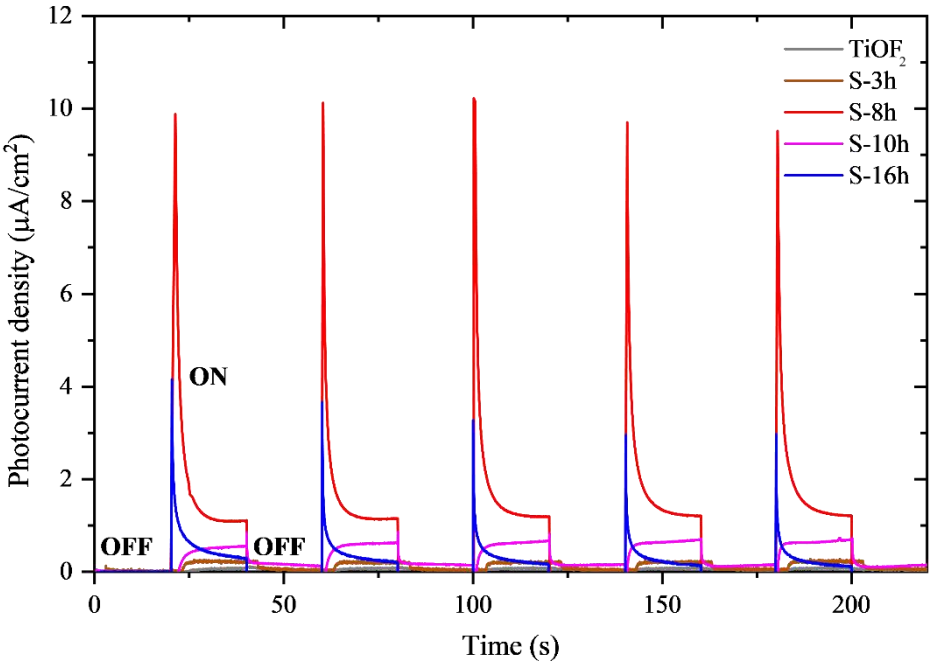

Figure S13. Photocurrent density vs. time measurements for selected $TiO_2/TiOF_2$ samples.

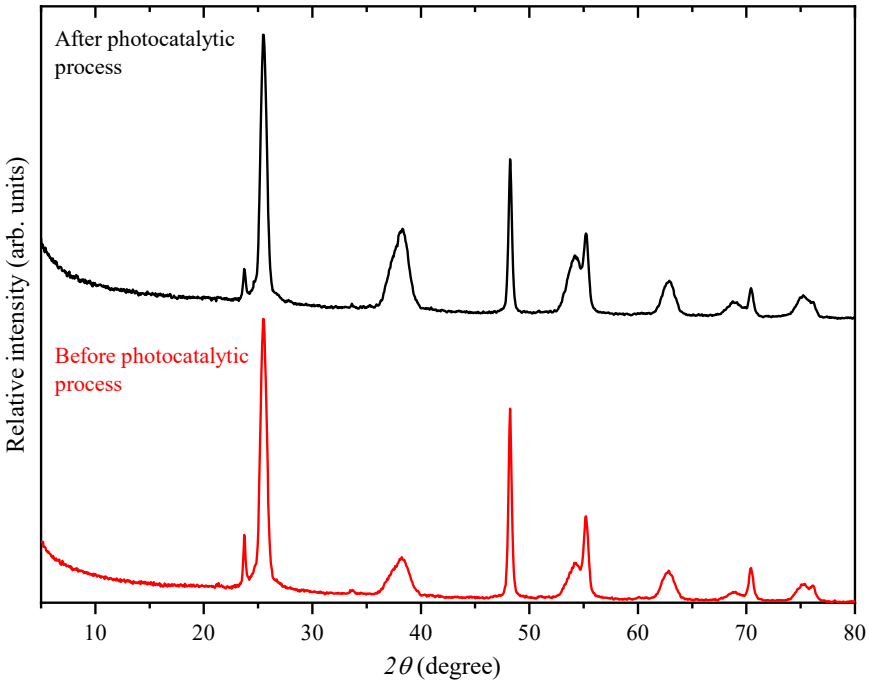

Figure S14. XRD patterns of the fresh S-8h $TiO_2/TiOF_2$ photocatalyst and the used photocatalyst after the MCL removal test.

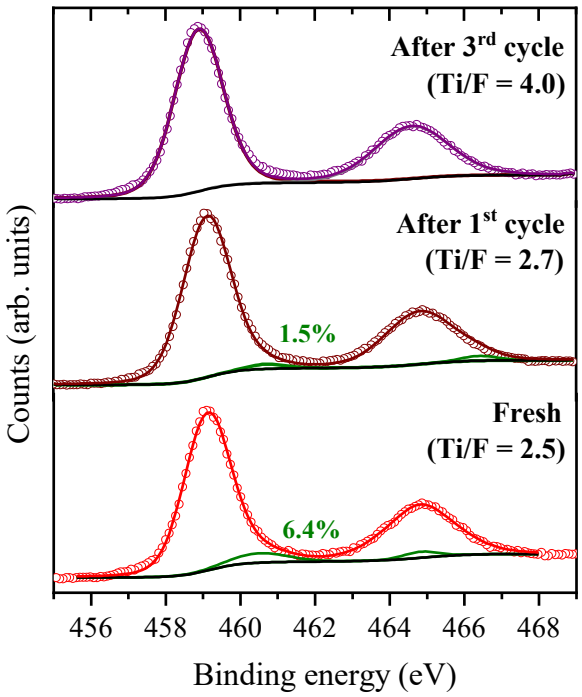

Figure S15. XPS spectra of the fresh S-8h $TiO_2/TiOF_2$ photocatalyst, and the used photocatalyst after the 1st and 3rd cycle of MCL degradation showing Ti2p signals with Gaussian fits and the corresponding Ti/F surface atomic ratio.

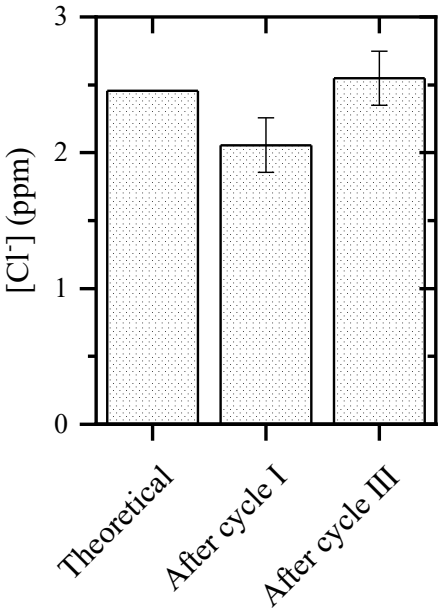

Figure S16. Cl^- concentration in the post-process water collected after the first and the third cycle using S-8h, in comparison to the theoretical value.

Table S1. Apparent kinetic rate constants for the MCL and CBZ degradation and the associated TOC conversion after 2 h of photocatalytic test with {0 0 1} TiO_2 and {0 0 1} $TiO_2/TiOF_2$ photocatalysts. Conditions: $[MCL]_0$ = 20 mg/dm^3; $[CBZ]_0$ = 14 mg/dm^3; [cat] = 1.0 g/dm^3.

Sample name	Photocatalytic process under UV-Vis light				Photocatalytic process under UV-A light			
	k_{MCL} (min^{-1})	X_{2h} TOC MCL (%)	k_{CBZ} (min^{-1})	X_{2h} TOC CBZ (%)	k_{MCL} (min^{-1})	X_{2h} TOC MCL (%)	k_{CBZ} (min^{-1})	X_{2h} TOC CBZ (%)
Photolysis	0.007	-	<0.001	-	<0.001	-	<0.001	-
S-6h	0.033	31	0.060	60	0.014	13	0.034	10
S-8h	0.044	59	0.070	51	0.028	70	0.078	40
S-10h	0.082	32	0.074	78	0.027	59	0.048	50
S-12h	0.053	22	0.071	7	0.045	18	0.045	16
S-16h	0.028	21	0.047	15	0.008	0	0.015	14

Table S2. Comparison of the photocatalytic performance with the literature.

Photocatalyst	Irradiation	Solution	Photocatalyst dosage (g·dm-^{3})	Rate constant (min^{-1})	Ref.
g-C_3N_4/TiO_2	24 W UV-A lamp λ_{max} = 365 nm, 3.25 mW/cm^2	CBZ, 10 ppm	0.1	0.0034	[11]
Ti_3C_2/TiO_2	300 W Xenon lamp with UG11 filter, aerated, light intensity not mentioned	CBZ, 14 ppm	2.0	0.056	[12]
FeS_2/Fe_2O_3	300 W Xenon lamp, light intensity not mentioned	CBZ, 2.5 ppm	0.8	0.0247	[13]
Al-doped ZnO/Fe_3O_4	15 W UV-A lamp, 3.3 mW/cm^2	CBZ, 1 ppm	0.5	0.079	[14]
Fe_3O_4@SiO_2/d-TiO_2/Pt	300 W Xenon lamp, 60 mW/cm^2, pH = 5.5 µl H_2O_2	CBZ, 14 ppm	0.5	0.030	[15]
S-10h	24 W UV-A lamp λ_{max} = 365 nm, 6 mW/cm^2	CBZ, 14 ppm	1.0	0.078	This work
S-10h	300 W Xenon lamp, 21 mW/cm^2	CBZ, 14 ppm	1.0	0.074	This work
$LaFeO_3$@TiO_2	1700 W Xenon lamp with filter (λ > 320 nm), 25 mW/cm^2	MCL, 20 ppm	1.0	0.0018	[16]
S-10h	300 W Xenon lamp, 21 mW/cm^2	MCL, 20 ppm	1.0	0.082	This work

Table S3. Bader charges for separated compounds and in heterojunction.

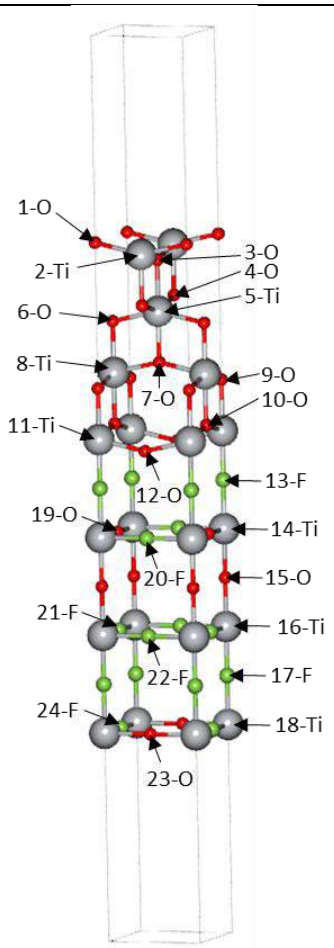

	No	Atom	Bader charge in heterojunction (e)	Bader charge separated (e)	Interface effect (e)
TiO_2 structure	1	O	-1.09569	-1.095925	-0.000235
	2	Ti	2.173393	2.173303	-0.000090
	3	O	-1.110932	-1.111525	-0.000593
	4	O	-1.077801	-1.077716	0.000085
	5	Ti	2.214556	2.214755	0.000199
	6	O	-1.12126	-1.121035	0.000225
	7	O	-1.102057	-1.101974	0.000083
	8	Ti	2.211906	2.211974	0.000068
	9	O	-1.094416	-1.094495	-0.000069
	10	O	-1.093058	-1.092811	0.000247
	11	Ti	2.190728	2.187264	-0.003464
	12	O	-1.085544	-1.092225	-0.006681
$TiOF_2$ structure	13	F	-0.564405	-0.550999	0.013406
	14	Ti	2.213933	2.212562	-0.001371
	15	O	-0.710102	-0.70984	0.000262
	16	Ti	2.117734	2.11760	-0.000134
	17	F	-0.575033	-0.574883	0.000150
	18	Ti	2.232746	2.232929	0.000183
	19	O	-0.976074	-0.977189	-0.001115
	20	F	-0.683455	-0.684121	-0.000666
	21	F	-0.703389	-0.703349	0.000040
	22	F	-0.703709	-0.703891	-0.000182
	23	O	-0.97455	-0.974874	-0.000324
	24	F	-0.684321	-0.684335	-0.000014
Total electron effect for TiO_2			-0.010235e		
Total electron effect for $TiOF_2$			0.010235e		

References:

[1] J. Tauc, Optical properties and electronic structure of amorphous Ge and Si, Mater. Res. Bull. 3 (1968) 37–46. https://doi.org/https://doi.org/10.1016/0025-5408(68)90023-8.

[2] C. Colbeau-Justin, M. Kunst, D. Huguenin, Structural influence on charge-carrier lifetimes in TiO_2 powders studied by microwave absorption, J. Mater. Sci. 38 (2003) 2429–2437. https://doi.org/10.1023/A:1023905102094.

[3] M.G. Méndez-Medrano, E. Kowalska, A. Lehoux, A. Herissan, B. Ohtani, D. Bahena, V. Briois, C. Colbeau-Justin, J.L. Rodríguez-López, H. Remita, Surface Modification of

TiO_2 with Ag Nanoparticles and CuO Nanoclusters for Application in Photocatalysis, J. Phys. Chem. C 120 (2016) 5143–5154. https://doi.org/10.1021/acs.jpcc.5b10703.

[4] P. Giannozzi, O. Andreussi, T. Brumme, O. Bunau, M. Buongiorno Nardelli, M. Calandra, R. Car, C. Cavazzoni, D. Ceresoli, M. Cococcioni, N. Colonna, I. Carnimeo, A. Dal Corso, S. de Gironcoli, P. Delugas, R. A. DiStasio Jr, A. Ferretti, A. Floris, G. Fratesi, G. Fugallo, R. Gebauer, U. Gerstmann, F. Giustino, T. Gorni, J. Jia, M. Kawamura, H-Y. Ko, A. Kokalj, E. Küçükbenli, M. Lazzeri, M. Marsili, N. Marzari, F. Mauri, N. L. Nguyen, H-V. Nguyen, A. Otero-de-la-Roza, L. Paulatto, S. Poncé, D. Rocca, R. Sabatini, B. Santra, M. Schlipf, A. P. Seitsonen, A. Smogunov, I. Timrov, T. Thonhauser, P. Umari, N. Vast, X. Wu, S. Baroni, Advanced capabilities for materials modelling with Quantum ESPRESSO, J. Condens. Matter Phys. 29 (2017). https://doi.org/https://doi.org/10.1088/1361-648X/aa8f79.

[5] P. Giannozzi, S. Baroni, N. Bonini, M. Calandra, R. Car, C. Cavazzoni, D. Ceresoli, G.L. Chiarotti, M. Cococcioni, I. Dabo, A. Dal Corso, S. De Gironcoli, S. Fabris, G. Fratesi, R. Gebauer, U. Gerstmann, C. Gougoussis, A. Kokalj, M. Lazzeri, L. Martin-Samos, N. Marzari, F. Mauri, R. Mazzarello, S. Paolini, A. Pasquarello, L. Paulatto, C. Sbraccia, S. Scandolo, G. Sclauzero, A.P. Seitsonen, A. Smogunov, P. Umari, R.M. Wentzcovitch, QUANTUM ESPRESSO: A modular and open-source software project for quantum simulations of materials, J. Condens. Matter Phys. 21 (2009). https://doi.org/10.1088/0953-8984/21/39/395502.

[6] S. Selcuk, A. Selloni, Facet-dependent trapping and dynamics of excess electrons at anatase TiO_2 surfaces and aqueous interfaces, Nat. Mater. 15 (2016) 1107–1112. https://doi.org/10.1038/nmat4672.

[7] P. Garcia-Muñoz, F. Fresno, C. Lefevre, D. Robert, N. Keller, Synergy effect between photocatalysis and heterogeneous photo-Fenton catalysis on Ti-doped $LaFeO_3$ perovskite for high efficiency light-assisted water treatment, Catal. Sci. Technol. 10 (2020) 1299–1310. https://doi.org/10.1039/c9cy02269d.

[8] P. Garcia-Muñoz, C. Lefevre, D. Robert, N. Keller, Ti-substituted $LaFeO_3$ perovskite as photoassisted CWPO catalyst for water treatment, Appl. Catal. B 248 (2019) 120–128. https://doi.org/10.1016/j.apcatb.2019.02.030.

[9] Y. Nosaka, A.Y. Nosaka, Understanding Hydroxyl Radical (•OH) Generation Processes in Photocatalysis, ACS Energy Lett. 1 (2016) 356–359. https://doi.org/10.1021/acsenergylett.6b00174.

[10] T. Hirakawa, K. Yawata, Y. Nosaka, Photocatalytic reactivity for $O2^{\cdot-}$ and $OH\cdot$ radical formation in anatase and rutile TiO_2 suspension as the effect of H_2O_2 addition, Appl. Catal. A 325 (2007) 105–111. https://doi.org/10.1016/j.apcata.2007.03.015.

[11] A. Kane, L. Chafiq, S. Dalhatou, P. Bonnet, M. Nasr, N. Gaillard, J.M. Dangwang Dikdim, G. Monier, A.A. Assadi, H. Zeghioud, g-C_3N_4/TiO_2 S-scheme heterojunction photocatalyst with enhanced photocatalytic Carbamazepine degradation and mineralization, J. Photochem. Photobiol. A Chem. 430 (2022) 113971. https://doi.org/10.1016/j.jsamd.2021.11.004.

[12] A. Grzegórska, P. Głuchowski, J. Karczewski, J. Ryl, I. Wysocka, K. Siuzdak, G. Trykowski, K. Grochowska, A. Zielińska-Jurek, Enhanced photocatalytic activity of accordion-like layered Ti_3C_2 (MXene) coupled with Fe-modified decahedral anatase particles exposing {1 0 1} and {0 0 1} facets, Chem. Eng. J. 426 (2021). https://doi.org/10.1016/j.cej.2021.130801.

[13] Q. Guo, G. Tang, W. Zhu, Y. Luo, X. Gao, In situ construction of Z-scheme FeS_2/Fe_2O_3 photocatalyst via structural transformation of pyrite for photocatalytic degradation of carbamazepine and the synergistic reduction of Cr(VI), J. Environ. Sci. 101 (2021) 351–360. https://doi.org/10.1016/j.jes.2020.08.029.

[14] A. Majumder, A.K. Gupta, M. Sillanpää, Insights into kinetics of photocatalytic degradation of neurotoxic carbamazepine using magnetically separable mesoporous Fe_3O_4 modified Al-doped ZnO: Delineating the degradation pathway, toxicity analysis and application in real hospital wastewater, Colloids Surf. A Physicochem. Eng. Asp. 648 (2022). https://doi.org/10.1016/j.colsurfa.2022.129250.

[15] S. Dudziak, Z. Bielan, P. Kubica, A. Zielińska-Jurek, Optimization of carbamazepine photodegradation on defective TiO_2-based magnetic photocatalyst, J. Environ. Chem. Eng. 9 (2021). https://doi.org/10.1016/j.jece.2021.105782.

[16] P. Garcia-Muñoz, F. Fresno, J. Ivanez, D. Robert, N. Keller, Activity enhancement pathways in $LaFeO_3@TiO_2$ heterojunction photocatalysts for visible and solar light driven degradation of myclobutanil pesticide in water, J. Hazard. Mater. 400 (2020) 123099. https://doi.org/10.1016/j.jhazmat.2020.123099.

4.5. Chapter V: $BiVO_4$ modification by vanadium precursor design and CuO_x sub-nanoclusters deposition for pharmaceuticals degradation and PMS activation under visible light

Based on **[P6]** M. Kowalkińska, A. Maximenko, A. Szkudlarek, K. Sikora, A. Zielińska-Jurek, *Addressing challenges of $BiVO_4$ light-harvesting ability through vanadium precursor engineering and sub-nanoclusters deposition for peroxymonosulfate-assisted photocatalytic pharmaceuticals removal*, Separation and Purification Technology, 351, 2024, 127643.

The main motivation of performing these studies was the formation of microcrystals by bismuth orthovanadate, which limits the light-harvesting ability, and the fast recombination of photogenerated charge carriers, which hinders its photocatalytic activity toward PhACs oxidation. In this regard, a dual approach was proposed to enhance the photoactivity – reducing the size of the precursor and interface modification.

First, self-synthesized ammonium metavanadate (NH_4VO_3) was for the first time applied to $BIVO_4$ fabrication. This vanadium precursor (NHV_W) exhibited smaller particles and a more stoichiometric structure than the commercial NH_4VO_3 from Merck (NHV_C). The comparison of both precursors is presented in Figure 4.11.

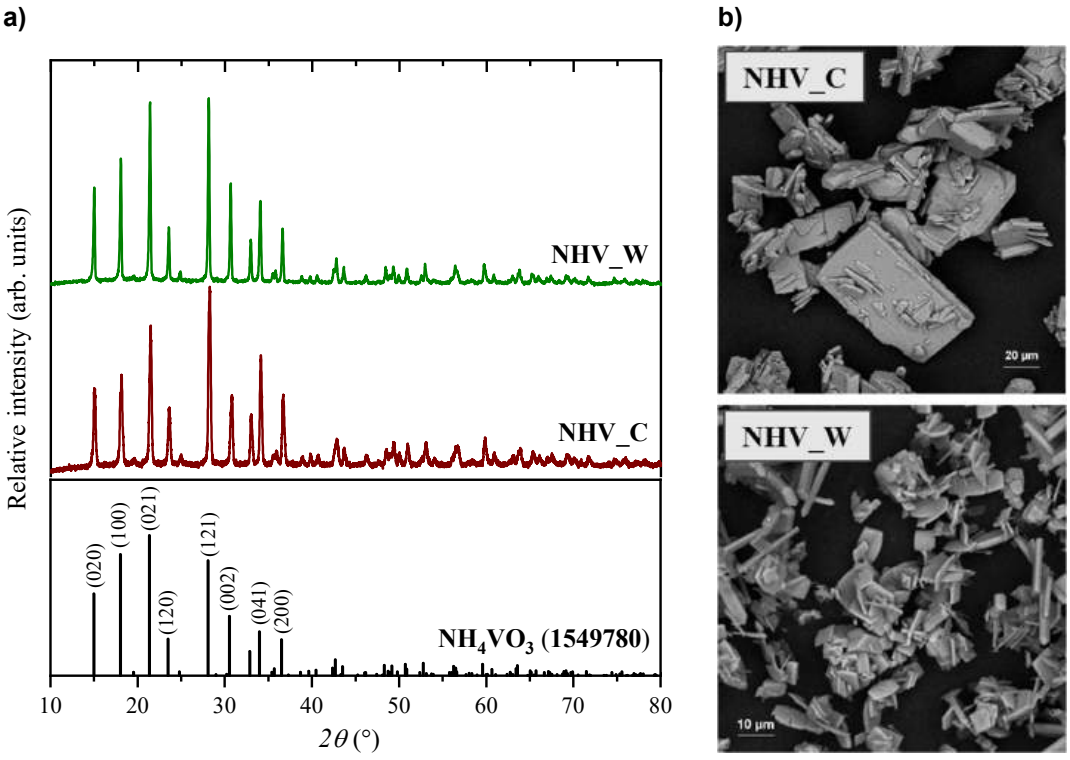

Figure 4.11. a) XRD pattern and **b)** SEM images of NH_4VO_3 precursors.

When the as-obtained precursor was used instead of the commercial counterpart, the resulting (m–s) $BiVO_4$ (BVO_NHV_W) possessed a lower particle size and better dispersion in water. These morphological changes resulted in significantly improved light absorption, as confirmed by local volume rate of photon absorption (LVRPA) analysis using a six-flux radiation model. The comparison of $BiVO_4$ photocatalysts is presented in Figure 4.12.

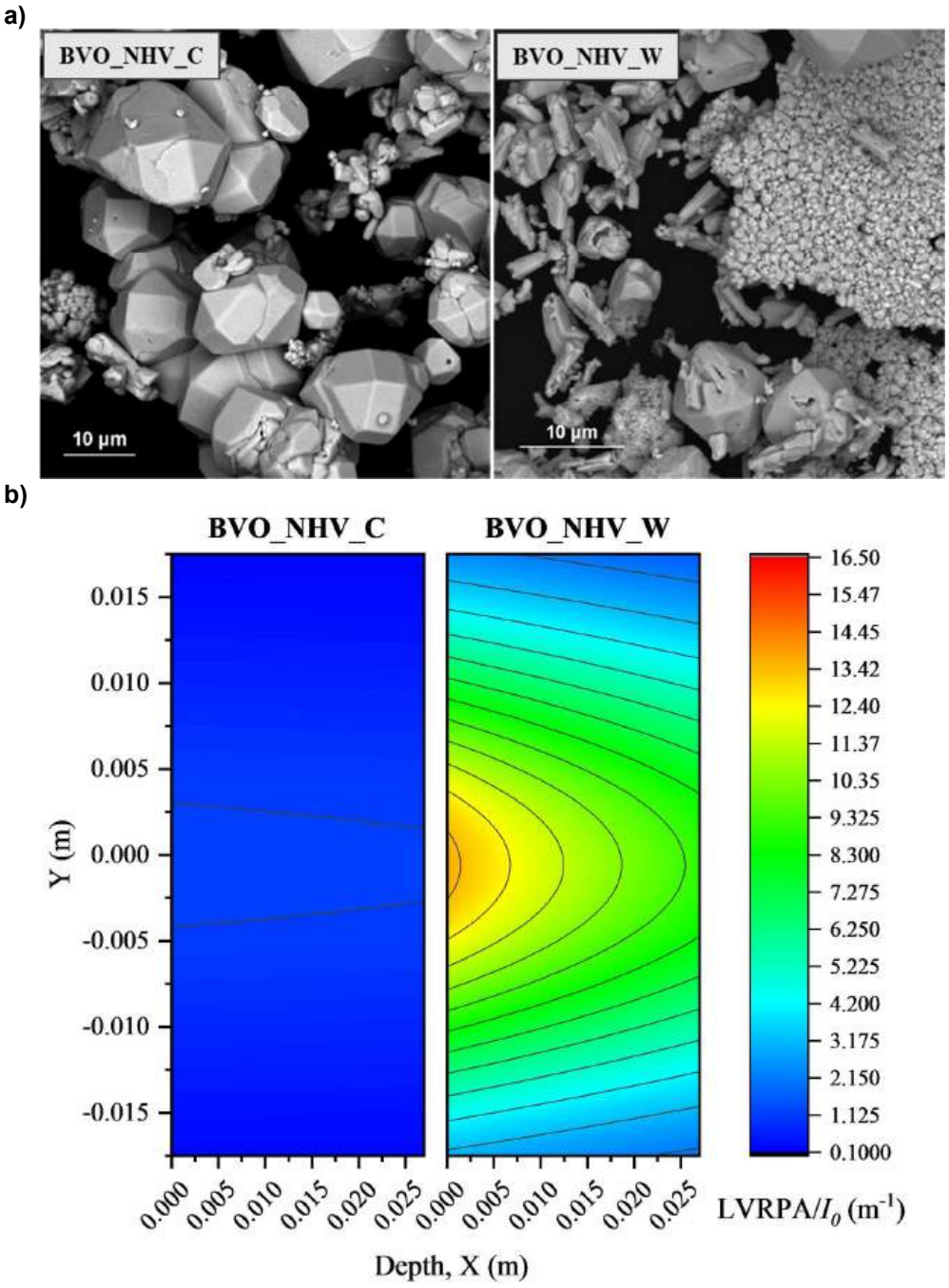

Figure 4.12. a) SEM images and **b)** corresponding LVRPA distribution in the cross-section of photoreactor of $BiVO_4$ photocatalysts.

These photocatalysts were investigated toward photocatalytic degradation of naproxen (NPX) and ofloxacin (OFL) under visible light (λ > 420 nm). In the second step, the interface of $BiVO_4$ was modified by copper species. X-ray absorption near edge structure (XANES) spectroscopy of Cu-K edge confirmed the presence of CuO_x sub-nanoclusters with mixed valence state between Cu(I) and Cu(II). The average oxidation state of copper species was +1.48 (Figure 4.13.a). This modification caused a several-fold increase in photocurrent response compared to pristine $BiVO_4$, indicating more efficient charge transport. As a consequence, the apparent kinetic rate constants for the photocatalytic degradation of NPX and OFL arisen 1.6- and 3.3-fold, respectively (Figure 4.13.b).

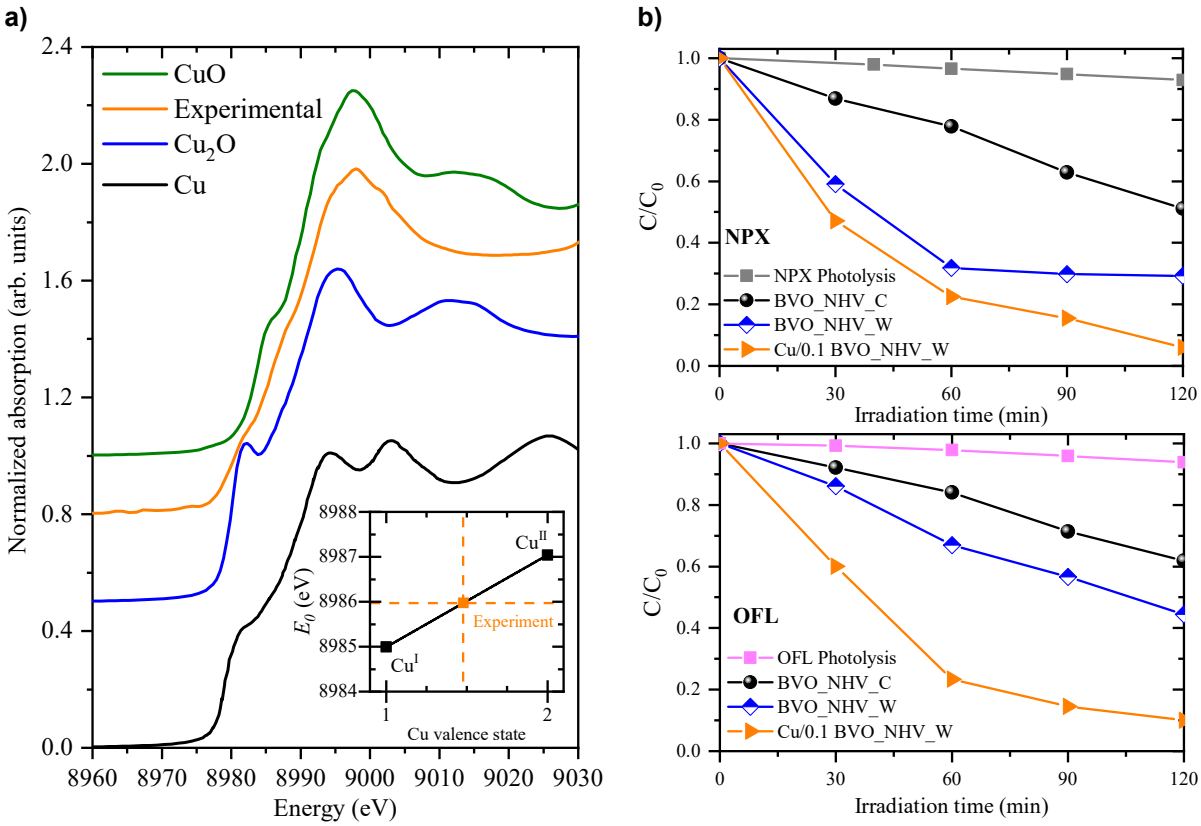

Figure 4.13. a) Normalized Cu–K edge absorption coefficient for sample Cu/0.1 BVO_NHV_W in relation to reference materials; inset shows the estimation of an average chemical state, **b)** Photocatalytic degradation of NPX and OFL over $BiVO_4$-based photocatalysts under visible light (λ > 420 nm).

Next to conventional heterogeneous photocatalysis, the $BiVO_4$-based semiconductors were also applied in peroxymonosulfate-assisted reactions under visible light. The presence of a low amount of PMS (0.1 mM) accelerated the degradation of PhACs, achieving complete degradation of NPX within 60 minutes and almost complete removal of ofloxacin (98.2%) within 120 minutes, as shown in Figure 4.14.

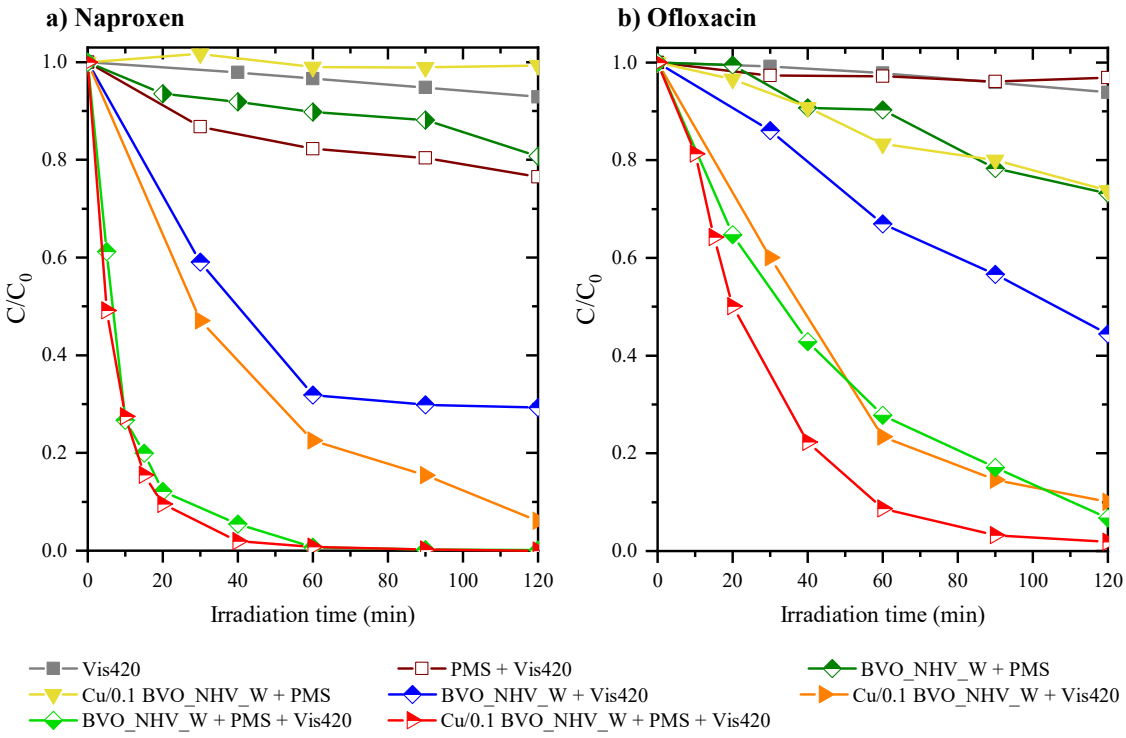

Figure 4.14. PMS-assisted photocatalytic degradation of **a)** NPX and **b)** OFL over $BiVO_4$-based photocatalysts under visible light (λ > 420 nm).

The combination $CuO_x/BiVO_4$/PMS/Vis420 showed satisfactory stability and reusability over three consecutive cycles, although excessive PMS concentrations were found to induce bismuth leaching, highlighting the importance of controlling oxidant dosage. Finally, ecological risk assessment was discussed by means of ECOSAR and Microtox bioassay using bioluminescent *Vibrio fischeri* bacteria. ECOSAR data showed the harmful effect of NPX and OFL intermediate products, which were more toxic than the initial compounds. However, the post-process wastewater after treatment of NPX solution with $CuO_x/BiVO_4$/PMS/Vis420 system exhibited a lower inhibition rate compared to unmodified photocatalysts, ensuring that the process remained environmentally safe. Although these results were not achieved for the OFL solution, the toxic effect is not permanent, as confirmed by the reduced gamma value (Γ).

The authors used ASTRA beamline of the National Synchrotron Radiation Centre SOLARIS (Cracow, Poland). Moreover, these studies were awarded twice – received distinction in the X edition of the Polish Academy of Sciences in Gdańsk Award for young scientists and Best Poster Award during 12th European Conference on Solar Chemistry and Photocatalysis: Energy and Environmental Applications (SPEA12), funded by the Royal Society of Chemistry

Separation and Purification Technology 351 (2024) 127643

Contents lists available at ScienceDirect

Separation and Purification Technology

journal homepage: www.elsevier.com/locate/seppur

Addressing challenges of $BiVO_4$ light-harvesting ability through vanadium precursor engineering and sub-nanoclusters deposition for peroxymonosulfate-assisted photocatalytic pharmaceuticals removal

Marta Kowalkińska [a,*], Alexey Maximenko [b], Aleksandra Szkudlarek [c], Karol Sikora [d], Anna Zielińska-Jurek [a,*]

[a] Department of Process Engineering and Chemical Technology, Faculty of Chemistry, Gdansk University of Technology, G. Narutowicza 11/12 Street, 80-233 Gdansk, Poland
[b] SOLARIS National Synchrotron Radiation Centre, Jagiellonian University, Czerwone Maki 98 Street, 30-392 Krakow, Poland
[c] AGH University of Krakow, Academic Centre for Materials and Nanotechnology, Av. Mickiewicza 30, 30-059 Krakow, Poland
[d] Department of Inorganic Chemistry, Faculty of Pharmacy, Medical University of Gdansk, M. Sklodowskiej-Curie 3a Street, 80-210 Gdansk, Poland

ARTICLE INFO

Keywords:
$BiVO_4$
Peroxymonosulfate
CuO_x sub-nanoclusters
LVRPA

ABSTRACT

In this study, we present a complex approach for increasing light utilisation and peroxymonosulfate (PMS) activation in $BiVO_4$-based photocatalyst. This involves two key considerations: the design of the precursor for $BiVO_4$ synthesis and interface engineering through CuO_x sub-nanoclusters deposition. The designed precursor of ammonium methavanadate (NH_4VO_3, NHV) leads to reduction in particle size, better dispersion and improved light harvesting ability, confirmed by the calculations of the local volume rate of photon absorption (LVRPA) using the Six-Flux Radiation Absorption-Scattering model. The morphological changes result in a significant improvement in photocatalytic activity under visible light for the degradation of pharmaceuticals (naproxen and ofloxacin) compared to the commercial NH_4VO_3. Additionally, CuO_x sub-nanoclusters were deposited on designed $BiVO_4$ and characterised using X-ray absorption near edge structure (XANES). The presence of sub-nanoclusters enhanced charge carriers separation, resulting in an increase in the apparent rate constants of 1.60 and 3.32-times for photocatalytic NPX and OFL removal, respectively. The application of obtained Vis light active photocatalysts in the presence of 0.1 mM PMS resulted in remarkably more efficient degradation of NPX (100 % within 60 min) and OFL (98.2 % within 120 min). PMS/Vis420/CuO_x/$BiVO_4$ system exhibited high stability and reusability in the subsequent cycles of photodegradation. However, high PMS dosage induced Bi leaching which may cause the instability of the photocatalyst. Finally, to address the environmental implications of pharmaceutical removal and adhere to the Guidelines for drinking-water quality, toxicity assessments using *Vibrio fischeri* bacteria were performed and compared to a quantitative structure–activity relationship (QSAR) model.

1. Introduction

Over the last few years, the level of development of the health system has risen sharply, contributing to improving the quality of human life and reducing mortality. One of the most important achievements of modern medicine was the discovery of numerous pharmaceuticals such as antibiotics and non-steroidal anti-inflammatory drugs (NSAIDs), which have helped treat many diseases. However, the widespread use of pharmaceuticals has led to their detection in trace amounts in surface and groundwater [1,2]. An example of a compound which is not susceptible to biological degradation is ofloxacin (OFL), a fluoroquinolone antibiotic with a broad spectrum of activity against both gram-positive and gram-negative bacteria, frequently detected in European effluents [3–6]. Simultaneously, naproxen (NPX) is a non-steroidal anti-inflammatory drug commonly used without prescription to treat pain and inflammation, which is the most frequently detected in surface- and groundwater in Poland [7]. Studies have shown that even at low concentrations, naproxen can have negative effects of long-term exposure on aquatic organisms, such as fish and invertebrates [8]. The presence of active pharmaceutical ingredients in water can be dangerous

* Corresponding authors.
E-mail addresses: marta.kowalkinska@pg.edu.pl (M. Kowalkińska), annjurek@pg.edu.pl (A. Zielińska-Jurek).

https://doi.org/10.1016/j.seppur.2024.127643
Received 9 February 2024; Received in revised form 11 April 2024; Accepted 22 April 2024
Available online 24 April 2024

to the environment for several reasons. First, they can accumulate in the tissues of aquatic organisms, and enter the food chain, potentially affecting human health through the consumption of contaminated seafood [9]. Moreover, antibiotics are toxic to aquatic life and can promote the growth of antibiotic-resistant bacteria and other pathogens, which can lead to the spread of drug-resistant infections in humans and animals [10]. These environmental dangers underscore the importance of reducing the release of pharmaceuticals into the environment and finding effective technology to remove them from wastewater.

Recently, Advanced Oxidation Processes (AOPs) have gained significant attention due to their ability to degrade a wide range of contaminants, including xenobiotics that resist conventional treatment methods. The most interesting advantage of these techniques is that they can effectively remove persistent organic pollutants from effluents, typically involving the generation of powerful oxidants that are capable of breaking down complex organic molecules into simpler, less harmful compounds [11–13]. Among AOP techniques, heterogeneous photocatalysis and sulfate-radical advanced oxidation processes (SR-AOP) have become the most extensively studied in the last few years. Peroxymonosulfate compounds (PMS) act as strong oxidising agents, capable of generating highly reactive sulfate radicals $SO_4^{\cdot-}$ under UV light or heat activation as well as transition metals presence [14–16]. Coupling photocatalysis with $SO_4^{\cdot-}$ generation in peroxymonosulfate-assisted photocatalysis (PAP) allows to enhance the degradation efficiency due to the generation of additional reactive species, such as hydroxyl radicals (·OH), through photocatalytic processes [17]. This synergistic combination results in the fast and efficient degradation of persistent pollutants, including pharmaceuticals, making peroxymonosulfate-assisted photocatalysis a promising technology for advanced water treatment applications with potential environmental and economic benefits [18–20].

However, the practical application of PAP processes for wastewater treatment remains challenging. Firstly, PMS concentration should be carefully controlled because it directly affects pH and generates high levels of sulfate ions, which may be toxic to aquatic life. The lowest threshold concentration for SO_4^{2-} is approximately 250 ppm suggested by the World Health Organization (WHO) in the Guidelines for Drinking-Water Quality (2004, updated in 2022) [21]. Although there is an increasing number of studies concerning SR-AOP, too high concentrations of PMS are used that exceed permitted standards [22]. Moreover, the side effects of activated PMS on in-situ environmental microorganisms in water have not been clear yet. The toxicity rate of degraded pharmaceuticals and their by-products is crucial for evaluation whether the process is environmentally friendly [23]. Therefore, a rationally designed system with appropriate photocatalyst type, which will be able to generate hydroxyl radicals upon irradiation and activate PMS at low dosage, will be crucial regarding the application of PAP processes.

Considering all the above aspects, bismuth orthovanadate ($BiVO_4$, BVO) has received considerable interest due to visible light activity, chemical stability and facile preparation methods [24–26]. Several studies have shown that $BiVO_4$ can also activate PMS, making this photocatalyst promising for PAP processes [27–29]. However, there are several drawbacks of BVO application in water treatment. Firstly, this photocatalyst suffers from low conduction band potential (~0.3–0.4 V vs. NHE) and fast recombination of photoinduced electron–hole pairs. Furthermore, $BiVO_4$ usually forms microcrystals with smooth facets and low surface area, resulting in poor photocatalyst dispersion in water [24,30,31]. Therefore, rational design of BVO material with satisfactory light harvesting and limited recombination rate is desired. One of the promising methods of promoting charge carriers separation is creating a heterojunction [28,32,33] or deposition of metal clusters [34]. Especially, modification by CuO_x species has captured extensive research interest due to the distinctive Cu^{2+}/Cu^{+} redox couple, which is beneficial for either enhancing photocatalytic activity or PMS activation [35]. Among existing CuO_x species, nanosized structures like nanoclusters have numerous advantages, including their low-coordination environment and unique electronic properties [34]. Therefore, the deposition of nanoclusters on $BiVO_4$ can guarantee the development of number of active sites in the final photocatalyst.

In this regard, a novel approach of $BiVO_4$ synthesis using self-synthesised ammonium metavanadate (NH_4VO_3, NHV) as a precursor is for the first time reported in this study. Local volume rate of photon absorption (LVRPA) analysis showed that the proposed precursor significantly improved the light harvesting ability of $BiVO_4$, compared to the photocatalyst in which commercial NH_4VO_3 was used. Moreover, the interface modification by CuO_x sub-nanoclusters enhanced visible light activity in reactions of naproxen and ofloxacin degradation, which are emerging organic pollutants present in water worldwide. The structure of interface-engineered photocatalysts was studied by X-ray absorption near edge structure (XANES). Finally, the toxicity assessment of post-process water was measured experimentally using *Vibrio fischeri* bacteria and compared to the quantitative structure–activity relationship (QSAR) model. Despite the existing reports describing the importance of light use by photocatalysts and the role of PMS on the toxicity rate, this topic remains new and represents an important study in the field of PAP processes.

2. Experimental section

For a two-step synthesis of $BiVO_4$ (BVO), vanadium(V) oxide (V_2O_5), ammonium acetate, sodium dodecyl sulfate (SDS), bismuth(III) nitrate pentahydrate ($Bi(NO_3)_3 \cdot 5\ H_2O$), hydroxylamine hydrochloride ($NH_2OH \cdot HCl$), copper chloride anhydrous ($CuCl_2$) were provided by Chemat (Poland) and used without further purification. For photocatalytic degradation of pharmaceuticals, naproxen (NPX), ofloxacin (OFL) and OXONE® with analytical grade was provided by Merck.

2.1. Synthesis of NH_4VO_3

The demonstrated synthesis of ammonium metavanadate (NHV) was based on Prześniak-Welenc *et al.* with the modifications [36]. 0.25 g V_2O_5 was dispersed in 300 cm^3 of 1.25 M solution of ammonium acetate in water using an ultrasonic bath for 30 min. Next, the yellow uniform mixture was left for 24 h. After this time, white solids precipitated from the initially yellow solution. This precipitate was separated by centrifugation (6000 rpm) and washed several times with anhydrous ethanol. The final product was dried at 40 °C under vacuum conditions (<100 mbar) to dry mass. This precursor was denoted as NHV_W, where the commercial NH_4VO_3, provided by Merck, was labeled as NHV_C.

2.2. Synthesis of $BiVO_4$ and interface modification

In a typical procedure, three 2 M nitric acid solutions were prepared separately: 2 mmol of NHV in 10 cm^3, 2 mmol of $Bi(NO_3)_3 \cdot 5\ H_2O$ in 10 cm^3 and 0.2 g SDS in 15 cm^3. These three solutions were stirred for 30 min and then mixed together. Subsequently, the mixture was diluted with water to volume 70 cm^3 and transferred to a 100 cm^3 Teflon-lined autoclave. The reactor was heated to 150 °C and kept at this temperature for 24 h in an electric oven. After natural cooling to room temperature, the obtained products were separated through centrifugation and thoroughly washed with deionised water and ethanol to remove the residual ions and surfactant. After drying at 80 °C to dry mass, the yellow powders were obtained. The $BiVO_4$ photocatalysts were denoted similar to NHV series, but with the BVO prefix added to the label.

Interface modification was carried out as follows: 1 g of SDS surfactant was dissolved in 90 cm^3 of water. Secondly, BVO_NHV_W powder was added to this solution. After obtaining a uniform mixture, 1.5 cm^3 of 0.1 M $CuCl_2$ aqueous solution was dropped into the mixture. After magnetic stirring for 1 h, 2.5 cm^3 of 0.2 M $NH_2OH \cdot HCl$ aqueous solution was slowly dropped into the above suspension. The mixture was kept for stirring overnight. The obtained product was collected by centrifugation, washed several times with distilled water and ethanol,

and dried at 50 °C under vacuum conditions (<100 mbar) to dry mass. To find the most optimum Cu/Bi content, several masses of BVO were used in the synthesis (0.075 g, 0.10 g and 0.125 g). CuO_x-modified samples were denoted as Cu-X BVO_NHV_W, where X is the mass of BVO_NHV_W photocatalyst used during modifications.

2.3. Material characterisation

The crystal structure and phase identification of as-synthesised samples were investigated by X-ray powder diffraction (Rigaku MiniFlex 600 X-Ray diffractometer, Tokyo, Japan) with Cu Kα radiation. Data were collected in a 2θ range of 10-80° with a scan speed of 1° min^{-1} and scan steps 0.01°. The Rietveld refinement, including specimen displacement, lattice parameters, polynomial coefficients for the background function, profile parameters, and Gaussian and Lorentzian profile coefficients, were performed with the HighScore Plus software package (Malvern Panalytical, Malvern, United Kingdom) and the Crystallography Open Database. The crystallite size was estimated on the basis of Scherrer's equation. The bond identification in samples was determined by Fourier-transform infrared spectroscopy (FTIR) in the transmittance mode. The FTIR Nicolet iS10 (Thermo Fisher Scientific, Waltham, MA, USA) spectrometer was used at room temperature in the wavenumber range from 4000 to 400 cm^{-1}. The pellets containing 95 % of potassium bromide and 5 % (wt.) of a photocatalyst were analysed in each measurement.

Morphologies of the as-prepared precursors and photocatalysts were investigated using scanning electron microscopy (Phenom Pro 6) with a back-scattered electron detector (BSE). Transmission electron microscopy (TEM) analysis was carried out using the ThermoFisher Tecnai TF 20 X-TWIN microscope. The water nanoparticle solution was drop-casted onto the Au TEM grid. The microscope is equipped with an Eagle 2 k HR camera and operates with Field Emission Gun. The primary beam energy was set to 200 keV. Selected area electron diffraction (SAED) was conducted using an aperture of 800 nm diameter.

The X-ray photoelectron spectroscopy (XPS) analysis was carried out to determine the surface chemical state. The sample was measured under ultra-high vacuum (UHV) conditions (Prevac, Poland). For XPS measurements, monochromatic Al Kα X-ray radiation ($E = 1486.7$ eV) was applied. All of the binding energies were adjusted in relation to the C 1 s peak at 285.0 eV.

X-ray absorption spectroscopy (XAS) at the Cu K edge was performed at the ASTRA beamline of SOLARIS National Synchrotron Radiation Centre (Kraków, Poland). The beamline utilised a double bend achromatic 1.3 Tesla bending magnet to generate the incident photon beam, with a critical energy of ~ 2 keV. A modified Lemonnier-type double crystal monochromator featuring a Ge(220) crystal pair was employed to monochromatise the beam. Slits were employed to shape the resulting monochromatic beam, which measured 7 × 1 mm at the sample position. The investigated CuO_x-modified $BiVO_4$ sample (Cu/0.1 BVO_NHV_W) was grinded in agate mortar and spread on the Kapton tape. Before measurements, Kapton tape was checked to exclude the presence of Cu species. Cu foil (provided by Exafs Company, Danville, USA) was used a reference between ionisation chamber I1 and I2 in order to calibrate and align collected spectra. Commercial CuO (Sigma Aldrich 241,741 100 g) and Cu_2O (Thermo Scientific 40188) were used as Cu^{II} and Cu^{I} reference materials. Copper oxides were measured in transmission mode, whereas CuO_x-modified $BiVO_4$ sample was measured in fluorescence mode with an integration time 8 s. For data processing and analysis, ATHENA software from Demeter software package was used [37].

The effect of pH on the surface charge was measured as zeta potential (mV) using Malvern Nano Zetasizer (Malvern Instruments Ltd., Malvern, UK). The concentration of the catalysts was 0.5 g · dm^{-3} in KCl solution (10^{-2} M). Measurements of the absorption spectra in the UV–Vis range were performed using Thermo Scientific's UV–Vis Spectrophotometer Evolution 220 with integrating sphere in order to determine absorption properties of the prepared materials and their optical band gap. Photoluminescence effect was measured by photoluminescence (PL) spectroscopy using Shimadzu spectrofluorophotometer RF-6000. Cut-off filter 400 nm was used during recording the emission spectra. For these measurements, powder photocatalysts were analysed.

The electrochemical properties were obtained using potentiostat–galvanostat Autolab PGSTAT204 (Metrohm Autolab) with a 0.5 M Na_2SO_4 solution as an electrolyte and a built-in software, Nova 2.1.4. was used for data analysis. Preparation of the electrode substrates modified with the as-synthesised photocatalysts, suitable for electrochemical measurements, was performed in three stages: dispersion preparation, deposition of the sample, and a surface blockage. Firstly, the sample suspension in water was sonicated for 15 min. Then, photocatalyst dispersion was dropped-cast onto carbon screen-printed electrodes with Ag/AgCl reference electrode (Metrohm DropSens 11*L*), followed by drying to evaporate the solvent completely. Finally, surface blockage was carried out by adding a small drop of Nafion (Sigma-Aldrich) onto the electrode. For photocurrent measurements, a switchable LED revolver (Instytut Fotonowy, Kraków, Poland) was used as a light source.

2.4. Determination of photocatalytic activity

The evaluation of photocatalytic activity toward pharmaceuticals degradation was carried out in a set-up presented in Fig. 1. The quartz reactor (1) with a volume 25 cm^3 was connected with thermostat to maintain the temperature 20 °C. The slurry suspension was stirred continuously with 800 rpm using a magnetic stirrer (2). As a visible light source, a 300 W xenon lamp (model 6271H, Oriel, USA) with a cut-off filter > 420 nm (3) and water IR filter (4), was used. In a typical reaction procedure, an appropriate concentration of catalyst in amount of 1 g · dm^{-3} was dispersed under stirring in an aqueous solution of pharmaceutical. The initial concentration of NPX and OFL was 15 mg · dm^{-3} and 20 mg · dm^{-3}, respectively. Prior to irradiation, the photocatalyst suspension was stirred for 45 min in the darkness to ensure the adsorption–desorption equilibrium. After the dark process, 0.1 cm^3 of PMS solution (25 mM) was added. The total PMS concentration in the reactor was 0.1 mM.

The degradation efficiency of pharmaceuticals was monitored using a high-performance liquid chromatography system (HPLC, model Shimadzu LC-6A), combined with a photodiode array detector (SPD-M20A) and C18 column (Phenomenex Gemini 5 μm; 150x4.6 mm). The detailed information about selected pharmaceuticals studied using HPLC were presented in Table 1. Bismuth, vanadium and copper leaching was checked by inductively coupled plasma optical emission spectroscopy method (ICP-OES SPECTRO BLUE TI, with seaspray nebuliser). Measurements were performed for wavelengths: 309.31 nm (vanadium), 223.06 nm (bismuth) and 324.75 nm (copper). The concentrations of SO_4^{2-} and F^- was monitored by Dionex ICS-1100 Ion Chromatography (Thermo Fisher Scientific). Dionex™ Combined Seven Anion Standard II was used to perform the quantitative analysis of the anions.

The high-performance LC-MS system employed consisted of an HCT Ultra spectrometer (Bruker Daltonics, Billerica, Massachusetts, US) with an ESI source coupled with an Agilent 1200 liquid chromatograph (Agilent Technologies, Santa Clara, California, US). Chromatographic separation was conducted on Gemini-NX 5 μm C18 110 Å, 4,6x150 mm (Phenomenex) column. Mobile phase A consisted of water with 0.1 % formic acid and phase B acetonitrile with 0.1 % formic acid. Gradient program was as follows: 0 min – 10 % B, 20 min – 90 % B, 22 min – 90 % B, 25 min – 10 % B, 30 min – 10 % B for NPX and 0 min – 1 % B, 5 min – 1 %, 20 min – 90 % B, 25 min – 1 % B, 30 min – 1 % B for OFL. The flow was set at 0.4 cm^3 · min^{-1}, and the injection volume was 50 mm^3. The column oven temperature was set to 25 °C and UV chromatograms were recorded at 214, 230 and 254 nm. Spectra were acquired in positive and negative ESI mode, the scanned mass range was 50–800 *m/z*. The parameters capillary voltage, drying gas flow, nebulising gas and source

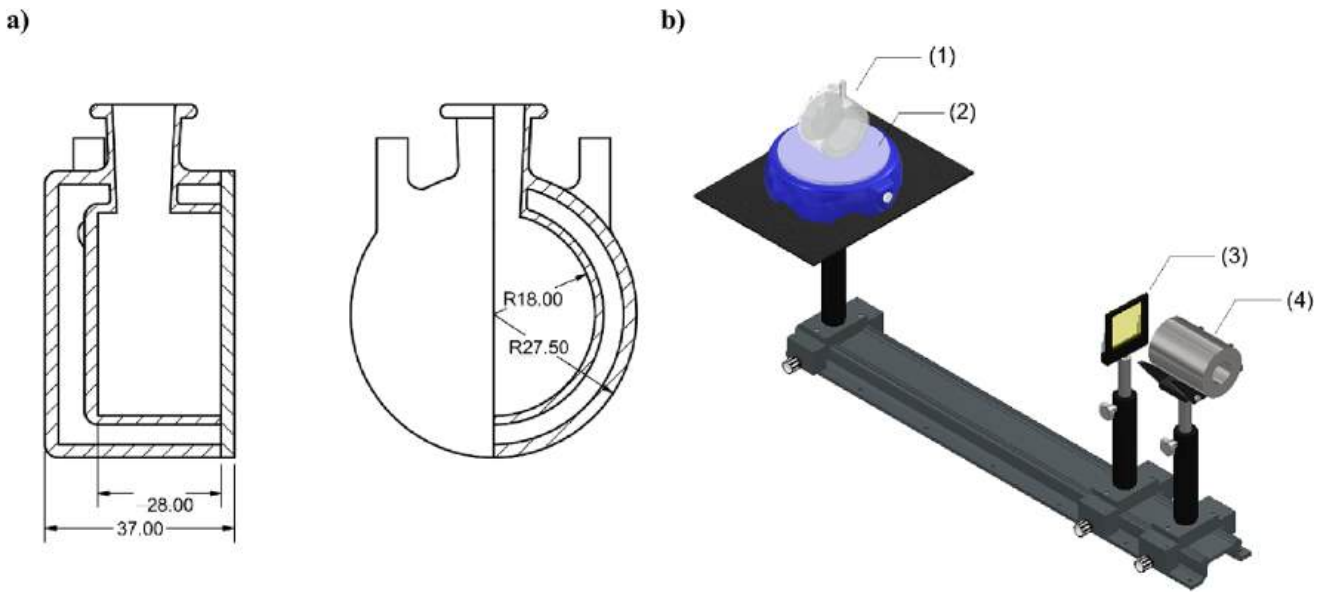

Fig. 1. Schematic illustration of **a)** quartz reactor and **b)** experimental set-up. For better clarity of illustrations, Xe lamp and thermostat were not presented.

Table 1
Detailed characteristics of selected pharmaceuticals.

Compound name	Chemical structure	pKa	Mobile phase (v/v)	Retention time (min)	Maximum absorbance (nm)
(S)-(+)-2-(6-Methoxy-2-naphthyl)propionic acid (**Naproxen, NPX**)	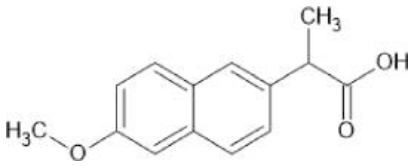	4.2	70 % acetonitrile, 30 % water with 0.1 % formic acid Flow rate 0.35 $cm^3 \bullet min^{-1}$	7.1	230
9-Fluoro-3-methyl-10-(4-methylpiperazin-1-yl)-7-oxo-3,7-dihydro-2H-[1,4] oxazino [2,3,4-ij]quinoline-6-carboxylic acid (**Ofloxacin, OFL**)	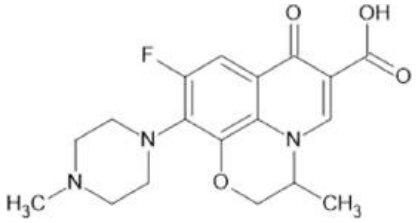	6.1 8.3	15 % acetonitrile, 85 % water with 0.1 % formic acid Flow rate 0.6 $cm^3 \bullet min^{-1}$	3.8	294

temperature was respectively: 4.0 kV, 10 $dm^3 \cdot min^{-1}$, 30 psi and 350 °C. Helium (99.999 %) was used as the collision gas in the ion trap. The mass spectrometer was operated in full scan and single ion monitoring (SIM).

Optical properties of the photocatalyst suspensions were determined for selected BVO-based materials to determine possible differences in their photon-absorption ability. Experimental procedure of the mass-specific extinction/absorption coefficient was based on the absorbance obtained from UV–Vis spectroscopy. Direct/scattered transmittance was measured through the water suspensions of various catalysts concentrations [38]. Measurements were performed in the wavelength range of 400–500 nm and the final absorbance was calculated as an average value in this region. The optical parameters β and κ for particular samples were used to numerical model of the local volume rate of photon absorption (LVRPA), following the six-flux model approach [39]. For calculations, the applied scattering probabilities in the forward, backward and side directions were 0.756, 0.132 and 0.028, respectively, based on Henyey-Greenstein phase function [40].

2.5. Toxicity rate

Microtox bioassay evaluated the toxicity of solutions treated during the PAP processes. The Microtox tests using the inhibition of luminescence from *Vibrio fischeri* bacteria as an acute reagent were performed on a Microtox model M500 (Microbics Corp., Carlsbad, California). The measurements of light output were carried out after 15 min. The addition of toxic compounds was indicated by a decrease in the light output. The toxicity was recorded as the percent decrease of light output, which was calculated using the formula (Equation (1):

$$Inhibition = \frac{I_S - I_e}{I_S} \cdot 100\% \quad (1)$$

in which I_s is the light level of blank and I_e – the light level of exposure sample. The reagents for the Microtox test were supplied by Microbic Corporation.

3. Results and discussion

3.1. Structural and morphological analyses of NHV and BVO, chemical state composition

To investigate the role of NHV precursor morphology, it is necessary to understand the crystal structure of ammonium metavanadate. Therefore, the crystal structure of NH_4VO_3 was visualised (Fig. 2a). This compound crystallises in an orthorhombic structure with space group Pbcm. A unit cell is composed of VO_4 tetrahedra, which form chains along *c* direction as a result of electrostatic interaction with intercalated NH_4^+ cations [41]. Therefore, the changes in lattice parameter *c* seem to be the most important for further structural characterisation. The phase identification of the self-obtained and commercial precursors is presented in Fig. 2b. The experimental XRD patterns of NHV samples are consistent with reference card 1549780, which corresponds to the ammonium metavanadate. In the case of NHV_W, which was synthesised from V_2O_5 reduction, no additional peaks ascribed to another phase were detected. Therefore, it can be assumed that single-phase NH_4VO_3 was successfully synthesised. Remarkably, when NHV_C and NHV_W are compared, the relative intensities of signals in the range of 20-35° can be noticed. The peak ascribed to (0 2 1) plane is the highest in the reference card, whereas in NHV_C the peak (1 2 1) is the most intense. Moreover, for commercial vanadium precursor, (0 0 2) signal is lower than (0 4 1), which is in opposite to the reference card and diffraction pattern of NHV_W. Finally, small differences can be observed in *c* parameters and volume cell, as a result of the interaction between VO_4 and intercalated NH_4^+ (Table 2). Rietveld refinement also revealed that NHV_C exhibits a non-stoichiometry at V1 position and the crystal structure of this compound deviated from the reference standard. The as-synthesised NHV_W is more stoichiometric and therefore less structural disorders are noticed in the crystal lattice.

The differences in morphology between commercial and as-prepared ammonium metavanadate were observed using scanning electron microscopy (SEM). SEM images of ammonium metavanadate (NHV) samples are presented in Fig. 2c. Commercial NH_4VO_3 exhibits non-uniform morphology with macrosized plate particles. In the case of NHV_W sample, plates are thinner and significantly smaller than NHV_C.

NHV precursors were further analysed by Fourier-transform infrared spectroscopy (FTIR) and compared with Standard Reference Database 69 from NIST Chemistry WebBook. FTIR spectra of NHV_C and NHV_W are presented in Fig. 2d. All bands in the standard reference spectrum are present in the ammonium metavanadate samples. The wide band above 3400 cm^{-1} corresponds to the O–H stretching vibration of the adsorbed H_2O molecules. The bands located at 3200, 2946, 2896 and 2799 cm^{-1} are assigned to the stretching vibration of N–H mode of the NH_4^+ group [42]. The characteristic band for ammonium cation is also located at 1413 cm^{-1}, which is due to N–H in-plane vibration mode. The presence of bands related to the vanadium–oxygen stretching vibrations is between 400 and 1115 cm^{-1}. The strong bands at 912 cm^{-1} for NHV_C and 919 cm^{-1} for NHV_W refer to V = O stretching modes. In-plane and out-of-plane V-O-V vibrations modes and are visible in the region between 860 cm^{-1} and 470 cm^{-1} [43]. Remarkably, the FTIR spectrum of NHV_W possesses sharper and narrower bands at 1413 cm^{-1}, 919 cm^{-1} and 660 cm^{-1} than the commercial precursor, which is more similar to the theoretical spectrum. Various intensities and widths of these bands, especially of V = O and V-O-V bonds may be a result of different interconnections between VO_4 tetrahedra and hydrogen bonds with

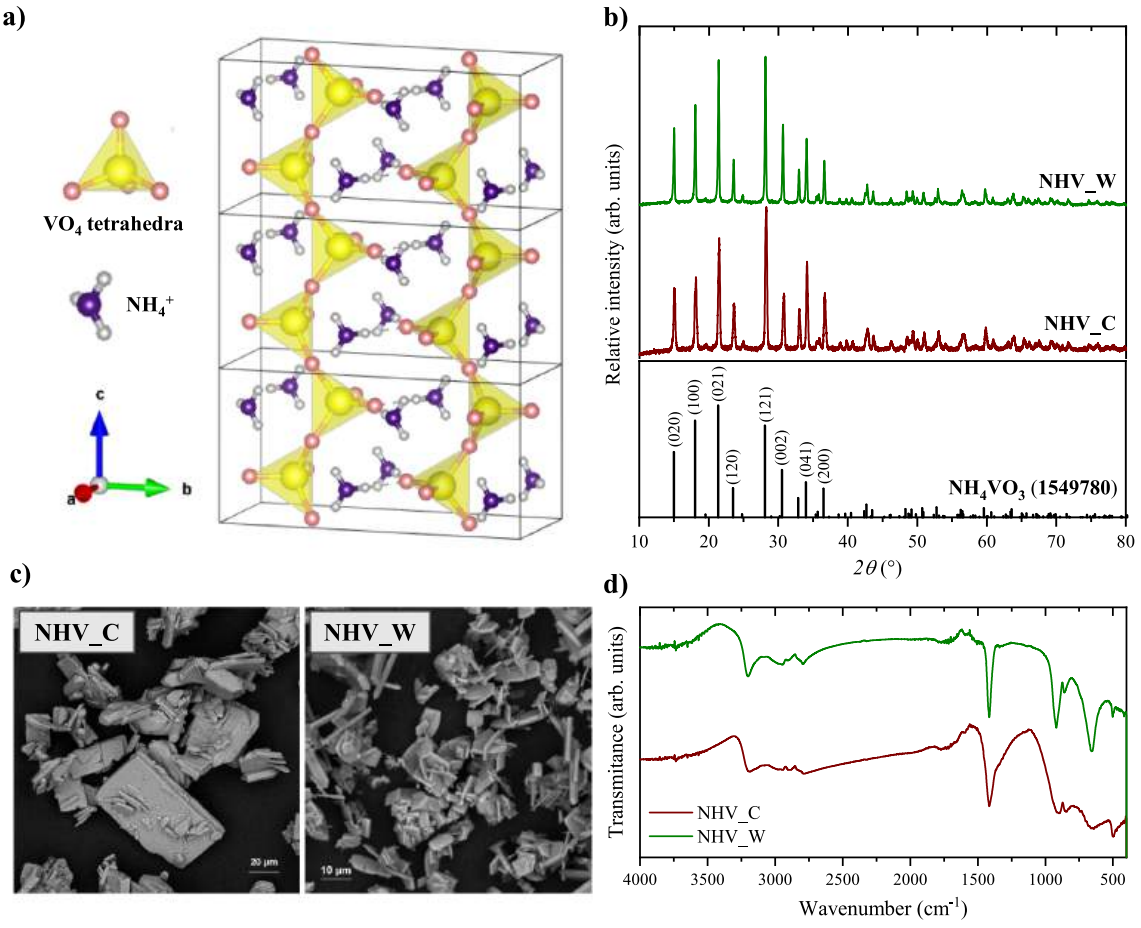

Fig. 2. a) Crystal structure of ammonium metavanadate visualised by VESTA3 programme [47]; Three unit cells arc shown to illustrate the chain arrangement of the VO_4 tetrahedra, b) XRD pattern, c) SEM images and d) FTIR spectra and of NHV precursors. Only the most intense XRD patterns were indexed.

Table 2
Structural parameters of NHV precursors and BVO-based photocatalysts.

Sample name	Crystallite size (nm) *	Lattice parameters			Volume cell (Å^3)	Occupancy at V position	Occupancy at Bi position
		a (Å)	*b* (Å)	*c* (Å)			
NHV_C	30	4.90227	11.78868	5.82003	336.347	0.73643	n/a
NHV_W	51	4.90406	11.78744	5.82645	336.806	0.92625	n/a
BVO_NHV_C	33	7.24992	11.69356	5.09807	309.057	0.81602	0.74800
BVO_NHV_W	42	7.24928	11.69401	5.09726	308.942	0.93948	0.89422
Cu/0.1 BVO_NHV_W	41	7.25412	11.69738	5.10215	309.236	0.86620	0.82508

* Crystallite size was calculated using Scherrer equation, based on the most intense peak in XRD pattern.

ammonium ions. Commercial ammonium metavanadate is produced via V_2O_5 dissolution in a hot sodium carbonate solution with the addition of potassium permanganate, which is further precipitated by ammonium salt [44]. Performing the synthesis of NHV_W in ammonium acetate without an oxidant agent and under mild conditions affected the interaction between VO_4^- and NH_4^+, resulting in a more stoichiometric structure of NH_4VO_3 [45,46]. Comparing these results with Rietveld refinement, it can be assumed that the as-synthesised precursor exhibits a more convenient crystal structure than the commercial one.

Furthermore, NHV samples were used for the preparation of photocatalysts. The XRD patterns of obtained bismuth orthovanadate (BVO) nanomaterials are presented in Fig. 3a. Both diffraction patterns for self-obtained BVO_NHV_C and commercial sample BVO_NHV_W are in agreement with the reference card 9013437, which corresponds to Clinobisvanite polymorph of $BiVO_4$ with monoclinic-scheelite structure. According to Table 2, it can be noticed that BVO_NHV_C exhibits more distinct non-stoichiometry than BVO_NHV_W, similarly to the NHV precursors. For the BVO_NHV_W sample, the occupancy at Bi and V positions is significantly higher and closer to the theoretical one (1.0). Therefore, it can be concluded that replacing the commercial precursor with NHV_W allows us to obtain more suitable crystal structure of $BiVO_4$.

SEM images presented in Fig. 3b prove that the reduction in precursor size influenced the morphology of the final BVO photocatalysts. BVO_NHV_C with polyhedra-shaped microcrystals and polydisperse nature were observed. In this case, few aggregates of small particles were noticed. On the contrary, these particles below 1 μm are predominant in BVO_NHV_W, synthesised from NHV_W. This photocatalyst also exhibited a polydisperse nature. However, replacing the ammonium metavanadate with NHV_W allowed for a reduction in size and formation of small particles. Two effects can be responsible for this result. Firstly, smaller particles have shorter VO_4 chains, which in solvent interacts with H^+ and water molecules and in consequence, hinder VO_4 condensation [48]. Secondly, the stoichiometry of the reagent is also a decisive factor for the crystal growth [49]. Similar observations were described in our previous study, in which the morphology of $TiOF_2$ precursor had a significant impact on the photocatalytic properties of F-doped TiO_2 [50]. Therefore, the morphology of the precursor and its stoichiometry affect the physicochemical properties and crystal structure of the final photocatalyst.

The most photocatalytic active sample of BVO_NHV_W was modified with CuO_x, as confirmed by transmission electron microscopy (TEM). Fig. 4a shows nanoparticles with average size (93 ± 27) nm, whereas EDX mapping (Figure S1 in Supplementary Materials) revealed uniform distribution of Bi, V and O. Size distribution of the particles is presented in Figure S2 in Supplementary Materials. Based on high-resolution TEM lattice fringe image (Fig. 4b), *d*-spacing value was calculated, being equal to 0.305 nm, which corresponds to (1 2 1) plane. In addition, to understand the nature of interface modifications, X-ray photoelectron spectroscopy (XPS) was performed (Figures S3 and S4 in Supplementary Materials). However, no signal, which can be attributed to Cu species was detected, probably because of the content below the sensitivity level. This obstacle is common for such subtle surface modifications at low amount [51]. Therefore, X-ray absorption near edge structure (XANES) spectroscopy of Cu-K edge (Fig. 4c) was performed for Cu/0.1 BVO_NHV_W. This measurement confirms the presence of copper species in this sample. Based on the values of edge energy positions (E_0) of the measured spectra, determined at the half of the edge step, and data from the literature, it can be assumed that copper exhibits mixed valence states between Cu^I and Cu^{II} [52–54]. The average oxidation state, which was + 1.48, was estimated from the plotted function between E_0 and Cu valence state (inset in Fig. 4c). The presented interface modification was performed as a chemical reduction of $CuCl_2$ with hydroxylamine hydrochloride as a reducing agent, so this procedure allows to partially oxidise Cu^{2+} ions. Due to the dissolved oxygen in the solution and aerobic conditions, deposited Cu^+ and Cu^{2+} further form CuO_x at $BiVO_4$ surface. The presence of metallic or partially reduced form is unlikely, because according to Nguyen *et al.*, Cu^I is resistant to reduction, whereas Cu^0 is more air-sensitive than copper cations [54]. Moreover, in the spectrum of interest, there are no characteristic features corresponding to metallic form of Cu, so the presence of Cu^0 was excluded. A linear combination fitting (LCF) of the sample's XANES spectrum using the

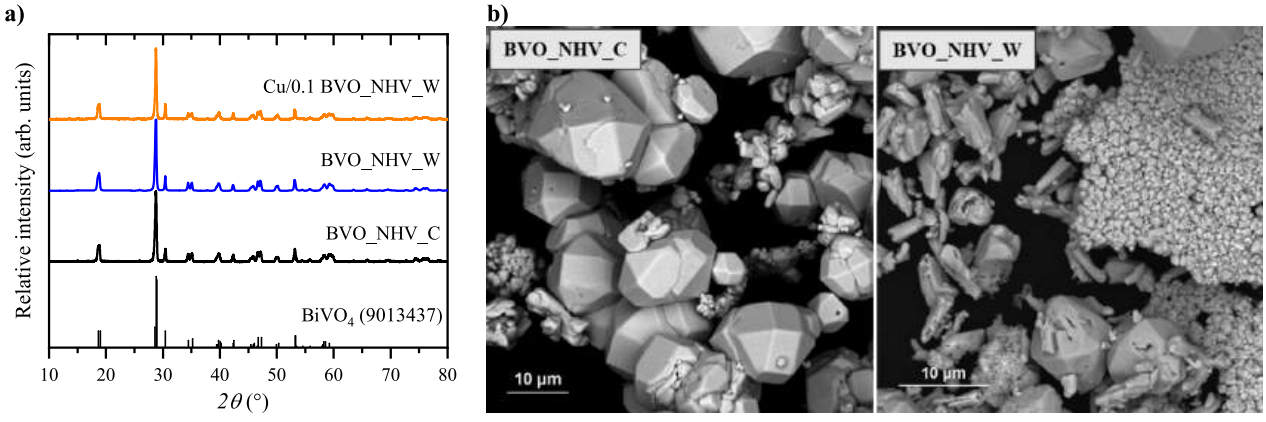

Fig. 3. **a)** XRD patterns of BVO and **b)** SEM images of BVO photocatalysts.

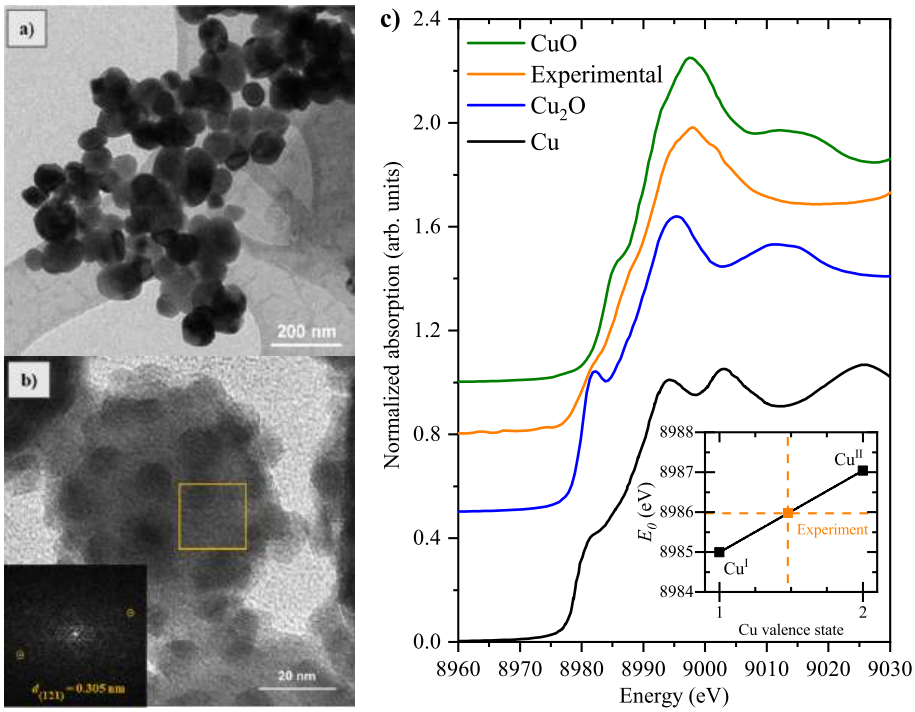

Fig. 4. a) TEM and **b)** HRTEM images of Cu/0.1 BVO_NHV_W; inset shows the calculated *d*-spacing, **c)** Normalised Cu–K edge absorption coefficient for Cu/0.1 BVO_NHV_W and reference samples; inset shows the relationship between Cu valence state and E_0 energy.

reference spectra of copper oxides was difficult to provide due to the differences in spectra features for crystalline Cu_2O and CuO powders and amorphous CuO_x nanoclusters. These features of CuO_x nanoclusters spectra are dependent on various factors such as size effects or oxygen content in the reaction environment [53–55]. Therefore, according to experimental results, synthesis conditions and existing literature, it can be concluded that the presence of sub-nanoclusters of mixed copper species is the most probable form of Cu present in Cu/0.1 BVO_NHV_W.

3.2. Optical and electrochemical properties

Absorption properties of the photocatalysts were investigated using diffuse-reflectance (DR) UV/vis spectroscopy, as presented in Fig. 5a. All samples, either pure BVO and Cu-modified, absorb light throughout the measuring range, so they are capable of utilising the full solar light spectrum. The wide band with high absorbance is noticed especially below 500 nm. However, replacing the commercial precursor to NHV_W allows to achieve slightly higher absorbance for BVO_NHV_W sample. Based on the Kubelka-Munk function transformation, the bandgaps (E_g) of these materials were calculated. All the E_g values are typical for monoclinic-scheelite $BiVO_4$ and correspond to Bi 6 s and V 3d transition [56]. Noticeably, two transitions are observed in samples BVO_NHV_W and Cu/0.1 BVO_NHV_W, which may suggest the presence of the additional state close to the conduction band. The CuO_x modification does not significantly influence the absorption properties compared to pure BVO_NHV_W.

Fig. 5b presents the photoluminescence (PL) spectra of the photocatalysts. All samples have an emission in a similar range with λ_{max} = 525 nm. The order of the PL intensity of the samples is BVO_NHV_W > Cu/0.1 BVO_NHV_W > BVO_NHV_C, indicating that hypothetically the recombination rate of BVO based on commercial NH_4VO_3 is lower than for BVO_NHV_W. In general, photoluminescence phenomena are connected with the radiative recombination process. Excited charge carriers tend to minimise their energy, therefore, recombination allows to release the excess of energy via photons or phonons. However, this effect causes a decrease in electrons and holes concentration, which is unfavourable for the photocatalytic process [57,58]. However, BVO_NHV_W may exhibit better absorption properties and light utilisation, so more electron-hole pairs may be generated. If the recombination rate was the same for these photocatalysts, in the case of BVO_NHV_W, more charge carriers would recombine, resulting in higher PL spectra. Liqiang *et al.* suggested that the photoluminescence signal may occur due to the defect binding of the photoinduced charge carriers. In this case, the stronger the emission signal, the higher the photocatalytic activity because oxygen vacancies and lattice distortions might favour reactions at the photocatalyst surface [59]. The effect of decreasing photoluminescence signal is clearly observed after CuO_x modification, so the formation of $CuO_x/BiVO_4$ heterojunction can effectively hinder the recombination of photogenerated electrons and holes.

In order to study the surface properties of the BVO-based photocatalysts, the zeta (ζ) potential, which determines the electrophoretic mobility of the particles, measured at different pH values was analysed. The ζ-potential evolution with the pH value is presented in Fig. 5c. Based on this relation, the isoelectric point (IEP) was determined as an OX axis intersection. The highest IEP value (equal to 3.8) was noticed for BVO_NHV_C. When the precursor is replaced from commercial to as-synthesised NHV_W, IEP decreases to 3.0. Finally, CuO_x modification causes a slight IEP shift to 3.4. Although the differences in isoelectric point values are small, the role of ammonium metavanadate is distinct in the region of negative ζ-potential. The values of ζ-potential in the pH range from 4.0 to 5.8 are more negative for BVO_NHV_W than for BVO_NHV_C. In this range, the negatively charged particles are stable in the dispersion during the degradation process [60]. For Cu/0.1 BVO_NHV_W the particles in basic conditions are less negatively charged which can be explained by different surface atom rearrangement and electronic distribution on the surface due to CuO_x modification of the sample.

The role of CuO_x modification for BVO photocatalysts was also investigated by electrochemical measurements. Firstly, the photocurrent response test LED light at λ_{max} = 426 nm was performed (Fig. 5d) to illustrate the changes in photoelectric properties. Cu/0.1 BVO_NHV_W

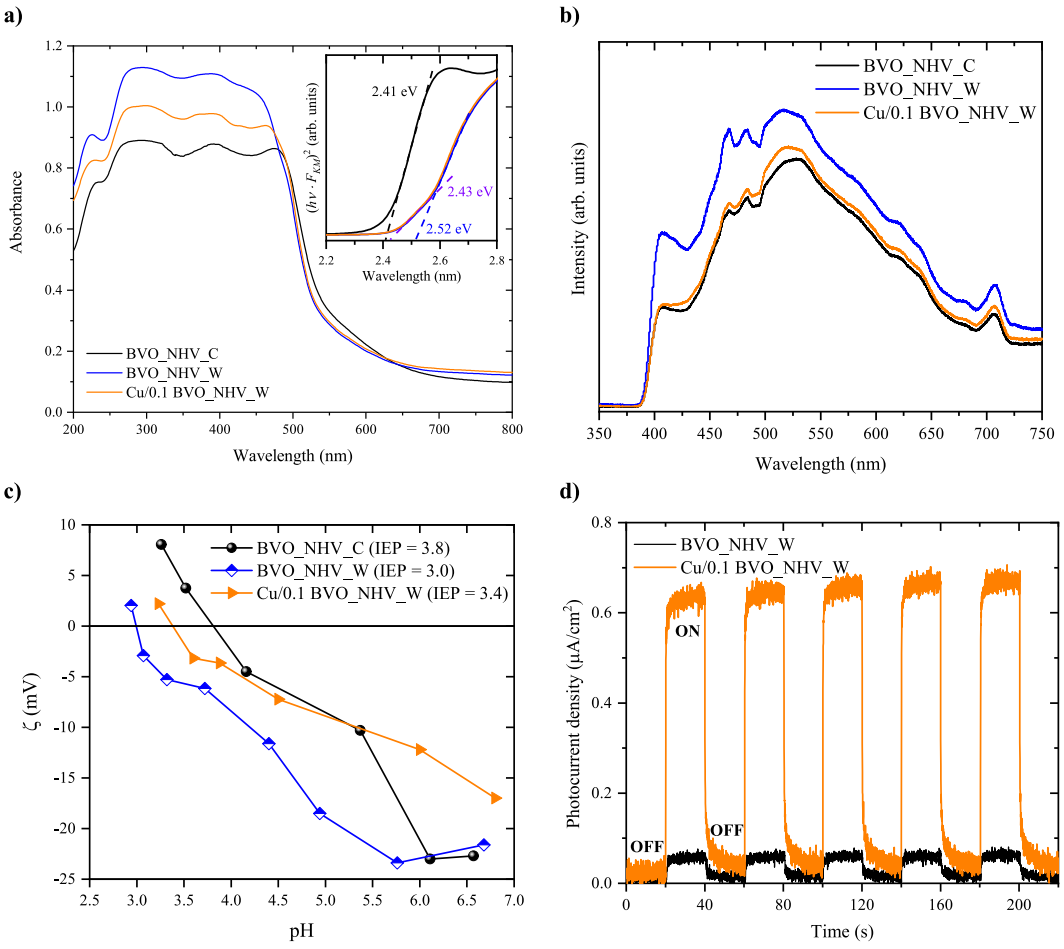

Fig. 5. a) DR/UV–Vis spectra and **b)** PL spectra of BVO-based photocatalysts (λ_{exc} = 315 nm), **c)** Zeta potential determined from the electrophoretic mobility in dependence of the pH, $I = 10^{-2}$ M KCl; **d)** Photocurrent density vs. time measurements of Cu/0.1 BVO_NHV_W compared with BVO_NHV_W under visible light (λ_{max} = 426 nm, P = 64 mW).

exhibits a 7.5-times higher photocurrent intensity than that of unmodified BVO_NHV_W, so interface modification allows for a significant improvement in visible light response. This result can be explained by the role of CuO_x nanoclusters presence. CuO or Cu_2O are p-type semiconductors, while $BiVO_4$ exhibits n-type conductivity [61]. Therefore, the formation of p-n junction allows to increase charge carriers separation and limits the recombination rate, which is beneficial for the photocatalytic performance of the final material [62].

3.3. Determination of photocatalytic activity, LVRPA analyses

The photocatalytic activity of the BVO-based photocatalysts was studied in reactions of naproxen (NPX) and ofloxacine (OFL) degradation under visible light (above 420 nm). Firstly, the effect of different NHV precursors was analysed. As can be seen in Fig. 6a-6d, both samples were able to degrade pharmaceutical compounds. However, in each case, the sample BVO_NHV_W prepared from as-synthesised precursor exhibited higher photocatalytic activity. The probable explanation was differences in light utilisation. Therefore, in the next step, the local volume rate of photon absorption (LVRPA) was calculated numerically for a cross-section of the reactor, following the six-flux model approach based on the Henyey-Greenstein phase function. The mass extinction coefficient (β) and mass absorption coefficient (κ) were determined for suspensions of both powders as dependence of the visible light spectral-average absorbance of the photocatalyst suspension on the photocatalyst dosage (Figure S6 in Supplementary Materials). LVRPA distribution in the cross-section of the photoreactor for the selected samples is presented in Fig. 6e. According to this graph, it can be noticed that BVO_NHV_C suspension has very limited optical properties, including low spectral-average mass extinction coefficient (β) and mass absorption coefficient (κ). Replacing the commercial precursor by a self-synthesised one caused significant improvement in LVRPA distribution and 7-times and 12.6-times rise of the β and κ coefficients, respectively. These results may be connected with the morphology of this photocatalyst, which possessed a higher content of small particles than the BVO_NHV_C sample. Moreover, better dispersion of BVO_NHV_W was also confirmed by ζ-potential, in which these particles were more negatively charged.

Based on the photocatalytic activity of BVO samples, BVO_NHV_W was selected for further modification. The interface modification had an impact on the final photocatalytic performance. The most efficient Cu/Bi parameter was when 0.1 g BVO_NHV_W was used for modification. Different contents were also studied and the results are presented in Figure S5 in Supplementary Materials. The presence of CuO_x clusters at BVO surface resulted in greater photocatalytic pharmaceuticals removal under visible light, achieving 93.9 % and 90 % removal of initial NPX and OFL in solution after 2 h of the process, respectively. Based on the calculated kinetic rate constants, fitted by a pseudo-first-order kinetic model, the modification by CuO_x allowed to increase the rate constants 1.18-times and 3.29-times for NPX and OFL removal, respectively. These observed degradation efficiencies are also higher or comparable with the latest literature regarding photocatalytic pharmaceuticals removal, presented in Table S1 in Supplementary Materials. Two effects can be responsible for enhanced photocatalytic activity. Firstly, due to interface modification, charge carriers separation is favoured, resulting in

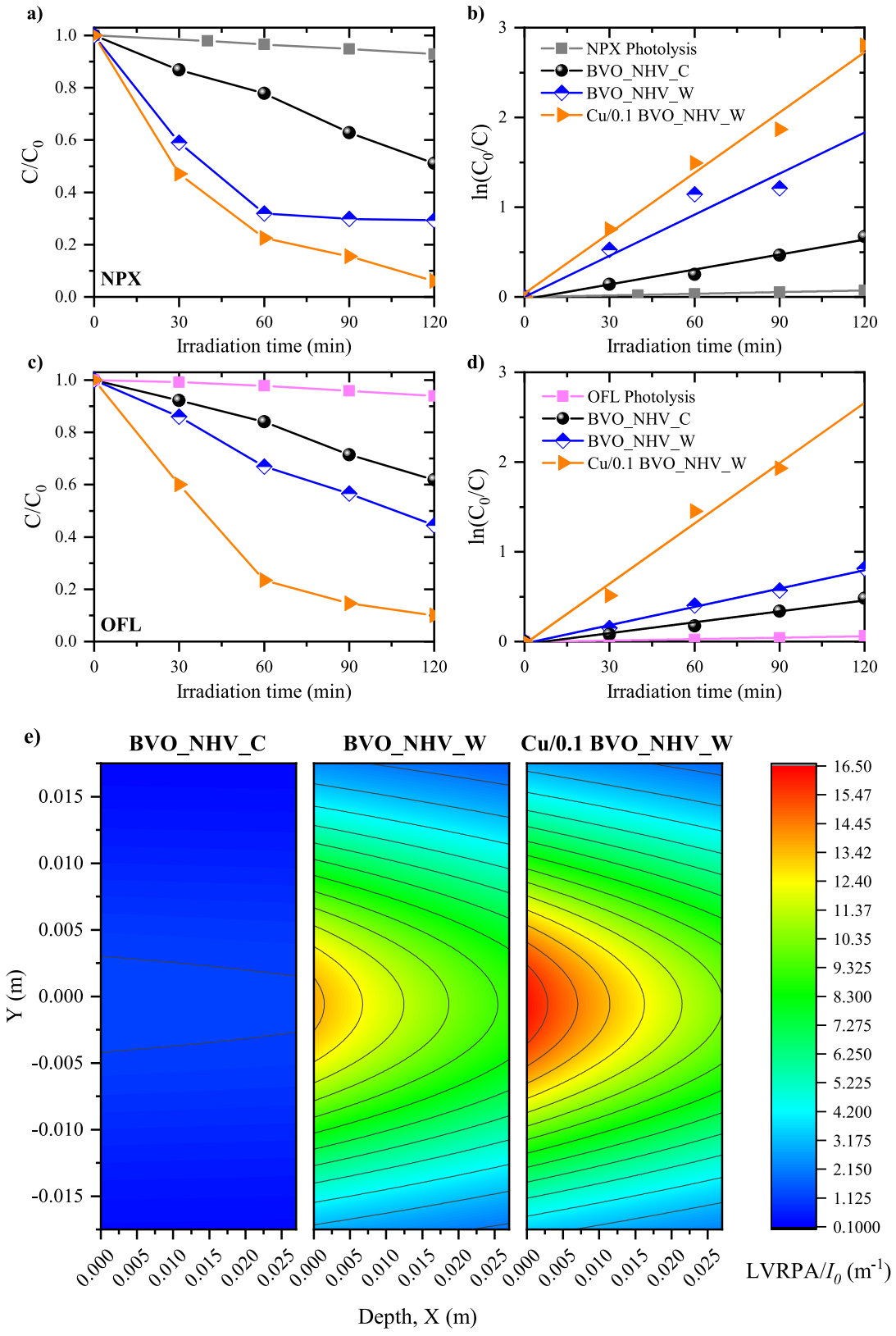

Fig. 6. Photocatalytic degradation of NPX **(a, b)** and OFL **(c, d)** using different BVO and the most efficient CuO_x-modified BVO under visible light ($\lambda > 420$ nm); Process parameters: $[NPX]_0 = 15$ ppm, $[OFL]_0 = 20$ ppm, [catalyst] = 1 g · dm^{-3}; **e)** LVRPA distribution in the cross-section of photoreactor for selected photocatalysts.

decreased signal on PL spectra and multiplied photocurrent density compared to pristine BVO_NHV_W. Secondly, the presence of CuO_x nanoclusters caused an improvement of LVRPA distribution and rise of the κ coefficient.

Based on ζ-potential analysis for Cu/0.1 BVO_NHV_W and literature values of pK_a for NPX and OFL molecule, it is possible to describe the interaction between the photocatalyst and pharmaceutical compound. Photocatalytic processes were performed in pH > pH_{IEP}. Therefore, the photocatalyst surface was negatively charged. NPX is an acidic compound with pK_a = 4.2, whereas OFL due to its amphoteric nature, is characterised by two pK_a values = 6.1 and 8.3 [63–65]. The pH of the mixture of photocatalyst in NPX and OFL solution were 5.2 and 6.7, respectively. At these conditions, NPX molecule is present in deprotonated form with a negative charge. Therefore, NPX degradation using Cu/0.1 BVO_NHV_W probably occurs in an aqueous solution instead of photocatalyst surface. In the case of fluoroquinolone antibiotic, OFL is zwitterionic due to two ionisable functional groups in the structure. Although the charge of OFL ion and photocatalyst surface are not opposite, adsorption may occur. Van Wieren *et al.* reported that photocatalytic OFL removal using TiO_2 was the highest at conditions where OFL was zwitterionic and TiO_2 had a net positive surface charge [63].

The selected photocatalysts were further used in the peroxymonosulfate-assisted photocatalysis (PAP) process to investigate the effect of PMS addition. As presented in Fig. 7a, 26 % of initial NPX concentration undergoes partial oxidation without photocatalyst in the PMS presence, which means that small amount of sulfate radicals are photogenerated under visible light. This effect is not observed in reaction with ofloxacin (Fig. 7b) and PMS cannot oxidise OFL without a photocatalyst. In both reactions, the presence of photocatalysts allows PMS to be partially activated without light introduction; however, the kinetics of dark reactions is significantly slower than pure photocatalysis. The simultaneous application of photocatalysts, PMS and visible light causes remarkably more efficient pharmaceutical degradation – ca. 100 % after 60 min (k_{NPX} = 0.0966 min^{-1}) and 98.2 % after 120 min (k_{OFL} = 0.0408 min^{-1}) for NPX and OFL removal, respectively. In both cases, the higher degradation rate was observed for Cu/0.1 BVO_NHV_W + PMS + Vis420, nevertheless the positive effect of CuO_x modification is more distinct for OFL degradation. Based on these results, it can be assumed that the most efficient PMS activator is the charge carriers transfer on the irradiated photocatalyst surface.

Ion chromatography (IC) revealed the presence of F^- in post-process wastewater after OFL degradation. These results, presented in Table S2 in Supplementary Materials indicate that $CuO_x/BiVO_4$/Vis420/PMS system is effective in the defluoridation of fluoroquinolone antibiotics.

3.4. *Effect of the process variables, stability and reusability of the photocatalyst*

To investigate the potential of as-prepared photocatalysts in real water environment, the effect of the inorganic anions such as Cl^-, NO_3^- and CO_3^{2-} on NPX and OFL degradation was studied. Fig. 8a and 8b show the ion strength effects of the three ions in the concentration of 2 mM. It can be noticed that carbonate, nitrate and chloride ions have a negative effect on pharmaceuticals degradation, especially for OFL removal. This decrease can be explained by the scavenging effect of inorganic ions due to their reaction with sulfate and hydroxyl radicals [66]. Moreover, the effect of humic acid (HA) as an example of natural organic matter at the concentration of 0.5 mM was also investigated. The HA presence caused a distinct decrease in the photocatalytic degradation of both pharmaceuticals. Especially for NPX degradation, the kinetics was the lowest compared to the experiments with addition of inorganic ions. Their inhibitory mechanism can be explained by several effects, including: competitive adsorption, ROS scavenging and inner filter effect [67].

Fig. 8c and 8d show the effect of the solution pH. Due to different chemical structure, NPX and OFL interacted diversely with photocatalyst/PMS system. What is common for both pharmaceuticals, is that an acidic environment (pH = 2.9) inhibits the degradation efficiency. At this condition, the surface of Cu/0.1 BVO_NHV_W is positively charged (pH < IEP), NPX molecule is neutral, whereas OFL forms cation. It can be seen that these conditions are unfavoured for pharmaceuticals degradation. For naproxen removal in PMS/Vis420/$CuO_x/BiVO_4$ system, a weak acidic environment is the most effective. What is worthy attention,

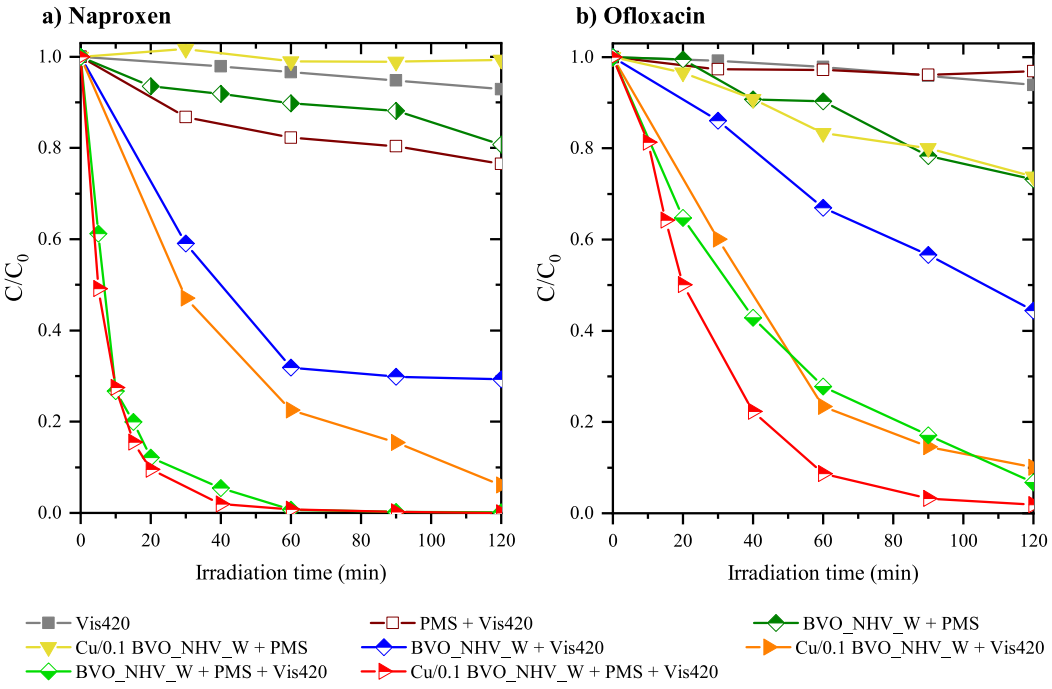

Fig. 7. Photocatalytic degradation of **a)** NPX and **b)** OFL using BVO and Cu-modified BVO under visible light (λ > 420 nm) with addition of PMS. Process parameters: $[NPX]_0$ = 15 ppm, $[OFL]_0$ = 20 ppm, [catalyst] = 1 g · dm^{-3}, [PMS] = 0.1 mM.

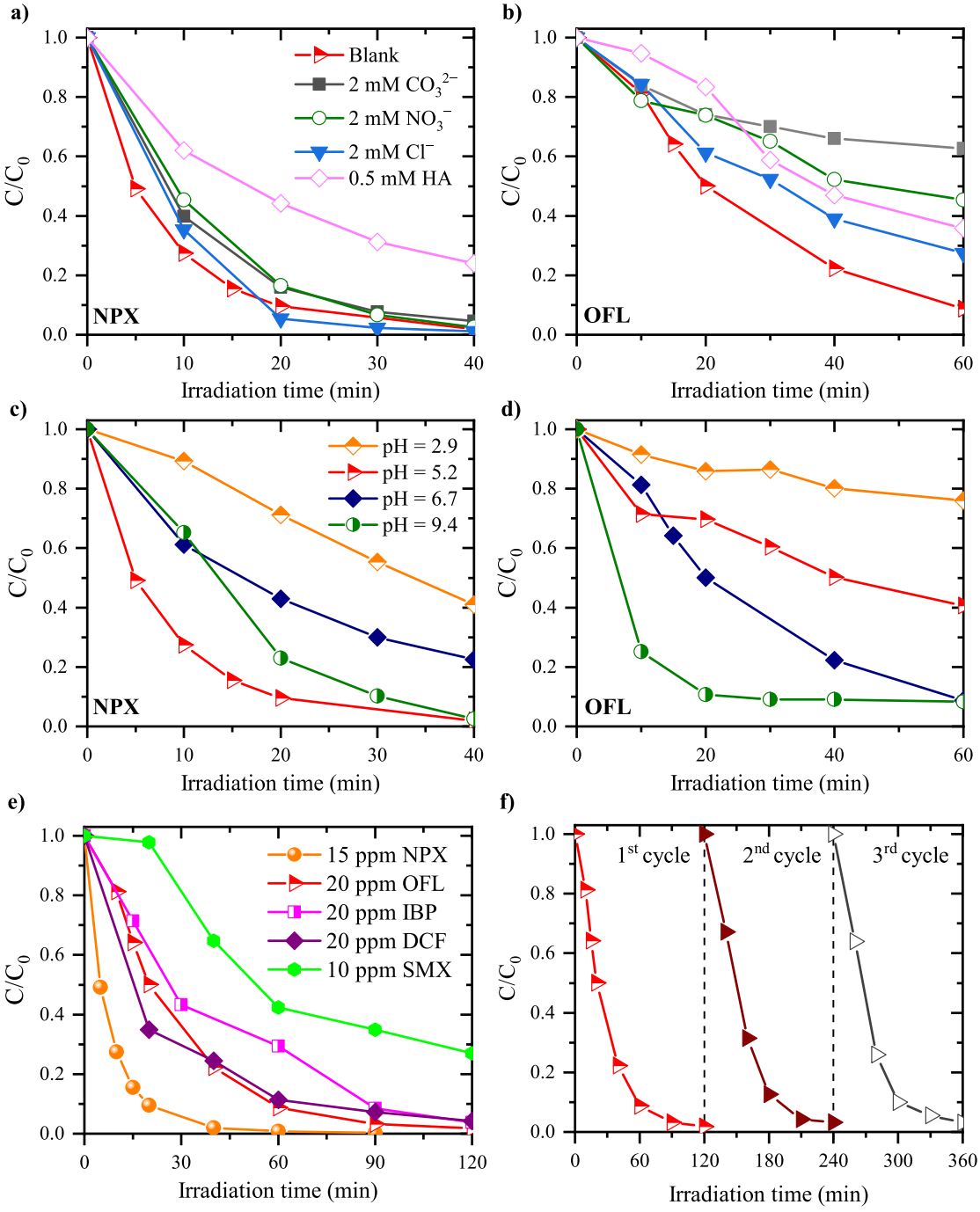

Fig. 8. Degradation of pharmaceuticals in PMS/Vis420/CuO_x/$BiVO_4$ system using using Cu/0.1 BVO_NHV_W: effect inorganic anions and HA presence **(a, b)**, pH of the solution **(c, d)**, **e)** comparison of selected pharmaceuticals**, f)** PMS-assisted photocatalytic OFL degradation after three subsequent cycles.

weak alkaline conditions (pH = 9.4) accelerated OFL removal. According to Qi et al., weak base can activate PMS [68], which also explains the high efficiency of NPX degradation. Overall results show that high kinetics of NPX degradation is maintained in the wide range of pH, whereas neutral/weak alkaline conditions are the most favourable for OFL removal.

The most efficient photocatalyst Cu/0.1 BVO_NHV_W was also studied in PMS-assisted degradation of ibuprofen (IBP), diclofenac (DCF) and sulfamethoxazole (SMX), as shown in Fig. 8e. PMS/Vis420/CuO_x/$BiVO_4$ system effectively degraded other pharmaceuticals from NSAIDs group, reaching 96.2 % IBP and 95.7 % DCF removal after 120 min of the PAP process, respectively. Notably, this system was also able to remove highly persistent antibiotic SMX with removal rates exceeding 73 % within 120 min. These results demonstrate the ability of the PMS/Vis420/CuO_x/$BiVO_4$ system to degrade a wide range of pharmaceutically active compounds.

The stability of Cu/0.1 BVO_NHV_W in PAP process was analysed as leaching of bismuth, vanadium and copper using the ICP-OES technique. The results are presented in Table S2 in Supplementary Materials. According to the Environmental Protection Agency (EPA), the permissible level of copper in drinking water is 1.3 mg/dm^3 [69]. Vanadium occurs naturally in surface water in a range from approximately 0.04 to 220 µg/dm^3 [70]. The observed presence of Cu and Bi in water after the process in the presence of 0.1 mM of PMS does not exceed the values reported by

EPA, so the effect of secondary risk pollution is not probable. However, increasing PMS concentration to 1 mM causes significant bismuth leaching and, consequently, ca. 4 % Bi loss from the composite. Therefore, the more PMS, the acidity of the environment reaction is increasing, which may cause instability of the final material. These results show the importance of controlling PMS concentration in PAP processes. Although the more PMS is added to the PAP process, the faster the kinetics of pharmaceuticals removal, more limitations may become like the stability of the material and secondary risk pollution.

The surface of Cu/0.1 BVO_NHV_W sample after the PAP process was investigated using XPS technique (Figure S7 in Supplementary Materials). The presence of potassium and sulfur was noticed, which is a result of PMS addition. S 2p region shows the S $2p_{3/2}$-S $2p_{1/2}$ doublet at 168.59 eV and 169.77 eV, which is typical for SO_4^{2-} [71]. Moreover, due to the interaction with molecules of pharmaceuticals and H_2O, higher signals ascribed to –OH, O-C-O-R and C-OH bonds were observed. Nevertheless, although the photocatalyst's surface is covered by residual pharmaceutical molecules and its by-products, no significant decrease in the photocatalytic activity was observed after 3 subsequent cycles toward OFL degradation (Fig. 8f). These results indicate that this material can be reused without regeneration and mass losses. Detailed results of error estimation and process variables effects are shown in Table S3 and S4 in Supplementary Materials.

3.5. Mechanism of PMS activation and ROS generation

For Cu/0.1 BVO_NHV_W sample, which was the most efficient catalyst, quenching experiments were performed to estimate the predominant reactive species in the PAP processes. For quenching experiments, ethanol (EtOH), *tert*-butanol (TBA) and *p*-benzoquinone (BQ) were selected as $SO_4^{\cdot-}$, ·OH and $O_2^{\cdot-}$ scavengers, respectively. The results in relation to pharmaceutical removal are presented in Fig. 9a. The elimination of particular species causes lower NPX and OFL degradation compared to the process without scavengers. In both processes, the presence of TBA and BQ significantly inhibited NPX and OFL removal, however, the lowest reaction kinetics was observed in the presence of $O_2^{\cdot-}$ scavenger. This observation can be surprising because benzoquinone can promote PMS activation and enhance the catalytic activity [72]. Based on this competitive effect, superoxide radicals are supposed to be the predominant ROS in the PAP process with Cu/0.1 BVO_NHV_W as a photocatalyst because more BQ reacts with $O_2^{\cdot-}$ radicals rather than with $SO_4^{\cdot-}$. This result can be a proof that electron transfer on photocatalyst surface was involved in the degradation of pharmaceuticals and played a crucial role in the generation of radicals. Superoxide radicals ($O_2^{\cdot-}$) are usually the product of one-electron molecular oxygen reduction, according to Equation (2) [73]:

$$e^- + O_2 \rightarrow O_2^{\bullet -} \quad (2)$$

The redox potential of the above reaction is − 0.33 V for the standard gas

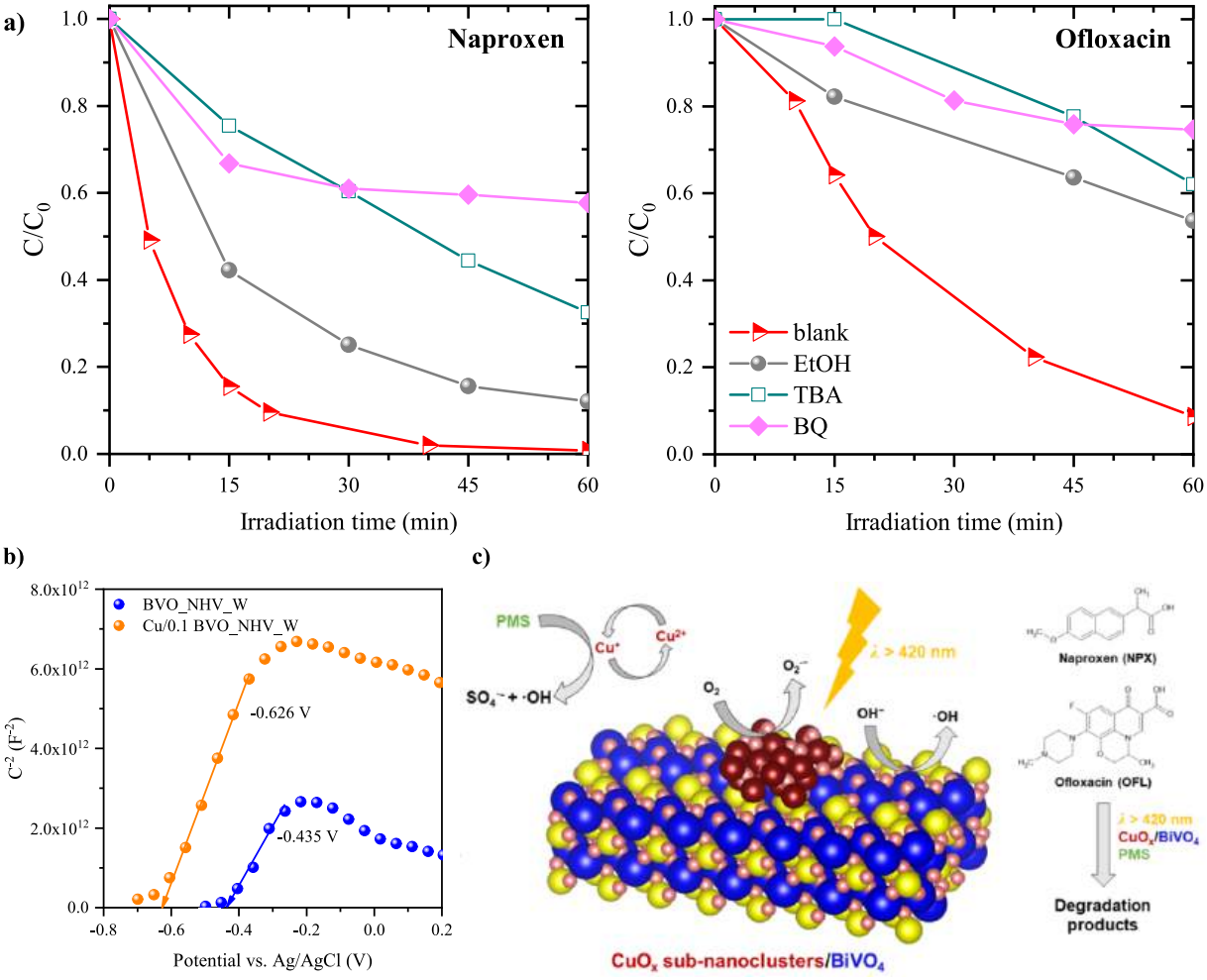

Fig. 9. a) Photocatalytic degradation of NPX and OFL using Cu/0.1 BVO_NHV_W photocatalyst under visible light (λ > 420 nm) with the addition of PMS in the presence of scavengers, **b)** Mott-Schottky plot of BVO_NHV_W and Cu/0.1 BVO_NHV_W, **c)** the proposed mechanism of enhanced NPX and OFL degradation in PMS/Vis420/CuO_x/$BiVO_4$ system.

state of 1 atm [73]. To check the possibility of generating superoxide radicals, Mott-Schottky analyses were performed and presented in Fig. 9b. The modification of $BiVO_4$ with sub-nanoclusters caused a shift of flatband potential towards more negative. Therefore, the modified photocatalyst exhibits resultant conduction and valence bands at − 0.34 V and 2.09 V, respectively (V vs. NHE), which enables to generate $O_2^{\cdot-}$ via single-electron reaction. According to the literature, due to favourable band position, copper oxides can also reduce molecular oxygen [74,75]. Without CuO_x modification, band position is not suitable for $O_2/O_2^{\cdot-}$ reaction, so sub-nanoclusters were supposed to be mainly responsible for their generation. Water oxidation to ·OH seems to be not preferencial for these photocatalysts, which is consistent with studies described by Nakabayashi *et al.* [76]. However, band position of $BiVO_4$ is suitable for both generating molecular oxygen and H_2O_2. Hydrogen peroxide can further participate in the generation of superoxide and hydroxyl radicals as presented below (Equations 3–5) [77–79].

$$O_2 + 2\ H^+ + 2\ e^- \rightarrow H_2O_2 \quad (3)$$

$$H_2O_2 + e^- \rightarrow \cdot OH + OH^- \quad (4)$$

$$H_2O_2 + h^+ \rightarrow O_2^{\bullet-} + 2\ H^+ \quad (5)$$

The possible mechanism of reactive species generation is as follows: when the photocatalyst is irradiated, electrons and holes are generated. In the case of PAP process, these charge carriers further participate in either generation of ROS, or PMS activation (Equations 6–9).

$$h^+ + OH^- \rightarrow \cdot OH \quad (6)$$

$$HSO_5^- + e^- \rightarrow SO_4^{\bullet-} + OH^- \quad (7)$$

$$HSO_5^- + e^- \rightarrow SO_4^{2-} + \cdot OH \quad (8)$$

$$SO_4^{\bullet-} + OH^- \rightarrow SO_4^{2-} + \cdot OH \quad (9)$$

Moreover, due to the presence of mixed copper oxides clusters, Cu^+/Cu^{2+} transfer occurs, enhancing the reactive species production in PAP process (Equations 10–15):

$$\equiv Cu^+ + HSO_5^- \rightarrow \equiv Cu^{2+} + \cdot OH + SO_4^{2-} \quad (10)$$

$$\equiv Cu^+ + HSO_5^- \rightarrow \equiv Cu^{2+} + OH^- + SO_4^{\bullet-} \quad (11)$$

$$\equiv Cu^{2+} + HSO_5^- \rightarrow \equiv Cu^+ + SO_5^{\bullet-} + H^+ \quad (12)$$

$$\equiv Cu^{2+} + e^- \rightarrow \equiv Cu^+ \quad (13)$$

$$HSO_5^- + e^- \rightarrow SO_4^{2-} + \cdot OH \quad (14)$$

$$SO_4^{\bullet-} + OH^- \rightarrow SO_4^{2-} + \cdot OH \quad (15)$$

In electron-deficient areas, $SO_5^{\cdot-}$ can be produced, which is a radical characterised by low redox potential (0.81 V) [19,61], according to Equations (12) and (16). However, $SO_5^{\cdot-}$ can participate in two reactions, resulting in formation of $SO_4^{\cdot-}$, as presented in Equation (17):

$$HSO_5^- + h^+ \rightarrow SO_5^{\bullet-} + H^+ \quad (16)$$

$$2\ H^+ + 2\ SO_5^{\bullet-} \rightarrow 2\ SO_4^{\bullet-} + H_2O \quad (17)$$

Despite the unsuitable band position of $BiVO_4$ to oxidise water to hydroxyl radicals, ·OH can be generated in different reactions, mainly reaction with H_2O_2 and PMS as well as OH^- oxidation. Moreover, it is probable that superoxide radicals can be formed and be the predominant ROS in PAP process. Finally, CuO_x present at the surface can act as a catalytic centre and participate in the generation of reactive species. Based on the above experimental results and related literature, a possible mechanism for the degradation of NPX and OFL in the PMS/Vis420/CuO_x/$BiVO_4$ system is presented in Fig. 9c.

3.6. Products identification, ECOSAR prediction vs. Experimental measurements of toxicity assessment

Ecological risk assessment is crucial for the application of PAP processes under visible light in wastewater treatment. However, detailed information about formed by-products is required. Therefore, liquid chromatography coupled with mass spectrometry (LC-MS) analysis was performed for PMS/Vis420/CuO_x/$BiVO_4$ system. Intermediate NPX and OFL products are depicted in Fig. 10a-b and detailed information is presented in Table S5 and Figure S8 in Supplementary Materials. Based on LC-MS analysis, three NPX by-products were identified: **N1** (m/z = 184.9), **N2** and **N3** (both m/z = 200.9). After 30 min of naproxen degradation, the signal coming from N3 increased the most compared to other by-products. Therefore, N3 is probably a transformation product of N2, which is consistent with the literature [80,81]. In the case of OFL degradation, two main products were detected – **O1** (m/z = 364.1) and **O2** (m/z = 378.1). Their signal was also increasing at the time of the PAP process, which proves the progressive NPX and OFL degradation.

Then, quantitative structure–activity relationship (QSAR) models are suitable tools for assessing the toxicity of pharmaceuticals and their intermediate products. To predict the toxicity of the NPX, OFL and their identified by-products, the Ecological Structure Activity Relationship Class Program (ECOSAR) was employed in relation to the acute and chronic toxicity of fish, daphnia, and green algae [82–84]. The summation of the lethal concentration (LC_{50}), effective concentration (EC_{50}) and chronic value (ChV) for several compounds is presented in Table 3. According to ECOSAR data, NPX and OFL molecules have no acute toxicity. The difference between these pharmaceuticals is in chronic toxicity – on the assumption that $10^2 > ChV > 10^1$, NPX exhibits harmful effects, highlighting the importance of its removal from wastewater. However, NPX degradation products are toxic or very toxic to that initial compound, especially N1 compound. Due to this fact, careful consideration of the ecological risk is essential during NPX degradation. In the case of OFL by-products, both O1 and O2 are not harmful to aquatic organisms.

Considering this aspect, the theoretical prediction was compared with the experiment using *Vibrio fischeri* bacteria as a bioindicator because according to G. G. Cash studies, ECOSAR predicts greater toxicity than experimental measurements using Microtox bioassay [85]. The experimental toxicity rate of post-process wastewater is presented in Fig. 10c. The experimental results of pure NPX and OFL solutions correlate with ECOSAR studies – ca. 49 % of bioluminescence inhibition was observed for NPX, whereas OFL exhibited almost non-toxic effect on bacteria. The progress of NPX removal in PAP process is clearly visible during comparison the systems with and without anchored CuO_x. After 120 min of process in PMS/Vis420/$BiVO_4$ system, luminescence inhibition is higher than before the reaction. When CuO_x nanoclusters were present in the photocatalyst, the luminescence was more intense, which successfully proves the decrease of toxicity assessment. This result highlights the importance of selecting the proper photocatalyst – a highly photoactive semiconductor will be able to generate more radicals, which induce the transformation of pharmaceuticals. Although pure BVO_NHV_W exhibits high photocatalytic activity under visible light, it seems to be insufficient considering environmental aspects, because there are still intermediate products that are harmful to aquatic life. Herein, only creating the heterojunction between $BiVO_4$ and CuO_x allows to degradation NPX effectively to non-toxic intermediates. Therefore, it can be concluded that Cu/0.1 BVO_NHV_W sample was not only non-toxic, but also the PAP process in the presence of this photocatalytic material leads to progressive NPX removal, together with its harmful by-products.

Although the toxicity rate of NPX was successfully decreased, OFL removal seems not to be optimistic. Although ECOSAR studies showed

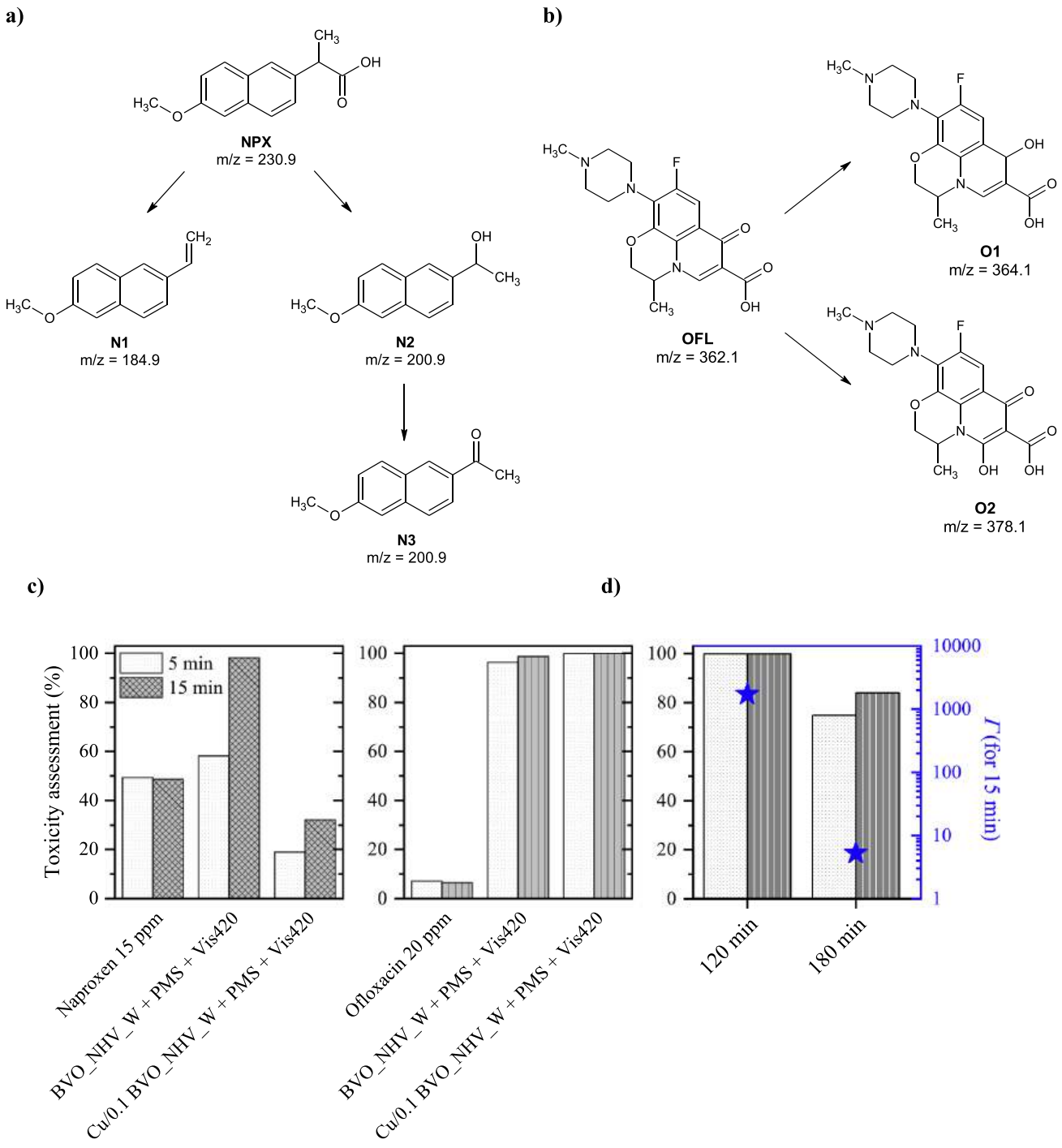

Fig. 10. Intermediate compounds of **a)** NPX and **b)** OFL detected by LC-MS, **c)** Microtox test with *Vibrio fischeri* bacteria of post-process solutions after 120 min of PAP process, **d)** the evolution of toxicity rate and Γ within time of OFL degradation using PAP process with Cu/0.1 BVO_NHV_W.

that detected by-products were not harmful to the environment, PMS/Vis420/CuO_x/$BiVO_4$ system leads to almost full inhibition of bioluminescence. Moreover, the gamma value (Γ), defined as the ratio of the light lost to the light remaining on time, significantly increased. Several studies have raised awareness that OFL degradation may increase the toxicity rate. For example, Calza *et al.* reported that the presence of piperazinic ring induced the toxicity of post-process solution after OFL degradation towards *Vibrio fischeri* bacteria. What is worthy of attention, this effect was not observed for ciprofloxacin, although this pharmaceutical and OFL have common structural nucleus [86]. Another explanation was reported by Carbajo *et al.*, who suggested the generation of formaldehyde during the oxidation process [87]. Finally, organic nitrogen products like amines can also be harmful for aquatic life [88]. ECOSAR studies of these compounds also suggest their harmful effect on the environment. Therefore, this high toxicity rate originates from formed by-products rather than the reaction system.

In this regard, two effects on toxicity assessment after OFL removal were investigated: the role of time prolongation of the PAP process (Fig. 10d) and PMS concentration (Figure S9 in Supplementary Materials). Fig. 10d shows that the toxicity rate is decreasing upon progressing OFL degradation in PMS/Vis420/CuO_x/$BiVO_4$ system with remarkably lower Γ value. This result indicates that toxic effect is not permanent and the harmful compounds can be effectively removed in PMS/Vis420/CuO_x/$BiVO_4$ system. What is worthy of attention, the

Table 3
Acute and chronic toxicity of NPX and OFL and selected transformation products for fish, daphnid and green algae, based on QSAR model. $LC_{50}/EC_{50}/ChV > 10^2$, not harmful, green label; $10^2 \geq LC_{50}/EC_{50}/ChV > 10^1$, harmful, yellow label; $10^1 \geq LC_{50}/EC_{50}/ChV > 10^0$, toxic, orange label; $LC_{50}/EC_{50}/ChV \leq 10^0$, very toxic, red label.

Compound	Acute toxicity (mg · dm^{-3})			Chronic toxicity *ChV* (mg · dm^{-3})		
	Fish (*LC$_{50}$*)	Daphnid (*LC$_{50}$*)	Green Algae (*EC$_{50}$*)	Fish	Daphnid	Green Algae
NPX	193	122	138	21.3	15.7	45.3
N1	1.77	1.22	2.07	0.218	0.208	0.845
N2	35.2	21.4	21.3	3.74	2.54	6.50
N3	24.0	14.9	15.8	2.60	1.84	5.01
OFL	$2.81 \cdot 10^5$	$1.30 \cdot 10^5$	$4.18 \cdot 10^4$	$2.16 \cdot 10^4$	$7.21 \cdot 10^3$	$6.97 \cdot 10^3$
O1	$4.13 \cdot 10^4$	$3.60 \cdot 10^3$	$5.52 \cdot 10^3$	$6.25 \cdot 10^3$	218	$1.46 \cdot 10^3$
O2	$4.48 \cdot 10^4$	$3.26 \cdot 10^3$	$7.14 \cdot 10^3$	$1.18 \cdot 10^4$	166	$1.66 \cdot 10^3$
HCHO	11.2	12.0	5.87	3.62	0.098	1.78
Piperazine	$1.14 \cdot 10^3$	98.3	154	179	5.89	40.5
N-phenylpiperazine	62.1	7.02	6.43	4.25	0.548	2.06
N-Phenylethylenediamine	204	20.7	23.4	19.2	1.46	6.93

increased PMS concentration does not change the toxicity assessment, although the kinetics of OFL degradation is higher. Therefore, considering economic and environmental aspects, there is no need to exaggerate with PMS concentration, because a higher kinetic rate constant does not influence on toxicity assessment. More important factor is to design the system which allows the efficient removal of pharmaceuticals and their derivatives as well as does not provide secondary risk pollution.

4. Conclusions

In this work, for the first time, $BiVO_4$-based photocatalysts were investigated in relation to their light-harvesting ability. To address this challenge, NH_4VO_3 was self-synthesised and used in $BiVO_4$ synthesis instead of the commercial counterpart. The application of designed vanadium precursor in BVO preparation leads to a reduction of particle size, dispersion stability and remarkably enhanced visible light absorption and scattering in $BiVO_4$, proved by LVRPA analyses. In consequence, changing the precursor allowed to improve the photocatalytic activity under visible light (>420 nm), reaching apparent kinetic rate constants 0.0140 min^{-1} and 0.0066 min^{-1} toward NPX and OFL removal, respectively.

Next, BVO_NHV_W sample was modified by sub-nanoclusters of mixed copper species with average oxidation state + 1.48, which presence was revealed by XANES measurements. This interface modification enhanced charge carriers separation and visible light response, resulting in an increase in the rate constants of 1.60 and 3.32-times for NPX and OFL removal, respectively. Finally, the addition of PMS at a low concentration of 0.1 mM accelerated the pharmaceuticals removal. PMS/Vis420/CuO_x/$BiVO_4$ system is capable of degrading various pharmaceutically active compounds. No significant decrease in the degradation efficiency was observed in three subsequent cycles of PAP process, indicating stability and reusability of Cu/0.1 BVO_NHV_W. Experiments with scavengers and Mott-Schottky measurements revealed that superoxide radicals can be formed and are the predominant reactive oxygen species that accelerated the PAP process.

Moreover, acute toxicity tests using *Vibrio fisheri* bacteria demonstrated that the proposed process can lower the toxicity rate in NPX removal. Based on QSAR models, these experimental results are vital, because NPX intermediate products are more toxic than undegraded molecules. In the case of fluoroquinolone antibiotic, increased toxicity rate and high Γ value were observed for OFL degradation. However, this effect is not permanent and the prolongation time of PAP process remarkably decreased the bioluminescence inhibition. Significantly, higher PMS concentration causes two negative effects: firstly, too high dosage induces Bi leaching and 4 % Bi loss from the photocatalyst, confirmed by ICP-OES analyses, secondly, despite the higher reaction kinetics, it does not lead to toxicity rate reduction.

In summary, the present study introduces new insight into $BiVO_4$-based photocatalyst preparation for improving light harvesting ability, which plays a crucial role in photocatalysis and peroxymonosulfate-assisted photocatalysis.

CRediT authorship contribution statement

Marta Kowalkińska: Writing – review & editing, Writing – original draft, Visualization, Methodology, Investigation, Formal analysis, Data curation, Conceptualization. **Alexey Maximenko:** Writing – review & editing, Investigation, Formal analysis. **Aleksandra Szkudlarek:** Writing – review & editing, Investigation, Formal analysis. **Karol Sikora:** Formal analysis. **Anna Zielińska-Jurek:** Writing – review & editing, Validation, Supervision, Resources, Project administration, Funding acquisition, Conceptualization.

Declaration of competing interest

The authors declare that they have no known competing financial interests or personal relationships that could have appeared to influence the work reported in this paper.

Data availability

Data will be made available on request.

Acknowledgments

The research was financially supported by the Polish National Science Centre, grant no. UMO-2021/43/B/ST5/02983. The authors used ASTRA beamline of the National Synchrotron Radiation Centre SOLARIS (Krakow, Poland). Alexey Maximenko acknowledges the Polish Ministry and Higher Education project: "Support for research and development with the use of research infrastructure of the National Synchrotron Radiation Centre SOLARIS" under contract nr 1/SOL/2021/2. The further development of the ASTRA beamline was supported within the EU Horizon2020 programme (952148-Sylinda).

Appendix A. Supplementary data

Supplementary data to this article can be found online at https://doi.org/10.1016/j.seppur.2024.127643.

References

[1] H. Wang, H. Xi, L. Xu, M. Jin, W. Zhao, H. Liu, Ecotoxicological effects, environmental fate and risks of pharmaceutical and personal care products in the water environment: a review, Sci. Total Environ. 788 (2021) 147819, https://doi.org/10.1016/j.scitotenv.2021.147819.

[2] Y. Yang, Y.S. Ok, K.H. Kim, E.E. Kwon, Y.F. Tsang, Occurrences and removal of pharmaceuticals and personal care products (PPCPs) in drinking water and water/sewage treatment plants: a review, Sci. Total Environ. 596–597 (2017) 303–320, https://doi.org/10.1016/j.scitotenv.2017.04.102.

[3] A. Pfau, Oral ofloxacin: a critical review of the new drug application, Clin. Infect. Dis. 16 (1993) 337, https://doi.org/10.1093/clind/16.2.337.

[4] R.H. Drew, B.S. Pharm, H.A. Gallis, Preview of new drugs potential for clinical application, Pharmacotherapy 8 (1988) 35–46, https://doi.org/10.1002/j.1875-9114.1988.tb04063.x.

[5] E. Korzeniewska, M. Harnisz, Sources, Occurrence, and environmental risk assessment of antibiotics and antimicrobial-resistant bacteria in aquatic environments of poland, Handbook of Environmental Chemistry 87 (2020) 179–193, https://doi.org/10.1007/978-3-030-12139-6_9.

[6] S. Rodriguez-Mozaz, I. Vaz-Moreira, S. Varela Della Giustina, M. Llorca, D. Barceló, S. Schubert, T.U. Berendonk, I. Michael-Kordatou, D. Fatta-Kassinos, J.L. Martinez, C. Elpers, I. Henriques, T. Jaeger, T. Schwartz, E. Paulshus, K. O'Sullivan, K.M. M. Pärnänen, M. Virta, T.T. Do, F. Walsh, C.M. Manaia, Antibiotic residues in final effluents of European wastewater treatment plants and their impact on the aquatic environment, Environ. Int. 140 (2020), https://doi.org/10.1016/j.envint.2020.105733.

[7] M. Caban, E. Lis, J. Kumirska, P. Stepnowski, Determination of pharmaceutical residues in drinking water in Poland using a new SPE-GC-MS(SIM) method based on Speedisk extraction disks and DIMETRIS derivatization, Sci. Total Environ. 538 (2015) 402–411, https://doi.org/10.1016/j.scitotenv.2015.08.076.

[8] D. Wojcieszyńska, U. Guzik, Naproxen in the environment: its occurrence, toxicity to nontarget organisms and biodegradation, Appl. Microbiol. Biotechnol. 104 (2020) 1849–1857, https://doi.org/10.1007/s00253-019-10343-x.

[9] O. Fawzi Suleiman Khasawneh, P. Palaniandy, Photocatalytic Degradation of Pharmaceuticals Using TiO2 Based Nanocomposite Catalyst-Review, Civil and Environmental Engineering Reports 29 (2019) 1–33, https://doi.org/10.2478/ceer-2019-0021.

[10] B.L. Phoon, C.C. Ong, M.S. Mohamed Saheed, P.L. Show, J.S. Chang, T.C. Ling, S. S. Lam, J.C. Juan, Conventional and emerging technologies for removal of antibiotics from wastewater, J. Hazard. Mater. 400 (2020) 122961, https://doi.org/10.1016/j.jhazmat.2020.122961.

[11] J. Gómez-Pastora, S. Dominguez, E. Bringas, M.J. Rivero, I. Ortiz, D.D. Dionysiou, Review and perspectives on the use of magnetic nanophotocatalysts (MNPCs) in water treatment, Chem. Eng. J. 310 (2017) 407–427, https://doi.org/10.1016/j.cej.2016.04.140.

[12] K.M. Lee, C.W. Lai, K.S. Ngai, J.C. Juan, Recent developments of zinc oxide based photocatalyst in water treatment technology: A review, Water Res. 88 (2016) 428–448, https://doi.org/10.1016/j.watres.2015.09.045.

[13] E. Mrotek, S. Dudziak, I. Malinowska, D. Pelczarski, Z. Ryżyńska, A. Zielińska-Jurek, Improved degradation of etodolac in the presence of core-shell ZnFe2O4/SiO2/TiO2 magnetic photocatalyst, Sci. Total Environ. 724 (2020), https://doi.org/10.1016/j.scitotenv.2020.138167.

[14] S. Wacławek, H.V. Lutze, K. Grübel, V.V.T. Padil, M. Černík, D.D. Dionysiou, Chemistry of persulfates in water and wastewater treatment: a review, Chem. Eng. J. 330 (2017) 44–62, https://doi.org/10.1016/j.cej.2017.07.132.

[15] J. Dan, P. Rao, Q. Wang, L. Dong, W. Chu, M. Zhang, Z. He, N. Gao, J. Deng, J. Chen, MgO-supported CuO with encapsulated structure for enhanced peroxymonosulfate activation to remove thiamphenicol, Sep. Purif. Technol. 280 (2022) 119782, https://doi.org/10.1016/j.seppur.2021.119782.

[16] K. Lalas, A. Petala, Z. Frontistis, I. Konstantinou, D. Mantzavinos, Sulfamethoxazole degradation by the CuOx/persulfate system, Catal. Today 361 (2021) 139–145, https://doi.org/10.1016/j.cattod.2020.01.047.

[17] S. He, Y. Chen, X. Li, L. Zeng, M. Zhu, Heterogeneous photocatalytic activation of persulfate for the removal of organic contaminants in water: a Critical Review, ACS ES&T Engineering 2 (2022) 527–546, https://doi.org/10.1021/acsestengg.1c00330.

[18] X. Wang, W. Lu, Z. Zhao, H. Zhong, Z. Zhu, W. Chen, In situ stable growth of β-FeOOH on g-C3N4 for deep oxidation of emerging contaminants by photocatalytic activation of peroxymonosulfate under solar irradiation, Chem. Eng. J. 400 (2020) 125872, https://doi.org/10.1016/j.cej.2020.125872.

[19] Y. Tian, Q. Li, M. Zhang, Y. Nie, X. Tian, C. Yang, Y. Li, pH-dependent oxidation mechanisms over FeCu doped g-C3N4 for ofloxacin degradation via the efficient peroxymonosulfate activation, J. Clean. Prod. 315 (2021) 1–10, https://doi.org/10.1016/j.jclepro.2021.128207.

[20] S. Feng, T. Xie, J. Wang, J. Yang, D. Kong, C. Liu, S. Chen, F. Yang, M. Pan, J. Yang, H. Du, H. Chen, Photocatalytic activation of PMS over magnetic heterojunction photocatalyst SrTiO3/BaFe12O19 for tetracycline ultrafast degradation, Chem. Eng. J. 470 (2023) 143900, https://doi.org/10.1016/j.cej.2023.143900.

[21] World Health Organization, Sulfate in Drinking-water Background document for development of WHO Guidelines for Drinking-water Quality (2004).

[22] X. Duan, S. Yang, S. Wacławek, G. Fang, R. Xiao, D.D. Dionysiou, Limitations and prospects of sulfate-radical based advanced oxidation processes, J. Environ. Chem. Eng. 8 (2020), https://doi.org/10.1016/j.jece.2020.103849.

[23] Z. Fang, R. Huang, P. Chelme-Ayala, Q. Shi, C. Xu, M. Gamal El-Din, Comparison of UV/Persulfate and UV/H2O2 for the removal of naphthenic acids and acute toxicity towards Vibrio fischeri from petroleum production process water, Sci. Total Environ. 694 (2019) 133686, https://doi.org/10.1016/j.scitotenv.2019.133686.

[24] C.V. Reddy, A. Nagar, N.P. Shetti, I.N. Reddy, S. Basu, J. Shim, R.R. Kakarla, Novel g-C3N4/BiVO4 heterostructured nanohybrids for high efficiency photocatalytic degradation of toxic chemical pollutants, Chemosphere 322 (2023) 138146, https://doi.org/10.1016/j.chemosphere.2023.138146.

[25] L. Chen, M. Zhang, J. Yang, Y. Li, Y. Sivalingam, Q. Shi, M. Xie, W. Han, Synthesis of BiVO4 quantum dots/reduced graphene oxide composites for CO2 reduction, Mater. Sci. Semicond. Process. 102 (2019) 104578, https://doi.org/10.1016/j.mssp.2019.06.013.

[26] X. Gao, C. Ma, Y. Liu, L. Xing, Y. Yan, Self-induced Fenton reaction constructed by Fe(III) grafted BiVO 4 nanosheets with improved photocatalytic performance and mechanism insight, Appl. Surf. Sci. 467–468 (2019) 673–683, https://doi.org/10.1016/j.apsusc.2018.10.172.

[27] J. Kang, Y. Tang, M. Wang, C. Jin, J. Liu, S. Li, Z. Li, J. Zhu, The enhanced peroxymonosulfate-assisted photocatalytic degradation of tetracycline under visible light by g-C3N4/Na-BiVO4heterojunction catalyst and its mechanism, J. Environ. Chem. Eng. 9 (2021) 105524, https://doi.org/10.1016/j.jece.2021.105524.

[28] X. Zheng, X. Zhang, Y. Cai, S. Zhao, S. Wang, Efficient degradation of bisphenol A with MoS2/BiVO4 hetero-nanoflower as a heterogenous peroxymonosulfate activator under visible-light irradiation, Chemosphere 289 (2022) 133158, https://doi.org/10.1016/j.chemosphere.2021.133158.

[29] H. Wang, Z. Long, R. Chen, H. Zhang, H. Shi, Y. Chen, Boosting PMS activation over BiVO4 piezo-photocatalyst to rapidly degrade tetracycline: Intermediates and mechanism, Sep. Purif. Technol. 331 (2024) 125598, https://doi.org/10.1016/j.seppur.2023.125598.

[30] Y. Deng, H. Zhou, Y. Zhao, B. Yang, M. Shi, X. Tao, S. Yang, R. Li, C. Li, Spatial separation of photogenerated charges on Well-Defined bismuth vanadate square nanocrystals, Small 18 (2022), https://doi.org/10.1002/smll.202103245.

[31] F. Wang, J. Zhang, C.C. Jin, X. Ke, F. Wang, D. Liu, Unveiling the effect of crystal facets on piezo-photocatalytic activity of BiVO4, Nano Energy 101 (2022) 107573, https://doi.org/10.1016/j.nanoen.2022.107573.

[32] Z. Long, X. Zheng, H. Shi, A. Photothermal-assisted, Construction of BiVO4/CoPc S-scheme heterojunctions with enhanced photothermal-assisted photocatalytic activity, Sci. China Mater. 67 (2024) 550–561, https://doi.org/10.1007/s40843-023-2773-9.

[33] R. Chen, H. Zhang, Y. Dong, H. Shi, Dual metal ions/BNQDs boost PMS activation over copper tungstate photocatalyst for antibiotic removal: Intermediate, toxicity assessment and mechanism, J. Mater. Sci. Technol. 170 (2024) 11–24, https://doi.org/10.1016/j.jmst.2023.07.005.

[34] Y. Chen, L. Soler, C. Cazorla, N.G. Bastús, V.F. Puntes, J. Llorca, Facet-engineered TiO2 drives photocatalytic activity and stability of supported noble metal clusters during H2 evolution, Nat. Commun. 14 (2023) 6165, https://doi.org/10.1038/s41467-023-41976-2.

[35] T. Han, H. Shi, Y. Chen, Facet-dependent CuO/{010}BiVO4 S-scheme photocatalyst enhanced peroxymonosulfate activation for efficient norfloxacin removal, J. Mater. Sci. Technol. 174 (2024) 30–43, https://doi.org/10.1016/j.jmst.2023.03.053.

[36] M. Prześniak-Welenc, M. Nadolska, B. Kościelska, K. Sadowska, Tailoring the size and shape-new path for ammonium metavanadate synthesis, Materials 12 (2019), https://doi.org/10.3390/ma12203446.

[37] B. Ravel, M. Newville, ATHENA, ARTEMIS, HEPHAESTUS: Data analysis for X-ray absorption spectroscopy using IFEFFIT, J. Synchrotron Radiat. 12 (2005) 537–541, https://doi.org/10.1107/S0909049505012719.

[38] E. Cako, S. Dudziak, P. Głuchowski, G. Trykowski, M. Pisarek, A. Fiszka Borzyszkowska, K. Sikora, A. Zielińska-Jurek, Heterojunction of (P, S) co-doped g-C3N4 and 2D TiO2 for improved carbamazepine and acetaminophen photocatalytic degradation Sep, Purif. Technol. 311 (2023), https://doi.org/10.1016/j.seppur.2023.123320.

[39] G. Li Puma, A. Brucato, Dimensionless analysis of slurry photocatalytic reactors using two-flux and six-flux radiation absorption-scattering models, Catal. Today 122 (2007) 78–90, https://doi.org/10.1016/j.cattod.2007.01.027.

[40] R. Acosta-Herazo, J. Monterroza-Romero, M.Á. Mueses, F. Machuca-Martínez, G. Li Puma, Coupling the Six Flux Absorption-Scattering Model to the Henyey-Greenstein scattering phase function: evaluation and optimization of radiation absorption in solar heterogeneous photoreactors, Chem. Eng. J. 302 (2016) 86–96, https://doi.org/10.1016/j.cej.2016.04.127.

[41] V. Synecek, F. Hanic, The crystal structure of ammonium metavanadate, Czech J. Phys. 4 (1954) 120–129, https://doi.org/10.1007/BF01687750.

[42] H.A. Abbood, H. Peng, X. Gao, B. Tan, K. Huang, Fabrication of cross-like NH4V4O10 nanobelt array controlled by CMC as soft template and photocatalytic activity of its calcinated product, Chem. Eng. J. 209 (2012) 245–254, https://doi.org/10.1016/j.cej.2012.08.027.

[43] G.S. Zakharova, C. Täschner, T. Kolb, C. Jähne, A. Leonhardt, B. Büchner, R. Klingeler, Morphology controlled NH4V3O8 microcrystals by hydrothermal synthesis, Dalton Trans. 42 (2013) 4897–4902, https://doi.org/10.1039/c3dt32550d.

[44] R.H. Baker, H. Zimmerman, R.N. Maxson, T. Moeller, W.W. Brandt, Ammonium metavanadate, Inorg. Synth. (1950) 117–188, https://doi.org/10.1002/9780470132340.ch30.

[45] S.H. Lee, J.M. Koo, S.G. Oh, S.S. Im, Facile synthesis of ammonium vanadate nanofibers by using reflux in aqueous V2O5 solution with ammonium persulfate, Mater. Chem. Phys. 194 (2017) 313–321, https://doi.org/10.1016/j.matchemphys.2017.03.053.

[46] X. Ren, Y. Liu, W. Guo, Morphology and crystal facet-dependent activation mechanism of persulfate by V2O5 nanomaterials for organic pollutants degradation, Sep. Purif. Technol. 253 (2020) 117501, https://doi.org/10.1016/j.seppur.2020.117501.
[47] K. Momma, F. Izumi, VESTA 3 for three-dimensional visualization of crystal, volumetric and morphology data, J. Appl. Cryst. 44 (2011) 1272–1276, https://doi.org/10.1107/S0021889811038970.
[48] V.I.E. Bruyère, P.J. Morando, M.A. Blesa, The dissolution of vanadium pentoxide in aqueous solutions of oxalic and mineral acids, J. Colloid Interface Sci. 209 (1999) 207–214, https://doi.org/10.1006/jcis.1998.5876.
[49] H. Hellevang, B.G. Haile, R. Miri, A Statistical approach to explain the solution stoichiometry effect on crystal growth rates, Cryst. Growth Des. 16 (2016) 1337–1348, https://doi.org/10.1021/acs.cgd.5b01466.
[50] M. Kowalkińska, J. Karczewski, A. Zielińska-Jurek, The Effect of titanium oxyfluoride morphology on photocatalytic activity of fluorine-doped titanium(IV) oxide, Crystals 13 (2023) 356, https://doi.org/10.3390/cryst13020356 Academic.
[51] X. Dong, Z. Chen, A. Tang, D.D. Dionysiou, H. Yang, Mineral modulated single atom catalyst for effective water treatment, Adv. Funct. Mater. 32 (2022), https://doi.org/10.1002/adfm.202111565.
[52] K. Ćwieka, Z. Bojarska, K. Czelej, D. Łomot, P. Dziegielewski, A. Maximenko, K. Nikiforow, L. Gradoń, M.Y. Qi, Y.J. Xu, J.C. Colmenares, Zero carbon footprint hydrogen generation by photoreforming of methanol over Cu/TiO2 nanocatalyst, Chem. Eng. J. 474 (2023), https://doi.org/10.1016/j.cej.2023.145687.
[53] Y. Liu, N. Marcella, J. Timoshenko, A. Halder, B. Yang, L. Kolipaka, M.J. Pellin, S. Seifert, S. Vajda, P. Liu, A.I. Frenkel, Mapping XANES spectra on structural descriptors of copper oxide clusters using supervised machine learning, J. Chem. Phys. 151 (2019), https://doi.org/10.1063/1.5126597.
[54] T.A.D. Nguyen, Z.R. Jones, B.R. Goldsmith, W.R. Buratto, G. Wu, S.L. Scott, T. W. Hayton, A Cu25 Nanocluster with Partial Cu(0) Character, J. Am. Chem. Soc. 137 (2015) 13319–13324, https://doi.org/10.1021/jacs.5b07574.
[55] B. Zandkarimi, G. Sun, A. Halder, S. Seifert, S. Vajda, P. Sautet, A.N. Alexandrova, Interpreting the Operando XANES of surface-supported subnanometer clusters: when fluxionality, oxidation state, and size effect fight, J. Phys. Chem. C 124 (2020) 10057–10066, https://doi.org/10.1021/acs.jpcc.0c02823.
[56] S. Wang, X. Wang, B. Liu, Z. Guo, K. Ostrikov, L. Wang, W. Huang, Vacancy defect engineering of BiVO4 photoanodes for photoelectrochemical water splitting, Nanoscale 13 (2021) 17989–18009, https://doi.org/10.1039/d1nr05691c.
[57] D.K. Pallotti, L. Passoni, P. Maddalena, F. Di Fonzo, S. Lettieri, Photoluminescence Mechanisms in Anatase and Rutile TiO2, The Journal of Physical Chemistry C 121 (2017) 9011–9021, https://doi.org/10.1021/acs.jpcc.7b00321.
[58] A.S. Rajashekharaiah, Y.S. Vidya, K.S. Anantharaju, G.P. Darshan, P. Lalitha, S. C. Sharma, H. Nagabhushana, Photoluminescence, thermoluminescence and photocatalytic studies of sonochemical synthesis of Bi2Zr2O7:Sm3+ nanomaterials, J. Mater. Sci. Mater. Electron. 31 (2020) 15627–15643, https://doi.org/10.1007/s10854-020-04126-8.
[59] J. Liqiang, Q. Yichun, W. Baiqi, L. Shudan, J. Baojiang, Y. Libin, F. Wei, F. Honggang, S. Jiazhong, Review of photoluminescence performance of nano-sized semiconductor materials and its relationships with photocatalytic activity, Sol. Energy Mater. Sol. Cells 90 (2006) 1773–1787, https://doi.org/10.1016/j.solmat.2005.11.007.
[60] R.P. Singh, K. Sharma, K. Mausam, Dispersion and stability of metal oxide nanoparticles in aqueous suspension: a review, Mater. Today:. Proc. 26 (2019) 2021–2025, https://doi.org/10.1016/j.matpr.2020.02.439.
[61] Y. Zhu, D. Li, S. Zuo, Z. Guan, S. Ding, D. Xia, X. Li, Cu2O/CuO induced non-radical/radical pathway toward highly efficient peroxymonosulfate activation, J. Environ. Chem. Eng. 9 (2021) 106781, https://doi.org/10.1016/j.jece.2021.106781.
[62] W. Wang, X. Huang, S. Wu, Y. Zhou, L. Wang, H. Shi, Y. Liang, B. Zou, Preparation of p-n junction Cu2O/BiVO4 heterogeneous nanostructures with enhanced visible-light photocatalytic activity, Appl Catal B 134–135 (2013) 293–301, https://doi.org/10.1016/j.apcatb.2013.01.013.
[63] E.M. Van Wieren, M.D. Seymour, J.W. Peterson, Interaction of the fluoroquinolone antibiotic, ofloxacin, with titanium oxide nanoparticles in water: Adsorption and breakdown, Sci. Total Environ. 441 (2012) 1–9, https://doi.org/10.1016/j.scitotenv.2012.09.067.
[64] X. Van Doorslaer, K. Demeestere, P.M. Heynderickx, H. Van Langenhove, J. Dewulf, UV-A and UV-C induced photolytic and photocatalytic degradation of aqueous ciprofloxacin and moxifloxacin: Reaction kinetics and role of adsorption, Appl Catal B 101 (2011) 540–547, https://doi.org/10.1016/j.apcatb.2010.10.027.
[65] D.Q. Zhang, T. Hua, R.M. Gersberg, J. Zhu, W.J. Ng, S.K. Tan, Carbamazepine and naproxen: Fate in wetland mesocosms planted with Scirpus validus, Chemosphere 91 (2013) 14–21, https://doi.org/10.1016/j.chemosphere.2012.11.018.
[66] Z. Honarmandrad, X. Sun, Z. Wang, M. Naushad, G. Boczkaj, Activated persulfate and peroxymonosulfate based advanced oxidation processes (AOPs) for antibiotics degradation - A review, Water Resour. Ind. 29 (2023) 100194, https://doi.org/10.1016/j.wri.2022.100194.
[67] D. Awfa, M. Ateia, M. Fujii, C. Yoshimura, Photocatalytic degradation of organic micropollutants: Inhibition mechanisms by different fractions of natural organic matter, Water Res. 174 (2020) 115643, https://doi.org/10.1016/j.watres.2020.115643.
[68] C. Qi, X. Liu, J. Ma, C. Lin, X. Li, H. Zhang, Activation of peroxymonosulfate by base: Implications for the degradation of organic pollutants, Chemosphere 151 (2016) 280–288, https://doi.org/10.1016/j.chemosphere.2016.02.089.
[69] National Research Council, Copper in Drinking Water (2000).
[70] Environmental Protection Agency, Toxicological Profile for Vanadium: Public health statement (2012).
[71] S. Vargas-Villanueva, D.A. Torres-Ceron, S. Amaya-Roncancio, I.D. Arellano-Ramírez, J.S. Riva, E. Restrepo-Parra, Study of the incorporation of S in TiO2/SO42− Coatings produced by PEO process through XPS and DFT, Appl. Surf. Sci. 599 (2022) 153811, https://doi.org/10.1016/j.apsusc.2022.153811.
[72] X. Liu, P. Shao, S. Gao, Z. Bai, J. Tian, Benzoquinone-assisted heterogeneous activation of PMS on Fe3S4 via formation of active complexes to mediate electron transfer towards enhanced bisphenol A degradation, Water Res. 226 (2022) 119218, https://doi.org/10.1016/j.watres.2022.119218.
[73] Y. Nosaka, A.Y. Nosaka, Generation and Detection of Reactive Oxygen Species in Photocatalysis, Chem. Rev. 117 (2017) 11302–11336, https://doi.org/10.1021/acs.chemrev.7b00161.
[74] M. Janczarek, E. Kowalska, On the origin of enhanced photocatalytic activity of copper-modified titania in the oxidative reaction systems, Catalysts 7 (2017), https://doi.org/10.3390/catal7110317.
[75] X. Qi, T. Jin, Y. Liu, Y. Tian, Y. Liu, S. Chi, J. Zhang, Y. Hu, D. Fang, J. Wang, Construction of a dual Z-scheme Cu|Cu2O/TiO2/CuO photocatalyst composite film with magnetic field enhanced photocatalytic activity, Sep. Purif. Technol. 301 (2022) 122019, https://doi.org/10.1016/j.seppur.2022.122019.
[76] Y. Nakabayashi, M. Nishikawa, N. Saito, C. Terashima, A. Fujishima, Significance of Hydroxyl Radical in Photoinduced Oxygen Evolution in Water on Monoclinic Bismuth Vanadate, J. Phys. Chem. C 121 (2017) 25624–25631, https://doi.org/10.1021/acs.jpcc.7b03641.
[77] H. Shi, Y. Li, X. Wang, H. Yu, J. Yu, Selective modification of ultra-thin g-C3N4 nanosheets on the (110) facet of Au/BiVO4 for boosting photocatalytic H2O2 production, Appl Catal B 297 (2021) 120414, https://doi.org/10.1016/j.apcatb.2021.120414.
[78] H. Shi, Y. Li, K. Wang, S. Li, X. Wang, P. Wang, F. Chen, H. Yu, Mass-transfer control for selective deposition of well-dispersed AuPd cocatalysts to boost photocatalytic H2O2 production of BiVO4, Chem. Eng. J. 443 (2022) 136429, https://doi.org/10.1016/j.cej.2022.136429.
[79] S. Dudziak, J. Karczewski, A. Ostrowski, G. Trykowski, K. Nikiforow, A. Zielińska-Jurek, Fine-Tuning the Photocatalytic Activity of the Anatase 1 0 1 facet through dopant-controlled reduction of the spontaneously present donor state density, ACS Materials Au (2024), https://doi.org/10.1021/acsmaterialsau.4c00008.
[80] R. Marotta, D. Spasiano, I. Di Somma, R. Andreozzi, Photodegradation of naproxen and its photoproducts in aqueous solution at 254 nm: a kinetic investigation, Water Res. 47 (2013) 373–383, https://doi.org/10.1016/j.watres.2012.10.016.
[81] M. Kowalkińska, K. Sikora, M. Łapiński, J. Karczewski, A. Zielińska-Jurek, Non-toxic fluorine-doped TiO2 nanocrystals from TiOF2 for facet-dependent naproxen degradation, Catal. Today 415 (2022) 113959, https://doi.org/10.1016/j.cattod.2022.11.020.
[82] P. Reuschenbach, M. Silvani, M. Dammann, D. Warnecke, T. Knacker, ECOSAR model performance with a large test set of industrial chemicals, Chemosphere 71 (2008) 1986–1995, https://doi.org/10.1016/j.chemosphere.2007.12.006.
[83] T. Ni, Z. Yang, H. Zhang, L. Zhou, W. Guo, L. Pan, Z. Yang, K. Chang, C. Ge, D. Liu, Peroxymonosulfate activation by Co3O4/SnO2 for efficient degradation of ofloxacin under visible light, J. Colloid Interface Sci. 615 (2022) 650–662, https://doi.org/10.1016/j.jcis.2022.02.024.
[84] Q. Su, J. Li, H. Yuan, B. Wang, Y. Wang, Y. Li, Y. Xing, Visible-light-driven photocatalytic degradation of ofloxacin by g-C3N4/NH2-MIL-88B(Fe) heterostructure: Mechanisms, DFT calculation, degradation pathway and toxicity evolution, Chem. Eng. J. 427 (2022), https://doi.org/10.1016/j.cej.2021.131594.
[85] G.G. Cash, Prediction of chemical toxicity to aquatic organisms: ECOSAR vs. Microtox® assay. Environmental Toxicology and Water, Quality 13 (1998) 211–216, https://doi.org/10.1002/(SICI)1098-2256(1998)13:3<211::AID-TOX2>3.0.CO;2-A.
[86] P. Calza, C. Medana, F. Carbone, V. Giancotti, C. Baiocchi, Characterization of intermediate compounds formed upon photoinduced degradation of quinolones by high-performance liquid chromatography/high- resolution multiple-stage mass spectrometry, Rapid Commun. Mass Spectrom. 22 (2008) 1533–1552, https://doi.org/10.1002/rcm.3537.
[87] J.B. Carbajo, A.L. Petre, R. Rosal, S. Herrera, P. León, E. García-Calvo, A. R. Fernández-Alba, J.A. Perdigón-Melón, Continuous ozonation treatment of ofloxacin: Transformation products, water matrix effect and aquatic toxicity, J. Hazard. Mater. 292 (2015) 34–43, https://doi.org/10.1016/j.jhazmat.2015.02.075.
[88] D. Calamari, R. Da Gasso, S. Galassi, A. Provini, M. Vighi, Biodegradation and toxicity of selected amines on aquatic organisms, Chemosphere 9 (1980) 753–762, https://doi.org/10.1016/0045-6535(80)90143-5.

Supplementary Materials

Addressing challenges of $BiVO_4$ light-harvesting ability through vanadium precursor engineering and sub-nanoclusters deposition for peroxymonosulfate-assisted photocatalytic pharmaceuticals removal

Marta Kowalkińska[1*], Alexey Maximenko[2], Aleksandra Szkudlarek[3], Karol Sikora[4], Anna Zielińska-Jurek[1*]

[1] Department of Process Engineering and Chemical Technology, Faculty of Chemistry, Gdansk University of Technology, G. Narutowicza 11/12 Street, 80-233 Gdansk, Poland

[2] SOLARIS National Synchrotron Radiation Centre, Jagiellonian University, Czerwone Maki 98, 30392 Cracow, Poland

[3] AGH University of Krakow, Academic Centre for Materials and Nanotechnology, av. Mickiewicza 30, 30-059 Krakow, Poland

[4] Department of Inorganic Chemistry, Faculty of Pharmacy, Medical University of Gdansk, M. Sklodowskiej-Curie 3a Street, 80-210 Gdansk, Poland

---

* Corresponding authors: marta.kowalkinska@pg.edu.pl (MK), annjurek@pg.edu.pl (AZJ)

TABLE OF CONTENTS

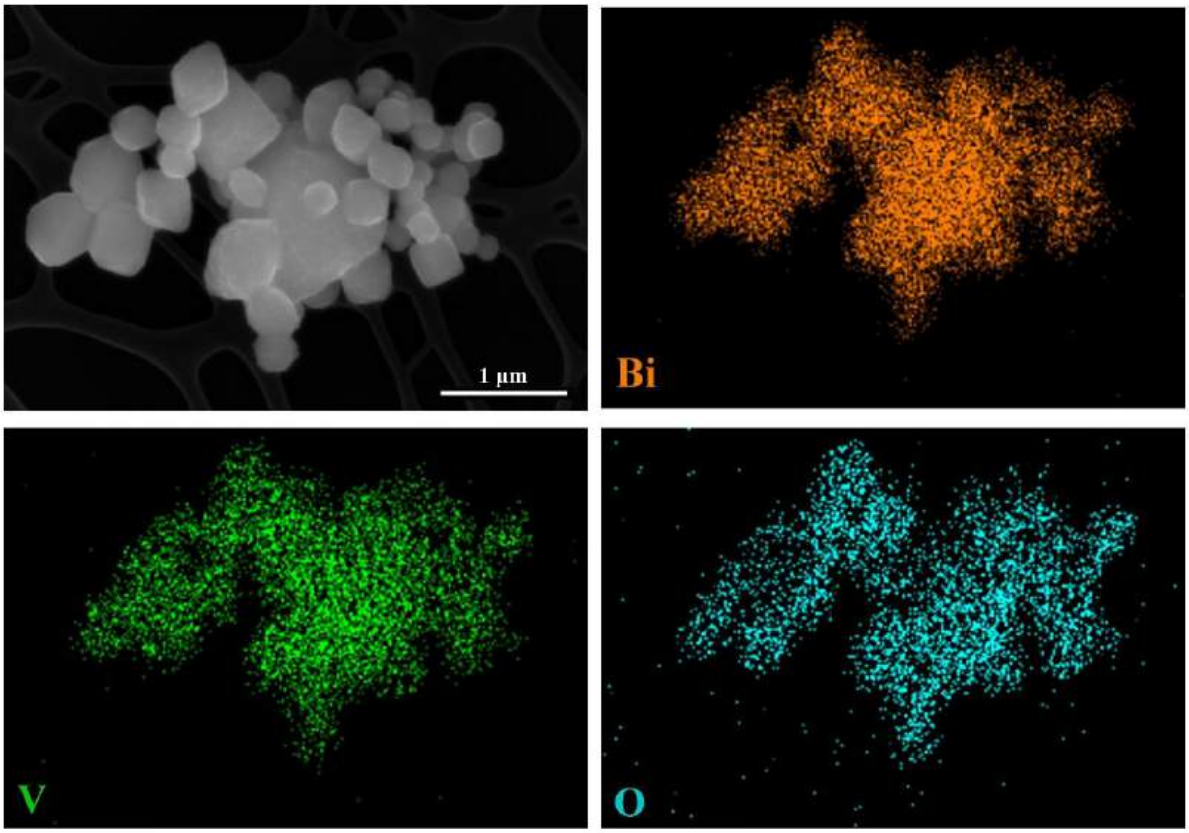

Figure S1. SEM mapping of Cu/0.1 BVO_NHV_W sample.

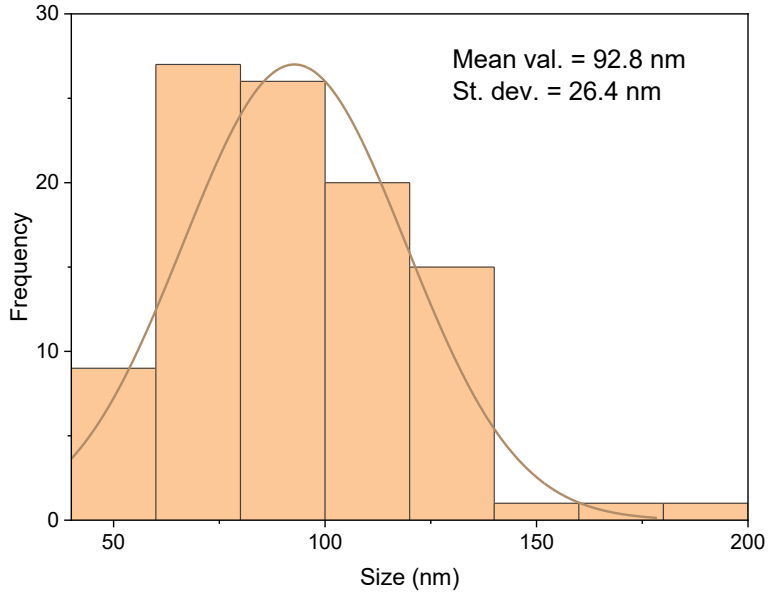

Figure S2. Size distribution of particles in Cu/0.1 BVO_NHV_W based on TEM image.

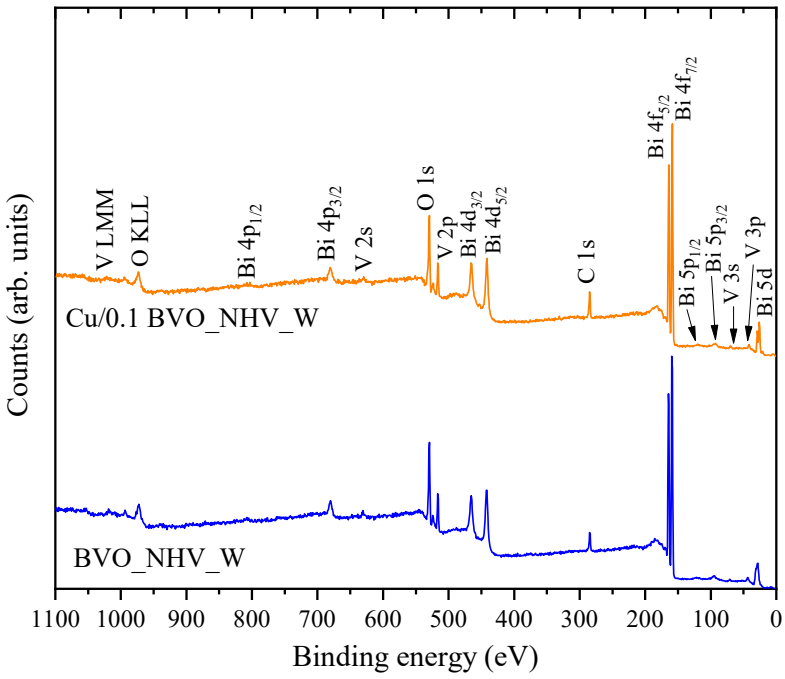

Figure S3. Survey scan of Cu/0.1 BVO_NHV_W and BVO_NHV_W samples.

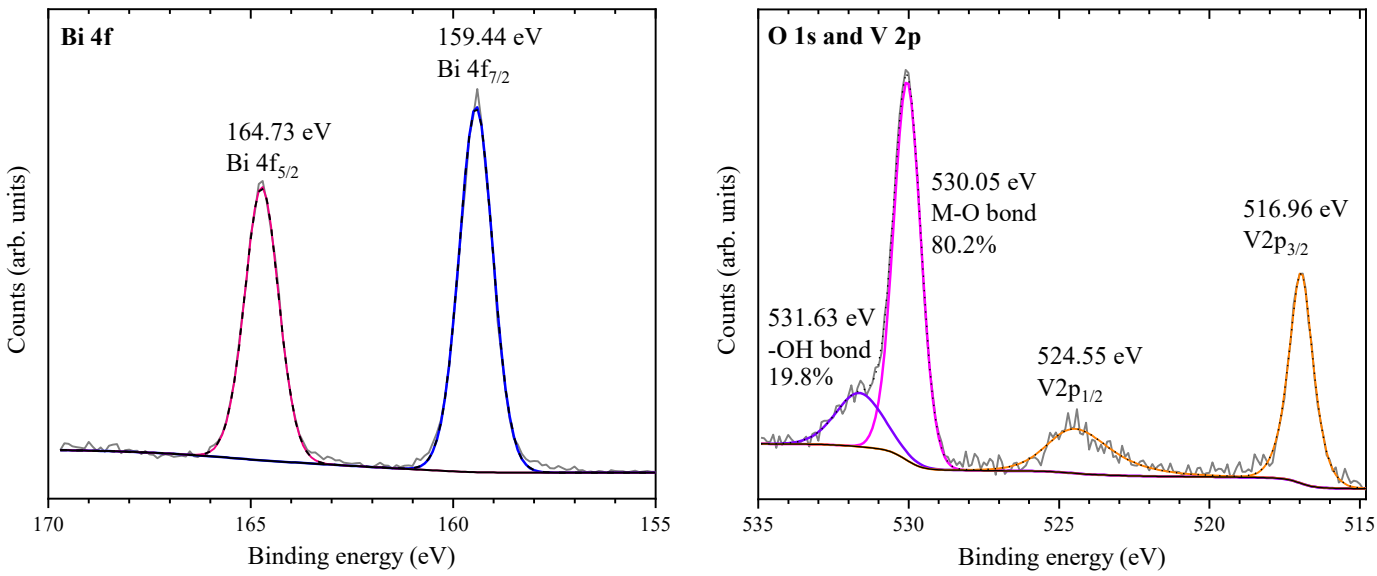

Figure S4. XPS spectra of BVO_NHV_W sample at Bi 4f, V 2p and O1s region.

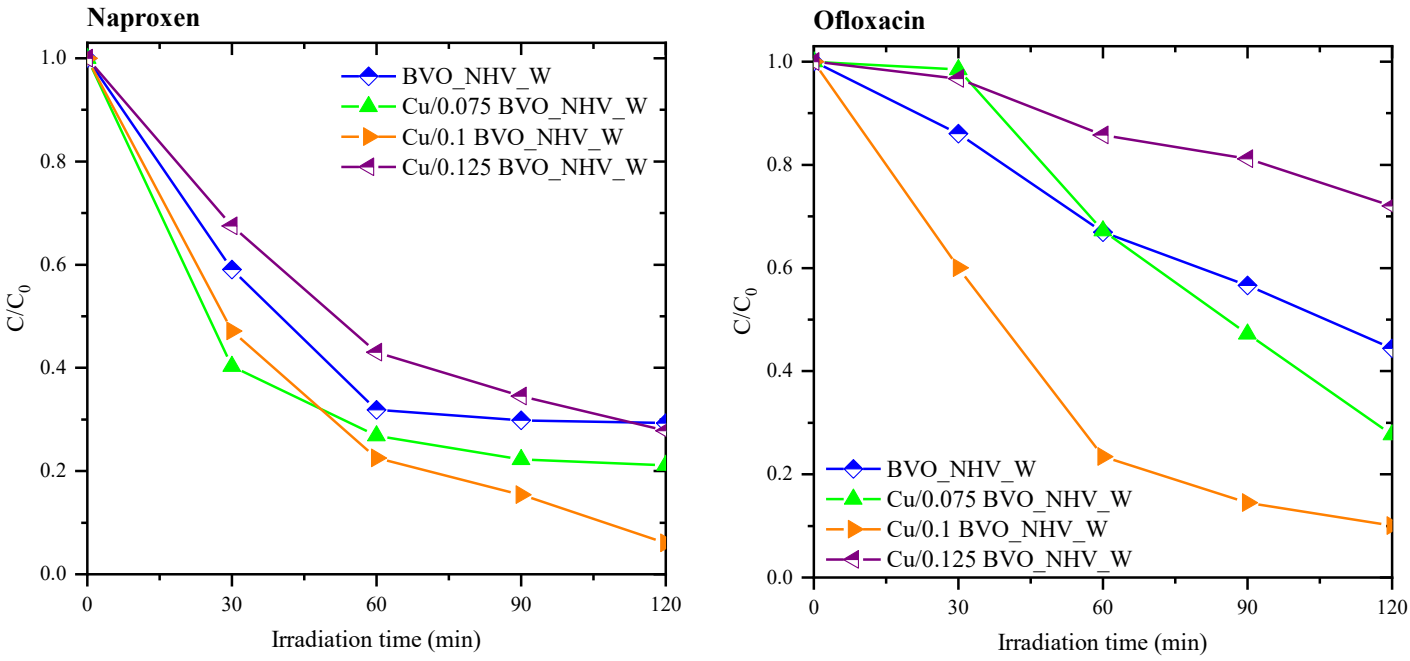

Figure S5. Effect of Cu/Bi content on photocatalytic NPX and OFL degradation.

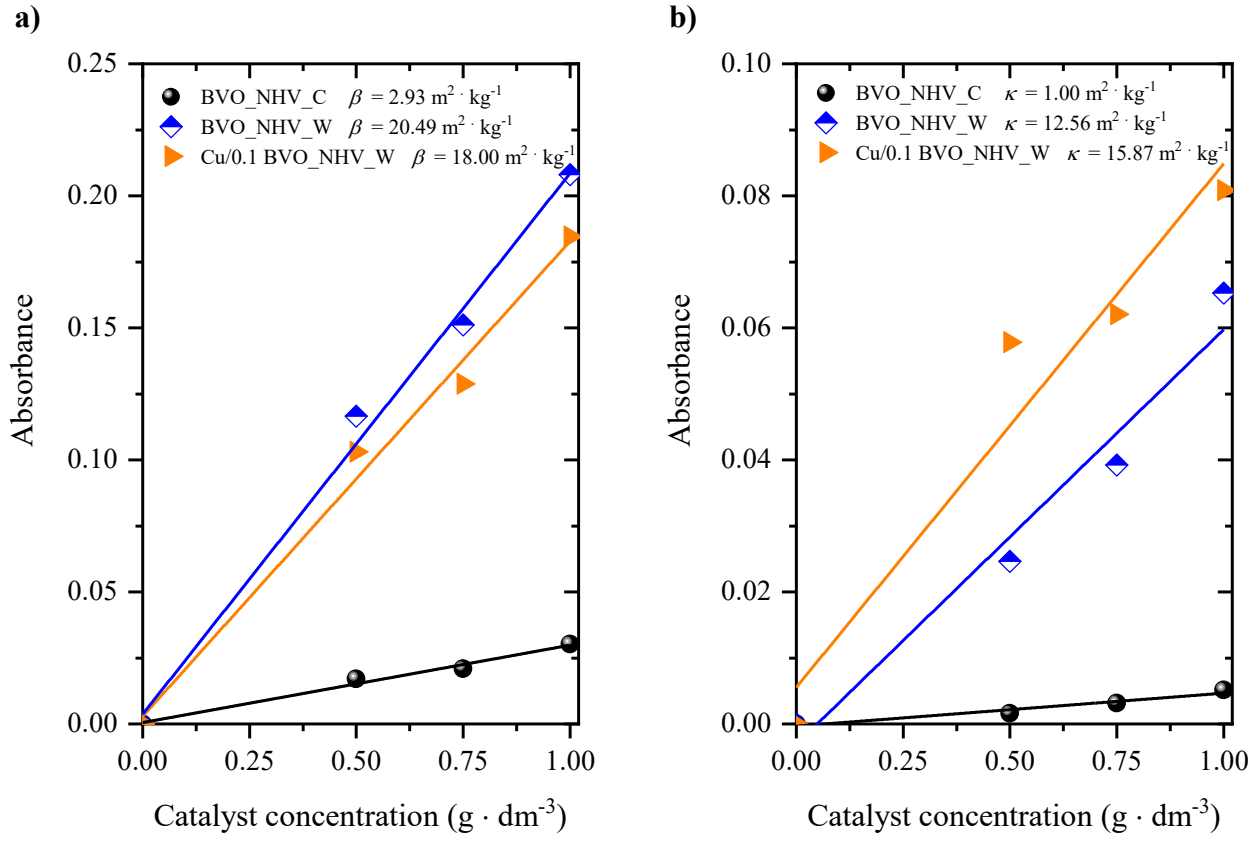

Figure S6. Dependence of the visible light spectral-average absorbance of the photocatalyst suspension on the photocatalyst dosage: **a)** without including scattered part of the radiation and **b)** including radiation scattered through the suspension. β and κ values are slopes of the fitted lines.

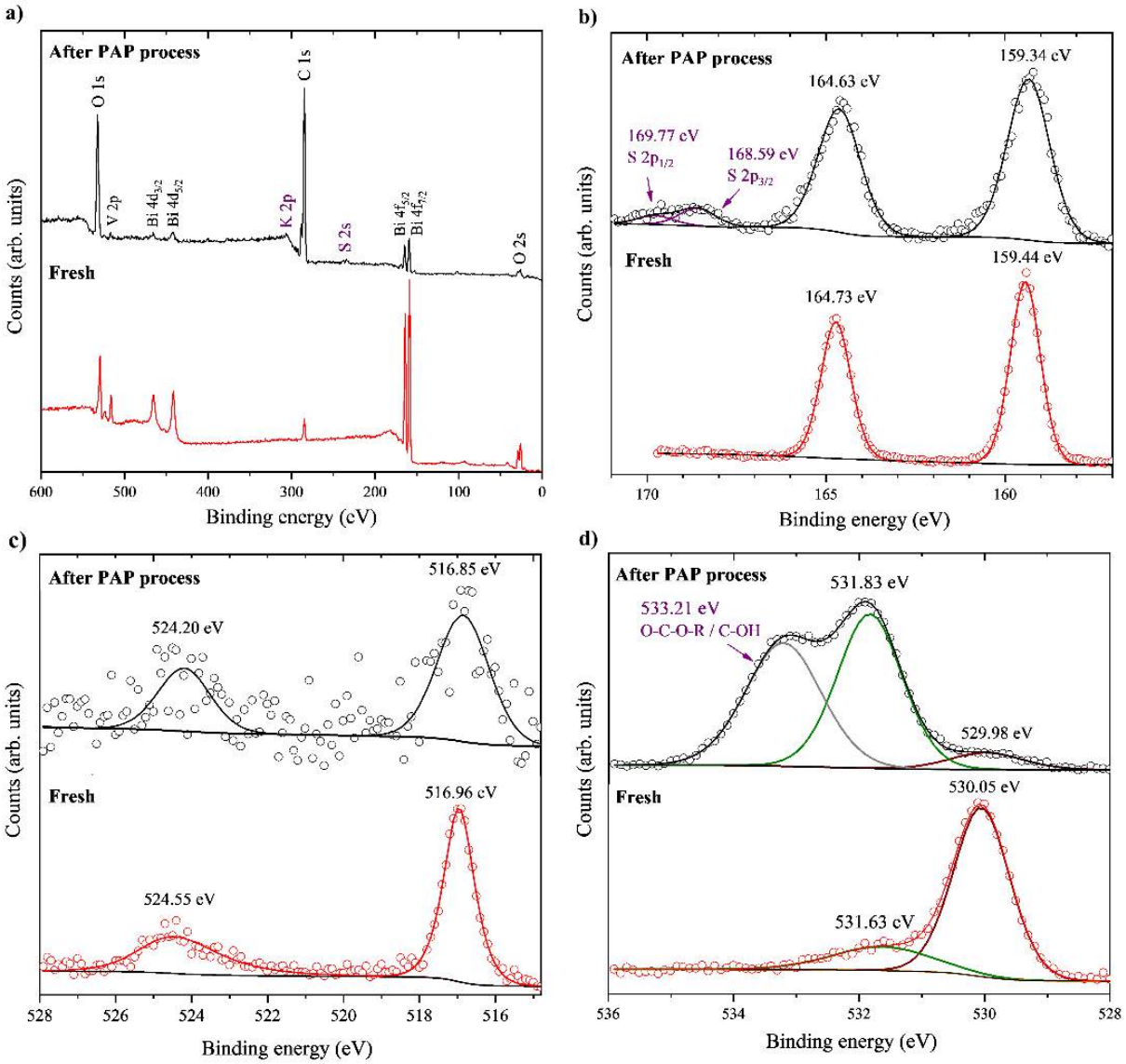

Figure S7. XPS spectra of fresh and used Cu/0.1 BVO_NHV_W sample: **a)** survey scan, **b)** Bi 4f and S 2p, **c)** V 2p and **d)** O 1s region.

a)

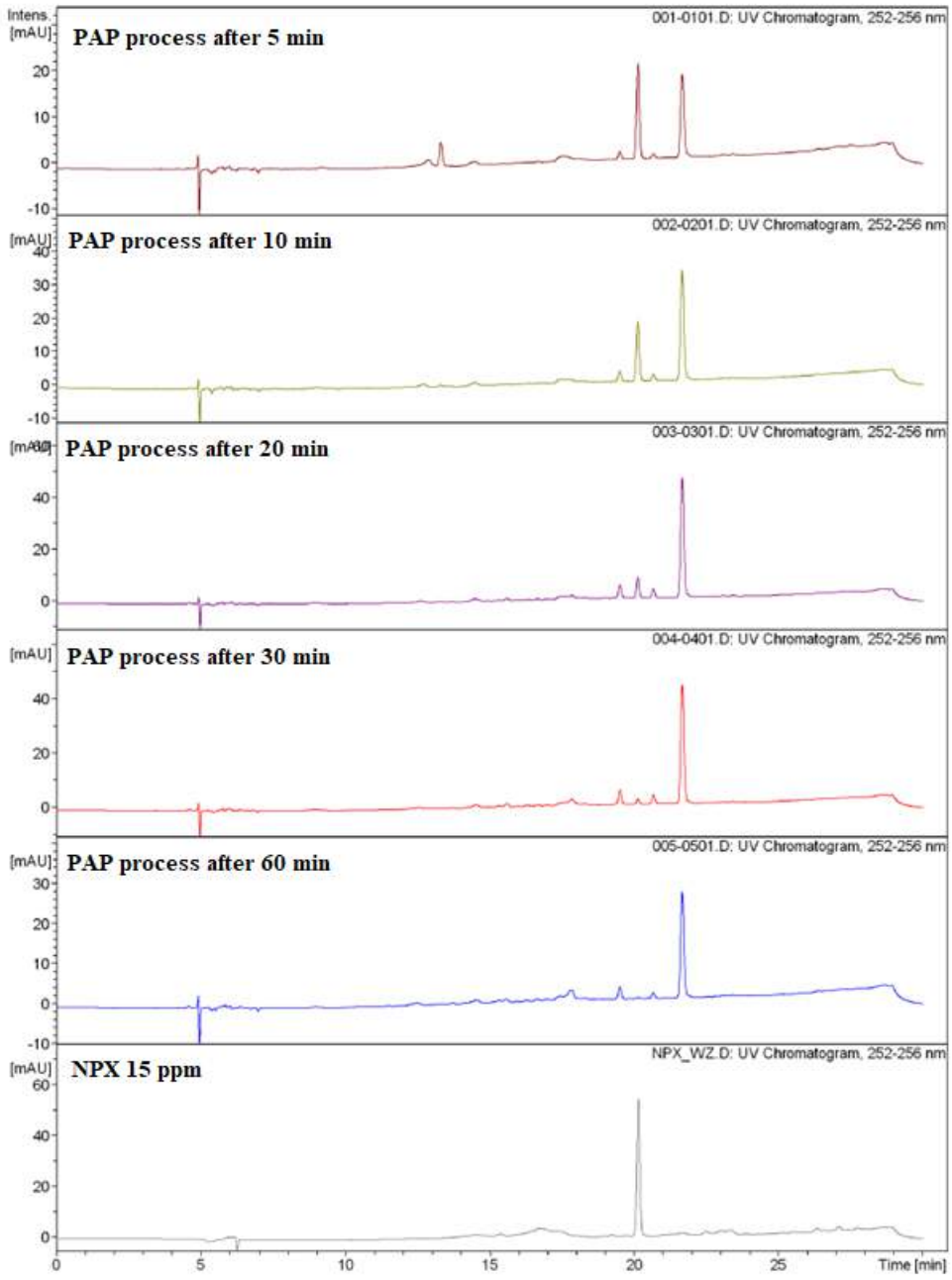
Intens.
[mAU]
001-0101.D: UV Chromatogram, 252-256 nm
PAP process after 5 min
002-0201.D: UV Chromatogram, 252-256 nm
PAP process after 10 min
003-0301.D: UV Chromatogram, 252-256 nm
PAP process after 20 min
004-0401.D: UV Chromatogram, 252-256 nm
PAP process after 30 min
005-0501.D: UV Chromatogram, 252-256 nm
PAP process after 60 min
NPX_WZ.D: UV Chromatogram, 252-256 nm
NPX 15 ppm
Time [min]

b)

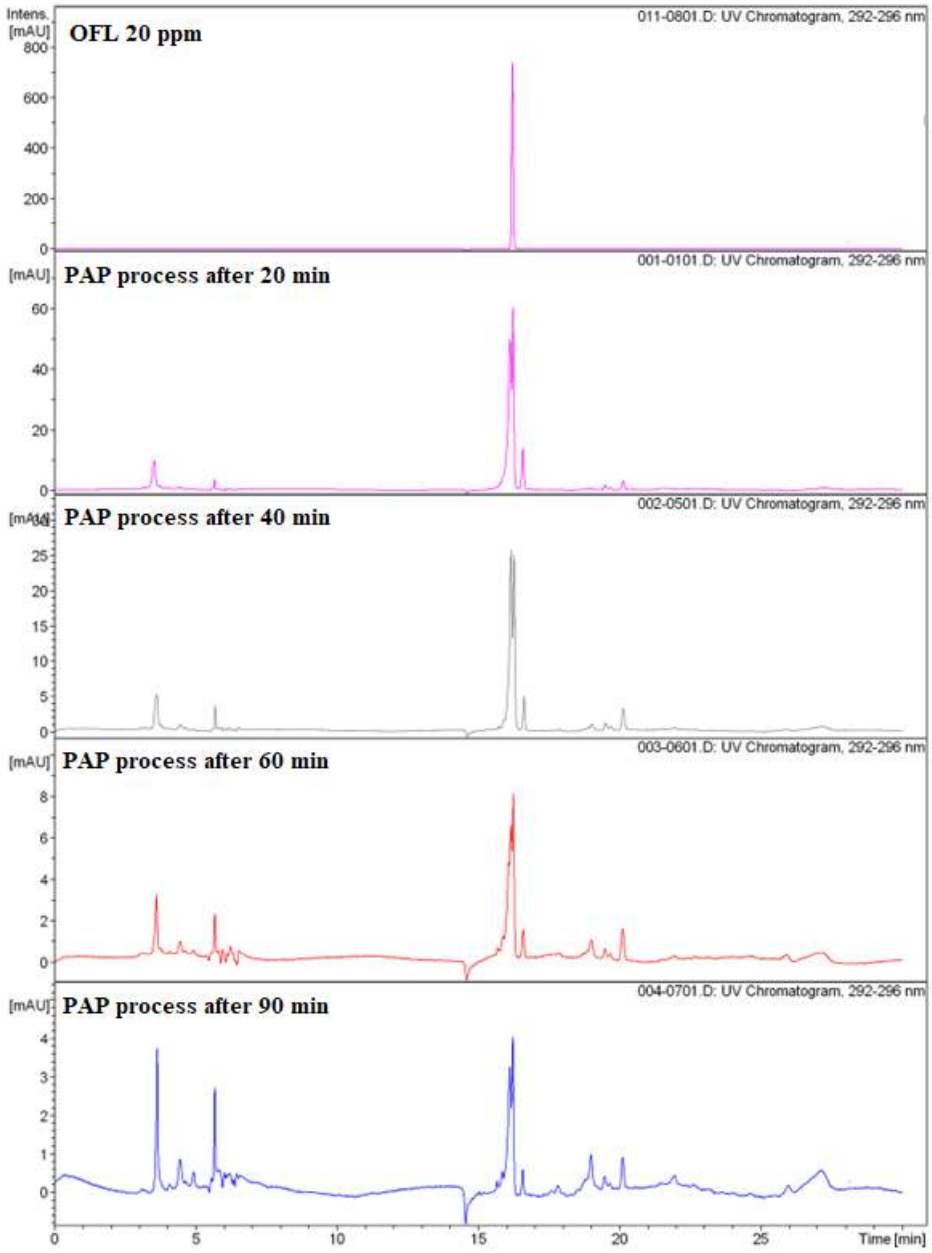

Figure S8. LC-MS chromatographs during **a)** NPX and **b)** OFL degradation in PMS/Vis420/CuO_x/$BiVO_4$ system.

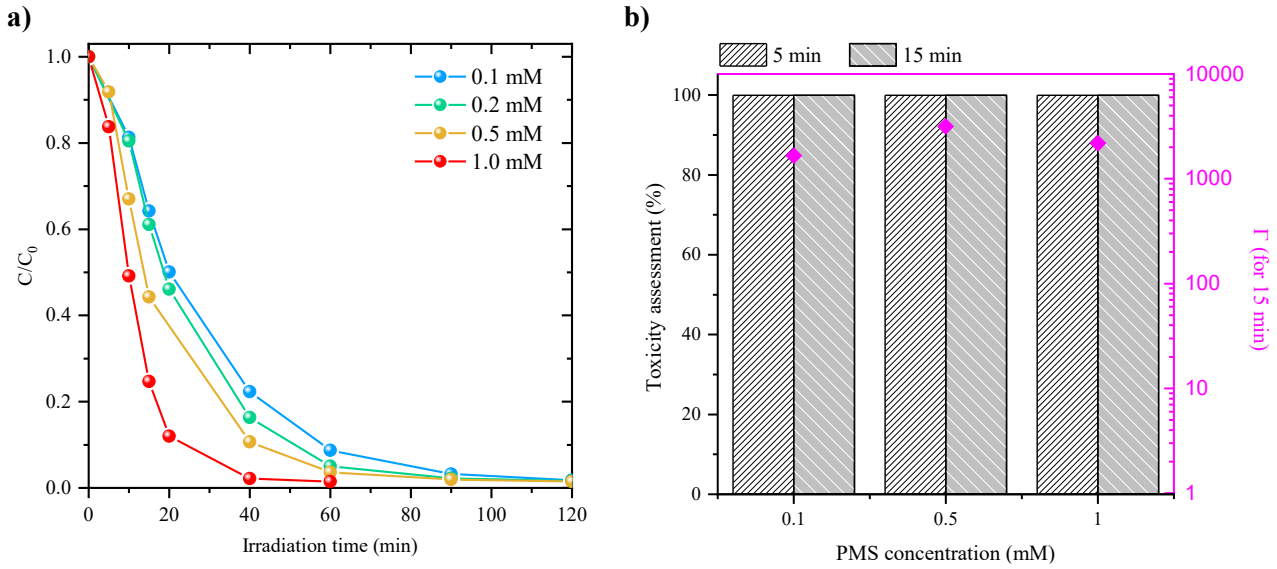

Figure S9. The effect of PMS concentration on **a)** OFL degradation and **b)** toxicity rate in PMS/Vis420/CuO_x/$BiVO_4$ system. Post-process wastewater was collected after 120 min of the process.

Table S1. Comparison of photocatalytic degradation of pharmaceutical drugs with reported literature.

Photocatalyst	**Irradiation and cut-off filter**	**NPX solution**	**Photocatalyst dosage (g·dm^{-3})**	**Rate constant (min^{-1})**	**Ref.**
S and W co-doped $BiVO_4$	150 W short arc lamp, λ > 420 nm	Acid, 10 ppm	1.0	0.007	[1]
H_2O_2-modified TiO_2	500 W metal halogen lamp, λ > 420 nm	Type of NPX not mentioned, 0.5 ppm	0.5	0.044	[2]
Bi_2MoO_6/g-C_3N_4	300 W Xenon lamp, λ > 420 nm	Type of NPX not mentioned, 10 ppm	0.2	0.033	[3]
Ag_I/g-C_3N_4	300 W Xenon lamp, λ > 400 nm	Not mentioned	0.2	0.069	[4]
Ag/AgI/ZnO	300 W Xenon lamp, λ > 400 nm	Acid, 2 ppm	0.1	0.083	[5]
Octahedral F-TiO_2	300 W Xenon lamp, λ > 420 nm	Acid, 15 ppm, aerated	0.5	0.009	[6]
Cu/ 0.1 BVO_NHV_W	300 W Xenon lamp, λ > 420 nm	Acid, 15 ppm	1.0	0.0224	This work
Photocatalyst	**Irradiation source**	**OFL solution**	**Photocatalyst dosage (g·dm^{-3})**	**Rate constant (min^{-1})**	**Ref.**
Co(II)-doped MoS_2	300 W Xe lamp, λ > 420 nm	20 ppm, pH = 8	0.1	0.0091	[7]
$CuFeO_2$	300 W Xe lamp, no filter	10 ppm, pH = 3.6	0.4	0.00918	[8]
Bi_2MoO_6/rGO/TiO_2	150 W tungsten lamp	$4 \cdot 10^{-5}$ M	0.4	0.0174	[9]
$BiFeO_3$	CFL Bulb (85 W)	10 ppm	0.5	0.0097	[10]
g-C_3N_4/NH_2-MIL88B(Fe)	300 W Xe, λ > 420 nm	10 ppm, pH = 5	0.25	0.0217	[11]
Cu/0.1 BVO_NHV_W	300 W Xenon lamp, λ > 420 nm	20 ppm	1.0	0.0219	This work

Table S2. Bi, V and Cu leaching and concentration of selected inorganic ions after PAP process with Cu/0.1 BVO_NHV_W using ICP-OES and ion chromatography.

Element	Concentration after PAP process with 0.1 mM PMS (mg · dm^{-3})	Concentration after PAP process with 1.0 mM PMS (mg · dm^{-3})
Cu	0.058 ± 0.005	0.050 ± 0.005
V	0.070 ± 0.005	0.194 ± 0.009
Bi	under sensitivity level	0.468 ± 0.016
SO_4^{2-}	18.98 ± 0.91	184.23 ± 9.12
F^-	0.535 ± 0.016	0.699 ± 0.049

Table S3. Calculations of relative errors.

NPX degradation using BVO_NHV_W + Vis420			OFL degradation using Cu/0.1 BVO_NHV_W + Vis420 + PMS		
	k (min^{-1})	R^2		k (min^{-1})	R^2
Repetition 1	0.0141	0.9981	Cycle I	0.0384	0.9963
Repetition 2	0.0126	0.9936	Cycle II	0.0338	0.9916
Repetition 3	0.0153	0.9927	Cycle III	0.0337	0.9903
Average	0.0140		**Average**	0.0353	
Standard deviation	0.001353		**Standard deviation**	0.002685	

Table S4. Calculations of process variables effects (CuO_x modification and PMS addition).

	Rate constants	
Process/Effect	**NPX degradation**	**OFL degradation**
BVO_NHV_W + Vis420 (k_1)	0.0140 min^{-1}	0.0066 min^{-1}
Cu/0.1 BVO_NHV_W + Vis420 (k_2)	0.0224 min^{-1}	0.0219 min^{-1}
Effect of CuO_x modification k_2/k_1	1.60	3.32
Cu/0.1 BVO_NHV_W + Vis420 + PMS (k_3)	0.0966 min^{-1}	0.0353 min^{-1}
Effect of PMS addition k_3/k_2	4.31	1.61
Effect of CuO_x modification and PMS addition k_3/k_1	6.90	5.35

Table S5. Detected intermediate products formed during PAP process for NPX and OFL degradation reaction with Cu/0.1 BVO_NHV_W. All compounds were detected in positive ionization mode.

m/z	t_R (min)	Compound name	Chemical structure
230.9	20.2	(S)-(+)-2-(6-methoxy-2-naphthyl)propionic acid (**NPX**)	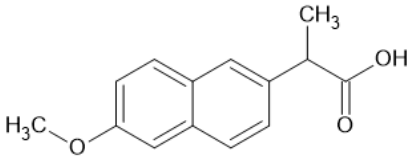
284.9	19.5	2-methoxy-6-vinylnaphthalene (**N1**)	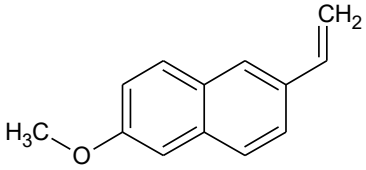
200.9	20.8	1-(6-methoxy-2-naphthyl)ethanol (**N2**)	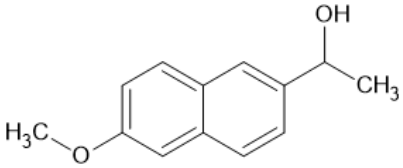
200.9	21.8	2-acetyl-6-methoxynaphthalene (**N3**)	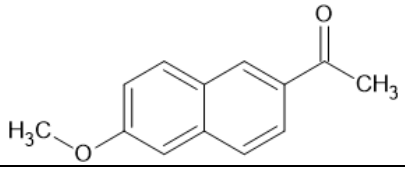
362.1	16.2	**OFL**	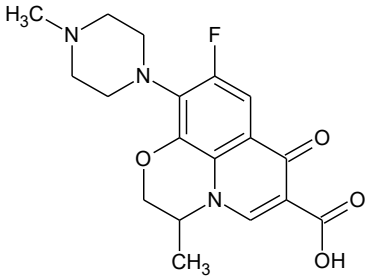
364.1	15.8	**O1**	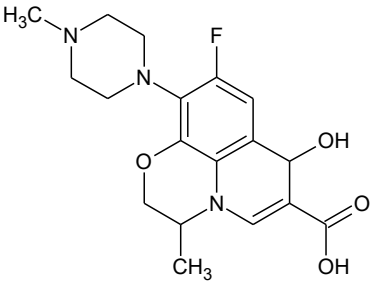
378.1	16.6	**O2**	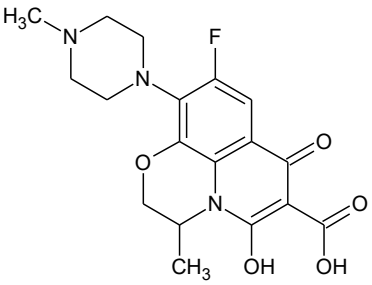

References:

[1] C. Regmi, Y. K. Kshetri, R. P. Pandey, & S. W. Lee, Visible-light-driven S and W co-doped dendritic BiVO4 for efficient photocatalytic degradation of naproxen and its mechanistic analysis. Molecular Catalysis, 453 (2018) 149–160. https://doi.org/10.1016/j.mcat.2018.05.008.

[2] G. Fan, J. Zhan, J. Luo, J. Zhang, Z. Chen, & Y. You, Photocatalytic degradation of naproxen by a H2O2-modified titanate nanomaterial under visible light irradiation. Catalysis Science and Technology, 9 (2019) 4614–4628. https://doi.org/10.1039/c9cy00965e.

[3] K. Fu, Y. Pan, C. Ding, J. Shi, & H. Deng, Photocatalytic degradation of naproxen by Bi2MoO6/g-C3N4 heterojunction photocatalyst under visible light: Mechanisms, degradation pathway, and DFT calculation. Journal of Photochemistry and Photobiology A: Chemistry, 412 (2021) 113235. https://doi.org/10.1016/j.jphotochem.2021.113235.

[4] F. Wang, Y. Wang, Y. Feng, Y. Zeng, Z. Xie, Q. Zhang, Y. Su, P. Chen, Y. Liu, K. Yao, W. Lv, & G. Liu, Novel ternary photocatalyst of single atom-dispersed silver and carbon quantum dots co-loaded with ultrathin g-C3N4 for broad spectrum photocatalytic degradation of naproxen. Applied Catalysis B: Environmental, 221 (2018) 510–520. https://doi.org/10.1016/j.apcatb.2017.09.055.

[5] C. Ding, K. Fu, M. Wu, S. Gong, J. Liu, J. Shi, & H. Deng, Photocatalytic performance and mechanism of AgI/Ag/ZnO composites as catalysts for the visible-light-driven degradation of naproxen. Journal of Photochemistry and Photobiology A: Chemistry, 414 (2021) 113283. https://doi.org/10.1016/j.jphotochem.2021.113283.

[6] M. Kowalkińska, K. Sikora, M. Łapiński, J. Karczewski, & A. Zielińska-Jurek, Non-toxic fluorine-doped TiO2 nanocrystals from TiOF2 for facet-dependent naproxen degradation. Catalysis Today, 415 (2022) 113959. https://doi.org/10.1016/j.cattod.2022.11.020.

[7] P. Chen, Y. Gou, J. Ni, Y. Liang, B. Yang, F. Jia, & S. Song, Efficient Ofloxacin degradation with Co(II)-doped MoS2 nano-flowers as PMS activator under visible-light irradiation. Chemical Engineering Journal, 401 (2020) 125978. https://doi.org/10.1016/j.cej.2020.125978.

[8] X. qiang Cao, F. Xiao, Z. wen Lyu, X. yu Xie, Z. xing Zhang, X. Dong, J. xiang Wang, X. jun Lyu, Y. zhen Zhang, & Y. Liang, CuFe2O4 supported on montmorillonite to activate peroxymonosulfate for efficient ofloxacin degradation. Journal of Water Process Engineering, 44 (2021) 102359. https://doi.org/10.1016/j.jwpe.2021.102359.

[9] A. Raja, N. Son, & M. Kang, Construction of visible-light driven Bi2MoO6-rGO-TiO2 photocatalyst for effective ofloxacin degradation. Environmental Research, 199 (2021) 111261. https://doi.org/10.1016/j.envres.2021.111261.

[10] G. Gupta, S. K. Kansal, A. Umar, & S. Akbar, Visible-light driven excellent photocatalytic degradation of ofloxacin antibiotic using BiFeO3 nanoparticles. Chemosphere, 314 (2023) 137611. https://doi.org/10.1016/j.chemosphere.2022.137611.

[11] Q. Su, J. Li, H. Yuan, B. Wang, Y. Wang, Y. Li, & Y. Xing, Visible-light-driven photocatalytic degradation of ofloxacin by g-C3N4/NH2-MIL-88B(Fe) heterostructure: Mechanisms, DFT calculation, degradation pathway and toxicity evolution. Chemical Engineering Journal, 427 (2022). https://doi.org/10.1016/j.cej.2021.131594.

4.6. Chapter VI: Facet-dependent naproxen degradation and PMS activation over $BiVO_4$ microcrystals

Followed by recent literature and studies presented in [P3], the investigation into crystal facets engineering was extended to $BiVO_4$ materials. Two effects of crystal facets exposition were considered – for photocatalytic NPX degradation and PMS activation during PMS-assisted photocatalysis. For comparison, $BiVO_4$ prepared *via* solid-state reaction was also included in these studies. As shown in Figure 4.15, single-phase compounds with high crystallinity were obtained. All the samples crystallized in the monoclinic scheelite structure, according to Rietveld refinement performed based on the reference card from the COD database.

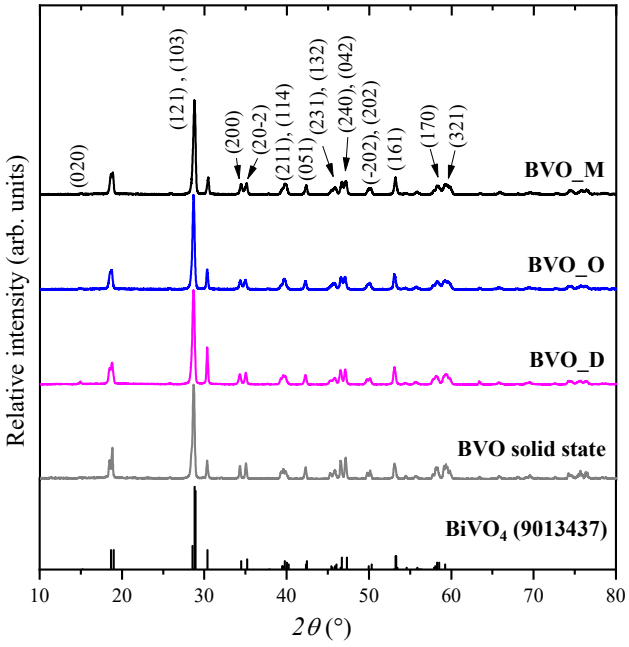

Figure 4.15. XRD patterns of facet-engineered $BiVO_4$.

Crystal facets identification was performed based on comparison of SEM images with the known crystal symmetry of (m–s) $BiVO_4$. The orientation between particular crystal planes was well-defined, resulted directly from the unit cell dimensions (lengths of vectors and angles between them). Therefore, geometrical analysis of crystals should be consistent with the as-obtained material shapes. When SDBS surfactant was used in hydrothermal synthesis, $BiVO_4$ octahedra were formed (Figure 4.16a). The measured angles from SEM images are in agreement with the geometrical construction of the bipyramids with exposed {1 2 0} and {0 2 1} crystal facets. These facets were identified in BVO_O sample, consistent with similar works [93,94]. The same approach was applied for the decahedra-shaped BVO_D photocatalyst (Figure 4.16b), and {0 1 0}, {1 1 0} and {0 1 1} crystal facets were identified, similarly to the published studies [95,131].

In case of BVO_M (Figure 4.16c), synthesized in the presence of SDS surfactant, this sample is similar to BVO_D, but more facets can be noticed, such as high-index {1 1 1} facets [92], together with the higher exposition of the {1 1 0} facets and lower share of the {0 1 0}. EDX spectroscopy confirmed the stoichiometry of the bulk samples, as presented in Table 4.3.

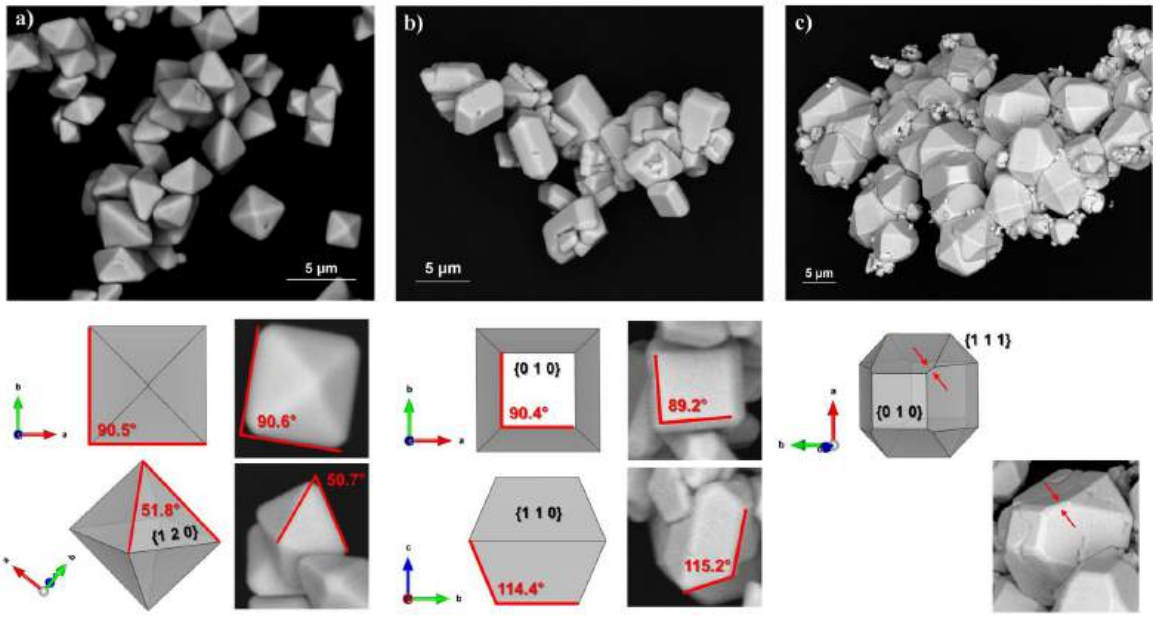

Figure 4.16. SEM images of **a)** BVO_O, **b)** BVO_D and **c)** BVO_M and their juxtaposition with geometrical configuration.

The analysis of surface chemical state was performed using XPS spectroscopy. Noteworthy, the surface atomic Bi:V ratio, presented in Table 4.3 was significantly higher than in the stoichiometric compound prepared *via* solid-state reaction (0.78). Therefore, it can be assumed that facets-engineered photocatalysts prepared under hydrothermal conditions possessed bismuth-rich surfaces. Deconvoluted XPS spectra of $BiVO_4$ samples at Bi 4f and V2p regions (Figures 4.17a-b) revealed well-defined Bi^{3+} doublets with peak separation of 5.3 eV, and V^{5+} species were detected, exhibiting a peak separation of 5.7 eV between V $2p_{3/2}$ and V $2p_{1/2}$ signals, respectively. Moreover, valence-band XPS (VB-XPS) spectra were performed to determine the VB position in relation to the Fermi level. As presented in Figure 4.17c and Table 4.3, the VB maximum of Bi-rich samples was higher than for the stoichiometric $BiVO_4$. Therefore, the crystal facets exposition and surface stoichiometry affected the band structure.

DR/UV-vis spectroscopy revealed that all the samples absorb light in the UV, blue and cyan range, indicating potential visible-light photocatalytic activity. Their band gap energies for BVO_O, BVO_D and BVO_M were 2.53 eV, 2.45 eV and 2.42 eV, respectively.

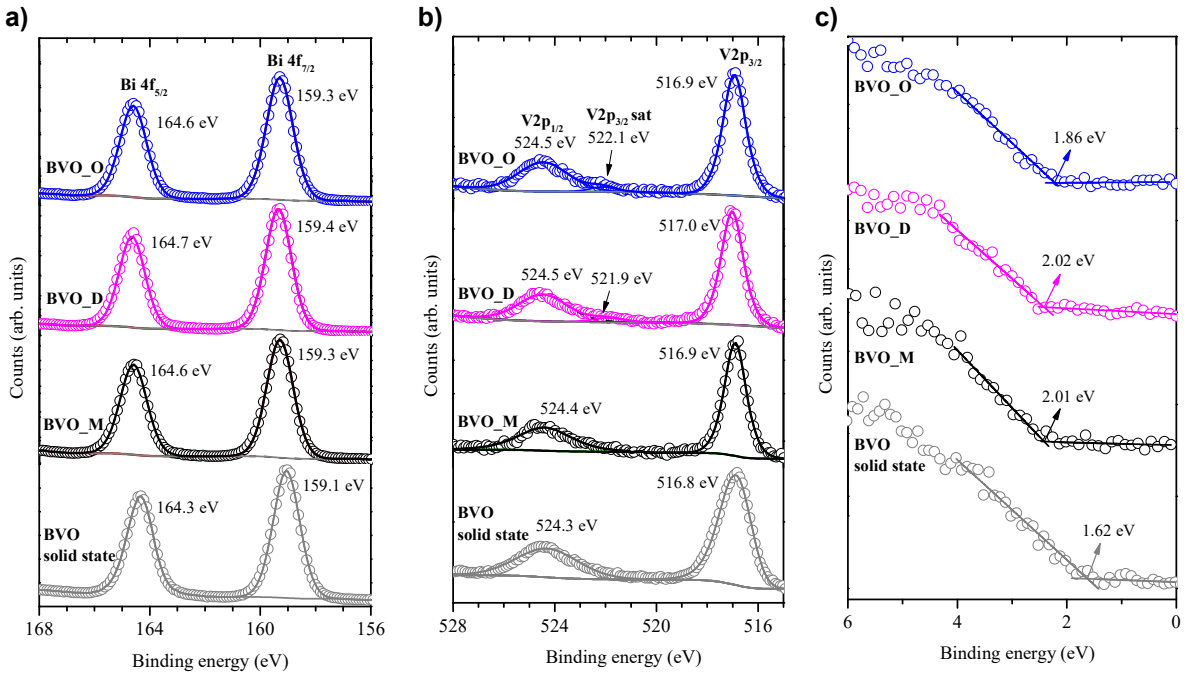

Figure 4.17. Deconvoluted XPS spectra at **a)** Bi4f and **b)** V2p regions with Gaussian/Lorentzian mixed-function, **c)** VB-XPS spectra of $BiVO_4$ samples.

Table 4.3. Results of specific surface area, elementary and surface analysis.

Sample name	S_{BET} (m^2/g)	EDS Bi:V ratio	Surface Bi:V	VB position (eV)
BVO_M	0.4	1.03	1.99	2.01
BVO_D	0.7	0.96	1.84	2.02
BVO_O	1.4	0.96	2.0	1.86
BVO solid state	not applicable	not applicable	0.78	1.62

The photocatalytic activity of facet-engineered $BiVO_4$ microcrystal materials was investigated toward NPX degradation under visible light (λ > 420 nm). Figures 4.18a-c present changes of NPX concentration during photocatalysis and PMS-assisted photocatalysis. As presented in Figure 4.18a, each photocatalyst interacted with the pollutant under visible light, led to a decrease in NPX concentration. The photocatalytic degradation rate followed the order BVO_O > BVO_D > BVO_M. However, after normalization the kinetic rate constants per specific surface area, BVO_O exhibited the lowest ratio. This control calculation suggests that the crystal facets effect is probably not observed for the pure photocatalytic process. The addition of PMS oxidant, depicted in Figure 4.18b, had two effects: acceleration of NPX degradation rate and TOC reduction from 10.09 mg/dm^3 (pure NPX solution) to 7.05 mg/dm^3 and 7.41 mg/dm^3 for BVO_O/PMS/Vis420 and BVO_D/PMS/Vis420 systems, respectively. As shown in Figure 4.18c, the highest enhancement of the kinetic rate constant without and in the presence of PMS was observed for BVO_D. This result suggests that {0 1 0} and {1 1 0} crystal facets of decahedral $BiVO_4$ are the most suitable for photocatalytic PMS

activation. This enhancement is not correlated with specific surface area and can be attributed to crystal facets effect.

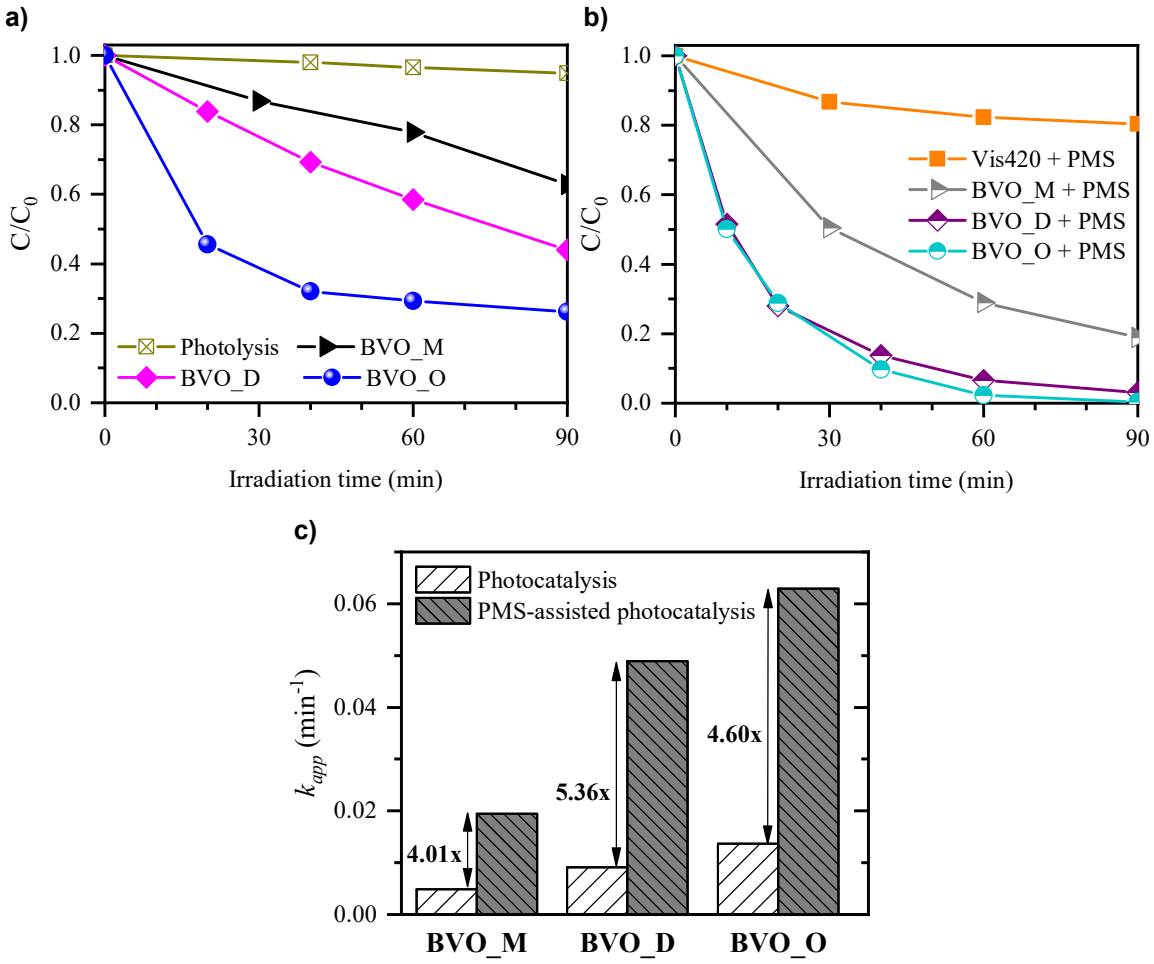

Figure 4.18. a) Photocatalytic and **b)** PMS-assisted photocatalytic degradation of NPX using facet-engineered $BiVO_4$ under visible light, **c)** enhancement of the kinetic rate constants without and in the presence of PMS.

During PMS-assisted photocatalysis, several ROS can be generated. Their identification was performed by three methods: quenching experiments (Figure 4.19a), fluorescence probe method with coumarin to determine the generation of •OH radicals (Figure 4.19b) and ESR spectroscopy (Figure 4.19c). Noteworthy, the first approach does not seem to be reliable for PMS-assisted photocatalysis due to the following reasons: (1) PMS interacts strongly with numerous scavengers such as NaN_3 and alcohols, and (2) there are no selective scavengers for sulfate radicals. In case of fluorescence probe method, no signals originated from 7-OHC were detected during pure photocatalysis with $BiVO_4$, which can be explained by an unsuitable band position for water oxidation [69,132]. When PMS was added to the reaction, fluorescence 7-OHC was observed, which can be attributed to enhanced ·OH generation. BVO_O sample achieved the highest production of 7-OHC, consistent with NPX degradation rate.

Finally, ESR spectroscopy was performed for BVO_O photocatalyst and PMS. Initial studies with numerous trapping agents did not detect signals attributed to the presence of $SO_4^{\bullet-}$ nor $^1O_2$. For all ESR spectra, a triplet of doublets described by spin Hamiltonian parameters [133,134] was observed, specific for hydroxyl radical in PBN-OH. When irradiation was introduced, a substantial increase in the signal intensity was noticed when the photocatalyst was present. Moreover, when tert-butyl alcohol and ethanol were introduced to BVO_O/PMS/Vis420 system, the intensity of the PBN-OH signal significantly decreased, indicating effective quenching of ·OH radicals. Generally, ethanol acts as a scavenger for both hydroxyl and sulfate radicals [47] and this ESR spectrum has a distinct difference spectrum, whose hyperfine coupling constants can be attributed to the formation of the PBN-CH(CH_3)OH adduct [133,134] with a low intensity signal from PBN-OH adduct. Therefore, the predominant ROS generated in BVO_O/PMS/Vis420 system were ·OH radicals.

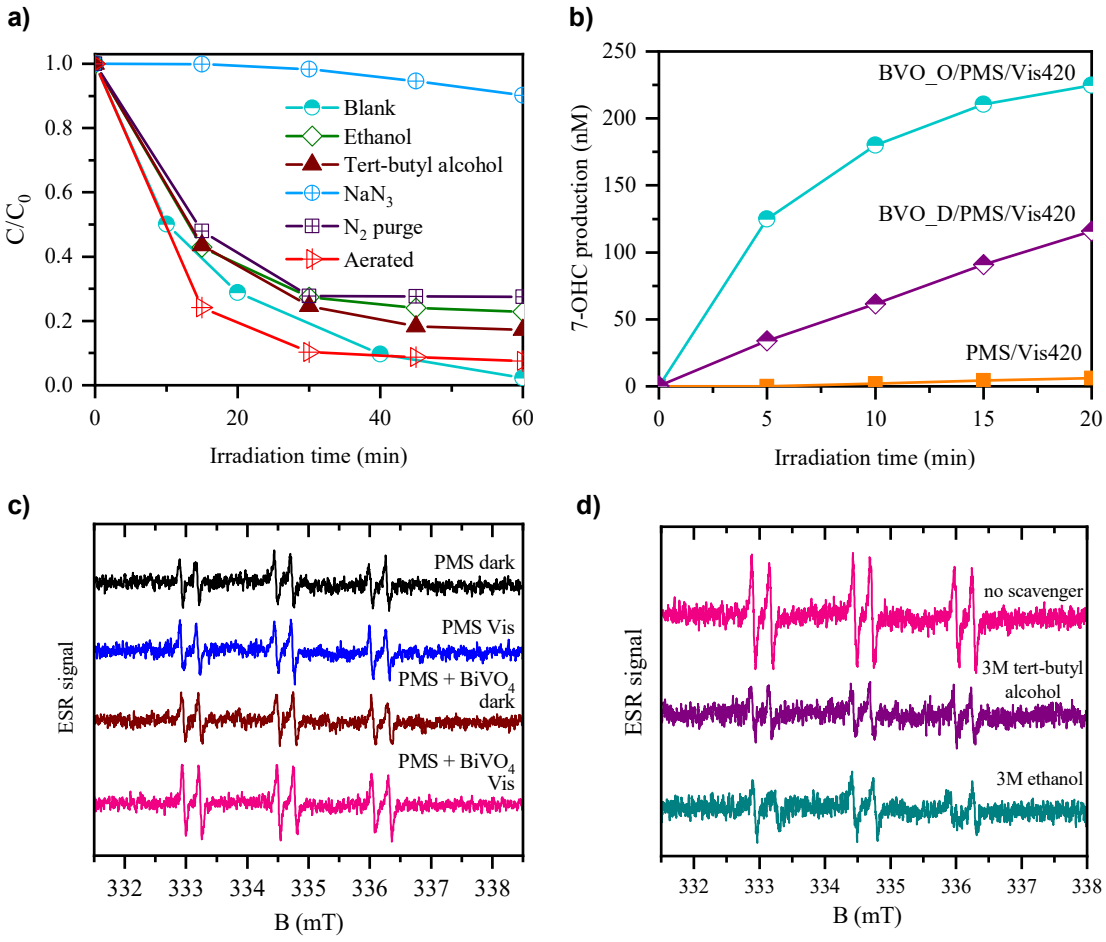

Figure 4.19. Detailed studies of the BVO_O/PMS/Vis420 system: **a)** NPX degradation over in the presence of scavengers and in specific gas conditions, **b)** 7-OHC evolution in PMS-assisted photocatalysis**, c)** ESR spectra of PMS activation with PBN as the trapping agent, **d)** the effect of scavengers on ESR signal with PBN.

Based on the presented findings about surface enrichment in bismuth, experiments were followed with DFT calculations to get better insight into their geometries and interactions with PMS. The systematic studies included relaxation of the bulk structure, stoichiometric surfaces and bismuth-enriched surfaces, followed by calculation of the electrostatic potential for the slab models, optimization of the PMS adsorption on the Bi-rich surfaces and final studies on the PMS activation.

The first part of the study included a detailed comparison between possible terminations of all stoichiometric facets. Noteworthy, considerations were constrained to structures that were both stoichiometric (that is, the full model had exactly a 1:1:4 ratio of the Bi:V:O atoms) and both top/bottom surfaces were equivalent. Furthermore, two aspects were included for comparison: (1) the non-equivalent nature of the [1 0 0] and [0 0 1] directions, due to the $\gamma \neq 90°$; and (2) possible termination with either undercoordinated Bi or V atoms at the topmost layer. The first aspect generally results in fact that {1 1 0} and {0 1 1} have slightly different dimensions and densities of the surface atoms, although otherwise having the same geometries. Analogically, in case of the {0 1 0}, two possible configurations can be considered: either with the surface atoms being bonded along the [1 0 -1] direction (configuration 1) or along the [1 0 1] direction (configuration 2). The second aspect connects with the possible termination with either undercoordinated Bi or V, in case of the {1 1 0} and {0 1 1} surfaces. Analogical problem of the Bi vs. V exposition is not present in case of the {0 1 0} and {1 2 0}. Table 4.4. shows the calculated surface energies of the final considered terminations.

Table 4.4. Simulated surface energies of the relaxed, stoichiometric models in vacuum.

Surface model	{0 1 0} Conf. 1	{0 1 0} Conf. 2	{0 1 1}-Bi	{0 1 1}-V	{1 1 0}-Bi	{1 1 0}-V	{1 2 0}
Surface energy (J/m^2)	0.280	0.354	0.175	0.470	0.196	0.528	0.503

Based on the obtained results, few conclusions can be reached. First of all, termination with either V or Bi has a significant effect on the surface energy, and Bi exposition is much more preferred. Although it must be noted that performed simulations are in a vacuum and cannot account for all further environmental effects, lower stability of the V-termination structures fits some of the recent results showing preferred vanadium leaching from the $BiVO_4$, especially under mild conditions [135,136]. Therefore, it is seems reasonable that Bi-rich surfaces might actually form in the real materials, as suggested from the XPS spectroscopy, especially when prepared hydrothermally, and some dissolution of both metals should occur. Secondly, the obtained results showed that due to the $\gamma \neq 90°$, a difference of approximately a few tens

of mJ/m^2 can be expected between possible configurations. Interestingly, the effect is relatively big for the {0 1 0}, where configuration 1 was found to be more stable and therefore will be considered in the further simulations. As for the {1 1 0} and {0 1 1}, the effect is lower, especially in case of the Bi terminations, and therefore only the {0 1 1}-Bi case was explored further to minimize overall computational cost.

Following simulations of the stoichiometric models, bismuth enrichment was modelled by adding the Bi atoms at the place where they would naturally exist if the $BiVO_4$ structure were further developed. Such structure can also be understood as the normal $BiVO_4$ with the V vacancy at the surface. Noteworthy, the analogical approach was recently applied by Lee *et al*. in their study of the non-stoichiometric $BiVO_4$ single crystals, where they both modelled and experimentally observed an analogical structure at the {0 1 0} surface [137]. Interestingly, they also observed that the additional Bi site at the surface has a preference to include two additional O atoms (+BiO_2). In this regard, the same structure of the Bi-rich {0 1 0} was applied here. On the other hand, there is no information about possible structures of the Bi-rich {0 1 1} and {1 2 0} facets. Therefore, for these models, the trials were started by including additional Bi atoms with all possible bridging O atoms, which would form in the final $BiVO_4$ structure. However, under such conditions, significant reconstruction of the surfaces occurred, and surface Bi atoms always tried to reduce coordination with oxygens. This fact can be reasonably connected with the known information about the structures of the BiO_X oxides, which are known to include Bi atoms often coordinated with 4-6 atoms [138,139], while in case of the $BiVO_4$, extended Bi polyhedra include 8 oxygens. In this regard, further trials included systematic reduction of the number of oxygen atoms bonded to the excess Bi. Ultimately, in each case, relative stability was achieved when the Bi enrichment included BiO_2-like sites, analogically to the {0 1 0} case. Comparison between the relaxed stoichiometric and Bi-rich surfaces of each facet is shown in Figure 4.20.

After finding the relatively stable geometries of the Bi-rich terminations of the {0 1 0}, {0 1 1} and {1 2 0}, further focus was placed on their electronic properties and interactions with PMS. To do so, the macroscopic average electrostatic potential of each surface was simulated, and the corresponding work function (Φ) was calculated as the difference between the vacuum level and the Fermi energy of each model (dotted line in Figure 4.20d). Interestingly, the addition of BiO_2 sites showed a different effect on the Φ, depending on the surface. In this regard, the effect is not dependent on the specific stoichiometry, but probably results from the specific geometry of the interface, which forms as a unique combination of the Bi excess and the initial geometry of each surface. Noteworthy, in case of the Bi-rich {0 1 1} control simulations revealed an increase of the

Φ value to be independent on the model size, with the same effect observed for the increased and decrease number of atomic layers, compared to the stoichiometric case.

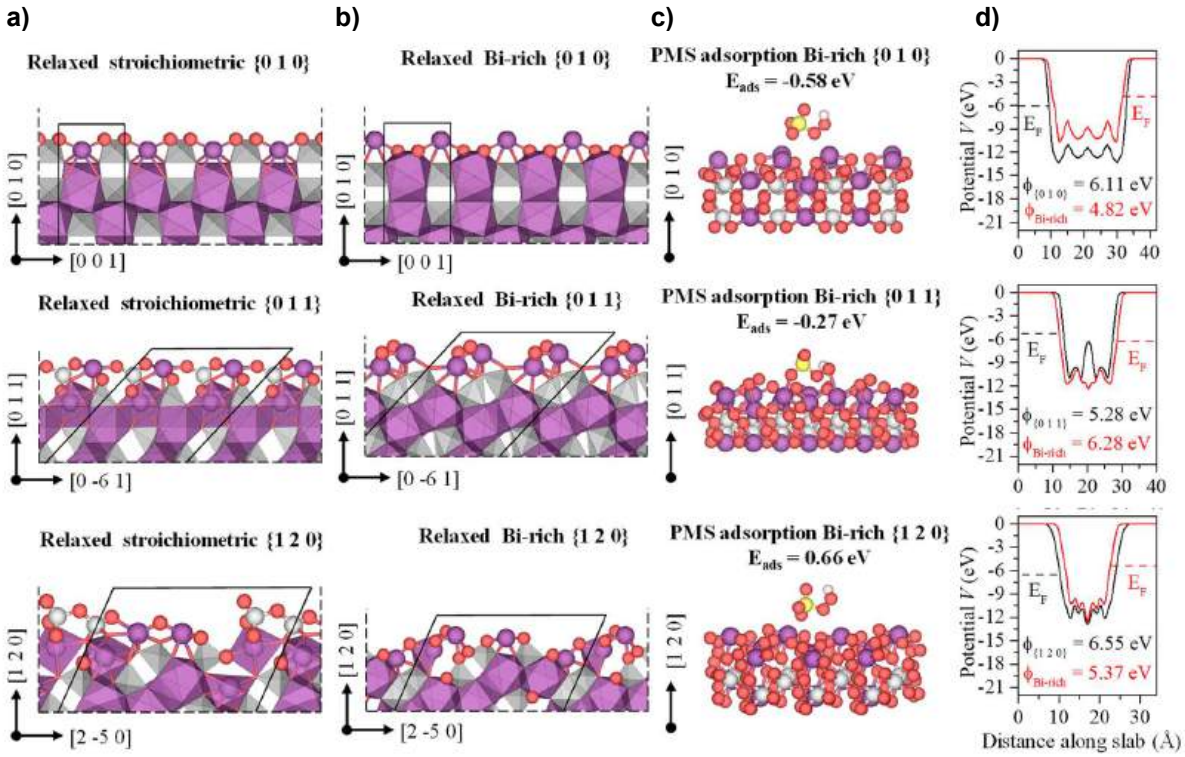

Figure 4.20. Relaxed models of the **a)** stoichiometric and **b)** bismuth-rich surface structures of the {0 1 0}, {0 1 1} and {1 2 0} $BiVO_4$ facets, together with **c)** PMS adsorption geometries and **d)** simulated potential profiles of each surface. In panels (a) and (b) only undercoordinated atoms are shown, while bulk-like structure is presented as corresponding coordination polyhedrons. Black and red lines in panel (d) correspond to stoichiometric and Bi-rich models, respectively. Violet, red, grey, yellow and white spheres are Bi, V, O, S and H atoms.

Further interactions with PMS were started by considering its adsorption on each Bi-rich surface. It should be noted that in order to do so, each surface model was expanded to cover around 10 Å in each direction, but its thickness was reduced by half to decrease the total number of atoms and required computational power. For these calculations, the bottom-most atomic layer was kept fixed. Figure 4.20 shows simulated adsorption geometries and calculated adsorption energies, with clear PMS preference to adsorb on the {0 1 0} and its aversion towards the {1 2 0}, when considered in their Bi-enriched forms. Noteworthy, preference to adsorb on the Bi-{0 1 0} connects well with the high enhancement of the BVO_D activity; however, it must be noted that overall adsorption energies (E_{ads}) are relatively low, on the edge between typical physical and chemical interactions (around 0.5 eV). Further transformation of the adsorbed molecule was studied in detail for the Bi-rich {0 1 0}. As shown in Figure 4.21, adsorption and dissociation of the PMS is further enhanced by its reduction, which results in an

exceptionally stable configuration of co-adsorbed SO_4 and OH units at the surface. Bader charge analysis confirmed that, compared to the initial state, an excess electron is effectively transferred to the PMS, but is equally delocalized between the resulting $[SO_4]^{-1.5}$ and $[OH]^{-0.5}$ groups. Any further desorption of each component destabilize the system; however, desorption of the ·OH is especially unfavored.

The results obtained for the Bi-rich {0 1 0} confirm the importance of the reduction process on the PMS transformation over $BiVO_4$. In fact, if the previously-calculated effect of the PMS addition on the photocatalytic activity was compared with the simulated work function value (energy needed to remove an electron) the trend is clearly inversely proportional, as could be expected at this point (Figure 4.21). This is both in agreement with the experimental findings on the enhanced ·OH production after PMS addition, otherwise unfavored for $BiVO_4$, as well as the electronic configuration of the HSO_5^-, which can be seen as electron-deficient, compared to the most stable SO_4^{2-} ion. This leads to the conclusion that electron availability can be seen as decisive for the PMS activation on the $BiVO_4$. In this regard, DFT calculations confirmed the importance of the electron withdrawal from the surface on the final effect of PMS addition, but also showed the complex effect of the possible Bi-rich structures on the simulated Φ values. Finally, it is worth noting that PMS reduction also stabilize adsorption and dissociation on the Bi-rich {1 2 0}, although the final structure is less stable than in case of the Bi-{0 1 0}, and the full transformation path was not simulated in this case. This suggests that PMS activation might still occur on the Bi-{1 2 0}, despite positive E_{ads}, as long as electron localization might precede its adsorption. Overall, the results reinforce the conclusion that redox processes are more important to the PMS activation than simple interaction with the $BiVO_4$ surface in its ground state, in accordance with the negligible activity of the system without the introduction of light.

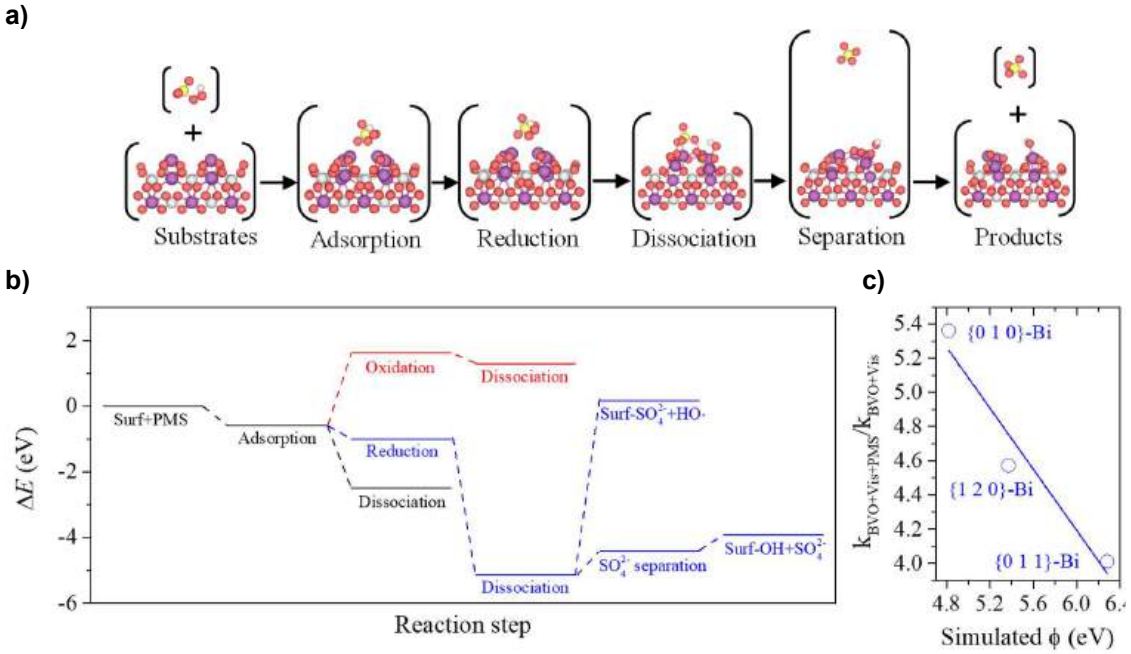

Figure 4.21. a) Schematic representation of the next steps of the PMS transformations on the Bi-rich {0 1 0} surface, **b)** the corresponding relative changes in the energy of the system and **c)** observed trend between calculated PMS effect and simulated Φ for each surface.

The presented study is part of a publication submitted to Chemical Engineering Journal: M. Kowalkińska, S. Dudziak, A. Szkudlarek, K. Nikiforow, A. Ostrowski, A. Zielińska-Jurek, *Mechanism insight into facet-dependent photocatalytic activation of peroxymonosulfates over $BiVO_4$ with bismuth-rich surface.*

5. CONCLUSIONS

The doctoral dissertation presents a systematic insight into the degradation of contaminants of emerging concern using heterogeneous photocatalysis and PMS-assisted photocatalysis. Two groups of potential photocatalysts were included in the PhD dissertation: based on scheelite-type-based compounds (alkaline-earth metal tungstates and molybdates, $BiVO_4$) and TiO_2 (F-TiO_2, {0 0 1} TiO_2/$TiOF_2$). Moreover, new procedures of precursor preparation, $TiOF_2$ and NH_4VO_3, were studied for the first time in terms of photocatalysts properties.

Firstly, the applicability of alkaline-earth metal tungstates and molybdates with a scheelite-type structure as photocatalysts was examined. Experimental results revealed that these compounds are able to degrade phenol under UV light, despite a wide band gap. The charge carrier lifetime was the key factor affecting the photocatalytic performance of these materials. $BaWO_4$ and $SrWO_4$, with the longest lifetime of photogenerated charge carriers, demonstrated the highest photocatalytic activity in the series. Electrochemical studies indicated that tungstates are more efficient photocatalysts than molybdates, due to possible conduction through charge carrier channels as well as more shallow electron traps.

Then, F-TiO_2 synthesized from $TiOF_2$ was examined, considering the crystal facets exposition of the final photocatalysts and the morphology of the precursor. $TiOF_2$ can also be used as a secondary phase in {0 0 1} TiO_2/$TiOF_2$ photocatalyst, significantly enhancing the photocatalytic activity due to a higher amount of photogenerated charge carriers and their improved separation.

Investigations of adjusting the morphology of the precursor and crystal facets exposition were extended to $BiVO_4$ materials. The replacement of commercial NH_4VO_3 with to as-synthesized one significantly enhanced the light utilization, confirmed by LVRPA calculations. Moreover, surface modification by sub-nanoclusters CuO_x and exposition of particular crystal facets were crucial for both photocatalytic activity and PMS activation.

The novelty of the presented doctoral dissertation could be summarized in the following statements:

- Demonstrating the potential of alkaline-earth metal tungstates and molybdates with scheelite-type structure for photocatalytic oxidation processes,
- Determining the dependence of $TiOF_2$ and NH_4VO_3 precursors morphology on the photocatalytic activity of F-TiO_2 and $BiVO_4$, respectively,
- Demonstrating crystal facets exposition effect on NPX degradation pathway, TOC conversion, toxicity rate and photocatalytic PMS activation,

- The content of $TiOF_2$ in {0 0 1} $TiO_2/TiOF_2$ photocatalyst can be controllable,
- High potential barriers exist within the $TiOF_2$ structure, which affects the optimum at a low level of $TiOF_2$ content (1.5%-6%) in {0 0 1} $TiO_2/TiOF_2$ photocatalyst,
- Deposition of CuO_x sub-nanoclusters on $BiVO_4$ enhances both the photocatalytic activity and PMS activation,
- The hydrothermal synthesis of facet-engineered $BiVO_4$ tends to form bismuth-rich surfaces,
- {1 2 0} crystal facets are the most photocatalytically active under visible light,
- The presence of {0 1 0} enhances photocatalytic PMS activation,
- There is a correlation between work function and enhancement of the degradation rate when PMS is added to the photocatalytic process.

LIST OF FIGURES AND TABLES

REFERENCES

[1] United Nations, *The Sustainable Development Goals Report* (2025). https://unstats.un.org/sdgs/report/2025/ (access date: 28.10.2025).

[2] N. H. Tran, M. Reinhard, and K. Y. H. Gin, *Occurrence and fate of emerging contaminants in municipal wastewater treatment plants from different geographical regions-a review.* Water Research, 133 (2018) 182–207.

[3] OW/ORD Emerging Contaminants Workgroup, *Aquatic Life Criteria for Contaminants of Emerging Concern Part I: General Challenges and Recommendations* (2008). https://www.epa.gov/wqc/contaminants-emerging-concern-including-pharmaceuticals-and-personal-care-products (access date: 28.10.2025).

[4] M. Brumovský, J. Bečanová, J. Kohoutek, M. Borghini, and L. Nizzetto, *Contaminants of emerging concern in the open sea waters of the Western Mediterranean.* Environmental Pollution, 229 (2017) 976–983.

[5] L. M. Lewis, A. V. Badkar, D. Cirelli, R. Combs, and T. F. Lerch, *The Race to Develop the Pfizer-BioNTech COVID-19 Vaccine: From the Pharmaceutical Scientists' Perspective.* Journal of Pharmaceutical Sciences, 112 (2023) 640–647.

[6] Departament Strategii i Analiz Miedzynarodowych, *Branża Farmaceutyczna: znaczenia polskich producentów na świecie* (2019). https://wspieramyeksport.pl/api/public/files/1709/www_PKO_BRANZA_FARMACEUTYCZNA_2019.pdf (access date: 28.10.2025).

[7] Rafał Momot, *Raport: Rynek Dystrybucji Farmaceutycznej w Polsce* (2016). https://pharmanet.org.pl/wp-content/uploads/2018/11/Rynek-Dystrybucji-Farmaceutycznej-2016.pdf (access date: 28.10.2025).

[8] C. Gadipelly, A. Pérez-González, G. D. Yadav, I. Ortiz, R. Ibáñez, V. K. Rathod, and K. V. Marathe, *Pharmaceutical industry wastewater: Review of the technologies for water treatment and reuse.* Industrial and Engineering Chemistry Research, 53 (2014) 11571–11592.

[9] The European Parliament, *Directive of The European Parliament and of The Council concerning urban wastewater treatment* (PE-CONS 85/1/24 REV 1) (Strasbourg, 2024). https://eur-lex.europa.eu/eli/dir/2024/3019/oj/eng (access date: 28.10.2025).

[10] M. Isidori, M. Lavorgna, A. Nardelli, A. Parrella, L. Previtera, and M. Rubino, *Ecotoxicity of naproxen and its phototransformation products.* Science of the Total Environment, 348 (2005) 93–101.

[11] M. DellaGreca, M. Brigante, M. Isidori, A. Nardelli, L. Previtera, M. Rubino, and F. Temussi, *Phototransformation and ecotoxicity of the drug Naproxen-Na.* Environmental Chemistry Letters, 1 (2003) 237–241.

[12] A. L. Jarvis, M. J. Bernot, and R. J. Bernot, *The effects of the psychiatric drug carbamazepine on freshwater invertebrate communities and ecosystem dynamics.* Science of the Total Environment, 496 (2014) 461–470.

[13] Y. Deng, A. Debognies, Q. Zhang, Z. Zhang, Z. Zhou, J. Zhang, L. Sun, T. Lu, and H. Qian, *Effects of ofloxacin on the structure and function of freshwater microbial communities.* Aquatic Toxicology, 244 (2022) 106084.

[14] J. Q. Xiong, S. J. Kim, M. B. Kurade, S. Govindwar, R. A. I. Abou-Shanab, J. R. Kim, H. S. Roh, M. A. Khan, and B. H. Jeon, *Combined effects of sulfamethazine and sulfamethoxazole on a freshwater microalga, Scenedesmus obliquus: toxicity, biodegradation, and metabolic fate.* Journal of Hazardous Materials, (2019) 138–146.

[15] A. G. Hornsby, R. Don Wauchope, and A. E. Herner, *Pesticide Properties in the Environment*, 1st edition, publisher Springer (1996).

[16] N. N. Melnikov, *Chemistry of pesticides*, 1st edition, publisher Springer (1971).

[17] A. L. Wilson, O. Courtenay, L. A. Kelly-Hope, T. W. Scott, W. Takken, S. J. Torr, and S. W. Lindsay, *The importance of vector control for the control and elimination of vector-borne diseases*. PLoS Neglected Tropical Diseases, 14 (2020) 1–31.

[18] M. Eddleston, L. Karalliedde, N. Buckley, R. Fernando, G. Hutchinson, G. Isbister, F. Konradsen, D. Murray, J. C. Piola, N. Senanayake, R. Sheriff, S. Singh, S. B. Siwach, and L. Smit, *Pesticide poisoning in the developing world — a minimum pesticides list.* Lancet, 360 (2002) 11631167.

[19] M. Peschka, J. Müller, T. P. Knepper, and P. Seel, *Trends in Pesticide Transport into the River Rhine*. The Rhine (Springer-Verlag, 2006), pp. 155–175.

[20] *Regulation (EC) No 1107/2009 of The European Parliament and of The Council of 21 October 2009 concerning the placing of plant protection products on the market and repealing Council Directives 79/117/EEC and 91/414/EEC* (2009). https://eur-lex.europa.eu/eli/reg/2009/1107/oj/eng (access date: 28.10.2025).

[21] G. Cortes, P. Rodriguez, D. Marinov, I. Sanseverino, and T. Lettieri, *Selection of substances for the 5th Watch List under the Water Framework Directive* (2025). https://doi.org/10.2760/956398 (access date: 28.10.2025).

[22] W. Hao, Y. Zhang, Y. Xie, B. Guo, J. Chang, J. Li, P. Xu, and H. Wang, *Myclobutanil accumulation, transcriptional alteration, and tissue injury in lizards (Eremias argus) treated with myclobutanil enantiomers.* Ecotoxicology and Environmental Safety, 171 (2019) 247–255.

[23] E. V. S. Motta, J. E. Powell, and N. A. Moran, *Glyphosate induces immune dysregulation in honey bees.* Animal Microbiome, 4 (2022).

[24] R. D. Burke, S. W. Todd, E. Lumsden, R. J. Mullins, J. Mamczarz, W. P. Fawcett, R. P. Gullapalli, W. R. Randall, E. F. R. Pereira, and E. X. Albuquerque, *Developmental neurotoxicity of the organophosphorus insecticide chlorpyrifos: from clinical findings to preclinical models and potential mechanisms.* Journal of Neurochemistry, 142 (2017) 162–177.

[25] M. A. Shalaby, H. Y. El Zorba, and R. M. Ziada, *Reproductive toxicity of methomyl insecticide in male rats and protective effect of folic acid.* Food and Chemical Toxicology, 48 (2010) 3221–3226.

[26] R. C. Gupta, A. Srivastava, and R. Lall, *Nutraceuticals in Veterinary Medicine*, publisher Springer (2019).

[27] X. Montané, O. Kowalczyk, B. Reig-Vano, A. Bajek, K. Roszkowski, R. Tomczyk, W. Pawliszak, M. Giamberini, A. Mocek-Płóciniak, and B. Tylkowski, *Current perspectives of the applications of polyphenols and flavonoids in cancer therapy.* Molecules, 25(15) (2020) 3342.

[28] J. Michałowicz, B. Bukowska, and W. Duda, *The differences in phenolic content in rivers exposed and non-exposed to anthropogenic contamination.* Chemosphere, 71 (2008) 735–741.

[29] W. Zhong, D. Wang, and Z. Wang, *Distribution and potential ecological risk of 50 phenolic compounds in three rivers in Tianjin, China.* Environmental Pollution, 235 (2018) 121–128.

[30] C. Hansch, S. C. Mckarns, C. J. Smith, and D. J. Doolittle, *Comparative QSAR evidence for a free-radical mechanism of phenol-induced toxicity.* Chemico-Biological Interactions, 127 (2000) 61-72.

[31] S. J. Sturla, *DNA adduct profiles: chemical approaches to addressing the biological impact of DNA damage from small molecules.* Current Opinion in Chemical Biology, 11 (2007) 293–299.

[32] J. Michałowicz and W. Duda, *Phenols – Sources and Toxicity.* Polish Journal of Environmental Studies, 16 (2007) 347–362.

[33] *Decision No 2455/2001/EC of The European Parliament and of The Council of 20 November 2001 establishing the list of priority substances in the field of water policy and amending Directive 2000/60/EC* (2000). https://eur-lex.europa.eu/eli/dec/2001/2455/oj/eng (access date: 28.10.2025).

[34] N. C. Saha, F. Bhunia, and A. Kaviraj, *Toxicity of phenol to fish and aquatic ecosystems. Bulletin of Environmental Contamination and Toxicology*, 63 (1999) 195–202.

[35] C. H. Lin, H. T. Leow, S. C. Huang, J. Nakamura, J. A. Swenberg, and P. H. Lin, *Induction of cytotoxicity, aldehydic DNA lesions, and poly(ADP-ribose) polymerase-1 activation by catechol derivatives of pentachlorophenol in calf thymus DNA and in human breast cancer cells.* Chemical Research in Toxicology, 18 (2005) 257–264.

[36] M. A. Valentovic and J. G. Ball, *2-Aminophenol and 4-aminophenol toxicity in renal slices from sprague-dawley and fischer 344 rats.* Journal of Toxicology and Environmental Health - Part A, 55 (1998) 225–240.

[37] H. Song and T. S. Chen, *P-Aminophenol-induced liver toxicity: Tentative evidence of a role for acetaminophen.* Journal of Biochemical and Molecular Toxicology, 15 (2001) 34–40.

[38] Y. Ma, H. Liu, J. Wu, L. Yuan, Y. Wang, X. Du, R. Wang, P. Wegesa Marwa, P. Petlulu, X. Chen, and H. Zhang, *The adverse health effects of bisphenol A and related toxicity mechanisms.* Environmental Research, 176 (2019) 108575.

[39] European Food Safety Authority (EFSA), *Scientific Opinion on the risks to public health related to the presence of bisphenol A (BPA) in foodstuffs: Executive summary.* EFSA Journal, 13 (2015) 3978.

[40] M. A. Oturan and J. J. Aaron, *Advanced oxidation processes in water/wastewater treatment: Principles and applications. A review.* Critical Reviews in Environmental Science and Technology, 44 (2014) 2577–2641.

[41] E. Pelizzetti and N. Serpone, Homogeneous and Heterogeneous Photocatalysis, 1st edition, publisher Springer (1986).

[42] S. He, Y. Chen, X. Li, L. Zeng, and M. Zhu, *Heterogeneous Photocatalytic Activation of Persulfate for the Removal of Organic Contaminants in Water: A Critical Review.* ACS ES&T Engineering, 2 (2022) 527–546.

[43] B. L. Phoon, C. C. Ong, M. S. Mohamed Saheed, P. L. Show, J. S. Chang, T. C. Ling, S. S. Lam, and J. C. Juan, *Conventional and emerging technologies for removal of antibiotics from wastewater.* Journal of Hazardous Materials, 400 (2020) 122961.

[44] I. M. Kolthoff and I. K. Miller, *Decomposition of Persulfate Ion in Aqueous Medium.* Journal of American Chemical Society, 73 (1951) 1–30.

[45] J. Flanagan, W. P. Griffith, and A. C. Skapski, *The Active Principle of Caro's Acid, HSO_5^-: X-Ray Crystal Structure of $KHSO_5 \cdot H_2O$.* Journal of the Chemical Society, Chemical Communications, 23 (1984) 1574–1575.

[46] J. Wang and S. Wang, *Activation of persulfate (PS) and peroxymonosulfate (PMS) and application for the degradation of emerging contaminants.* Chemical Engineering Journal, 334 (2018) 1502–1517.

[47] W. Da Oh, Z. Dong, and T. T. Lim, *Generation of sulfate radical through heterogeneous catalysis for organic contaminants removal: Current development, challenges and prospects.* Applied Catalysis B: Environmental, 194 (2016) 169–201.

[48] Q. Fang, H. Yang, S. Ye, P. Zhang, M. Dai, X. Hu, Y. Gu, and X. Tan, *Generation and identification of $^1O_2$ in catalysts/peroxymonosulfate systems for water purification.* Water Research, 245 (2023) 120614.

[49] M. Kohantorabi, G. Moussavi, and S. Giannakis, *A review of the innovations in metal- and carbon-based catalysts explored for heterogeneous peroxymonosulfate (PMS) activation, with focus on radical vs. non-radical degradation pathways of organic contaminants.* Chemical Engineering Journal, 411 (2021) 127957.

[50] S. Mao, P. Zhao, Y. Wu, C. Liu, M. Xia, and F. Wang, *Promoting charge migration of $Co(OH)_2$/g-C_3N_4 by hydroxylation for improved PMS activation: Catalyst design, DFT calculation and mechanism analysis.* Chemical Engineering Journal, 451 (2023) 138503.

[51] G. P. Anipsitakis and D. D. Dionysiou, *Radical generation by the interaction of transition metals with common oxidants.* Environmental Science and Technology, 38 (2004) 3705–3712.

[52] X. Duan, X. Niu, J. Gao, S. Wacławek, L. Tang, and D. D. Dionysiou, *Comparison of sulfate radical with other reactive species.* Current Opinion in Chemical Engineering, 38 (2022) 100867.

[53] W. Ren, C. Cheng, P. Shao, X. Luo, H. Zhang, S. Wang, and X. Duan, *Origins of Electron-Transfer Regime in Persulfate-Based Nonradical Oxidation Processes.* Environmental Science and Technology, 56 (2022) 78–97.

[54] B. Ohtani, *Chapter 5 - Principle of Photocatalysis and Design of Active Photocatalysts,* New and Future Developments in Catalysis, publisher Elsevier (2013).

[55] J. Schneider, M. Matsuoka, M. Takeuchi, J. Zhang, Y. Horiuchi, M. Anpo, and D. W. Bahnemann, *Understanding TiO_2 Photocatalysis: Mechanisms and Materials.* Chemical Reviews, 114 (2014) 9919–9986.

[56] H. Gnaser, B. Huber, and C. Ziegler, *Nanocrystalline TiO_2 for Photocatalysis*. Encyclopedia of Nanoscience and Nanotechnology, 6 (2004) 505–535.

[57] Y. Nosaka and A. Y. Nosaka, *Generation and Detection of Reactive Oxygen Species in Photocatalysis.* Chemical Reviews, 117 (2017) 11302–11336.

[58] L. Wang and J. Yu, *Principles of photocatalysis.* Interface Science and Technology (2023), pp. 1–52.

[59] X. Li, J. Yu, and M. Jaroniec, *Hierarchical photocatalysts.* Chemical Society Reviews, 45 (2016) 2603–2636.

[60] I. Rapti, C. Kosma, T. Albanis, and I. Konstantinou, *Solar photocatalytic degradation of inherent pharmaceutical residues in real hospital WWTP effluents using titanium dioxide on a CPC pilot scale reactor.* Catalysis Today, 423 (2023) 113884.

[61] H. Zhang and J. F. Banfield, *Structural characteristics and mechanical and thermodynamic properties of nanocrystalline TiO_2.* Chemical Reviews, 114 (2014) 9613–9644.

[62] J. Zhang, P. Zhou, J. Liu, and J. Yu, *New understanding of the difference of photocatalytic activity among anatase, rutile and brookite TiO_2.* Physical Chemistry Chemical Physics, 16 (2014) 20382–20386.

[63] K. Momma and F. Izumi, *VESTA 3 for three-dimensional visualization of crystal, volumetric and morphology data.* Journal of Applied Crystallography, 44 (2011) 1272–1276.

[64] D. T. T. Trinh, W. Khanitchaidecha, D. Channei, and A. Nakaruk, *Synthesis, characterization and environmental applications of bismuth vanadate.* Research on Chemical Intermediates, 45 (2019) 5217–5259.

[65] S. Tokunaga, H. Kato, and A. Kudo, *Selective preparation of monoclinic and tetragonal $BiVO_4$ with scheelite structure and their photocatalytic properties.* Chemistry of Materials, 13 (2001) 4624–4628.

[66] A. Kudo, K. Omori, and H. Kato, *A novel aqueous process for preparation of crystal form-controlled and highly crystalline $BiVO_4$ powder from layered vanadates at room temperature and its photocatalytic and photophysical properties.* Journal of the American Chemical Society, 121 (1999) 11459–11467.

[67] A. Kudo, K. Ueda, H. Kato, and I. Mikami, *Photocatalytic O_2 evolution under visible light irradiation on $BiVO_4$ in aqueous $AgNO_3$ solution,* Catalysis Letters 53 (1998) 229–230.

[68] Q. Zhang, M. Liu, W. Zhou, Y. Zhang, W. Hao, Y. Kuang, H. Liu, D. Wang, L. Liu, and J. Ye, *A novel Cl^- modification approach to develop highly efficient photocatalytic oxygen evolution over $BiVO_4$ with AQE of 34.6%.* Nano Energy, 81 (2021). 105651.

[69] Y. Nakabayashi, M. Nishikawa, N. Saito, C. Terashima, and A. Fujishima, *Significance of Hydroxyl Radical in Photoinduced Oxygen Evolution in Water on Monoclinic Bismuth Vanadate.* Journal of Physical Chemistry C, 121 (2017) 25624–25631.

[70] P. Garcia-Muñoz, F. Fresno, C. Lefevre, D. Robert, and N. Keller*, Highly robust $La_{1-x}Ti_xFeO_3$ dual catalyst with combined photocatalytic and photo-CWPO activity under visible light for 4-chlorophenol removal in water.* Applied Catalysis B: Environmental, 262 (2020) 118310.

[71] K. Spilarewicz, K. Mróz, M. Kobielusz, and W. Macyk, *When the fate of electrons matters — strategies for correct heterojunction classification in photocatalysis.* Current Opinion in Chemical Engineering, 45 (2024) 101041.

[72] D. Hermosilla, M. Cortijo, and C. P. Huang, *The role of iron on the degradation and mineralization of organic compounds using conventional Fenton and photo-Fenton processes.* Chemical Engineering Journal, 155 (2009) 637–646

[73] Y. Xin, Y. Wang, Z. Jiang, B. Deng, and Z. J. Jiang, *Advances in the Removal of Organic Pollutants from Water by Photocatalytic Activation of Persulfate: Photocatalyst Modification Strategy and Reaction Mechanism.* ChemSusChem, 17 (2024) 202400254.

[74] K. Żelechowska, *Nanotechnologia w chemii i medycynie,* Wydawnictwo Politechniki Gdańskiej (2014).

[75] B. Dręczewski, A. Herman, and P. Wroczyński, *Nanotechnologia Stan Obecny I Perspektywy,* Wydawnictwo Politechniki Gdańskiej (1997).

[76] A. Fujishima, X. Zhang, and D. A. Tryk, *TiO_2 photocatalysis and related surface phenomena.* Surface Science Reports, 63 (2008) 515–582.

[77] B. Ohtani, Y. Ogawa, and S. Nishimoto, *Photocatalytic Activity of Amorphous-Anatase Mixture of Titanium(IV) Oxide Particles Suspended in Aqueous Solutions.* Journal of Physical Chemistry B, 5647 (1997) 3746–3752.

[78] D. R. Hummer, J. D. Kubicki, P. R. C. Kent, J. E. Post, and P. J. Heaney, *Origin of nanoscale phase stability reversals in titanium oxide polymorphs.* Journal of Physical Chemistry C, 113 (2009) 4240–4245.

[79] A. Navrotsky, *Nanoscale effects on thermodynamics and phase equilibria in oxide systems.* ChemPhysChem, 12 (2011) 2207–2215.

[80] S. Kundu and A. Patra, *Nanoscale strategies for light harvesting.* Chemical Reviews, 117 (2017) 712–757.

[81] Y. Wang, H. Sun, H. M. Ang, M. O. Tadé, and S. Wang, *3D-hierarchically structured MnO_2 for catalytic oxidation of phenol solutions by activation of peroxymonosulfate: Structure dependence and mechanism.* Applied Catalysis B: Environmental, 164 (2015) 159–167.

[82] J. Zheng, Y. Zhang, T. Hu, T. Lv, and C. Meng, *New Strategy for the Morphology-Controlled Synthesis of V_2O_5 Microcrystals with Enhanced Capacitance as Battery-type Supercapacitor Electrodes.* Crystal Growth and Design, 18 (2018) 5365–5376.

[83] M. Maisano, M. V. Dozzi, and E. Selli, *Searching for facet-dependent photoactivity of shape-controlled anatase TiO_2.* Journal of Photochemistry and Photobiology C: Photochemistry Reviews, 28 (2016) 29–43.

[84] S. Dudziak, M. Kowalkińska, and A. Zielińska-Jurek, *Chapter 3: Crystal Facet Engineering of TiO_2 from Theory to Application.* Updates on Titanium Dioxide, publisher IntechOpen (2023).

[85] G. Liu, J. C. Yu, G. Q. Lu, and H. M. Cheng, *Crystal facet engineering of semiconductor photocatalysts: Motivations, advances and unique properties.* Chemical Communications, 47 (2011) 6763–6783.

[86] W. J. Ong, L. L. Tan, S. P. Chai, S. T. Yong, and A. R. Mohamed, *Highly reactive {001} facets of TiO_2-based composites: Synthesis, formation mechanism and characterization.* Nanoscale, 6 (2014) 1946–2008.

[87] Z. Xiong, Z. Lei, Y. Li, L. Dong, Y. Zhao, and J. Zhang, *A review on modification of facet-engineered TiO_2 for photocatalytic CO_2 reduction.* Journal of Photochemistry and Photobiology C: Photochemistry Reviews, 36 (2018) 24–47.

[88] H. G. Yang, C. H. Sun, S. Z. Qiao, J. Zou, G. Liu, S. C. Smith, H. M. Cheng, and G. Q. Lu, *Anatase TiO_2 single crystals with a large percentage of reactive facets.* Nature, 453 (2008) 638–641.

[89] S. Liu, J. Yu, and M. Jaroniec, *Anatase TiO_2 with dominant high-energy {001} facets: Synthesis, properties, and applications.* Chemistry of Materials, 23 (2011) 4085–4093.

[90] S. Selcuk and A. Selloni, *Facet-dependent trapping and dynamics of excess electrons at anatase TiO_2 surfaces and aqueous interfaces.* Nature Materials, 15 (2016) 1107–1112.

[91] S. Xie, Z. Shen, H. Zhang, J. Cheng, Q. Zhang, and Y. Wang, *Photocatalytic coupling of formaldehyde to ethylene glycol and glycolaldehyde over bismuth vanadate with controllable facets and cocatalysts.* Catalysis Science and Technology, 7 (2017) 923–933.

[92] Y. Zhang, H. Gong, Y. Zhang, K. Liu, H. Cao, H. Yan, and J. Zhu, *The Controllable Synthesis of Octadecahedral $BiVO_4$ with Exposed {111} Facets*. European Journal of Inorganic Chemistry, 2017 (2017) 2990–2997.

[93] M. Han, X. Chen, T. Sun, O. K. Tan, and M. S. Tse, *Synthesis of mono-dispersed m-$BiVO_4$ octahedral nano-crystals with enhanced visible light photocatalytic properties.* CrystEngComm, 13 (2011) 6674–6679.

[94] X. Zhai, Z. Li, Z. Lu, G. Wang, P. Li, Y. Gao, X. Huang, W. Huang, H. Uji-i, and G. Lu, *Synthesis of 42-faceted bismuth vanadate microcrystals for enhanced photocatalytic activity.* Journal of Colloid and Interface Science, 542 (2019) 207–212.

[95] R. Li, F. Zhang, D. Wang, J. Yang, M. Li, J. Zhu, X. Zhou, H. Han, and C. Li, *Spatial separation of photogenerated electrons and holes among {010} and {110} crystal facets of $BiVO_4$*. Nature Communications, 4 (2013) 1432.

[96] Y. Zhao, X. Liu, B. Ma, Y. Li, X. Fan, F. Zhang, G. Zhang, and W. Peng, *Facet Dependent Activity of Fe(III) Species Modified TiO_2 for Simulated Sunlight Driven Fenton-like Reactions*. ACS Applied Materials and Interfaces, 14 (2022) 52940–52950.

[97] J. Low, J. Yu, M. Jaroniec, S. Wageh, and A. A. Al-Ghamdi, *Heterojunction Photocatalysts.* Advanced Materials, 29 (2017) 1601694.

[98] Q. Xu, L. Zhang, J. Yu, S. Wageh, A. A. Al-Ghamdi, and M. Jaroniec, *Direct Z-scheme photocatalysts: Principles, synthesis, and applications.* Materials Today, 21 (2018) 1042–1063.

[99] M. Liras, M. Barawi, and V. A. De La Peña O'Shea, *Hybrid materials based on conjugated polymers and inorganic semiconductors as photocatalysts: From environmental to energy applications.* Chemical Society Reviews, 48 (2019) 5454–5487.

[100] W. Li and S. Ismat Shah, *Semiconductor Nanoparticles for Photocatalysis.* Encyclopedia of Nanoscience and Nanotechnology, 9 (2004) 669–695.

[101] L. Yuan, Z. Geng, J. Xu, F. Guo, and C. Han, *Metal-Semiconductor Heterostructures for Photoredox Catalysis: Where Are We Now and Where Do We Go?* Advanced Functional Materials, 31 (2021) 2101103.

[102] W. Hou and S. B. Cronin, *A review of surface plasmon resonance-enhanced photocatalysis*. Advanced Functional Materials, 23 (2013) 1612–1619.

[103] F. Fresno, A. Iglesias-Juez, and J. M. Coronado, *Photothermal Catalytic CO_2 Conversion: Beyond Catalysis and Photocatalysis*, Topics in Current Chemistry, 381 (2023) 21.

[104] B. Qiao, A. Wang, X. Yang, L. F. Allard, Z. Jiang, Y. Cui, J. Liu, J. Li, and T. Zhang, Single-atom catalysis of CO oxidation using Pt_1/FeO_x. Nature Chemistry, 3 (2011) 634–641.

[105] H. Liang, B. J. Liu, B. Tang, S. C. Zhu, S. Li, X. Z. Ge, J. Le Li, J. R. Zhu, and F. X. Xiao, *Atomically Precise Metal Nanocluster-Mediated Photocatalysis*. ACS Catalysis, 12 (2022) 4216–4226.

[106] T. Li, R. Zhang, N. Fang, Y. Shi, J. Li, C. He, and Y. Chu, *Metal cluster-mediated photocatalysis: synthesis, characterization and application.* Nanoscale, 17 (2025) 9834–9869.

[107] A. Wang, J. Li, and T. Zhang, *Heterogeneous single-atom catalysis.* Nature Reviews Chemistry, 2 (2018) 65–81.

[108] S. Saedy, N. Hiemstra, D. Benz, H. Van Bui, M. Nolan, and J. R. van Ommen, *Dual promotional effect of Cu_xO clusters grown with atomic layer deposition on TiO_2 for photocatalytic hydrogen production*. Catalysis Science and Technology, 12 (2022) 4511–4523.

[109] J. Miao, Y. Zhu, J. Lang, J. Zhang, S. Cheng, B. Zhou, L. Zhang, P. J. J. Alvarez, and M. Long, S*pin-State-Dependent Peroxymonosulfate Activation of Single-Atom M-N Moieties via a Radical-Free Pathway*. ACS Catalysis, 11 (2021) 9569–9577.

[110] K. Vinodgopal and P. V Kamat, *Enhanced Rates of Photocatalytic Degradation of an Azo Dye Using SnO_2/TiO_2 Coupled Semiconductor Thin Films.* Environmental Science & Technology, 29 (1995) 841–845.

[111] Y. Lv, P. Chen, J. J. Foo, J. Zhang, W. Qian, C. Chen, and W. J. Ong, *Dimensionality-dependent MoS_2 toward efficient photocatalytic hydrogen evolution: from synthesis to modifications in doping, surface and heterojunction engineering.* Materials Today Nano, 18 (2022) 100191.

[112] N. Imanuella, K. H. Ng, L. A. Tuyen, and N. Q. Hung, *Inverted F-scheme heterojunction: Introduction and experimental validation using CdS/Co_3O_4 nanocage photocatalytic composite.* Applied Catalysis B: Environmental, 358 (2024) 124401.

[113] T. Y. Liang, S. J. Chan, A. S. Patra, P. L. Hsieh, Y. A. Chen, H. H. Ma, and M. H. Huang, *Inactive Cu_2O Cubes Become Highly Photocatalytically Active with Ag_2S Deposition.* ACS Applied Materials and Interfaces, 13 (2021) 11515–11523.

[114] S. H. Lee, J. M. Koo, S. G. Oh, and S. S. Im, *Facile synthesis of ammonium vanadate nanofibers by using reflux in aqueous V_2O_5 solution with ammonium persulfate.* Materials Chemistry and Physics, 194 (2017) 313–321.

[115] M. Kowalkińska, *Synteza amonowych związków wanadu.* Praca inżynierska, Wydział Fizyki Technicznej i Matematyki Stosowanej, (2019).

[116] V. Synecek and F. Hanic, *The crystal structure of ammonium metavanadate.* Czechoslovak Journal of Physics, 4 (1954) 120–129.

[117] H. M. Rietveld*, A Profile Refinement Method for Nuclear and Magnetic Structures.* Journal of Applied Crystallography, 2 (1969) 65.

[118] B. Ravel and M. Newville, *ATHENA, ARTEMIS, HEPHAESTUS: Data analysis for X-ray absorption spectroscopy using IFEFFIT.* Journal of Synchrotron Radiation, 12 (2005) 537–541.

[119] J. Tauc, *Optical properties and electronic structure of amorphous Ge and Si.* Materials Research Bulletin, 3 (1968) 37–46.

[120] Y. Nosaka and A. Y. Nosaka, *Understanding Hydroxyl Radical (•OH) Generation Processes in Photocatalysis.* ACS Energy Letters, 1 (2016) 356–359.

[121] P. Giannozzi, O. Andreussi, T. Brumme, O. Bonau, M. Buongiorno Nardelli, M. Calandra, R. Car, C. Cavazzoni, D. Ceresoli, M. Cococcioni, N. Colonna, I. Carnimeo, A. Dal Corso, S. de Gironcoli, P. Delugas, R.A. DiStasio Jr., A. Ferretti, A. Floris, G. Fratesi, G. Fugallo, R. Gebauer, U. Gerstmann, F. Giustino, T. Gorni, J. Jia, M. Kawamura, H-Y. Ko, A. Kokalj, E. Küçükbenli, M. Lazzeri, M. Marsili, N.

Marzari, F. Mauri, N.L. Nguyen, A. Otero-de-la-Roza, L. Paulatto, S. Poncé, D. Rocca, R. Sabatini, B. Santra, M. Schlipf, A.P. Seitsonen, A. Smogunov, I. Timrov, T. Thonhauser, P. Umari, N. Vast, X. Wu, S. Baroni, J. Phys.: Condens. Matter 29 (2017) 465901, *Advanced capabilities for materials modelling with Quantum ESPRESSO.* Journal of Physics: Condensed Matter, 29 (2017), 465901.

[123] R. F. W. Bader, *Atom in Molecules: A Quantum Theory,* publisher Oxford University Press (1994).

[124] J. P. Perdew, K. Burke, and M. Ernzerhof, *Generalized Gradient Approximation Made Simple.* Physical Review Letters, 77 (1996) 3865–3868.

[125] L. C. Hsu and P. E. Galli, *Origin of the scheelite-powellite series of minerals.* Economic Geology, 68 (1973) 681–696.

[126] X. Han, Q. Kuang, M. Jin, Z. Xie, and L. Zheng, *Synthesis of Titania Nanosheets with a High Percentage of Exposed (001) Facets and Related Photocatalytic Properties.* Journal of the American Chemical Society, 131 (2009) 3152–3153.

[127] N. Feng, H. Lin, H. Song, L. Yang, D. Tang, F. Deng, and J. Ye, *Efficient and selective photocatalytic CH_4 conversion to CH_3OH with O_2 by controlling overoxidation on TiO_2.* Nature Communications, 12 (2021) 4652.

[128] L. Ye, J. Mao, T. Peng, L. Zan, and Y. Zhang, *Opposite photocatalytic activity orders of low-index facets of anatase TiO_2 for liquid phase dye degradation and gaseous phase CO_2 photoreduction.* Physical Chemistry Chemical Physics, 16 (2014) 15675–15680.

[129] M. Kowalkińska, S. Dudziak, J. Karczewski, J. Ryl, G. Trykowski, and A. Zielińska-Jurek, *Facet effect of TiO_2 nanostructures from $TiOF_2$ and their photocatalytic activity*. Chemical Engineering Journal, 404 (2021) 126493.

[130] S. Dudziak, M. Kowalkińska, J. Karczewski, M. Pisarek, K. Siuzdak, A. Kubiak, K. Siwińska-Ciesielczyk, and A. Zielińska-Jurek, *Solvothermal growth of {0 0 1} exposed anatase nanosheets and their ability to mineralize organic pollutants. The effect of alcohol type and content on the nucleation and growth of TiO_2 nanostructures.* Applied Surface Science, 563 (2021) 150360.

[131] H. Shi, Y. Li, X. Wang, H. Yu, and J. Yu, *Selective modification of ultra-thin g-C_3N_4 nanosheets on the (110) facet of Au/$BiVO_4$ for boosting photocatalytic H_2O_2 production.* Applied Catalysis B: Environmental, 297 (2021) 120414.

[132] M. Kowalkińska, A. Maximenko, A. Szkudlarek, K. Sikora, and A. Zielińska-Jurek, *Addressing challenges of $BiVO_4$ light-harvesting ability through vanadium precursor engineering and sub-nanoclusters deposition for peroxymonosulfate-assisted photocatalytic pharmaceuticals removal.* Separation and Purification Technology, 351 (2024) 127643.

[133] G. R. Buettner, *Spin Trapping - Electron-Spin-Resonance Parameters of Spin Adducts.* Free Radical Biology & Medicine, 3 (1987) 259–303.

[134] N. J. F. Dodd and A. N. Jha, *Photoexcitation of aqueous suspensions of titanium dioxide nanoparticles: An electron spin resonance spin trapping study of potentially oxidative reactions.* Photochemistry and Photobiology, 87 (2011) 632–640.

[135] S. Zhang, M. Rohloff, O. Kasian, A. M. Mingers, K. J. J. Mayrhofer, A. Fischer, C. Scheu, and S. Cherevko, *Dissolution of $BiVO_4$ Photoanodes Revealed by Time-Resolved Measurements under Photoelectrochemical Conditions.* Journal of Physical Chemistry C, 123 (2019), 23410–23418.

[136] H. Wen, Z. Pan, X. Wang, K. Li, Q. Wang, J. Luo, H. Fu, L. Zhang, and Z. Wang, *Dissolution behaviors of a visible-light-responsive photocatalyst $BiVO_4$: Measurements and chemical equilibrium modeling.* Journal of Hazardous Materials, 443 (2023) 130187.

[137] D. Lee, W. Wang, C. Zhou, X. Tong, M. Liu, G. Galli, and K. S. Choi, *The impact of surface composition on the interfacial energetics and photoelectrochemical properties of $BiVO_4$.* Nature Energy, 6 (2021) 287–294.

[138] G. Malmros, *The Crystal Structure of α-Bi_2O_3.* Acta Chemica Scandinavica, 24 (1970) 384–396.

[139] F. D. Hardcastle and I. E. Wachs, *The molecular structure of bismuth oxide by Raman spectroscopy.* Journal of Solid State Chemistry, 97 (1992) 319–331.

CO-AUTHORS' STATEMENTS OF CONTRIBUTION

Professor Anna Zielińska-Jurek, PhD. DSc. Eng.
Department of Process Engineering and Chemical Technology,
Faculty of Chemistry,
Gdańsk University of Technology,
Gabriela Narutowicza 11/12,
80-233, Gdańsk, Poland

Gdańsk, 30.10.2025

Statement of Contribution

I have contributed to the publications which constitute a part of dissertation of Marta Kowalkińska in the following way:

- M. Kowalkińska, P. Głuchowski, T. Swebocki, T. Ossowski, A. Ostrowski, W. Bednarski, J. Karczewski, A. Zielińska-Jurek, *Scheelite-Type Wide-Bandgap ABO_4 Compounds (A = Ca, Sr, and Ba; B = Mo and W) as Potential Photocatalysts for Water Treatment*, Journal of Physical Chemistry C 125(46) (2021), 25497-25513,
- M. Kowalkińska, K. Sikora, M. Łapiński, J. Karczewski, A. Zielińska-Jurek, *Non-toxic fluorine-doped TiO_2 nanocrystals from $TiOF_2$ for facet-dependent naproxen degradation*, Catalysis Today 413 (2023), 113959,
- M. Kowalkińska, J. Karczewski, A. Zielińska-Jurek, *The Effect of Titanium Oxyfluoride Morphology on Photocatalytic Activity of Fluorine-Doped Titanium (IV) Oxide*, Crystals 13(2) (2023), 356.
- M. Kowalkińska, N. Keller, F. Fresno, C. Colbeau-Justin, A. Zielińska-Jurek, *Insight into charge carrier dynamics and interface design of {0 0 1} TiO_2 coupled with $TiOF_2$ for photocatalytic degradation of contaminants of emerging concern*, Applied Surface Science 695 (2025) 162893.
- M. Kowalkińska, A. Maximenko, A. Szkudlarek, K. Sikora, A. Zielińska-Jurek, *Addressing challenges of $BiVO_4$ light-harvesting ability through vanadium precursor engineering and sub-nanoclusters deposition for peroxymonosulfate-assisted photocatalytic pharmaceuticals removal*, Separation and Purification Technology 351 (2024) 127643.

In the above publications I have supervised the experimental works, helped to shape the concept of the studies and discussed the results. I contributed to the draft and revised versions of the manuscripts.

- S. Dudziak, M. Kowalkińska, A. Zielińska-Jurek, „*Crystal Facet Engineering of TiO_2 from Theory to Application*", from the book "*Updates on Titanium Dioxide*", IntechOpen, 2023,

In the above publication I initiated the research topic and contributed to the draft and revised versions of the book chapter.

Professor Anna Zielińska-Jurek, PhD. DSc. Eng.

Assoc. Prof. Paweł Głuchowski, PhD. DSc.
Division of Optical Spectroscopy,
Institute of Low Temperature and Structural Research,
Polish Academy of Sciences,
50-422, Wrocław, Poland

Wrocław, 16.10.2025

Statement of Contribution

I have contributed to the publication which constitutes a part of PhD dissertation of Marta Kowalkińska in the following way:

M. Kowalkińska, P. Głuchowski, T. Swebocki, T. Ossowski, A. Ostrowski, W. Bednarski, J. Karczewski, A. Zielińska-Jurek, *Scheelite-Type Wide-Bandgap ABO_4 Compounds (A = Ca, Sr, and Ba; B = Mo and W) as Potential Photocatalysts for Water Treatment*, Journal of Physical Chemistry C 125(46) (2021), 25497-25513.

In the above publication I have performed photoluminescence and time-resolved photoluminescence spectra analysis and helped in description of optical properties of the photocatalysts.

Assoc. Prof. Paweł Głuchowski, PhD. DSc.

Tomasz Swebocki, PhD
Institute of Nanotechnology and Materials Science,
Faculty of Physics and Applied Mathematics,
Gdańsk University of Technology,
Gabriela Narutowicza 11/12,
80-233, Gdańsk, Poland

Gdańsk, 13.10.2025

Statement of Contribution

I have contributed to the publication which constitutes a part of PhD dissertation of Marta Kowalkińska in the following way:

M. Kowalkińska, P. Głuchowski, T. Swebocki, T. Ossowski, A. Ostrowski, W. Bednarski, J. Karczewski, A. Zielińska-Jurek, *Scheelite-Type Wide-Bandgap ABO_4 Compounds (A = Ca, Sr, and Ba; B = Mo and W) as Potential Photocatalysts for Water Treatment*, Journal of Physical Chemistry C 125(46) (2021), 25497-25513.

In the above publication I have performed electrochemical studies (cyclic voltammetry, electrochemical impedance spectroscopy, Mott-Schottky analysis), including electrode preparation, and described the results.

Tomasz Swebocki, PhD

Professor Tadeusz Ossowski, PhD. DSc. Eng.
Department of Analytical Chemistry,
Faculty of Chemistry,
University of Gdańsk,
Gdańsk 80-308, Poland

Gdańsk, 16.10.2025

Statement of Contribution

I have contributed to the publication which constitutes a part of PhD dissertation of Marta Kowalkińska in the following way:

M. Kowalkińska, P. Głuchowski, T. Swebocki, T. Ossowski, A. Ostrowski, W. Bednarski, J. Karczewski, A. Zielińska-Jurek, *Scheelite-Type Wide-Bandgap ABO_4 Compounds (A = Ca, Sr, and Ba; B = Mo and W) as Potential Photocatalysts for Water Treatment*, Journal of Physical Chemistry C 125(46) (2021), 25497-25513.

In the above publication I supervised the performed electrochemical studies (cyclic voltammetry, electrochemical impedance spectroscopy, Mott-Schottky analysis), and revised the manuscript draft.

Professor Tadeusz Ossowski, PhD. DSc. Eng.

Adam Ostrowski, PhD. Eng.
Department of Auxetics, Functional Materials
and Computer Simulations,
Institute of Molecular Physics,
Polish Academy of Sciences,
Smoluchowskiego 17
60-179 Poznań, Poland

Poznań, 16.10.2025

Statement of Contribution

I have contributed to the publication which constitutes a part of PhD dissertation of Marta Kowalkińska in the following way:

M. Kowalkińska, P. Głuchowski, T. Swebocki, T. Ossowski, A. Ostrowski, W. Bednarski, J. Karczewski, A. Zielińska-Jurek, *Scheelite-Type Wide-Bandgap ABO_4 Compounds (A = Ca, Sr, and Ba; B = Mo and W) as Potential Photocatalysts for Water Treatment*, Journal of Physical Chemistry C 125(46) (2021), 25497-25513.

In the above publication I have performed and described electron paramagnetic resonance (EPR) spectroscopy studies, helped in analysis of reactive oxygen species (ROS) generation and revised the manuscript draft.

Adam Ostrowski

Adam Ostrowski, PhD. Eng.

Assoc. Prof. Waldemar Bednarski, PhD
Department of Auxetics, Functional Materials
and Computer Simulations,
Institute of Molecular Physics,
Polish Academy of Sciences,
Smoluchowskiego 17
60-179 Poznań, Poland

Poznań, 16.10.2025

Statement of Contribution

I have contributed to the publication which constitutes a part of PhD dissertation of Marta Kowalkińska in the following way:

M. Kowalkińska, P. Głuchowski, T. Swebocki, T. Ossowski, A. Ostrowski, W. Bednarski, J. Karczewski, A. Zielińska-Jurek, *Scheelite-Type Wide-Bandgap ABO_4 Compounds (A = Ca, Sr, and Ba; B = Mo and W) as Potential Photocatalysts for Water Treatment*, Journal of Physical Chemistry C 125(46) (2021), 25497-25513.

In the above publication I supervised the performed electron paramagnetic resonance (EPR) spectroscopy studies and revised the manuscript draft.

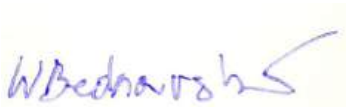

Assoc. Prof. Waldemar Bednarski, PhD

Assoc. Prof. Jakub Karczewski, PhD. DSc. Eng.
Institute of Nanotechnology and Materials Science,
Faculty of Physics and Applied Mathematics,
Gdańsk University of Technology,
Gabriela Narutowicza 11/12,
80-233, Gdańsk, Poland

Gdańsk, 31.07.2025

Statement of Contribution

I have contributed to the publications which constitute a part of PhD dissertation of Marta Kowalkińska in the following way:

- M. Kowalkińska, P. Głuchowski, T. Swebocki, T. Ossowski, A. Ostrowski, W. Bednarski, J. Karczewski, A. Zielińska-Jurek, *Scheelite-Type Wide-Bandgap ABO_4 Compounds (A = Ca, Sr, and Ba; B = Mo and W) as Potential Photocatalysts for Water Treatment*, Journal of Physical Chemistry C 125(46) (2021), 25497-25513,
- M. Kowalkińska, K. Sikora, M. Łapiński, J. Karczewski, A. Zielińska-Jurek, *Non-toxic fluorine-doped TiO_2 nanocrystals from $TiOF_2$ for facet-dependent naproxen degradation*, Catalysis Today 413 (2023), 113959,
- M. Kowalkińska, J. Karczewski, A. Zielińska-Jurek, *The Effect of Titanium Oxyfluoride Morphology on Photocatalytic Activity of Fluorine-Doped Titanium (IV) Oxide*, Crystals 13(2) (2023), 356.

In the above studies I have performed scanning electron microscope studies, including sample preparation, and energy-dispersive X-ray spectroscopy analyses.

Assoc Prof. Jakub Karczewski, PhD. DSc. Eng.

Assoc. Prof. Karol Sikora, PhD. DSc.
Department of Inorganic Chemistry,
Faculty of Pharmacy,
Medical University of Gdańsk,
M. Skłodowskiej-Curie 3a Street,
80-210 Gdańsk, Poland

Gdańsk, 27.10.2025

Statement of Contribution

I have contributed to the publications which constitute a part of PhD dissertation of Marta Kowalkińska in the following way:

- M. Kowalkińska, K. Sikora, M. Łapiński, J. Karczewski, A. Zielińska-Jurek, *Non-toxic fluorine-doped TiO_2 nanocrystals from $TiOF_2$ for facet-dependent naproxen degradation,* Catalysis Today 413 (2023) 113959,
- M. Kowalkińska, A. Maximenko, A. Szkudlarek, K. Sikora, A. Zielińska-Jurek, *Addressing challenges of $BiVO_4$ light-harvesting ability through vanadium precursor engineering and sub-nanoclusters deposition for peroxymonosulfate-assisted photocatalytic pharmaceuticals removal,* Separation and Purification Technology 351 (2024) 127643.

In the above studies I was responsible for identification of by-products after photocatalytic and peroxymonosulfate-assisted photocatalytic degradation of pharmaceuticals using liquid chromatography combined with mass spectrometry (LC-MS).

Assoc. Prof. Karol Sikora, PhD. DSc.
Katedra i Zakład Chemii Nieorganicznej
Gdański Uniwersytet Medyczny
dr hab. Karol Sikora

ADIUNKT

Assoc. Prof. Marcin Łapiński, PhD. DSc. Eng.
Institute of Nanotechnology and Materials Science,
Faculty of Physics and Applied Mathematics,
Gdańsk University of Technology,
Gabriela Narutowicza 11/12,
80-233, Gdańsk, Poland

Gdańsk, 13.10.2025

Statement of Contribution

I have contributed to the publication which constitutes a part of PhD dissertation of Marta Kowalkińska in the following way:

M. Kowalkińska, K. Sikora, M. Łapiński, J. Karczewski, A. Zielińska-Jurek, *Non-toxic fluorine-doped TiO_2 nanocrystals from $TiOF_2$ for facet-dependent naproxen degradation,* Catalysis Today 413 (2023) 113959.

In the above publication I have performed X-ray photoelectron spectroscopy measurements, deconvoluted the signals and helped interpret chemical nature of the observed states.

Zastępca Dyrektora
ds. infrastruktury badawczej
dr hab. inż. Marcin Łapiński, prof. PG
INSTYTUT NANOTECHNOLOGII
I INŻYNIERII MATERIAŁOWEJ

Assoc. Prof. Marcin Łapiński, PhD. DSc. Eng.

Nicolas Keller, PhD
Institut de Chimie et Procédés pour l'Energie,
l'Environnement et la Santé (ICPEES)
CNRS/University of Strasbourg,
25 rue Becquerel,
67087 Strasbourg, France

Strasbourg, 02.10.2025

Statement of Contribution

I have contributed to the publication which constitutes a part of PhD dissertation of Marta Kowalkińska in the following way:

M. Kowalkińska, N. Keller, F. Fresno, C. Colbeau-Justin, A. Zielińska-Jurek, *Insight into charge carrier dynamics and interface design of {0 0 1} TiO_2 coupled with $TiOF_2$ for photocatalytic degradation of contaminants of emerging concern*, Applied Surface Science 695 (2025) 162893.

In the above study I have supervised the experiments, helped to analyse and describe measurements performed at the University of Strasbourg and revised the final version of the manuscript.

ICPEES
Institut de Chimie et Procédés pour l'Energie,
l'Environnement et la Santé
UMR 7515 CNRS - UNIV. Strasbourg / ECPM
25 rue Becquerel
67087 STRASBOURG Cedex / FRANCE

Nicolas Keller, PhD

Fernando Fresno, PhD
Instituto de Catálisis y Petroleoquímica
Consejo Superior de Investigaciones Científicas
Marie Curie 2
28049 Madrid, Spain

Madrid, 06.10.2025

Statement of Contribution

I have contributed to the publication which constitutes a part of PhD dissertation of Marta Kowalkińska in the following way:

M. Kowalkińska, N. Keller, F. Fresno, C. Colbeau-Justin, A. Zielińska-Jurek, *Insight into charge carrier dynamics and interface design of {0 0 1} TiO_2 coupled with $TiOF_2$ for photocatalytic degradation of contaminants of emerging concern*, Applied Surface Science 695 (2025) 162893.

In the above study I have performed and described time-resolved fluorescence measurements, and revised the final version of the manuscript.

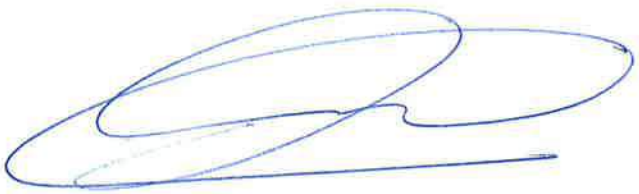

Fernando Fresno, PhD

Christophe COLBEAU-JUSTIN
Professeur des Universités
Institut de Chimie-Physique – CNRS UMR 8000
Université Paris-Saclay
Tel : (33 1) 69-15-66-95
e-mail : christophe.colbeau-justin@universite-paris-saclay.fr

Orsay, 17th of October 2025

STATEMENT OF CONTRIBUTION

I have contributed to the publication which constitutes a part of PhD dissertation of Marta Kowalkińska in the following way:

M. Kowalkińska, N. Keller, F. Fresno, C. Colbeau-Justin, A. Zielińska-Jurek, *Insight into charge carrier dynamics and interface design of {0 0 1} TiO_2 coupled with $TiOF_2$ for photocatalytic degradation of contaminants of emerging concern*, Applied Surface Science 695 (2025) 162893.

In the above study I have performed and described time-resolved microwave conductivity (TRMC) measurements.

Pr. Christophe COLBEAU-JUSTIN

Alexey Maximenko, PhD
SOLARIS National Synchrotron Radiation Centre,
Jagiellonian University,
Czerwone Maki 98 Street,
30-392 Kraków, Poland

Kraków, 22.09.2025

Statement of Contribution

I have contributed to the publication which constitute a part of PhD dissertation of Marta Kowalkińska in the following way:

M. Kowalkińska, A. Maximenko, A. Szkudlarek, K. Sikora, A. Zielińska-Jurek, *Addressing challenges of $BiVO_4$ light-harvesting ability through vanadium precursor engineering and sub-nanoclusters deposition for peroxymonosulfate-assisted photocatalytic pharmaceuticals removal*, Separation and Purification Technology 351 (2024) 127643.

In the above publication I have performed X-ray absorption spectroscopy (XAS) measurements, performed data processing and analysis, helped in interpretation of the results and reviewed the manuscript draft.

Alexey Maximenko

Alexey Maximenko, PhD

Aleksandra Szkudlarek, PhD. Eng.
AGH University of Krakow,
Academic Centre for Materials and Nanotechnology,
Adama Mickiewicza 30,
30-059 Kraków, Poland

Kraków, 13.10.2025

Statement of Contribution

I have contributed to the publication which constitutes a part of PhD dissertation of Marta Kowalkińska in the following way:

M. Kowalkińska, A. Maximenko, A. Szkudlarek, K. Sikora, A. Zielińska-Jurek, *Addressing challenges of $BiVO_4$ light-harvesting ability through vanadium precursor engineering and sub-nanoclusters deposition for peroxymonosulfate-assisted photocatalytic pharmaceuticals removal*, Separation and Purification Technology 351 (2024) 127643.

In the above publication I have performed transmission electron microscope studies, including sample preparation, and energy-dispersive X-ray spectroscopy analyses, and revised the manuscript draft.

A. Szkudlarek

Aleksandra Szkudlarek, PhD Eng.

Szymon Dudziak, PhD. Eng.
Department of Process Engineering and Chemical Technology,
Faculty of Chemistry,
Gdańsk University of Technology,
Gabriela Narutowicza 11/12,
80-233, Gdańsk, Poland

Gdańsk, 10.10.2025

Statement of Contribution

I have contributed to the publications which constitute a part of dissertation of Marta Kowalkińska in the following way:

S. Dudziak, M. Kowalkińska, A. Zielińska-Jurek, „*Crystal Facet Engineering of TiO_2 from Theory to Application*", from the book "*Updates on Titanium Dioxide*", IntechOpen, 2023,

In the above study I was co-responsible for chapter idea and its content. I was mainly responsible for describing the geometries and properties of TiO_2 crystal facets from computations; as well as co-responsible for the description of the existing preparation methods.

Szymon Dudziak, PhD. Eng.